Agenzia Nazionale per le Nuove Tecnologie,
l'Energia e lo Sviluppo Economico Sostenibile

Ministero dello Sviluppo Economico

RICERCA DI SISTEMA ELETTRICO

Monte Carlo results for selected ex-core radiation responses

K.W. Burn

Report RdS/2010/84

MONTE CARLO RESULTS FOR SELECTED EX-CORE RADIATION RESPONSES

K.W. Burn, ENEA

Settembre 2010

Report Ricerca di Sistema Elettrico
Accordo di Programma Ministero dello Sviluppo Economico – ENEA
Area: Produzione e fonti energetiche
Tema: Nuovo Nucleare da Fissione

Responsabile Tema: Stefano Monti, ENEA

ENEA	Ricerca Sistema Elettrico	Sigla di identificazione	Distrib.	Pag.	di
		NNFISS – LP2 – 016	L	1	316

Titolo ed Autori

IRIS: Monte Carlo Results for Selected Ex-Core Radiation Responses. Open Version

Kenneth W. Burn

Descrittori

Tipologia del documento: Rapporto Tecnico

Collocazione contrattuale: Accordo di Programma ENEA-MSE: tema di ricerca "Nuovo Nucleare da Fissione". Linea progettuale LP2 Reattori INTD

Argomenti trattati: Ingegneria nucleare, Fisica dei reattori nucleari, Neutronica, Schermaggio delle radiazioni, Metodi Montecarlo, PWR, Generazione 3+, IRIS

Sommario

Results for ex-core radiation responses in the IRIS reactor design obtained with the Monte Carlo method are presented at the preliminary design stage.
The responses include pressure vessel damage, dose during running outside the biological shield and in the seismic isolator zone, maintenance doses in the pressure vessel well and in the cavities inside the containment vessel above and below the main deck level, doses at EOL around an extracted steam generator and around the extracted reflector and barrel, EOL activity of the reflector and barrel and EOL activity of the pressure vessel liner, pressure vessel, concrete liner and concrete surrounding the pressure vessel well. Substitution of the concrete surrounding the pressure vessel well by carbon steel is considered (only in terms of EOL activity).

Note

This report is a public version of the restricted access report: ENEA NNFISS–LP2–007.

Copia n. **In carico a:**

REV.	DESCRIZIONE	DATA		REDAZIONE	CONVALIDA	APPROVAZIONE
2			NOME			
			FIRMA			
1			NOME			
			FIRMA			
0	EMISSIONE	27.08.2010	NOME	K. W. Burn	F. Padoani	S. Monti
			FIRMA			

INDEX

1. OBJECTIVE AND SCOPE

This work was carried out in the period November 2007 to October 2009. It used as starting point work done by the Politecnico di Milano in the period 2002-2003 (references cited in the text). It was coordinated by Westinghouse and Georgia Tech. (see acknowledgements) through frequent conference calls and workshops (the latter roughly every six months, sometimes within the IRIS team meetings, sometimes outside).

With the IRIS design as at roughly the beginning of 2008, the objectives were:

- to calculate the pressure vessel (PV) damage from all radiation types and to verify whether the bottom shield, present in the design at the end of 2007, could be removed.
- to calculate the dose during running in the control room.
- to calculate the activity at end-of-life (EOL) of the PV, concrete liner and concrete in the PV well.
- to calculate the dose around an extracted activated steam generator during a maintenance period.
- to calculate some doses during maintenance operations in the zones between the PV and the containment vessel.

Subsequently during the work the objectives were expanded to include estimations of:

- the dose during maintenance operations in the PV well.
- the dose during running in the zone under the reactor, housing the seismic isolators and the lifetime dose to the isolators themselves.
- the dose around the extracted reflector and barrel at EOL.

The radiation source was the fission rate in the reactor core. The fission neutrons contribute directly to some responses (neutron damage to the vessel, neutron dose during running), indirectly, via the production of prompt gamma rays, to others (gamma damage to the vessel, gamma dose during running) and also indirectly, through activation, activity and delayed gamma rays, to doses at various times after shut-down and after various lengths of operation.

Not included are other radiation sources such as spent fuel assemblies outside the core, waste tanks, deposits in pumps, deposits in pipes, deposits in filters, etc. As far as the latter are concerned, note that in general only fixed structure activation sources are considered, and not transported sources such as deposits, plating, etc.

Furthermore the presence of ^{16}N ($T_{1/2}$: 7.1 s) as a radiation source in the primary coolant was ignored. This was justifiable for the calculation of the doses during maintenance operations which were assumed to be never less than 24 h after shutdown. Instead for the calculation of the dose during running [around the seismic isolators (§11 and §16.6) and especially in the control room (§6 and §16.2)], **this may not be justified**. (For example the time for the primary water to get from the core to the upper part of the PV, at a similar level to accessible parts of the reactor building, is not very much longer than the half life of ^{16}N.)

Accident scenarios were not considered. Notwithstanding, some of the results, such as the source from gaseous and volatile fission products, might be employed for accident studies.

2. STRUCTURE

Chapter 3 cites the tools employed for the study: codes and data and mentions any modifications to standard codes that were made for this work. Also the in-house variance reduction vehicle is summarised.

Chapter 4 describes the basic calculational model: the fission source in the core with its spatial and energy distribution and the geometry and materials from the core out to the concrete of the PV well.

In chapter 5 the results for radiation damage to the pressure vessel are presented, both for the reference configuration (§5.1) and for a number of variations around this configuration (Fig. 18). For these results, a 60 year lifetime is assumed. It is shown that the bottom shield is redundant from the point of view of PV damage.

In chapter 6 the geometrical and material model is extended out to the control room. Dose results are generated for a 1 m thick biological shield. As the important radiation path from the core to the control room is through the lower part of the steam generators, new doses are generated with an improved modeling of this zone. Finally the thickness of the biological shield was increased from 1m to 1.5 m and dose results are presented for the new thickness.

In chapter 7 the maximum activities after two different irradiation times (60 and 100 years) and four different cooling times (7 days, 60 days, 2 years and 10 years) of the PV liner, PV, concrete liner and concrete in the PV well are calculated. The activities are calculated for the most important nuclides and compared with the clearance levels. The same results are generated with borated concrete. Average activities are also generated for the PV liner and PV (both separately and together).

In chapter 8 activation doses in the PV well are generated for 100 year irradiation time (10 years for the fuel assemblies) and 1 day cooling. The source in the active core (responsible for most of the dose) is checked with other codes and data. Variations on the reference are: 3 days cooling for the core and the plena, 4 times the reference cobalt content in the barrel and isolation of the cobalt contribution to the dose from the PV.

In chapter 9 an improved modeling of the steam generators and inclusion of their lower supports is presented.

Chapter 10 presents results for the dose during maintenance operations in the cavities between the PV and the containment vessel and outside the PV well. First the modeling of the various structures in these zones that are activated is introduced. The spatial division of these structures to score the neutron flux is discussed. The dose after 100 years irradiation (10 years for active core and plena) and 1 day cooling is presented at a variety of points throughout these cavities. An estimate is made of the dose from structure that has not been explicitly modeled (employing the “Gross Structure Constant”). Variations on the reference are: 3 days cooling for the core and the plena, 4 times the reference cobalt content in selected structures between the PV and the containment, isolation of the cobalt contribution to the dose from the PV and voiding the secondary circuit and removing the end flange of the inlet nozzle.

In chapter 11 the dose results in the zone under the reactor, housing the seismic isolators are presented.

In chapter 12 the doses around an extracted steam generator are presented, under the conditions of 100 year irradiation and 1 day cooling. A variation on the reference is 4 times the reference cobalt content in the lower support structure and bottom header.

In chapter 13 the doses around the extracted reflector and barrel are presented, under the conditions of 100 year irradiation and 2 year cooling. The activity of the reflector and barrel are also given. Only for the dose results, a variation on the reference is 4 times the reference cobalt content in the reflector and barrel.

Chapter 14 deals with the substitution of the concrete in the PV well by carbon steel and considers the activity of this steel at EOL [100 years operation and four different cooling times (7 days, 60 days, 2 years and 10 years)].

In chapter 15 some quality control considerations are made concerning the internal consistency of the Monte Carlo calculations.

Chapter 16 gives summary results and concluding remarks. (Note that here the results for radiation damage to the pressure vessel assume a 100 year lifetime.)

3. CALCULATIONAL TOOLS

3.1 Codes

For the neutron and gamma ray (prompt or activation gamma's) transport, MCNP5 [1] (RSICC-NEA distribution) was employed for the calculations with all 89 core assemblies modeled in a homogeneous fashion (see §4.2.1). Instead MCNPX2.6.d [2] (β test version) was employed for the calculations with the 40 outer assemblies modeled pin-by-pin and the 49 inner assemblies modeled homogeneously. (Use of the two codes was called for because of computer memory problems with the MPI implementation of MCNP5 for the mixed pin-by-pin/homogeneous core model.)

For the activation and activity calculations and generation of the activation gamma ray source, FISPACT (2001 version) [3] was employed together with the option of the XMAS 172 energy group structure.

3.2 Nuclear Data and Physics

With both MCNP-based codes, the cross-sections available with MCNP5 were employed:

– neutron cross-sections: all from the "ACTIA" file (Appendix G in [1], [4] and [5]) (based on ENDF/B-VI Release 8) with the exception of: ^{2}H, ^{10}B, ^{11}B, C_{nat}, ^{17}O, ^{31}P, Zr_{nat}, ^{93}Nb, Mo_{nat}, ^{235}U and ^{238}U which were from the ENDF66 file (Appendix G in [1], [6] and [7]) (based on ENDF/B-VI Release 6) and Sn_{nat} from the ENDL-92 file (Appendix G in [1], and [8]) (based on ENDL data).

– thermal neutron data libraries: hydrogen in light water from the SAB2002 file (based on ENDF/B-VI Release 3) (Appendix G in [1], and [9]). Note that, due to an oversight, older data from the TMCCS file (based on ENDF/B-III) (*ibid.*) were employed in the pressure vessel damage calculations.

– photon cross-sections: all from the "MCPLIB04" file (Appendix G in [1], [10] and [11]) (based on ENDF/B-VI Release 8).

FISPACT employs EAF2001 data [12] that originate from a number of sources (JEF-2.2, EFF-2.4, ENDF/B-VI, JENDL-3.2/A and IRDF-90.2).

Dpa cross-sections

Neutron dpa cross-sections for ^{50}Cr, ^{52}Cr, ^{53}Cr, ^{54}Cr, ^{55}Mn, ^{54}Fe, ^{56}Fe, ^{57}Fe, ^{58}Fe, ^{58}Ni and ^{60}Ni were used from the BISERM data library [13], obtained with the IOTA code [14]. Results were also verified independently, employing neutron dpa cross-sections for all the components of the pressure vessel (see §4.2.12) from a library based on JEFF-3.1 [15].

Photon dpa cross-sections were employed for Fe only (Table 3 in [16]).

Neutron and photon flux-to-dose response functions

For the dose tallies, neutron and photon flux-to-dose response functions were taken from [17]. (For neutrons, the maximum dose equivalent along the diameter of the ICRU sphere was used. For photons, up to and including 3 MeV, the H*(10) (ambient dose equivalent) values were used; above 3 MeV the maximum dose equivalent along the diameter of the ICRU sphere was used.) The same flux-to-dose response functions were employed both for the normal tallies and for the mesh tallies.

Temperature of neutron data

All neutron cross-sections employed, including those in the core, were doppler broadened to 20°C. (This should be slightly conservative.) Then the elastic scattering cross-section in the thermal range was adjusted to 300°C with the free gas thermal treatment model for all cross-sections of materials within the pressure vessel including the vessel itself. (Also with the same model the velocity of the target nucleus was adjusted to 300°C.) Instead for all cross-sections of materials outside the pressure vessel, a temperature of 20°C was employed for the thermal treatment with the free gas model.

At energies less than 4 eV, the S(α,β) data employed for hydrogen attached to the water molecule were at two different temperatures: 300°K and 600°K (600°K everywhere within the vessel, 300°K outside).

Physics options within MCNP/X

When data tables were available, the probability table treatment in the unresolved resonance energy range was employed.

For photons, the options chosen were “detailed physics” with coherent scattering and production of bremsstrahlung photons with the thick target bremsstrahlung model, but with no Doppler energy broadening. For the damage calculations, because of the threshold energy for γ dpa, an energy cut-off of 700 keV was employed. In this case these options are surely not necessary and the “simple physics” could have been used.

3.3 Variance reduction

The method employed was the DSA (Direct Statistical Approach) (see for example [18]). The DSA currently runs with MCNPX2.1.5 [19]. Therefore small changes needed to be made to the inputs for MCNP5 to be compatible with the older MCNPX2.1.5. (The inputs for MCNPX2.6.d, employed for the calculations with the 40 outer assemblies modeled pin-by-pin, were run with the DSA. Instead variance reduction parameters generated with the DSA for the case of all-smeared assemblies were converted to the appropriate format in the inputs that contained the pin-by-pin description in the outer assemblies.)

Because of the very different variance reduction parameters required for neutrons compared with gamma rays, usually separate runs were made for the neutron responses and for the gamma responses. In the n-γ runs (with no source biasing), the standard DSA cell-importance mode was employed. Instead in the neutron-only runs (with an aggressive source biasing – see §4.1.1) the DSA weight-line mode was employed [20]. In both cases the resulting optimized variance

reduction parameters were converted to a weight window so as to be used in the standard versions MCNP5 and MCNPX2.6.d. [It is worthwhile noting that the parameter in MCNP/MCNPX that controls the maximum amount of splitting / Russian roulette (MXSPLN) is given much higher values, typically 100 or greater, than its default value of 5.] Strong source biasing was also employed in the gamma-only runs (i.e. activation gamma's). Therefore the DSA weight-line mode was also employed in these calculations.

In all DSA calculations, the multi-response capability [18] was employed. For the calculation of the pressure vessel responses (fluxes, dpa'a and activation rates) the neutron flux in 4 energy groups (> 7 MeV, 1 – 7 MeV, 100 keV – 1 MeV and < 1 eV) in various spatial segments was employed with typically a total of 12 responses of interest. (The range 1 eV – 100 keV is then automatically covered through the neutron transport mechanism.) For the activation rates in the geometry outside the PV, the neutron flux in 3 energy groups (> 1 keV, 1 eV – 1 keV and < 1 eV) in various spatial segments was employed. For the gamma damage calculations to the PV, the gamma flux in 4 energy groups (> 6 MeV, 3 – 6 MeV, 1 MeV – 3 MeV and < 1 MeV) in various spatial segments was employed with again typically 12 responses of interest. (Although with the data used [16], the gamma dpa threshold is 1 MeV and the effective lowest energy is roughly 4 MeV.) For the dose calculations (neutron and prompt gamma's and activation gamma's) the dose rate was directly employed as response-of-interest, albeit at a number of different spatial points (usually surface or volume segments).

The above energy division concerns the fluxes to be used as scoring the responses-of-interest. In the transport process, the variance reduction parameters were defined for neutrons in typically 10 energy groups (> 11.5 MeV, 8 - 11.5 MeV, 5.5 – 8 MeV, 2 – 5.5 MeV, 500 keV – 2 MeV, 100 – 500 keV, 10 – 100 keV, 100 eV – 10 keV, 1 – 100 eV and < 1 eV) and for gamma's in typically 6 energy groups (> 5 MeV, 3 - 5 MeV, 1.5 – 3 MeV, 700 keV – 1.5 MeV, 200 – 700 keV, < 200 keV). The spatial grouping of the MCNP cells (of which there were typically around 2500) was into around 50 "macrocells" for the earlier limited geometries (up to the PV well) and around 80 macrocells for the later geometries that included the control room and the various structures between the PV and the containment.

The optimum variance reduction parameters (cell importances or weight lines) were then generated in a matrix of 50×10 or 80×10 phase space cells for the neutron runs and a matrix of 50×6 or 80×6 phase space cells for the gamma runs. For the n-γ runs, two matrices were employed for the neutrons and for the gamma's. The optimisation was then carried out in the presence of up to 12 responses-of-interest.

If possible, the optimised variance reduction parameters already generated for a previous set of responses were employed in a new calculation. Usually this was not possible. (It would actually have been possible in more cases if the standard DSA cell-importance mode had been more often employed rather than the weight-line mode.) Therefore the optimization procedure usually had to be rerun (for a total of 10 – 20 times).

4. BASIC CALCULATIONAL MODEL OUT TO THE PRESSURE VESSEL WELL

4.1 Source description

The fission source provided by WEC for running at 1000 MW (th) assumed 1/4 core azimuthal symmetry [21], [22]. There were two distinct spatial descriptions: pin-by-pin or smeared over each pin assembly. Both descriptions included the same axial variation: 37 axial bins distributed non-uniformly (with a finer binning at the top and bottom of the core). For each spatial bin (axial bin and assembly for the smeared case or axial bin and pin for the pin-by-pin case), the probability of the fissioning isotope was given for four isotopes: ^{235}U, ^{238}U, ^{239}Pu and ^{241}Pu.

Two representative sources have been generated for each spatial description: an average source and a maximum source, the latter to be used for (high) instantaneous dose calculations during operation [23]. In all results presented here, the average source was employed. MCNP inputs have also been generated for the maximum source (both with the smeared assembly description and with the pin-by-pin description in the outer assemblies) but have not been used.

As a first model it was decided to choose a single isotope and therefore separate the space and energy variables. For the reference calculation ^{235}U was chosen. Fig.1 shows the fission spectra of ^{238}U, ^{239}Pu and ^{241}Pu normalized to that of ^{235}U (see §4.1.1). Probably a more conservative and realistic spectrum for the reference calculation would have been to use ^{239}Pu and not ^{235}U. The choice of ^{235}U is considered in §5.1.1 (and in §7.4) where spectral safety factors are defined. In §5.3 a comparison is made with results generated from a ^{241}Pu fission source spectrum.

4.1.1 Source energy description

MCNP/X allows a continuous energy analytic description of the fission spectrum. For the fissionable nuclides of interest here, the Watt fission spectrum is used for ^{235}U, ^{238}U and ^{239}Pu and the Maxwell fission spectrum for ^{241}Pu, each spectrum with the recommended parameters for the particular nuclide (Appendix H in [1]).

It was desired to flag different parts of the source energy spectrum to see their differential contributions to selected results of interest. It was not possible to effect this with the continuous, analytic, source fission spectrum. Therefore a group-wise source fission spectrum was generated from the analytic one in 200 energy bins. It is thought that this introduced negligible error with respect to the analytic spectrum. Whilst the 200 bins were employed for the sampling of the source energy, they were grouped into 20 macro energy bins for the source energy flagging.

The high energy tail of the fission spectrum provides the major contribution to ex-core neutron responses. This is particularly the case in IRIS where the pressure vessel is much farther from the core compared to conventional designs. Therefore a strong source biasing was applied (in the 20 macro energy bins which represented the first level of sampling). This source biasing was only applied for the neutron-only runs. In the n-γ runs (with all the responses gamma) no source energy biasing was applied because the gamma's are mainly born in the reactor internals (principally the reflector and barrel) and, as progenitors, have neutrons from the higher probability part of the fission spectrum.

4.1.2 Source spatial description

The spatial source description was made compatible with the core geometry description (see §4.2.1). This resulted in two models:

- the source smeared over each of the 89 assemblies
- the source smeared over each of the 49 inner assemblies whilst maintaining a pin-by-pin description for the outer ring of 40 assemblies.

In both models the WEC axial description was preserved with the 37 axial bins [24].

To try to maintain a minimum of quality control, it was decided not to employ a "SOURCE" subroutine but to use the capabilities of the "SDEF" logic within MCNP/X. This proved possible with the 89 assembly-smeared source model but not with the model involving a mixture of smeared inner assemblies and pin-by-pin outer assemblies. For this model, it was necessary to modify MCNPX2.6.d (employed as discussed in §3.1 instead of MCNP5 for the mixed model). Such modification annulled to a great extent the reason for not employing a "SOURCE" subroutine.

For both spatial source models it was necessary to convert the WEC source format to that requested by the chosen "SDEF" logic (requiring also an expansion from 1/4 core to full core with the 89 assembly-smeared source model). For this purpose ad-hoc fortran programs were written. Although tested with various sources, including an artificially skewed source [25], these represent a diminution of quality control. Furthermore some manual data manipulation is still required to transfer sections of the outputs of these fortran programs to the appropriate array in "SDEF", implying a further reduction of quality control.

4.2 Geometrical and material description

4.2.1 Core: active zone

Radial description

Reference calculation: Standard Westinghouse 17x17 fuel (the fuel data is given in [26] and [27]). A variation was to employ an assembly referred to as the "Enhanced Moderation lattice", which features the same fuel dimensions (clad and pellet) as the Standard Westinghouse fuel, but with a slightly larger pitch between the rods. The enhanced moderation improves neutron thermalization, and thereby increases fuel utilization under typical LWR fuel management schemes. An MCNP model of the Standard fuel assembly design (one of the outer assemblies) is shown in Fig. 2.

For the case of smeared assemblies, the same composition was adopted (radially) for all the assemblies. That is, 1/2 the assembly-assembly gap was included on all four sides of each assembly, in the composition of the assembly. The same was done for the 28 assemblies that have 1 or 2 faces that correspond to the outer surface of the core.

For the core with the Enhanced Moderation fuel assemblies, the reflector dimensions are given in [28]. Water gaps between the core and the reflector are calculated accordingly (going from the smallest core/reflector dimension to the largest):

– *smeared outer assemblies*: cm. 0.744, 0.735, 0.731, 0.727;

– *pin-by-pin outer assemblies*: cm. 0.973, 0.964, 0.960, 0.956 (from the outer surface of the cladding of the outer pin to the inner surface of the reflector).

The inner reflector dimensions were not defined for the Standard Westinghouse 17x17 fuel assembly. These were taken instead from [27] and produced the following core-reflector gaps (going from the smallest core/reflector dimension to the largest):

– *smeared outer assemblies*: cm. 0.746, 0.738, 0.733, 0.729;

– *pin-by-pin outer assemblies*: cm. 0.944, 0.935, 0.931, 0.926 (from the outer surface of the cladding of the outer pin to the inner surface of the reflector).

Fig. 3 shows a section of the MCNP model at the core centre for the case with the Standard Westinghouse 17x17 fuel and all assembly compositions smeared. (Note the change of colour of the materials in this and all following figures compared with Fig. 2.) Fig. 4 shows the same section for the core with the Enhanced Moderation fuel assemblies. Fig. 5 shows a quarter core section at the core centre for the case of the core with the Standard Westinghouse 17x17 fuel, inner assemblies smeared and outer assemblies modeled pin-by-pin.

Axial description

For both the Standard Westinghouse 17x17 fuel and the Enhanced Moderation fuel assembly, the active length of the core is taken from [21]. This is the length at the operating temperature. The corresponding variation of water density along the axial length of the core is given in [29]. Linear interpolation was employed to generate average water densities in 10 axial segments from the bottom to the top of the core [30], the first and last segments corresponding to the two end blankets. Fig. 6 shows an axial section of the MCNP model of the Standard fuel assemblies core with all the assemblies smeared.

Compositions

The fuel density for both the full-enriched and low-enriched (blanket) parts was taken as 10.412 g cm^{-3} (from the UO_2 theoretical density reduced by a density factor). The full-enriched part was taken as 4.95% (by wt) enrichment in ^{235}U and the blankets as 2.10%. Simple chemical stoichiometry was assumed.

Zircaloy-4 composition and density (6.553 g cm^{-3}) was taken from [31].

With these geometrical and material data, smeared compositions were generated in each of the 10 axial segments for the Standard Westinghouse fuel assemblies [32] and the Enhanced Moderation fuel assemblies [33]. Note that grids and sleeves, accounting for < 0.01 Zircaloy-4 volume fraction [34], have been neglected.

4.2.2 Core: regions between the core plates and the active zone

The only data available for the regions between the lower plate and the active zone and between the active zone and the upper plate (plena, end plug, nozzle, grid, springs, etc.) has been homogenized into 8 axial regions above the active zone and 7 axial regions below the active zone [35]. These data were used both for the Standard Westinghouse fuel assemblies (with both the pin-by-pin and the smeared description of the active zone) and for the Enhanced Moderation fuel assemblies. From these data, MCNP-compatible data were generated [36], employing the same

composition for steel as that used previously by PoliMi - AISI-304L [37] (7.85 g cm^{-3}) and for inconel from [38] [8.1 g cm^{-3}, % (assumed by weight) Ni 61, Cr 22.5, Fe 15.1, Al 1.4].

The hypothesis of homogeneous compositions in these regions is likely not conservative which is an important issue for the radiation impinging on the lower part of the PV. However:

– it was thought that this should not be too large an effect

– the results will show that the a much higher neutron flux impinges on the vessel due to radial rather than axial leakage from the lower part of the core.

Thus this non-conservative modeling is probably acceptable.

Fig. 7 shows the MCNP model of the region between the active core and the top plate and Fig. 8 shows the region between the active core and the bottom plate. Both Fig. 7 and Fig. 8 are for the core with Standard 17x17 fuel.

4.2.3 Bottom core plate

The position of the bottom core plate with respect to the lower surface of the active zone is defined by [35]. The dimensions are taken from [39]. The water channel lattice in [39] has been modeled explicitly. The water density is taken as 0.74264 g cm^{-3} - the temperature at the bottom of the active region [29]. The steel is taken as AISI-304L steel from [37] (7.85 g cm^{-3}). There is assumed no structure within each water channel.

Fig. 9 shows a radial section of the MCNP model of the bottom core plate for the Standard fuel assemblies and Fig. 10 shows the same for the Enhanced Moderation fuel assemblies.

4.2.4 Top core plate

The position of the top core plate with respect to the upper surface of the active zone is defined by [35]. A drawing of the top plate was not available.

The thickness is apparently 76 mm [40]. {n.b. The quoted thickness of the bottom plate of the "Reactor Internals" is also 76 mm [41]. This plate is assumed by the author not to be the top plate of the core because the former rests on the thicker part of the reflector that follows the core's radial cartesian shape [28], [42]. Instead the lower surface of the core top plate in the developed model is approximately 23.5 cm below the top surface of the thicker part of the reflector (using [21], [28], [35] and from [42] that the lower surface of the reflector rests on the upper surface of the core bottom plate).}

The outer surfaces of the top plate are assumed to be identical to the inner surfaces of the reflector.

The structure is assumed the same as the bottom plate, AISI-304L steel [37] (7.85 g cm^{-3}).

The water channels in the top plate were taken conservatively as 1 water channel of diameter 6.47 inch per fuel assembly, in the same lattice structure as the fuel assemblies [43]. The water density is taken as 0.65027 g cm^{-3} - the temperature at the top of the active region [29]. There is assumed no assembly structure within each water channel.

Fig. 11 shows a radial section of the MCNP model of the top core plate for the Standard fuel assemblies and Fig. 12 shows the same for the Enhanced Moderation fuel assemblies.

4.2.5 Region above the top plate and within the reflector and the barrel

The "Reactor Internals" [41] have not been modeled, neither is any structure present between the core top plate and the bottom plate of the "Reactor Internals". All the region is filled with water at 0.65027 g cm^{-3} - the temperature at the top of the active region [29] (see for example Fig. 6).

4.2.6 Reflector

The reflector has been modeled faithfully as in [28] with a lower thicker part whose inner surface follows the core's radial cartesian shape and an upper thinner part whose inner surface is cylindrical. From [42] the lower surface of the reflector rests on the upper surface of the core bottom plate. The reflector material is AISI-304L steel [37] (7.85 g cm^{-3}).

The lower thicker part of the reflector (height 518.2 cm [28]) is modeled as a homogeneous mixture of 90% by vol. AISI-304L and 10% by vol. water (at 0.74264 g cm^{-3}) to simulate the many small water tubes for cooling [44] (using data from [26], Table 2.5).

As discussed in §4.2.1, the inner radial dimensions of the reflector are defined in [28] for the Enhanced Moderation core assemblies. For the core with Standard Westinghouse 17x17 fuel assemblies, the inner radial dimensions were chosen so as to approximately maintain the fuel assembly-reflector water gap and are given in §4.2.1. See Figs. 3-8 and 11-12.

4.2.7 Barrel

The barrel is modeled as a simple cylinder with a thicker annular "foot" as in [45]. The bottom surface of the annular foot corresponds to the lower surface of the bottom core plate whilst the top surface of the annular foot corresponds to the point at which the outer radius of the bottom core plate changes [39], [42]. See for example Fig. 6.

The barrel material is AISI-304L steel [37] (7.85 g cm^{-3}).

4.2.8 Radial interstitial water within barrel

The water channel between the core and the reflector of thickness 0.72-0.75 cm (for smeared outer core Standard assemblies) or thickness 0.92-0.95 cm (for pin-by-pin outer core Standard assemblies) is modeled explicitly with density 0.74264 g cm^{-3}. For the Enhanced Moderation assemblies, the channel is of thickness 0.72-0.75 cm (for smeared outer core assemblies) or thickness 0.95-0.98 cm (for pin-by-pin outer core assemblies).

The water channel between the reflector and the barrel of thickness 1.5 cm and with density 0.74264 g cm^{-3} is also modeled explicitly.

The water channel between the upper part of the bottom core plate and the inner surface of the barrel is 5 mm thick whilst that between the lower part of the bottom core plate and the inner surface of the barrel is 2.5 mm thick. Both channels have water of density 0.74264 g cm^{-3}.

4.2.9 Lower barrel annular support with its eight azimuthal supports

The data are given in [46]. The lower annular "foot" of the barrel fits into the annular support with coincident surfaces. The lower inner surface of the annular support is identical to the outer surface of the lower part of the bottom plate. Then some simplifications were made:

The angular surface near the top of the annular support which looks from [46] to be slightly curved (in the vertical section) was made conical. The point at which this surface meets the outer vertical surface of the annular support (diameter 315 cm) was estimated by eye from [46]. The rounded corners both on the inside and outside of the bottom of the annular support were approximated as conical surfaces. Fig. 13 shows an axial section of the MCNP model of the lower barrel annular support.

The "surge orifices" in the eight azimuthal supports were ignored. The inner radius of the azimuthal supports is not quoted. It was estimated by eye from [46] and for simplicity assumed cylindrical (around the core axis). The outer/upper surface of the azimuthal supports was assumed conical (around the core axis). Although the angle between the inner and outer/upper surfaces of each of the azimuthal supports is quoted (65°), the point at which the outer/upper surface intersects with the outer surface of the lower barrel annular support is not quoted. This was estimated by eye from [46].

From [42] we see that the azimuthal supports rest on the PV. Fig. 14 shows an axial section of the MCNP model of two of the eight azimuthal supports.

The material of both the lower barrel annular support and the eight azimuthal supports is AISI-304L steel [37] (7.85 g cm^{-3}).

4.2.10 Bottom shield

For the reference calculation, the bottom shield was not modeled. The shield is in the form of a spherical cap, intersecting the 8 azimuthal supports of the lower barrel annular support. It is shown in [42] and in [46] where it is quoted with thickness 15 cm. In [47] (left side) the position of the bottom shield (and of the lower part of the PV) is defined with respect to the lower surface of the lower annular "foot" of the barrel and therefore with respect to the core bottom plate. The upper limit of the bottom shield is not quoted, but is taken conservatively as the lower surface of the flange (at 176.52 cm below the focal centre point – see [46]). Fig. 15 shows an axial section of the MCNP model of the bottom shield.

The material of the bottom shield is AISI-304L steel [37] (7.85 g cm^{-3}).

4.2.11 Between the core and the pressure vessel

Currently no other structure below the core, and no structure above the core or in the downcomer has been modeled. Water above the core and within the barrel (which is modeled to the top of the geometry) has the density: 0.65027 g cm^{-3} - the temperature at the top of the active region [29]. Water below the core and in the downcomer has the density: 0.74264 g cm^{-3} - the temperature at the bottom of the active region [29]. This may not be conservative, especially for the downcomer.

4.2.12 Pressure vessel liner and vessel

The vessel data is taken from [48]. The position of the vessel with respect to the core is given by [47] (left side). The point at which the thickness of the vessel changes from 28 cm to 14 cm was taken as the point {quoted in [47] (left side)} where the thickness begins to reduce from 28 cm (see Fig. 16). This is therefore conservative (for responses outside the vessel in this direction).

The vessel liner is 5 mm thick [49]. The material of the vessel liner is taken as AISI-304L steel [37] (7.85 g cm^{-3}).

The material composition of the pressure vessel is taken from [50], density 7.833 g cm^{-3} [51].

Note there is no vessel support skirt below the vessel [42], [48].

4.2.13 Concrete liner and concrete outside the PV

The steel liner of the concrete was taken as 2 cm thick (identical to the value for the previous PoliMi calculations [52]) and as steel type, AISI-304L [37] (7.85 g cm^{-3}).

The inner radius of the cylindrical part of the concrete was taken as 4 m [53]. From section A-A of [54] the thickness of the surrounding concrete was estimated as 1 m (both in the radial cylindrical part and in the bottom well).

The position of the PV with respect to the concrete well (and therefore also with respect to the centre of the 22.5 m diameter containment vessel) was established from [53] and [48]. [The common point is the plane of support of the vessel skirt (although the skirt is not currently modeled)]. Fig. 17 shows the concrete surrounding the PV (section through the azimuthal supports of the bottom plate annular support).

The concrete composition (Portland) was taken from [55], density 2.3 g cm^{-3} from [56] (composition also suggested by PoliMi [57]). The presence of reinforcement rods (“rebar”) was neglected. This is not conservative for the PV responses. However the effect should be very small.

Note that [53] and [54] employ a 22.5 m diameter containment vessel.

5. RESULTS FOR PRESSURE VESSEL DAMAGE

The scheme of the various geometrical and source models is shown in Fig. 18. Most calculations were made with all the assemblies, including the 40 outer assemblies, smeared because of issues concerning the local computing environment (these calculations were made with MCNP5 with MPI under AIX whilst the reference calculation with the 40 outer assemblies pin-by-pin was made with MCNPX2.6.d with MPICH under LINUX). [In Fig. 18 actually the first calculation was that in the bottom left corner (Enhanced Moderation fuel assemblies; thinner reflector; including bottom shield; ^{235}U fission spectrum; 40 outer assemblies smeared), then we worked our way up the diagram, with some variations left and right until we arrived at the reference calculation at the top.]

As far as the coupled neutron-gamma calculations are concerned, because of the threshold on the dpa cross-section [16] a gamma energy cut-off of 700 keV was employed in all the vessel damage runs.

Results will be presented in detail only for the reference calculation. Then results for the other calculations will be summarised as variations with respect to the results of the reference calculation.

n.b. The gamma dpa calculations initially employed an erroneous interpretation of the response function defined in [16] which led to an underestimate of the total gamma dpa results (by a factor of between 1.15 and 1.2). The results presented for the reference calculation in Figs. 40 – 46 in §5.1 have been corrected (actually the ratios in Figs. 41 and 42 did not change). All the other gamma dpa results (in Fig. 47, case "A" in §5.2, case "B" in §5.3, case "C" in §5.4, case "D" in §5.5 and case "F" in §5.7) employed the initial, erroneous interpretation of the gamma dpa response function. However none of these results are absolute values but instead are all differences or ratios. In this case we estimate that the error involved through the use of the erroneous response function is negligible.

5.1 Reference calculation (Case "R")

The results for the neutron fluences are shown in Figs. 19 – 25, for the neutron dpa's in Figs. 26 – 32, for the gamma fluences in Figs. 33 – 39 and for the gamma dpa's in Figs. 40 – 46.

(Note that although the illustration in each figure is for the all-homogeneous assembly case, the reference case is with the 40 outer assemblies pin-by-pin).

5.1.1 Contributions from different parts of the fission spectrum

Fig. 47 shows the contribution to the neutron and gamma dpa results on the cylindrical and spherical segments of the pressure vessel inner surface shown in Fig. 27 as a function of the energy of the fission neutrons. Shown also is the ^{235}U fission spectrum.

Discussion

As expected, the high energy (low probability) tail of the fission spectrum provides all the contributions to the neutron dpa, with the maximum contribution probability around 10 MeV for the dpa to the cylindrical part of the vessel and slightly less for the dpa to the spherical part of the vessel. Instead the part of the fission spectrum responsible for gamma dpa to the vessel is at a much lower energy (maximum around 2 MeV) as the gamma's are born in the reflector and the barrel.

As a consequence although uncertainties in the fission spectrum or in the fissioning nuclide (see Fig. 1) should not lead to uncertainties in the gamma-induced dpa or damage, such uncertainties do have an impact on the uncertainty of the neutron-induced dpa or damage. (However in §5.3 it is noted that the neutron-induced dpa below the azimuthal struts is unchanged in going from a ^{235}U fission spectrum to a ^{241}Pu one.)

Taking into account Figs. 1 and 47, it was decided to include a "Spectral Safety Factor" of 1.3 on the neutron-induced damage results outside the azimuthal struts for the UO_2 core and 1.5 for a 100% MOX core [58]. (These factors are not included in the results in Figs. 19 – 32). These factors are checked in §5.3 where results obtained using a ^{241}Pu fission spectrum are compared with those from a ^{235}U fission spectrum.

Note that the Spectral Safety Factors are intended to take into account the fact that in both the UO_2 and the MOX cores there are four possible fissioning nuclides: ^{235}U, ^{238}U, ^{239}Pu and ^{241}Pu (in different proportions) whilst only one, ^{235}U, is actually modeled. They are also intended to take into account the fact that we are using an analytic spectrum that is an approximation for the actual fission spectrum of ^{235}U.

5.2 Smearing the 40 outer assemblies (both source and geometry) (Case "A")

The variations in the vessel responses in going from case "R" to case "A" are summarised as follows:

– The neutron fluences and neutron-induced dpa's increase by a factor of between 1.16 and 1.18 at all energies on both the cylindrical and the spherical parts (above the azimuthal struts) of the PV.

– Instead on the segment of the PV underneath the azimuthal struts, there is a greater variation in both the neutron fluence and neutron-induced dpa, depending on the energy. This increase is by a factor of 1.12 above 1 MeV, this factor rising to around 1.25 both above 100 keV and for the total.

– The gamma fluences and gamma-induced dpa's increase by a factor of 1.23 at all energies on the cylindrical part and by a factor of between 1.25 and 1.26 at all energies on the spherical part (above the azimuthal struts).

5.2.1 The neutron flux leaking from the pressure vessel (for purposes of comparison)

For comparison purposes with other plant designs, it is of interest to report the flux leaking from the pressure vessel around the core mid-plane. Note that this is not the maximum flux leaking from the vessel because a) as already shown, the flux impinging on the spherical part of the vessel is higher than that on the cylindrical part around the core mid-plane and b) the spherical part of the vessel is 14 cm thick, half the thickness of the part around the core mid-plane. However as we see from Fig. 17, leaking neutrons from the spherical part of the pressure vessel are much less important for responses above the core within or outside the containment vessel compared with leaking neutrons from the cylindrical part of the pressure vessel. The fluxes are tallied over the same segment as that shown in Fig. 20 (and over 360° as in Fig. 20) but on the outer surface of the 28 cm thick cylindrical vessel.

	Φ_n (n cm^{-2} s^{-1})
> 1 MeV	4.9E+2
>100 keV	5.2E+3
total	1.2E+4

Note these values must be adjusted downwards by a factor of around 1.17 to provide reference values as discussed in the first paragraph of §5.2.

5.2.2 Further examination of neutron fluence and neutron-induced dpa underneath the azimuthal struts

As the neutron-induced dpa on the PV underneath the azimuthal struts is comparable to the maximum value on the spherical part of the PV just above the azimuthal struts (for the reference case 1.30E-7 and 1.04E-7 respectively and for case "A" 1.61E-7 and 1.22E-7 respectively although the value above the struts is averaged over 360°), it is of interest to sub-divide the segment underneath the struts.

Referring to Figs. 23 or 30, we imagine subdividing the intersection of the strut with the PV as illustrated in the lower left corner into 5 roughly equal segments, in moving towards the bottom of the spherical part of the PV, while leaving the other dimension as illustrated in the top right corner of the figure unsegmented. This produces the following variations (down the page represents moving towards the bottom of the spherical part of the PV) with respect to the mean value over the whole strut intersection with the PV:

Φ_n (> 100 keV)	DPA (tot)
0.53	0.71
1.34	1.28
1.76	1.63
1.12	1.07
0.39	0.51

[Note that the strut at 22.5° to the horizontal (E-W), rather than the one at 67.5° to the horizontal actually has slightly higher flux and dpa values (presumably due to the different source assembly powers). The results presented in Figs. 23 and 30 are for the struts at 67.5° to the horizontal as shown. The results in the above table include the additional factor for the strut at 22.5° to the horizontal, which is around 1.08 for both the flux above 100 keV and total dpa.]

Thus we note that there is an appreciable variation under each strut, that, with a finer segmentation, we may hypothesize gives a factor of 2.5 times the neutron-induced dpa as a maximum value under the strut at 22.5° to E-W compared with the average value under the strut at 67.5° to E-W. Note that this estimate of 2.5 is not necessarily conservative as we have not investigated the variation in the responses in the other dimension (over the 20 cm thickness [46] of the strut). This will be borne in mind.

5.2.3 Comparison of neutron-induced dpa using BISERM and JEFF-3.1 data

The comparison of the dpa results was first made for the cylindrical segment of the vessel inner surface shown in Fig. 27 (note the results in Fig. 27 are for the reference case whilst the results here are for case A):

	DPA (> 1 MeV)	DPA (> 100 keV)	DPA (tot)
BISERM data:	3.3E-8	3.8E-8	3.8E-8
JEFF-3.1 data:	3.1E-8	3.6E-8	3.7E-8

The same comparison was made for the spherical segment of the vessel inner surface shown in Fig. 27:

	DPA (> 1 MeV)	DPA (> 100 keV)	DPA (tot)
BISERM data:	1.0E-7	1.2E-7	1.2E-7
JEFF-3.1 data:	9.8E-8	1.1E-7	1.2E-7

and for the segment of the vessel inner surface under the azimuthal struts shown in Fig. 30:

	DPA (> 1 MeV)	DPA (> 100 keV)	DPA (tot)
BISERM data:	1.5E-8	1.1E-7	1.4E-7
JEFF-3.1 data:	1.5E-8	1.1E-7	1.4E-7

The BISERM results differ from those shown in Figs. 27 and 30 by the correction factors given in the first paragraph of §5.2 for going from the reference case to case “A”. We see a good agreement between the BISERM results and the JEFF-3.1 results both in the harder neutron spectrum on the cylindrical and spherical segments and in the softer neutron spectrum under the azimuthal struts. The results for the finer subdivision of the segments of the pressure vessel under the azimuthal struts (and including the factor for the strut at 22.5° to the horizontal), presented in §5.2.2 for the BISERM data, are shown below for both sets of data:

DPA (tot) (BISERM data)	DPA (tot) (JEFF-3.1 data)
0.71	0.71
1.28	1.26
1.63	1.59
1.07	1.07
0.51	0.50

Thus the variation of the response under the azimuthal struts in one of the dimensions (and including the different struts), is confirmed.

5.3 Employing a ^{241}Pu fission spectrum (case "B")

Compared with case "A":

– The neutron fluences and neutron-induced dpa's on the cylindrical part of the pressure vessel are higher by a factor between 1.52 and 1.63 (dpa's nearer the higher value, fluences nearer the lower value). Instead on the spherical part of the pressure vessel the factor is lower, between 1.37 and 1.48 with again the dpa's nearer the higher value and fluences nearer the lower value.

– The situation is different underneath the azimuthal struts. Here both the neutron fluence and neutron-induced dpa's above 1 MeV are raised by a factor of 1.43. Instead the neutron fluence and neutron-induced dpa's above 100 keV as well as the total fluence and total dpa are virtually unchanged. (We remind ourselves that underneath the azimuthal struts the dpa from neutrons > 1 MeV accounts for about 15% of the total neutron-induced dpa.) Thus as a consequence the maximum value of the total neutron-induced dpa, which in Cases "R" and "A" looked comparable underneath the azimuthal struts and just above the azimuthal struts on the spherical part of the PV, is in this case at the latter point.

– The gamma fluences and gamma-induced dpa's at the pressure vessel are unchanged.

Discussion

The higher results obtained with the ^{241}Pu fission spectrum are consistent with the Spectral Safety Factors of §5.1.1.

5.4 Reducing the reflector thickness (case "C")

The geometry as shown in Fig. 3 is modified by reducing the thickness of the reflector to that shown in Fig. 4 whilst however maintaining the core size shown in Fig. 3 (i.e. retaining the Standard fuel assemblies). The wider gap between the outer fuel assemblies and the reflector is filled with water previously in the narrow gap.

It should also be mentioned that the density of the water outside the active zone was slightly lower than in case "A" due to a mistake, subsequently corrected in cases "A", "B" and "R". The difference in results should however mainly be due to the different reflector thickness.

Compared with case "A":

– The neutron fluences and neutron-induced dpa's on the cylindrical part of the pressure vessel are higher by a factor of 2.22. On the spherical part of the pressure vessel the factor is slightly higher, around 2.29.

– The situation is again different underneath the azimuthal struts. Here both the neutron fluence and neutron-induced dpa's above 1 MeV are raised by a factor of about 1.75. Instead the neutron fluence and neutron-induced dpa's above 100 keV as well as the total fluence and dpa are lower, the fluences by a factor of around 0.75 and the dpa's by a factor of around 0.90. As in case "B", the maximum value of the total neutron-induced dpa, which in cases "R" and "A" looked comparable underneath the azimuthal struts and just above the azimuthal struts on the spherical part of the PV, is at the latter point.

– The gamma fluences above 4 MeV and above 8 MeV and the gamma-induced dpa's at all energies reduce by a factor of around 0.75 on both the cylindrical and spherical parts (above the azimuthal struts). (This factor is around 0.80 for the total gamma fluence.)

5.5 Changing from the Standard to the Enhanced Moderation assemblies (case "D")

The geometry is now that shown in Fig. 4. Compared with case "C":

– The neutron fluences and neutron-induced dpa's on the cylindrical part of the pressure vessel are higher by a factor of between 1.55 and 1.60. On the spherical part of the pressure vessel the factor is slightly lower, between 1.45 and 1.50.

– Underneath the azimuthal struts the neutron fluence and neutron-induced dpa's above 1 MeV are higher by a factor of about 1.33. Instead the neutron fluence and neutron-induced dpa's above 100 keV as well as the total fluence and dpa are higher by a factor of about 1.40. As in cases "B" and "C", the maximum value of the total neutron-induced dpa, which in cases "R" and "A" looked comparable underneath the azimuthal struts and just above the azimuthal struts on the spherical part of the PV, is at the latter point.

– The gamma fluences and the gamma-induced dpa's at all energies increase by a factor between 2.10 and 2.15.

5.5.1 The neutron flux leaking from the pressure vessel (for purposes of comparison)

In an analogous fashion to what was done for case "A" in §5.2.1, for comparison purposes with other plant designs, it is of interest to report the flux leaking from the pressure vessel around the core mid-plane. The fluxes are tallied over the same segment as that shown in Fig. 20 (and over 360° as in Fig. 20) but on the outer surface of the 28 cm thick cylindrical vessel.

	ϕ_n (n cm^{-2} s^{-1})
> 1 MeV	1.8E+3
>100 keV	1.8E+4
total	4.7E+4

If we adjust these values by the factor: 1÷1.575 (§5.5) to go from case "D" back to case "C" and successively by the factor 1÷2.22 (§5.4) to go from case "C" back to case "A", we obtain consistent leakage flux values to those cited in §5.2.1. The factor of 1.17, mentioned in §5.2.1, to adjust these values downwards to provide reference values is assumed to be approximately valid for the model of case "D".

5.6 Changing from the Standard to the Enhanced Moderation assemblies, simultaneously reducing the reflector thickness

This is equivalent to going from case "A" to case "D". The appropriate factors can be extracted as accumulative (multiplicative) values from the factors given in §5.4 and §5.5.

5.7 Adding a bottom shield (case "F")

The geometry is shown in Fig. 15 and is described in §4.2.10. Compared with case "D":

– The neutron and gamma fluences and neutron and gamma-induced dpa's on the cylindrical part of the pressure vessel are of course unchanged. The results on the spherical part of the vessel not directly underneath the shield are also unchanged. (That is, considering for example Fig. 26 and comparing with Fig. 15, the results in the upper four segments of the spherical part of the vessel.)

– On the spherical part of the pressure vessel underneath the shield, the neutron fluence above 1 MeV is reduced by a factor of 0.56 in the segment that is partially occluded by the shield. This factor then reduces to 0.24 at the bottom of the vessel. Instead the neutron fluence above 100 keV has higher factors: 0.64 reducing to 0.37 at the bottom of the vessel, but with a rise to 0.92 in the annular segment that includes the struts. This trend is accentuated for the total flux with a factor of 0.82 reducing to 0.71 at the bottom of the vessel, but now with a factor of 1.33 in the annular segment that includes the struts. Underneath the struts, the factor is 0.50 for the fluence above 1 MeV, 1.20 for the fluence above 100 keV and 1.36 for the total fluence, whilst between the struts these factors are 0.34, 0.65 and 1.20 respectively.

– On the spherical part of the pressure vessel underneath the shield, the neutron-induced dpa above 1 MeV is reduced by a factor of 0.54 in the segment that is partially occluded by the shield. This factor then reduces to 0.21 at the bottom of the vessel. For the neutron-induced dpa above 100 keV, the same factors are 0.57 and 0.25 respectively and for the total neutron-induced dpa they are 0.58 and 0.25 respectively. Underneath the struts, the factor is 0.41 for the neutron-induced dpa above 1 MeV, 1.04 for the neutron-induced dpa above 100 keV and 1.10 for the total neutron-induced dpa, whilst between the struts these factors are 0.32, 0.40 and 0.43 respectively.

– The gamma fluences and the gamma-induced dpa's at all energies decrease by a factor of around 0.4 in the segment that is partially occluded by the shield. This factor then reduces to below 0.05 in all other segments that are underneath the shield.

Discussion

In the cases with the thinner reflector ("C", "D", "E", "F"), the maximum neutron-induced damage to the vessel is at a point that is unaffected by the presence of the shield. In the cases with the thicker reflector ("A", "B", "R"), the neutron-induced damage is comparable underneath the struts and just above the struts. Just above the struts, the shield makes no difference. Underneath the struts, the shield actually increases the total neutron-induced dpa by 10%. Such an effect may be accentuated with a thicker reflector.

The maximum gamma-induced damage to the vessel is on the cylindrical part of the vessel where the shield has no effect.

5.8 Addressing the spatial distribution of the fission source (case "E")

It was of interest to examine the model of a homogeneous spatial fission source in the active zone (similar to that used in the previous analysis [59], where however only the outer 15-17 cm thick stratum was considered with an assumed 1/2 of the average specific core power). Instead here a source throughout the active zone, including the upper and lower blankets was

considered. (Although we concur that the inner assemblies give a negligible contribution to the leakage contributon flux from the core.)

A homogeneous source with a specific power equal to the average specific core power always overestimates the vessel damage responses presented here: PV fluences and dpa's.

A homogeneous source with a specific power equal to half the average specific core power underestimates on the cylindrical part and overestimates on the spherical part of the vessel the vessel damage responses presented here: PV fluences and dpa's. The overestimates can reach a factor of 2, although they are generally around 1.5.

This only concerns neutron responses: neutron fluences and neutron-induced dpa's. The verification has not been made for the gamma responses.

5.9 Calculated upper limits and damage limits

The upper limit for the fast neutron fluence (> 1 MeV) over the PV lifetime required for licensing is 2E+19 n cm^{-2} [60], [61] and for a surveillance programme is 1E+17 n cm^{-2} [60], [61], [62]. There are approximately three orders of magnitude between the calculated result in §5.1 for the maximum fast neutron fluence in 60 years functioning at 100% power and the latter limit. However as we have seen the maximum neutron-induced dpa at the PV is not necessarily where the fast neutron fluence (> 1 MeV) is a maximum. Furthermore the maximum gamma-induced dpa at the PV is around two orders of magnitude greater than the maximum neutron-induced dpa (see §5.1).

5.9.1 Reference case

The maximum result of 6.8E+13 n cm^{-2} in Fig. 19 for the fast neutron fluence (> 1 MeV) over the PV lifetime of 60 years has been averaged over the circumference of the spherical part of the PV. This should be multiplied by 1.21 from Fig. 22 to account for the maximum around the azimuth, giving 8.2E+13 n cm^{-2}. This should be further multiplied by the "Spectral Safety Factor" (§5.1.1) to give 1.1E+14 n cm^{-2} for a UO_2 core and 1.2E+14 n cm^{-2} for a 100% MOX core, factors of **approximately 900** and **850** respectively below the surveillance limit.

In terms of total neutron-induced dpa, the maximum result of 1.0E-7 on the spherical part of the PV in Fig. 26 (at exactly the same location as the fast neutron fluence of 6.8E+13 n cm^{-2}) over the PV lifetime of 60 years has been averaged over the circumference. This should be multiplied by 1.20 from Fig. 29 to account for the maximum around the azimuth, giving 1.2E-7. This should be further multiplied by the "Spectral Safety Factor" (§5.1.1) to give 1.6E-7 for a UO_2 core and 1.8E-7 for a 100% MOX core (where the total neutron-induced dpa results of 1.6E-7 and 1.8E-7 are at exactly the same location as the above fast neutron fluences of 1.1E+14 n cm^{-2} and 1.2E+14 n cm^{-2}).

Instead, the total neutron dpa result averaged under the azimuthal struts of 1.3E-7 in Fig. 30 should be multiplied by the factor 2.5 to account for the difference between the strut at 22.5° to (E-W) and the one at 67.5° and to account for the maximum value in the middle of the strut (see §5.2.2). (This assumes the transferability of the results in §5.2.2 for case "A" to the reference case.) This gives 3.3E-7, substantially higher than the value outside the struts (and we remember that the factor 2.5 is not necessarily a conservative estimate).

Thus for the UO_2 core we may hypothesise a fictitious equivalent maximum fast neutron fluence by forming the ratio: 3.3E-7÷1.6E-7 and multiply it by 1.1E+14 to give: 2.2E+14 n cm^{-2}. For the MOX core, the ratio is 3.3E-7÷1.8E-7 multiplied by 1.2E+14 to give a virtually identical value. We are then a factor of **approximately 500** (or less given that the factor 2.5 is not necessarily conservative) below the surveillance limit. (Note that here we have employed as conversion factor for total neutron-induced dpa to fast neutron fluence the value outside the azimuthal struts. This is because the neutron spectrum outside the struts should be more typical of the usual neutron spectrum at the PV in PWR's compared with the spectrum under the struts.)

Taking into account gamma damage, the maximum gamma-induced dpa is 1.8E-5 (Fig. 40). This should be multiplied by 1.05 from Fig. 42 to account for the maximum around the azimuth, giving 1.9E-5. In this case, for the UO_2 core, we may hypothesise a fictitious equivalent maximum fast neutron fluence by forming the ratio: 1.9E-5÷1.6E-7 and multiplying it by 1.1E+14 to give: 1.3E+16 n cm^{-2}. For the MOX core we have an identical value. Here we have employed the same conversion factor for total neutron-induced dpa to fast neutron fluence as above, i.e. on the spherical part of the PV just above the struts. Instead if we employ as conversion factor the ratio of total neutron-induced dpa to fast neutron fluence at the point on the cylindrical part of the PV where the gamma dpa is maximum, we obtain:

1.9E-5×(2.1E+13×1.19)÷(3.3E-8×1.19) = 1.2E+16 n cm^{-2} (from Figs. 19, 21, 26 and 28), virtually the same result.

We are in both cases a factor of **approximately 8** below the surveillance limit.

Note that these results are for a 60 year lifetime at 100% load.

5.9.2 Case "D" (Enhanced Moderation fuel assemblies with thinner reflector)

We apply the factors listed in §5.4 and §5.5 when moving from case "A", through case "C" to case "D". Also we assume that the factors listed in §5.2 when moving from case "R" to case "A" are the same as those we would have when moving from a hypothetical (in the sense that it has not been treated) case "R_D" to case "D", where case "R_D" is like case "D" but with the 40 outer assemblies modeled pin-by-pin both for the fission source and for the geometry. (This assumption may, if anything, be conservative as one would expect a thicker reflector to accentuate the differences between the pin-by-pin and the homogeneous assembly description.)

Then we have: an estimated maximum result of 2.3E+14 (6.8E+13×2.29×1.475) n cm^{-2} for the fast neutron fluence (> 1 MeV) over the PV lifetime of 60 years which has been averaged over the circumference of the spherical part of the PV. This should be multiplied by 1.21 from Fig. 22 to account for the maximum around the azimuth, giving 2.8E+14 n cm^{-2}. This should be further multiplied by the "Spectral Safety Factor" (§5.1.1) to give 3.6E+14 n cm^{-2} for a UO_2 core and 4.2E+14 n cm^{-2} for a 100% MOX core, factors of **approximately 275** and **240** respectively below the surveillance limit

In terms of neutron-induced dpa, an estimated maximum result of 3.4E-7 (1.0E-7×2.29×1.475) on the spherical part of the PV (at exactly the same location as the fast neutron fluence of 2.3E+14 n cm^{-2}) over the PV lifetime of 60 years has been averaged over the circumference. This should be multiplied by 1.20 from Fig. 29 to account for the maximum around the azimuth, giving 4.1E-7. This should be further multiplied by the "Spectral Safety Factor" (§5.1.1) to give 5.3E-7 for a UO_2 core and 6.1E-7 for a 100% MOX core (where the neutron-induced dpa results of 5.3E-7 and 6.1E-7 are at exactly the same location as the above

fast neutron fluences of 3.6E+14 n cm^{-2} and 4.2E+14 n cm^{-2}). Instead the estimated result averaged under the azimuthal struts of 1.6E-7 (1.3E-7×0.90×1.40) should be multiplied by the factor 2.5 to account for the difference between the strut at 22.5° to (E-W) and the one at 67.5° and to account for the maximum value in the middle of the strut (see §5.2.2). (This assumes the transferability of the results in §5.2.2 for case "A" to both the reference case and to case "D".) This gives 4.0E-7, lower now than the result outside the struts. (Although the factor 2.5 for the variation under the struts was not necessarily conservative, probably the result outside the struts still remains higher than that underneath.)

Thus for the UO_2 core we have an estimated maximum fast neutron fluence of 3.6E+14 n cm^{-2} and for the MOX core we have 4.2E+14. We are then a factor of **approximately 300** below the surveillance limit for the UO_2 core and a factor of **approximately 250** below the surveillance limit for the MOX core.

Taking into account gamma damage, the estimated maximum gamma-induced dpa is 2.9E-5 (1.8E-5×0.75×2.125). This should be multiplied by 1.05 from Fig. 42 to account for the maximum around the azimuth, giving 3.0E-5. In this case, for the UO_2 core we may hypothesise a fictitious equivalent maximum fast neutron fluence by forming the ratio: 3.0E-5÷5.3E-7 and multiplying it by 3.6E+14 to give: 2.0E+16 n cm^{-2}. For the MOX core we have an identical value. Here we have again employed the same conversion factor for total neutron-induced dpa to fast neutron fluence as above, i.e. on the spherical part of the PV just above the struts. Instead if we employ as conversion factor the ratio of total neutron-induced dpa to fast neutron fluence at the point on the cylindrical part of the PV where the gamma dpa is maximum, we obtain:

3.0E-5×(2.1E+13×1.19×2.22×1.575)÷(3.3E-8×1.19×2.22×1.575) = 1.9E+16 n cm^{-2}, again virtually the same result.

We are in both cases a factor of **approximately 5** below the surveillance limit.

Note that these results are for a 60 year lifetime at 100% load.

6. DOSE DURING RUNNING OUTSIDE THE BIOLOGICAL SHIELD

6.1 Calculational model: geometrical and material description

6.1.1 Between the pressure vessel and the containment vessel

The geometry modeling was firstly based on the 22.5 m diameter containment vessel. The following drawings were used: [53], [63], [54], [64] and [65]. All concrete thicknesses were taken as 1 m even if not quoted, apart from in the region between the PSS cavities and the main deck (between the main deck and 12.75-9.5=3.25 m below the main deck [63]) which will be described below. The concrete filling in the bottom of the PSS cavities [63] was not modeled. The four vertical struts in the PSS cavities [54] (section A-A) were modeled. As discussed in §4.2.13, the concrete composition (Portland) was taken from [55], density 2.3 g cm^{-3} from [56] Reinforcement rods were not modeled.

The thickness of the sleeve surrounding the pressure vessel above the main deck (the anti-missile shield) was taken in these calculations as 1 foot (30.48 cm) [66]. (In subsequent calculations, this thickness was drastically reduced – see §10.1.) It was originally by mistake modeled as concrete, then subsequently changed to steel [66]. The steel was as always taken as AISI-304L steel [37] (7.85 g cm^{-3}). For the calculations in which the sleeve was concrete, its composition and presence has no bearing on the results.

The region between the PSS cavities and the main deck was modeled employing the 3-D figure in the top right corner of [54] and, for the measurements, [65] (assuming the latter is to scale). Note that the penetrations ("slots") in the 1 m thick concrete sleeve around the vessel that house the inlet nozzles are not quoted and were modeled from [54] and [65]. From [65] the slots were estimated as being exactly 1 m wide.

The radii of the inlet nozzles were firstly taken from section A-A of [42] as 9.656 in (24.52624 cm). They were firstly assumed bare (no walls, no flanges). In the first model, they were also, in an arbitrary manner, truncated at the same outer radius as that of the 1 m thick concrete sleeve surrounding the pressure vessel.

For the moment no floor grills or tanks were modeled in the cavities or in the region above the main deck.

The containment vessel was taken as 1 in thick steel [67], again assumed as AISI-304L steel [37] (7.85 g cm^{-3}). This was subsequently seen to be an error in interpreting the text in [67] and the thickness is actually 1.75 in. The results in §6 employ 1 in, whilst 1.75 in was employed in all subsequent sections, in particular in §10.

All concrete was assumed without rebar.

After the initial modeling effort, it was decided to move to a 25 m diameter containment vessel. For this the following drawings were used: [68], [69], [70], [71] and [72]. The new measurements were taken from these references {for example the cavities containing the CVCS equipment were moved further out (compare [72] and [65])}. However the 1 m thick concrete sleeve surrounding the pressure vessel in the region between the PSS cavities and the main deck was modeled as in [54] rather than [70] (see attachment to [66]).

The above represents the first model for the geometry between the pressure and containment vessel. It is shown in Figs. 48-50 (vertical sections through the inlet nozzles moving

progressively to smaller scale) and in Figs. 51-53 (horizontal sections at various heights). [Note in these figures, the first model of the steam generators is present (§6.1.2).] Subsequently a second model was generated with an improved description of the inlet nozzles, including the tube wall and flange where the tube enters the pressure vessel.

The second model employed ANSALDO drawings for the inlet nozzle, wall and flange. Firstly the radius of the inlet nozzles was modified slightly from 24.52624 cm to 24.546 cm ([73] section B-B). The outer diameter of the inlet nozzle pipe in the thinnest part is given as 24 in [74], giving a wall thickness of 5.934 cm.

The outer limit of the inlet nozzle pipe including flange is 552.7 cm from the core axis ([75] vertical section). The end thickness of the flange at the end of the inlet nozzle pipe is not quoted and is taken arbitrarily as 10 cm. The radial (axis that of the inlet nozzle) extension of the end flange does not seem to be quoted and is ignored, although from the drawings it looks substantial. (This end flange would actually play an important role in the shielding in its current position. However its present position is not defined for shielding purposes and therefore is subject to possible future modification – if it is further away from the pressure vessel its shielding function diminishes.)

Instead the flanges where the inlet nozzles penetrate the pressure vessel have been modeled as simple cones. The point where the cone starts is given in [74] as 410.31 cm from the reactor axis. Also in [74] the thickness where the flange meets the pressure vessel is given as 60 cm. Observing the flange section in [74], we see that such a conical representation should be conservative.

Figs. 54-57 show vertical sections of the second model and Figs. 58-59 show horizontal sections. Note in these figures, the second model of the steam generators is present (§6.1.2).

6.1.2 Steam generators

Although the steam generators are situated within the pressure vessel, their presence is relevant only for the selected responses calculated outside the pressure vessel. For this reason their modeling is described here.

First model

In a first model the steam generators were homogenized, applying some reduction factors to the density as such a homogenization by itself is not conservative. The dimensions were taken from [73] (distance of bottom of S.G. from axis of inlet nozzles: 44.5 cm; height and radius of S.G.: 914.5 cm and 82 cm respectively). (The position of the inlet nozzles with respect to the bottom of the pressure vessel, and therefore with respect to the core, is given in [48]. The result is that in the present model, the bottom surface of the steam generators is at a distance of 72.392 cm from the top surface of the top core plate or at a distance of 120.632 cm from the top surface of the upper blanket of the active zone.) From [76] the centre of each S.G. is at 226.825 cm from the reactor axis.

As far as the composition is concerned, the following rationale was followed:

- The volume of each S.G. is: $\pi \times 82^2 \times 914.5 = 1.9318E+7$ cm^3.
- From [73] the total mass is 38441 kg.

– From [73] subtract SA15 (822 kg) and SA13 (582 kg) as they are outside our S.G. model volume. This leaves 37037 kg.
– Of this 37037 kg, 17458 kg is SA20 ("tube bundle") whose composition is given in [77]. We apply a guessed factor of 0.6667 to account for the non-conservative nature of the homogeneous model of the bundles. This then produces a smeared density of SA20 in the 1.9318E+7 cm^3 of 0.60248 g cm^{-3} (6.53458E-3 atom cm^{-1} b^{-1}) with the following fractions:

	g cm^{-3} (unnormalized)	atom cm^{-1} b^{-1} (normalised)
Ni	0.18226	5.49467E-01
Cu	0.0001571	4.37451E-04
Fe	0.03142	9.95513E-02
Mn	0.001571	5.05990E-03
C	0.00006285	9.25900E-04
S	0.00001571	8.66947E-05
Cr	0.09270	3.15463E-01
P	0.00004714	2.69299E-04
Co	0.00005028	1.50964E-04
Si	0.001571	9.89768E-03
N	0.0001571	1.98514E-03
Al	0.001571	1.03026E-02
Ti	0.001257	4.64552E-03
Mo	0.0006285	1.15927E-03
Nb	0.0003142	5.98412E-04

– The remaining 19579 kg of the 37037 kg was taken as generic stainless steel. Therefore adopting the usual steel - AISI-304L [37] (7.85 g cm^{-3}, or 8.5440E-2 atom cm^{-1} b^{-1}), smearing the mass in the 1.9318E+7 cm^3 and again applying the same guessed factor of 0.6667 to account for the non-conservative nature of the homogeneous model, we obtain an atom density for this AISI-304L of 7.35412E-3 atom cm^{-1} b^{-1} with the following isotopic normalised fractions:

^{54}Fe	0.040534927
^{56}Fe	0.636311673
^{57}Fe	0.014695211
^{58}Fe	0.001955663
^{50}Cr	0.008784231
^{52}Cr	0.169395152
^{53}Cr	0.01920805
^{54}Cr	0.00478129
^{58}Ni	0.064171419
^{60}Ni	0.024718716
^{61}Ni	0.001074505
^{62}Ni	0.003425994
^{64}Ni	0.0008725
^{55}Mn	0.010070668

– Assuming the density of the SA20 is the same as that of the AISI-304L (7.85 g cm^{-3}), the total volume not occupied by the SA20 or AISI-304L in each S.G. is: 1.9318E+7

– (37037×1000) ÷7.85 = 1.4600E+7 cm^3. To account for water vapour or voids within the structure, in 90% of this volume (guessed), insert water at 0.74264 g cm^{-3} (7.44894E-2 atom cm^{-1} b^{-1}), giving a resultant reduced water density of 5.06673E-2 atom cm^{-1} b^{-1} throughout each S.G.

– The final S.G. composition is a sum of the three components: SA20, AISI-304L and water with their smeared densities as above.

Second model

Following recommendations from the Bologna workshop of Oct. 2008, a second model was developed with the following features:

A separate bottom header modeled as a steel parallelepiped of height 73 cm [73], [74], width 95 cm [73] and maximum depth 164 cm [73] (i.e. the diameter of the steam generator tube), the depth of the parallelepiped delimited by the circumference of the steam generator tube (Fig. 58). The thicknesses of the walls of the approximate parallelepiped were taken as 10 cm in all three dimensions [73], [74]. We neglect the steel tubes that finish within the bottom header and assume that it is full of water (secondary circuit). The hole in the steel wall of diameter 25.4 cm on the outer side, shown in [73] is explicitly modeled. The shroud around the bottom header is neglected.

Assuming a true parallelepiped (i.e. neglecting the delimitation by the circumference of the S.G. tube), the volume of steel in this model of the bottom header is 564940 cm^3 and assuming a density of 7.85 g cm^{-3} the mass is 4435 kg. Assuming the top header is identical we have a total header mass of 8813 kg. This seems reasonable as comparing with that given in [73] of 12092 kg, we know we have underestimated the steel in each header by examination of the section of each header in [74]. Furthermore we have neglected the "center support" [73], [74].

From [74] we see that the bottom header is symmetric about the inlet nozzle. Therefore the lower surface of the bottom header is at 36.5 cm below the axis of the inlet nozzle. We ignore the lower support and assume that the lower surface of the bottom header is the lower surface of the S.G. (In the first model the lower surface of the S.G. was at 44.5 cm below the inlet nozzle axis.) In this model, the bottom surface of the steam generators is at a distance of 80.392 cm from the top surface of the top core plate or at a distance of 128.632 cm from the top surface of the upper blanket of the active zone. This should be conservative for all dose calculations apart from the activation of the S.G. itself, for which this should be revisited.

The bottom header is modeled as AISI-304L with composition from [37] and density 7.85 g cm^{-3}.

Again assuming a true parallelepiped, the water within the bottom header has a volume of 572400 cm^3. The actual volume is 439600 cm^3 [78], lower as expected. This water has a density of 0.8386 g cm^{-3} [78].

For the rest of the S.G., the top header is ignored as is the "center support" (ext. diameter 61 cm [73]). Thus the rest of the S.G. is modeled as a cylinder of radius 82 cm with axis at 226.825 cm from the core axis [76], with lower surface identical to the upper surface of the bottom header (i.e. at 36.5 cm above the inlet nozzle axis) and upper surface 820 cm above the lower surface [73] (thus including part of the tube bundle in the top header and not concentrating the tube bundle in a smaller volume to give a too high density and non-conservative results). (Note that the length of the S.G. in the first model was 914.5 cm.)

In this volume of $\pi \times 82^2 \times 820$ = 1.732174E+7 cm^3, put from [73]:

– 17458 kg of SA20 (tube bundle, composition is given in [77], with a modified density compared with the first model of 8.14 g cm^{-3} [79]);
– 3698 × 820÷914.5 = 3316 kg SA24 (shroud, assume AISI-304L, composition from [37], density 7.85 g cm^{-3});
– 1760 kg SA21 (tube bundle support, assume AISI-304L, composition from [37], density 7.85 g cm^{-3}).

This then produces a volume of 2.79134E+6 cm^3 occupied by the steel and leaves (1.732174E+7 – 2.79134E+6) = 1.453040E+7 cm^3 occupied by the primary and secondary water.

From [78] the volume of water within the tube bundle is given as 2.8910E+6 cm^3, with density 0.8386 g cm^{-3}. The rest of the water, assumed all primary, then occupies 1.45304E+7 - 2.8910E+6 = 1.16394E+7 cm^3 and is given density 0.74264 g cm^{-3}. [Note the volume of the primary water in the steam generators is actually 74.757E+6÷8 = 9.345E+6 cm^3 ([80] p. 43).]

With these geometrical and material data, a smeared composition was generated for the part of the steam generator above the bottom header [81].

In contrast to the first model, no guessed factors are applied to account for the non-conservative nature of the homogeneous model or to account for the presence of water vapour or voids.

6.1.3 Outside the containment vessel

The reactor building model was based on [82] but assuming an azimuthal symmetry based on the South direction ([82]). All walls and floors were assumed to be concrete and to be 1 m thick (apart from the concrete just outside the containment vessel below –13.5M in [82] which was modeled to scale). As discussed in §4.2.13, the concrete composition (Portland) was taken from [55], density 2.3 g cm^{-3} from [56]. Reinforcement rods were not modeled.

We refer to the concrete wall directly outside the containment vessel as the "biological shield" (currently assumed to be 1 m thick). The concrete wall outside the biological shield was moved in an arbitrary fashion closer to the biological shield (to a distance of 1 m). The radial dividing walls between the areas just outside the biological shield (see for example [83] and [84]) were not modeled.

Figure 60 shows a vertical section of the model out to the wall outside the biological shield. Figs 61 and 62 show two horizontal sections, the first through the inlet nozzles, the second just above the main deck.

6.2 Source and core description

The source and core descriptions were that of case "A" in §5.2 above [^{235}U fission spectrum, average source (see §4.1), both the source and the geometry smeared in all 89 assemblies of the active zone, Standard assemblies, thick reflector, etc.].

6.3 Results for dose during running outside the biological shield

Neutron and gamma doses were first generated at the outer surface of the biological shield in a rather coarse grid: a single axial interval at the third floor and two axial intervals at the fourth floor – see Fig. 63, and 8 azimuthal intervals – see Figs. 64 (third floor) and 65 (fourth floor). The first model of the steam generators and the first model for the geometry between the pressure and containment vessel (absence of wall and flanges of inlet nozzles) were employed. The dose results are in Table 6.1 (note for case "A" and with no safety factors yet).

The neutron dose is negligible compared with the gamma dose and from now on will be ignored. Furthermore, on the fourth floor the gamma dose is due to gamma's born from neutron collisions within (and not including) the pressure vessel. (Gamma's born in and outside the pressure vessel account for less than 0.1 % of the dose.) The contributing gamma's are actually those born in the barrel and the outer part of the reflector (at or just above the upper part of the active zone). (Note this latter information was obtained with an in-house patched version of MCNPX2.4.k [85].)

Given that the gamma's born in the barrel and reflector are the predominant contributors to the dose outside the biological shield, the streaming path from the barrel, past or through the lower part of the steam generators, through the pressure vessel and through the cavities between the pressure and containment vessels, acquires importance. (In Figs. 48-50 this is from the upper part of the core in a straight line going upwards at around 30° to the horizontal.) This implied an improved modeling of the lower part of the steam generators as discussed in §6.1.2 and illustrated in Figs. 54-59.

A calculation was made with this improved modeling of the steam generator but without the improved modeling of the inlet nozzles wall and flange discussed in §6.1.1. The results for the gamma dose at the fourth floor are in Table 6.2.

The second steam generator model reduces slightly the dose and moves the maximum from the upper part to the lower part of the fourth floor.

Furthermore a consideration of Figures 50 and 52 leads one to predict the presence of four "hot spots", two each in the E and W directions respectively in line with (but above) the inlet nozzles. A relatively fine tally mesh was adopted, using the "meshtal" option of MCNP5 employing a total of 250 tallies: 10 axial bins on the fourth floor only, and 25 azimuthal bins. The azimuthal bins consisted of four groups of 5 bins each, clustered around the projection of the inlet nozzles in the E and W directions on the outer surface of the biological shield. (They are defined in Table 6.3.) The axial bins were distributed equally over the 3.43 m height of the fourth floor, the first axial bin being the lowest one. The dose results are in Table 6.3.

We see a maximum dose in the third axial interval (68.66-102.99 cm from the floor) and in the azimuthal bins: 5, 9, 17 and 21, giving an average dose in these bins of 0.76 μSv/h. Looking at the results in the above table, we may estimate that the maximum calculated dose should not be greater than 1 μSv/h. (Note this could be verified using a finer spatial and angular grid.) This is to be compared with 0.24 μSv/h from Table 6.2 in the coarser azimuthal segments E and W.

The dose was then calculated for the improved steam generator model together with the improved model for the inlet nozzles. The results for the gamma dose at the fourth floor are in Table 6.4.

The improved modeling of the inlet nozzles roughly halves the dose. The finer mesh then gives the results in Table 6.5. Compared with the previous results for the bare inlet nozzle, we see

a reduction of slightly more than a factor of 2, with an average dose in the third axial interval (68.66-102.99 cm from the floor) and in the azimuthal bins: 5, 9, 17 and 21, of 0.31 μSv/h.

Finally the thickness of the biological shield was increased from 1 to 1.5 m maintaining the second steam generator model and the improved modeling of the inlet nozzles. The results for the gamma dose at the fourth floor are in Table 6.6. We see a factor of around 20 reduction in the dose. The finer mesh gives the results in Table 6.7 where we see that the factor of 20 with respect to the previous results is maintained, also in the dose values at the "hot spots".

Discussion

As all the dose is from gamma's born in or near the core, the "Spectral Safety Factor" (§5.1.1) is taken as unity.

As the source and core descriptions were from case "A", the results should be slightly conservative with respect to the reference case. [Assuming the transferability of results for damage to the PV to the doses outside the biological shield, the gamma results should be a factor of ~1.25 too high (§5.2).]

The 1 in rather than 1.75 in CV thickness adds a further element of conservativeness. Furthermore no rebars were modeled in any of the concrete walls, either within or outside the CV. Rebars will reduce the gamma dose.

Finally a possible non-conservative factor: the concrete adopted [55], [56], [57] has 1% by weight of hydrogen, which looks a "fresh" concrete. As discussed in §7.1.3, in [86] it is shown that the water content in a concrete shield at equilibrium is around 54% of the initial water content. In [86] it is stated that "a factor of 50% reduction in the water content of the shield ..... results in a factor of three increase in the gamma ray dose rate". This refers to a 2.65 m thick concrete shield. Here we have 1.5 m (assuming no other concrete is traversed between the PV and the outside of the biological shield). However as noted above, gamma's born in the concrete outside the PV give a very small fraction of the total dose, so this is largely irrelevant.

If a working hypothesis is of a maximum dose in the control room of 0.25 μSv/h, then after the inclusion of safety factors – still to be defined – to our calculated result of ~ 0.015 μSv/h, we should be well below that limit with a 1.5 m thick biological shield. Instead with a 1 m biological shield, at ~ 0.3 – 0.35 μSv/h we were over that limit, even before applying safety factors.

Table 6.1

Doses in μSv/h during running at outer surface of biological shield (see Figs. 63-65)

Floor		neutron dose	gamma dose
3rd	N	~ 5E-8	~ 2E-5
3rd	NE	~ 8E-8	~ 2E-5
3rd	E	~ 1E-7	1.3E-4
3rd	SE	~ 1E-7	1.5E-5
3rd	S	~ 2E-6	8.6E-3
3rd	SW	~ 1E-7	1.3E-5
3rd	W	~ 1E-7	1.3E-4
3rd	NW	~ 5E-8	~ 1E-5
4th (lower)	N	~ 8E-7	5.4E-3
4th (lower)	NE	~ 2E-6	6.4E-3
4th (lower)	E	~ 4E-6	0.31
4th (lower)	SE	~ 1E-6	6.4E-3
4th (lower)	S	~ 2E-6	5.5E-2
4th (lower)	SW	~ 1E-6	6.9E-3
4th (lower)	W	~ 4E-6	0.27
4th (lower)	NW	~ 8E-7	6.3E-3
4th (upper)	N	~ 1E-6	8.3E-2
4th (upper)	NE	~ 2E-6	7.7E-2
4th (upper)	E	~ 4E-6	0.32
4th (upper)	SE	~ 2E-6	8.0E-2
4th (upper)	S	~ 3E-6	0.12
4th (upper)	SW	~ 1.5E-6	7.5E-2
4th (upper)	W	2.4E-6	0.33
4th (upper)	NW	9.5E-7	7.7E-2

Table 6.2

Doses in μSv/h during running at outer surface of biological shield (see Figs. 63-65) with improved modeling of the lower part of the steam generators

Floor		gamma dose
4th (lower)	N	2.1E-3
4th (lower)	NE	3.1E-3
4th (lower)	E	0.24
4th (lower)	SE	3.1E-3
4th (lower)	S	4.2E-2
4th (lower)	SW	3.2E-3
4th (lower)	W	0.24
4th (lower)	NW	~ 1E-2
4th (upper)	N	4.3E-2
4th (upper)	NE	4.7E-2
4th (upper)	E	0.20
4th (upper)	SE	4.8E-2
4th (upper)	S	7.0E-2
4th (upper)	SW	4.8E-2
4th (upper)	W	0.20
4th (upper)	NW	5.2E-2

Table 6.3

Dose (μSv/h) during running at outer surface of biological shield (see Figs. 63-65) with improved modeling of the lower part of the steam generators;
azimuthal bins (down); axial bins (across) [Note: for the azimuthal bins, 0° is the N direction (see Figs. 64 and 65), they then proceed anticlockwise, so that 90° is the W direction, etc.]
The colour code denotes range of fractional statistical error: black: < 0.1; blue: 0.1-0.2; green: 0.2-0.3; magenta: 0.3-0.5; red: > 0.5.

		1	2	3	4	5	6	7	8	9	10
1	(0° - 63.13°)	0.001	0.001	0.001	0.002	0.005	0.016	0.033	0.041	0.040	0.037
2	(63.13° - 65.70°)	0.005	0.007	0.013	0.061	0.299	0.120	0.260	0.241	0.189	0.160
3	(65.70° - 68.04°)	0.012	0.022	0.029	0.057	0.103	0.190	0.376	0.478	0.454	0.319
4	(68.04° - 71.09°)	0.130	0.455	0.535	0.471	0.474	0.487	0.452	0.464	0.414	0.348
5	(71.09° - 74.29°)	0.167	0.572	0.724	0.646	0.566	0.470	0.460	0.376	0.353	0.288
6	(74.29° - 77.80°)	0.121	0.396	0.488	0.435	0.403	0.335	0.293	0.260	0.254	0.206
7	(77.80° - 102.20°)	0.037	0.108	0.116	0.107	0.081	0.081	0.070	0.059	0.054	0.052
8	(102.20° - 105.71°)	0.114	0.432	0.427	0.417	0.378	0.351	0.280	0.265	0.221	0.198
9	(105.71° - 108.91°)	0.162	0.604	0.744	0.673	0.595	0.542	0.514	0.381	0.312	0.267
10	(108.91° - 111.96°)	0.111	0.448	0.503	0.442	0.443	0.423	0.565	0.516	0.407	0.366
11	(111.96° - 114.30°)	0.011	0.019	0.027	0.042	0.064	0.164	0.345	0.411	0.423	0.321
12	(114.30° - 116.87°)	0.005	0.005	0.006	0.012	0.027	0.074	0.143	0.194	0.186	0.164
13	(116.87° - 243.13°)	0.016	0.017	0.016	0.016	0.017	0.027	0.046	0.054	0.049	0.044
14	(243.13° - 245.70°)	0.004	0.006	0.005	0.010	0.023	0.064	0.176	0.208	0.173	0.156
15	(245.70° - 248.04°)	0.011	0.021	0.024	0.037	0.062	0.132	0.327	0.441	0.419	0.328
16	(248.04° - 251.09°)	0.118	0.517	0.499	0.441	0.442	0.418	0.434	0.472	0.430	0.353
17	(251.09° - 254.29°)	0.183	0.708	0.893	0.734	0.556	0.508	0.472	0.364	0.352	0.282
18	(254.29° - 257.80°)	0.136	0.483	0.482	0.453	0.363	0.349	0.309	0.216	0.217	0.184
19	(257.80° - 282.20°)	0.031	0.096	0.106	0.096	0.085	0.074	0.074	0.056	0.045	0.040
20	(282.20° - 285.71°)	0.125	0.438	0.388	0.409	0.429	0.385	0.323	0.257	0.241	0.189
21	(285.71° - 288.91°)	0.174	0.591	0.692	0.663	0.579	0.499	0.437	0.400	0.372	0.288
22	(288.91° - 291.96°)	0.118	0.447	0.480	0.508	0.517	0.492	0.444	0.511	0.452	0.386
23	(291.96° - 294.30°)	0.012	0.021	0.027	0.031	0.065	0.147	0.298	0.421	0.390	0.287
24	(294.30° - 296.87°)	0.005	0.006	0.007	0.011	0.021	0.078	0.152	0.220	0.173	0.196
25	(296.87° - 360°)	0.001	0.001	0.001	0.002	0.005	0.016	0.033	0.043	0.042	0.040

Table 6.4

Doses in μSv/h during running at outer surface of biological shield (see Figs. 63-65) with improved modeling of the lower part of the steam generators and with the improved model for the inlet nozzles

Floor		gamma dose
4th (lower)	N	5.8E-4
4th (lower)	NE	1.2E-3
4th (lower)	E	0.13
4th (lower)	SE	1.2E-3
4th (lower)	S	3.5E-2
4th (lower)	SW	1.2E-3
4th (lower)	W	0.12
4th (lower)	NW	1.2E-3
4th (upper)	N	1.4E-2
4th (upper)	NE	1.5E-2
4th (upper)	E	9.1E-2
4th (upper)	SE	1.6E-2
4th (upper)	S	2.9E-2
4th (upper)	SW	1.6E-2
4th (upper)	W	9.1E-2
4th (upper)	NW	1.5E-2

Table 6.5

Doses in μSv/h during running at outer surface of biological shield (see Figs. 63-65) with improved modeling of the lower part of the steam generators and with the improved model for the inlet nozzles;
azimuthal bins (down); axial bins (across) [Note: for the azimuthal bins, 0° is the N direction (see Figs. 64 and 65), they then proceed anticlockwise, so that 90° is the W direction, etc.]
The colour code denotes range of fractional statistical error: black: < 0.1; blue: 0.1-0.2; green: 0.2-0.3; magenta: 0.3-0.5; red: > 0.5.

		1	2	3	4	5	6	7	8	9	10
1	(0° - 63.13°)	0.000	0.000	0.000	0.001	0.001	0.006	0.012	0.013	0.013	0.011
2	(63.13° - 65.70°)	0.001	0.003	0.002	0.004	0.009	0.030	0.050	0.038	0.046	0.058
3	(65.70° - 68.04°)	0.006	0.012	0.012	0.025	0.032	0.058	0.104	0.157	0.104	0.095
4	(68.04° - 71.09°)	0.061	0.216	0.249	0.225	0.220	0.216	0.215	0.208	0.165	0.177
5	(71.09° - 74.29°)	0.075	0.278	0.287	0.233	0.231	0.221	0.187	0.177	0.183	0.138
6	(74.29° - 77.80°)	0.070	0.262	0.258	0.261	0.221	0.181	0.127	0.093	0.091	0.063
7	(77.80° - 102.20°)	0.021	0.074	0.079	0.071	0.062	0.051	0.042	0.029	0.024	0.017
8	(102.20° - 105.71°)	0.063	0.233	0.229	0.254	0.212	0.167	0.139	0.106	0.084	0.086
9	(105.71° - 108.91°)	0.074	0.271	0.292	0.258	0.246	0.231	0.214	0.169	0.124	0.129
10	(108.91° - 111.96°)	0.053	0.251	0.214	0.216	0.225	0.206	0.218	0.209	0.180	0.165
11	(111.96° - 114.30°)	0.006	0.011	0.014	0.016	0.028	0.064	0.153	0.148	0.144	0.125
12	(114.30° - 116.87°)	0.002	0.003	0.003	0.003	0.006	0.025	0.060	0.072	0.060	0.054
13	(116.87° - 243.13°)	0.013	0.014	0.013	0.013	0.012	0.014	0.019	0.019	0.016	0.014
14	(243.13° - 245.70°)	0.002	0.003	0.003	0.003	0.010	0.034	0.046	0.069	0.044	0.053
15	(245.70° - 248.04°)	0.006	0.010	0.017	0.019	0.028	0.064	0.159	0.145	0.162	0.104
16	(248.04° - 251.09°)	0.060	0.238	0.237	0.265	0.214	0.243	0.266	0.226	0.169	0.142
17	(251.09° - 254.29°)	0.084	0.300	0.304	0.340	0.228	0.187	0.199	0.145	0.152	0.121
18	(254.29° - 257.80°)	0.080	0.269	0.259	0.230	0.198	0.183	0.155	0.120	0.078	0.064
19	(257.80° - 282.20°)	0.025	0.075	0.079	0.078	0.057	0.046	0.039	0.027	0.022	0.021
20	(282.20° - 285.71°)	0.071	0.248	0.259	0.262	0.225	0.167	0.144	0.107	0.089	0.069
21	(285.71° - 288.91°)	0.078	0.291	0.357	0.306	0.272	0.233	0.207	0.206	0.137	0.119
22	(288.91° - 291.96°)	0.068	0.213	0.279	0.258	0.265	0.203	0.229	0.229	0.214	0.147
23	(291.96° - 294.30°)	0.006	0.014	0.021	0.021	0.024	0.061	0.118	0.165	0.127	0.096
24	(294.30° - 296.87°)	0.002	0.003	0.003	0.004	0.007	0.017	0.053	0.059	0.054	0.050
25	(296.87° - 360°)	0.000	0.000	0.000	0.001	0.002	0.004	0.011	0.013	0.014	0.012

Table 6.6

Doses in μSv/h during running at outer surface of biological shield (see Figs. 63-65) with improved modeling of the lower part of the steam generators, with the improved model for the inlet nozzles and with 1.5 m thick biological shield

Floor		gamma dose
4th (lower)	N	1.2E-5
4th (lower)	NE	4.6E-5
4th (lower)	E	5.8E-3
4th (lower)	SE	4.2E-5
4th (lower)	S	1.7E-3
4th (lower)	SW	5.1E-5
4th (lower)	W	5.5E-3
4th (lower)	NW	5.4E-5
4th (upper)	N	5.2E-4
4th (upper)	NE	6.0E-4
4th (upper)	E	4.5E-3
4th (upper)	SE	5.5E-4
4th (upper)	S	1.2E-3
4th (upper)	SW	6.0E-4
4th (upper)	W	4.5E-3
4th (upper)	NW	5.4E-4

Table 6.7

Doses in μSv/h during running at outer surface of biological shield (see Figs. 63-65) with improved modeling of the lower part of the steam generators, with the improved model for the inlet nozzles and with 1.5 m thick biological shield;
azimuthal bins (down); axial bins (across) [Note: for the azimuthal bins, 0° is the N direction (see Figs. 64 and 65), they then proceed anticlockwise, so that 90° is the W direction, etc.]
The colour code denotes range of fractional statistical error: black: < 0.1; blue: 0.1-0.2; green: 0.2-0.3; magenta: 0.3-0.5; red: > 0.5.

		1	2	3	4	5	6	7	8	9	10
1	(0° - 63.13°)	0.000	0.000	0.000	0.000	0.000	0.000	0.000	0.001	0.001	0.001
2	(63.13° - 65.70°)	0.000	0.000	0.000	0.000	0.000	0.001	0.001	0.001	0.001	0.002
3	(65.70° - 68.04°)	0.000	0.001	0.000	0.001	0.003	0.003	0.003	0.004	0.006	0.006
4	(68.04° - 71.09°)	0.001	0.005	0.012	0.011	0.010	0.011	0.010	0.009	0.009	0.007
5	(71.09° - 74.29°)	0.001	0.007	0.013	0.012	0.010	0.011	0.010	0.008	0.007	0.006
6	(74.29° - 77.80°)	0.002	0.007	0.012	0.013	0.013	0.010	0.008	0.008	0.006	0.003
7	(77.80° - 102.20°)	0.000	0.002	0.004	0.004	0.003	0.003	0.002	0.002	0.001	0.001
8	(102.20° - 105.71°)	0.001	0.006	0.012	0.011	0.012	0.010	0.007	0.006	0.005	0.004
9	(105.71° - 108.91°)	0.002	0.008	0.016	0.017	0.013	0.012	0.010	0.008	0.006	0.006
10	(108.91° - 111.96°)	0.001	0.007	0.013	0.011	0.009	0.008	0.009	0.009	0.008	0.008
11	(111.96° - 114.30°)	0.000	0.001	0.001	0.001	0.001	0.002	0.004	0.008	0.006	0.006
12	(114.30° - 116.87°)	0.000	0.000	0.000	0.000	0.000	0.001	0.002	0.003	0.003	0.003
13	(116.87° - 243.13°)	0.001	0.001	0.001	0.001	0.001	0.001	0.001	0.001	0.001	0.001
14	(243.13° - 245.70°)	0.000	0.000	0.000	0.000	0.000	0.001	0.001	0.002	0.002	0.002
15	(245.70° - 248.04°)	0.000	0.001	0.001	0.001	0.002	0.002	0.004	0.006	0.007	0.005
16	(248.04° - 251.09°)	0.001	0.008	0.014	0.013	0.015	0.011	0.011	0.012	0.011	0.008
17	(251.09° - 254.29°)	0.001	0.008	0.016	0.017	0.011	0.011	0.010	0.009	0.007	0.006
18	(254.29° - 257.80°)	0.002	0.008	0.017	0.013	0.010	0.008	0.008	0.007	0.004	0.003
19	(257.80° - 282.20°)	0.000	0.002	0.004	0.003	0.003	0.002	0.002	0.002	0.001	0.001
20	(282.20° - 285.71°)	0.001	0.007	0.011	0.012	0.014	0.007	0.008	0.005	0.004	0.004
21	(285.71° - 288.91°)	0.001	0.010	0.016	0.013	0.015	0.015	0.010	0.010	0.008	0.006
22	(288.91° - 291.96°)	0.001	0.008	0.010	0.012	0.010	0.011	0.009	0.009	0.007	0.009
23	(291.96° - 294.30°)	0.000	0.000	0.001	0.001	0.001	0.003	0.004	0.006	0.005	0.004
24	(294.30° - 296.87°)	0.000	0.000	0.000	0.000	0.000	0.001	0.002	0.003	0.002	0.002
25	(296.87° - 360°)	0.000	0.000	0.000	0.000	0.000	0.000	0.000	0.000	0.001	0.001

7. EOL ACTIVITY IN PV LINER, PV, CONCRETE LINER AND CONCRETE

7.1 Calculational model: materials and geometry

The source and core descriptions were that of case "A" in §5.2 above [^{235}U fission spectrum, average source (see §4.1), both the source and the geometry smeared in all 89 assemblies of the active zone, Standard assemblies, thick reflector, etc.]. The same geometry model as that employed for the PV damage calculations in §4 was used. Note that this assumes a 22.5 m diameter CV which places the concrete in the PV well slightly nearer the PV compared with a 25 m diameter CV.

7.1.1 Pressure vessel liner and pressure vessel

Neutron and gamma transport

The compositions of the PV and its liner have been defined in §4.2.12.

Activation

A 200 ppm by weight content of Co is assumed in the PV liner [87] p.14, [88] p.6. Instead the PV is arbitrarily assumed to contain 30 ppm Co by weight.

7.1.2 Steel liner of concrete

Neutron and gamma transport

The composition of the steel liner has been defined in §4.2.13.

Activation

A 200 ppm by weight content of Co is assumed in the liner [87] p.14, [88] p.6.

7.1.3 Concrete

Neutron and gamma transport

The concrete composition was based on that already employed in previous sections [55], [56], [57] with some *caveats*:

Water composition:

In [86] it is shown that the water content at equilibrium is around 54% of the initial water content. The initial hydrogen content in [86] is 0.75% by weight (all due to water). Instead in the concrete composition adopted here [55], [57], the hydrogen content is 1.0%. Thus a maximum hydrogen content is taken as in [55], [57] (i.e. 1.0% by weight) while a minimum hydrogen content is chosen as $0.54 \times 0.75 = 0.41\%$ by weight. This is reasonably consistent with [89]

where maximum and minimum values of hydrogen content of 1% and 0.33% by weight were used.

Rebars:

From [86] rebar steel was taken as 3% by weight of the total. In an arbitrary fashion, the diameter of the rebars was taken as 1 in (2.54 cm). This seems a typical value. Assuming a density of 7.87 g cm^{-3} for the rebars (taking AISI 1005 steel [90] and maintaining 2.3 g cm^{-3} for the concrete [56]) and a regular square lattice, we obtain a distance between adjacent rebars of 23.78 cm. This looks too large. Therefore some more or less arbitrary changes were made: the 3% was taken as by volume rather than by weight and the diameter of the rebars was reduced from 25.4 mm to 15.875 mm (5/8 in). These new values produced a distance of 8.123 cm between adjacent rebars which looks more reasonable.

To examine various models of the rebar in the concrete, a semi-infinite slab geometry was employed with four different concrete models:

1. Portland concrete [55], [56], [57] without rebar.
2. A homogeneous mix of 97% by vol. Portland concrete, 3% by vol. rebar. For the rebar we assume AISI 1005 steel [90], with a composition: (% by weight) C 0.06; Mn 0.35; P 0.04, S 0.05, Fe 99.5.
3. An explicit square lattice of rebar cylindrical rods in a concrete matrix with the rod dimensions and lattice step defined above (see Fig. 66).
4. Rebar plates in a concrete matrix with each plate having the same volume as one line of rods and the distance between plates equal to the lattice step (see Fig. 67).

The neutron leakage spectrum from the 14 cm thick part of the PV was employed as source spectrum impinging on the concrete surface. The $^{59}Co(n,\gamma)$ reaction rate was examined in the rebars and in the concrete and the $^{151}Eu(n,\gamma)$ reaction rate in the concrete. Although not relevant here as ratios of the reaction rates were examined, the concentrations employed were (see following section "*Activation*") rebar: 100 ppm ^{59}Co, concrete: 25 ppm ^{59}Co, 4 ppm Eu (containing 47.9% at. ^{151}Eu). The standard was taken as model 2 above. Two different hydrogen contents were employed in the concrete: 1% by weight as in standard Portland concrete and 0.41% by weight (see above).

(n,γ) reaction rate / (n,γ) reaction rate in concrete-rebar model 2:

Concrete/rebar model	$^{59}Co(n,\gamma)$ in concrete	$^{151}Eu(n,\gamma)$ in concrete	$^{59}Co(n,\gamma)$ in rebar
1 (1% H in concrete)	1.37	1.42	1.37
2 (1% H in concrete)	1	1	1
3 (1% H in concrete)	1.04	1.05	0.84
4 (1% H in concrete)	1.00	1.00	0.92
1 (0.41% H in concrete)	1.45	1.53	1.45
2 (0.41% H in concrete)	1	1	1
3 (0.41% H in concrete)	1.03	1.04	0.87
4 (0.41% H in concrete)	0.99	0.99	0.94

(n,γ) reaction rate / (n,γ) reaction rate in concrete-rebar model with 1% H in concrete:

Concrete/rebar model	^{59}Co(n,γ) in concrete	^{151}Eu(n,γ) in concrete	^{59}Co(n,γ) in rebar
1 (0.41% H in concrete)	1.10	1.06	1.10
2 (0.41% H in concrete)	1.04	0.98	1.04
3 (0.41% H in concrete)	1.04	0.97	1.08
4 (0.41% H in concrete)	1.04	0.97	1.06

We see that the preferred model 2 is a good approximation to the explicit model 3 at both hydrogen contents. With the higher hydrogen content, the ^{59}Co(n,γ) reaction rate in rebar is overestimated by 20% while the ^{59}Co(n,γ) and ^{151}Eu(n,γ) reaction rates in concrete are slight underestimates by up to 5%. With the lower hydrogen content, the differences are slightly less. The differences between the two hydrogen contents for the models 2, 3 and 4 are less than 5% for the reaction rates in concrete and less than 10% for the reaction rates in rebar. (Note that these results concern the reaction rates integrated over the whole volume, not the peak values. It is assumed that the peak value will be higher for the higher hydrogen content.) Therefore with some small correction factors, model 2 is adopted (the homogeneous concrete / rebar mix) and with 1.0% hydrogen content by weight.

There are instead substantial differences between model 1 (absence of rebar) and the other three models, indicating important spectral differences in the concrete matrix. Less rebar in the concrete leads to higher average activities. Presumably the difference in the maximum activity will be even greater (with less rebar, a higher thermal neutron peak nearer the surface of the concrete). This will be borne in mind when the uncertainty in the results is estimated.

Activation

100 ppm Co was assumed in the rebar [57].

Reasonable “upper” values for the contents of trace elements in the concrete were gleaned from a number of sources ([57], [91], [92], [89], [93], [94]) and were (ppm by weight):

Co:	25
Eu:	4
Cs:	4
Li:	30
Ba:	250
Th:	4
U:	3

Subsequently, following discussions and referring to data from [95], the value for Co was changed from 25 to 10 and that for Eu was changed from 4 to 1 ppm by weight. These are the values employed to calculate the activities.

7.1.4 Question of the impurities perturbing the neutron fluxes

Normally low concentrations of impurities do not perturb the neutron flux. Thus the effect on the resulting activity is linear (doubling their concentrations, doubles the activity due to these impurities).

To estimate whether this holds in this case, Figs. 68 to 72 show the following cross-sections in the range 10^{-3} eV – 10 MeV: ^{59}Co(n,γ), ^{151}Eu(n,γ), AISI-304L (PV liner and concrete liner) total, PV-steel total and the homogeneous mix of 97% by vol. Portland concrete, 3% by vol. rebar (§7.1.3), total, respectively. These cross-sections were employed by MCNP and are based on ENDF/B-VI evaluations.

The impurity hypotheses of ^{59}Co and ^{151}Eu are summarised as follows:

material	^{59}Co ppm		^{151}Eu ppm	
	by weight	by atom	by weight	by atom
PV liner	200	188		
PV	30	28		
concrete liner	200	188		
concrete/rebar mix	10 (concrete) 100 (rebar)	6 (mixture)	0.475 (concrete)	0.052 (mixture)

Bearing in mind the above atom fractions, comparing the ^{59}Co(n,γ)^{60}Co cross-section (Fig. 68) with the steel and concrete total cross-sections (Figs. 70 to 72) and comparing the ^{151}Eu(n,γ)^{152}Eu cross-section (Fig. 69) with the concrete total cross-section (Fig. 72), we see that neither the cobalt nor the europium should have an impact on the neutron fluxes. Therefore the effect on the activity of different concentrations should be linear.

7.2 Calculational model for finding the maximum activities: spatial binning of the neutron fluxes

The segmentation of the geometry to average the neutron fluxes for the search for the maximum EOL activities is shown in Fig. 73. Fig. 74 shows the same segmentation in a larger scale. Figs. 75 and 76 show details of Fig. 74.

From these figures we see that the 28 cm thick cylindrical part of the PV is divided into four equal thicknesses of 7 cm each over a height of approximately 160 cm centred slightly above the core centre and around 360°. The 14 cm thick spherical part of the PV is divided into four equal thicknesses of 3.5 cm each over the height segment just above the azimuthal struts where the flux impinging on the inner surface of the vessel outside the azimuthal struts is a maximum (see Fig. 19) and around 360°. Also the part of the PV underneath the azimuthal struts where the flux impinging on the PV is a maximum (Fig. 23) is divided in the same way. This is done for the struts at 22.5° to E-W (Fig. 77).

The PV liner is axially segmented in the same way as the PV but with a single thickness. Thus there are three segments.

The concrete is segmented into four inner thicknesses each of 3 cm. There are seven axial segments on the cylindrical part and two radial segments on the lower spherical part (see Figs. 73 - 76). The concrete liner is segmented in the same way as the concrete, but with a single thickness.

7.3 Results for activation rates of PV liner, PV, concrete liner and concrete in PV well

To find the zones of maximum activity in the PV liner, PV, steel liner and concrete, the zones of maximum reaction rates of ^{59}Co(n,γ) and ^{151}Eu(n,γ) were searched for using MCNP and the spatial segmentation shown in Figs. 73 to 77.

From Table 7.1, we see that the maximum activation in the PV liner and PV is underneath the azimuthal struts and in the inner part of the PV.

From Table 7.2, we see that the activation in the concrete liner and concrete is quite widely distributed around the lower part of the PV well with the maximum values around the corner between the bottom and the cylindrical lateral part. In the concrete, the peak is at a thickness of between 6 and 9 cm.

Given that the maximum values of activation to the PV liner and PV are under the azimuthal struts and given that we have seen in §5.2.2 that there is a reasonably strong variation of the neutron flux under each azimuthal strut, it is necessary to look for a maximum activation under the struts. Therefore the same sub-segmentation was carried out as that made in §5.2.2. That is, five roughly equal segments of the section shown in the bottom left corner of Fig. 23 were considered with the other section shown in the top right corner of Fig. 23 left unsegmented. This produces variations in the ^{60}Co production rate with respect to the mean value over the whole strut intersection with the PV in Table 7.1 shown in Table 7.3.

We see a similar variation to that found in §5.2.2 for the neutron-induced dpa. In a similar fashion to what was done in §5.2.2 and §5.9, we employ a safety factor of 2.5 to account for the variation under the struts compared with the average value, bearing in mind, as before, that 2.5 is not necessarily a conservative estimate because of the variation in the other dimension (§5.2.2).

As the activation to the concrete liner and concrete shows a maximum roughly behind the azimuthal struts, it is necessary also in this case to estimate the maximum around the azimuth. To this end the concrete liner and concrete was segmented into a 40 cm thickness behind the two azimuthal struts which are at 22.5° to EW (we remember that each strut is 20 cm thick). This gave a factor of 8% higher activation of either cobalt or europium in the concrete thickness between 6 and 9 cm and 4 % higher cobalt activation in the concrete liner. We employ safety factors of 1.1 for the concrete liner and 1.15 for the concrete to account for this azimuthal maximum.

Furthermore as discussed in §7.1.3, we require factors to account for the employment of the homogeneous rebar/concrete model compared with the explicit lattice and to account for the uncertainty in the hydrogen content. (Note no factors are employed to account for the uncertainty in the rebar content.) These are taken as:

- Cobalt in concrete: $1.04^2 = 1.08$
- Europium in concrete: 1.05
- Cobalt in rebar: $0.84 \times 1.08 = 0.91$

For all nuclides in the rebar we adopt the same value as for cobalt in the rebar. For all nuclides in the concrete apart from europium we adopt the same value as for cobalt in the concrete. Note that the factors generated in §7.1.3 were for the reaction rates integrated over the whole volume, not the maximum values. The lower hydrogen content would both lower the maximum in Table 7.2 (where 1% hydrogen by weight was employed) and move it to a greater depth in the concrete.

7.4 Results for maximum EOL activity in PV liner, PV, concrete liner and concrete in PV well

In FISPACT, two different irradiation times were considered: 60 years and 100 years, both at 100% load [running at 1000 MW (th)]. Four cooling times were considered: 7 days, 60 days, 2 years and 10 years.

With all the above factors included, the activities in the zones of the PV liner, PV, concrete liner, rebar in concrete and the concrete itself which show maximum activation rates for the two reactions of interest in Tables 7.1 and 7.2, are presented in terms of selected nuclides in the following Tables 7.4 to 7.8 respectively.

The criterion for selection was a non-negligible presence compared with the clearance level. The clearance levels are taken from IAEA data [96]. If an isotope is absent from [96], the clearance level was taken from [97]. In this case it is calculated. It turned out that no isotope was selected that had a clearance level taken from [97], i.e. they all had negligible amounts.

Discussion

As the source and core descriptions were from case “A”, the results should be slightly conservative with respect to the reference case. [We assume by a factor ~1.25 which is the factor for the total neutron flux under the azimuthal struts (§5.2). (Instead from §5.2 the factor for the total neutron flux on the spherical part of the PV just above the azimuthal struts is between 1.16 and 1.18.)] A further element of conservativeness for the concrete and rebar is present due to the employment of the maximum hydrogen content (1% by weight) to generate the neutron fluxes when lower hydrogen contents should lower the peak value for the activation and activity. Instead a non-conservative assumption in the model may be the amount of rebar – less rebar will raise the activities (§7.1.3).

The question arises as to whether a “Spectral Safety Factor” (§5.1.1) needs to be applied to account for the uncertainty in the high energy tail of the fission spectrum and for the presence of higher actinides with a harder fission spectrum (see Fig. 1). Fig. 78 (analogous to Fig. 47 for the dpa) shows the contribution to the ^{59}Co(n,γ) reaction rate in the first 1/4 thickness of the PV under the azimuthal struts and to the ^{59}Co(n,γ) and ^{151}Eu(n,γ) reaction rates in the outer bottom part of the PV well as a function of the energy of the fission neutrons. Shown also is the ^{235}U fission spectrum. As far as the activation of the PV liner and PV is concerned, from Fig. 78 one might be inclined to apply a small spectral safety factor to the cobalt activation. However in §5.3 it was seen that the neutron-induced dpa below the azimuthal struts is unchanged in going from a ^{235}U fission spectrum to a ^{241}Pu one. Therefore we retain consistency with the neutron-induced dpa results and apply no spectral safety factor to these results. As far as the concrete activation is concerned, we see in Fig. 78 that the cobalt and europium results are identical in terms of source spectral contributions. Comparing Fig. 78 with Fig. 47 and bearing in mind Fig. 1, we see that the

spectral safety factor should be substantially less than the value adopted for the neutron-induced dpa results in the PV outside the azimuthal struts [1.3 for the UO_2 core and 1.5 for a 100% MOX core (§5.1.1)]. In an arbitrary fashion we employ 1.1 for the UO_2 core and 1.2 for a 100% MOX core.

Because of the lengths of either of the irradiation times considered compared with the half lives of ^{60}Co (5.27 years) and of ^{152}Eu (13.52 years), at EOL the creation rates via ^{59}Co(n,γ) and ^{151}Eu(n, γ) should be nearly equal to the decay rates of ^{60}Co and ^{152}Eu respectively. Whilst this is the case for ^{60}Co, for ^{152}Eu the creation rate is 50% higher than the decay rate. The creation rates are calculated with MCNP employing cross-sections from the ENDF66 file (Appendix G in [1], [6] and [7]). (Although this is based on ENDF/B-VI Release 6, the ^{151}Eu data is actually from ENDF/B-VI Release 0.) The decay rates are calculated with FISPACT that employs EAF2001 data [12] that originate from a number of sources (§3.2). Thus there is firstly the question of the quality of the basic data and furthermore in FISPACT there is the question of averaging the neutron fluxes into the 172 group XMAS structure. At the moment it looks that a factor of 2 safety factor could be applied to the results for the ^{152}Eu activity to account for these data uncertainties.

In conclusion, we ignore the facts that the results are for case A rather than for the reference case, that a maximum hydrogen content in the concrete was used to generate the neutron fluxes (which should give a higher maximum with depth in the concrete) and that the rebar content may be less than that assumed. (The first two lead to conservative results, the third is non-conservative.) We also ignore the fact that the factor 2.5 for the variation of the activation rate under the azimuthal struts is not necessarily conservative. We apply a factor to the maximum cobalt activation rates in the concrete and in the concrete liner of 1.1 for the UO_2 core and 1.2 for the MOX core. In a similar way we apply a factor to the maximum europium activation rate in the concrete of 2.2 (1.1×2) for the UO_2 core and 2.4 (1.2×2) for the MOX core. Then with these safety factors we see from Tables 7.4 – 7.8 that for **100 years irradiation and 10 years cooling**:

– in the PV liner the maximum ^{60}Co activity is a factor of 55 above the IAEA clearance level.

– in the PV the maximum ^{60}Co activity is a factor of 5.8 above the IAEA clearance level.

– in the steel liner of the concrete, the maximum ^{60}Co activity is 8% below the IAEA clearance level for the UO_2 core and at the IAEA clearance level for the MOX core.

– in the rebar in the concrete, the maximum ^{60}Co activity is 10% above the IAEA clearance level for the UO_2 core and 20% above the IAEA clearance level for the MOX core.

– in the concrete, the maximum ^{60}Co activity is a factor 7.5 below the IAEA clearance level for the UO_2 core and a factor 6.9 below the IAEA clearance level for the MOX core, whilst the maximum ^{152}Eu activity is 41% above the IAEA clearance level for the UO_2 core and 54% above the IAEA clearance level for the MOX core.

Here we have considered each radioactive nuclide independently rather than summing the ratios of their activities to the clearance level activities. We have assumed the impurity levels given in §7.1.1, §7.1.2 and §7.1.3. (We estimate in §7.1.4 that the activities should be proportional to the impurity concentrations.) We have not applied any safety factor to account for transport model or data uncertainties (apart from for the ^{151}Eu activation cross-section).

If we consider cooling times less than 10 years, then from Tables 7.4 to 7.8 we see that other nuclides apart from ^{60}Co and ^{152}Eu must be considered. For example it will be shown in §14 that for ^{54}Mn [which is produced via ^{54}Fe(n,p), a threshold reaction]: a) zones of maximum ^{60}Co

or ^{152}Eu activity are not the same zones as those of maximum ^{54}Mn activity; b) there is a substantial variation of the ^{54}Mn activity within each zone. Thus care should be taken in considering the activities at 2 years and less cooling.

7.5 Results for maximum EOL activity in PV liner, PV, concrete liner and concrete in PV well with concrete boration

Borating the concrete to 1E+21 atom natural boron cm^{-3} [95] (0.775% by weight), reduces the differences between the various rebar-in-concrete models and modifies the results in §7.1.3 as follows:

(n,γ) reaction rate / (n,γ) reaction rate in concrete-rebar model 2:

Concrete/rebar model	^{59}Co(n,γ) in concrete	^{151}Eu(n,γ) in concrete	^{59}Co(n,γ) in rebar
1 (1% H in concrete)	1.00	1.02	1.00
2 (1% H in concrete)	1	1	1
3 (1% H in concrete)	1.00	1.03	1.00
4 (1% H in concrete)	1.01	1.03	1.03

We see that the differences between the various models are strongly reduced and the models are essentially all equivalent.

The cobalt and europium activation rates in Tables 7.1 and 7.2 are modified according to the Tables 7.9 and 7.10 respectively. (Note in these tables the activation rates with borated concrete are relative to the rates without boration.)

Discussion

The conclusions for the ^{60}Co and ^{152}Eu activities with concrete boration follow directly from the results for their respective activation rates:

– borating the concrete makes no difference to the maximum cobalt activity in the PV liner or PV.

– borating the concrete reduces the maximum cobalt activity in the concrete liner by a factor 1.8. As a consequence at 10 years after shut-down the ^{60}Co activity is close to 50% of the IAEA clearance for the UO_2 core and 55% of the IAEA clearance for the MOX core. Instead at 2 years after shut-down we are still nearly 50% above IAEA clearance for the UO_2 core and nearly 60% above IAEA clearance for the MOX core. Note that this is without considering safety factors on the calculational results to account for transport model or data uncertainties.

As far as the concrete itself is concerned, from Tables 7.2 and 7.10, borating the concrete moves the point of maximum activation of the cobalt or europium from the depth 6-9 cm to the depth 0-3 cm (in both cases in the outer part of the bottom of the PV well). Taking into account the factors for employment of the homogeneous rebar/concrete model compared with the explicit lattice both with and without boration whilst assuming the other factors are the same (variation in activation rate with hydrogen content in the concrete, azimuthal maximum behind the azimuthal struts), we obtain the following results:

– borating the concrete reduces the maximum cobalt activity in the rebar in the concrete by a factor 3.8. As a consequence at 10 years after shut-down the ^{60}Co activity is just under 30% of the IAEA clearance for the UO_2 core and just over 30% of the IAEA clearance for the MOX core. Instead at 2 years after shut-down down the ^{60}Co activity is just over 80% of the IAEA clearance for the UO_2 core and 90% of the IAEA clearance for the MOX core.

– borating the concrete reduces the maximum cobalt activity in the concrete by a factor 4.8. As a consequence at just 7 days after shut-down the ^{60}Co activity is a factor of roughly 9.5 below the IAEA clearance level for the UO_2 core and a factor of roughly 8.5 below the IAEA clearance level for the MOX core.

– borating the concrete reduces the maximum europium activity in the concrete by a factor 18.5. As a consequence at 10 years after shut-down the ^{152}Eu activity is a factor of roughly 13 below the IAEA clearance level for the UO_2 core and a factor of roughly 12 below the IAEA clearance level for the MOX core. At 7 days after shut-down the ^{152}Eu activity is a factor of roughly 7.5 below the IAEA clearance level for the UO_2 core and a factor of roughly 7 below the IAEA clearance level for the MOX core.

In all these results safety factors on the calculational results to account for transport model or data uncertainties have not yet been included apart from for the ^{151}Eu activation cross-section.

As was the case in the absence of boration, care should be taken in considering cooling times of 2 years and less, when other nuclides may become important for the total activity. For example boration will have a substantially lower effect on the production of ^{54}Mn.

7.6 Results for average EOL activity in PV liner and PV

Given that the maximum EOL activities in the PV liner and in the PV are above the IAEA clearance levels, with or without concrete boration, it is of interest to estimate the average activities over various axial (height) segments. This could be relevant if, in melting the metal down, the maximum activity would be reduced below the clearance level and if such a procedure would be acceptable from a regulatory point of view.

The PV liner and PV were axially subdivided as shown in Fig. 79. Also shown in Fig. 79 is the homogenized model of the steam generator support structure (below the steam generator bottom header). (This will be discussed in detail in §9 where a better heterogeneous model of the structure is introduced.) Such a homogeneous model is not conservative and it will be borne in mind that the activities in the top three segments are consequently underestimated.

The axial subdivision was made to see at what point above the core the average activity goes below the clearance level. For example if the pressure vessel is cut, the point at which the lowest cut can be made so that both cut segments have average activities below the C.L. Actually it seems from [48] that the natural cut plane is just above the inlet nozzles. In this case the lower part of the vessel below the cut consists of all 9 axial segments of Fig. 79.

A single irradiation time of 100 years was considered at 100% load [running at 1000 MW (th)]. Four cooling times were considered: 7 days, 60 days, 2 years and 10 years.

The results (without any safety factors) for the pressure vessel liner are shown in Tables 7.11 and 7.12. Table 7.11 shows the cumulative values from the bottom of the vessel, going upwards (segment 1 is at the bottom of the vessel, segment 4 is the highest one on the spherical

part, segment 5 is the lowest one on the cylindrical part, segment 9 is the highest one on the cylindrical part). Table 7.12 shows the differential segment values.

The results (again without any safety factors) for the pressure vessel are shown in Tables 7.13 and 7.14. Table 7.13 shows the cumulative values from the bottom of the vessel, going upwards and Table 7.14 shows the differential segment values.

In the case that the pressure vessel liner cannot be detached from the pressure vessel, the results for their aggregation (without any safety factors) are shown in Tables 7.15 and 7.16. Table 7.15 shows the cumulative values from the bottom of the vessel, going upwards and Table 7.16 shows the differential segment values.

Discussion

As discussed in §7.4, the source and core descriptions were from case "A" and therefore the results should be slightly conservative with respect to the reference case (from §5.2 by a factor of around 1.17 on both the cylindrical and the spherical parts).

As far as the possible application of "Spectral Safety Factor" (§5.1.1) is concerned, rather than adopt the S.S.F. of unity for the $^{59}Co(n,\gamma)$ reaction rate in the first 1/4 thickness of the PV under the azimuthal struts (from Fig. 78 examined in §7.4), because of spectral differences we adopt instead the S.S.F.'s for the $^{59}Co(n,\gamma)$ and $^{151}Eu(n,\gamma)$ reaction rates in the outer bottom part of the PV well. In §7.4 these were estimated as 1.1 for the UO_2 core and 1.2 for a 100% MOX core.

Also as mentioned above, the activities in the top three segments are underestimated due to non-conservative modeling of the steam generators. Finally further safety factors would need to be supplied to account for transport model or data uncertainties.

We see from Table 7.11 that even **after 10 years cooling the lower part of the pressure vessel liner is still substantially above the C.L.** even taking all nine segments (cutting just above the inlet nozzles). We see instead from Table 7.12 that **after 2 years cooling that if we cut above the 6th axial segment, the upper part of the pressure vessel liner should be below the clearance** (bearing on mind the above considerations of safety factors).

We see from Table 7.13 that **after 10 years cooling, cutting the pressure vessel anywhere will leave an average activity of the lower part below the clearance level** (with safety factors of up to 3). Instead after 2 years cooling, even taking all nine segments (cutting the pressure vessel just above the inlet nozzles) leaves an average activity that is at the limit (without safety factors). From Table 7.14 we see that **above the 6th axial segment, the average activity of the pressure vessel is more than an order of magnitude below the C.L. after 60 days cooling**.

In the case that the pressure vessel liner is left joined to the pressure vessel, we see from Table 7.15 that up to and including 2 years cooling, no cut can be made that leaves the lower part below the clearance level. **At 10 years cooling, a cut can be safely made between the 5th and 6th axial segments for the lower part of the PV + liner (and of course the upper part) to be below the C.L. For any chance of making a lower cut, safety factors would need to be defined properly.** From Table 7.16 we see that cutting between the 5th and 6th axial segments allows the upper part to be below the C.L. at 2 years cooling whilst cutting between the third and fourth axial segments allows the upper part to be below the C.L. at 10 years cooling.

The average activity in the pressure vessel after 10 years is all due to ^{60}Co. Instead up to and including 2 years after shut-down the activity is mainly from ^{54}Mn. This is not the case in the PV liner where the ^{60}Co activity predominates, also at 2 years after shut-down. (The differences are due both to differences in the composition as well as the assumptions of cobalt impurities.) This is also not the case for the maximum activity to the pressure vessel under the azimuthal struts (§7.4 – Table 7.5) where again the ^{60}Co activity predominates at 2 years after shut-down. In this case the differences are due to differences in the neutron spectrum under the struts compared with over 360°.

Table 7.1

Activation rates ^{59}Co(n,γ)^{60}Co/g/s in various parts of the PV liner and PV (for segments see Fig. 74) (Co impurities in §7.1.1)

	PV liner	PV 1/4 t	PV 2/4 t	PV 3/4 t	PV 4/4 t
Cylindrical part (opposite core mid-plane) over 360°	0.90	0.036	0.0088	0.0065	0.0077
Spherical part (just above azimuthal struts) over 360°	3.1	0.19	0.054	0.031	0.028
Under two azimuthal struts at 22.5° to EW	8.1	0.87	0.49	0.28	0.12

Table 7.2

Activation rates in various parts of the concrete liner and concrete; $^{59}Co(n,\gamma)^{60}Co/g/s$ (in black) (Co impurities in §7.1.2 and §7.1.3); $^{151}Eu(n,\gamma)^{152}Eu/g/s$ (in red) (Eu impurity in §7.1.3); (for segments see Figs. 73 and 74)

	Inner part of well	Outer part of well	Concrete liner	Concrete (3 cm)	Concrete (3 cm)	Concrete (3 cm)	Concrete (3 cm)
Cylindrical part (opposite core mid-plane) over 360°			0.091	0.0085 0.028	0.011 0.040	0.011 0.043	0.010 0.038
Cylindrical part (opposite lower part of PV) over 360°			0.16	0.015 0.050	0.020 0.070	0.020 0.073	0.018 0.068
“			0.21	0.020 0.065	0.025 0.090	0.026 0.098	0.024 0.090
“			0.24	0.023 0.075	0.030 0.11	0.030 0.11	0.028 0.11
“			0.26	0.025 0.083	0.032 0.12	0.032 0.12	0.029 0.11
“			0.26	0.025 0.083	0.032 0.11	0.032 0.12	0.029 0.11
Bottom of PV well (concrete liner) over 360°	0.25	0.28					
Bottom of PV well (concrete 3 cm) over 360°	0.023 0.075	0.028 0.090					
“	0.030 0.11	0.036 0.13					
“	0.030 0.11	0.037 0.14					
“	0.027 0.10	0.033 0.13					

Table 7.3

Variation of the activation rate of $^{59}Co(n,\gamma)^{60}Co$/g/s in the PV liner and PV under the azimuthal struts (down the page represents moving towards the bottom of the spherical part of the PV – see for example Fig. 23) ($^{59}Co(n,\gamma)^{60}Co$/g/s: value / mean value under azimuthal strut)

Under the two azimuthal struts at 22.5° to EW	PV liner	PV 1/4 t	PV 2/4 t	PV 3/4 t	PV 4/4 t
	0.51	0.46	0.41	0.41	0.51
	1.4	1.3	1.3	1.2	1.2
	1.6	1.6	1.5	1.4	1.3
	1.0	1.0	1.1	0.94	1.0
	0.34	0.37	0.34	0.42	0.47

Table 7.4

Activity at EOL in Bq/g in PV liner in zone that contains the maximum ^{60}Co activity

Irradiation	Cooling	^{51}Cr	^{54}Mn	^{55}Fe	^{59}Fe	^{57}Co	^{58}Co	^{60}Co	^{59}Ni	^{63}Ni
60 years	7 days	91.4	1.1	85.2	3.3	0.098	2.1	20.1	0.14	12.6
	60 days	24.3	1.0	82.2	1.4	0.086	1.3	19.8	0.14	12.6
	2 years	-	0.23	51.6	-	0.016	0.0018	15.5	0.14	12.4
	10 years	-	-	6.8	-	-	-	5.4	0.14	11.7
100 years	7 days	91.4	1.1	85.2	3.3	0.098	2.1	20.1	0.23	18.4
	60 days	24.3	1.0	82.2	1.4	0.086	1.3	19.8	0.23	18.4
	2 years	-	0.23	51.6	-	0.016	0.0018	15.5	0.23	18.2
	10 years	-	-	6.8	-	-	-	5.4	0.23	17.2
IAEA Clearance		100	0.1	1000	1	1	1	0.1	100	100

Table 7.5

Activity at EOL in Bq/g in PV in zone that contains the maximum ^{60}Co activity

Irradiation	Cooling	^{51}Cr	^{54}Mn	^{55}Fe	^{59}Fe	^{58}Co	^{60}Co	^{63}Ni	^{99}Mo
60 years	7 days	0.74	1.2	71.4	3.1	0.12	2.2	0.50	1.0
	60 days	0.20	1.1	68.9	1.4	0.073	2.1	0.50	-
	2 years	-	0.25	43.3	-	-	1.7	0.49	-
	10 years	-	-	5.7	-	-	0.58	0.47	-
100 years	7 days	0.74	1.2	71.4	3.1	0.12	2.2	0.73	1.0
	60 days	0.20	1.1	68.9	1.4	0.073	2.1	0.73	-
	2 years	-	0.25	43.3	-	-	1.7	0.72	-
	10 years	-	-	5.7	-	-	0.58	0.68	-
IAEA Clearance		100	0.1	1000	1	1	0.1	100	10

Table 7.6

Activity at EOL in Bq/g in steel liner of concrete in PV well in zone that contains the maximum ^{60}Co activity

Irradiation	Cooling	^{51}Cr	^{54}Mn	^{55}Fe	^{59}Fe	^{58}Co	^{60}Co	^{63}Ni
60 years	7 days	2.8	0.080	2.3	0.066	0.15	0.31	0.39
	60 days	0.73	0.072	2.2	0.029	0.092	0.31	0.39
	2 years	-	0.017	1.4	-	-	0.24	0.39
	10 years	-	-	0.19	-	-	0.084	0.36
100 years	7 days	2.8	0.080	2.3	0.066	0.15	0.31	0.56
	60 days	0.73	0.072	2.2	0.029	0.092	0.31	0.56
	2 years	-	0.017	1.4	-	-	0.24	0.56
	10 years	-	-	0.19	-	-	0.084	0.53
IAEA Clearance		100	0.1	1000	1	1	0.1	100

Table 7.7

Activity at EOL in Bq/g in rebar in concrete in PV well in zone that contains the maximum ^{60}Co activity

Irradiation	Cooling	^{54}Mn	^{55}Fe	^{59}Fe	^{60}Co
60 years	7 days	0.051	12.6	0.32	0.39
	60 days	0.045	12.2	0.14	0.38
	2 years	0.010	7.7	-	0.29
	10 years	-	1.01	-	0.10
100 years	7 days	0.051	12.6	0.32	0.39
	60 days	0.045	12.2	0.14	0.38
	2 years	0.010	7.7	-	0.29
	10 years	-	1.01	-	0.10
IAEA Clearance		0.1	1000	1	0.1

Table 7.8

Activity at EOL in Bq/g in concrete in PV well in zone that contains the maximum ^{60}Co (and ^{152}Eu) activity

Irradiation	Cooling	^{3}H	^{40}K	^{60}Co	^{134}Cs	^{152}Eu	^{154}Eu
60 years	7 days	1.9	0.50	0.046	0.012	0.10	0.0085
	60 days	1.9	0.50	0.045	0.012	0.10	0.0085
	2 years	1.7	0.50	0.035	0.0066	0.094	0.0073
	10 years	1.1	0.50	0.012	-	0.061	0.0039
100 years	7 days	2.0	0.50	0.046	0.012	0.11	0.0085
	60 days	2.0	0.50	0.045	0.012	0.11	0.0085
	2 years	1.7	0.50	0.035	0.0066	0.097	0.0073
	10 years	1.1	0.50	0.012	-	0.064	0.0039
IAEA Clearance		100	10	0.1	0.1	0.1	0.1

Irradiation	Cooling	^{208}Tl	^{220}Rn	^{228}Ra	^{228}Th	^{232}Th	^{234m}Pa	^{234}U	^{238}U
60 years	7 days	0.0079	0.020	0.020	0.020	0.020	0.046	0.046	0.046
	60 days	0.0072	0.020	0.020	0.020	0.020	0.046	0.046	0.046
	2 years	0.0073	0.020	0.020	0.020	0.020	0.046	0.046	0.046
	10 years	0.0073	0.020	0.020	0.020	0.020	0.046	0.046	0.046
100 years	7 days	0.0079	0.020	0.020	0.020	0.020	0.046	0.046	0.046
	60 days	0.0072	0.020	0.020	0.020	0.020	0.046	0.046	0.046
	2 years	0.0073	0.020	0.020	0.020	0.020	0.046	0.046	0.046
	10 years	0.0073	0.020	0.020	0.020	0.020	0.046	0.046	0.046
IAEA Clearance		1	1	1	1	1	1	1	1

Table 7.9

Activation rates $^{59}Co(n,\gamma)^{60}Co$/g/s in various parts of the PV liner and PV with 1E+21 atom natural boron cm^{-3} relative to values with no boration (for segments see Fig. 74)

	PV liner	PV 1/4 t	PV 2/4 t	PV 3/4 t	PV 4/4 t
Cylindrical part (opposite core mid-plane) over 360°	1.00	1.00	1.00	0.99	0.87
Spherical part (just above azimuthal struts) over 360°	1.00	1.00	0.99	0.96	0.82
Under two azimuthal struts at 22.5° to EW	1.00	1.00	1.00	1.00	1.00

Table 7.10

Activation rates $^{59}Co(n,\gamma)^{60}Co$/g/s (in black), $^{151}Eu(n,\gamma)^{152}Eu$/g/s (in red) in various parts of the concrete liner and concrete with 1E+21 atom natural boron cm^{-3} relative to values with no boration (for segments see Figs. 73 and 74)

	Inner part of well	Outer part of well	Concrete liner	Concrete (3 cm)	Concrete (3 cm)	Concrete (3 cm)	Concrete (3 cm)
Cylindrical part (opposite core mid-plane) over 360°			0.57	0.29 0.082	0.19 0.055	0.15 0.042	0.11 0.033
Cylindrical part (opposite lower part of PV) over 360°			0.55	0.28 0.081	0.18 0.054	0.14 0.042	0.11 0.033
“			0.55	0.28 0.081	0.18 0.053	0.14 0.041	0.11 0.034
“			0.56	0.28 0.080	0.19 0.054	0.14 0.042	0.11 0.034
“			0.54	0.28 0.081	0.19 0.055	0.14 0.042	0.11 0.033
“			0.55	0.28 0.083	0.19 0.055	0.14 0.042	0.11 0.033
Bottom of PV well (concrete liner) over 360°	0.54	0.55					
Bottom of PV well (concrete 3 cm) over 360°	0.29 0.081	0.28 0.082					
“	0.19 0.054	0.19 0.055					
“	0.13 0.041	0.14 0.043					
“	0.11 0.033	0.11 0.034					

Table 7.11

Ratio of average Bq/g to IAEA C.L. in each of nine lower parts of PV liner (axial segments 1 to 9 from bottom to top: see Fig. 79) (100 year irradiation time)

IAEA CL		100	0.1	1000	1	1	1	0.1	100	100	
Cooling time:	lower part, axial segments:	^{51}Cr	^{54}Mn	^{55}Fe	^{59}Fe	^{57}Co	^{58}Co	^{60}Co	^{59}Ni	^{63}Ni	SUM
7 d	1	2.5E-01	2.4E+01	2.1E-02	4.5E-01	2.7E-01	4.3E+00	1.8E+01	5.6E-04	5.1E-02	4.7E+01
	1 – 2	5.4E-01	1.7E+01	4.4E-02	1.1E+00	1.7E-01	3.1E+00	4.3E+01	1.3E-03	1.1E-01	6.5E+01
	1 – 3	4.7E-01	2.7E+01	3.9E-02	8.9E-01	2.7E-01	4.9E+00	3.6E+01	1.1E-03	9.8E-02	6.9E+01
	1 – 4	3.7E-01	2.3E+01	3.1E-02	7.0E-01	2.5E-01	4.3E+00	2.8E+01	8.5E-04	7.7E-02	5.7E+01
	1 – 5	2.4E-01	1.8E+01	2.0E-02	4.5E-01	2.1E-01	3.2E+00	1.8E+01	5.6E-04	5.1E-02	4.0E+01
	1 – 6	2.2E-01	1.6E+01	1.8E-02	4.1E-01	1.9E-01	2.9E+00	1.6E+01	5.0E-04	4.6E-02	3.6E+01
	1 – 7	2.0E-01	1.5E+01	1.7E-02	3.8E-01	1.8E-01	2.7E+00	1.5E+01	4.7E-04	4.3E-02	3.4E+01
	1 – 8	1.9E-01	1.4E+01	1.6E-02	3.5E-01	1.7E-01	2.5E+00	1.4E+01	4.3E-04	3.9E-02	3.1E+01
	1 – 9	1.7E-01	1.3E+01	1.5E-02	3.2E-01	1.5E-01	2.3E+00	1.3E+01	4.0E-04	3.6E-02	2.9E+01
60 d	1	6.5E-02	2.1E+01	2.0E-02	2.0E-01	2.4E-01	2.6E+00	1.7E+01	5.6E-04	5.1E-02	4.2E+01
	1 – 2	1.4E-01	1.5E+01	4.2E-02	4.6E-01	1.5E-01	1.9E+00	4.2E+01	1.3E-03	1.1E-01	6.0E+01
	1 – 3	1.3E-01	2.4E+01	3.7E-02	3.9E-01	2.3E-01	2.9E+00	3.5E+01	1.1E-03	9.8E-02	6.3E+01
	1 – 4	9.8E-02	2.1E+01	3.0E-02	3.0E-01	2.2E-01	2.5E+00	2.7E+01	8.5E-04	7.7E-02	5.2E+01
	1 – 5	6.5E-02	1.6E+01	2.0E-02	2.0E-01	1.9E-01	1.9E+00	1.8E+01	5.6E-04	5.1E-02	3.6E+01
	1 – 6	5.9E-02	1.4E+01	1.8E-02	1.8E-01	1.7E-01	1.7E+00	1.6E+01	5.0E-04	4.6E-02	3.3E+01
	1 – 7	5.4E-02	1.3E+01	1.7E-02	1.7E-01	1.6E-01	1.6E+00	1.5E+01	4.7E-04	4.3E-02	3.0E+01
	1 – 8	5.0E-02	1.2E+01	1.5E-02	1.5E-01	1.4E-01	1.5E+00	1.4E+01	4.3E-04	3.9E-02	2.8E+01
	1 – 9	4.6E-02	1.1E+01	1.4E-02	1.4E-01	1.3E-01	1.4E+00	1.3E+01	4.0E-04	3.6E-02	2.6E+01
2 y	1	3.4E-09	4.8E+00	1.3E-02	5.8E-06	4.3E-02	3.6E-03	1.4E+01	5.6E-04	5.0E-02	1.9E+01
	1 – 2	7.6E-09	3.4E+00	2.7E-02	1.4E-05	2.7E-02	2.6E-03	3.3E+01	1.3E-03	1.1E-01	3.7E+01
	1 – 3	6.6E-09	5.3E+00	2.3E-02	1.1E-05	4.2E-02	4.1E-03	2.8E+01	1.1E-03	9.7E-02	3.3E+01
	1 – 4	5.2E-09	4.7E+00	1.9E-02	9.0E-06	4.0E-02	3.6E-03	2.2E+01	8.5E-04	7.6E-02	2.6E+01
	1 – 5	3.4E-09	3.6E+00	1.2E-02	5.8E-06	3.4E-02	2.7E-03	1.4E+01	5.6E-04	5.0E-02	1.8E+01
	1 – 6	3.0E-09	3.2E+00	1.1E-02	5.3E-06	3.1E-02	2.5E-03	1.3E+01	5.0E-04	4.5E-02	1.6E+01
	1 – 7	2.8E-09	3.0E+00	1.0E-02	4.9E-06	2.9E-02	2.3E-03	1.2E+01	4.7E-04	4.2E-02	1.5E+01
	1 – 8	2.6E-09	2.8E+00	9.6E-03	4.5E-06	2.6E-02	2.1E-03	1.1E+01	4.3E-04	3.9E-02	1.4E+01
	1 – 9	2.4E-09	2.5E+00	8.8E-03	4.1E-06	2.4E-02	1.9E-03	1.0E+01	4.0E-04	3.6E-02	1.3E+01
10 y	1	0.0E+00	7.3E-03	1.7E-03	0.0E+00	2.5E-05	0.0E+00	4.8E+00	5.6E-04	4.8E-02	4.8E+00
	1 – 2	0.0E+00	5.2E-03	3.5E-03	0.0E+00	1.6E-05	0.0E+00	1.2E+01	1.3E-03	1.1E-01	1.2E+01
	1 – 3	0.0E+00	8.2E-03	3.1E-03	0.0E+00	2.5E-05	0.0E+00	9.7E+00	1.1E-03	9.2E-02	9.8E+00
	1 – 4	0.0E+00	7.2E-03	2.4E-03	0.0E+00	2.3E-05	0.0E+00	7.5E+00	8.5E-04	7.2E-02	7.6E+00
	1 – 5	0.0E+00	5.4E-03	1.6E-03	0.0E+00	2.0E-05	0.0E+00	4.9E+00	5.6E-04	4.7E-02	5.0E+00
	1 – 6	0.0E+00	4.9E-03	1.5E-03	0.0E+00	1.8E-05	0.0E+00	4.4E+00	5.0E-04	4.3E-02	4.5E+00
	1 – 7	0.0E+00	4.6E-03	1.4E-03	0.0E+00	1.7E-05	0.0E+00	4.1E+00	4.7E-04	4.0E-02	4.2E+00
	1 – 8	0.0E+00	4.2E-03	1.3E-03	0.0E+00	1.5E-05	0.0E+00	3.8E+00	4.3E-04	3.7E-02	3.8E+00
	1 – 9	0.0E+00	3.9E-03	1.2E-03	0.0E+00	1.4E-05	0.0E+00	3.5E+00	4.0E-04	3.4E-02	3.5E+00

Table 7.12

Ratio of average Bq/g to IAEA C.L. in each of nine axial segments of PV liner (segments 1 to 9 from bottom to top: see Fig. 79) (100 year irradiation time)

IAEA CL		100	0.1	1000	1	1	1	0.1	100	100	
Cooling time:	Axial segment	^{51}Cr	^{54}Mn	^{55}Fe	^{59}Fe	^{57}Co	^{58}Co	^{60}Co	^{59}Ni	^{63}Ni	SUM
7 d	1	2.5E-01	2.4E+01	2.1E-02	4.5E-01	2.7E-01	4.3E+00	1.8E+01	5.6E-04	5.1E-02	4.7E+01
	2	6.6E-01	1.4E+01	5.3E-02	1.3E+00	1.3E-01	2.6E+00	5.3E+01	1.5E-03	1.4E-01	7.2E+01
	3	3.9E-01	3.7E+01	3.3E-02	7.1E-01	3.7E-01	6.8E+00	2.8E+01	9.0E-04	8.2E-02	7.4E+01
	4	1.7E-01	1.7E+01	1.4E-02	3.0E-01	2.2E-01	3.1E+00	1.2E+01	3.8E-04	3.5E-02	3.3E+01
	5	1.2E-01	1.2E+01	1.1E-02	2.2E-01	1.8E-01	2.2E+00	9.0E+00	2.8E-04	2.6E-02	2.4E+01
	6	2.5E-02	2.5E+00	2.2E-03	4.5E-02	3.9E-02	4.4E-01	1.8E+00	5.6E-05	5.1E-03	4.9E+00
	7	2.5E-03	2.3E-01	2.2E-04	4.7E-03	4.7E-03	4.1E-02	1.9E-01	5.7E-06	5.2E-04	4.7E-01
	8	3.3E-04	1.4E-02	2.8E-05	6.4E-04	3.8E-04	2.4E-03	2.6E-02	7.6E-07	6.9E-05	4.3E-02
	9	8.3E-05	2.3E-04	6.6E-06	1.6E-04	8.0E-06	3.9E-05	6.6E-03	1.9E-07	1.7E-05	7.1E-03
60 d	1	6.5E-02	2.1E+01	2.0E-02	2.0E-01	2.4E-01	2.6E+00	1.7E+01	5.6E-04	5.1E-02	4.2E+01
	2	1.8E-01	1.3E+01	5.1E-02	5.7E-01	1.2E-01	1.6E+00	5.2E+01	1.5E-03	1.4E-01	6.7E+01
	3	1.0E-01	3.3E+01	3.2E-02	3.1E-01	3.3E-01	4.0E+00	2.8E+01	9.0E-04	8.2E-02	6.6E+01
	4	4.4E-02	1.5E+01	1.4E-02	1.3E-01	1.9E-01	1.8E+00	1.2E+01	3.8E-04	3.5E-02	2.9E+01
	5	3.3E-02	1.1E+01	1.0E-02	9.8E-02	1.5E-01	1.3E+00	8.8E+00	2.8E-04	2.6E-02	2.1E+01
	6	6.6E-03	2.2E+00	2.1E-03	2.0E-02	3.4E-02	2.6E-01	1.8E+00	5.6E-05	5.1E-03	4.3E+00
	7	6.7E-04	2.0E-01	2.2E-04	2.1E-03	4.1E-03	2.4E-02	1.9E-01	5.7E-06	5.2E-04	4.2E-01
	8	8.8E-05	1.2E-02	2.7E-05	2.8E-04	3.3E-04	1.4E-03	2.5E-02	7.6E-07	6.8E-05	4.0E-02
	9	2.2E-05	2.0E-04	6.4E-06	7.2E-05	7.0E-06	2.3E-05	6.4E-03	1.9E-07	1.7E-05	6.8E-03
2 y	1	3.4E-09	4.8E+00	1.3E-02	5.8E-06	4.3E-02	3.6E-03	1.4E+01	5.6E-04	5.0E-02	1.9E+01
	2	9.2E-09	2.9E+00	3.2E-02	1.7E-05	2.1E-02	2.2E-03	4.1E+01	1.5E-03	1.4E-01	4.4E+01
	3	5.5E-09	7.5E+00	2.0E-02	9.2E-06	5.9E-02	5.8E-03	2.2E+01	9.0E-04	8.1E-02	2.9E+01
	4	2.3E-09	3.4E+00	8.7E-03	3.9E-06	3.5E-02	2.6E-03	9.3E+00	3.8E-04	3.4E-02	1.3E+01
	5	1.7E-09	2.5E+00	6.5E-03	2.9E-06	2.8E-02	1.9E-03	6.9E+00	2.8E-04	2.5E-02	9.4E+00
	6	0.0E+00	5.0E-01	1.3E-03	5.8E-07	6.2E-03	3.8E-04	1.4E+00	5.6E-05	5.1E-03	1.9E+00
	7	0.0E+00	4.6E-02	1.4E-04	6.0E-08	7.4E-04	3.5E-05	1.5E-01	5.7E-06	5.1E-04	1.9E-01
	8	0.0E+00	2.8E-03	1.7E-05	0.0E+00	6.1E-05	2.0E-06	2.0E-02	7.6E-07	6.8E-05	2.3E-02
	9	0.0E+00	4.6E-05	4.0E-06	0.0E+00	1.3E-06	3.3E-08	5.1E-03	1.9E-07	1.7E-05	5.1E-03
10 y	1	0.0E+00	7.3E-03	1.7E-03	0.0E+00	2.5E-05	0.0E+00	4.8E+00	5.6E-04	4.8E-02	4.8E+00
	2	0.0E+00	4.4E-03	4.2E-03	0.0E+00	1.2E-05	0.0E+00	1.4E+01	1.5E-03	1.3E-01	1.4E+01
	3	0.0E+00	1.1E-02	2.6E-03	0.0E+00	3.4E-05	0.0E+00	7.6E+00	9.0E-04	7.6E-02	7.7E+00
	4	0.0E+00	5.2E-03	1.1E-03	0.0E+00	2.0E-05	0.0E+00	3.2E+00	3.8E-04	3.2E-02	3.3E+00
	5	0.0E+00	3.8E-03	8.5E-04	0.0E+00	1.6E-05	0.0E+00	2.4E+00	2.8E-04	2.4E-02	2.4E+00
	6	0.0E+00	7.6E-04	1.7E-04	0.0E+00	3.6E-06	0.0E+00	4.9E-01	5.6E-05	4.8E-03	4.9E-01
	7	0.0E+00	7.0E-05	1.8E-05	0.0E+00	4.3E-07	0.0E+00	5.1E-02	5.7E-06	4.8E-04	5.2E-02
	8	0.0E+00	4.2E-06	2.3E-06	0.0E+00	3.5E-08	0.0E+00	6.9E-03	7.6E-07	6.4E-05	7.0E-03
	9	0.0E+00	7.0E-08	5.3E-07	0.0E+00	0.0E+00	0.0E+00	1.8E-03	1.9E-07	1.6E-05	1.8E-03

Table 7.13

Ratio of average Bq/g to IAEA C.L. in each of nine lower parts of PV (axial segments 1 to 9 from bottom to top: see Fig. 79) (100 year irradiation time)

IAEA CL		100	0.1	1000	1	1	0.1	100	10	
Cooling time:	lower part, axial segments:	^{51}Cr	^{54}Mn	^{55}Fe	^{59}Fe	^{58}Co	^{60}Co	^{63}Ni	^{99}Mo	SUM
7 d	1	8.3E-04	1.3E+01	3.9E-03	8.7E-02	1.2E-01	4.9E-01	4.2E-04	1.3E-03	1.3E+01
	1 – 2	1.1E-03	9.2E+00	7.7E-03	2.3E-01	8.8E-02	1.3E+00	9.1E-04	4.3E-03	1.1E+01
	1 – 3	1.2E-03	1.4E+01	6.8E-03	1.8E-01	1.4E-01	1.0E+00	7.9E-04	3.1E-03	1.6E+01
	1 – 4	9.9E-04	1.3E+01	5.5E-03	1.4E-01	1.2E-01	7.8E-01	6.2E-04	2.4E-03	1.4E+01
	1 – 5	4.8E-04	6.6E+00	2.6E-03	6.2E-02	6.3E-02	3.5E-01	2.8E-04	1.1E-03	7.1E+00
	1 – 6	4.2E-04	5.8E+00	2.2E-03	5.4E-02	5.5E-02	3.1E-01	2.4E-04	9.7E-04	6.2E+00
	1 – 7	3.9E-04	5.3E+00	2.0E-03	5.0E-02	5.0E-02	2.8E-01	2.2E-04	8.8E-04	5.6E+00
	1 – 8	3.5E-04	4.7E+00	1.8E-03	4.5E-02	4.5E-02	2.5E-01	2.0E-04	8.0E-04	5.1E+00
	1 – 9	3.1E-04	4.3E+00	1.7E-03	4.0E-02	4.1E-02	2.3E-01	1.8E-04	7.2E-04	4.6E+00
60 d	1	2.2E-04	1.1E+01	3.8E-03	3.8E-02	7.2E-02	4.8E-01	4.2E-04	0.0E+00	1.2E+01
	1 – 2	3.0E-04	8.2E+00	7.4E-03	9.9E-02	5.2E-02	1.3E+00	9.1E-04	6.2E-09	9.6E+00
	1 – 3	3.2E-04	1.3E+01	6.6E-03	7.8E-02	8.2E-02	9.8E-01	7.9E-04	4.1E-09	1.4E+01
	1 – 4	2.6E-04	1.1E+01	5.3E-03	6.1E-02	7.2E-02	7.6E-01	6.2E-04	2.7E-09	1.2E+01
	1 – 5	1.3E-04	5.8E+00	2.5E-03	2.7E-02	3.7E-02	3.4E-01	2.8E-04	1.4E-09	6.3E+00
	1 – 6	1.1E-04	5.1E+00	2.2E-03	2.4E-02	3.3E-02	3.0E-01	2.4E-04	1.2E-09	5.5E+00
	1 – 7	1.0E-04	4.7E+00	2.0E-03	2.2E-02	3.0E-02	2.8E-01	2.2E-04	1.1E-09	5.0E+00
	1 – 8	9.2E-05	4.2E+00	1.8E-03	2.0E-02	2.7E-02	2.5E-01	2.0E-04	9.9E-10	4.5E+00
	1 – 9	8.3E-05	3.8E+00	1.6E-03	1.8E-02	2.4E-02	2.2E-01	1.8E-04	9.0E-10	4.1E+00
2 y	1	0.0E+00	2.6E+00	2.4E-03	1.1E-06	1.0E-04	3.8E-01	4.2E-04	0.0E+00	2.9E+00
	1 – 2	0.0E+00	1.9E+00	4.7E-03	2.9E-06	7.5E-05	9.9E-01	9.0E-04	0.0E+00	2.8E+00
	1 – 3	0.0E+00	2.9E+00	4.1E-03	2.3E-06	1.2E-04	7.7E-01	7.8E-04	0.0E+00	3.7E+00
	1 – 4	0.0E+00	2.5E+00	3.3E-03	1.8E-06	1.0E-04	6.0E-01	6.1E-04	0.0E+00	3.1E+00
	1 – 5	1.6E-12	1.3E+00	1.5E-03	8.0E-07	5.3E-05	2.7E-01	2.7E-04	0.0E+00	1.6E+00
	1 – 6	1.4E-12	1.2E+00	1.4E-03	7.0E-07	4.7E-05	2.4E-01	2.4E-04	0.0E+00	1.4E+00
	1 – 7	1.3E-12	1.1E+00	1.2E-03	6.4E-07	4.2E-05	2.2E-01	2.2E-04	0.0E+00	1.3E+00
	1 – 8	1.2E-12	9.5E-01	1.1E-03	5.8E-07	3.8E-05	2.0E-01	2.0E-04	0.0E+00	1.1E+00
	1 – 9	1.1E-12	8.6E-01	1.0E-03	5.2E-07	3.5E-05	1.8E-01	1.8E-04	0.0E+00	1.0E+00
10 y	1	0.0E+00	3.9E-03	3.1E-04	0.0E+00	0.0E+00	1.3E-01	4.0E-04	0.0E+00	1.4E-01
	1 – 2	0.0E+00	2.8E-03	6.2E-04	0.0E+00	0.0E+00	3.5E-01	8.5E-04	0.0E+00	3.5E-01
	1 – 3	0.0E+00	4.4E-03	5.4E-04	0.0E+00	0.0E+00	2.7E-01	7.4E-04	0.0E+00	2.8E-01
	1 – 4	0.0E+00	3.9E-03	4.4E-04	0.0E+00	0.0E+00	2.1E-01	5.8E-04	0.0E+00	2.1E-01
	1 – 5	0.0E+00	2.0E-03	2.0E-04	0.0E+00	0.0E+00	9.5E-02	2.6E-04	0.0E+00	9.7E-02
	1 – 6	0.0E+00	1.8E-03	1.8E-04	0.0E+00	0.0E+00	8.3E-02	2.3E-04	0.0E+00	8.5E-02
	1 – 7	0.0E+00	1.6E-03	1.6E-04	0.0E+00	0.0E+00	7.6E-02	2.1E-04	0.0E+00	7.8E-02
	1 – 8	0.0E+00	1.5E-03	1.5E-04	0.0E+00	0.0E+00	6.8E-02	1.9E-04	0.0E+00	7.0E-02
	1 – 9	0.0E+00	1.3E-03	1.3E-04	0.0E+00	0.0E+00	6.2E-02	1.7E-04	0.0E+00	6.3E-02

Table 7.14

Ratio of average Bq/g to IAEA C.L. in each of nine axial segments of PV (segments 1 to 9 from bottom to top: see Fig. 79) (100 year irradiation time)

IAEA CL		100	0.1	1000	1	1	0.1	100	10	
Cooling time:	Axial segment	^{51}Cr	^{54}Mn	^{55}Fe	^{59}Fe	^{58}Co	^{60}Co	^{63}Ni	^{99}Mo	SUM
7 d	1	8.3E-04	1.3E+01	3.9E-03	8.7E-02	1.2E-01	4.9E-01	4.2E-04	1.3E-03	1.3E+01
	2	1.3E-03	7.8E+00	9.2E-03	2.8E-01	7.5E-02	1.6E+00	1.1E-03	5.5E-03	9.8E+00
	3	1.2E-03	2.0E+01	5.8E-03	1.3E-01	1.9E-01	6.9E-01	6.5E-04	1.7E-03	2.1E+01
	4	5.9E-04	9.2E+00	2.8E-03	5.9E-02	8.7E-02	3.3E-01	2.9E-04	8.9E-04	9.7E+00
	5	2.4E-04	3.7E+00	1.2E-03	2.5E-02	3.5E-02	1.5E-01	1.1E-04	5.0E-04	3.9E+00
	6	5.1E-05	7.4E-01	2.6E-04	6.0E-03	7.0E-03	3.6E-02	2.4E-05	1.3E-04	7.9E-01
	7	6.7E-06	6.9E-02	4.3E-05	1.4E-03	6.5E-04	9.4E-03	4.0E-06	4.2E-05	8.1E-02
	8	1.3E-06	4.1E-03	1.2E-05	4.8E-04	3.9E-05	3.6E-03	1.2E-06	1.7E-05	8.3E-03
	9	5.0E-07	1.4E-04	4.8E-06	2.2E-04	1.7E-06	1.6E-03	5.1E-07	7.3E-06	2.0E-03
60 d	1	2.2E-04	1.1E+01	3.8E-03	3.8E-02	7.2E-02	4.8E-01	4.2E-04	0.0E+00	1.2E+01
	2	3.4E-04	7.0E+00	8.9E-03	1.2E-01	4.5E-02	1.6E+00	1.1E-03	8.6E-09	8.7E+00
	3	3.3E-04	1.8E+01	5.6E-03	5.6E-02	1.1E-01	6.8E-01	6.5E-04	1.7E-09	1.9E+01
	4	1.6E-04	8.2E+00	2.7E-03	2.6E-02	5.2E-02	3.3E-01	2.9E-04	0.0E+00	8.6E+00
	5	6.3E-05	3.3E+00	1.1E-03	1.1E-02	2.1E-02	1.4E-01	1.1E-04	7.8E-10	3.4E+00
	6	1.4E-05	6.6E-01	2.5E-04	2.6E-03	4.2E-03	3.5E-02	2.4E-05	0.0E+00	7.0E-01
	7	1.8E-06	6.2E-02	4.2E-05	6.0E-04	3.9E-04	9.2E-03	4.0E-06	0.0E+00	7.2E-02
	8	3.5E-07	3.7E-03	1.1E-05	2.1E-04	2.3E-05	3.6E-03	1.2E-06	0.0E+00	7.5E-03
	9	1.3E-07	1.3E-04	4.6E-06	9.5E-05	1.0E-06	1.6E-03	5.1E-07	0.0E+00	1.8E-03
2 y	1	0.0E+00	2.6E+00	2.4E-03	1.1E-06	1.0E-04	3.8E-01	4.2E-04	0.0E+00	2.9E+00
	2	0.0E+00	1.6E+00	5.6E-03	3.6E-06	6.4E-05	1.2E+00	1.1E-03	0.0E+00	2.8E+00
	3	0.0E+00	4.0E+00	3.5E-03	1.6E-06	1.6E-04	5.3E-01	6.4E-04	0.0E+00	4.6E+00
	4	0.0E+00	1.8E+00	1.7E-03	7.6E-07	7.4E-05	2.6E-01	2.8E-04	0.0E+00	2.1E+00
	5	2.4E-12	7.4E-01	7.0E-04	3.3E-07	3.0E-05	1.1E-01	1.1E-04	0.0E+00	8.5E-01
	6	0.0E+00	1.5E-01	1.6E-04	7.7E-08	5.9E-06	2.7E-02	2.4E-05	0.0E+00	1.8E-01
	7	0.0E+00	1.4E-02	2.6E-05	1.8E-08	5.5E-07	7.2E-03	3.9E-06	0.0E+00	2.1E-02
	8	0.0E+00	8.3E-04	7.0E-06	6.1E-09	3.3E-08	2.8E-03	1.1E-06	0.0E+00	3.6E-03
	9	0.0E+00	2.9E-05	2.9E-06	2.5E-09	1.1E-09	1.3E-03	5.0E-07	0.0E+00	1.3E-03
10 y	1	0.0E+00	3.9E-03	3.1E-04	0.0E+00	0.0E+00	1.3E-01	4.0E-04	0.0E+00	1.4E-01
	2	0.0E+00	2.4E-03	7.4E-04	0.0E+00	0.0E+00	4.3E-01	1.0E-03	0.0E+00	4.3E-01
	3	0.0E+00	6.1E-03	4.6E-04	0.0E+00	0.0E+00	1.9E-01	6.1E-04	0.0E+00	1.9E-01
	4	0.0E+00	2.8E-03	2.2E-04	0.0E+00	0.0E+00	8.9E-02	2.7E-04	0.0E+00	9.2E-02
	5	0.0E+00	1.1E-03	9.2E-05	0.0E+00	0.0E+00	3.9E-02	1.0E-04	0.0E+00	4.1E-02
	6	0.0E+00	2.3E-04	2.1E-05	0.0E+00	0.0E+00	9.6E-03	2.3E-05	0.0E+00	9.9E-03
	7	0.0E+00	2.1E-05	3.5E-06	0.0E+00	0.0E+00	2.5E-03	3.7E-06	0.0E+00	2.6E-03
	8	0.0E+00	1.3E-06	9.3E-07	0.0E+00	0.0E+00	9.8E-04	1.1E-06	0.0E+00	9.8E-04
	9	0.0E+00	4.4E-08	3.8E-07	0.0E+00	0.0E+00	4.4E-04	4.7E-07	0.0E+00	4.4E-04

Table 7.15

Ratio of average Bq/g to IAEA C.L. in each of nine lower parts of PV and PV liner (axial segments 1 to 9 from bottom to top: see Fig. 79) (100 year irradiation time)

IAEA CL		100	0.1	1000	1	1	1	0.1	100	100	10	
Cooling time:	lower part, axial segments:	^{51}Cr	^{54}Mn	^{55}Fe	^{59}Fe	^{57}Co	^{58}Co	^{60}Co	^{59}Ni	^{63}Ni	^{99}Mo	SUM
7 d	1	8.9E-03	1.3E+01	4.5E-03	9.9E-02	1.6E-02	2.6E-01	1.1E+00	2.3E-05	2.1E-03	1.3E-03	1.5E+01
	1 – 2	1.9E-02	9.5E+00	8.9E-03	2.5E-01	1.0E-02	1.9E-01	2.7E+00	5.2E-05	4.6E-03	4.2E-03	1.3E+01
	1 – 3	1.7E-02	1.5E+01	7.9E-03	2.0E-01	1.6E-02	2.9E-01	2.2E+00	4.4E-05	4.0E-03	3.0E-03	1.7E+01
	1 – 4	1.3E-02	1.3E+01	6.3E-03	1.6E-01	1.5E-02	2.6E-01	1.7E+00	3.5E-05	3.2E-03	2.3E-03	1.5E+01
	1 – 5	5.9E-03	6.8E+00	2.9E-03	7.1E-02	8.9E-03	1.3E-01	7.5E-01	1.5E-05	1.4E-03	1.1E-03	7.8E+00
	1 – 6	5.1E-03	6.0E+00	2.6E-03	6.2E-02	7.8E-03	1.2E-01	6.5E-01	1.3E-05	1.2E-03	9.5E-04	6.8E+00
	1 – 7	4.7E-03	5.5E+00	2.4E-03	5.7E-02	7.1E-03	1.1E-01	6.0E-01	1.2E-05	1.1E-03	8.7E-04	6.2E+00
	1 – 8	4.2E-03	4.9E+00	2.1E-03	5.1E-02	6.4E-03	9.5E-02	5.4E-01	1.1E-05	1.0E-03	7.8E-04	5.6E+00
	1 – 9	3.8E-03	4.5E+00	1.9E-03	4.6E-02	5.8E-03	8.6E-02	4.9E-01	1.0E-05	9.0E-04	7.1E-04	5.1E+00
60 d	1	2.4E-03	1.2E+01	4.3E-03	4.3E-02	1.4E-02	1.5E-01	1.0E+00	2.3E-05	2.1E-03	0.0E+00	1.3E+01
	1 – 2	5.1E-03	8.4E+00	8.6E-03	1.1E-01	9.1E-03	1.1E-01	2.6E+00	5.2E-05	4.6E-03	6.0E-09	1.1E+01
	1 – 3	4.4E-03	1.3E+01	7.6E-03	8.9E-02	1.4E-02	1.7E-01	2.1E+00	4.4E-05	4.0E-03	3.9E-09	1.6E+01
	1 – 4	3.5E-03	1.2E+01	6.1E-03	6.9E-02	1.3E-02	1.5E-01	1.6E+00	3.5E-05	3.1E-03	2.6E-09	1.3E+01
	1 – 5	1.6E-03	6.1E+00	2.8E-03	3.1E-02	7.7E-03	7.9E-02	7.3E-01	1.5E-05	1.4E-03	1.4E-09	6.9E+00
	1 – 6	1.4E-03	5.3E+00	2.5E-03	2.7E-02	6.8E-03	6.9E-02	6.4E-01	1.3E-05	1.2E-03	1.2E-09	6.1E+00
	1 – 7	1.2E-03	4.9E+00	2.3E-03	2.5E-02	6.2E-03	6.3E-02	5.9E-01	1.2E-05	1.1E-03	1.1E-09	5.5E+00
	1 – 8	1.1E-03	4.4E+00	2.0E-03	2.2E-02	5.6E-03	5.7E-02	5.3E-01	1.1E-05	1.0E-03	9.7E-10	5.0E+00
	1 – 9	1.0E-03	4.0E+00	1.9E-03	2.0E-02	5.1E-03	5.1E-02	4.8E-01	1.0E-05	9.0E-04	8.8E-10	4.5E+00
2 y	1	1.1E-10	2.6E+00	2.7E-03	1.3E-06	2.6E-03	2.2E-04	8.1E-01	2.3E-05	2.1E-03	0.0E+00	3.5E+00
	1 – 2	2.5E-10	1.9E+00	5.4E-03	3.3E-06	1.7E-03	1.6E-04	2.1E+00	5.2E-05	4.6E-03	0.0E+00	4.0E+00
	1 – 3	2.2E-10	3.0E+00	4.8E-03	2.6E-06	2.6E-03	2.5E-04	1.7E+00	4.4E-05	4.0E-03	0.0E+00	4.6E+00
	1 – 4	1.7E-10	2.6E+00	3.8E-03	2.0E-06	2.4E-03	2.2E-04	1.3E+00	3.5E-05	3.1E-03	0.0E+00	3.9E+00
	1 – 5	7.7E-11	1.4E+00	1.8E-03	9.1E-07	1.4E-03	1.1E-04	5.8E-01	1.5E-05	1.4E-03	0.0E+00	2.0E+00
	1 – 6	6.6E-11	1.2E+00	1.6E-03	8.0E-07	1.2E-03	9.8E-05	5.0E-01	1.3E-05	1.2E-03	0.0E+00	1.7E+00
	1 – 7	6.0E-11	1.1E+00	1.4E-03	7.3E-07	1.1E-03	9.0E-05	4.6E-01	1.2E-05	1.1E-03	0.0E+00	1.6E+00
	1 – 8	5.4E-11	9.9E-01	1.3E-03	6.6E-07	1.0E-03	8.1E-05	4.1E-01	1.1E-05	9.9E-04	0.0E+00	1.4E+00
	1 – 9	4.9E-11	8.9E-01	1.2E-03	5.9E-07	9.2E-04	7.3E-05	3.7E-01	1.0E-05	8.9E-04	0.0E+00	1.3E+00
10 y	1	0.0E+00	4.0E-03	3.6E-04	0.0E+00	1.5E-06	0.0E+00	2.8E-01	2.3E-05	2.0E-03	0.0E+00	2.9E-01
	1 – 2	0.0E+00	2.9E-03	7.1E-04	0.0E+00	9.6E-07	0.0E+00	7.2E-01	5.2E-05	4.3E-03	0.0E+00	7.2E-01
	1 – 3	0.0E+00	4.5E-03	6.3E-04	0.0E+00	1.5E-06	0.0E+00	5.8E-01	4.4E-05	3.7E-03	0.0E+00	5.9E-01
	1 – 4	0.0E+00	4.0E-03	5.0E-04	0.0E+00	1.4E-06	0.0E+00	4.5E-01	3.5E-05	2.9E-03	0.0E+00	4.6E-01
	1 – 5	0.0E+00	2.1E-03	2.4E-04	0.0E+00	8.1E-07	0.0E+00	2.0E-01	1.5E-05	1.3E-03	0.0E+00	2.0E-01
	1 – 6	0.0E+00	1.8E-03	2.1E-04	0.0E+00	7.2E-07	0.0E+00	1.8E-01	1.3E-05	1.1E-03	0.0E+00	1.8E-01
	1 – 7	0.0E+00	1.7E-03	1.9E-04	0.0E+00	6.5E-07	0.0E+00	1.6E-01	1.2E-05	1.0E-03	0.0E+00	1.6E-01
	1 – 8	0.0E+00	1.5E-03	1.7E-04	0.0E+00	5.9E-07	0.0E+00	1.4E-01	1.1E-05	9.3E-04	0.0E+00	1.5E-01
	1 – 9	0.0E+00	1.4E-03	1.5E-04	0.0E+00	5.3E-07	0.0E+00	1.3E-01	1.0E-05	8.4E-04	0.0E+00	1.3E-01

Table 7.16

Ratio of average Bq/g to IAEA C.L. in each of nine axial segments of PV and PV liner (segments 1 to 9 from bottom to top: see Fig. 79) (100 year irradiation time)

IAEA CL		100	0.1	1000	1	1	1	0.1	100	100	10	
Cooling time:	Axial segment	^{51}Cr	^{54}Mn	^{55}Fe	^{59}Fe	^{57}Co	^{58}Co	^{60}Co	^{59}Ni	^{63}Ni	^{99}Mo	SUM
7 d	1	8.9E-03	1.3E+01	4.5E-03	9.9E-02	1.6E-02	2.6E-01	1.1E+00	2.3E-05	2.1E-03	1.3E-03	1.5E+01
	2	2.3E-02	8.0E+00	1.1E-02	3.1E-01	8.0E-03	1.6E-01	3.3E+00	6.3E-05	5.6E-03	5.3E-03	1.2E+01
	3	1.4E-02	2.1E+01	6.7E-03	1.5E-01	2.3E-02	4.1E-01	1.6E+00	3.6E-05	3.3E-03	1.6E-03	2.3E+01
	4	6.1E-03	9.5E+00	3.2E-03	6.7E-02	1.3E-02	1.9E-01	7.2E-01	1.5E-05	1.4E-03	8.6E-04	1.0E+01
	5	2.3E-03	3.8E+00	1.3E-03	2.9E-02	5.7E-03	7.1E-02	2.9E-01	5.9E-06	5.4E-04	4.9E-04	4.2E+00
	6	4.7E-04	7.7E-01	2.9E-04	6.6E-03	1.3E-03	1.4E-02	6.6E-02	1.2E-06	1.1E-04	1.3E-04	8.6E-01
	7	4.9E-05	7.2E-02	4.6E-05	1.4E-03	1.5E-04	1.3E-03	1.2E-02	1.4E-07	1.3E-05	4.1E-05	8.8E-02
	8	6.9E-06	4.3E-03	1.2E-05	4.8E-04	1.2E-05	7.8E-05	4.0E-03	2.8E-08	2.3E-06	1.6E-05	8.9E-03
	9	1.9E-06	1.4E-04	4.8E-06	2.2E-04	2.4E-07	2.3E-06	1.7E-03	9.7E-09	7.9E-07	7.2E-06	2.1E-03
60 d	1	2.4E-03	1.2E+01	4.3E-03	4.3E-02	1.4E-02	1.5E-01	1.0E+00	2.3E-05	2.1E-03	0.0E+00	1.3E+01
	2	6.1E-03	7.2E+00	1.0E-02	1.4E-01	7.0E-03	9.5E-02	3.2E+00	6.3E-05	5.6E-03	8.4E-09	1.1E+01
	3	3.8E-03	1.8E+01	6.5E-03	6.4E-02	2.0E-02	2.4E-01	1.6E+00	3.6E-05	3.3E-03	1.6E-09	2.0E+01
	4	1.6E-03	8.4E+00	3.0E-03	2.9E-02	1.2E-02	1.1E-01	7.0E-01	1.5E-05	1.4E-03	0.0E+00	9.3E+00
	5	6.1E-04	3.4E+00	1.3E-03	1.3E-02	5.0E-03	4.2E-02	2.9E-01	5.9E-06	5.4E-04	7.7E-10	3.7E+00
	6	1.2E-04	6.8E-01	2.8E-04	2.9E-03	1.1E-03	8.5E-03	6.4E-02	1.2E-06	1.1E-04	0.0E+00	7.6E-01
	7	1.3E-05	6.4E-02	4.5E-05	6.2E-04	1.3E-04	7.9E-04	1.2E-02	1.4E-07	1.3E-05	0.0E+00	7.8E-02
	8	1.8E-06	3.8E-03	1.1E-05	2.1E-04	1.1E-05	4.6E-05	3.9E-03	2.8E-08	2.3E-06	0.0E+00	8.0E-03
	9	5.0E-07	1.3E-04	4.6E-06	9.4E-05	2.1E-07	1.4E-06	1.7E-03	9.7E-09	7.9E-07	0.0E+00	1.9E-03
2 y	1	1.1E-10	2.6E+00	2.7E-03	1.3E-06	2.6E-03	2.2E-04	8.1E-01	2.3E-05	2.1E-03	0.0E+00	3.5E+00
	2	3.0E-10	1.6E+00	6.5E-03	4.0E-06	1.3E-03	1.4E-04	2.5E+00	6.3E-05	5.6E-03	0.0E+00	4.2E+00
	3	1.8E-10	4.1E+00	4.1E-03	1.9E-06	3.6E-03	3.5E-04	1.2E+00	3.6E-05	3.3E-03	0.0E+00	5.4E+00
	4	7.7E-11	1.9E+00	1.9E-03	8.6E-07	2.1E-03	1.6E-04	5.5E-01	1.5E-05	1.4E-03	0.0E+00	2.5E+00
	5	3.1E-11	7.7E-01	8.0E-04	3.7E-07	9.1E-04	6.0E-05	2.3E-01	5.9E-06	5.3E-04	0.0E+00	1.0E+00
	6	0.0E+00	1.5E-01	1.8E-04	8.5E-08	2.0E-04	1.2E-05	5.1E-02	1.2E-06	1.1E-04	0.0E+00	2.1E-01
	7	0.0E+00	1.4E-02	2.8E-05	1.8E-08	2.4E-05	1.1E-06	9.6E-03	1.4E-07	1.2E-05	0.0E+00	2.4E-02
	8	0.0E+00	8.6E-04	7.2E-06	6.0E-09	1.9E-06	6.6E-08	3.1E-03	2.8E-08	2.2E-06	0.0E+00	4.0E-03
	9	0.0E+00	2.9E-05	2.9E-06	2.5E-09	3.9E-08	1.7E-09	1.3E-03	9.7E-09	7.8E-07	0.0E+00	1.4E-03
10 y	1	0.0E+00	4.0E-03	3.6E-04	0.0E+00	1.5E-06	0.0E+00	2.8E-01	2.3E-05	2.0E-03	0.0E+00	2.9E-01
	2	0.0E+00	2.5E-03	8.5E-04	0.0E+00	7.4E-07	0.0E+00	8.9E-01	6.3E-05	5.3E-03	0.0E+00	9.0E-01
	3	0.0E+00	6.3E-03	5.3E-04	0.0E+00	2.1E-06	0.0E+00	4.3E-01	3.6E-05	3.1E-03	0.0E+00	4.4E-01
	4	0.0E+00	2.9E-03	2.5E-04	0.0E+00	1.2E-06	0.0E+00	1.9E-01	1.5E-05	1.3E-03	0.0E+00	2.0E-01
	5	0.0E+00	1.2E-03	1.1E-04	0.0E+00	5.3E-07	0.0E+00	7.9E-02	5.9E-06	5.0E-04	0.0E+00	8.1E-02
	6	0.0E+00	2.4E-04	2.3E-05	0.0E+00	1.2E-07	0.0E+00	1.8E-02	1.2E-06	1.0E-04	0.0E+00	1.8E-02
	7	0.0E+00	2.2E-05	3.7E-06	0.0E+00	1.4E-08	0.0E+00	3.4E-03	1.4E-07	1.2E-05	0.0E+00	3.4E-03
	8	0.0E+00	1.3E-06	9.5E-07	0.0E+00	1.1E-09	0.0E+00	1.1E-03	2.8E-08	2.1E-06	0.0E+00	1.1E-03
	9	0.0E+00	4.4E-08	3.8E-07	0.0E+00	0.0E+00	0.0E+00	4.6E-04	9.7E-09	7.4E-07	0.0E+00	4.6E-04

8. MAINTENANCE DOSES IN THE PRESSURE VESSEL WELL

8.1 Calculational model for the neutron transport: materials and geometry

The source and core models were identical to those employed for the EOL activity in the PV, steel liner and concrete (§7.1).

The materials to be activated may be conveniently divided into those within the pressure vessel and those outside, including the pressure vessel itself.

For the zones including and outside the pressure vessel (the PV liner, the PV, the steel concrete liner and the reinforced concrete), the material description and in particular the assumed impurities, are identical to those employed to estimate the EOL activities and are given in §7.1.1, §7.1.2 and §7.1.3.

For zones within the pressure vessel (the active core, the upper and lower plena regions, the bottom and top plates, the reflector, the barrel, the bottom plate annular support and the eight azimuthal supports), the compositions are those discussed in §4.2.1 to §4.2.4, §4.2.6, §4.2.7 and §4.2.9.

Where AISI-304L steel [37] is employed in the plena regions (see §8.1.2), in the bottom and top plates, in the reflector, in the barrel, in the bottom plate annular support and in the eight azimuthal supports, a 200 ppm by weight content of Co is assumed (of course only with respect to the steel parts of the plena regions, reflector and bottom and top plates).

8.1.1 Core

No impurities were assumed; i.e. the compositions for the activation were identical to those employed for the transport and discussed in §4.2.1 (with the model of all 89 core assemblies smeared).

8.1.2 Upper and lower plena regions

In these regions (seven between the bottom plate and the active core and eight between the active core and the top plate), both AISI-304L steel and inconel are employed (§4.2.2). A 200 ppm by weight content of Co is assumed in the AISI-304L and a 300 ppm by weight content of Co in the inconel. For the estimation of the activation, these zones were then averaged into a single zone between the bottom plate and the active core and a single zone between the active core and the top plate. The result for these single zones with both AISI-304L steel and inconel is as follows:

– doubling the cobalt impurity in the steel causes a 75% increase in the total cobalt content of the lower plenum region and a 88% increase in the total cobalt content of the upper plenum region.

– doubling the cobalt impurity in the inconel causes a 25% increase in the total cobalt content of the lower plenum region and a 12% increase in the total cobalt content of the upper plenum region.

8.2 Calculational model for the neutron transport: spatial binning of the neutron fluxes

The segmentation of the geometry to average the neutron fluxes for the calculation of the EOL activities is shown in Figs. 80 to 84.

Fig. 80 shows the axial division of the active region into three zones: the lower and upper 65 cm (including the lower and upper blankets) and the middle 3 m (precisely 298.598 cm). Note that all 89 assemblies were considered. Fig. 80 also shows the division of the thick part of the reflector (that is composed of 90% by vol. AISI-304L and 10% by vol. water) into 6 axial zones and 2 radial zones. The outer radial zone of the reflector, just visible, is 2.5 cm thick. The lower and upper plena are considered as 1 zone each and comprise all 89 assemblies.

Fig. 81 shows the axial division of the barrel into eight segments (the upper part above the top segment is ignored). It also shows the upper cylindrical part of the reflector (composed of 100% AISI-304L) which like the lower part is divided into two radial zones with the outer one 2.5 cm thick. In this case the inner zone is also 2.5 cm thick. The steel of the top plate is considered as a single zone whilst the steel of the bottom plate is divided into two axial zones.

Fig. 82 illustrates again the axial division of the bottom plate and also the segmentation of the bottom plate annular support into five zones, four surface zones and an inner volume zone. The upper, outer and inner surface zones are all 2.5 cm thick. The lower surface zone is thicker.

Fig. 83 shows again the segmentation of the bottom plate annular support and also the division of the azimuthal supports into an upper and inner 2.5 cm thick surface segment together with an inner volume segment. These segments are further subdivided into a part near the PV and a part near the bottom plate annular support.

Fig. 84 shows that there is also a lateral subdivision of the azimuthal supports into two 2.5 cm thick surface segments. The inner 2.5 cm thick surface segment is also shown. As before, the lateral surface segments are subdivided into a part near the PV and a part near the bottom plate annular support.

Fig. 85 shows the segmentation of the pressure vessel. There are five axial divisions of the cylindrical part and four polar divisions of the spherical part. There is no azimuthal sub-division around the inlet nozzles but there is a sub-division of the struts at 22.5° to E-W (Fig. 86). There is also a depth sub-division of 1/4T – 3/4T for both the cylindrical and spherical parts (7 – 21 cm for the cylindrical part and 3.5 – 10.5 cm for the spherical part). From Table 7.1 this depth sub-division is judged to be conservative (possibly overly so under the azimuthal struts). Figs. 87-90 show details of Fig. 85. Note in some of these figures there is shown the homogenized model of the steam generator support structure (below the steam generator bottom header). This will be discussed in detail in §9.1.1.

Fig. 91 shows the subdivision of the concrete. This subdivision was made based on the results in Table 7.2 (compare Figs. 91 and 73). The concrete side wall is divided radially into two depths: 12 cm, then 9 cm and axially into four segments. The concrete at the bottom part of the PV well is divided into the same two depths and into two radial segments. The same homogeneous concrete-rebar model was adopted as that in §7.1.3. The concrete was not borated. The concrete liner is not segmented depth-wise but is segmented axially and radially in an identical fashion to the concrete. Note the same geometry model as in §7 was used which assumes a 22.5 m diameter CV and which places the concrete in the PV well slightly nearer the PV compared with a 25 m diameter CV.

8.3 Calculational model for the activation gamma transport: materials and geometry

The model for the gamma transport was the same as that for the neutron transport described in §8.1 apart from the density of the water within the pressure vessel (including the water homogenised with other material in the core and lower and upper plenum regions and in the reflector) which was set to 1 g cm^{-3}. {The resulting smeared compositions for the Standard Westinghouse fuel assemblies, now identical in each of the eight central, higher enrichment axial segments and with lower and upper blankets identical (see Fig. 6), are given in [98] and for the seven lower plenum regions and eight upper plenum regions in [99]. ([98] and [99] may be compared with the compositions during running in [32] and [36] respectively.)}

8.4 Results

8.4.1 Activation and activity

In FISPACT for all zones apart from the active core and plena regions, two different irradiation times were considered: 60 years and 100 years, both at 100% load [running at 1000 MW (th)]. For the active core and plena regions, a single irradiation time of 10 years was considered, at 100% load. Two cooling times were considered: 1 and 3 days.

Active core

As far as the core is concerned, FISPACT is not written for burn-up calculations. (In the manual it is written that it "can treat trace amounts of actinides that are able to fission".

In this particular case, irradiating the fresh fuel with a constant spectrum leaves roughly one quarter the number of ^{235}U atoms remaining after 10 years. Given assembly shuffling and spectral changes with burn-up it is not conservative to employ this model, even if renormalising to the total number of fissions over 10 years (as there will be a preponderance of fission products created in the earlier part of the 10 year interval and a lack of fission products created in the latter part of the 10 year interval).

A solution at first looked to be to irradiate with an artificially low flux and then normalise to the expected number of fissions. However in this case there would be no burn-up of fission products.

The solution adopted was to retain the correct estimated flux levels but artificially maintain the actinide inventory through fictitious reactions (see acknowledgements). Furthermore so as to generate a reasonable mix of fission products, an average fuel composition rather than fresh fuel was employed, which was [100] (atom fractions):

^{235}U:	1.41E-02
^{238}U:	9.79E-01
^{239}Pu:	5.24E-03
^{241}Pu:	1.39E-03

Note that through natural decay, the ^{241}Pu inventory was not actually constant over the 10 year interval but was about 10% less at the end compared with the beginning.

In the FISPACT output the following message typically appeared:

```
+-------------------------------------------------+
|                 W A R N I N G                   |
|                 -------------                   |
|   Ratio of Fission Products/Fissions differs    |
|              from 2 by   74.8 %                 |
|                                                 |
+-------------------------------------------------+
```

However when the total number of fissions in each axial interval were summed:

lower 65 cm:	1.145E+27
middle 3 m:	6.668E+27
upper 65 cm:	1.140E+27
total:	8.953E+27

and compared with the total number of atoms produced by FISPACT between A=50 and A=200 inc.:

lower 65 cm:	1.998E+27
middle 3 m:	1.164E+28
upper 65 cm:	1.990E+27
total:	1.563E+28

there was seen to be a 12-13% discrepancy only from a ratio of 2. To compensate for the slight lack of fission products compared with fissions, the results are adjusted by multiplying by the factor 1.15 (2×0.8953÷1.563). Note furthermore that the above total number of fissions in 10 years is equivalent to around 910 MW [assuming 3.121E+10 fissions/joule (200 MeV/fission)]. This is slightly lower than the expected value of 1000 MW so the results are further adjusted by multiplying by the factor of 1.1.

Finally a version of ORIGEN [101] was run to try to check the FISPACT results. The running conditions were made as near as possible those of the FISPACT runs (see acknowledgements), resulting in a 7 year irradiation of the middle 3 m at a power of 744.9 MW and a 9 year irradiation of the upper and lower 65 cm at a power of 127.8 MW (each).

On comparing the results with those from FISPACT it was seen that ORIGEN produced 3.64E+6 g fission products after scaling the irradiation times up to 10 years, compared with 3.07E+6 g in FISPACT (atoms produced between A=50 and A=200 inc). When multiplied by the above factor of 1.15 this gives 3.53E+6 g and further multiplied by the above factor of 1.1 gives 3.88E+6 g.

Without scaling the irradiation times, 24 hours after shut-down the total gamma source with ORIGEN was 2.10E+19 MeV/s whilst that with FISPACT was 2.04E+19 MeV/s again after multiplying by both the factors 1.15 (because according to FISPACT nearly all the gamma power is from fission products whilst ORIGEN gives 80% of the gamma power from fission products) and 1.1.

The total gamma spectrum at 24 hours after shut-down from FISPACT (without the adjustment factors 1.15 and 1.1) is compared with that from ORIGEN in Fig. 92. Note that the spectra are normalised to 1 watt of fission power. The FISPACT total gamma spectrum at 24 hours after shut-down (without the adjustment factors 1.15 and 1.1) is also compared in Fig. 93 with the gamma spectrum obtained with the Westinghouse in-house methodology on a 3400 MW(th) core [102]. In both cases the agreement looks reasonable in the energy range of interest (between around 1 and 3 MeV).

Plena

Interpreting in a conservative manner data from [103], it was decided to assign 2% of gaseous fission products to the upper plenum and 2% to the lower plenum. Subsequently volatile fission products were added and then to be conservative, any fission product with boiling point < 1000°C. Thus we have: Se, Br, Kr, Rb, Cd, Te, I, Xe and Cs.

A total of 129 isotopes of these elements, produced by FISPACT after 10 years running, were allowed to decay for 24 hours. After multiplying by both the factors 1.15 and 1.1, the resulting gamma source was 7.07E+18 MeV/s, or around 35% of the total gamma source from the active core. The two unnormalized spectra (without the adjustment factors 1.15 and 1.1) are compared in Fig. 94.

2% of this gamma source was smeared over the lower plenum region.

8.4.2 Gamma doses

The spatial sub-division of the core described in §8.4.1 into 3 axial zones with no radial sub-division should produce conservative results for the gamma dose from this contribution, both in the axial and radial directions (especially in the latter).

Fig. 95 shows the division of the region under consideration into surface segments (in red) and volume segments (in black) over which the average dose after shutdown is calculated. The lower part of the outer surface of the PV is divided into six segments: A1 to A5 are symmetric around the azimuth whilst surface A6 in Fig. 96 is under the two azimuthal struts at 22.5° to EW. The lower part of the side wall is divided into five segments: B1 to B5 whilst the inner surface of the concrete liner in the bottom of the well is divided into two segments: C1 and C2 (Fig. 95). The volume between the PV and the concrete is divided into seven segments: D1 to D7.

Table 8.1 shows the doses after 1 day cooling (and 100 years running at 100% load for all components apart from the active core and plena for which the time was 10 years) at the various surfaces and regions of Fig. 95 from the various activated zones. No safety factors are included but the adjustment factors 1.15 and 1.1 for the core active region and for the gaseous and volatile fission products in the plena (§8.4.1) are included. The contribution from the activated structure is not given separately from that from the fission products in the lower plenum as the activated structure contribution is very low (around 1.5% of the total) compared with the fission products contribution.

Note in Table 8.1 the azimuthal supports of the bottom plate annular support are not present as, given the contributions from the bottom plate annular support and from the PV liner and PV, they were judged to be unimportant.

Discussion

From Table 8.1 we see that the active core, lower plenum and barrel are the predominant contributors to the dose at 24 hours after shut-down in the PV well.

The **maximum calculated dose** without safety factors, at the outer surface of the PV directly below the core (segment A5) at 24 h after shut-down is around **50 μSv/h**. The cobalt impurity assumption in the steel of 200 ppm is relatively unimportant here. A first gross estimate of safety factors on the source and transport model (in particular the homogeneous lower plenum region) is a factor 3, **giving ~ 150 μSv/h**.

For the contributions from components other than the active core and lower plenum, the uncertainty on the source should be much lower. However as ^{60}Co predominates, the uncertainty is on the cobalt impurity level (200 ppm in stainless steel, 30 ppm in carbon steel)..

8.4.3 Gamma doses from core and lower plenum after 3 days cooling

The contributions to the doses from the active core and lower plenum (for the latter only the fission product part) were calculated allowing 3 days cooling. The results are shown in Table 8.2 as a fraction of the respective dose contributions after 1 day cooling.

Discussion

From Table 8.2 we see that there is a conspicuous difference between the average decay constant in the active core and in the lower plenum (the latter including only gaseous and volatile fission products §8.4.1). Whilst the dose from the active core after 3 days cooling is 85-88% of that after 1 day, that from the lower plenum is 45-49% of the 1 day dose.

8.4.4 Gamma doses with four times the reference cobalt content in the barrel

The cobalt content in the barrel was increased from 200 to 800 ppm by weight. After a 100 year irradiation time followed by a 1 day cooling time the doses at the same points as in Table 8.1 were calculated. They are shown in Table 8.3 as a ratio of the dose with 800 ppm cobalt to the dose with 200 ppm.

Discussion

From Table 8.3 we see that the results lie between around 3.15 and 3.45 for a 4 times increase in cobalt. Thus scaling the dose rate linearly with cobalt content greater than 200 ppm by weight is conservative but not excessively so.

8.4.5 Gamma doses from the cobalt in the PV

The contribution to the dose rates from the 30 ppm by weight of cobalt in the pressure vessel was calculated. Conditions were a 100 year irradiation time followed by a 1 day cooling. The results are shown in Table 8.4 as a ratio of this dose contribution to the total dose contribution from the pressure vessel (including the 30 ppm by weight of cobalt with a total dose contribution as in Table 8.1).

Discussion

In Table 8.4 we see that the cobalt at such a low impurity level is responsible for a small fraction of the total dose from the PV with the model assumption of no structure between the barrel and the PV. Neutron spectrum effects are however important as we see from the ratio below the azimuthal struts (zones A6, C1, D5, etc.).

Table 8.1

Doses in the PV well in μSv/h after 100 years running (10 years for active core and plena) and 1 day cooling (for dose zones see Figs. 95 and 96)

	Active core	reflector	barrel	lower plenum	bottom plate	annular support	PV liner	PV	concrete liner	rebar	concrete	total
A1	9.8	0.9	2.6	0.02	0.001	0	0.001	0.20	0.13	0.01	0.15	13.8
A2	11.4	1.4	4.3	0.3	0.003	0.03	0.001	0.32	0.18	0.01	0.22	18.2
A3	8.4	1.6	6.4	0.7	0.007	0.3	0.001	0.42	0.20	0.01	0.26	18.3
A4	1.8	0.2	1.7	0.8	0.33	0.6	0.002	0.27	0.20	0.01	0.23	6.1
A5	26.8	0.01	0.1	22.0	1.2	0.06	0.001	0.28	0.20	0.01	0.17	50.8
A6	0.6	0.08	0.5	0.4	0.11	0.1	0.002	0.45	0.21	0.01	0.22	2.7
B1	6.0	0.6	1.7	0.08	0.003	0.01	0	0.09	0.25	0.01	0.18	8.9
B2	6.4	0.7	2.3	0.2	0.005	0.02	0.001	0.12	0.33	0.01	0.24	10.3
B3	5.3	0.7	2.4	0.3	0.009	0.06	0.001	0.12	0.38	0.01	0.29	9.6
B4	3.9	0.6	2.2	0.3	0.015	0.1	0.001	0.11	0.39	0.01	0.31	7.9
B5	2.4	0.4	1.7	0.3	0.033	0.1	0.001	0.09	0.41	0.01	0.30	5.7
C1	2.6	0.15	0.8	1.7	0.20	0.1	0.001	0.09	0.40	0.01	0.26	6.3
C2	16.9	0.03	0.1	13.1	0.53	0.07	0.001	0.11	0.39	0.01	0.23	31.5
D1	8.1	0.8	2.5	0.1	0.003	0.01	0.001	0.14	0.23	0.01	0.22	12.1
D2	8.6	1.0	3.1	0.3	0.005	0.02	0.001	0.19	0.27	0.01	0.26	13.8
D3	8.2	1.1	3.5	0.4	0.006	0.05	0.001	0.21	0.28	0.01	0.28	14.0
D4	4.9	0.8	3.0	0.4	0.016	0.1	0.001	0.16	0.33	0.01	0.32	10.0
D5	1.9	0.2	1.2	0.8	0.18	0.3	0.001	0.13	0.33	0.01	0.30	5.4
D6	8.0	0.04	0.2	6.8	0.61	0.1	0.001	0.12	0.33	0.01	0.28	16.5
D7	20.8	0.03	0.1	16.5	0.73	0.04	0.001	0.15	0.31	0.01	0.24	38.9

Table 8.2

Ratio of dose rate in the PV well after 10 years running for active core and plena and 3 days cooling to dose rate after 1 day cooling (for dose zones see Figs. 95 and 96)

	Active core	reflector	barrel	lower plenum	bottom plate	annular support	PV liner	PV	concrete liner	rebar	concrete	total
A1	0.87			0.49								
A2	0.87			0.47								
A3	0.87			0.46								
A4	0.87			0.45								
A5	0.86			0.45								
A6	0.87			0.39 (!)								
B1	0.88			0.47								
B2	0.87			0.47								
B3	0.87			0.46								
B4	0.87			0.46								
B5	0.87			0.45								
C1	0.87			0.45								
C2	0.85			0.46								
D1	0.88			0.47								
D2	0.87			0.47								
D3	0.87			0.47								
D4	0.87			0.46								
D5	0.87			0.45								
D6	0.86			0.45								
D7	0.85			0.46								

(!): poor statistics

Table 8.3

Ratio of dose rate in the PV well after 100 years running and 1 day cooling with 800 ppm by weight of cobalt in the barrel to dose rate with 200 ppm by weight of cobalt (for dose zones see Figs. 95 and 96)

	Active core	reflector	barrel	lower plenum	bottom plate	annular support	PV liner	PV	concrete liner	rebar	concrete	total
A1			3.14									
A2			3.24									
A3			3.32									
A4			3.35									
A5			3.46 (!)									
A6			3.71 (!)									
B1			3.18									
B2			3.22									
B3			3.28									
B4			3.30									
B5			3.30									
C1			3.35									
C2			3.45									
D1			3.20									
D2			3.22									
D3			3.28									
D4			3.31									
D5			3.34									
D6			3.39									
D7			3.39									

(!): poor statistics

Table 8.4

Ratio of dose rate in the PV well after 100 years running and 1 day cooling with activation source only cobalt in the PV (at 30 ppm by weight) to dose rate with all activation sources in the PV (for dose zones see Figs. 95 and 96)

	Active core	reflector	barrel	lower plenum	bottom plate	annular support	PV liner	PV	concrete liner	rebar	concrete	total
A1								0.065				
A2								0.060				
A3								0.060				
A4								0.24				
A5								0.075				
A6								0.42				
B1								0.063				
B2								0.066				
B3								0.077				
B4								0.091				
B5								0.11				
C1								0.14				
C2								0.12				
D1								0.064				
D2								0.061				
D3								0.062				
D4								0.087				
D5								0.16				
D6								0.14				
D7								0.095				

9. IMPROVED MODELING OF THE STEAM GENERATORS

9.1 Geometrical and material description

9.1.1 Steam generator lower supports

First (homogeneous) model

The total mass of the "Steam Generator Support Lower Assembly' is given in [104] as 1436 kg. Also from [104], the lower surface of the S.G. support is given as 90 cm below the axis of the inlet nozzles. With the second model of the steam generators (§6.1.2) this gives the lower surface of the S.G. support zone as 53.5 cm (90 – 36.5) below the lower surface of the S.G. bottom header.

The horizontal cross-section of the S.G. support is taken from [105] as rectangular but with the two sides beside the barrel and the pressure vessel respectively having the circular shape of the steam generators (radius 82 cm - §6.1.2). The other two sides, which are planes, are estimated from [105] to be 61 cm apart.

With the given mass, this then produces an average steel density in the volume under consideration of 2.748 g cm^{-3}. The rest of the volume is occupied by water at the density of the downcomer (0.74264 g cm^{-3} - §4.2.11). The reduced density steel is then homogenized with the water.

Vertical and horizontal cross-sections of the homogenized lower support model are shown in Figs. 97 and 98 respectively.

Second (heterogeneous) model

Employing [105] (the version with details outside the frame of the drawing) and [106], a more realistic model was developed with:

– two "I" shaped beams following the shapes of the barrel and pressure vessel with azimuthal extensions 30° (estimated) and 24° (estimated) respectively. The height of the beams (including the two ends) is estimated as 45.5 cm. Their lower surface is at the lower surface of the S.G. support zone (at 53.5 cm below the lower surface of the S.G. bottom header). The thickness of the middle part of the beams is estimated as 3 cm. The height of each of the end parts is estimated as 4 cm.

– two "T" shaped beams (but with the top part of the "T" ignored) of an estimated thickness of 3 cm, 47 cm apart (centre-to-centre), over the same height as the "I" shaped beams and orthogonal to them.

– a steel mass over a 12 cm (estimated) height below the lower header, of rectangular shape 70×61 cm^2 (both estimated) to model the "Centering Ring" together with its housing.

A vertical cross-section through the radial centre of the heterogeneous lower support model can be seen in Figs. 99 and 100 showing the two "I" shaped beams and the steel mass modeling the "Centering Ring" and housing. Fig. 101 shows a vertical cross-section through one of the "T" shaped beams detailing the intersection with the "I" shaped beams and with the "Centering Ring" and housing.

Four horizontal cross-sections at the lower end, middle and upper end of the "I" shaped beams and between the "I" shaped beams and the lower header are shown in Figs. 102, 103, 104 and 105 respectively.

9.1.2 Steam generators: third model

Further refinements were made to the second steam generator model of §6.1.2 as follows:

- the density of the water in the lower header was reduced by 2% [107].
- to account in an approximate fashion for the difference in volume of the secondary circuit water in the lower header between the model value (572400 cm^3) and the quoted value (439600 cm^3) (§6.1.2 – *Second model*), given that the density of the water around the lower header is 0.74264 g cm^{-3}, the density of the secondary water within the bottom header was reduced from its current value in the second model of 0.8386 (× 0.98) g cm^{-3} to:
  $0.8386 \times 0.98 \times 4396 \div 5724 + 0.74264 \times (5724 - 4396) \div 5724 = 0.80346$ g cm^{-3}.
- the "center support" (ext. diameter 61 cm [73]) was included in the steel part. The inner diameter is not quoted. In an arbitrary fashion, 2 cm thick steel walls were assumed.

As in the second model, we ignore the top header and assume a height of 820 cm above the top surface of the bottom header. Now, in this volume, to the steel of the second steam generator model (§6.1.2), *viz.*:

- 17458 kg of SA20 (tube bundle, density 8.14 g cm^{-3});
- $3698 \times 820 \div 914.5 = 3316$ kg SA24 (shroud, density 7.85 g cm^{-3});
- 1760 kg SA21 (tube bundle support, density 7.85 g cm^{-3}),

we add: $820 \times \pi \times (30.5^2 - 28.5^2) \times 7.85 = 2386$ kg steel "center support" (density 7.85 g cm^{-3}), producing a total volume of steel of 3.09532E+6 cm^3 (previously 2.79134E+6 cm^3 in the second model).

Now we consider separately the recirculation water within the "center support" or central column, with volume: $820 \times \pi \times 28.5^2 = 2.09244E+6$ cm^3. From [107] we assign a constant density of 0.658 g cm^{-3} to this water over the whole height.

We also consider separately the secondary water within the tube bundle, which from [78] is given as 2.8910E+6 cm^3, but instead of assigning the density 0.8386 g cm^{-3} as in the second model, we assign seven different densities as suggested in [107] according to the RELAP model cells.

The remaining volume of 9.24294E+6 cm^3 (previously 1.16394E+7 cm^3 in the second model) is assumed to be occupied by the primary water. [As noted in §6.1.2 *Second model*, the volume of the primary water in the steam generators is quoted as 9.345E+6 cm^3 ([80] p. 43). The volumes in the third model therefore seem quite consistent.] From [107] we adopt a density corresponding to the axial position of the chosen secondary density. Taking now the length of the steam generators in the RELAP model cells 1-50 as being between the lower and upper headers (747 cm), we have the following water densities from [107]:

RELAP cell [107]	cm above bottom header	Water densities (g cm^{-3}) secondary	primary	recirculation
1 – 5	0 – 74.7	0.789061	0.738276	0.658
6 – 10	74.7 – 149.4	0.531735	0.732858	0.658
11 – 15	149.4 – 224.1	0.325015	0.725413	0.658
16 – 20	224.1 – 298.8	0.233510	0.719409	0.658
21 – 30	298.8 – 448.2	0.0979563	0.704112	0.658
31 – 40	448.2 – 597.6	0.0390832	0.677787	0.658
41 – 50	597.6 – 747	0.0261414	0.661727	0.658

The total height of the steam generators above the bottom header is then reduced from 820 cm to 747 cm and the top header is ignored.

With these geometrical and material data, smeared compositions were generated in each of seven homogeneous axial zones of steel and primary, secondary and recirculation water (according to the RELAP cells in the above table) for the part of the steam generators above the bottom header [108]. A vertical cross-section of this model is shown in Fig. 106.

Finally as far as the bypass water surrounding the steam generators is concerned, from [107] we assign a density of 0.74264 g cm^{-3} up to a height of 209 cm above the top surface of the bottom header ("7/25" of the 747 cm between the two headers) and 0.6676 g cm^{-3} to the water above this. Fig. 107 shows a vertical cross-section, off-centre of the steam generators, where we see the division between the two bypass water densities (around the height of the bottom of the steel anti-missile shield).

9.1.3 Materials

From §6.1.2 the bottom header of the steam generator (second and third models) is AISI-304L with composition from [37] and density 7.85 g cm^{-3}. 200 ppm by weight cobalt impurity is assumed. The same material and cobalt impurity is assumed for the steel structure in the second heterogeneous model of the steam generator lower support as described in §9.1.1. The homogenized part of the steam generators above the bottom header were assumed to receive a much lower neutron flux compared with the bottom header and consequently to have a negligible activity compared with that of the bottom header.

9.2 Calculational model: spatial binning of the neutron fluxes

The segmentation of the geometry to average the neutron fluxes for the calculation of the EOL activities is shown in Figs. 108 to 115.

Fig. 108 shows a vertical cross-section of the steam generator heterogeneous lower support and header in a radial direction between the two "T" beams showing a single vertical segmentation of the lower and upper parts of the "I" beams and a division of the middle part into two segments, the division being just 6 cm above the lower part. There is also a vertical division

of the “Centering Ring” model into a lower 4 cm and an upper 8 cm. Finally the lower header is divided equally into a lower part and an upper part.

Fig. 109 shows a vertical cross-section of the steam generator heterogeneous lower support and header through one of the “T” beams showing the same vertical division as for the “I” beams as well as the radial division into four radial segments.

Figs. 110, 111 and 112 show horizontal cross-sections of the steam generator heterogeneous lower support through the lower, middle and upper parts of the “I” beams respectively.

Figs. 113, 114 and 115 are horizontal cross-sections of the steam generator lower header, through the bottom wall, lower part and middle part respectively. We see a division into five radial segments, with the inner segment containing only the inner wall opposite the inlet channel. The vertical division, into two parts was shown in Figs. 108 and 109. The same radial subdivision is present in the upper and lower parts.

9.3 Results

The activation gamma ray doses in the accessible areas in the cavities under the main deck are reported in §10. The contributions from the steam generator lower support and lower header are negligible compared with the other contributions. Only in the special conditions of a void secondary circuit and the end flange of the inlet nozzle removed, does the dose contribution become non-negligible (§10.10). Finally in §12 the dose results are presented around a bare steam generator (i.e. extracted from the core).

10. MAINTENANCE DOSES BETWEEN THE PRESSURE VESSEL AND THE CONTAINMENT VESSEL

10.1 Calculational model for generating the neutron fluxes: geometrical and material description

The final model of the geometry up to and including the pressure vessel [comprising the second (heterogeneous) model of the steam generator lower supports (§9.1.1), the explicit steam generator bottom header (§6.1.2), the third model of the steam generators (§9.1.2) and inlet nozzle walls and flange according to ANSALDO drawings (§6.1.1)] was extended by adding structure in the cavities between the pressure vessel and containment vessel. The only other modification was a substantial reduction in the thickness of the anti-missile sleeve from 1 foot (30.48 cm) [109], [110] (and a consistent use of steel as its material). Note that no rebar was employed in any part of the modeled concrete.

10.1.1 Emergency boron tanks

The outer and inner diameters were taken from [68]. The position of the EBT's is taken from [72] assuming to scale (45° from E-W; for the distance from the core axis, see [110]). For simplicity the tanks are assumed cylindrical.

The internal volume of each EBT was taken from [111]. With the assumed cylindrical shape, this produces a lower height than that quoted in [68]. However this is not for a cylindrical shape but for a cylinder with a hemisphere above and below. (With the adopted internal volume and wall thicknesses, if the realistic shape of the EBT tanks as shown in [68] is modeled, this gives a total external height that is nearly precisely the quoted height.) Note the volume from [111] is not consistent with that quoted in [80] p. 45, but the above considerations lend weight to the former value which was that adopted.

The distance of the centre of each EBT from the main deck is taken from [69] (assuming to scale). The walls are assumed AISI-304L [37] (7.85 g cm^{-3}). The EBT's are assumed full of borated water at density 1 g cm^{-3}, the boron concentration taken from [112], the ^{10}B enrichment from [113].

The dimensions, positions and boron data are fully described in [110].

10.1.2 LGMS injection tanks

The (assumed) outer diameter is quoted in [68], [80] p. 44. The thickness of the walls is taken from [114]. The distance of the centre of each LGMS tank from the main deck is taken from [68] (assuming to scale). Similarly the distance of the centre of each LGMS tank from the reactor axis is estimated from [68]. The two LGMS tanks are modeled as truncated tori, the truncation point being estimated from [72] to attempt to approximately conserve the volume (and not the surface area). The truncation planes resulted as at 19.2° to N-S and 4.7° to E-W. This, with the truncation planes truncating the inner rather than the outer volume, gives an inner volume of each LGMS tank that is rather less than that quoted [80] p. 44. We assume that they are full of normal water at 1 g cm^{-3}.

The dimensions and positions are fully described in [110].

The steel of the walls was the same as that adopted for the EBT's.

10.1.3 ADS quench tank

The dimensions are estimated from [72] assuming to scale. The tank occupies the whole height of the cavity direction E below the main deck. This gives a height (after taking away the gratings – see §10.1.4) that is consistent with that given in [80] p. 44. The thickness of the walls is taken from [114]. The top of the tank is left open.

Wishing to maintain the same trapezoidal section as for the tank shown in [72] (i.e. with vertical walls), it was necessary to move the outer surface that is farthest from the core towards the core axis by a small amount. The outer surface that is nearest the core was then also moved the same amount towards the core.

Filling up the tank to the main deck level produced a volume of water nearly identical to that quoted in [80] p. 44.

The dimensions and positions are fully described in [110].

The steel of the walls was the same as that adopted for the EBT's.

10.1.4 Gratings

Following [111], at the level of the main deck we have modeled gratings above the DVI valve rooms (E and W), the cavity for the feed pipes (S) and the pits for the CVCS equipment (N and NE) (i.e. all the cavities in the main deck up to the anti-missile shield which in this calculation was steel). The grating was modeled as homogeneous 5 mm thick steel, always the same composition as all other steel employed, apart from the pressure vessel.

10.1.5 Water pipes

The feedwater pipes shown in [64] were modeled as a steel-water-steel sandwich (1cm steel, 3 cm water, 1 cm steel) on the whole floor of the cavity below the main deck in the south direction and just on the part of the floor near the pressure vessel of the DVI Valve room cavities (E and W) and the cavities housing the inlet nozzles (NE and NW).

10.1.6 Illustration of tanks, gratings and water pipes

Vertical sections in direction WNW-ESE through the inlet nozzles illustrating the LGMS tank "B" and in direction SW-NE illustrating the EBT "B" and the LGMS tank "A" are shown in Figs. 116 and 117 respectively. Fig. 118 is a vertical section in direction W-E showing the ADS quench tank.

A horizontal section at the midplane of the LGMS tanks is shown in Fig. 119, illustrating both LGMS tanks and both EBT's. Fig. 120 is a horizontal section through the inlet nozzles showing the ADS Quench tank. Fig. 121 shows three horizontal sections of the ADS Quench tank: just below the top (note there is no lid), at the inlet nozzles and just above the base.

Fig. 122 is a horizontal section at the main deck showing the modeled gratings whilst Fig. 123 is a horizontal section at the floor of the cavities under the main deck showing the upper steel part of the water pipe model. Fig. 124 is a vertical section of the water pipe model.

In Figs. 116-119 we see the new, reduced thickness, steel anti-missile shield.

10.2 Source and core description

The source and core descriptions were that of case "A" in §5.2 above [^{235}U fission spectrum, average source (see §4.1), both the source and the geometry smeared in all 89 assemblies of the active zone, Standard Westinghouse 17x17 fuel assemblies, thick reflector, etc.].

10.3 Calculational model for generating the activation sources: spatial binning of the neutron fluxes

There are eight distinct steel structures outside the PV up to and including the CV: the inlet nozzle walls, the anti-missile shield, the water pipe model, the main deck gratings, the ADS quench tank walls, the LGMS tank walls, the EB tank walls and the containment vessel. As previously, each component must be spatially segmented in such a way that the neutron flux-induced activation source is reasonably constant throughout each segment or, less strictly, that the consequent activation dose at chosen points should not vary when making the segmentation finer.

The inlet nozzle walls were segmented into three radial parts plus the end cap. A further division was made into an upper and a lower part making a total of eight segments. A horizontal section of one nozzle is shown in Fig. 125 and a vertical section in Fig. 126. Fig. 127 shows another vertical section, orthogonal to that shown in Fig. 126.

The segmentation of the anti-missile shield into four vertical sections is shown in Fig. 128. The thickness was not subdivided.

The radial segmentation of the water pipe model is shown in Fig. 129 with a detail of the inner part in Fig. 130. The part of the sandwich above the water was treated separately from the part below the water (see Fig. 124).

The radial segmentation of the main deck gratings is shown in Fig. 131.

The ADS quench tank walls were segmented as follows: a single front wall, a single bottom and a back wall divided vertically into two parts (see Fig. 132). Fig. 133 shows the segmentation of the side walls into four roughly equal parts: inner-lower, inner-upper, outer-lower and outer-upper. A vertical section through the front wall is shown in Fig. 134 whilst Fig. 135 is the same for the back wall. Finally Figs. 136 and 137 are horizontal sections through the middle part and through the bottom respectively.

The LGMS tank walls are segmented as follows: each tank is divided into two cylindrical end caps and the toroidal wall into four azimuthal segments – see Figs. 138 and 139 for tanks A (West) and B (East) respectively. Fig. 140 shows that these azimuthal divisions were chosen to correspond to the gap in the concrete wall surrounding the PV well where the inlet nozzles are located (and therefore where the steam generators are also located). The azimuthal segments that may experience a direct neutron leakage flux from the PV (at 4-o-clock, 5-o-clock, 7-o-clock and

8-o-clock – see Fig. 140) are divided into three polar segments: inner-lower, inner-upper and outer: see Fig. 141. The other azimuthal segments (at 3.30, 4.30, 7.30 and 8.30 – see Fig. 140) are divided into two polar segments: inner and outer: see Fig. 142. The cylindrical end caps of the tanks are not subdivided.

The EB tank walls are divided into three segments: bottom, top and side walls (see Fig. 143). There is no subdivision of the side walls (see Fig. 144).

The neutron fluxes were only tallied in the part of the containment vessel that is directly exposed, i.e. not behind concrete. The part below the main deck in the South direction was taken as a single segment – see Figs. 145 and 146. The part above the main deck and outside the missile shield (see Fig. 147) was divided into 18 azimuthal segments (see Fig. 148), like grapefruit slices.

Having presented the neutron fluxes to FISPACT, the irradiation time adopted was 100 years at 100% load [running at 1000 MW (th)]. Two cooling times were considered: 1 and 3 days. For all steel structures outside the PV including the inlet nozzle walls and flanges, AISI-304L steel [37] was employed assuming a 200 ppm by weight content of Co.

Sources inside the pressure vessel including the pressure vessel itself

As well as activation sources in structures situated outside the pressure vessel (including the inlet nozzle walls and flanges), treated above, there are also dose contributions from activation sources within the pressure vessel (including the PV itself). With the exception of the steam generator structure (lower support and lower header), these sources have been described in §8 and the same sources (apart from those in the PV liner and PV which are discussed in the next two paragraphs) are employed for the dose here. The sources in the steam generator structure are discussed in §9.

The activation sources in the PV liner and PV have been regenerated using the third model of the steam generators (§9.1.2), the heterogeneous steam generator supports (§9.1.1) and the explicit steam generator bottom header (§6.1.2), as well as the ANSALDO data for the inlet nozzle walls and flanges (§6.1.1). [Previously in §8 the neutron fluxes employed for the activation sources in the PV liner and PV were generated with the homogeneous steam generator support model (§9.1.1) and the second model of the steam generators (§6.1.2), see for example Figs. 85 and 87.]

The new geometry for generating the neutron fluxes in the PV liner and PV is shown in Figs. 149 and 150. The same 5 axial segments and 2 radial segments in the cylindrical part of the PV as previously are employed. Note that the activation source in the spherical part of the PV liner and PV was ignored when calculating the activation doses in the cavities above and below the main deck.

10.4 Calculational model for the activation gamma transport: materials and geometry

The model for the gamma transport was as in §10.1 apart from the density of the water within the pressure vessel (including the water homogenised with other material in the core and lower and upper plenum regions and in the reflector) which was set to 1 g cm^{-3} (as in §8.3). In addition, as after shut-down the secondary circuit might be voided [115], the water within the inlet nozzles and steam generator bottom header was voided. (This was irrelevant for the results

in §8.) The composition of the homogenised steam generators above the lower header was not changed from that during operation as, although after shut-down the secondary water within the steam generators might be voided, the primary water would be at 1 g cm^{-3}. Leaving the primary water in the steam generators at its density during operation should more than compensate for not voiding the secondary water, as can be seen from the volumes of the steam generator occupied by the primary and secondary water [108].

10.5 Activity dose points between the PV and CV

Particular attention was firstly paid to the dose around the inlet nozzles to evaluate the streaming of activation gamma rays from within the PV past the nozzles and into the cavities.

The dose from all sources, within and outside the PV was then calculated at the following places:

- at a number of points in air both in the cavities below the main deck and above it;
- on surface segments of each of the activated structures listed in §10.3.

Defining now these dose "points":

Using the "meshtal" capability in MCNP5 [1], points of maximum dose (only from streaming gamma rays from the core out to and including the barrel) were found on the same circumference as the end of the inlet nozzles at radius 552.7 cm (see Fig. 151) and over the height of the cavities below the main deck level (see Fig. 152). Having found these points of maximum streaming dose, the streaming path was extrapolated a further 1 m into the cavities and the dose was calculated at this point. Fig. 153 shows the position of this point projected onto the plane through the axis of the inlet nozzles. Fig. 154 shows the actual position of this dose point (at a height of 40.5 cm above the inlet nozzle axis, or 120 cm above the concrete floor of the cavity). Fig. 155 shows the streaming path between this point and the core. Note that these particular doses were only calculated for the most important sources within the PV: the active core, the upper plenum, the inner part of the reflector and the barrel. (The dose due to the activated steam generator bottom header was also calculated at the point shown in Figs. 153 - 155 although the main streaming path from this source is lower down, through the inlet nozzle pipe.)

"l-E", "l-W", "l-S": Fig. 156 shows the dose points in air in the cavities below the main deck level (where the total dose from all activated components was calculated). These points were all at a height of 162 cm above the concrete floor of the cavity (precisely half the height of the cavities).

"u-WSW", "u-ENE", "u-N": Fig. 157 shows the three dose points in the cavity above the main deck level, all at a height of 175 cm above the gratings. Unlike the dose points in the cavities below the main deck level shown in Fig. 156, two of these points: "u-WSW" and "u-ENE" "see" past the inlet nozzle wall and flange through to the pressure vessel and barrel. For these two points as well as for dose point "u-N", in Figs. 158, 159 and 160 we show vertical sections through the reactor axis and each dose point, u-WSW, u-ENE and u-N respectively. We remind ourselves that the active core and barrel have a finite dimension into/out of the page in these figures.

"IN-u", "IN-l", "IN-cap": three segments on the surface of the inlet nozzles: the end of the radial surface, upper and lower segments and the end axial surface (see Figs. 161, 162 and 163). Note that although all 8 nozzles are considered together, in the dose results where there is a high

asymmetric azimuthal effect (e.g. source in walls of ADS quench tank), the particular inlet nozzle experiencing the highest dose is reported.

"Wpi": a segment on the upper surface of the inner part of the water pipe model (see Fig. 164). Note, as for the inlet nozzles, the highest dose around the azimuth is reported in some cases of high azimuthal asymmetry.

"ADS": the lower, inner quadrants of the side surfaces of the ADS quench tank (see Figs. 165 and 166).

"CV-l-S": Figs. 167 and 168 are horizontal and vertical sections showing the inner surface of the part of the containment vessel in the South direction below the main deck.

"GR-i-l", "GR-i-u": lower and upper surfaces respectively of the inner part of the gratings at main deck level (see Fig. 169). As for the water pipe model, the highest dose around the azimuth is reported in some cases of high azimuthal asymmetry.

"AMS": outer surface of lower segment of anti-missile shield (see Fig. 170). As for the gratings, the highest dose around the azimuth is reported in some cases of high azimuthal asymmetry, however in an approximate fashion relying on other results.

"EBT-b", "EBT-s": the bottom and side surfaces respectively of the two EB tanks (see Figs. 171 and 172 respectively). As for the anti-missile shield, the highest dose around the azimuth of each tank is reported in some cases of high azimuthal asymmetry, again however in an approximate fashion relying on other results.

"LGMS": the union of the two inner and lower poloidal segments of the toroidal surfaces at azimuthal directions 4-o-clock and 8-o-clock (see Fig. 140) (see Figs. 173 and 174).

"CV-u": segment of inner surface of containment vessel above the main deck and outside the anti-missile shield. The segment covers an azimuthal angle of ±15° around the North direction (see Figs. 175 and 176).

Note that the doses at the points "l-E", "l-W", "l-S" and "u-WSW", "u-ENE", "u-N" (as well as at the point shown in Figs. 153 - 155) are actually estimated at single points in space (using the "next event estimator" [1]). All other dose results are averages over surface segments. Whilst it is usually the case in Monte Carlo simulations that doses over surface segments are more reliable than doses calculated at points, instead here the opposite is the case. Thus between the PV and CV the most reliable (total) doses are those at the points "l-E", "l-W", "l-S" and "u-WSW", "u-ENE", "u-N".

10.6 Results for maintenance doses between the PV and CV

Partial dose results from the streaming activation gamma rays from within the pressure vessel in the gap between the inlet nozzles and the concrete (Figs. 151 and 152) are shown in Table 10.1. The sources are the active core, upper plenum, the inner part of the reflector, the barrel and the pressure vessel. Conditions are 100 years running (10 years for active core and plena) and 1 day cooling. The adjustment factors 1.15 and 1.1 on the source from the core and plenum (§8.4.1) are included, but no safety factors are included.

Partial doses 1 m further out in the cavities along the streaming path (see Figs. 153, 154 and 155) are given in Table 10.2. The sources are again the active core, upper plenum, the inner part of the reflector and the barrel but now include the steam generator bottom header and exclude the

pressure vessel. (As noted in the previous section, the streaming path from the SG bottom header is actually lower down at the level of the inlet nozzles.)

The objective of calculating and reporting the partial doses in Tables 10.1 and 10.2 was to verify the consistency with the results in the following Table 10.3, where both partial and total doses are reported.

Table 10.3 shows the total doses from all non-negligible contributions at the surface segments and dose points listed in §10.5. Not reported is the contribution from the PV liner, which is negligible as is also the contribution from the steam generator lower support. Conditions are again 100 years running (10 years for active core and plena) and 1 day cooling. The bold typed results represent doses from the contact structure. The yellow background results are from sources within the pressure vessel. The turquoise background results are from sources outside the pressure vessel.

In Table 10.3, results with an asterisk are estimates of the maximum dose on the area segment. [For example the inner part of the lower surface of the gratings model GR-i-l (Fig. 169) exhibits a maximum dose from the source in the ADS tank wall (Fig. 129) in the ESE and ENE directions, the side of the EBT tanks (Fig. 172) exhibits a maximum dose from the source in the anti-missile shield in the part directly opposite the shield (same Figure), etc.] Also the results in Table 10.3 from the sources in the reflector and upper plenum are extrapolated from the results with the active core source, employing the results in Tables 8.1 and 10.1.

We see that the partial dose results in Table 10.1 are similar to those for the lower part of the outer section of the inlet nozzle in Table 10.3. The latter doses include all dose contributions and may therefore be considered as maximum doses in accessible areas in the cavities outside the inlet nozzles.

Also estimates may be made of the total doses at 6.52 m from the reactor axis in Table 10.2 by adding the turquoise background doses for point l-E in Table 10.3 (2.2E-4 μSv/h) to the partial doses in Table 10.2 giving a total of 6.1E-4 μSv/h in air along a streaming path at approximately 1 m from the inlet nozzles (compare maximum 2.7E-3 at the inlet nozzles in Table 10.3). Thus the two sets of results look reasonably consistent.

Finally referring to Table 10.3 it should be mentioned that the doses from structures within the PV (yellow background) are in general relatively low compared with the doses from structures outside the PV (turquoise background) only because of the higher density of the primary water at shut-down compared with during running.

Only a limited number of steel structures have been modeled between the PV and CV whilst in reality more steel structure will be present. Therefore approximate enveloping values are obtained by multiplying all the dose contributions from structure outside the PV (with the exception of the contact structure, given in bold type in Table 10.3) by some constant. This constant (the “Gross Structure Constant”, or GSC) was given two values: 4 and 16. GSC=4 means that the doses from all active structures outside the PV not in contact with the particular dose point are multiplied by a factor of 4. GSC=16 means that the doses from all active structures outside the PV not in contact with the particular dose point are multiplied by a factor of 16.

This then converts the results in Table 10.3 to those in Table 10.4. We see now that the contribution to the dose from locally activated structure between the PV and CV accounts for nearly all of the total dose (apart from the lower surface and end cap of the inlet nozzles). However the total doses in Table 10.4 are still low, although they do not yet contain safety factors apart from the GSC, the hypothesised structure multiplier.

10.7 Gamma doses from core and upper plenum after 3 days cooling

It was desired to generate similar results to those in Table 10.3 for the source in the active core and plenum at 3 days after shut-down (as was done in §8.4.3 and Table 8.2 for the doses in the PV well). This proved statistically difficult.

The dose in the gaps between the inlet nozzles and the concrete (see Fig. 151) and behind the concrete wall surrounding the PV well in the cavities under the main deck in the East, West and South directions (see Fig. 151) had previously been calculated for the gamma source in the active core at 1 and 3 days after shut-down. However this was with the wrong primary water density (that during running rather than after shut-down).

Because:

1) the results in Table 8.2 did not change when the primary water density was corrected from its value during running to its value after shut-down;

2) the ratio of the above doses from the active core at 3 days after shut-down to 1 day after shut-down in the gaps between the inlet nozzles and the concrete and behind the concrete wall surrounding the PV well was 0.84 – 0.85, similar to the values in Table 8.2;

it seems that adopting the value **0.88** from Table 8.2 for the ratio of dose from the active core at 3 days after shut-down to 1 day after shut-down for all the dose points between the PV and CV in the cavities below and above the main deck, should be if anything slightly conservative.

No attempt was made to do the same thing for the source in the top plenum. Instead given the consistency of the results for the active core contribution around the end of the inlet nozzles and in the PV well, we hypothesise the same ratio for the contribution of the top plenum as for the bottom plenum in §8.4.3. That is, the ratio of this dose contribution at 3 days after shut-down to 1 day after shut-down is around **0.48** (see Table 8.2) for all dose points between the PV and CV below and above the main deck.

10.8 Results for maintenance doses between the PV and CV with four times the reference cobalt content in the steel of the inlet nozzles and main deck gratings

The cobalt content in the steel of both the inlet nozzles walls and flange and the main deck gratings model was increased from 200 to 800 ppm by weight. After a 100 year irradiation time followed by a 24 hour cooling time the doses at the same points as in Table 10.3 were calculated. They are shown in Table 10.5 as a ratio of dose with 800 ppm cobalt to dose with 200 ppm.

Discussion

A small fraction of the dose is seen to be from non-cobalt sources, this fraction being larger for the gratings compared with the inlet nozzles, presumably due to neutron spectral effects. We see that scaling the dose linearly with cobalt impurity at impurity levels greater than 200 ppm leads to a slightly conservative dose estimate.

10.9 Gamma doses from the cobalt in the PV

The contribution to the dose rates from the 30 ppm by weight of cobalt in the pressure vessel was calculated. Conditions were a 100 year irradiation time followed by a 1 day cooling. The results are shown in Table 10.6 as a ratio of this dose contribution to the total dose contribution from the pressure vessel (including the 30 ppm by weight of cobalt with a total dose contribution as in Table 10.3).

Discussion

In Table 10.6 we see that the cobalt in the PV is responsible for a substantially greater fraction of the total PV contribution (around 20%) compared with the situation in the PV well [below 10% apart from in the shadow of the azimuthal struts (see Table 8.4)]. This is presumably due to the thicker PV (28 cm rather than 14 cm).

The results in Table 10.6 were somewhat noisy. The fraction of the dose contribution from the PV due to the cobalt in the PV is expected to be slightly lower for dose points that are either in direct sight of the PV and/or nearer (in terms of attenuation) and vice versa for dose points not in direct sight of the PV and/or farther. From the results in Table 10.6, we hypothesise that the former group have cobalt dose fractions in the range 0.14 – 0.19, the latter group instead in the range 0.19 – 0.25.

10.10 Removing the end flange of the inlet nozzle

Vertical and horizontal sections with the outer flange of the inlet nozzle removed (and still with the secondary circuit water in the steam generator bottom header and in the inlet nozzle voided) are shown in Figs. 177 and 178 respectively.

The same segmentation of the bottom header for scoring the neutron fluxes to calculate the activation source was employed as described in §9.2 (see Figs. 108 and 113-115).

At 1 day after shut-down and 100 years running, the dose at the open end of the inlet nozzles from the activated steam generator lower header is 1.7E-2 μSv/h. (Note this is a calculational result and contains no safety factors for modeling and nuclear data uncertainties.) That from the steam generator lower support is negligible. This dose must be added to the other contributions for the segment "IN-cap" in Tables 10.3 and 10.4, giving a value of **1.8E-2 μSv/h** without a GSC constant, **1.9E-2 μSv/h** with a GSC constant of 4, or **2.1E-2 μSv/h** with a GSC constant of 16. We see that under these conditions, the contribution from the steam generator bottom header is predominant.

Table 10.1

Maximum doses from various sources within the PV in the gap between the inlet nozzles and the concrete at the radius of the end of the inlet nozzles (see Figs. 151 and 152) in μSv/h after 100 years running (10 years for active core and plena) and 1 day cooling

source:	active core:	upper plenum	inner part of reflector	barrel	PV
μSv/h:	8.8E-4	7.0E-5	1.3-5	7.9-5	1.6E-4

Table 10.2

Maximum doses from various sources within the PV in the cavity below the main deck at 6.52 m from the reactor axis (see Figs. 153, 154 and 155) in μSv/h after 100 years running (10 years for active core and plena) and 1 day cooling

source:	active core:	upper plenum	inner part of reflector	barrel	SG bottom header
μSv/h:	3.3E-4	1.3E-5	5.4-6	2.5-5	1.6-5

Table 10.3

Doses in the cavities between the PV and CV in μSv/h after 100 years running (10 years for active core and plena) and 1 day cooling (for dose points see §10.5 and Figs. 156-176) (for 1.2-3 read 1.2E-3)

	active core	reflector (a)	barrel	upper plenum (b)	SG bottom header	PV	inlet nozzle walls	water pipe model	ADS tank walls	main deck gratings	EB tank walls	LGMS tank walls	anti-missile shield	CV	total
IN-l	9.2-4	4.2-5	1.2-4	7.3-5	1.7-5	1.6-4	**1.1-3**	2.2-4	1.8-5*	4.5-6*	8.3-8*	1.4-6*	1.0-6	3.7-6*	2.7-3
IN-u	1.4-4	5.3-6	1.5-5	1.1-5	2.7-5	2.0-5	**4.8-4**	3.9-5*	2.1-5*	2.2-5*	4.5-7*	4.7-6*	1.5-5	1.6-5*	8.2-4
IN-cap	2.8-5	1.9-5	5.3-5	2.2-6	3.1-4	4.6-6	**2.6-4**	1.3-4*	3.6-5*	1.9-5*	2.7-7*	5.3-6*	2.8-6	1.2-5*	8.8-4
WPi	4.8-5	1.1-5	3.2-5	3.8-6	5.3-6	6.5-5	4.9-4	**1.3-3**	2.4-5*	1.2-5*	1.4-7*	3.4-6*	2.8-6	9.9-6*	2.0-3
l-E	2.7-6	2.5-7	7.0-7	2.1-7	1.5-6	1.5-6	2.3-5	5.1-5	7.4-5	2.9-5	1.3-6	8.0-6	1.5-5	1.6-5	2.2-4
l-W	3.7-6	3.9-7	1.1-6	2.9-7	1.5-6	2.9-6	1.4-5	1.9-5	3.8-9	3.9-5	1.1-6	1.2-5	2.8-5	2.4-5	1.5-4
l-S	3.4-6	4.2-7	1.2-6	2.7-7	1.1-6	4.3-6	9.5-6	6.1-5	1.4-8	2.6-5	7.3-9	6.3-6	2.4-5	4.0-5	1.8-4
ADS	8.9-6	3.9-7	1.1-6	7.1-7	2.5-6	7.7-6	1.4-5	9.9-6	**2.8-4**	1.4-5	4.2-7	4.4-6	1.5-5	7.7-6	3.6-4
CV-l-S	1.9-6	2.5-7	7.2-7	1.5-7	3.3-7	2.4-6	3.9-6	2.5-5	6.1-9	1.7-5	9.5-9	3.6-6	1.3-5	**9.7-5**	1.6-4
GR-i-l	2.3-5	2.5-6	7.1-6	1.8-6	2.8-6	3.3-5	4.1-5	3.0-5*	3.3-5*	**1.9-4**	5.0-6*	2.1-5*	7.1-5	3.2-5*	4.9-4
GR-i-u	1.8-5	1.3-6	3.6-6	1.4-6	1.9-6	2.6-5	3.2-5	2.4-5*	1.7-5*	**1.8-4**	7.0-6*	3.5-5*	1.3-4	5.0-5*	5.3-4
AMS	1.6-6	3.0-6	8.6-6	1.3-7	6.0-7	3.4-6	1.1-5	3.3-6*	6.0-6*	2.2-5*	8.0-6*	2.6-5*	**6.8-4**	3.9-5*	8.1-4
u-WSW	1.1-5	2.9-6	8.4-6	8.8-7	7.5-7	2.9-5	2.0-5	8.1-6	1.3-8	3.3-5	1.4-6	4.1-5	1.6-4	4.0-5	3.6-4
u-ENE	9.1-6	4.6-7	1.3-6	7.2-7	5.8-7	4.0-6	7.1-6	5.2-6	1.4-5	3.2-5	4.3-6	9.3-6	6.1-5	6.9-5	2.2-4
u-N	7.5-7	6.0-7	1.7-6	6.0-8	9.3-8	1.7-6	4.9-6	4.9-7	7.4-7	1.9-5	5.7-6	2.9-6	1.4-4	6.6-5	2.4-4
EBT-b	5.5-7	2.3-7	6.5-7	4.4-8	5.1-8	7.5-7	1.4-6	8.8-7	4.6-6*	2.3-5	**5.1-5**	1.2-6	4.9-5	1.4-5	1.5-4
EBT-s	8.9-7	9.5-7	2.7-6	7.1-8	7.2-8	3.9-6	5.7-6*	3.4-6*	7.2-6*	1.1-5	**5.8-5**	6.6-6*	1.2-4*	6.9-5*	2.9-4
LGMS	1.1-5	6.7-7	1.9-6	8.8-7	6.8-7	5.7-6	8.4-6	6.4-6	1.7-5*	3.4-5	8.9-7	**1.4-4**	6.2-5	1.2-5	3.0-4
CV-u	4.2-7	1.3-6	3.8-6	3.3-8	8.2-8	2.0-6	1.5-6	5.2-7	3.9-7	4.7-6	2.0-6	2.2-6	4.0-5	**1.3-4**	1.9-4

"*": estimate made of highest dose over the defined area segment (usually around the azimuth)

"(a)": results made proportional to barrel results employing as constant of proportionality the factor 0.35=0.22/0.62 [0.22 = inner reflector / barrel dose in cavity below main deck (Table 10.2); 0.62 = inner reflector / total reflector dose for point A2 in Table 8.1]

"(b)": results made proportional to active core results employing as constant of proportionality the dose in the gap between inlet nozzles and concrete evaluated beside end of inlet nozzles (Table 10.1)

Table 10.4

Doses in the cavities between the PV and CV in μSv/h after 100 years running (10 years for active core and plena) and 1 day cooling, assuming 4 and 16 times the modeled steel structure between the PV and CV (for dose points see §10.5 and Figs. 156-176) (for 1.2-3 read 1.2E-3)

	active core	reflector	barrel	upper plenum	SG bottom header	PV	Explicit structures between PV and CV with GSC=4	Total (GSC=4)	Explicit structures between PV and CV with GSC=16	Total (GSC=16)
IN-l	9.2-4	4.2-5	1.2-4	7.3-5	1.7-5	1.6-4	2.1-3	3.4-3	5.1-3	6.4-3
IN-u	1.4-4	5.3-6	1.5-5	1.1-5	2.7-5	2.0-5	9.5-4	1.1-3	2.4-3	2.6-3
IN-cap	2.8-5	1.9-5	5.3-5	2.2-6	3.1-4	4.6-6	1.1-3	1.5-3	3.5-3	3.9-3
WPi	4.8-5	1.1-5	3.2-5	3.8-6	5.3-6	6.5-5	3.5-3	3.7-3	1.0-2	1.0-2
l-E	2.7-6	2.5-7	7.0-7	2.1-7	1.5-6	1.5-6	8.7-4	8.8-4	3.5-3	3.5-3
l-W	3.7-6	3.9-7	1.1-6	2.9-7	1.5-6	2.9-6	5.5-4	5.6-4	2.2-3	2.2-3
l-S	3.4-6	4.2-7	1.2-6	2.7-7	1.1-6	4.3-6	6.7-4	6.8-4	2.7-3	2.7-3
ADS	8.9-6	3.9-7	1.1-6	7.1-7	2.5-6	7.7-6	5.4-4	5.6-4	1.3-3	1.3-3
CV-l-S	1.9-6	2.5-7	7.2-7	1.5-7	3.3-7	2.4-6	3.5-4	3.6-4	1.1-3	1.1-3
GR-i-l	2.3-5	2.5-6	7.1-6	1.8-6	2.8-6	3.3-5	1.1-3	1.2-3	3.9-3	4.0-3
GR-i-u	1.8-5	1.3-6	3.6-6	1.4-6	1.9-6	2.6-5	1.4-3	1.5-3	4.9-3	5.0-3
AMS	1.6-6	3.0-6	8.6-6	1.3-7	6.0-7	3.4-6	1.1-3	1.1-3	2.5-3	2.5-3
u-WSW	1.1-5	2.9-6	8.4-6	8.8-7	7.5-7	2.9-5	1.2-3	1.3-3	4.9-3	5.0-3
u-ENE	9.1-6	4.6-7	1.3-6	7.2-7	5.8-7	4.0-6	8.1-4	8.3-4	3.2-3	3.2-3
u-N	7.5-7	6.0-7	1.7-6	6.0-8	9.3-8	1.7-6	9.6-4	9.6-4	3.8-3	3.8-3
EBT-b	5.5-7	2.3-7	6.5-7	4.4-8	5.1-8	7.5-7	4.3-4	4.3-4	1.6-3	1.6-3
EBT-s	8.9-7	9.5-7	2.7-6	7.1-8	7.2-8	3.9-6	9.5-4	9.6-4	3.6-3	3.6-3
LGMS	1.1-5	6.7-7	1.9-6	8.8-7	6.8-7	5.7-6	7.0-4	7.2-4	2.4-3	2.4-3
CV-u	4.2-7	1.3-6	3.8-6	3.3-8	8.2-8	2.0-6	3.4-4	3.5-4	9.5-4	9.6-4

Table 10.5

Ratio of dose rate in the cavities between the PV and CV (100 years running, 1 day cooling) with 800 ppm by weight of cobalt in the steel of the inlet nozzles and main deck gratings to dose rate with 200 ppm by weight of cobalt (for dose points see §10.5 and Figs. 156-176)

	active core	reflector	barrel	upper plenum	SG bottom header	PV	inlet nozzle walls	water pipe model	ADS tank walls	main deck gratings	EB tank walls	LGMS tank walls	anti-missile shield	CV	total
IN-l							**3.42**			3.19					
IN-u							**3.47**			3.16					
IN-cap							**3.47**			3.12					
WPi							3.47			3.18					
l-E							3.37			3.17					
l-W							3.42			3.18					
l-S							3.46			3.22					
ADS							3.48			3.09					
CV-l-S							3.68			3.25					
GR-i-l							3.47			**3.25**					
GR-i-u							3.51			**3.25**					
AMS							3.61			3.26					
u-WSW							3.46			3.21					
u-ENE							3.58			3.21					
u-N							3.64			3.22					
EBT-b							3.22			3.24					
EBT-s							3.73			3.18					
LGMS							3.74			3.21					
CV-u							3.37			3.22					

Table 10.6

Ratio of dose rate in the cavities between the PV and CV (100 years running, 1 day cooling) with activation source only cobalt in the PV (at 30 ppm by weight) to dose rate with all activation sources in the PV (for dose points see §10.5 and Figs. 156-176)

	active core	reflector	barrel	upper plenum	SG bottom header	PV	inlet nozzle walls	water pipe model	ADS tank walls	main deck gratings	EB tank walls	LGMS tank walls	anti-missile shield	CV	total
IN-l						0.19									
IN-u						0.25									
IN-cap						0.14									
WPi						0.23									
l-E						0.19									
l-W						0.20									
l-S						0.20									
ADS						0.24									
CV-l-S						0.22									
GR-i-l						0.17									
GR-i-u						0.16									
AMS						0.15									
u-WSW						0.14									
u-ENE						0.19									
u-N						0.17									
EBT-b						0.25									
EBT-s						0.14									
LGMS						0.19									
CV-u						0.14									

11. DOSES DURING RUNNING IN THE AREA UNDER THE REACTOR, HOUSING THE SEISMIC ISOLATORS

11.1 Calculational model

The source and core descriptions were that of case "A" in §5.2 [^{235}U fission spectrum, average source (see §4.1), both the source and the geometry smeared in all 89 assemblies of the active zone, Standard Westinghouse 17x17 fuel assemblies, thick reflector, etc.]. A minimum thickness of 2 m of concrete was laid under the containment vessel. Then below the surface where the dose was scored, a further 1 m of concrete was laid to provide a neutron albedo (see Fig. 179). Note in Fig. 179 the scoring surface is shown in red and the surfaces employed for variance reduction are also shown.

No rebar was employed in any of the modeled concrete.

Two different doses were calculated: biological whole body dose with the neutron and photon flux-to-dose response functions taken from [17] (units: Sievert) and absorbed dose (units: Gray). To calculate the latter a rubber composition $(C_5H_8)_n$ was assumed [116] page 309, with an assumed density of 1.6 g cm^{-3} (a density of between 1.2 and 1.65 g cm^{-3} is given in [116] page 315).

11.2 Results

As well as the normal radial reduction in the dose expected due to the limited radial extent of the source, there is an enhanced effect due to the greater concrete penetration required with increasing radius (see Fig. 179). To estimate the maximum dose on the axis, the doses were calculated in annular rings of radii: 0-75, 75-150, 150-225, 225-300 and 300-375 cm and then extrapolated to a maximum value at zero radius. The neutron and γ doses were calculated separately. The neutron and gamma doses are shown in Figs. 180 and 181 respectively. The statistical errors are also present in the two figures but are too small to be seen (of the order of 2 – 3% for the neutron doses and 1 – 2 % for the gamma doses). Note these are statistical rather than systematic errors.

From Figs. 180 and 181, extrapolating to a point on the axis we obtain the following maximum doses in the seismic isolator area:

	μSv/h	μGy/h
neutron:	**5.5E-9**	**3.3E-10**
gamma:	**1.6E-2**	**1.5E-2**

Note these results do not take into account modeling and nuclear data uncertainties.

12. ACTIVATION DOSE AROUND BARE STEAM GENERATOR

12.1 Calculational model for generating the neutron fluxes: geometrical and material description

The calculational model employed the second (heterogeneous) model of the steam generator supports (§9.1.1) with the separate, explicit bottom header from the second model of the steam generators (§6.1.2) and with, above the bottom header, the third model of the steam generators. Also the segmentation of the geometry to average the neutron fluxes has been described in §9.2 and is shown in Figs. 108 to 115. Again the source and core description were that of case "A" in §5.2 [^{235}U fission spectrum, average source (see §4.1), both the source and the geometry smeared in all 89 assemblies of the active zone, Standard Westinghouse 17x17 fuel assemblies, thick reflector, etc.].

12.2 Calculational model: activation and activity

In FISPACT a 100 year irradiation time at 100% load [running at 1000 MW (th)] was assumed followed by a 24 hour cooling time. A 200 ppm by weight content of Co was assumed in the steel of the steam generator supports and bottom header. Activation of the part of the steam generator above the bottom header was ignored.

12.3 Results for doses around bare, extracted steam generator

The points at which the dose was calculated, assuming the steam generator is extracted together with its bottom header and lower support, are shown in Fig. 182. On the inner (core) side, there are two different heights, beside the lower part of the bottom header and beside the lower end of the "I" shaped beams. The doses are also reported underneath the steam generator support on the inner (core) side. There are three distances: at the surface, at 1m from the surface and at 10 m from the surface. The points at 10 m from the surface are not shown in Fig. 182. The doses are shown in Table 12.1.

The dose component due to the steam generator lower support has also been evaluated at 72 hours after shut-down. The doses were between 97 and 98% of the 24 hour values.

Discussion

Apart from for the dose point in contact with the bottom header, the dose from the lower support predominates. The difference between the contributions from the lower support and bottom header indicate that the dose from the structure of the steam generator immediately above the bottom header can certainly be neglected, at least for those dose points considered and more generally for dose points at distances of 1 m or more from the lower part of the steam generator.

The highest dose is actually underneath rather than beside the inner side of the steam generators, again as expected if we examine for example Fig. 152.

12.4 Results for doses around bare, extracted steam generator with four times the reference cobalt content

The cobalt content in both the steam generator lower support structure and the steam generator bottom header was increased from 200 to 800 ppm by weight. After a 100 year irradiation time followed by a 24 hour cooling time the doses at the same points as in Table 12.1 were calculated. They are shown in Table 12.2 as a ratio of dose with 800 ppm cobalt to dose with 200 ppm.

Discussion

At 24 hours after shut-down, there is a substantial fraction of the dose from non-cobalt sources, especially from the lower header (ratios of around 2.5 means that at the reference cobalt impurity level of 200 ppm only about 50% of the dose is from cobalt). The lower support, which accounts for nearly all the dose, has a ratio of around 3. This means that at the reference cobalt impurity level of 200 ppm, about 67% of the total dose is from cobalt. Assuming that the dose scales linearly with the cobalt impurity concentration (at concentrations greater than 200 ppm) is therefore conservative.

Table 12.1

Dose rate in μSv/h in the presence of an extracted, bare, steam generator (including bottom header and lower support) (100 years running, 24 hours cooling) (for dose points see Fig. 182)

Axial position (see Fig. 182)	Position with respect to SG surface	Dose from SG lower header	Dose from SG lower support	Total
Beside inner (core) side of lower part of bottom header	at surface	15.4	5.2	20.6
Beside inner (core) side of lower part of "I" shaped beams of lower support	at surface	0.021	4014.	4014.
Below inner (core) side of lower support	at surface	0.066	4744.	4744.
Beside inner (core) side of lower part of bottom header	1 m from surface	0.74	50.2	50.9
Beside inner (core) side of lower part of "I" shaped beams of lower support	1 m from surface	0.51	56.6	57.1
Below inner (core) side of lower support	1 m from surface	0.043	87.1	87.1
Beside inner (core) side of lower part of bottom header	10 m from surface	0.0097	0.68	0.69
Beside inner (core) side of lower part of "I" shaped beams of lower support	10 m from surface	0.0098	0.66	0.67
Below inner (core) side of lower support	10 m from surface	0.0021	0.96	0.96

Table 12.2

Ratio of dose rate in the presence of an extracted, bare, steam generator (including bottom header and lower support) (100 years running, 24 hours cooling) with 800 ppm by weight of cobalt in the steel to dose rate with 200 ppm by weight of cobalt (for dose points see Fig. 182)

Axial position (see Fig. 182)	Position with respect to SG surface	Dose from SG lower header	Dose from SG lower support	Total
Beside inner (core) side of lower part of bottom header	at surface	2.55	3.04	2.67
Beside inner (core) side of lower part of "I" shaped beams of lower support	at surface	3.61 (!)	3.03	3.03
Below inner (core) side of lower support	at surface	3.44 (!)	3.04	3.04
Beside inner (core) side of lower part of bottom header	1 m from surface	2.51	2.97	2.96
Beside inner (core) side of lower part of "I" shaped beams of lower support	1 m from surface	2.54	2.93	2.93
Below inner (core) side of lower support	1 m from surface	2.51	3.02	3.02
Beside inner (core) side of lower part of bottom header	10 m from surface	2.51	2.95	2.94
Beside inner (core) side of lower part of "I" shaped beams of lower support	10 m from surface	2.51	2.94	2.93
Below inner (core) side of lower support	10 m from surface	2.42	3.02	3.02

(!): poor statistics

13. EOL ACTIVITY IN REFLECTOR AND BARREL AND CONSEQUENT ACTIVATION DOSE AROUND BARE REFLECTOR AND BARREL

13.1 Calculational model for generating the neutron fluxes: geometrical and material description

The calculational model was identical to that employed in §8.1 for the maintenance doses in the PV well. Also the segmentation of the geometry to average the neutron fluxes was identical to that described in §8.2 and is shown in Fig. 81.

13.2 Calculational model: activation and activity

In FISPACT a 100 year irradiation time at 100% load [running at 1000 MW (th)] was assumed followed by a 2 year cooling time. A 200 ppm by weight content of Co was assumed in the steel.

13.3 Results for EOL activity in reflector and barrel

To obtain the average activity in the reflector and barrel, the total activity was divided by the total mass. For both the total activity and mass, all the reflector was considered, both the part whose inner surface follows the outer shape of the active core and which contains 90% by volume steel and the upper part whose inner surface is cylindrical and which contains 100% steel. Instead only the part of the barrel below the top surface of the upper part of the reflector was considered (see Fig. 81).

The average activities of selected nuclides in the reflector are shown in Table 13.1 and in the barrel are shown in Table 13.2. The selection is somewhat arbitrary and is according to the specific activities rather than the activities relative to their respective clearance levels. As in §7.4 the clearance levels are from [96] and [97].

Discussion

No safety factors are attached to the results in Tables 13.1 and 13.2. The only element of conservativeness is the employment of the source and active core models of case “A”, which in §5.2 were shown to be a factor of around 1.23 too high for γ production (during running) in the barrel and reflector.

13.4 Results for doses around bare, extracted reflector and barrel

The points at which the dose was calculated, assuming the reflector and barrel are extracted together from the core, are shown in Fig. 183. There are five different heights, the highest one at the centre of the active zone. There are three radii: at the surface, at 1m from the surface and at 10 m from the surface. The points at 10 m from the surface are not shown in Fig. 183. The doses are shown in Table 13.3. As for the activities, these are for 100 years running and 2 years cooling.

Discussion

The same remarks as in §13.3 apply.

13.5 Results for doses around bare, extracted reflector and barrel with four times the reference cobalt content

The cobalt content in both the reflector and barrel was increased from 200 to 800 ppm by weight. After a 100 year irradiation time followed by a 2 year cooling time the doses at the same points as in Table 13.3 were calculated. They are shown in Table 13.4 as a ratio of dose with 800 ppm cobalt to dose with 200 ppm.

Discussion

At 2 years after shut-down, the dose from the barrel is nearly all due to cobalt (values near 4). The dose from the reflector includes also a relatively small fraction from other isotopes (a ratio of 3.5 means that at the reference cobalt impurity level of 200 ppm about 83% of the dose is from cobalt). As the barrel provides most of the dose, to a very good approximation the dose scales linearly with the cobalt impurity concentration (at concentrations greater than 200 ppm).

Table 13.1

Average Bq/g of selected nuclides in reflector at EOL

Irradiation	Cooling	^{49}V	^{54}Mn	^{55}Fe	^{59}Fe	^{57}Co	^{58}Co	^{60}Co
100 years	2 years	7.8E+3	2.1E+7	7.2E+8	6.0E+2	6.3E+4	1.7E+5	1.4E+8
Clearance		766	0.1	1000	1	1	1	0.1

Irradiation	Cooling	^{59}Ni	^{63}Ni	^{65}Zn
100 years	2 years	2.2E+6	2.6E+8	9.0E+2
IAEA Clearance		100	100	0.1

Table 13.2

Average Bq/g of selected nuclides in barrel at EOL

Irradiation	Cooling	^{49}V	^{54}Mn	^{55}Fe	^{59}Fe	^{57}Co	^{58}Co	^{60}Co
100 years	2 years	4.0E+2	7.9E+5	2.2E+8	1.3E+2	3.1E+3	7.3E+3	3.3E+7
Clearance		766	0.1	1000	1	1	1	0.1

Irradiation	Cooling	^{59}Ni	^{63}Ni
100 years	2 years	9.2E+5	8.9E+7
IAEA Clearance		100	100

Table 13.3

Dose rate in Sv/h in the presence of an extracted, bare, reflector and barrel (100 years running, 2 years cooling)

Axial position (from top to bottom – see Fig. 183)	Position with respect to barrel	Dose from barrel	Dose from reflector	Total
1 (opposite core mid-plane)	at surface	36.5	7.6	44.1
2	at surface	36.7	7.6	44.3
3	at surface	24.6	5.4	30.0
4	at surface	23.4	4.6	28.0
5 (bottom of reflector)	at surface	4.5	1.2	5.7
1 (opposite core mid-plane)	1 m from surface	12.5	3.6	16.1
2	1 m from surface	11.4	3.4	14.8
3	1 m from surface	8.2	2.4	10.6
4	1 m from surface	6.5	1.7	8.2
5 (bottom of reflector)	1 m from surface	5.4	1.4	6.8
1 (opposite core mid-plane)	10 m from surface	0.54	0.22	0.76
2	10 m from surface	0.53	0.22	0.75
3	10 m from surface	0.52	0.21	0.73
4	10 m from surface	0.51	0.20	0.71
5 (bottom of reflector)	10 m from surface	0.51	0.20	0.71

Table 13.4

Ratio of dose rate in the presence of an extracted, bare, reflector and barrel (100 years running, 2 years cooling) with 800 ppm by weight of cobalt in the reflector and barrel to dose rate with 200 ppm by weight of cobalt

Axial position (from top to bottom – see Fig. 183)	Position with respect to barrel	Ratio of doses from barrel	Ratio of doses from reflector	Ratio of total doses
1 (opposite core mid-plane)	at surface	3.87	3.53	3.81
2	at surface	3.86	3.52	3.80
3	at surface	3.90	3.67	3.86
4	at surface	3.91	3.67	3.87
5 (bottom of reflector)	at surface	3.96	3.80	3.93
1 (opposite core mid-plane)	1 m from surface	3.87	3.54	3.79
2	1 m from surface	3.87	3.53	3.79
3	1 m from surface	3.88	3.57	3.81
4	1 m from surface	3.88	3.61	3.83
5 (bottom of reflector)	1 m from surface	3.88	3.65	3.84
1 (opposite core mid-plane)	10 m from surface	3.87	3.54	3.77
2	10 m from surface	3.87	3.55	3.78
3	10 m from surface	3.87	3.54	3.78
4	10 m from surface	3.87	3.53	3.78
5 (bottom of reflector)	10 m from surface	3.87	3.54	3.78

14. CHANGING THE CONCRETE IN THE PV WELL TO CARBON STEEL: IMPACT ON EOL ACTIVITY

14.1 Calculational model for generating the neutron fluxes: geometrical and material description

The calculational model was identical to that employed in §7.1 for the EOL activity in the PV liner, PV, concrete liner and concrete in the PV well (i.e. case "A" for the core - §5.2) apart from the substitution of the concrete liner and concrete by a 35 cm thickness of carbon steel (with an identical composition to that of the pressure vessel [50], [51]). The inner surface of the carbon steel is identical to the previous inner surface of the concrete (and the steel liner of the concrete is absent).

14.2 Calculational model: activation and activity

As in §7.1.1 a 30 ppm by weight impurity of cobalt is assumed in the carbon steel.

Given that we have seen in §7 (Table 7.5) that at cooling times up to 2 years, ^{54}Mn gives a non-negligible contribution to the total activity (with respect to the clearance levels), in the search for the maximum activity the reaction ^{54}Fe(n,p)^{54}Mn is employed as well as the usual ^{59}Co(n,γ)^{60}Co. [Note that ^{54}Fe(n,p)^{54}Mn is typically responsible for more that 98% of the production of ^{54}Mn in the PV. This cross-section is shown in Fig. 184. ^{54}Fe constitutes 5.5% (at.) of the total number of atoms in the carbon steel. Also ^{54}Mn has a half life of 312 days.]

To find the zones of maximum activity in the carbon steel, the zones of maximum reaction rates of ^{59}Co(n,γ) and ^{54}Fe(n,p) were searched for using MCNP and the spatial segmentation shown in Figs. 185, 186 and 187. From these figures we see that the axial segmentation of the cylindrical part and the radial segmentation of the lower spherical part of the carbon steel substituting the concrete is made in an identical fashion to the previous concrete (§7.2 and Figures 73 and 74). Instead depth-wise the carbon steel is divided into 11 segments of 3 cm each (with a 2 cm thickness remaining at the outside).

14.3 Results for activation rates in the carbon steel in PV well

The activation rates for ^{59}Co(n,γ)^{60}Co and ^{54}Fe(n,p)^{54}Mn are shown in Table 14.1 (that is made in a similar style to Table 7.2).

As far as the ^{59}Co(n,γ)^{60}Co reaction is concerned, we see that the results decrease continuously with depth (i.e. no thermal peak) with the maximum values around the corner between the spherical bottom part and the cylindrical lateral part (as was the case previously for the concrete). Furthermore as discussed in §7.3 there will be a maximum around the azimuth due to the presence of the azimuthal struts. This will be taken into account with a safety factor of 1.1 like that of the concrete liner in §7.3 (this only for the ^{60}Co activity in zones that are in the shade of the struts). Given that the carbon steel provides a greater neutron albedo than the previous concrete, the result in Table 14.1 of 0.0082 reactions/g/s in the first 3 cm thickness near the core mid-plane looks consistent with the result of 0.0077 reactions/g/s from Table 7.1 in the outer 7 cm thickness of the PV.

As far as the $^{54}Fe(n,p)^{54}Mn$ reaction is concerned, we see that again the results decrease continuously with depth but with the maximum located higher up the cylindrical lateral part compared with $^{59}Co(n,\gamma)^{60}Co$ results. As expected, there is a much sharper decrease with depth compared with cobalt, so that it is necessary to define a safety factor to extrapolate the results up to the surface. We employ for this the factor 1.2 (the approximate square root of the ratio of 0.16 to 0.11 – see Table 14.1) only for the ^{54}Mn activity.

14.4 Results for maximum EOL activity in the carbon steel in PV well

In FISPACT a single irradiation time of 100 years was considered at 100% load [running at 1000 MW (th)]. Four cooling times were considered: 7 days, 60 days, 2 years and 10 years.

With the above factors included, the activities in the two zones of the carbon steel which show maximum activation rates for the two reactions of interest in Table 14.1 are presented in terms of selected nuclides in Tables 14.2 and 14.3. (The nuclides are selected with the same criterion as in §7.4.) Table 14.2 shows selected activities in the first 3 cm of the carbon steel in the lateral part [where in Table 14.1 the $^{54}Fe(n,p)^{54}Mn$ reaction shows a maximum of 0.16 g^{-1} s^{-1}]. Table 14.3 shows selected activities in the first 3 cm of the carbon steel in the bottom outer part [where in Table 14.1 the $^{59}Co(n,\gamma)^{60}Co$ reaction shows a maximum of 0.021 g^{-1} s^{-1}].

Discussion

Comparing the FISPACT results in Tables 14.2 and 14.3 with the MCNP results in Table 14.1 (we remind ourselves of the different sources of the data as discussed in §7.4), after removing the factors 1.1 and 1.2 from the results in Tables 14.2 and 14.3 we see an excellent agreement between the creation (via the above single reactions only) and decay rates:

	MCNP (creation)	FISPACT (7 day decay time)
^{54}Mn (lateral)	0.16	0.17
^{54}Mn (bottom)	0.087	0.090
^{60}Co (lateral)	0.019	0.019
^{60}Co (bottom)	0.021	0.021

As in §7.4, there is a slight conservative bias due to the source and core descriptions being from case "A" which we ignore. Following §7.4 we employ "spectral safety factors" of 1.1 for the UO_2 core and 1.2 for a 100% MOX core to the ^{60}Co activity results. Instead for the ^{54}Mn activity, given that it is created through a threshold reaction (Fig. 184), we use the "spectral safety factors" employed in §5.1.1 for the neutron-induced damage results to the vessel outside the azimuthal struts (1.3 for the UO_2 core and 1.5 for the 100% MOX core). [It seems reasonable to use these values as although we are now outside the 14 cm thick part of the vessel, the cross-section shows a maximum at around 8 MeV whilst the neutron dpa cross-section increases up to 20 MeV.]

Then with these safety factors we see from Tables 14.2 and 14.3 that in the carbon steel substituting the concrete in the PV well **for 100 years irradiation**:

– after 10 years cooling, the maximum ^{60}Co activity is 7% and 8% of the IAEA clearance level for the UO_2 and MOX cores respectively. All other nuclides give negligible activities.

– after 2 years cooling, the maximum ^{60}Co activity is 20% and 22% of the IAEA clearance level for the UO_2 and MOX cores respectively. Instead the maximum ^{54}Mn activity is 53% and 62% of the IAEA clearance level for the UO_2 and MOX cores respectively.

Here we have not applied any safety factor to account for transport model or data uncertainties. **Therefore although it looks as if at 10 years after shut-down all materials outside the PV are normally disposable, at 2 years the margin is too low to affirm this.**

Table 14.1

Activation rates in various parts of the carbon steel in the PV well; $^{59}Co(n,\gamma)^{60}Co$/g/s (in black) (Co impurities in §14.2); $^{54}Fe(n,p)^{54}Mn$/g/s (in blue); (for segments see Figs. 185 and 186) (for 1.2-3 read 1.2E-3)

	Inner part of well	Outer part of well	Carb. Steel (3 cm)	Carb. Steel (3 cm)	Carb. Steel (3 cm)	Carb. Steel (3 cm)	Carb. Steel (3 cm)	Carb. Steel (3 cm)	Carb. Steel (3 cm)	Carb. Steel (3 cm)	Carb. Steel (3 cm)	Carb. Steel (3 cm)	Carb. Steel (3 cm)
Cylindrical part (opposite core mid-plane) over 360°			8.2-3 1.4-2	7.3-3 8.6-3	6.6-3 5.3-3	5.9-3 3.2-3	5.2-3 2.0-3	4.6-3 1.2-3	4.0-3 7.5-4	3.5-3 4.5-4	2.9-3 2.7-4	2.4-3 1.7-4	2.2-3 1.1-4
Cylindrical part (opposite lower part of PV) over 360°			1.4-2 1.1-1	1.3-2 7.0-2	1.1-2 4.5-2	1.0-2 2.8-2	9.0-3 1.7-2	7.8-3 1.1-2	6.8-3 6.4-3	5.7-3 3.9-3	4.7-3 2.4-3	3.8-3 1.5-3	3.0-3 8.7-4
“			1.7-2 1.5-1	1.5-2 1.0-1	1.4-2 6.3-2	1.2-2 4.0-2	1.1-2 2.5-2	9.8-3 1.5-2	8.6-3 9.2-3	7.2-3 5.6-3	5.9-3 3.4-3	4.7-3 2.1-3	4.0-3 1.2-3
“			1.9-2 1.6-1	1.8-2 1.1-1	1.6-2 6.6-2	1.5-2 4.0-2	1.3-2 2.4-2	1.2-2 1.5-2	1.0-2 9.1-3	8.7-3 5.6-3	7.3-3 3.4-3	6.1-3 2.0-3	5.1-3 1.3-3
“			2.1-2 1.4-1	1.9-2 9.0-2	1.8-2 5.4-2	1.6-2 3.2-2	1.5-2 1.9-2	1.3-2 1.1-2	1.2-2 6.9-3	1.0-2 4.2-3	8.4-3 2.5-3	7.4-3 1.5-3	6.8-3 9.1-4
“			2.1-2 1.1-1	2.0-2 6.3-2	1.8-2 3.6-2	1.7-2 2.1-2	1.5-2 1.2-2	1.4-2 7.0-3	1.2-2 4.1-3	1.1-2 2.4-3	9.2-3 1.5-3	7.9-3 9.0-4	7.3-3 5.2-4
Bottom of PV well; Carbon Steel (3 cm) over 360°	2.0-2 1.1-1	2.1-2 8.7-2											
“	1.9-2 7.6-2	2.0-2 5.7-2											
“	1.7-2 4.9-2	1.9-2 3.6-2											
“	1.6-2 3.1-2	1.8-2 2.2-2											
“	1.5-2 1.9-2	1.7-2 1.4-2											
“	1.4-2 1.2-2	1.5-2 8.3-3											
“	1.3-2 7.2-3	1.4-2 5.0-3											
“	1.1-2 4.5-3	1.2-2 3.1-3											
“	1.0-2 2.7-3	1.1-2 1.9-3											
“	9.0-3 1.7-3	9.7-3 1.1-3											
“	8.4-3 1.0-3	8.5-3 6.7-4											

Table 14.2

Activity at EOL in Bq/g in carbon steel in zone that contains the maximum ^{54}Mn activity

Irradiation	Cooling	^{51}Cr	^{54}Mn	^{55}Fe	^{59}Fe	^{58}Co	^{60}Co	^{63}Ni	^{99}Mo
100 years	7 days	0.010	0.20	0.64	0.028	0.017	0.019	0.004	0.012
	60 days	0.003	0.18	0.62	0.012	0.010	0.019	0.004	-
	2 years	-	0.041	0.39	-	-	0.015	0.004	-
	10 years	-	-	0.051	-	-	0.005	0.004	-
IAEA Clearance		100	0.1	1000	1	1	0.1	100	10

Table 14.3

Activity at EOL in Bq/g in carbon steel in zone that contains the maximum ^{60}Co activity

Irradiation	Cooling	^{51}Cr	^{54}Mn	^{55}Fe	^{59}Fe	^{58}Co	^{60}Co	^{63}Ni	^{99}Mo
100 years	7 days	0.007	0.11	0.65	0.032	0.009	0.024	0.005	0.014
	60 days	0.002	0.096	0.62	0.014	0.005	0.023	0.005	-
	2 years	-	0.022	0.39	-	-	0.018	0.004	-
	10 years	-	-	0.052	-	-	0.0063	0.004	-
IAEA Clearance		100	0.1	1000	1	1	0.1	100	10

15. SOME QUALITY CONTROL CONSIDERATIONS

This report is not written as a quality assurance document. Notwithstanding, we make the following remarks from the QC perspective:

– The modeling of the geometry should be reasonably secure. Many two-dimensional plots have been made, appearing in the report and not, that suggest a reasonably faithful correspondence of the geometry model to the technical drawings.

– The above plots however only show different materials or voids. There has not been any kind of independent check on the material compositions and total densities, as present in the MCNP input files. Here there are two separate issues:

  – The definition of the materials and the creation of mixtures: EXCEL files were used to create the mixtures. These files are cited in the text when present in the e-room and if not, are in any case available.

  – The insertion of the materials with the correct total density in the right cell in the geometry. This particular issue is considered significant.

– Apart from a few "point flux" estimations (some dose points in §10, §12 and §13), radiation responses have been tallied in volume or on surface segments. The volumes or areas of these segments were calculated analytically, where possible, or estimated where an analytic solution was not found. In all cases where the volumes or areas were estimated and in nearly all cases where an analytic solution was used, a statistical check was made (voiding the geometry and employing a simple source: either mono-directional on a plane or inwardly-directed on a sphere). The same procedure was employed for the volume segments required by FISPACT (fluxes in units of cm^{-2} s^{-1} and total numbers of atoms of each nuclide starting from the atomic densities). If the result required from FISPACT is the gamma source, then the volume segment is not in fact used (i.e. it cancels). If instead the specific activities are required (as in §7 and §14), the volume segments are used.

– The flux-to-dose response functions employed (§3.2) were more commonly used in high energy applications. No other response functions have been used to check them.

– As far as the dpa response functions are concerned, just two sets were employed for the neutron values (§3.2 and §5.2.3). It is assumed that these two sets are independent. Instead for the gamma values just one set was used (§3.2). In the gamma case this leads to a degree of uncertainty in the results (see §16.1).

– As far as the spatial distribution of the fission source is concerned (§4.1.2), extensive effort was made to check the conversion from the format supplied by WEC to that required by MCNP. The difference in results for the neutron flux impinging on the vessel between cases "R" and "A" looks reasonable and as might be expected, as does the difference between the homogeneous distribution case "E" and case "D" (see Fig. 18 and §5.8). However as discussed in §4.1.2, doubts must remain on this item.

– Instead as far as the energy distribution of the source is concerned, the MCNP input is simple and straightforward and errors should not creep in here.

– As far as the activation, activity and delayed gamma source is concerned (with FISPACT), there has been shown to be consistency between MCNP results for the creation rates

of ^{60}Co and ^{54}Mn and FISPACT results for the decay rate, under specific circumstances (see discussions in §7.4 and §14.4). Instead for ^{152}Eu there were important differences between the two rates (§7.4), differences that were credited to cross-section differences. (It may also be reported that simple trials have been made with FISPACT with standard thermal neutron spectra impinging on cobalt and sodium, comparing the results with analytic solutions.) EXCEL files were employed to calculate the number of atoms of each nuclide, including impurities, required by FISPACT. These files are available. However the conversion of "fraction by weight" (the usual way that the amount of impurity is defined) to "fraction by atom" (required by FISPACT) was usually made in a dummy MCNP run. (MCNP automatically lists the atomic and weight fractions for each component of each material and the atomic and weight densities of each material.) The outputs of these dummy MCNP runs have been discarded.

– The interfaces MCNP–FISPACT (for example for the neutron fluxes which must be inverted) and FISPACT–MCNP (for the activation gamma source) are essentially manual.

– Concerning the definition of the gamma activation source in MCNP, there are well-known sampling problems in MCNP with multiple sources, dependent distributions and cell (or "ccc") rejection (see for example the MCNP user forum of 2006). Here for the activation gamma sources, the rejection probability was made constant for each source in a run (for example each source within the steam generator lower support) by varying the size of the sampling volume containing the source. Such a procedure involves a reduction of quality control.

16. SUMMARY OF RESULTS

16.1 Damage to the Pressure Vessel (§5)

Whilst previously in §5 a 60 year lifetime at 100% load was assumed, here we consider a 100 year lifetime at 100% load

Fast neutron fluence (> 1 MeV)

For a 100 year lifetime for the reference case (Standard Westinghouse 17x17 fuel assemblies, "thick" reflector), the calculated results for the fast neutron fluence (> 1 MeV) are a factor **500 below** the surveillance limit of 1E+17 n cm^{-2} ([60], [61], [62]) for a 100% MOX core (§5.9.1). This factor is approximately **140** with the Enhanced Moderation fuel assemblies with the thinner reflector (case "D" §5.9.2). Any structure that has not been modeled between the barrel and the PV will lower the fast neutron flux on the PV.

These results do not take into account modeling and data uncertainties (but do include a factor accounting for uncertainty in the high energy tail of the fission distribution - §5.1.1). As far as the modeling uncertainties are concerned, firstly the homogenization of the regions between the active core and the core bottom plate (§4.2.2) may not be conservative for streaming in the downward direction [although the maximum fast neutron flux on the PV is due to radial rather than downward, axial, leakage from the core (Fig. 19)]. So some margin [~40% = (6.8-4.8)÷4.8, see Fig. 19] is present here. Secondly the density of the water between the barrel and the PV may be a slight overestimate (§4.2.11). This would certainly increase the maximum fast neutron flux on the PV.

Neither the above modeling uncertainties, nor nuclear data uncertainties should reduce the above factors of 500 and 140 to values that would require a more systematic uncertainty analysis.

Neutron dpa

The greater distance between the barrel and the PV and the consequent presence of various contributing channels (*viz.* through the steel azimuthal struts as well as the downcomer) brings into question the conventional measure of damage limits with fast neutron fluence. Neutron spectral differences at the PV compared with conventional (generation ≤III) PWR's were accounted for by employing the neutron dpa to attempt to provide an equivalent fast neutron fluence. This brought the above factor of 500 for the reference core down to **270** (§5.9.1) and left the above factor of **140** for the core with the Enhanced Moderation lattice unchanged (§5.9.2). **The conclusions in the above section "Fast neutron fluence (> 1 MeV)" thus remain unchanged when considering neutron spectrum variations in this way.**

Gamma dpa

The greater distance between the barrel and the PV changes the ratio of fast neutron flux to gamma flux impinging on the PV. Gamma dpa responses were employed ([16]) to again provide an equivalent fast neutron fluence to allow a comparison with the surveillance limit. This brought the above factors of 270 and 140 (that took into account neutron spectral variations) for the

reference and the core with the Enhanced Moderation lattice down to just **approximately 5** (§5.9.1) and **3** respectively (§5.9.2). [The presence or absence of the neutron shield (§5.7) makes no difference here.]

In the gamma case there is a greater uncertainty attached to the dpa response function compared with the neutron case. Then if we remember that we must take into account geometric and material modeling and cross-section and source uncertainties (including the model uncertainties mentioned in the above paragraphs such as the density of the water in the downcomer), the factor of 3 in the case of the Enhanced Moderation lattice core implies that at some design stage further investigation, such as an uncertainty analysis, would be required.

16.2 Doses during running outside the biological shield (§6)

A relatively low dose rate of 0.25 μSv/h was adopted as the maximum individual dose rate in a permanently manned zone such as the control room. Such a low dose rate was not driven by the individual limit but by the desire to keep the collective dose low [117].

With a 1 m thick normal concrete biological shield, the maximum calculated dose in the control room was ~ 0.3 – 0.35 μSv/h. This reduced to ~ 0.015 μSv/h with a 1.5 m thick shield.

As discussed in §6.3, the predominant contributors to the dose outside the biological shield are the gamma's born in the barrel and reflector. [In this case the "spectral safety factor" (§5.1.1) is unity.] The gamma's follow a streaming path from the core out of the pressure vessel and through the gap in the concrete surrounding the PV well around the inlet nozzles (see for example Figs. 57 – 61). Under these circumstances, the model contains a number of conservative assumptions (§6.3):

- the source and core description that assumes homogeneous outer assemblies;
- a too thin containment vessel (§6.1.1);
- an absence of rebar in the concrete.

To these we may add further assumptions, all conservative:

- an absence of any structure between the barrel and the PV;
- the absence of the steam generator lower support model in these calculations (this is directly in the streaming path and will certainly make a difference);
- as discussed in §6.1.1, a presumed conservative modeling of the inlet nozzle walls and flanges;
- also as discussed in §6.1.1, the absence of floor gratings at the main deck level, tanks, etc.

Note that the non-conservative assumption of the hydrogen content of the concrete is as mentioned in §6.3 irrelevant as neutrons outside the PV have no impact on the dose.

Other modeling uncertainties (for example possible deviations from density homogeneities in the concrete of the biological shield) can raise the dose as can also nuclear data uncertainties. As far as the latter are concerned, rather than neutron or gamma ray cross-sections, the uncertainty and incompleteness of the n-γ cross-sections is mainly responsible for the uncertainty (and possible underestimation) in the dose. Also the presence of impurities tends to increase the

production of prompt gamma rays. This would usually be a problem for the concrete, but again, as there is a low neutron flux outside the PV, this is not relevant.

Finally the not-fine-enough angular and spatial binning of the scoring surface for the dose results in Tables 6.3, 6.5 and 6.7 should be borne in mind. For Table 6.3 this was grossly estimated as giving rise to a factor 1.3 (1 ÷ 0.76) increase.

Taking all these elements into account, a relatively low safety factor of 2 may be hypothesised to apply to the above dose results. This implies that with a 1.5 m thick biological shield, we are still a factor of 8 below the 0.25 μSv/h threshold assumed here.

16.3 EOL activity in PV liner, PV, concrete liner and concrete of PV well (§7)

The source and core descriptions were from case "A", so the results should be slightly conservative with respect to the reference case (§7.4).

Maximum activities without concrete boration

Assuming the impurity concentrations given in §7.1.1 - §7.1.3, after 100 years irradiation and 10 years cooling, ^{60}Co is the only important isotope in the PV liner, PV (even at the low reference concentration of 30 ppm), concrete liner and rebar. Instead in the concrete matrix, ^{60}Co is relatively unimportant compared with ^{152}Eu. The calculational results (§7.4) that include only safety factors to account for the uncertainty in the high energy tail of the fission distribution and to account for the uncertainty in the ^{151}Eu(n,γ)^{152}Eu cross-section indicate that for the MOX core:

- in the PV liner and PV, the maximum ^{60}Co activity is a factor of just over 50 and just under 6 respectively above the IAEA clearance level (and furthermore the results employ a factor of 2.5 that is not necessarily conservative to account for the variation of activity under the azimuthal struts).
- in the steel liner of the concrete and in the rebar in the concrete, the maximum ^{60}Co activity is around the IAEA clearance level.
- in the concrete matrix, the maximum ^{60}Co activity is a factor of nearly 7 below the IAEA clearance level, whilst the maximum ^{152}Eu activity is roughly 50% above the IAEA clearance level.

Instead for the UO_2 core the activities are slightly lower in the concrete (plus rebar and liner) but not by much.

Taking into account uncertainties in modeling and nuclear data, the above results imply that it is unlikely that any of the above materials can be disposed of normally, with some *caveats*: This conclusion is for the impurity concentrations given in §7.1.1 - §7.1.3. The results are for the source and core description that assumes homogeneous outer assemblies [this provides a conservative factor of around 1.2 (§7.4)], for an assumed maximum 1% by weight hydrogen content (which should again overestimate the result) and for an assumed 3% by volume rebar (which should underestimate the result if there is less rebar). Only if a number of conditions are met might the concrete liner, concrete and rebar be disposable:

- reducing the cobalt impurity in the steel liner substantially below its hypothesised value of 200 ppm;

- reducing the cobalt impurity in the rebar substantially below its hypothesised value of 100 ppm;
- reducing the uncertainty in the results by employing the core pin-by-pin model and the explicit lattice rebar model;
- reducing the uncertainty in the results by employing a better average (with time) hydrogen content in the concrete and a known rebar content;
- being able to remove the safety factor of 2 on the $^{151}Eu(n,\gamma)^{152}Eu$ cross-section.

Note that the idea of a sacrificial layer of the concrete, beyond which the concrete can be disposed of normally, would, because of neutron thermalization, involve a layer of a thickness substantially greater than 12 cm (see Table 7.2).

Maximum activities with concrete boration

Borating the concrete to 0.775% by weight (§7.5):

- makes no difference to the maximum ^{60}Co activities in the PV liner and PV.
- reduces the maximum ^{60}Co activity in the concrete liner by a factor of nearly 2.
- reduces the maximum ^{60}Co activity in the rebar by a factor of nearly 4.
- reduces the maximum ^{60}Co activity in the concrete matrix by a factor of nearly 5.
- reduces the maximum ^{152}Eu activity in the concrete matrix by a factor of nearly 20.

Furthermore the point of maximum activity in the concrete is moved from a depth of around 9 cm to near the surface.

Taking into account uncertainties in modeling and nuclear data, the above results imply that with a reasonable assumption of concrete boration [95], it is very likely that the concrete outside the PV can be disposed of normally. It is probable also that the concrete liner would be able to be disposed of normally.

Average activities in the PV liner and PV

In the expectation that melting metal components can equate the maximum activity to the average activity and thereby lower the maximum activity below the clearance level, the average activities in axial segments of the PV and PV liner were calculated. The calculational results (§7.6) showed:

- **After 10 years cooling**, cutting the pressure vessel anywhere leaves both parts with an average activity below the clearance level. Cutting at the worst place leaves the lower part with a calculated activity a factor of 3 below the C.L. (Table 7.13). **The whole lower half of the PV (segments 1-9, Table 7.13) has an activity that is more than a factor 10 below the C.L.** Such a factor will amply cover modeling and data uncertainties.
- Instead **after 10 years cooling, the lower part of the pressure vessel liner is still substantially above the C.L. even taking all nine segments (cutting just above the inlet nozzles) (Table 7.11).** Only if we cut above the 6th axial segment

(see Fig. 79), the upper part of the pressure vessel liner should be below the clearance.

– If instead the PV liner is left joined to the PV, **after 10 years cooling the whole lower half of the PV + liner** (segments 1-9, Table 7.15**) has an activity that is slightly less than a factor 10 below the C.L.** Again at 10 years cooling, any axial segment of the pressure vessel + liner has a calculated average activity below the clearance level (although too close to be below after safety factors are taken into account) (Table 7.16). **Cutting anywhere above the 5th axial segment should leave both upper and lower parts of the PV + liner below the C.L.** (Table 7.15).

16.4 Maintenance doses in the PV well (§8)

As for the EOL activities in the PV well (§16.3), the results for the maintenance doses are for the source and core description that assumes homogeneous outer assemblies (§8.1). It is not clear what degree of conservativeness this provides for activation gamma's born in the core. Probably the factor is greater than that for prompt gamma's (around 1.25 – see §5.2). This of course only applies in the radial direction, not in the axial direction underneath the core.

We have seen from Table 8.1 that the core, lower plenum, reflector and barrel are responsible for all the maintenance dose in the PV well in proportions that depend on where the dose point is situated (see Fig. 95). The spatial binning of the neutron fluxes (§8.2) shown in Figs. 80 – 84 leads to conservative results for all these regions.

Although employing an inappropriate tool to calculate the gamma source in the active core (and therefore also in the plena), the resulting source compares reasonably with two independent evaluations (§8.4.1 and Figs. 92 and 93). A lifetime of 10 in-core years is a conservative estimate. The assignment of 2% of all the fission products with boiling point < 1000°C to the lower plenum is apparently also conservative.

As possible offsets, there is the homogenization of the lower plenum region (in this context this includes everything between the bottom plate and the active zone) and in general the presence of impurities not accounted for.

Considering the volume "D7" (Fig. 95) for the maximum volumetric dose (rather than the surface "A5" as in §8.4.2) and following the above considerations adopting a safety factor of 3 as in §8.4.2, **we have just under 120 μSv/h in the PV well below the PV with the maximum hypothesis of irradiation time (10 years fuel assemblies, 100 years rest) at 1 day after shut-down.** With the same safety factor, **this dose reduces to ~ 80 μSv/h at 3 days after shut-down** (§8.4.3, Tables 8.1 and 8.2).

Instead considering the volume "D3" (Fig. 95) for the maximum volumetric dose in the radial direction and adopting the same safety factor of 3 (although it should be less in the radial direction), **we have ~ 42 μSv/h in the PV well beside the PV with the maximum hypothesis of irradiation time (10 years fuel assemblies, 100 years rest) at 1 day after shut-down.** With the same safety factor, **this dose reduces to ~ 38 μSv/h at 3 days after shut-down** (§8.4.3, Tables 8.1 and 8.2).

The contributions of the barrel and reflector, shown in Table 8.1, scale roughly with the cobalt content (§8.4.4 and Table 8.3). For example, **four times the reference cobalt impurity concentration in the reflector and barrel changes the dose at 1 day after shut-down in**

volume "D3" from the ~42 μSv/h above to just under 75 μSv/h (from §8.4.4, Tables 8.1 and 8.3 and assigning the same cobalt dose factor to the reflector as was found in the barrel) whilst leaving **the dose of just under 120 μSv/h in volume "D7" (above) virtually unchanged.**

Note that the "Spectral Safety Factor" (§5.1.1 and §7.4) is unity because nearly all the activation gamma's come from in, or near, the core. Note also that the density of the primary water after shut-down for the gamma transport was taken as 1 g cm^{-3}.

16.5 Maintenance doses in cavities between the PV and the containment (§10)

Again the source and core descriptions are for the model that assumes homogeneous outer assemblies (§10.2). This introduces a degree of conservativeness that has not been quantified (and that is different for each of the gamma sources: in the activated core, in the activated barrel and outside the PV).

The quality of the activation sources in the core, plena, reflector and barrel has been discussed in §16.4. The spatial binning of the neutron fluxes in the pressure vessel (Figs. 149 and 150) should be conservative. Just as for the dose during running outside the biological shield, the gamma's born inside the pressure vessel (apart from those originating in the steam generator bottom header) follow a streaming path through the gap in the concrete surrounding the PV well around the inlet nozzles (see for example Figs. 57 – 61). As in §16.2 we then have a number of conservative assumptions in the model for these gamma's:

- an absence of any structure between the barrel and the PV;
- as discussed in §6.1.1, a presumed conservative modeling of the inlet nozzle walls and flanges.

Note that in contrast to the model of §16.2, the steam generator lower support model was present in these calculations (§10.1).

Instead the gamma source in the steam generator bottom header is not necessarily conservative, as greater structure between the barrel and the PV and in particular around the SG lower support zone should raise the activation source in the SG bottom header.

As far as the activation sources in the structures outside the pressure vessel are concerned, there is clearly a large uncertainty involved. The structures are mocked-up in an approximate fashion, their volumes may be larger and there are certainly more of them. Also the spatial binning of the neutron fluxes in the structures outside the pressure vessel (Figs. 125 – 148) is not necessarily conservative. All these uncertainties were taken into account with the introduction of the "Gross Structure Constant" (GSC) (§10.6) and its assigned values of 4 or 16 (the latter value probably leads to conservative results, the former possibly not). [Note that the "Spectral Safety Factor" (§5.1.1 and §7.4) might be non-unity for activation outside the pressure vessel, but it is convenient to include it within the GSC value.]

The increased water density in the primary after shut-down compared with during running leads to a weighting of the dose results in favour of extra-PV sources. The possible voiding of the secondary water means that the steam generator bottom header has some local importance outside the inlet nozzle cap. Both these effects weigh the activation dose towards the sources that are more uncertain and not necessarily conservative.

However the calculated doses at 1 day after shut-down in the cavities between the PV and the containment are actually very low. With the GSC=16, there is a maximum dose above

the water pipe model (Figs. 162 and 164) of 0.010 μSv/h and in the cavity above the main deck (Fig. 158) of 0.0050 μSv/h (§10.6 and Table 10.4). Whilst most of the considerations on the uncertainty of the doses in the PV well (§16.4) apply also here for the sources within the PV, for the sources outside the PV, the GSC is intended to cover them. Therefore the same safety factor of 3 as for the maintenance doses in the PV well is adopted, **producing at 1 day after shut-down a dose of 0.030 μSv/h above the water pipes below the main deck and 0.015 μSv/h in the cavity above the main deck.**

At 3 days after shut-down, from §10.7 and Table 10.4 the above doses of 0.030 μSv/h and 0.015 μSv/h remain unchanged.

Four times the reference cobalt concentrations in the steel structures both within and outside the PV change the above doses at 1 day after shut-down of 0.030 μSv/h above the water pipes below the main deck and 0.015 μSv/h in the cavity above the main deck to 0.104 μSv/h and 0.047 μSv/h respectively (employing §10.8, §10.9, Tables 10.3, 10.5 and 10.6 and extrapolating the results in Table 8.3).

Removing the end flange of the inlet nozzle produces a calculated dose of 0.021 μSv/h at the end of the inlet nozzles with a GSC value of 16. The contribution to this dose from the activated SG bottom header is 0.017 μSv/h (with a negligible contribution from the SG lower support) (§10.10). Because of uncertainties in the geometric modeling of the SG lower support zone and possible neutron streaming pathways through steel not included in the current model (for example the absence in the model of structure above the core top plate), a safety factor of 5 is assigned to the contribution from the SG bottom header. With the above safety factor of 3 on the remaining part of the dose, **we have a dose of virtually 0.1 μSv/h at the end of the inlet nozzles under these conditions.** [Note that the "Spectral Safety Factor" (§5.1.1 and §7.4) is considered unity for this result.]

16.6 Dose during running in the area housing the seismic isolators (§11)

Assuming 2 m of concrete below the containment vessel (and a further 1 m of concrete within the containment vessel in the pressure vessel well) (Fig. 179), the neutron dose is negligible, while the gamma calculated dose is 0.016 μSv/h (§11.2). A rubber composition for the isolators is assumed that produces an absorbed dose that is 0.015 μGy/h, very nearly the same as the (biological) dose equivalent.

The contributing gamma's are created in the core and the bottom plate. This means that no "Spectral Safety Factor" (§5.1.1) is assigned. Although the source and core descriptions are again for the model that assumes homogeneous outer assemblies (§11.1), this does not provide conservative results in this case because the contributing transport path is axial rather than radial.

Possible sources of non-conservativeness in the geometric model are the homogenization of the zone between the bottom plate and the active core and the lack of homogeneity of the concrete. As usual, there are of course nuclear data uncertainties and in particular the uncertainty and incompleteness of the n-γ cross-sections.

A gross estimate of the global uncertainty is to give a safety factor of 5, leading to a biological dose of 0.080 μSv/h and an absorbed dose of 0.075 μGy/h.

16.7 Maintenance dose around an extracted steam generator (§12)

Again the source and core descriptions are for the model that assumes homogeneous outer assemblies. As the main contributing path to neutron activation of the steam generator lower support (which provides nearly all the dose) is for the neutrons to exit the core radially (see Fig. 99), this introduces an element of conservativeness. However the geometry modeling of the steam generator lower support (§9.1.1 and Figs. 99 to 106) is not necessarily conservative, neither is the geometry segmentation of either the lower support or the lower header for the averaging of the neutron fluxes (§12.1 and Figs. 108 to 115).

A concern exists that steel structure that has not been modeled below the steam generator lower support can provide a streaming path for neutrons that exit the barrel radially. Also steel structure that has not been modeled does exist above the top core plate. This may decrease the neutron attenuation between the top plate and the inner side of the steam generator lower support and bottom header (see Fig. 99). However it is not thought that this will be very relevant to the activation of the lower support.

Finally the "Spectral Safety Factor" following the discussion in §7.4 (concerning the activation of the PV liner and PV) should be unity.

Following these considerations, a safety factor of 3 is (grossly) estimated to be applied to the results in Table 12.1. **The doses underneath the steam generator after 100 years irradiation and 1 day cooling are then: just under 15 mSv/h at the surface, 260 μSv/h at 1 m below the surface and just under 3 μSv/h at 10 m below the surface. The maximum doses beside the steam generator are: 12 mSv/h at the surface, slightly over 170 μSv/h at 1 m from the surface and 2 μSv/h at 10 m from the surface.**

The above results are for the reference 200 ppm cobalt impurity. **In the SG lower support, cobalt accounts for roughly 2/3 of the dose** (§12.4 and Table 12.2). Thus for example, four times the reference cobalt content gives three times the above doses.

16.8 EOL activity in reflector/barrel and consequent activation dose around extracted reflector/barrel (§13)

The source and core descriptions are for the model that assumes homogeneous outer assemblies implying ~25% degree of conservativeness (§13.3). A low safety factor of 1.2 is then assigned to the results for the activities in Tables 13.1 and 13.2. No "Spectral Safety Factor" is assigned. **After 100 years irradiation and 2 years cooling, the most important isotopes in the reflector are (factor over C.L.): ^{54}Mn(3E+8), ^{55}Fe (1E+6), ^{60}Co (2E+9) and ^{63}Ni (3E+6). The most important isotopes in the barrel are (factor over C.L.): ^{54}Mn(9E+6), ^{55}Fe (3E+5), ^{60}Co (4E+8) and ^{63}Ni (1E+6).** (Cobalt impurity assumption is 200 ppm.)

The calculated dose results, given in Table 13.3 are also assigned the safety factor of 1.2. **The maximum doses beside the reflector/barrel are: slightly over 53 Sv/h at the surface, just under 20 Sv/h at 1 m from the surface and just under 1 Sv/h at 10 m from the surface**. This dose scales quite closely with the cobalt content (§13.5).

16.9 Changing the concrete in the PV well to carbon steel: impact on EOL activity (§14)

The source and core descriptions were from case "A", so as usual the results should be slightly conservative with respect to the reference case (§7.4). Assuming 30 ppm cobalt impurity in the steel, **after 100 years irradiation and 10 years cooling the activity (all ^{60}Co) is an order of magnitude below the clearance level for UO_2 or MOX fuel. At 2 years cooling the total activity is just under the clearance level.** At 2 years cooling the ^{54}Mn activity is roughly three times the ^{60}Co activity. So a greater cobalt impurity will not change the results too much.

Taking into account data and model uncertainties, all materials outside the PV should be normally disposable around 4 – 6 years after shut-down.

Note in substituting the concrete around the PV well by carbon steel, possible changes in other ex-core radiation responses have not been considered. The maintenance doses at 1 day after shut-down in the PV well (§8) and in the cavities between PV and containment around the main deck level (§10) will certainly increase. However their current levels are low enough for such increase to be probably acceptable. Also the dose outside the biological shield (§6) will increase but probably by little. The neutron-induced damage to the pressure vessel will also increase a little but it is the gamma-induced damage that is driving the total damage and this will remain unchanged.

Acknowledgements

ENEA: Lodovico Casalini provided substantial support and back-up.

Georgios Glinatsis ran the ORIGEN calculations.

Isaac Habert as always provided informatics support.

Carlo Petrovich advised on the use of FISPACT.

The informatics group at ENEA Frascati and in particular Pietro D'Angelo and Salvatore Podda.

ENSA: Jesús Collado provided information on the steel of the PV and on the position of the core internals.

Georgia Tech.: Bojan Petrovic directed the project and gave general backup.

Mangiarotti Nuclear: Fabio Berra supplied the steam generator drawings.

ORNL: Jeffrey O. Johnson provided the reference for the gamma dpa cross-sections, supplied advice on where dpa is calculated in the vessel and gave general support.

Politecnico di Milano: Carlo Lombardi provided the shielding documents produced by PoliMi and the data on clearance levels. He proposed the idea of substituting the concrete in the PV well by carbon steel (§14). He also reminded us in a timely fashion that after shut-down the density of the water within the PV is 1 g cm^{-3}.

Enrico Padovani provided support on the PoliMi shielding activity.

Westinghouse: Fausto Franceschini coordinated the project, gave general backup and reviewed this report. He also supplied the fission source in the IRIS core (both the average source, the maximum source and a skewed source for testing purposes) and information on dose zoning.

Andrea Maioli provided useful input on the IRIS system as a whole and on the structure.

Gary D. Storrick provided useful advice on the IRIS system.

The Westinghouse shielding group brought to attention the question of the ^{16}N source.

REFERENCES

[1] X-5 Monte Carlo Team, "MCNP – A General Monte Carlo N-Particle Transport Code, Version 5", LA-UR-03-1987, Los Alamos National Laboratory, April 24, 2003 (Revised 10/3/05).

[2] J.S. Hendricks *et al.*, "MCNPX, VERSION 26D", LA-UR-07-4137, Los Alamos National Laboratory June 20, 2007

[3] R.A. Forrest: "FISPACT-2001: User Manual", UKAEA FUS 450, Dec. 2001

[4] S. C. Frankle, R. C. Reedy, and P. G. Young, "ACTI - An MCNP Data Library for Prompt Gamma-ray Spectroscopy", Proc. of the 12th Biennial Radiation Protection and Shielding Topical Meeting, Santa Fe, NM (April 15-19, 2002)

[5] http://laws.lanl.gov/projects/data/nuclear/mcnpdata/acti.html

[6] J. M. Campbell, S. C. Frankle, and R. C. Little, "ENDF66: A Continuous-energy Neutron Data Library for MCNP4C", Proc. of the 12th Biennial Radiation Protection and Shielding Topical Meeting, Santa Fe, NM (April 15-19, 2002)

[7] http://laws.lanl.gov/projects/data/nuclear/mcnpdata/endf66.html

[8] http://laws.lanl.gov/projects/data/nuclear/mcnpdata/textendl92.html

[9] http://laws.lanl.gov/projects/data/nuclear/mcnpdata/sab_data.html

[10] M. C. White, "Photoatomic Data Library MCPLIB04: A New Photoatomic Library Based On Data From ENDF/B-VI Release 8", LANL internal memorandum X-5:MCW-02-111 and LA-UR-03-1019 (2002)

[11] http://laws.lanl.gov/projects/data/nuclear/mcnpdata/mcplib.html

[12] R.A. Forrest and J. Kopecky: "The European Activation File: EAF-2001 cross section library", UKAEA FUS 451, Dec. 2001

[13] Yu.A Korovin *et al.*, "BISERM-2. Nuclear Data Library for Evaluation of Radiation Effects in Materials Induced by Neutrons of Intermediate Energies", IAEA-NDS-203 (March 1997)

[14] A. Konobeyev, K. Voukelatou, "Displacement Cross-Sections for Materials Irradiated with Neutrons and Protons at the Energies up to 1 GeV". Private communication, April 2003

[15] O. Cabellos, package NEA-1768 ZZ-MCJEFF3.1NEA (http://www.nea.fr/html/dbdata/JEFF/processed/report_mcjeff31-v36.pdf) (2005)

[16] E.D. Blakeman, "Neutron and Gamma Fluxes and dpa Rates for HFIR Vessel Beltline Region (Present and Upgrade Designs)", ORNL/TM-13693 (Nov. 2000)

[17] M. Pelliccioni, "Overview of Fluence-to-Effective Dose and Fluence-to-Ambient Dose Equivalent Conversion Coefficients for High Energy Radiation Calculated with the FLUKA Code", *Rad. Prot. Dosim.*, **88**-**4**, 279-297 (2000)

[18] K.W. Burn *et al.*: "Variance Reduction with Multiple Responses", Proc. conf. "Monte Carlo 2000", Lisbon, 2000, pp. 687-695 (Springer) and citations in that paper

[19] L.S. Waters (ed.), "MCNPX™ USER'S MANUAL Version 2.1.5", TPO-E83-G-UG-X-00001, Revision 0, Los Alamos National Laboratory Nov. 14, 1999

[20] K.W. Burn: "A New Weight-Dependent Direct Statistical Approach Model", *Nucl. Sci. Eng.* **125** 128-170 (1997)

[21] F. Franceschini: e-room file: "asm_standard.txt"

[22] F. Franceschini: e-room file: "pin_standard.txt"

[23] F. Franceschini, 8th IRIS shielding conference call minutes (A. Maioli, 28th Feb. 2008)

[24] F. Franceschini: e-room file: "all_core_ax_sum.txt"

[25] F. Franceschini: e-room files: "asm_skew.txt" and "pin_skew.txt"

[26] WCAP-16062-P Rev.1 "IRIS Plant Description Document"

[27] F. Franceschini: e-room file: "IRIS_Core_Dim_r1.xls"

[28] ENSA I9219CRQ08 rev.0 (24th May 2007)

[29] F. Franceschini: e-room file: "dens_prfl.txt"

[30] K.W. Burn: e-room file: "core.water.densities.xls"

[31] K.Tonoike *et al.*, J. Nucl. Sci. and Technology, **40-4**, 238 (Apr. 2003)

[32] K.W. Burn: e-room file: "std.AP.smear.core.xls"

[33] K.W. Burn: e-room file: "enhan.mod.smear.core.xls"

[34] F. Franceschini: e-mail of 10th April, 2008

[35] F. Franceschini: e-room file: "fuel_ax_model_r1.doc"

[36] K.W. Burn: e-room file: "fuel-to-plates.xls"

[37] CRC Handbook of Chemistry and Physics, 52nd Edition, 1971-2, page F-127 [adopted values were: (% by wt.): Fe: 70; Cr: 19; Ni: 10; Mn: 1]

[38] http://www.hpalloy.com/alloys/descriptions/INCONEL601.html

[39] ENSA I9219CRQ06 rev.1 (29th Feb. 2008)

[40] J.M. Collado, private communication (Atlanta, 7th-8th March, 2008)

[41] ENSA I9219CRQ05 rev.0 (24th May 2007)

[42] ENSA I9219CRQ00 rev.1 (29th Feb. 2008)

[43] F. Franceschini: e-room file: "UpCorePlate_EqD.xls" (incorporates e-mail of 14th March, 2008 with attachment)

[44] B. Petrovic, private communication (Atlanta, 7th-8th March, 2008)

[45] ENSA I9219CRQ04 rev.1 (29th Feb. 2008)

[46] ENSA I9219CRQ07 rev.1 (29th Feb. 2008)

[47] ENSA %TDM_ID %REVISION "Estudio Fondo Inferior"

[48] ENSA I9219CRQ01 rev.1 (29th Feb. 2008)

[49] J.M. Collado, private communication (Atlanta, 7th-8th March, 2008)

[50] J.M. Collado: e-room file: "SA508.pdf" [commented article: "Specification for Quenched and Tempered Vacuum-Treated carbon and Alloy Steel Forgings for Pressure Vessel", SA-508/SA-508M (2007)]; (attachment to e-mail of 11th March, 2008)

[51] F. Franceschini: e-mail of 14th March, 2008

[52] E. Padovani, private communication

[53] WEC IRIS 1101-001 rev.X (28th June 2007)

[54] WEC IRIS 1110-001 rev.A (25th July 2007)

[55] Jaeger *et al.*: Engineering Compendium on Radiation Shielding, vol. II, p.173, table 9.1.12-76 (column 1), Springer-Verlag, 1975

[56] *idem* p.136 table 9.1.12-26

[57] C. Lombardi, E. Padovani: e-room file: "Conc.Comp.Rev1.doc"

[58] F. Franceschini: attachment to e-mail of 27th Oct. 2008 (draft minutes of Bologna shielding workshop)

[59] A. Cammi, C. Lombardi, E. Padovani:"IRIS Internal Shields – Update at Apr. 2002", IRIS 7th team Meeting, Arlington, VA, April, 2002

[60] B. Petrovic: e-room file: "IRIS_SHIELD._OBJ.rev3.pdf"

[61] U.S. Nuclear Regulatory Commission: "Calculational and Dosimetry Methods for determining Pressure Vessel Neutron Fluence", Regulatory Guide 1.190 (March 2001)

[62] U.S. Nuclear Regulatory Commission: "Appendix H to Part 50 – Reactor Vessel Material Surveillance Program Requirements" (19th Dec. 2007) (http://www.nrc.gov/reading-rm/doc-collections/cfr/part050/part050-apph.html)

[63] WEC IRIS 1102-001 rev.X (28th June 2007)

[64] WEC IRIS 1120-001 rev.X (28th June 2007)

[65] WEC IRIS 1130-001 rev.X (28th June 2007)

[66] A. Maioli: 2nd e-mail of 21st Oct, 2008 (with attachment: "IRIS - Notes on layout.doc 4")

[67] M.D.Carelli *et al.*: "The Design and Safety Features of the IRIS Reactor", Nucl.Eng. & Design vol.230 p.151 (2004)

[68] WEC IRIS 1101-001 rev.A (12th July 2007)

[69] WEC IRIS 1102-001 rev.A (16th July 2007)

[70] WEC IRIS 1110-001 (25th July 2007)

[71] WEC IRIS 1120-001 rev.A (12th July 2007)

[72] WEC IRIS 1130-001 rev.A (12th July 2007)

[73] ANSALDO IR-DWF-00-001 rev.2 (1st Feb. 2006)

[74] ANSALDO-IR-DWF-11-001 rev.1 (20th Apr. 2004)

[75] ANSALDO-IR-DWF-00-000 rev.2 (9th May 2006)

[76] ANSALDO IR-DWF-10-000 rev.0 (23rd Jan. 2006)

[77] ANSALDO IR-SPV-20-AESC001 rev.0 (23rd May 2005), page 9

[78] F. Franceschini: e-room file: "SG_data_ansaldo.doc"

[79] J.R. Davis: ASM Specialty Handbook, "Nickel, Cobalt, and Their Alloys", The Materials Information Society, ASM International Handbook Committee, p.33

[80] G. D. Storrick: e-room file: "IRIS Integral System Test Specification Rev 1.pdf"

[81] K.W. Burn: e-room file: "SG.model2.xls"

[82] WEC IRIS 1201-001 rev.A (17th July 2007)

[83] WEC IRIS 1230-001 rev.A (17th July 2007)

[84] WEC IRIS 1240-001 rev.A (18th July 2007)

[85] H. Grady Hughes *et al.* MCNPX User's Manual Version 2.4.0, LA-CP-02-408, Sept.2002

[86] A.H. Fero: "Use of SSTRs and a Multi-Component Shield Assembly to Measure Radiation Penetrating the Reactor Biological Shield in the Presence of Radiation Streaming from Other Sources", Reactor Dosimetry: Radiation Metrology and Assessment, ASTM STP 1398 [J.G. Williams, D.W. Vehar, F.H. Ruddy, D.M. Gilliam (Eds.), American Society for Testing and Materials, West Conshohocken, PA, 2001]

[87] A. Cammi, C. Lombardi, E. Padovani: "IRIS Internal Shields – Update at Apr. 2002", IRIS 7th Team Meeting, Arlington VA, April 2002

[88] A. Cammi, C. Lombardi, E. Padovani: "Internal Lateral Shields – Update at Aug. 2002", IRIS 8th Team Meeting, Rio de Janeiro, August 2002

[89] T. Matsumura, T. Hattori, T. Kawabe: "Assessment of Activation of Concrete Wall for Decommissioning of Nuclear Power Plants", ASTM STP 1398 [J.G. Williams, D.W. Vehar, F.H. Ruddy, D.M. Gilliam (Eds.), American Society for Testing and Materials, West Conshohocken, PA, 2001] (Table 1)

[90] http://efunda.com/materials/alloys/carbon_steels/low_carbon.cfm

[91] A. Suzuki *et al.*: "Trace Elements with Large Activation Cross Section in Concrete Materials in Japan", J. of Nucl. Science & Technology, **38-7** 542 (2001) (average over aggregates, Table 3)

[92] L.R. Carroll: "Predicting Long-Lived, Neutron-Induced Activation of Concrete in a Cyclotron Vault", CAARI 2000, Conf. on Applications of Accelerators in Research and Industry, Denton, Nov. 2000, page 6

[93] M. Kinno *et al.*: "Correlation between Tritium and ^{152}Eu Induced in Various Types of Concrete by Thermal Neutron Irradiation" J. of Nucl. Science and Technology, **39-3** 215 (2002) (Table 9)

[94] Free University of Brussels, "Evaluation of the Radiological and Economic Consequences of Decommissioning Particle Accelerators", Report EUR19151 (EC Nuclear Safety and the Environment, 1999) (Tables 4.3 and 4.4)

[95] M. Kinno *et al.*: "Development of Low–Activation Reinforced Concrete Design Methodology–1: Manufacture Of Low–Activation Concrete" Nucl. Technology **168** 564-570 (2009)

[96] IAEA: "Application of the Concepts of Exclusion, Exemption and Clearance", Safety Standards Series No.RS-G-1.7, IAEA Vienna, 2004

[97] R.A. Forrest: "The European Activation File: EAF-2007 biological, clearance and transport libraries", UKAEA FUS 538, March 2007

[98] K.W. Burn: e-room file: "AP.smear.core.shtdwn.xls"

[99] K.W. Burn: e-room file: "fueltoplates.shtdwn.xls"

[100] F. Franceschini, e-mail of 13th Feb. 2009

[101] S.M. Bowman and L.C. Leal: "ORIGEN-ARP: Automatic Rapid Process for Spent Fuel Depletion, Decay, and Source Term Analysis", NUREG/CR-0200, Revision 6, Volume 1, Section D1, ORNL/NUREG/CSD-2/VI/R6 (March 2000)

[102] F. Franceschini, e-mail of 20th March 2009

[103] H. Bailly, D. Ménessier, C. Prunier (eds.): "The Nuclear Fuel of Pressurized Water Reactors and Fast Neutron Reactors", Series: Collection du Commissariat à l'Energie Atomique, Lavoisier Publishing, Paris 1999 (p. 113, Fig. 3.1.7)

[104] ANSALDO Camozzi IR-DWF-00-001 rev.2 (1st Feb. 2006)

[105] ANSALDO Camozzi IR-DWF-00-002 rev.2 (9th May 2006)

[106] ANSALDO Camozzi IR-DWF-10-000 rev.0 (23rd Jan. 2006)

[107] B.Petrovic, "IRIS – Axial coolant density distribution in the SG region for shielding analysis", attachment to e-mail of 26th Dec. 2008

[108] K.W. Burn: e-room file: "SG.model3.xls"

[109] D. Grgic´, e-mail of 8th Jan. 2009 (including previous e-mails from A. Maioli)

[110] K.W. Burn: "IRIS: Monte Carlo Results for Selected Ex-Core Radiation Responses", ENEA NNFISS–LP2–007 (2010)

[111] A. Maioli, e-mail of 13th Nov. 2008

[112] D. Grgic´, private communication

[113] WEC "IRIS Plant Description Document", WCAP-16062-NP rev. 0, sec. 1.5.1, para. 17, (21st March 2003)

[114] A. Maioli, e-mail of 21st Dec. 2008

[115] A. Maioli, e-mail of 14th Jan. 2010
G. D. Storrick, e-mail of 15th Jan. 2010

[116] Jaeger *et al.*: Engineering Compendium on Radiation Shielding, vol. II, Springer-Verlag, 1975

[117] B.Petrovic, e-mail of 13th May 2009

Figure 1. Fission spectra from thermal neutron-induced fission in ^{239}Pu (Watt) and ^{241}Pu (Maxwell) and 1MeV neutron-induced fission in ^{238}U (Watt) relative to thermal neutron-induced fission in ^{235}U (Watt), each spectrum employing the recommended fission spectra constants from the MCNP5 manual.

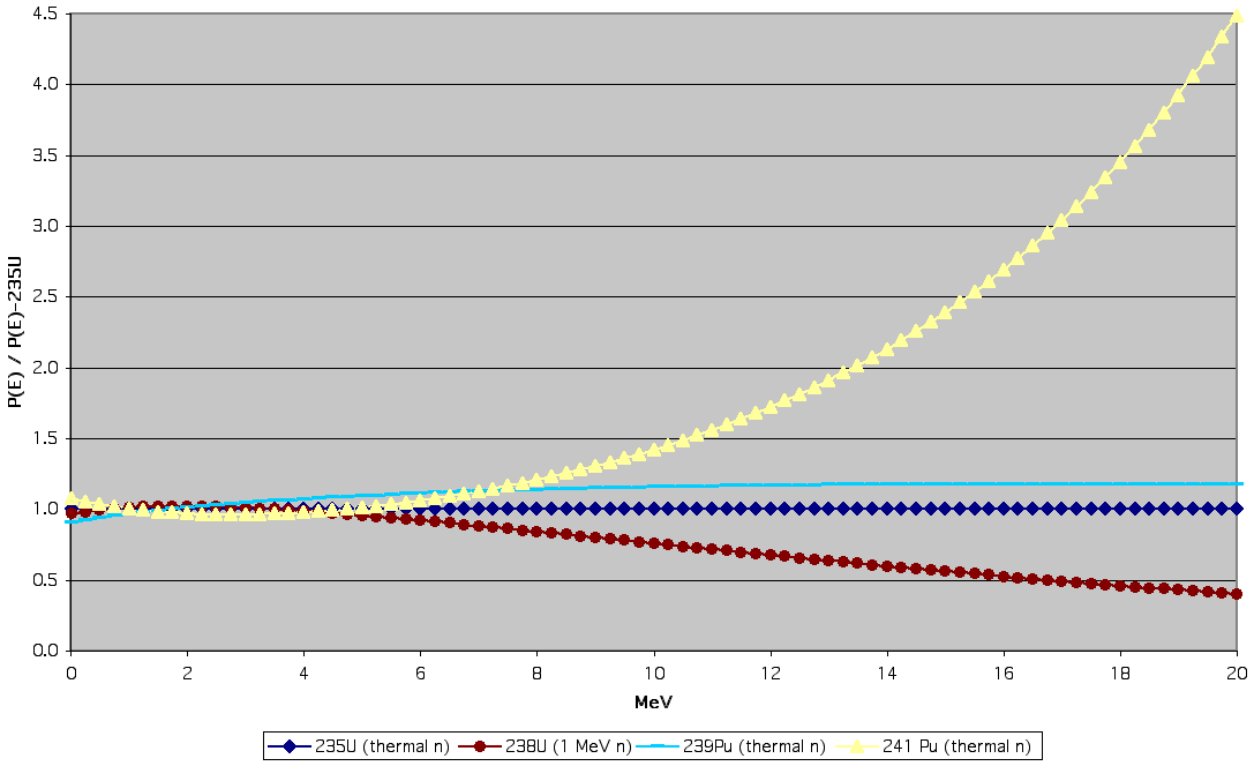

Figure 2. MCNP pin-by-pin model of an outer assembly (Standard 17x17 fuel) (the white material is the fuel).

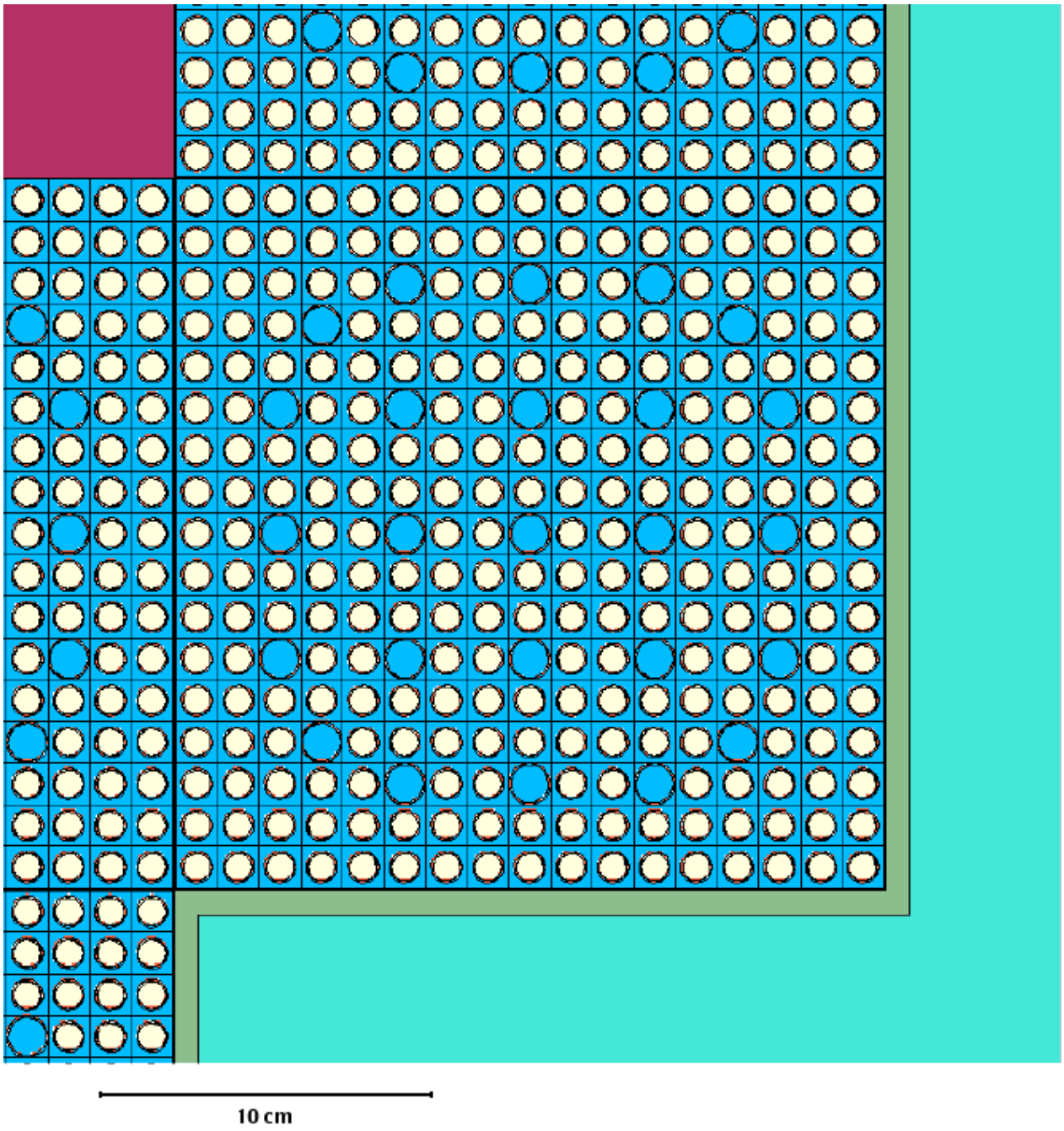

Figure 3. Cross-section of the MCNP model at the core centre for Standard Westinghouse 17x17 fuel assemblies, all assembly compositions smeared.

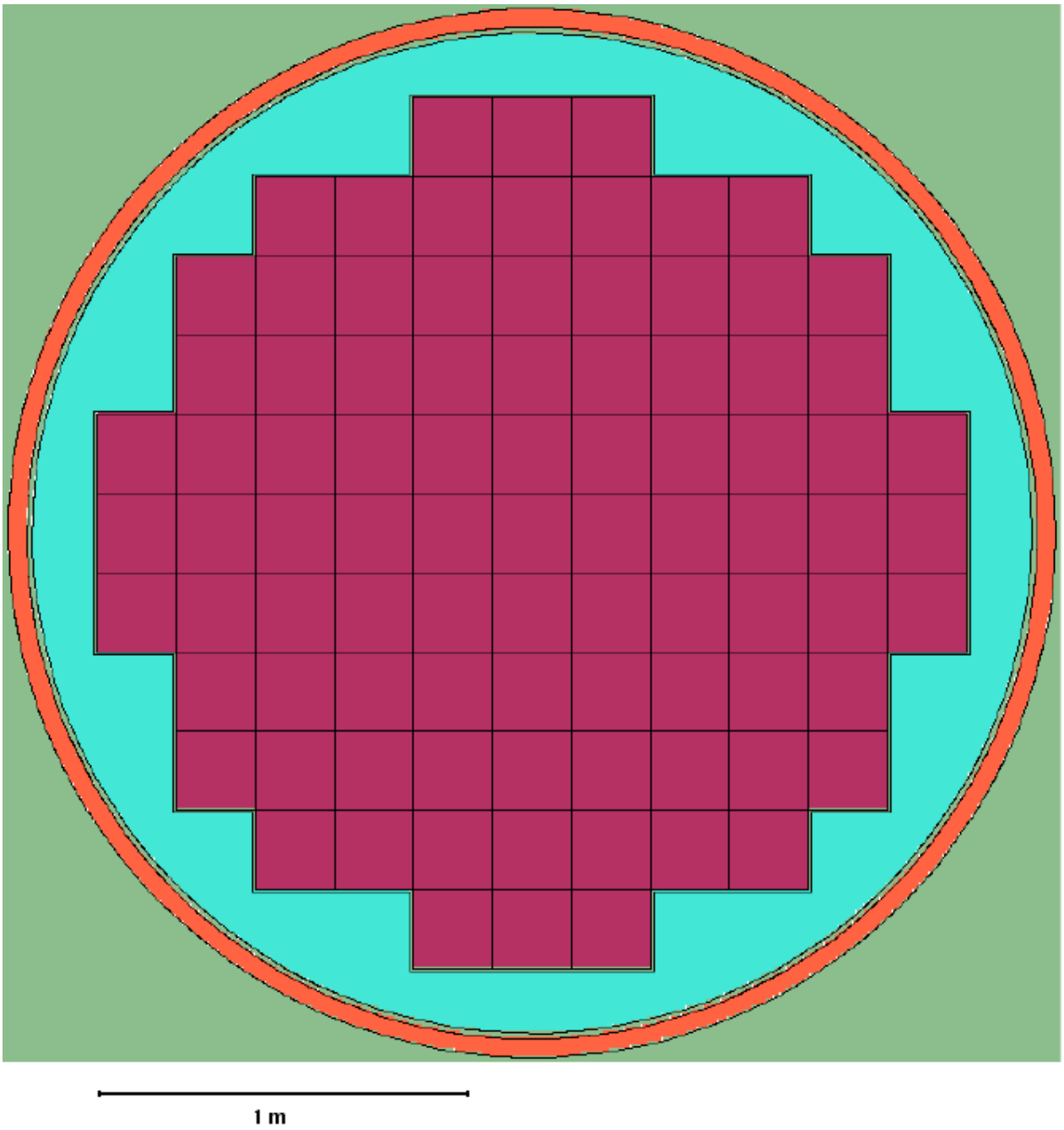

Figure 4. Cross-section of the MCNP model at the core centre for the Enhanced Moderation fuel assemblies, all assembly compositions smeared.

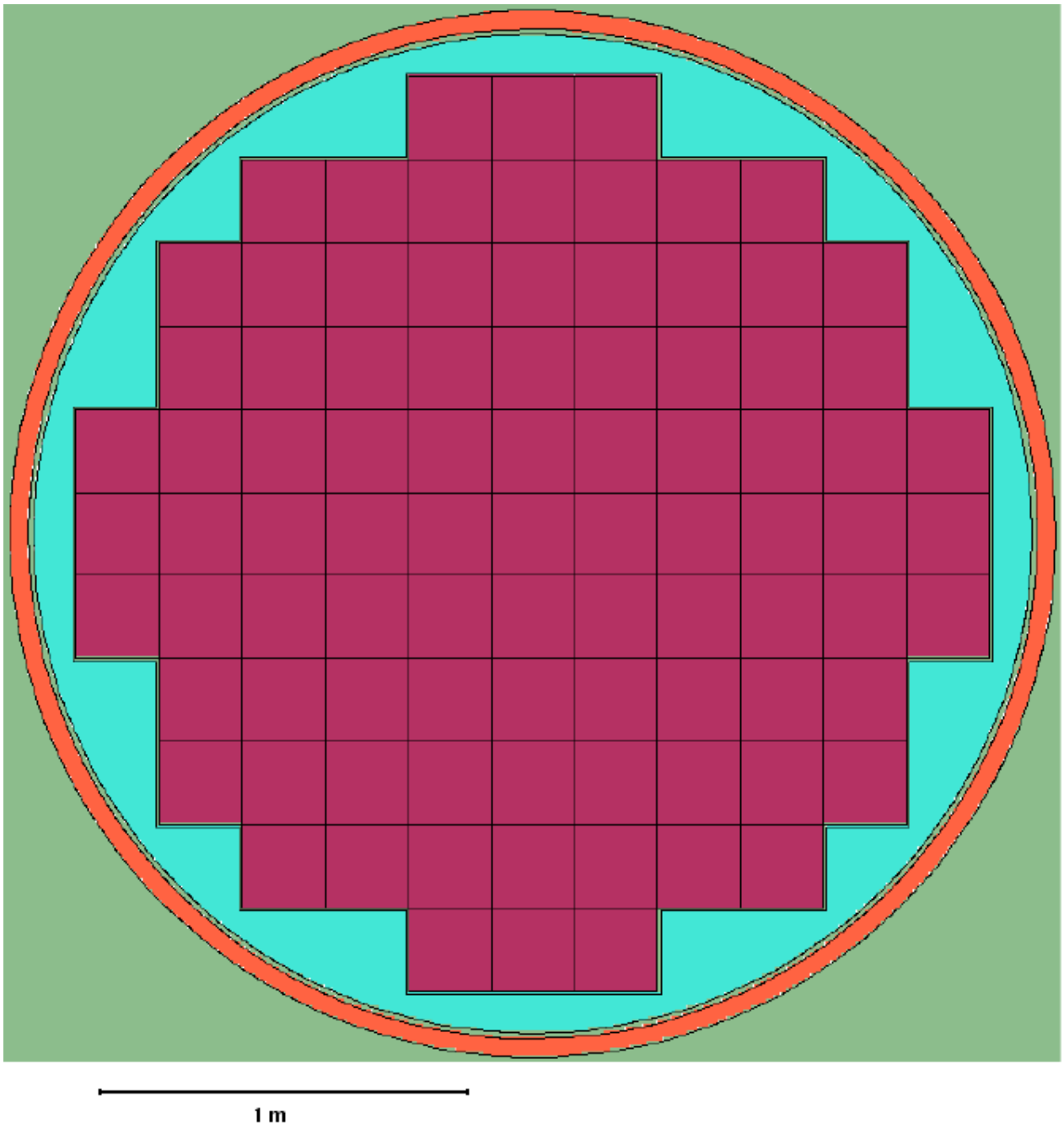

Figure 5. Quarter core cross-section of the MCNP model at the core centre for Standard Westinghouse fuel assemblies, inner assemblies smeared, outer assemblies modeled pin-by-pin.

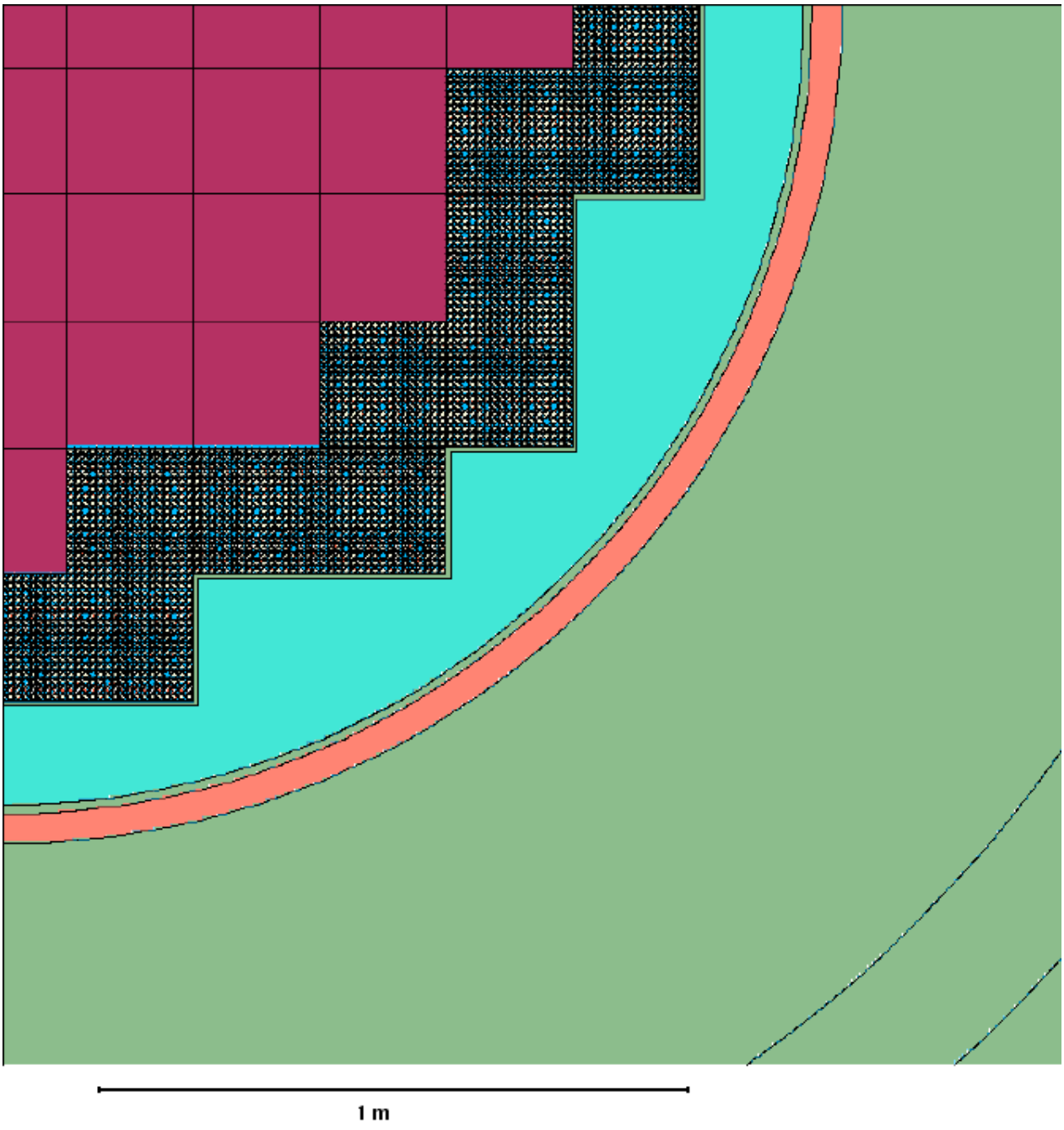

Figure 6. Axial cross section of the MCNP model of the Standard fuel assemblies core (all assemblies smeared).

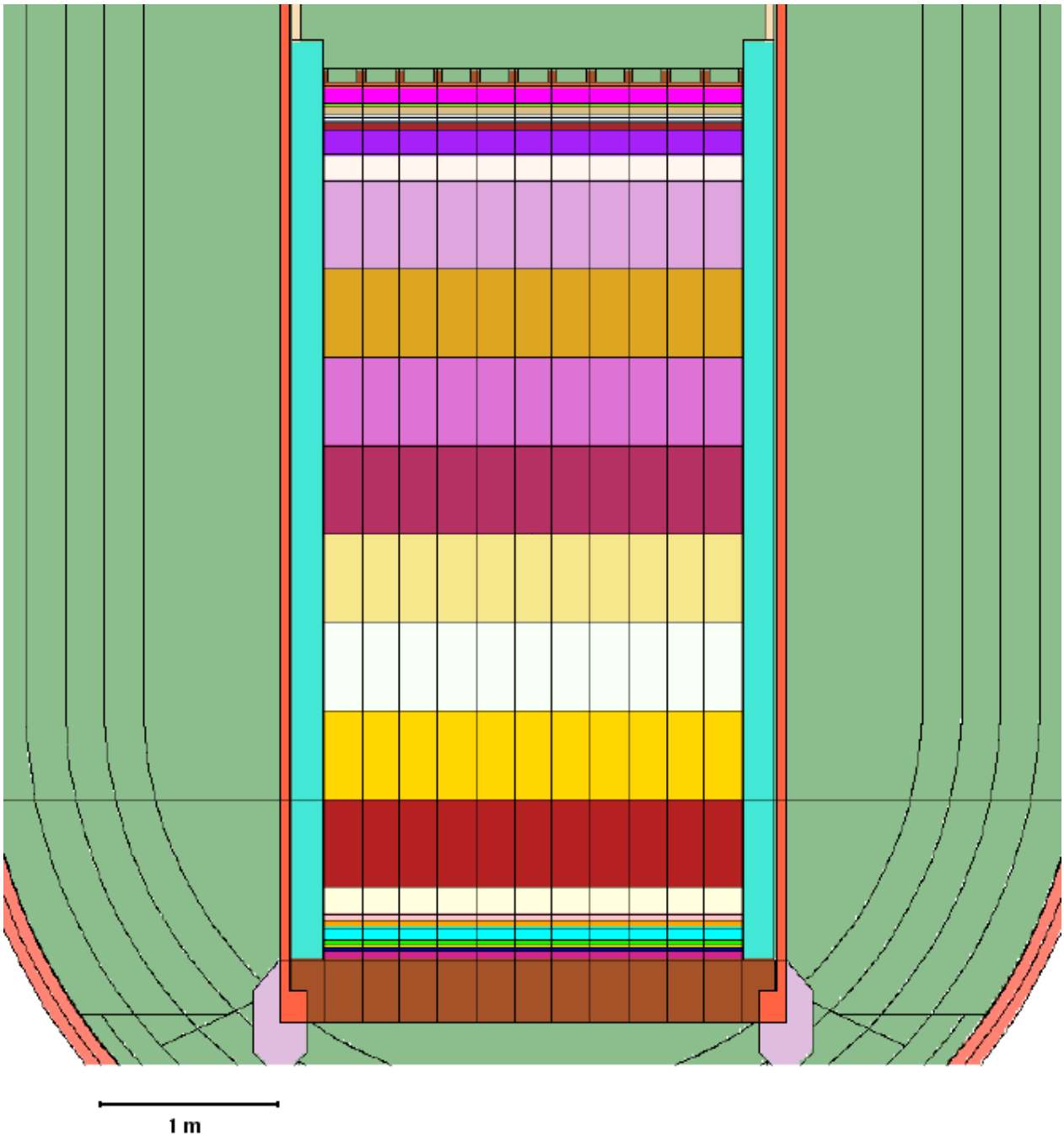

Figure 7. The MCNP model of the region between the active core and the top plate for the Standard assemblies core (the white zone just above the mauve zone is the upper blanket).

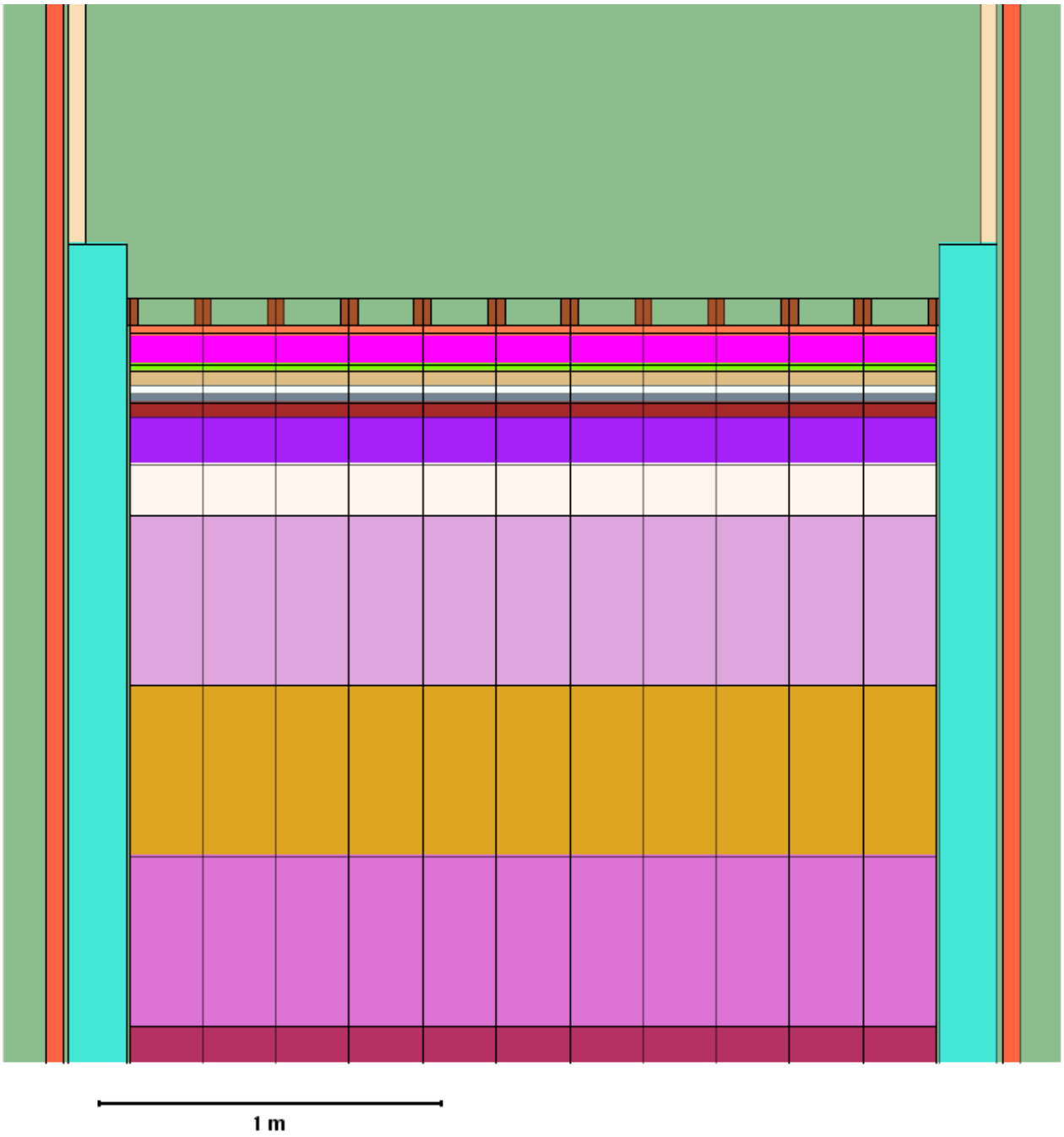

Figure 8. MCNP model of the region between the active core and the bottom plate, for the Standard assemblies core (the white zone just under the brown zone is the lower blanket).

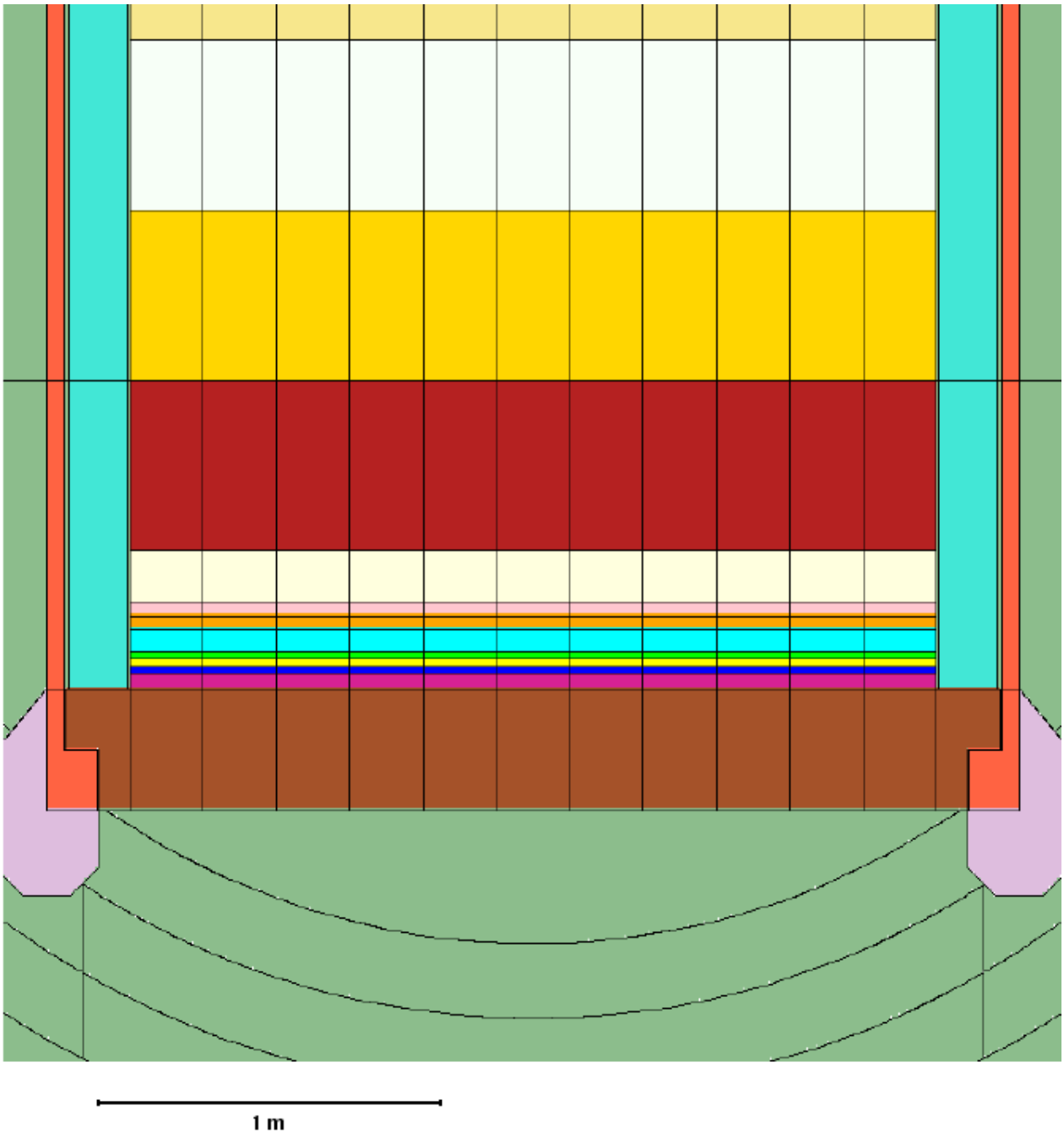

Figure 9. Radial cross section of the MCNP model of the bottom core plate for the Standard fuel assemblies.

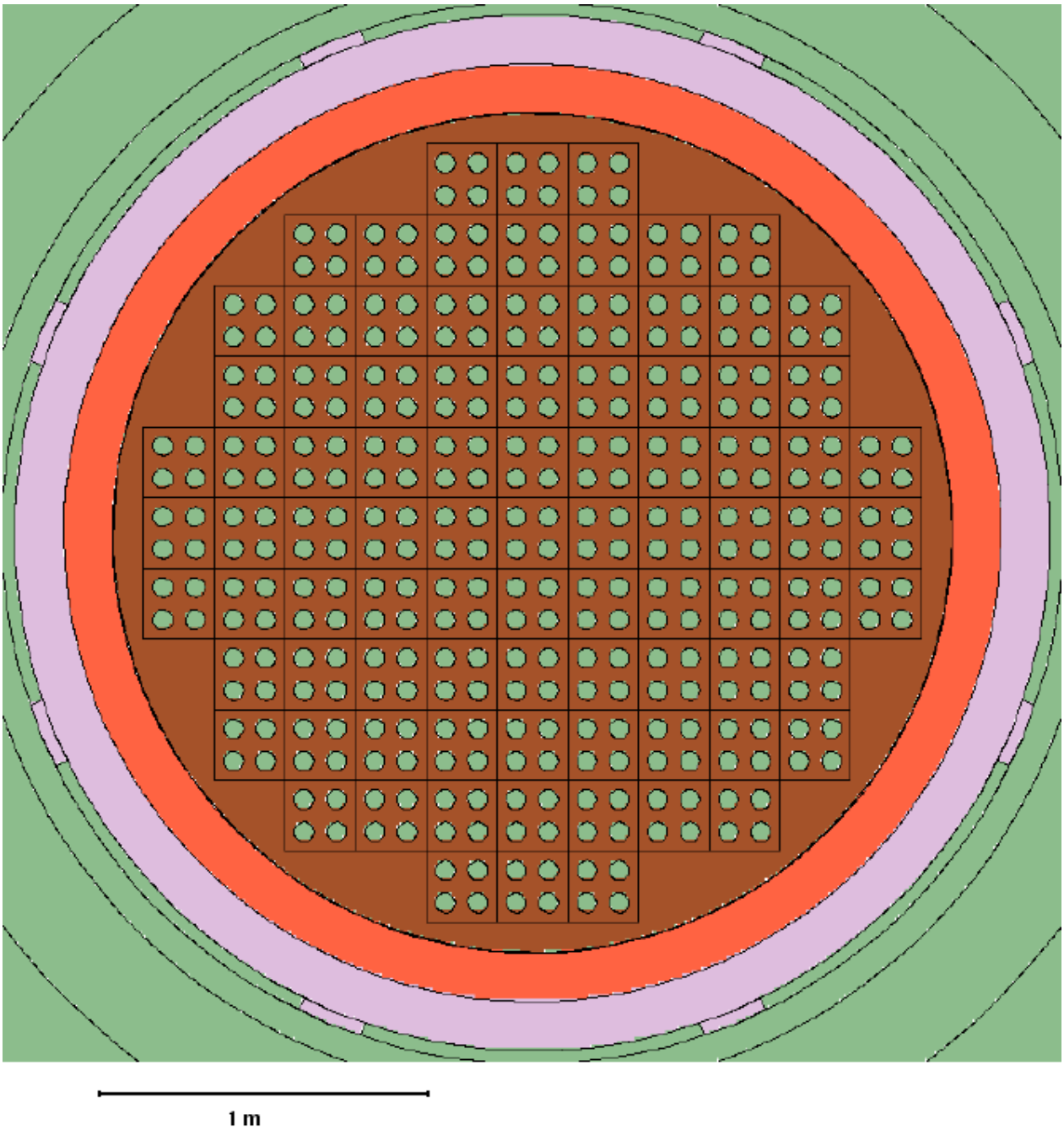

Figure 10. Radial cross section of the MCNP model of the bottom core plate for the Enhanced Moderation fuel assemblies.

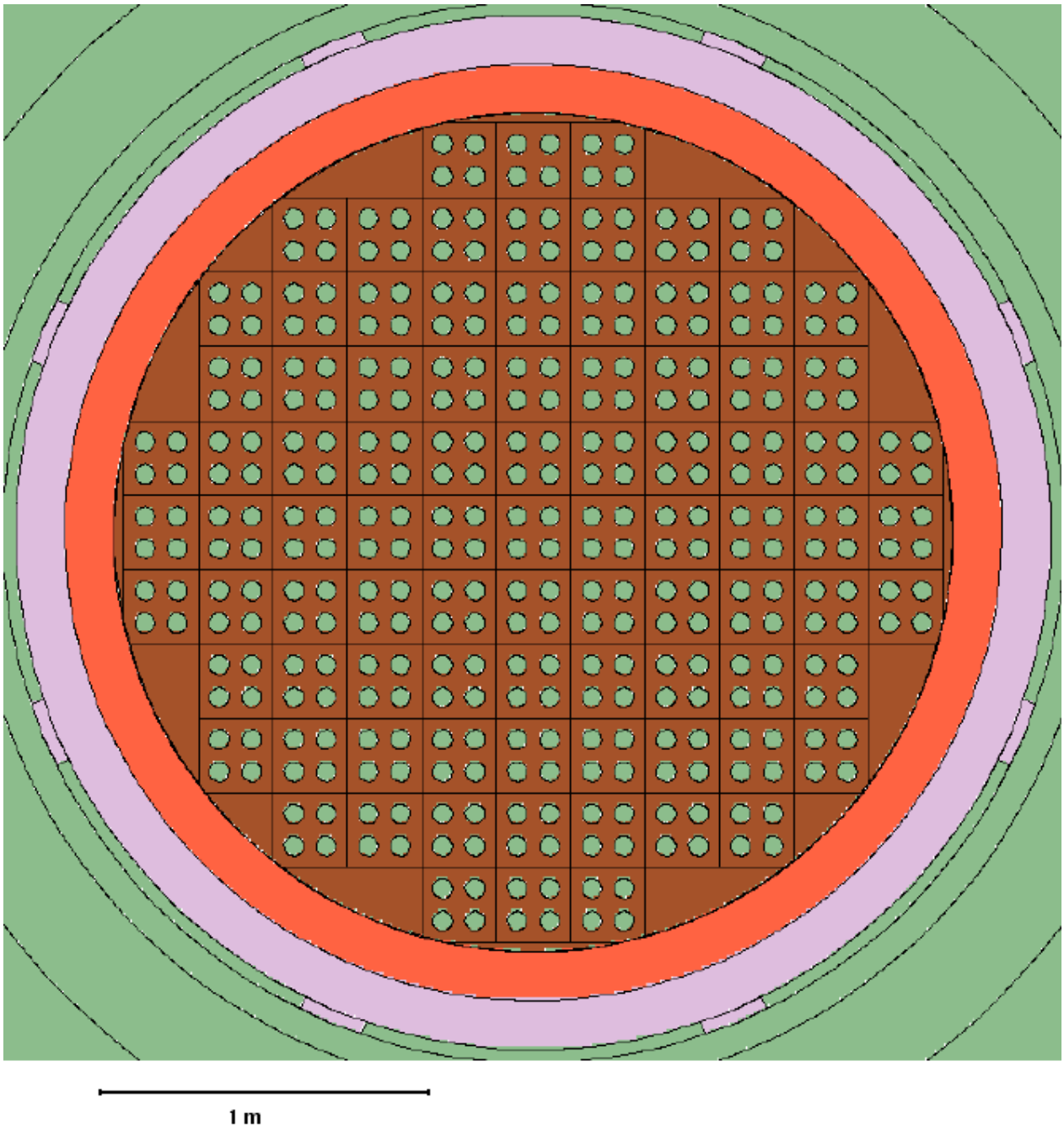

Figure 11. Radial cross section of the MCNP model of the top core plate for the Standard fuel assemblies.

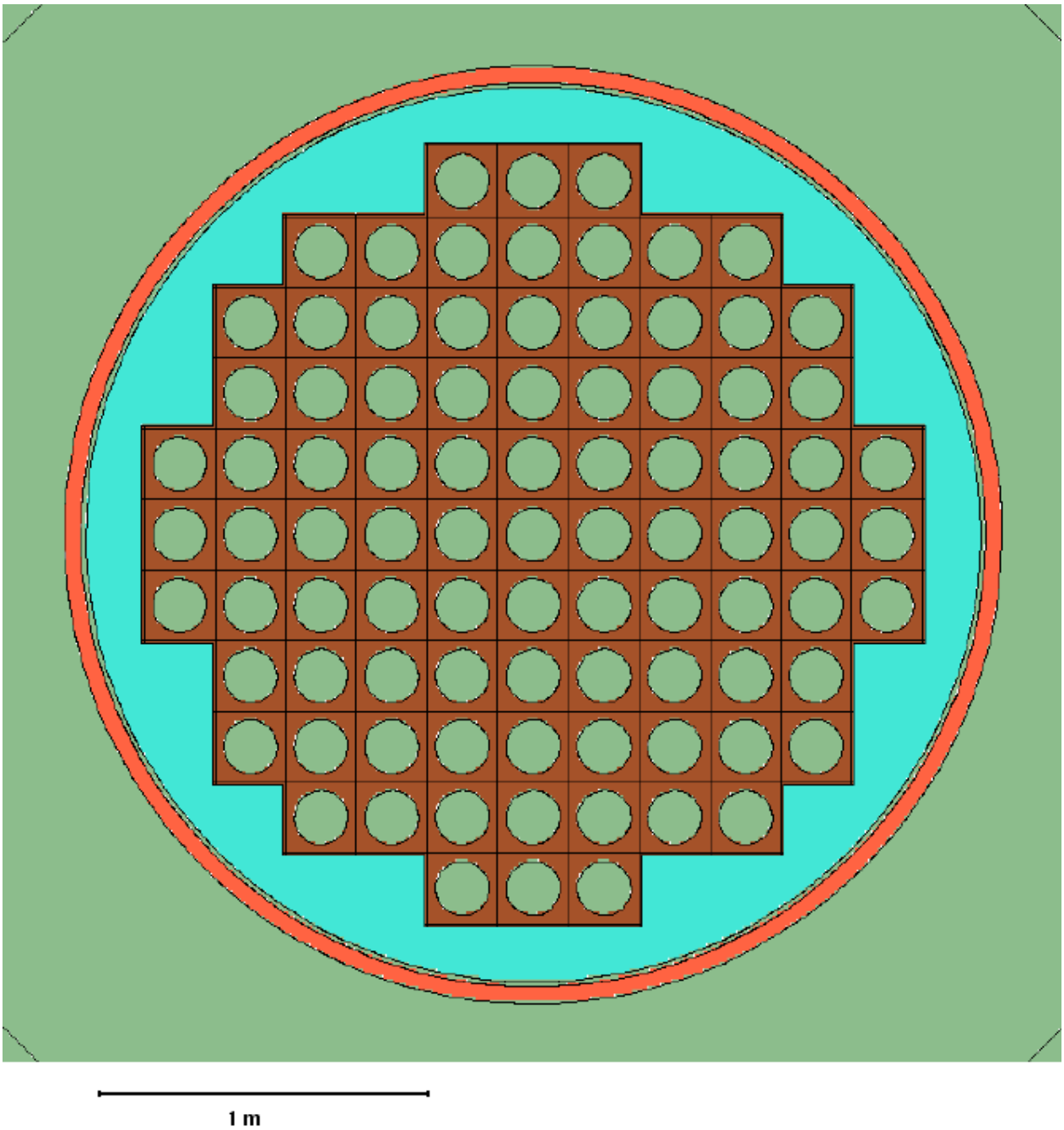

Figure 12. Radial cross section of the MCNP model of the top core plate for the Enhanced Moderation fuel assemblies.

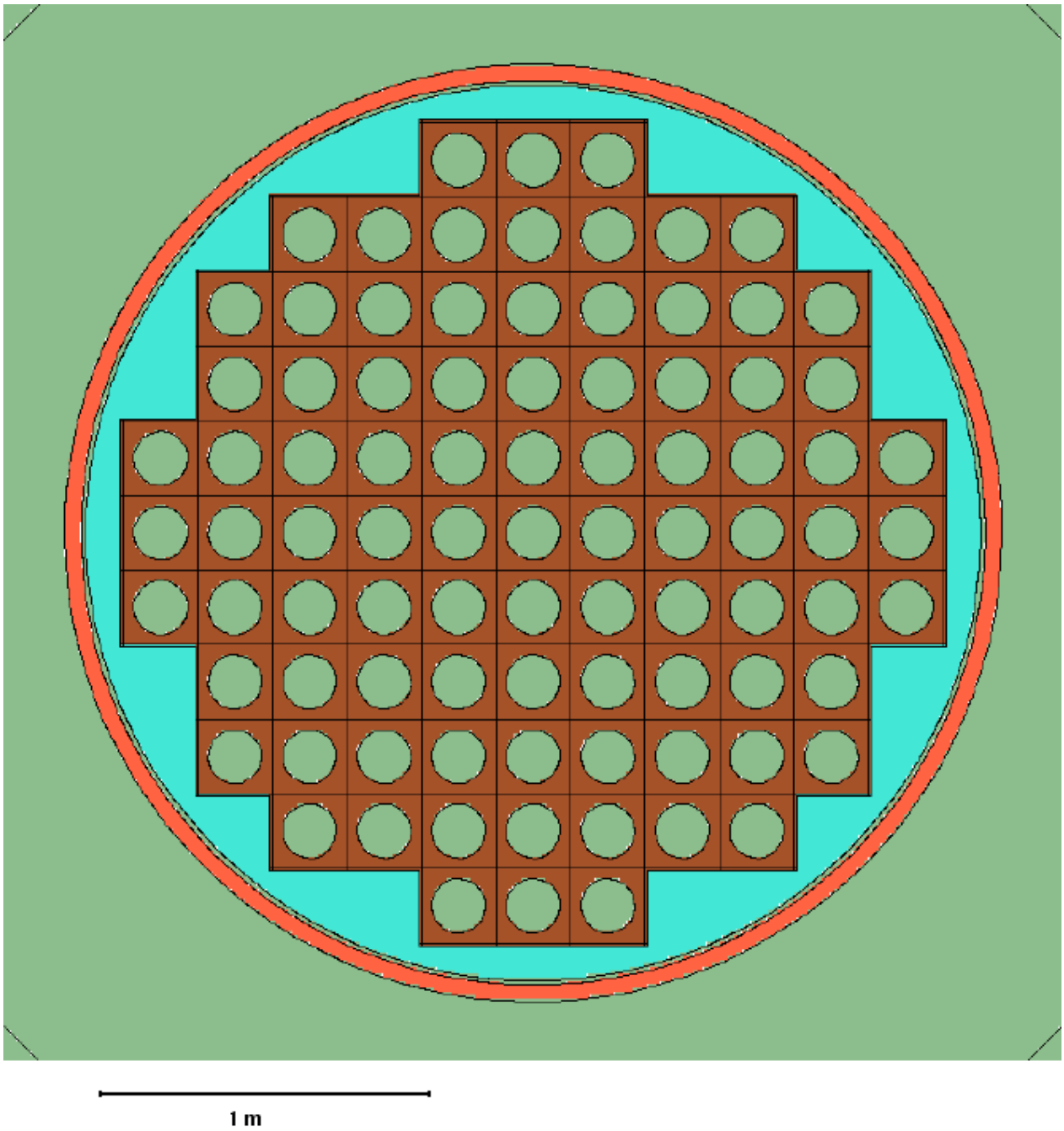

Figure 13. Axial cross section of the MCNP model of the lower barrel annular support.

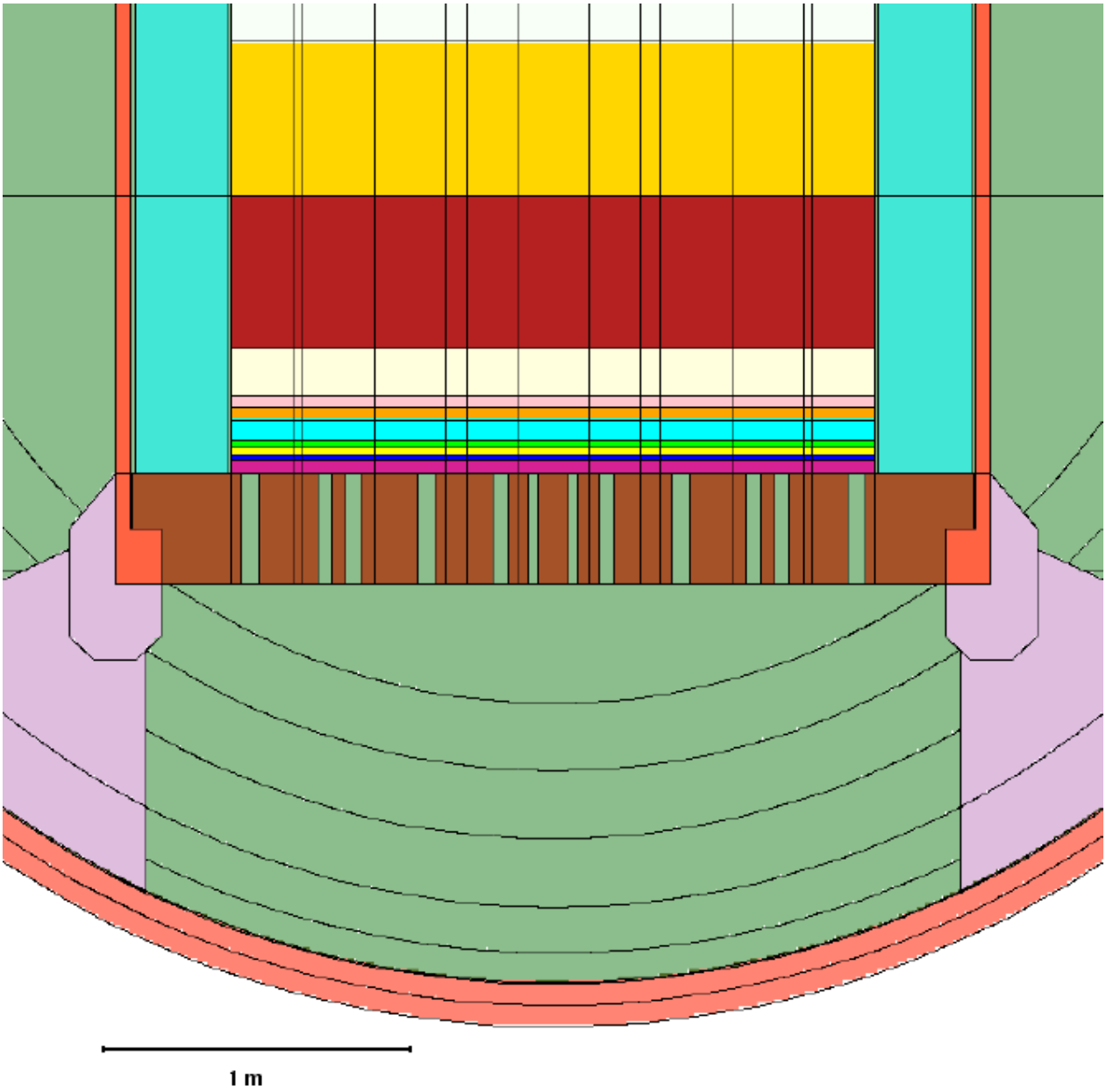

Figure 14. Axial cross section of the MCNP model of two of the eight azimuthal supports.

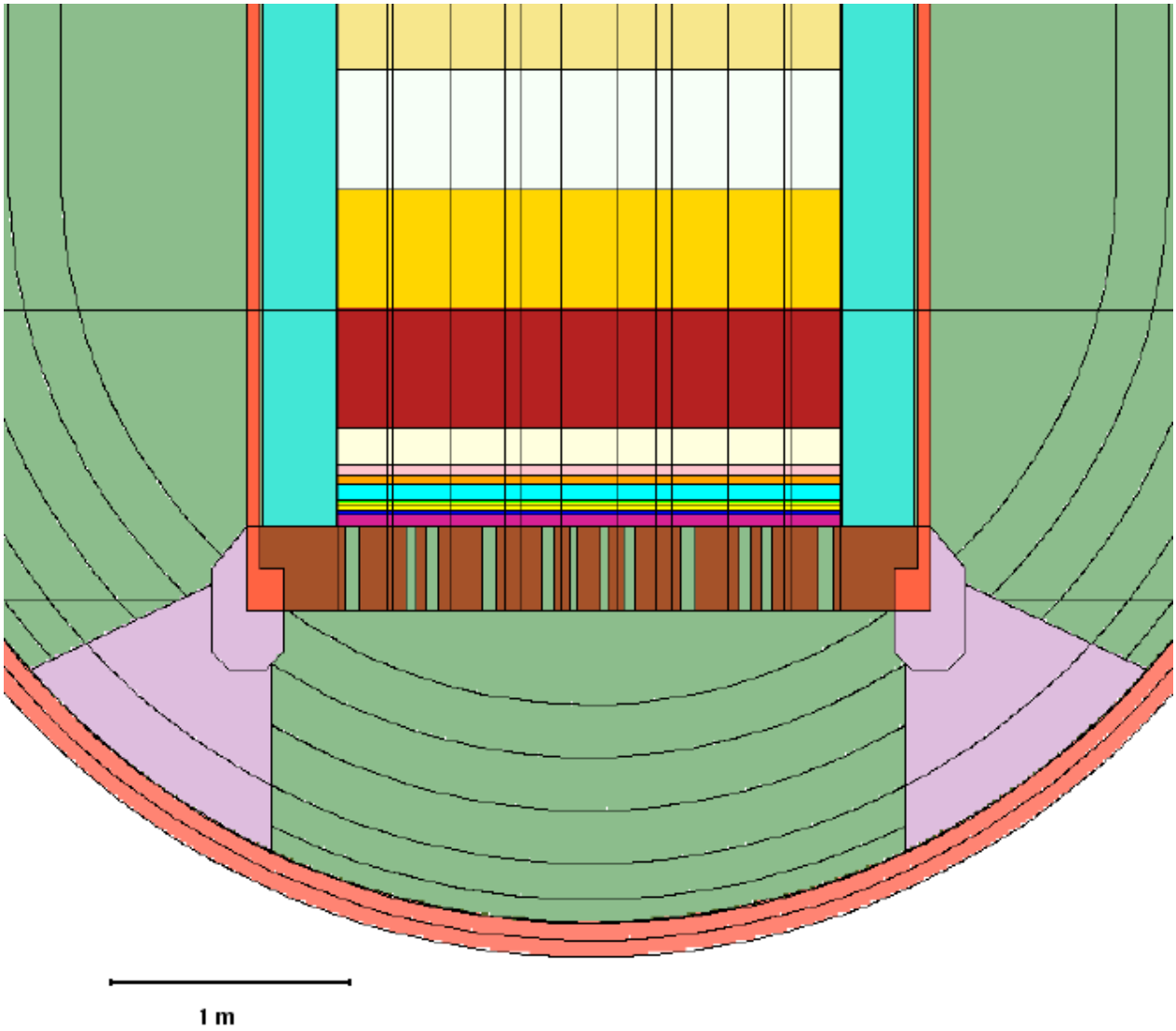

Figure 15. MCNP model of the bottom shield.

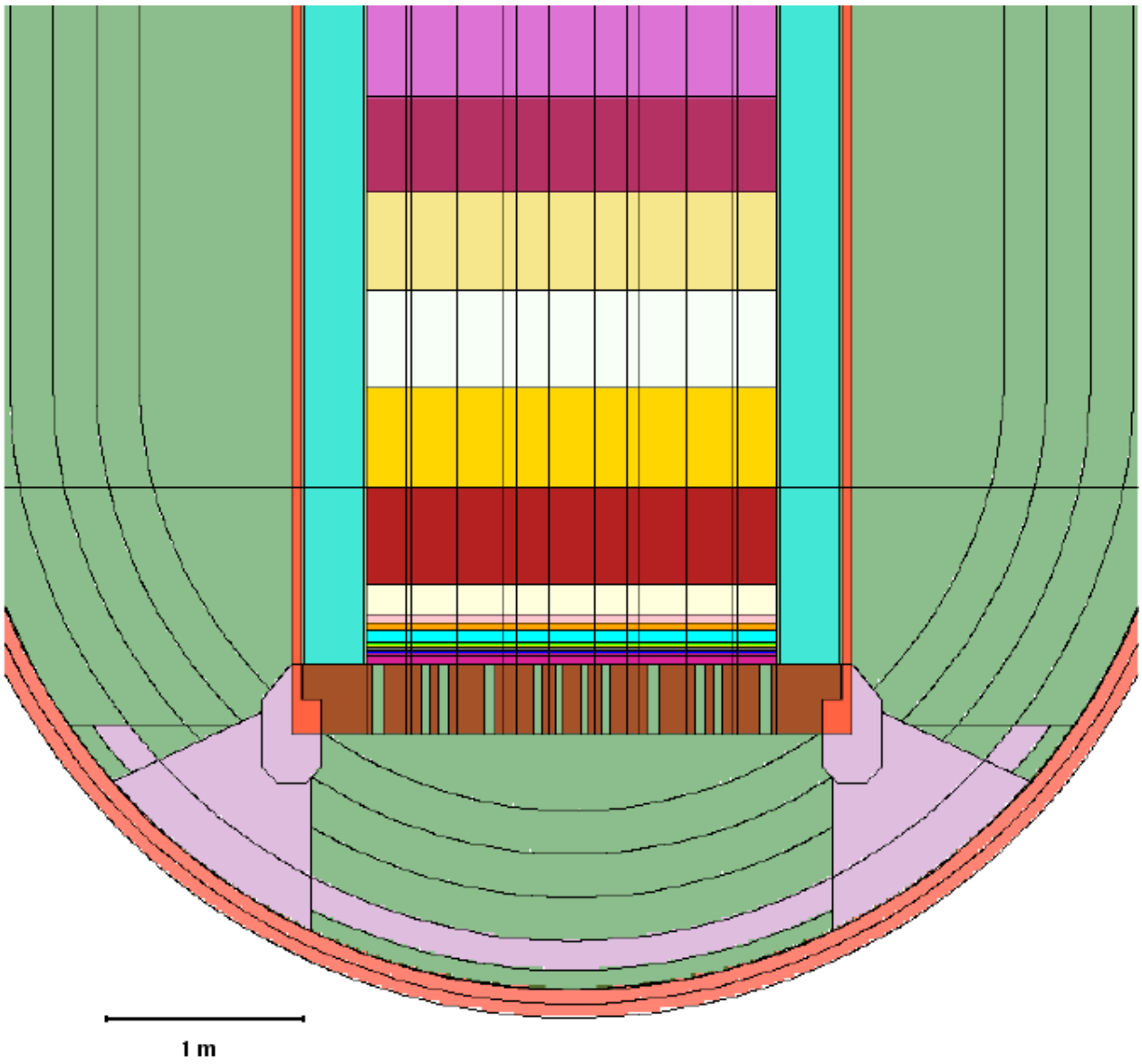

Figure 16. MCNP model of the pressure vessel and PV cavity.

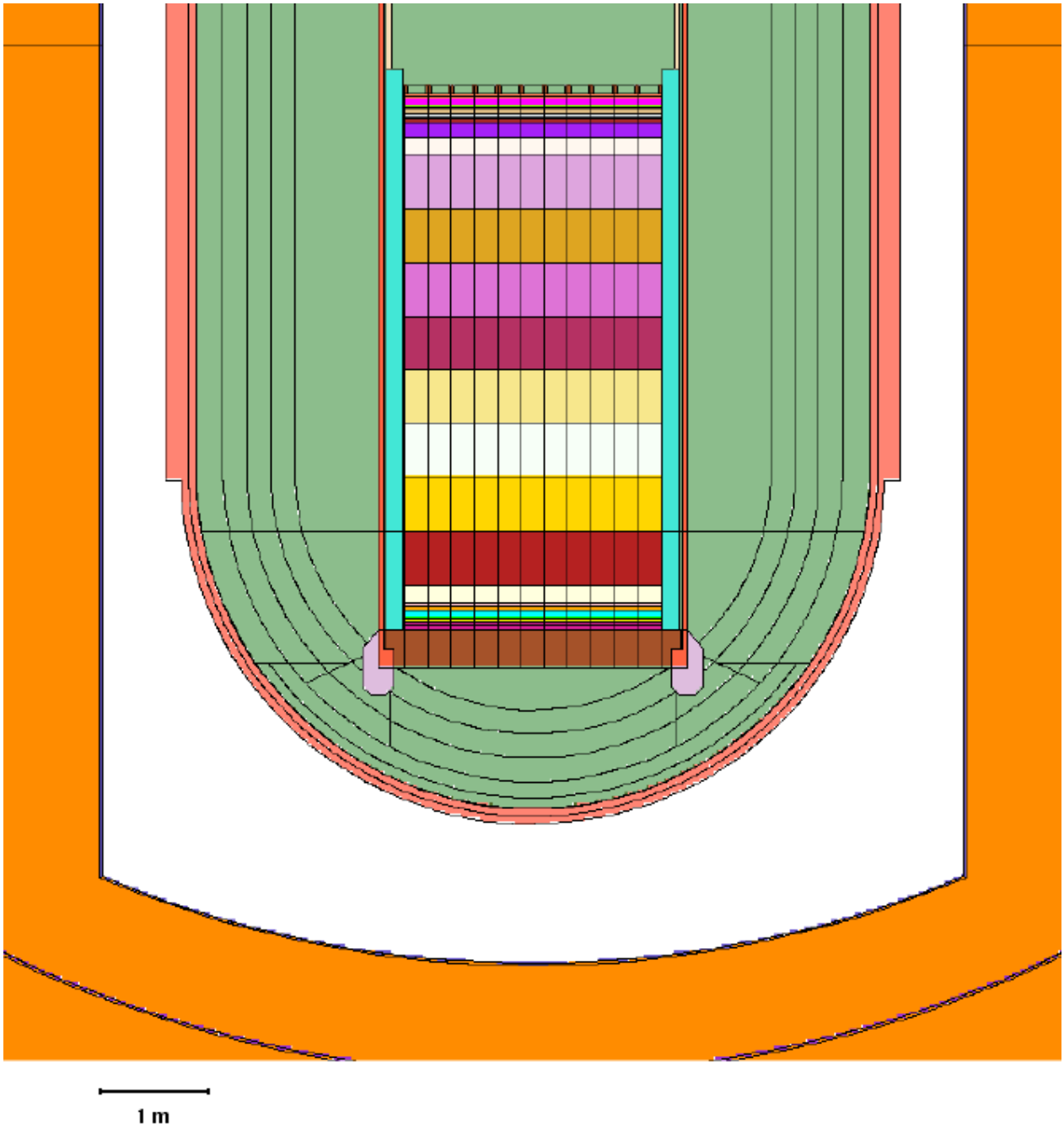

Figure 17. Concrete surrounding the PV.

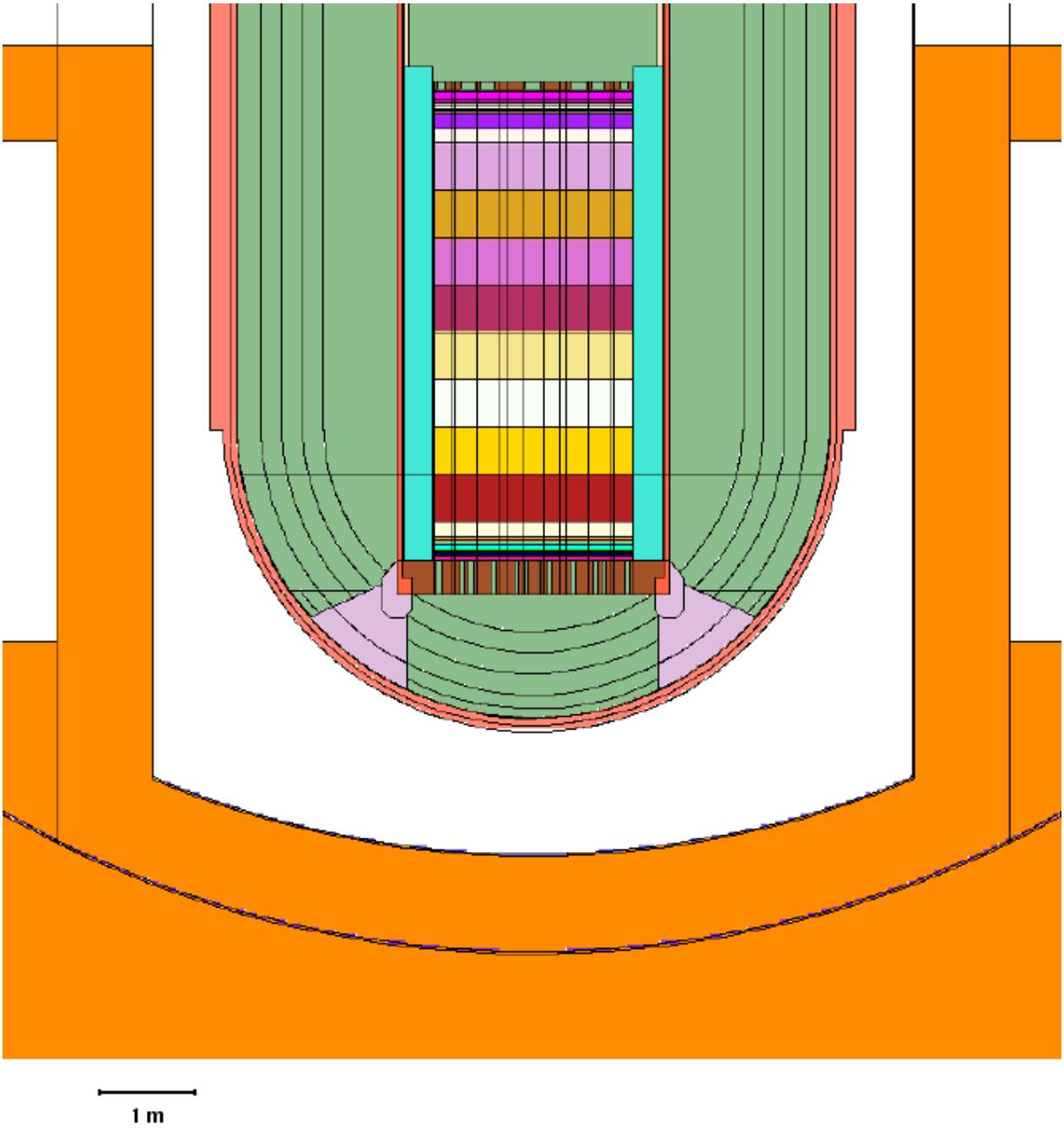

Figure 18. The scheme of the various geometrical and source models for the Pressure Vessel damage calculations.

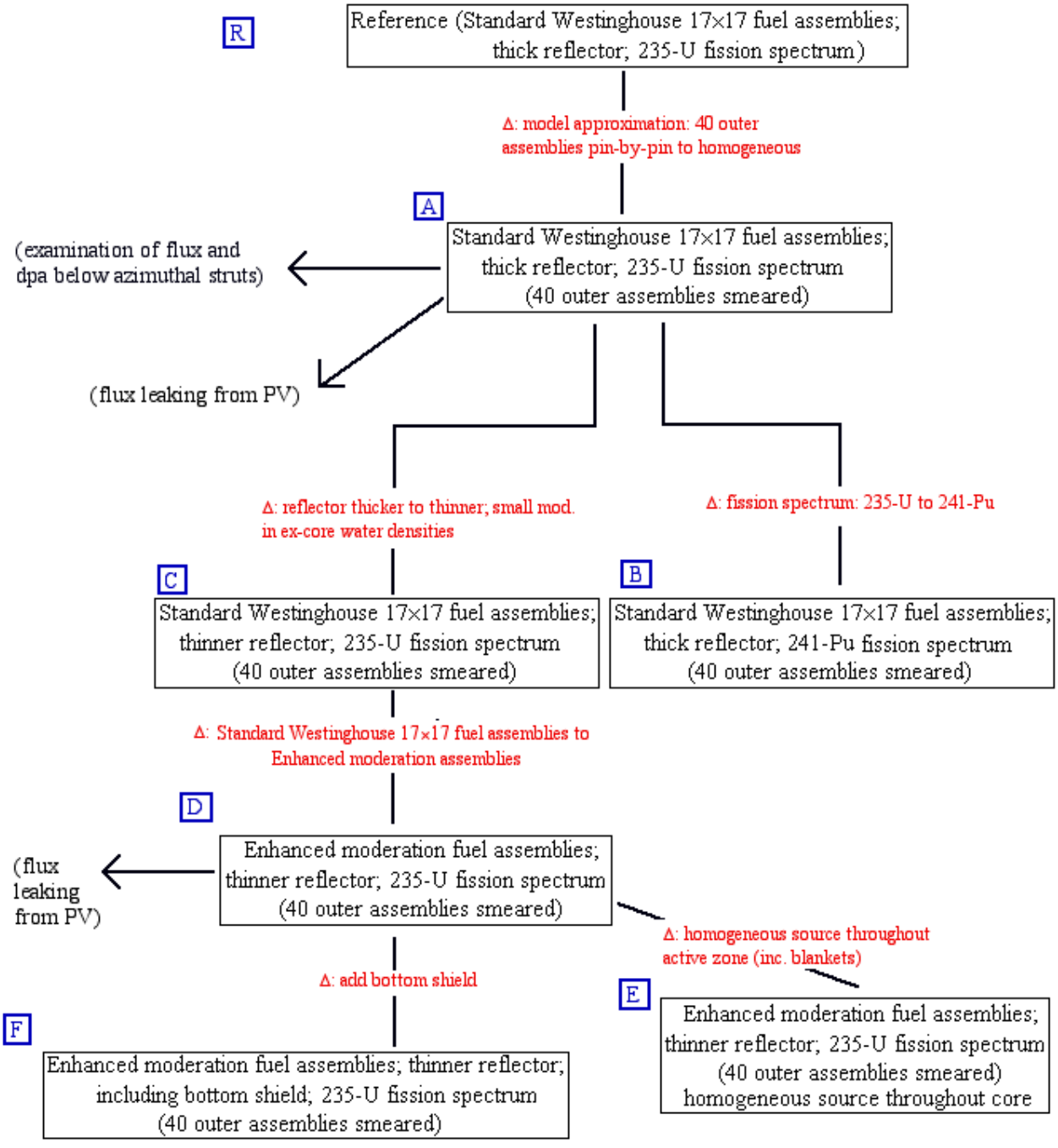

Figure 19. Reference case: Neutron fluences at segments of the inner surface of the pressure vessel (between the vessel cladding and the vessel) averaged around the circumference for 60 years continuous running at 1000 MW.

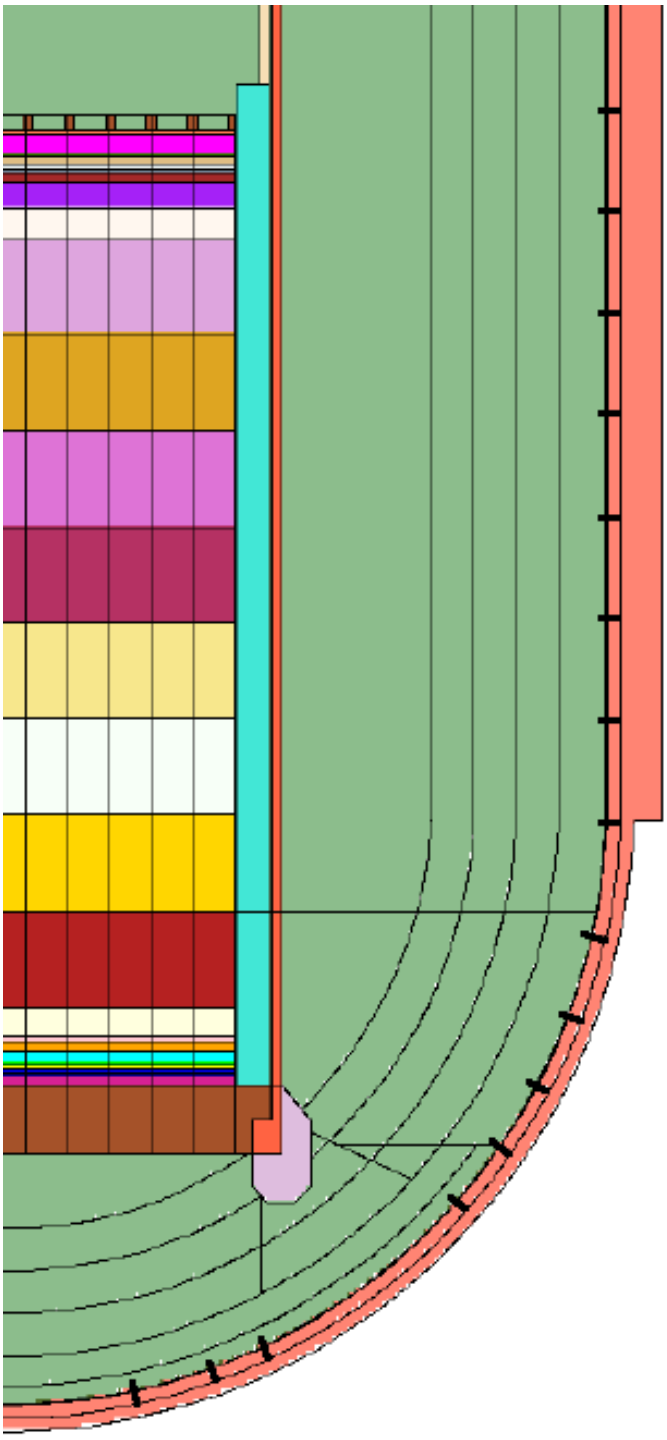

Φ_n (> 1 MeV) (n / cm^2)	Φ_n (> 100 keV) (n / cm^2)	Φ_n (tot) (n / cm^2)
4.8E+12	9.2E+12	2.0E+13
1.2E+13	2.3E+13	5.1E+13
1.9E+13	3.5E+13	7.6E+13
2.1E+13	3.9E+13	8.4E+13
2.1E+13	3.9E+13	8.4E+13
2.1E+13	3.9E+13	8.4E+13
2.0E+13	3.8E+13	8.2E+13
2.2E+13	3.9E+13	8.4E+13
3.3E+13	5.7E+13	1.2E+14
4.9E+13	8.6E+13	1.9E+14
6.5E+13	1.1E+14	2.5E+14
6.8E+13	1.2E+14	2.7E+14
2.7E+13	1.5E+14	5.5E+14
4.8E+13	8.7E+13	1.9E+14
4.4E+13	7.8E+13	1.7E+14
3.4E+13	6.0E+13	1.3E+14

Figure 20. Reference case: Neutron fluences at two segments of the inner surface of the pressure vessel (between the vessel cladding and the vessel) and averaged over the inner 1/4 or 1/2 depths, averaged around the circumference for 60 years continuous running at 1000 MW.

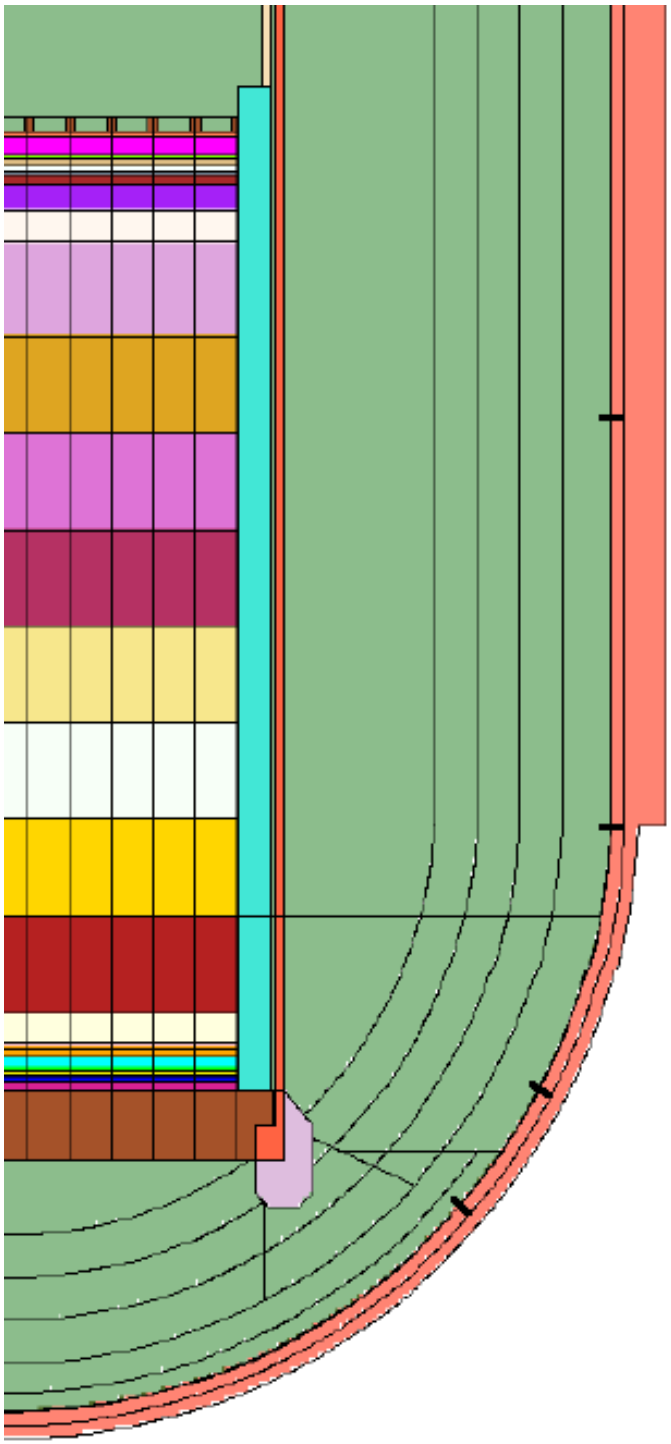

Φ_n (> 1 MeV) (n / cm^2)	Φ_n (> 100 keV) (n / cm^2)	Φ_n (tot) (n / cm^2)
(at PV inner surface)		
2.1E+13	3.9E+13	8.4E+13
(averaged over inner 1/4 thickness)		
1.5E+13	3.6E+13	5.8E+13
(at PV inner surface)		
6.6E+13	1.2E+14	2.6E+14
(averaged over inner 1/2 thickness)		
4.8E+13	1.0E+14	1.6E+14

Figure 21. Reference case: Azimuthal variation of the neutron fluences at the upper (cylindrical) segment of the inner surface of the pressure vessel with respect to the result for the average around the circumference shown in Figure 20.

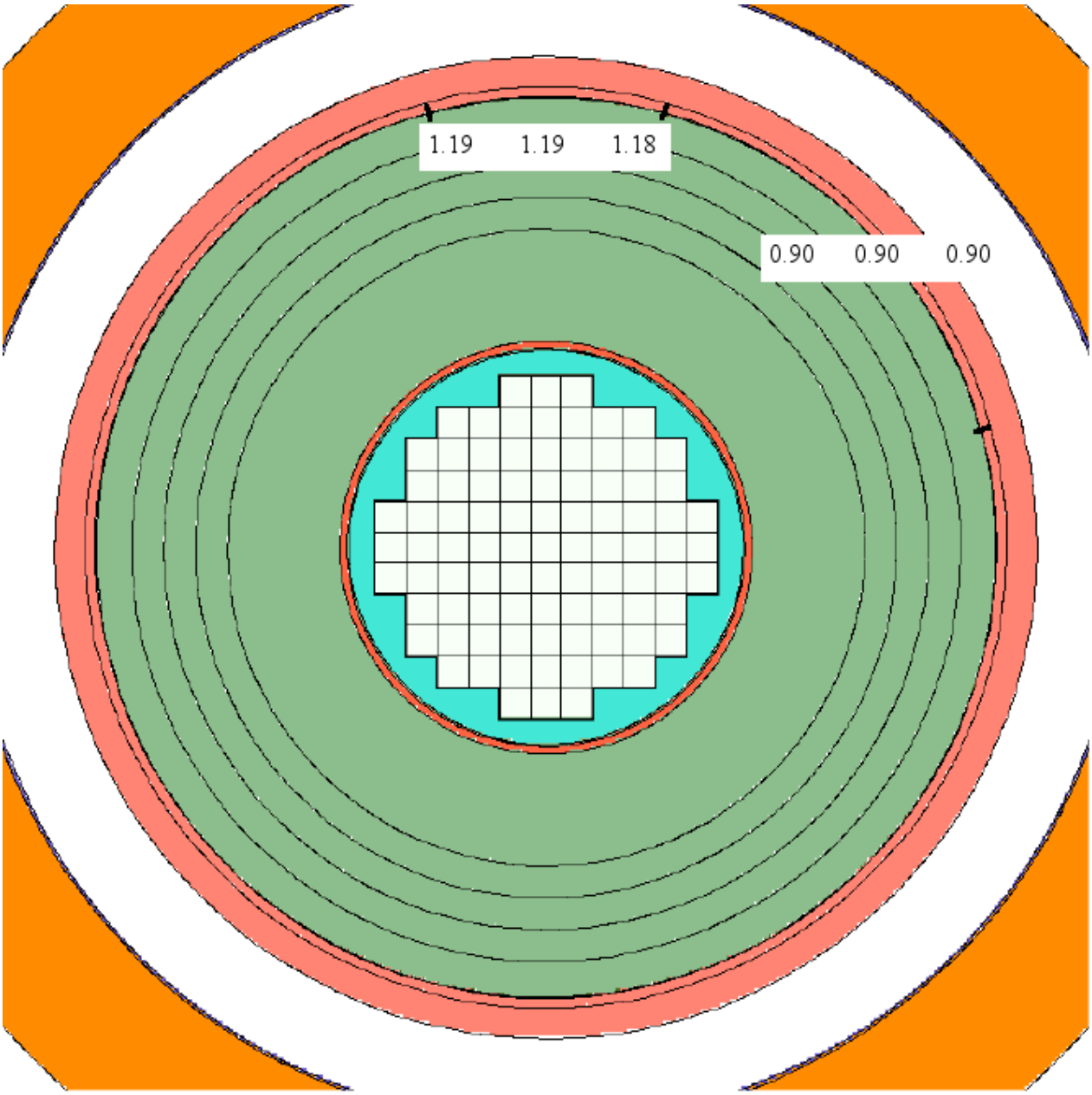

Figure 22. Reference case: Azimuthal variation of the neutron fluences at the lower (spherical) segment of the inner surface of the pressure vessel with respect to the result for the average around the circumference shown in Figure 20.

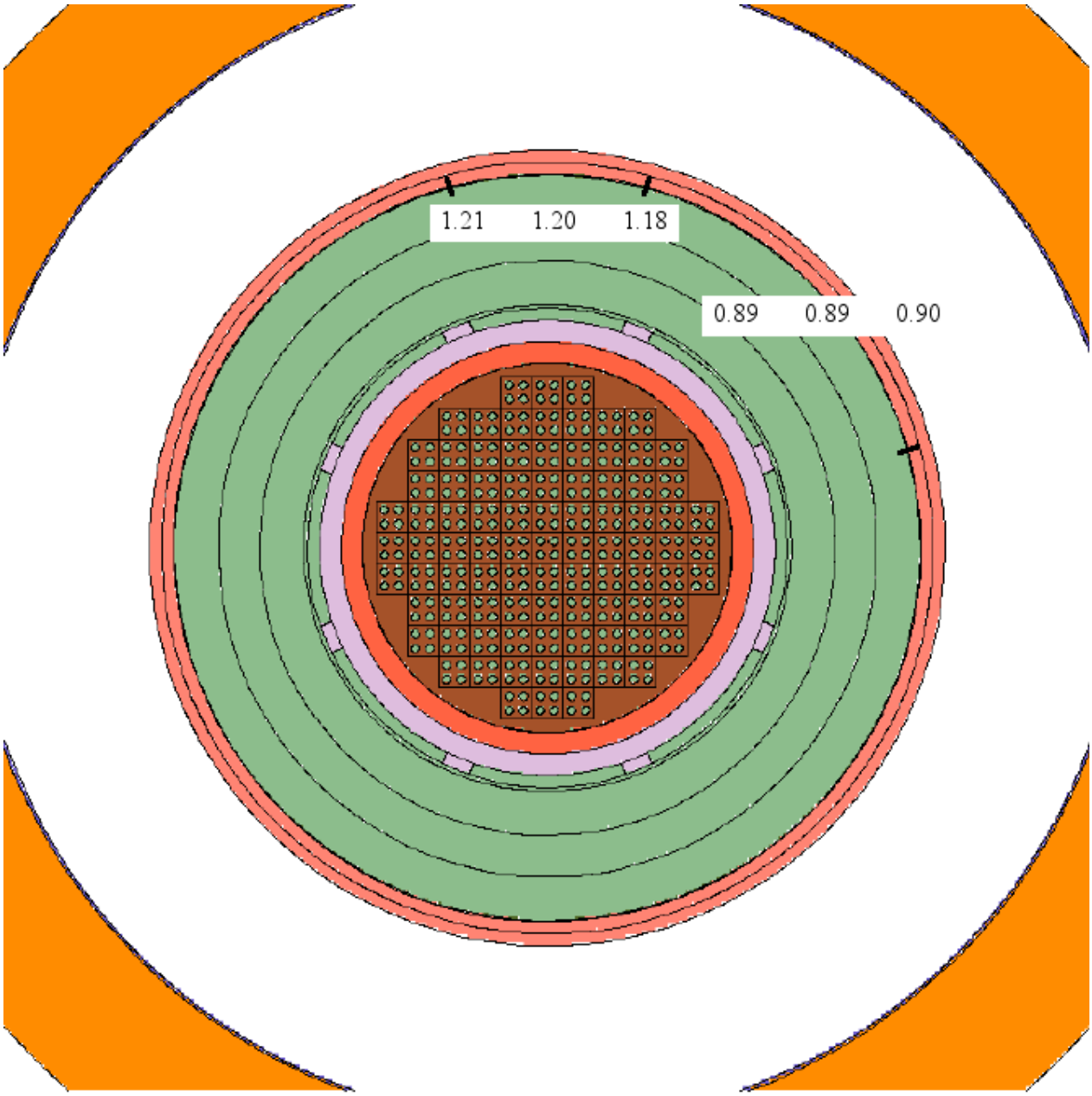

Figure 23. Reference case: Neutron fluences at a segment of the inner surface of the pressure vessel (between the vessel cladding and the vessel) and averaged over the inner 1/2 depth, at the point where the azimuthal struts rest on the vessel, for 60 years continuous running at 1000 MW.

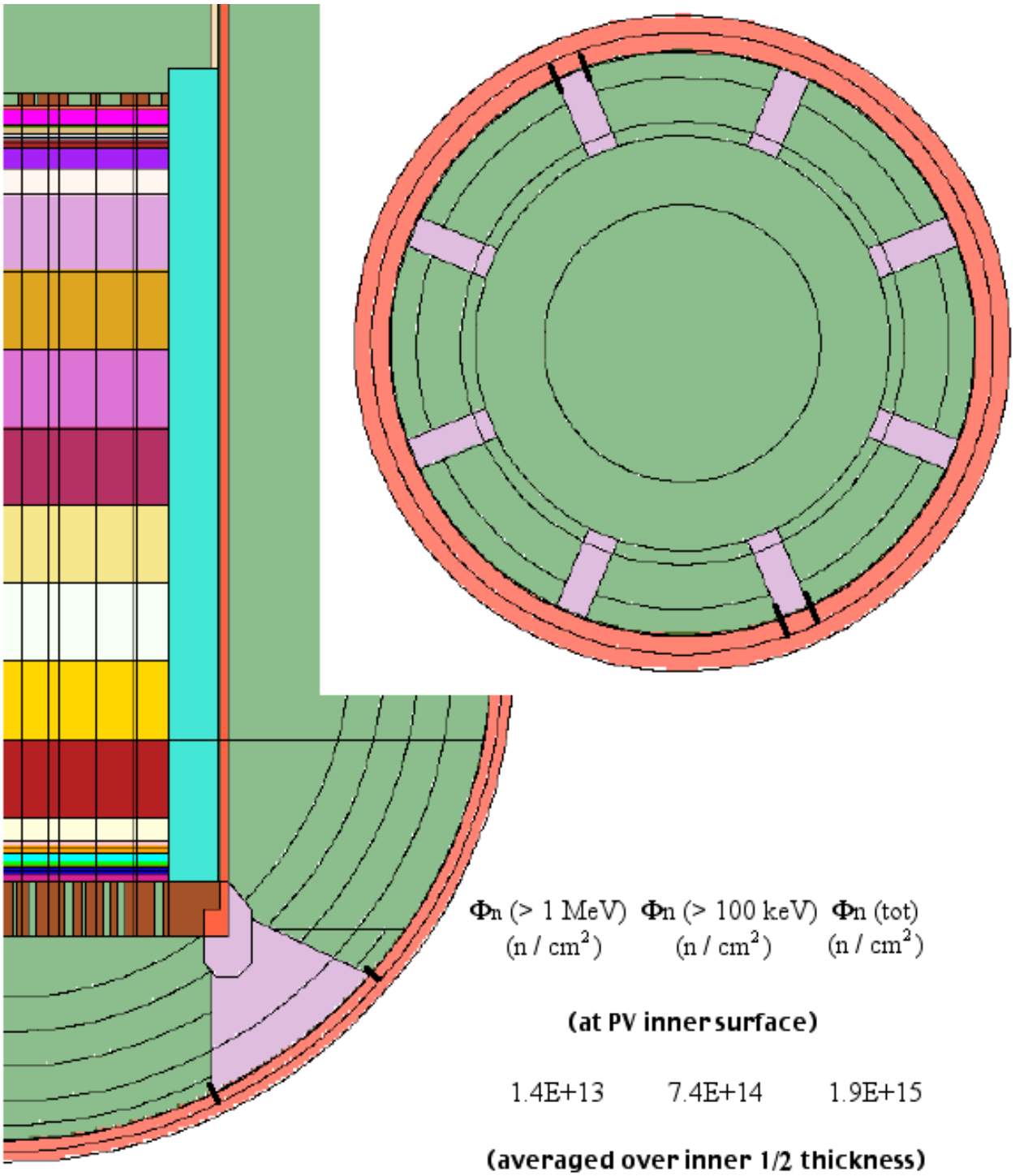

Φ_n (> 1 MeV) (n / cm^2)	Φ_n (> 100 keV) (n / cm^2)	Φ_n (tot) (n / cm^2)
(at PV inner surface)		
1.4E+13	7.4E+14	1.9E+15
(averaged over inner 1/2 thickness)		
1.0E+13	4.7E+14	1.3E+15

Figure 24. Reference case: Neutron fluences at a segment of the inner surface of the pressure vessel (between the vessel cladding and the vessel) between the azimuthal struts, for 60 years continuous running at 1000 MW.

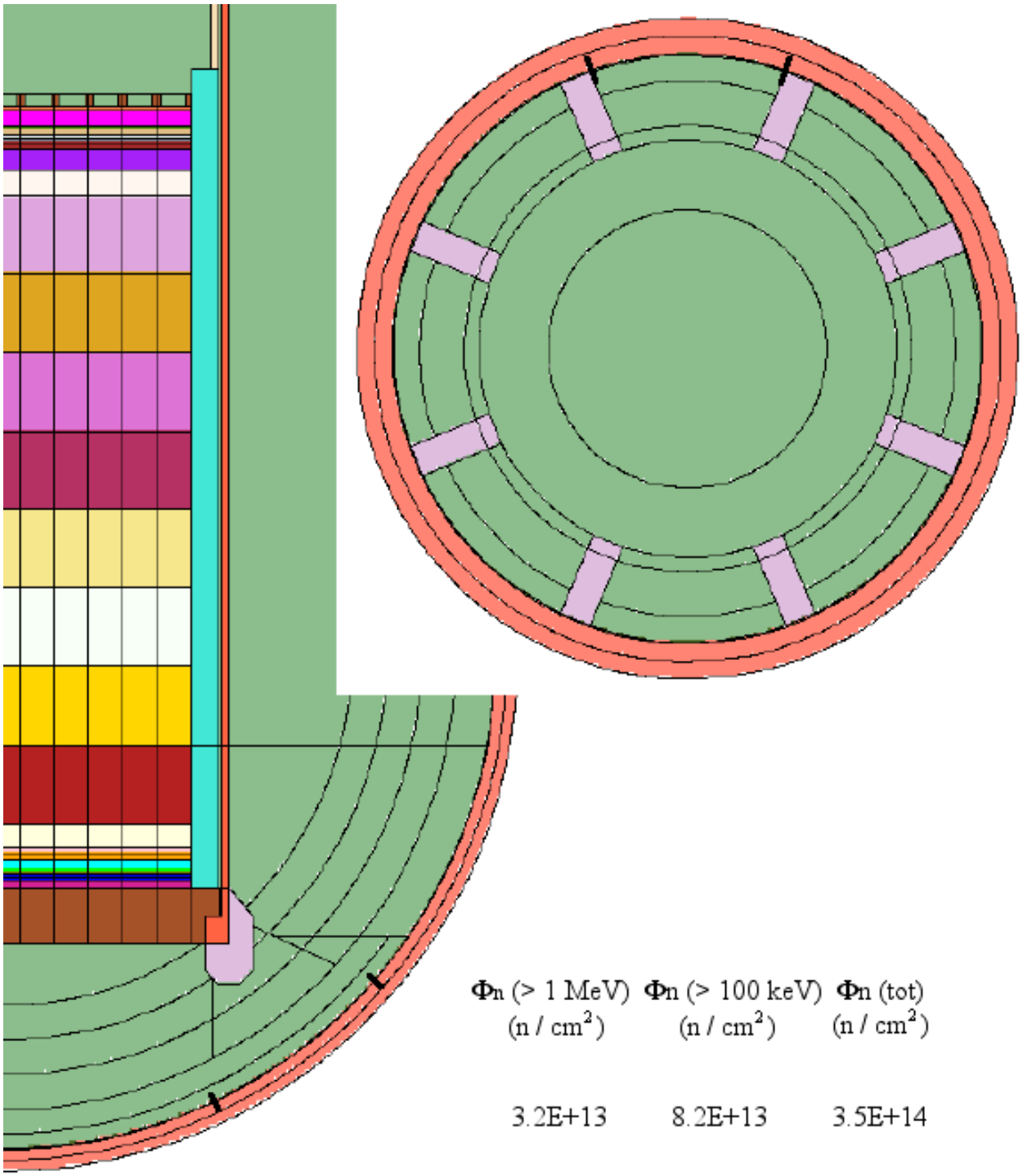

Figure 25. Reference case: Neutron fluences at two segments of the inner surface of the pressure vessel (between the vessel cladding and the vessel) between the azimuthal struts, for 60 years continuous running at 1000 MW.

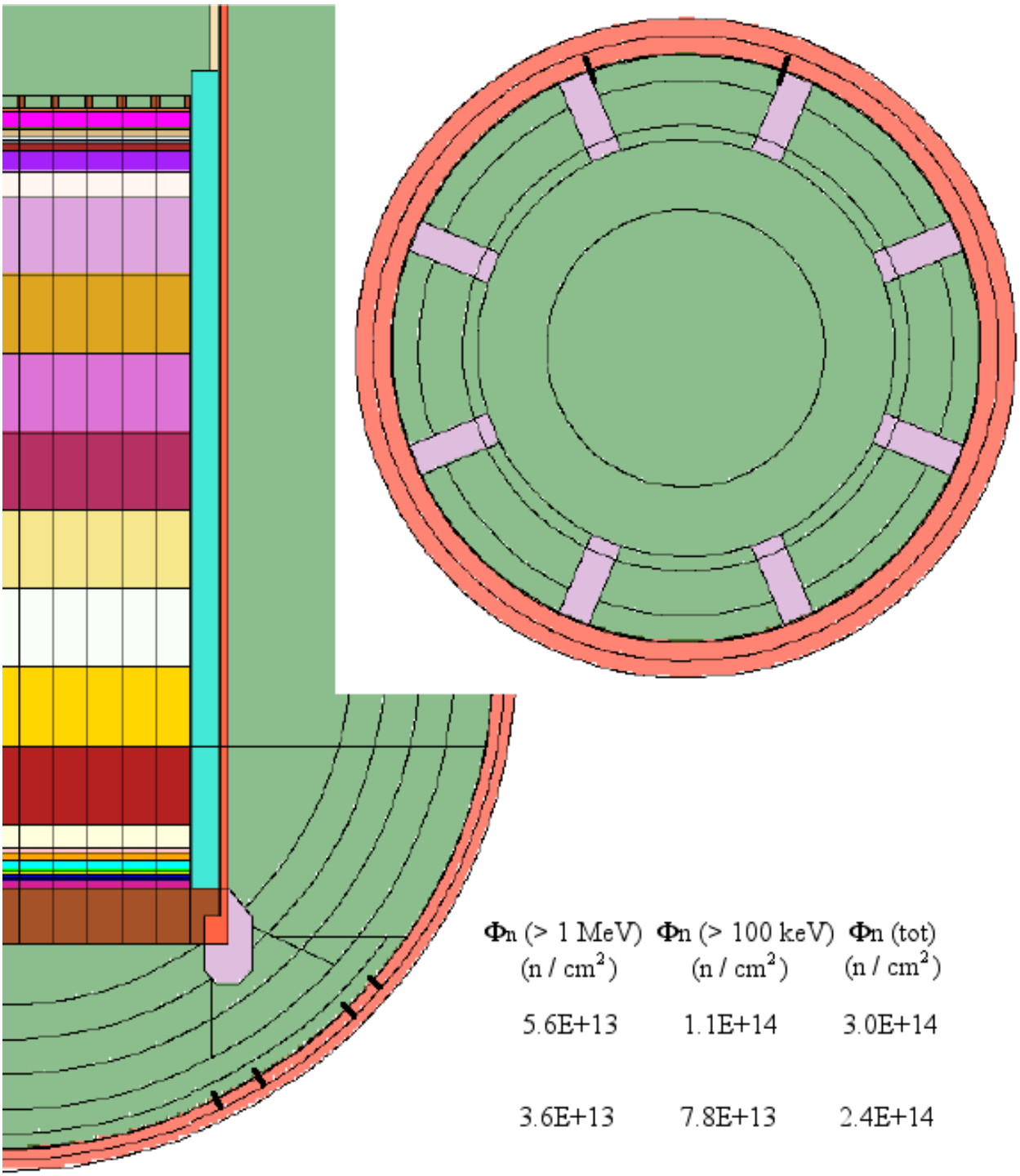

Φ_n (> 1 MeV) (n / cm^2)	Φ_n (> 100 keV) (n / cm^2)	Φ_n (tot) (n / cm^2)
5.6E+13	1.1E+14	3.0E+14
3.6E+13	7.8E+13	2.4E+14

Figure 26. Reference case: Neutron dpa's at segments of the inner surface of the pressure vessel (between the vessel cladding and the vessel) averaged around the circumference for 60 years continuous running at 1000 MW.

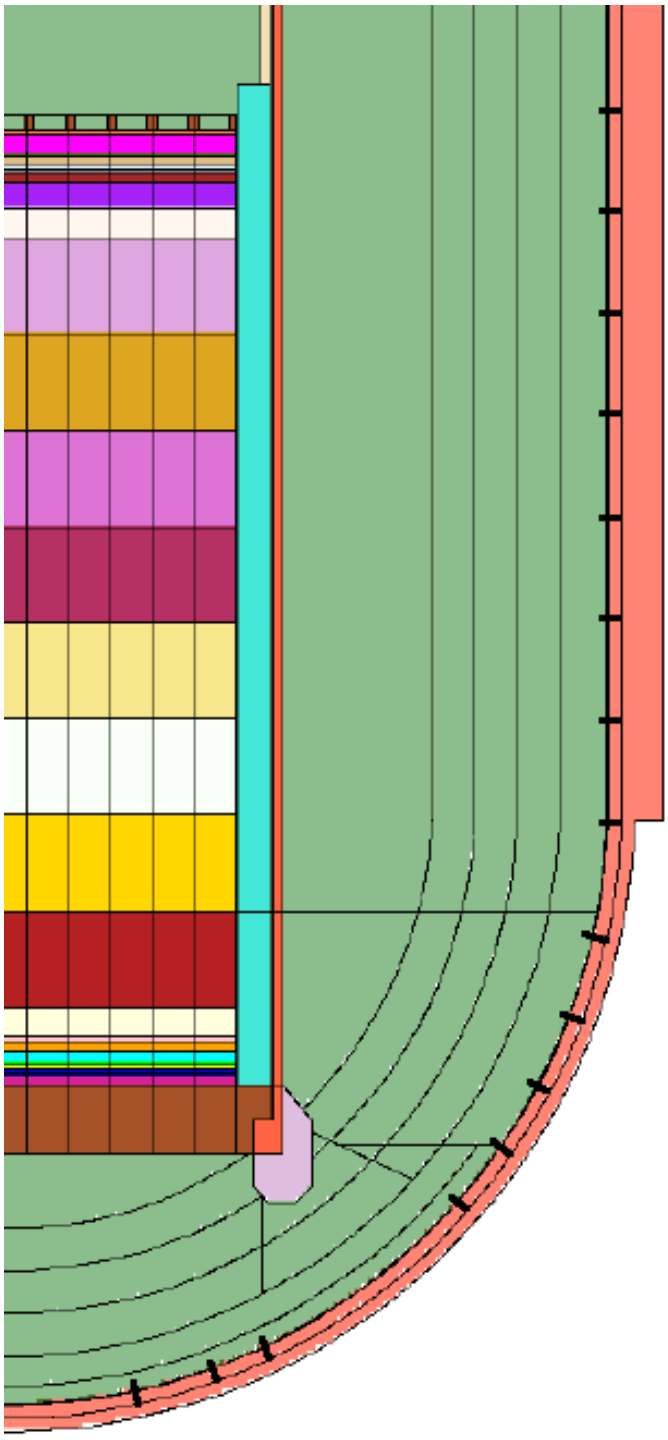

DPA n (> 1 MeV)	DPA n (> 100 keV)	DPA n (tot)
6.6E-9	7.7E-9	7.8E-9
1.7E-8	2.0E-8	2.0E-8
2.5E-8	3.0E-8	3.0E-8
2.8E-8	3.3E-8	3.3E-8
2.8E-8	3.3E-8	3.3E-8
2.8E-8	3.3E-8	3.3E-8
2.7E-7	3.2E-8	3.2E-8
2.9E-8	3.4E-8	3.4E-8
4.3E-8	5.0E-8	5.1E-8
6.5E-8	7.5E-8	7.6E-8
8.6E-8	9.9E-8	1.0E-7
8.8E-8	1.0E-7	1.0E-7
3.4E-8	5.4E-8	6.0E-8
6.4E-8	7.4E-8	7.5E-8
5.8E-8	6.7E-8	6.9E-8
4.5E-8	5.2E-8	5.3E-8

Figure 27. Reference case: Neutron dpa's at two segments of the inner surface of the pressure vessel (between the vessel cladding and the vessel) and averaged over the inner 1/4 or 1/2 depths, averaged around the circumference for 60 years continuous running at 1000 MW.

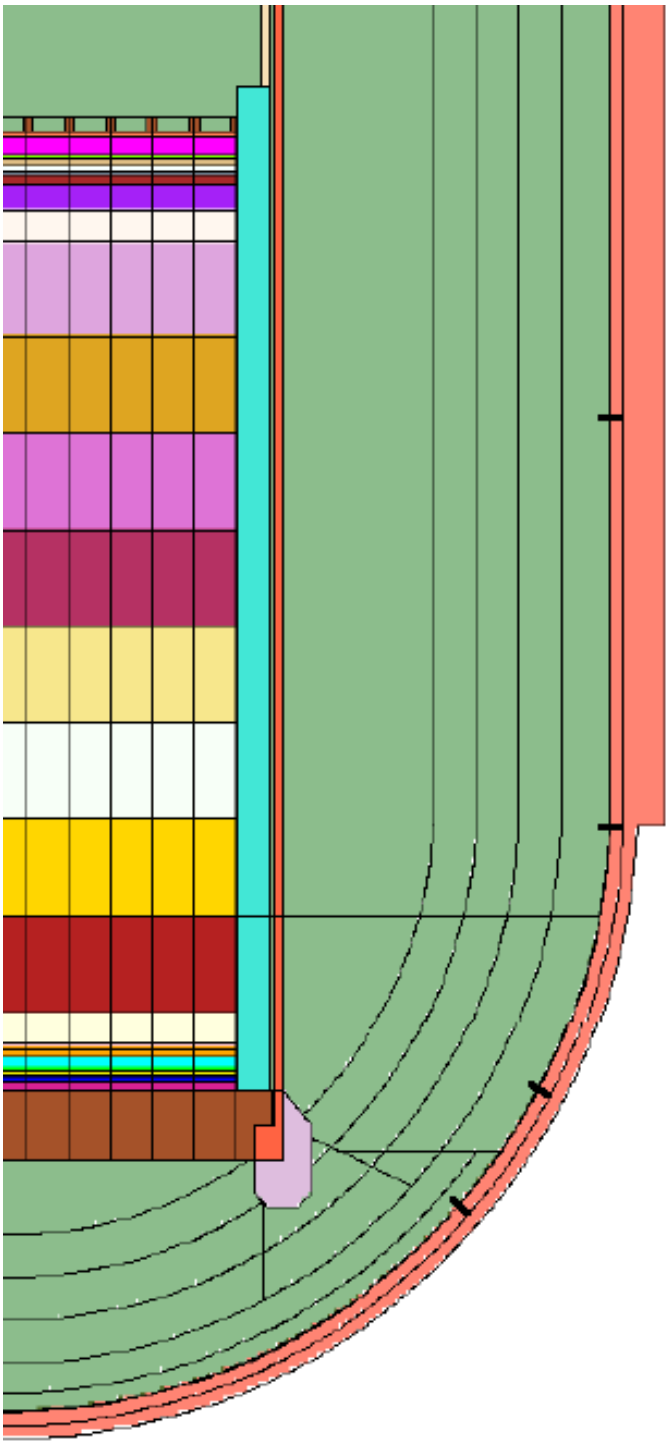

DPA n (> 1 MeV)	DPA n (> 100 keV)	DPA n (tot)
(at PV inner surface)		
2.8E-8	3.3E-8	3.3E-8
(averaged over inner 1/4 thickness)		
1.9E-8	2.4E-8	2.4E-8
(at PV inner surface)		
8.7E-8	1.0E-7	1.0E-7
(averaged over inner 1/2 thickness)		
5.8E-8	7.2E-8	7.3E-8

Figure 28. Reference case: Azimuthal variation of the neutron dpa's at the upper (cylindrical) segment of the inner surface of the pressure vessel with respect to the result for the average around the circumference shown in Figure 27.

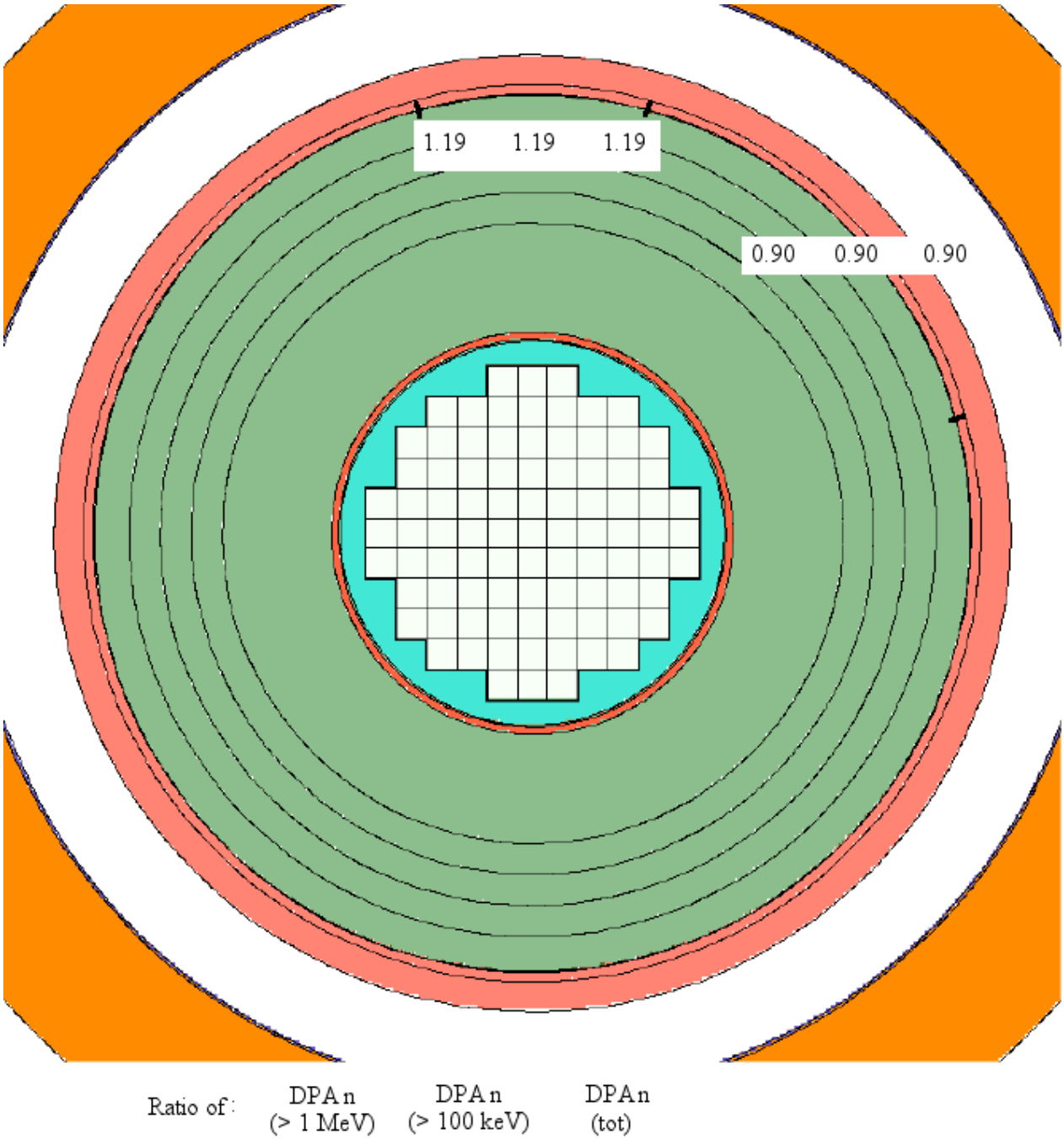

Figure 29. Reference case: Azimuthal variation of the neutron dpa's at the lower (spherical) segment of the inner surface of the pressure vessel with respect to the result for the average around the circumference shown in Figure 27.

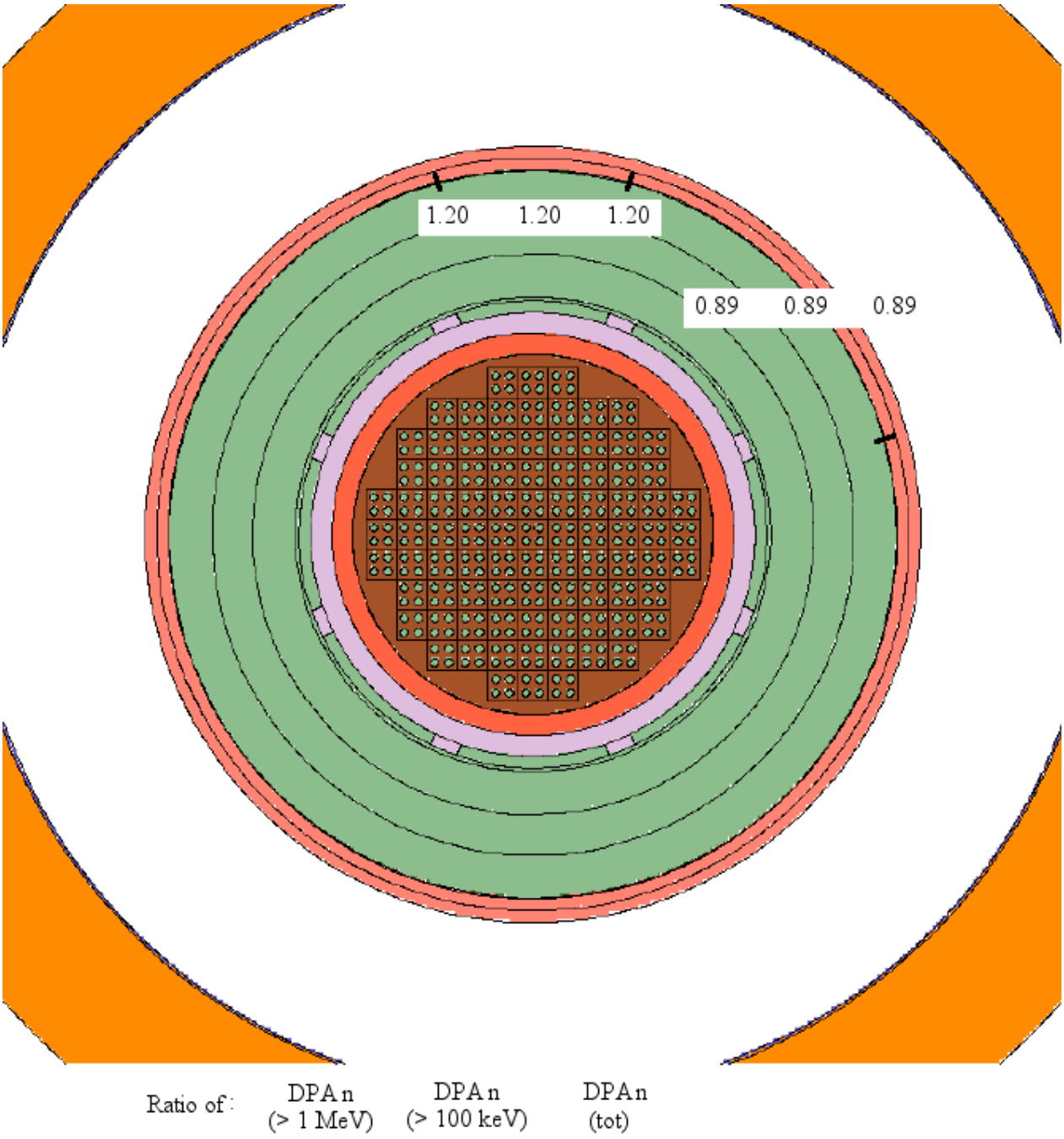

Figure 30. Reference case: Neutron dpa's at a segment of the inner surface of the pressure vessel (between the vessel cladding and the vessel) and averaged over the inner 1/2 depth, at the point where the azimuthal struts rest on the vessel, for 60 years continuous running at 1000 MW.

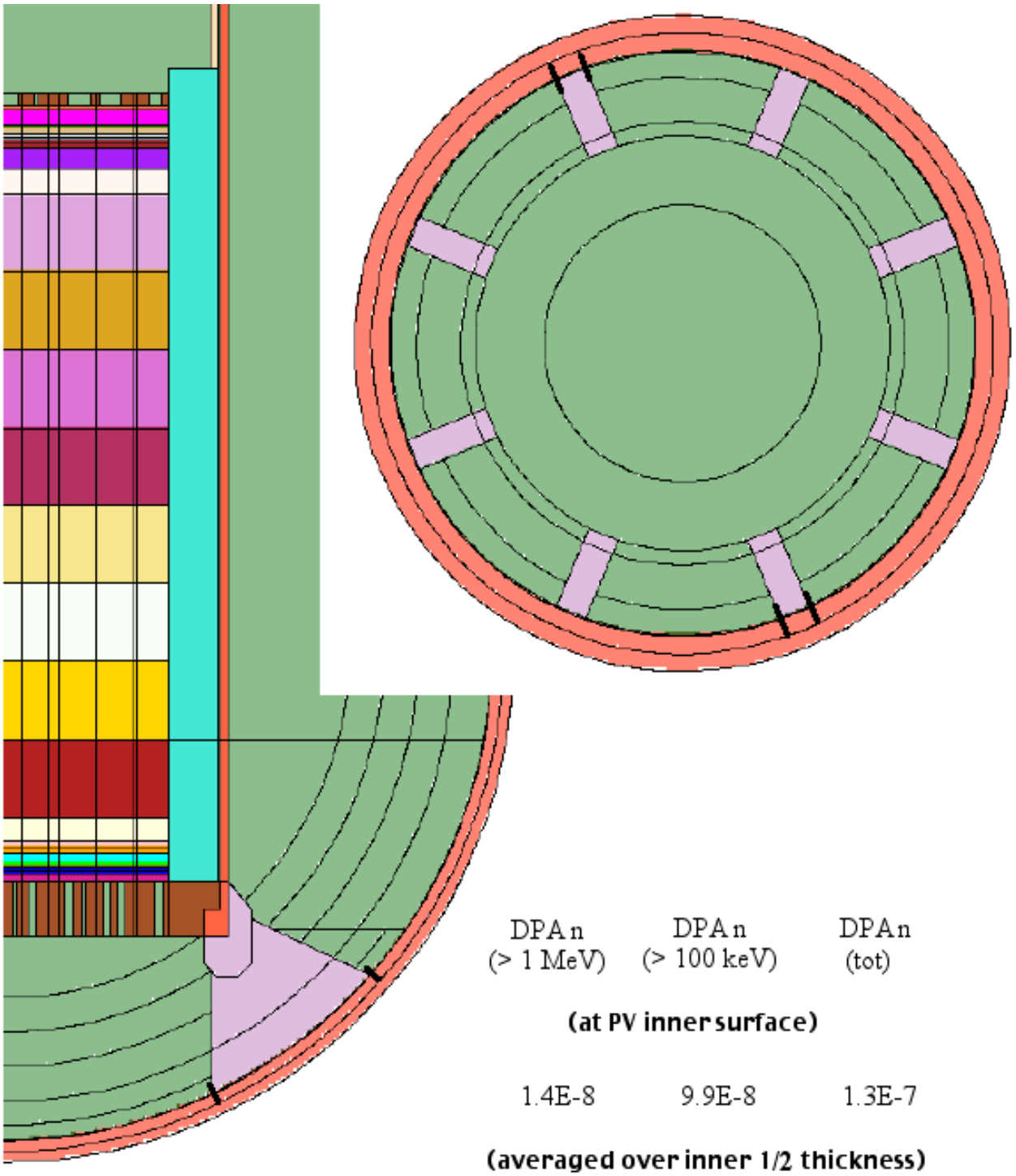

DPA n (> 1 MeV)	DPA n (> 100 keV)	DPA n (tot)
(at PV inner surface)		
1.4E-8	9.9E-8	1.3E-7
(averaged over inner 1/2 thickness)		
9.8E-9	6.9E-8	8.8E-8

Figure 31. Reference case: Neutron dpa's at a segment of the inner surface of the pressure vessel (between the vessel cladding and the vessel) between the azimuthal struts, for 60 years continuous running at 1000 MW.

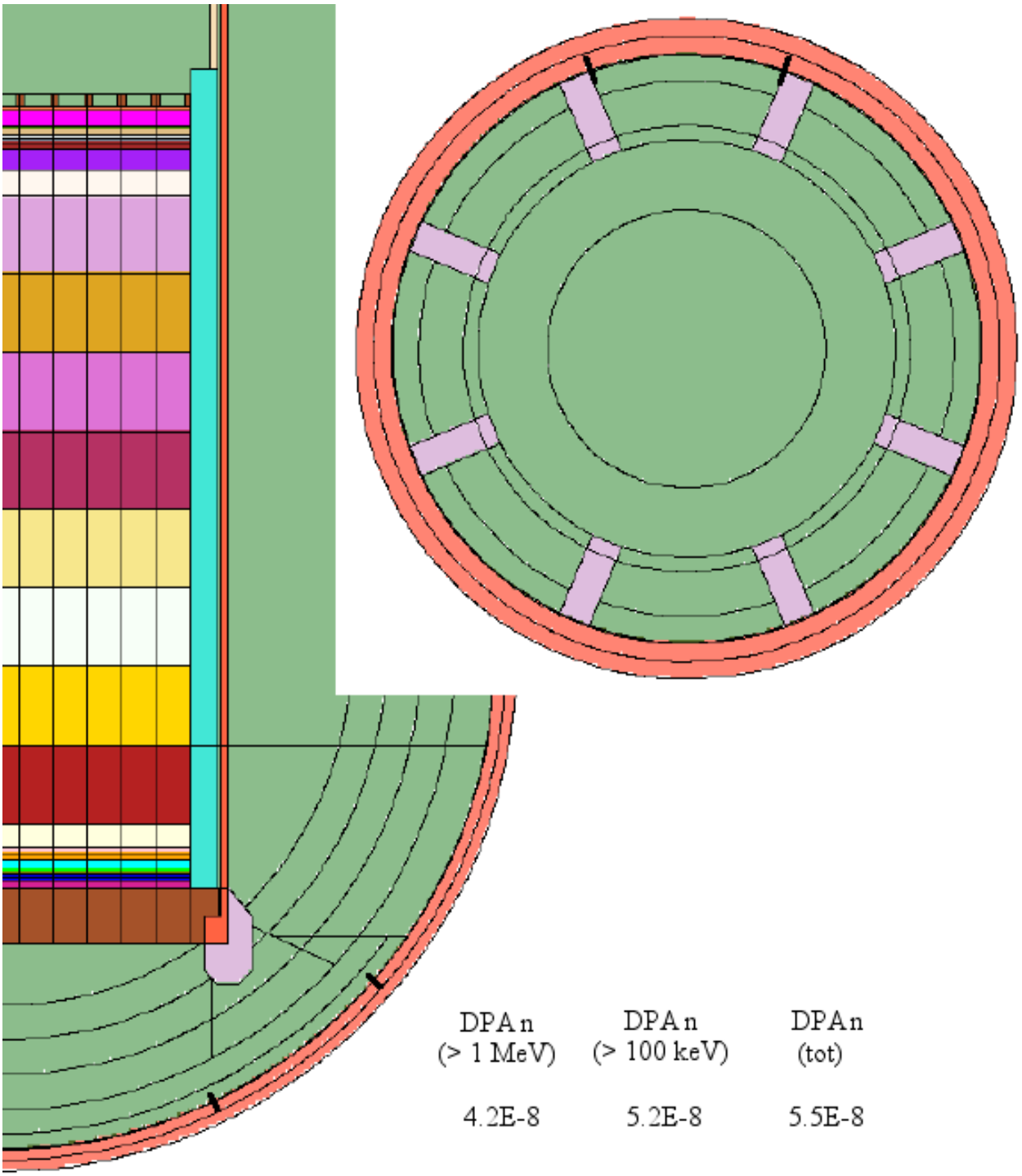

Figure 32. Reference case: Neutron dpa's at two segments of the inner surface of the pressure vessel (between the vessel cladding and the vessel) between the azimuthal struts, for 60 years continuous running at 1000 MW.

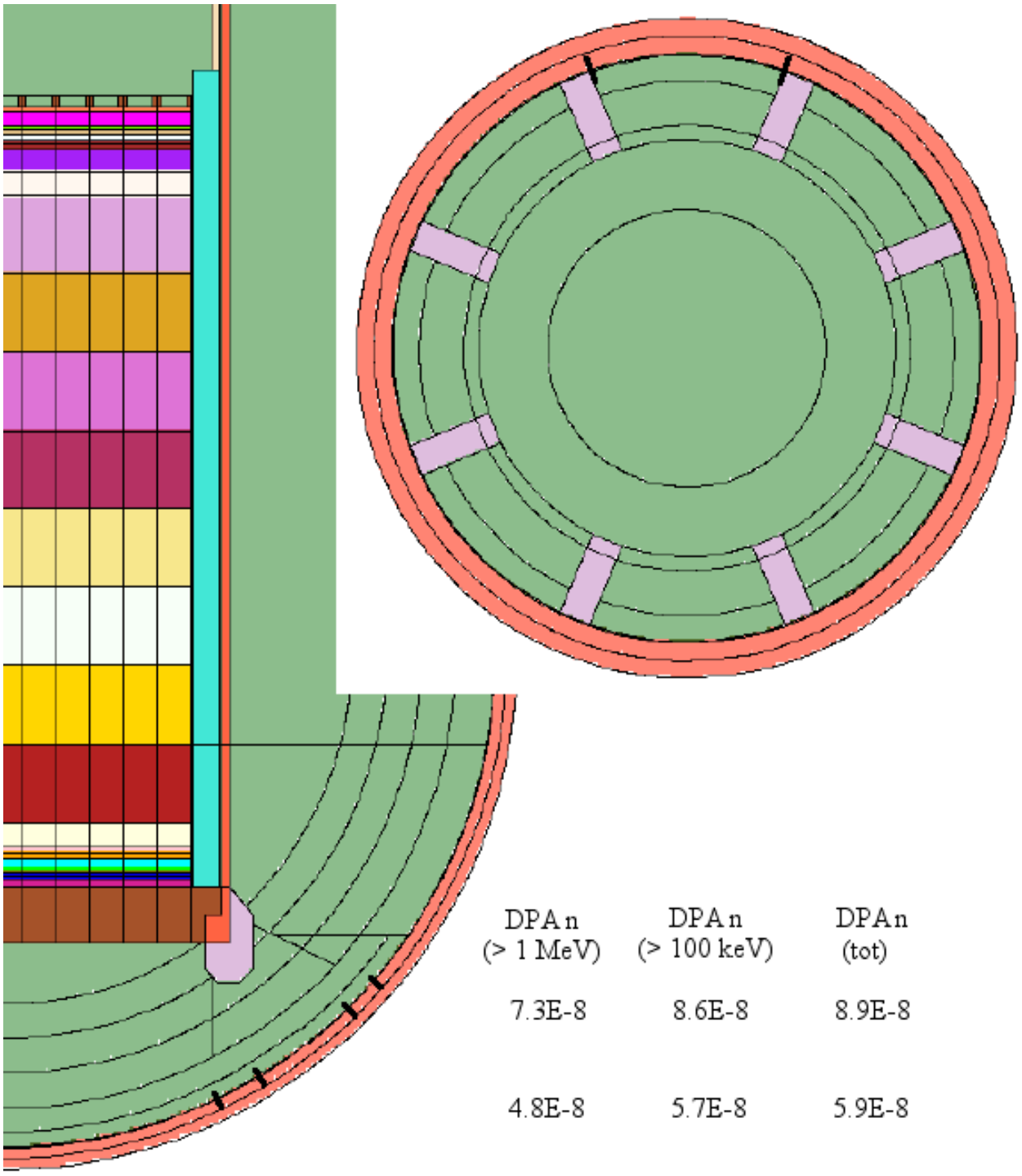

Figure 33. Reference case: Gamma fluences at segments of the inner surface of the pressure vessel (between the vessel cladding and the vessel) averaged around the circumference for 60 years continuous running at 1000 MW. (Results within brackets denote poor statistical quality.)

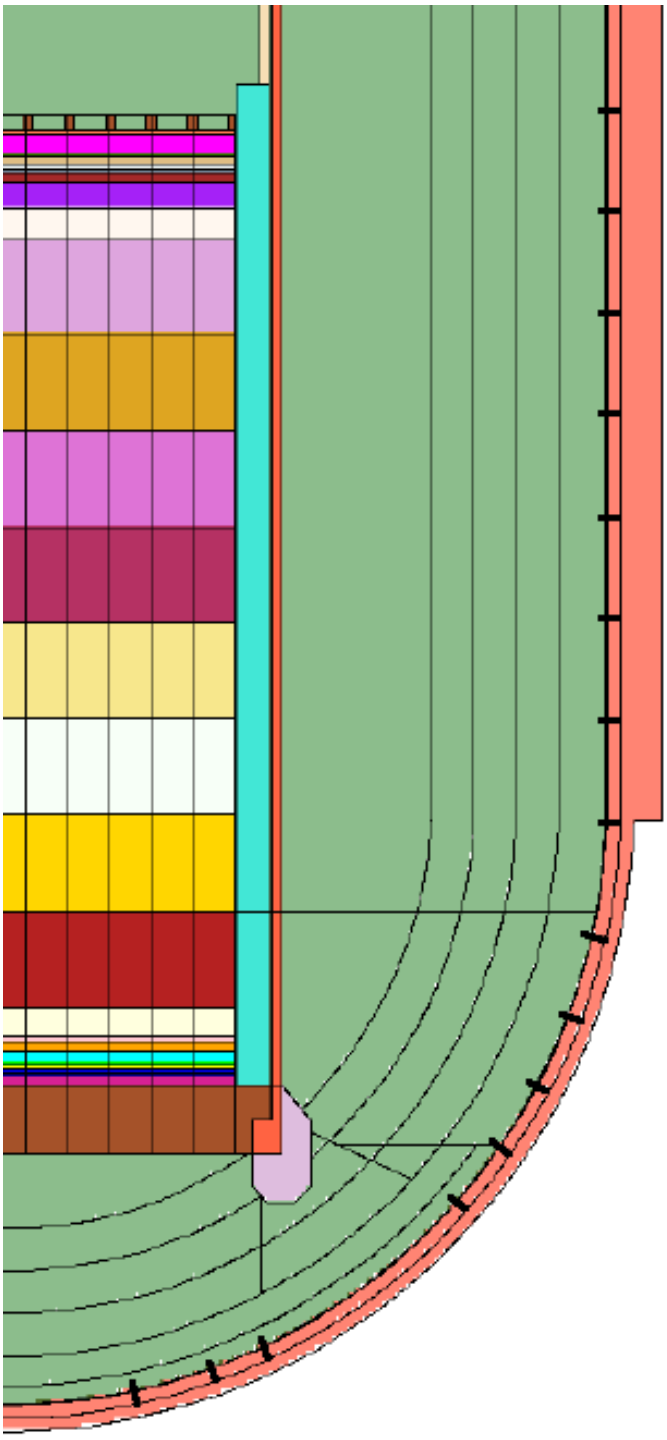

$\Phi\gamma(>8\,MeV)$ (γ / cm^2)	$\Phi\gamma(>4\,MeV)$ (γ / cm^2)	$\Phi\gamma(>700\,keV)$ (γ / cm^2)
2.6E+17	1.5E+18	3.4E+18
4.6E+17	2.6E+18	6.0E+18
6.3E+17	3.5E+18	8.3E+18
7.4E+17	4.1E+18	9.6E+18
7.7E+17	4.3E+18	1.0E+19
7.6E+17	4.3E+18	1.0E+19
6.9E+17	3.9E+18	9.2E+18
6.2E+17	3.5E+18	8.2E+18
5.7E+17	3.2E+18	7.7E+18
5.3E+17	2.9E+18	7.1E+18
4.4E+17	2.5E+18	6.2E+18
3.4E+17	1.9E+18	4.8E+18
9.1E+16	5.2E+17	1.4E+18
(3.8E+16)	(2.4E+17)	(6.9E+17)
(5.5E+16)	(3.7E+17)	(9.0E+17)
(6.7E+16)	(3.3E+17)	(8.1E+17)

Figure 34. Reference case: Gamma fluences at two segments of the inner surface of the pressure vessel (between the vessel cladding and the vessel) and averaged over the inner 1/4 or 1/2 depths, averaged around the circumference for 60 years continuous running at 1000 MW.

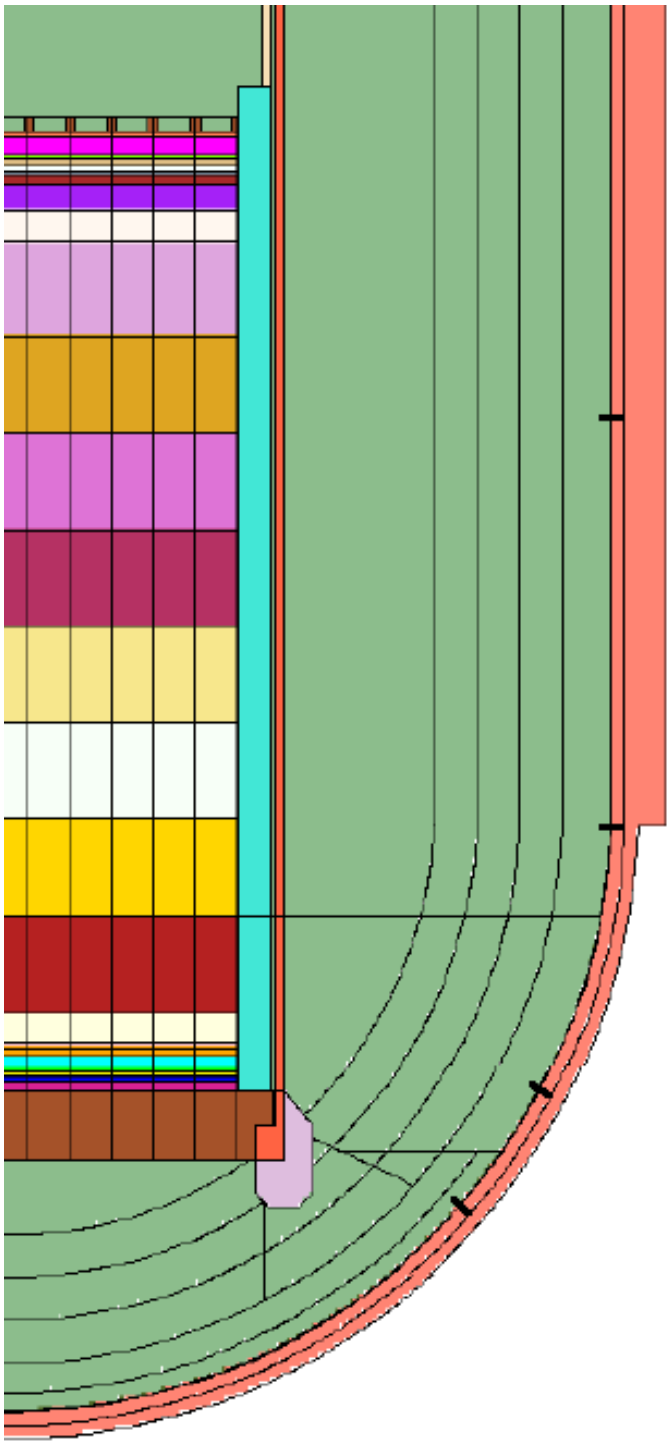

$\Phi\gamma(>8\,MeV)$ (γ / cm^2)	$\Phi\gamma(>4\,MeV)$ (γ / cm^2)	$\Phi\gamma(>700\,keV)$ (γ / cm^2)
(at PV inner surface)		
7.4E+17	4.1E+18	9.7E+18
(averaged over inner 1/4 thickness)		
3.4E+17	2.0E+18	5.1E+18
(at PV inner surface)		
4.0E+17	2.2E+18	5.5E+18
(averaged over inner 1/2 thickness)		
1.9E+17	1.1E+18	2.9E+18

Figure 35. Reference case: Azimuthal variation of the gamma fluences at the upper (cylindrical) segment of the inner surface of the pressure vessel with respect to the result for the average around the circumference shown in Figure 34.

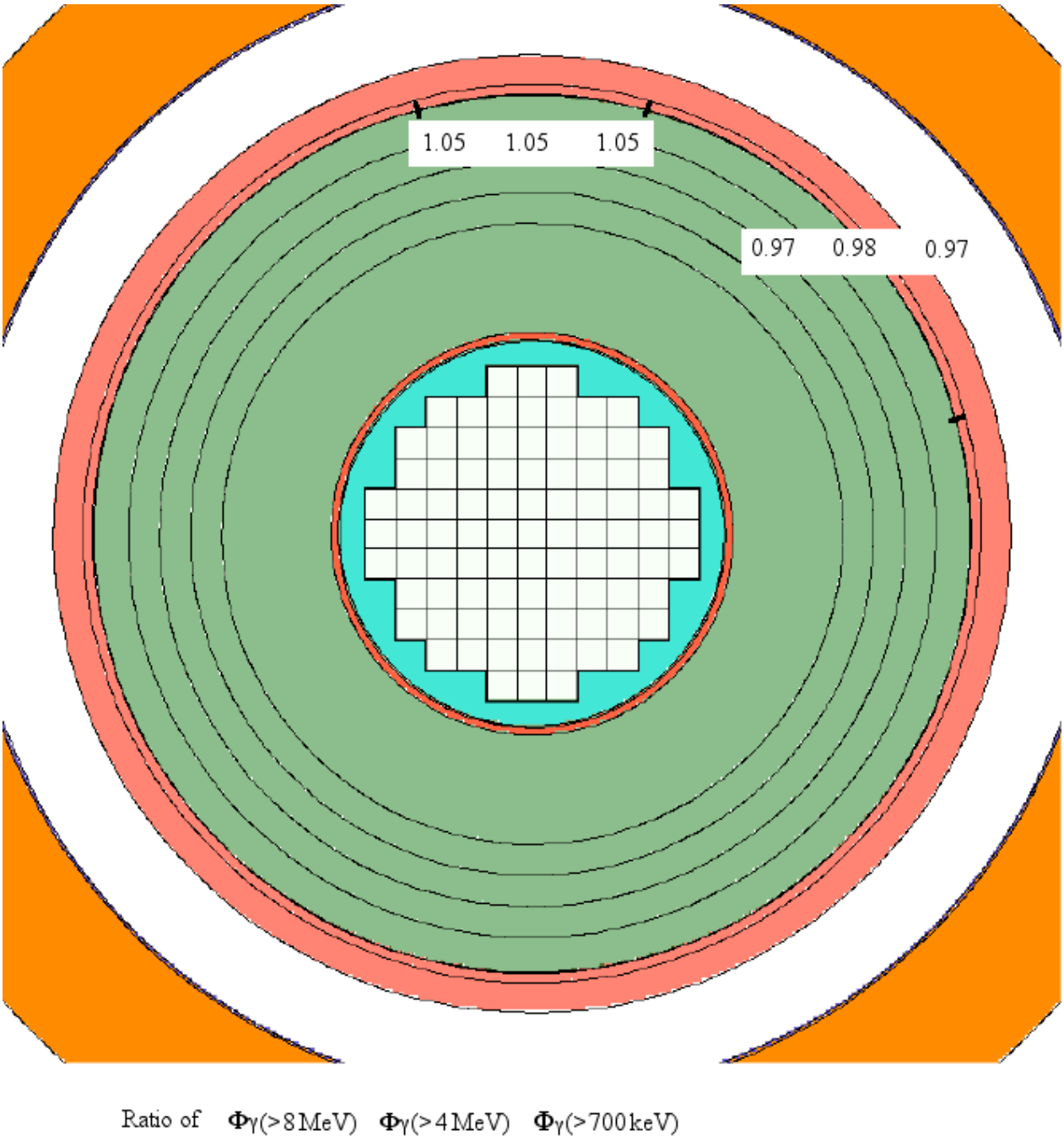

Figure 36. Reference case: Azimuthal variation of the gamma fluences at the lower (spherical) segment of the inner surface of the pressure vessel with respect to the result for the average around the circumference shown in Figure 34.

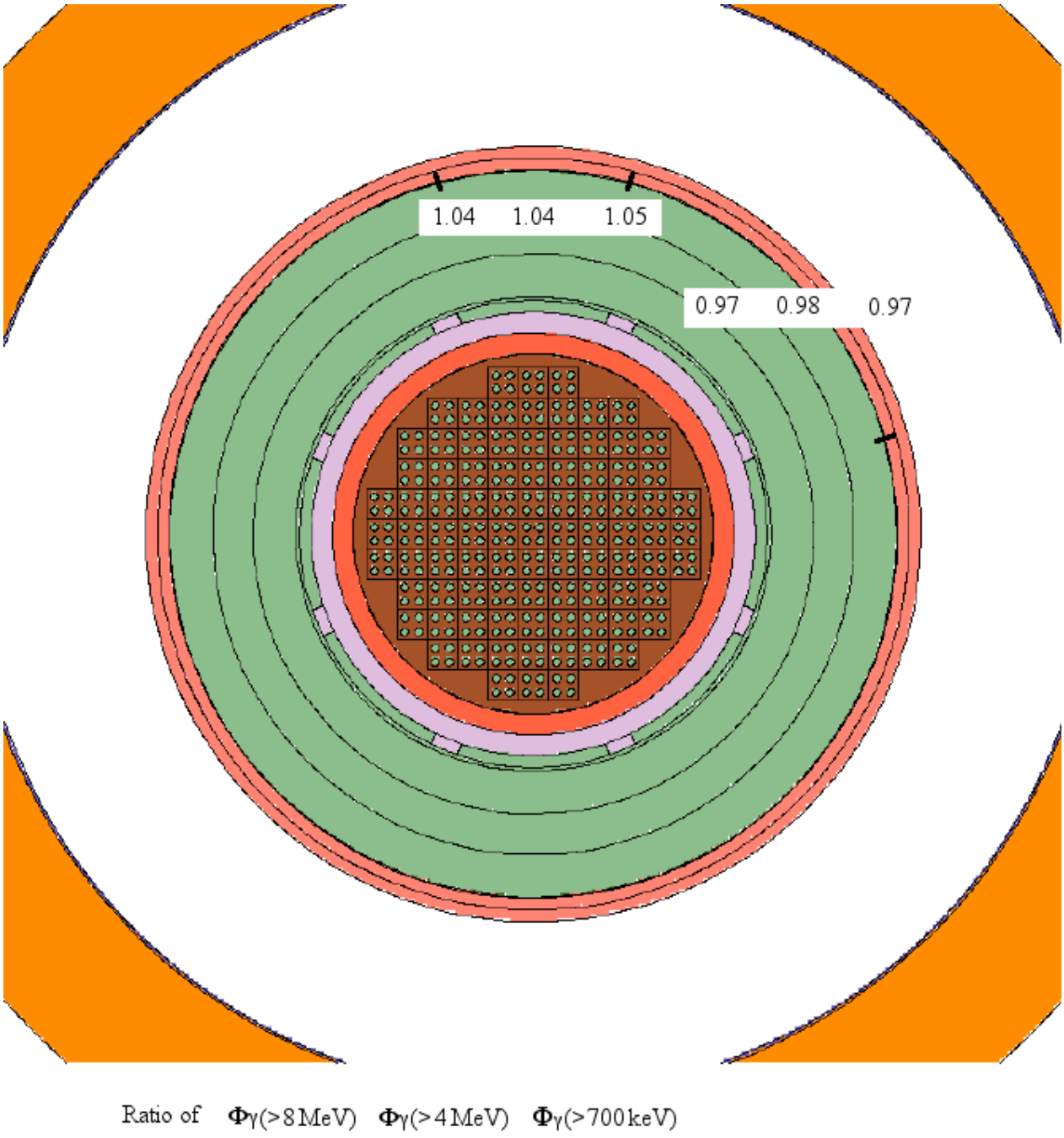

Figure 37. Reference case: Gamma fluences at a segment of the inner surface of the pressure vessel (between the vessel cladding and the vessel) and averaged over the inner 1/2 depth, at the point where the azimuthal struts rest on the vessel, for 60 years continuous running at 1000 MW.

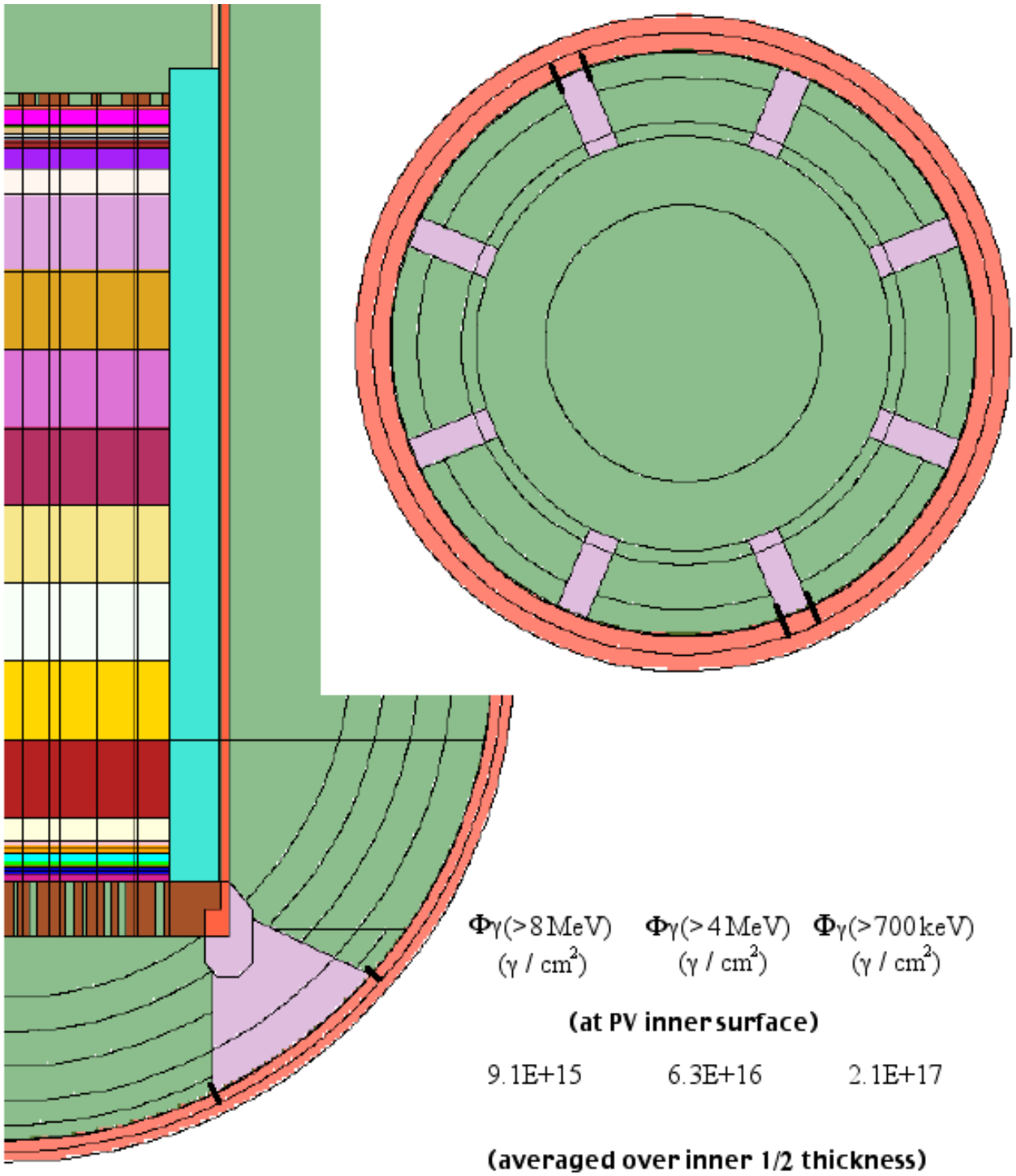

Figure 38. Reference case: Gamma fluences at a segment of the inner surface of the pressure vessel (between the vessel cladding and the vessel) between the azimuthal struts, for 60 years continuous running at 1000 MW.

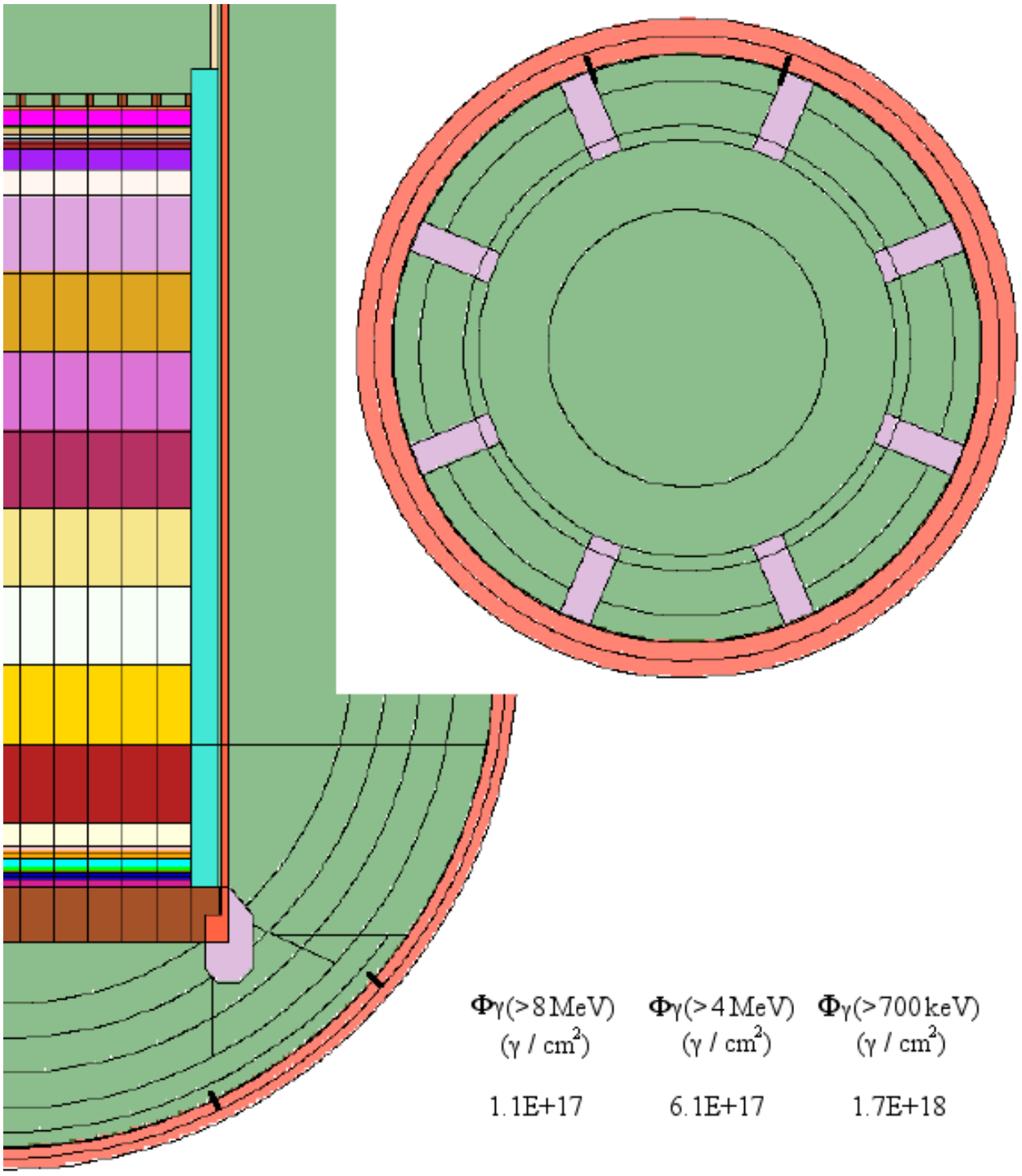

Figure 39. Reference case: Gamma fluences at two segments of the inner surface of the pressure vessel (between the vessel cladding and the vessel) between the azimuthal struts, for 60 years continuous running at 1000 MW. (Results within brackets denote poor statistical quality.)

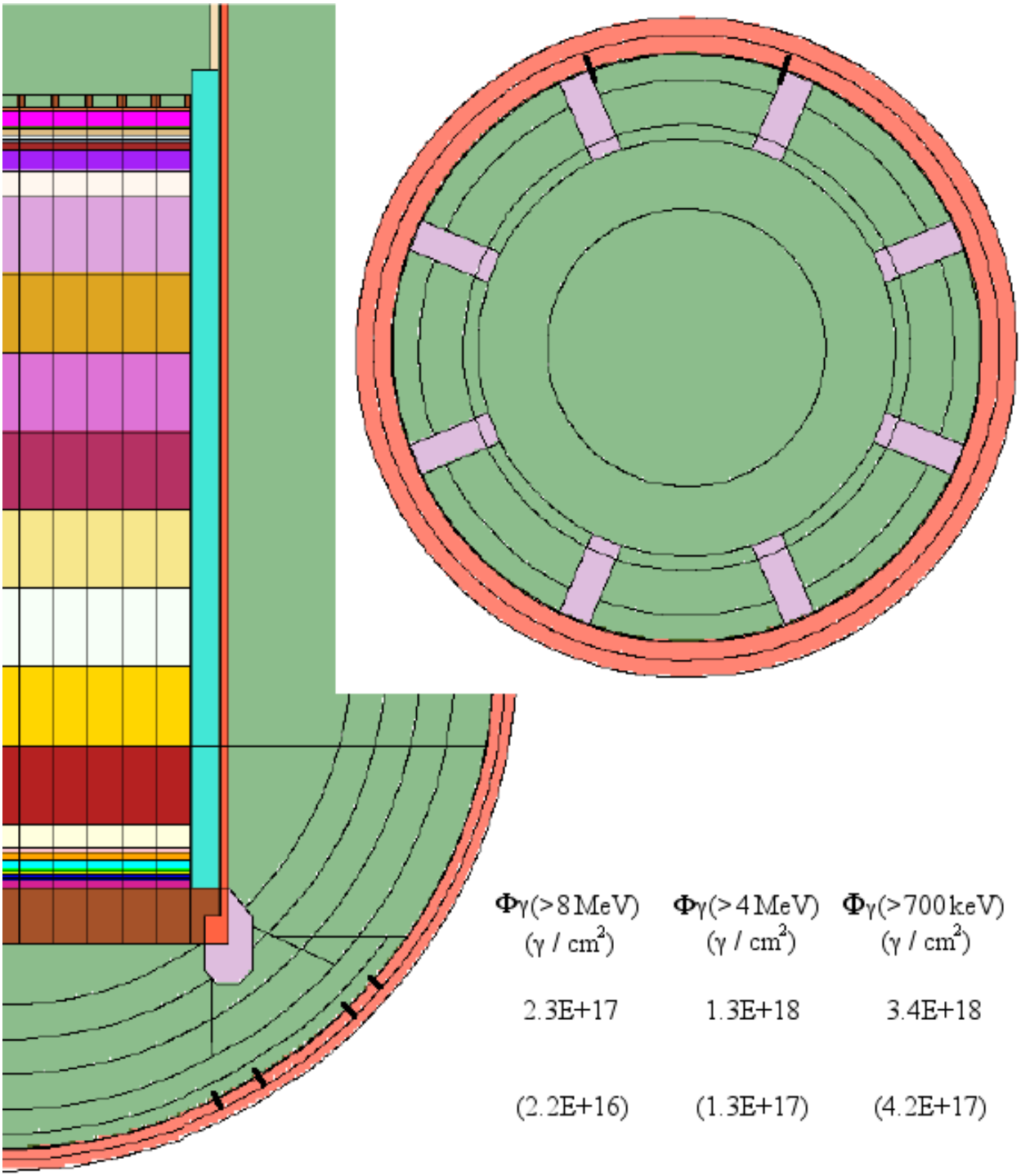

$\Phi\gamma(>8\,MeV)$ (γ / cm^2)	$\Phi\gamma(>4\,MeV)$ (γ / cm^2)	$\Phi\gamma(>700\,keV)$ (γ / cm^2)
2.3E+17	1.3E+18	3.4E+18
(2.2E+16)	(1.3E+17)	(4.2E+17)

Figure 40. Reference case: Gamma dpa's at segments of the inner surface of the pressure vessel (between the vessel cladding and the vessel) averaged around the circumference for 60 years continuous running at 1000 MW. (Results within brackets denote poor statistical quality.)

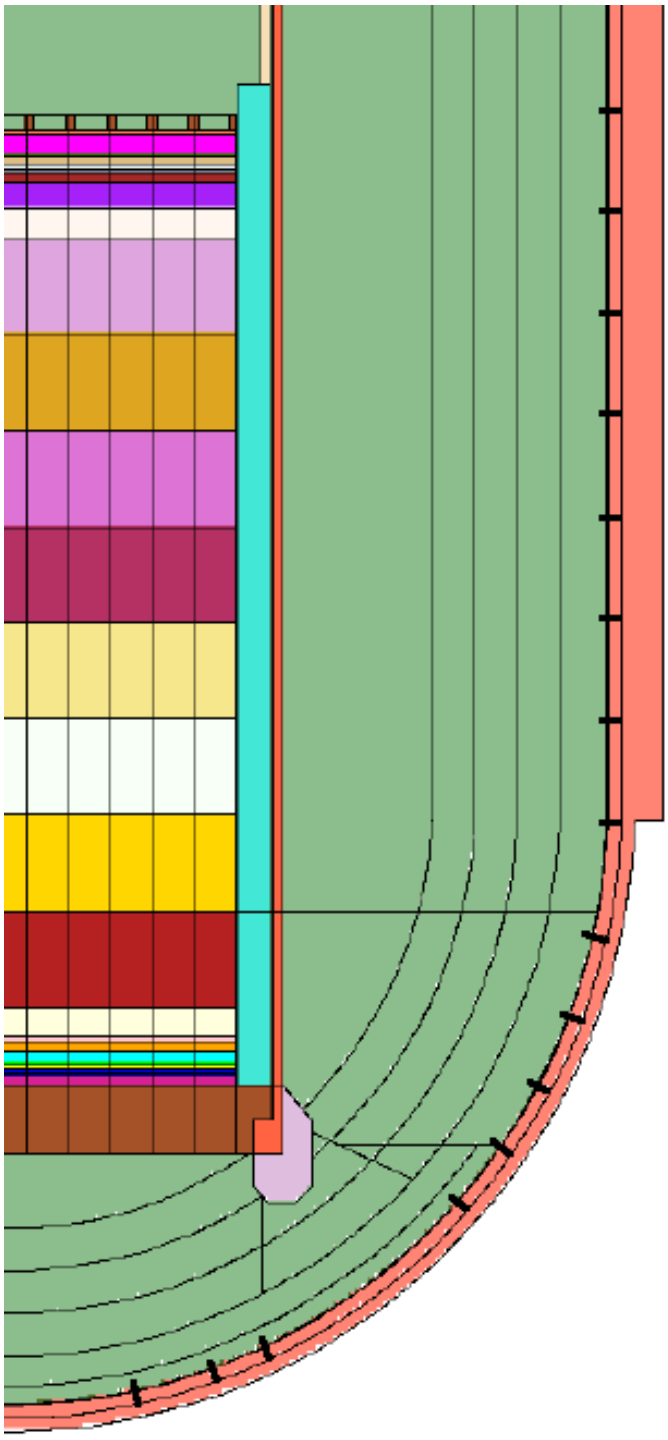

DPAγ (>8MeV)	DPAγ (>4MeV)	DPAγ (tot)
1.6E-6	5.5E-6	6.0E-6
2.9E-6	9.6E-6	1.1E-5
3.9E-6	1.3E-5	1.4E-5
4.6E-6	1.5E-5	1.7E-5
4.8E-6	1.6E-5	1.8E-5
4.7E-6	1.6E-5	1.7E-5
4.3E-6	1.5E-5	1.6E-5
3.9E-6	1.3E-5	1.4E-5
3.6E-6	1.2E-5	1.3E-5
3.3E-6	1.1E-5	1.2E-5
2.8E-6	9.4E-6	1.0E-5
2.1E-6	7.2E-6	7.9E-6
5.7E-7	2.0E-6	2.2E-6
(2.4E-7)	(8.9E-7)	(1.0E-6)
(3.5E-7)	(1.4E-6)	(1.5E-6)
(4.2E-7)	(1.2E-6)	(1.4E-6)

Figure 41. Reference case: Gamma dpa's at two segments of the inner surface of the pressure vessel (between the vessel cladding and the vessel) and averaged over the inner 1/4 or 1/2 depths, averaged around the circumference for 60 years continuous running at 1000 MW.

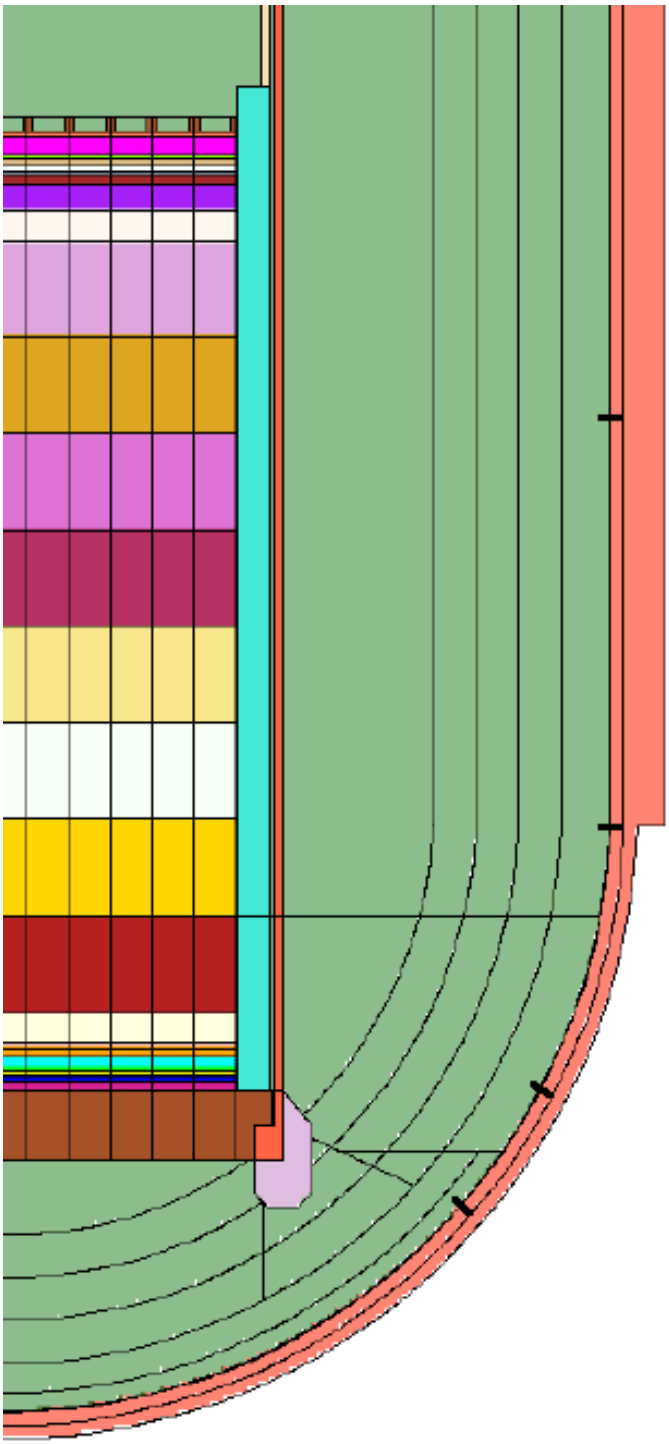

DPAγ (>8MeV)	DPAγ (>4MeV)	DPAγ (tot)
(at PV inner surface)		
4.6E-6	1.5E-5	1.7E-5
(averaged over inner 1/4 thickness)		
2.2E-6	7.5E-6	8.4E-6
(at PV inner surface)		
2.5E-6	8.4E-6	9.2E-6
(averaged over inner 1/2 thickness)		
1.2E-6	4.2E-6	4.6E-6

Figure 42. Reference case: Azimuthal variation of the gamma dpa's at the upper (cylindrical) segment of the inner surface of the pressure vessel with respect to the result for the average around the circumference shown in Figure 41.

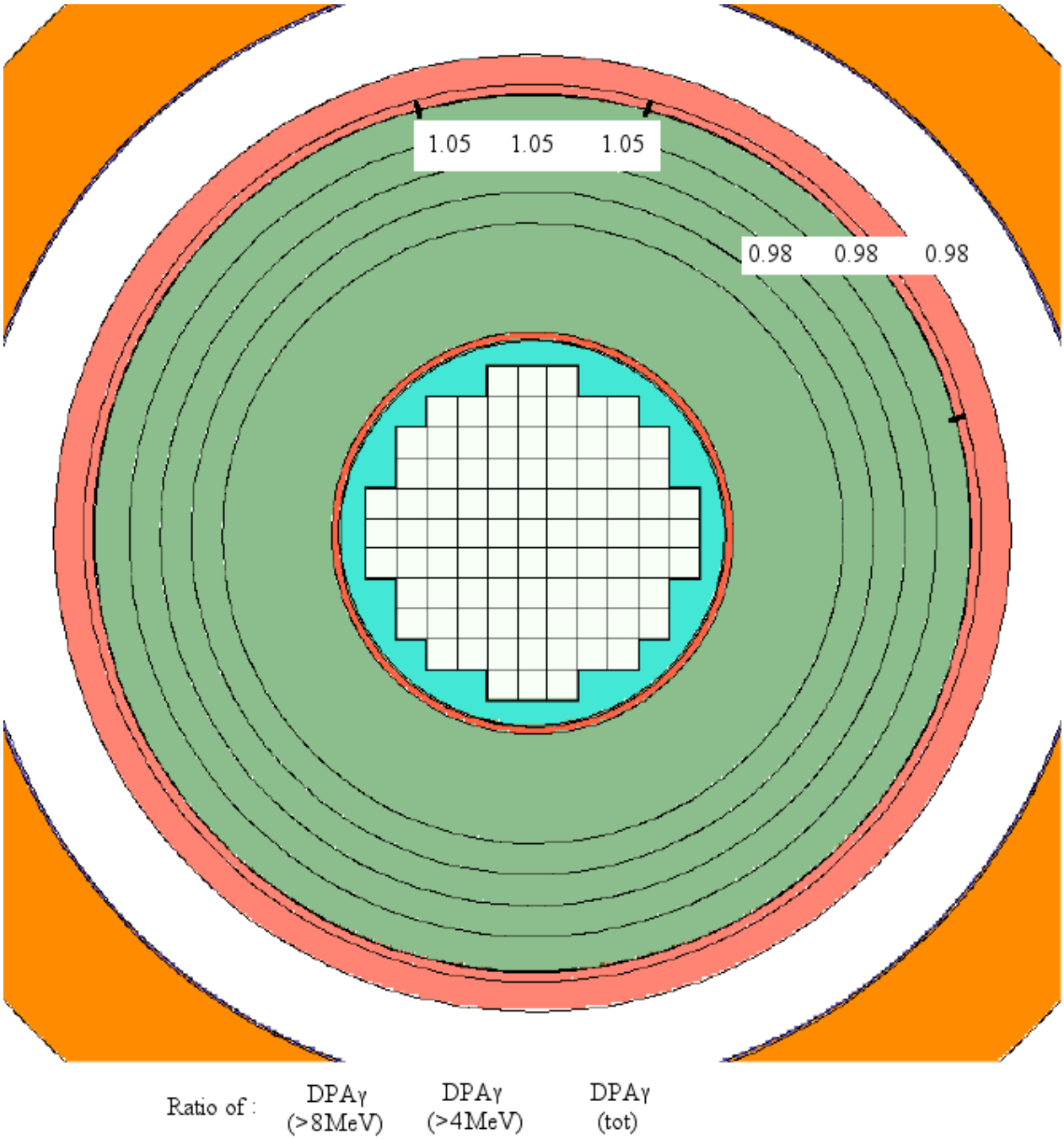

Figure 43. Reference case: Azimuthal variation of the gamma dpa's at the lower (spherical) segment of the inner surface of the pressure vessel with respect to the result for the average around the circumference shown in Figure 41.

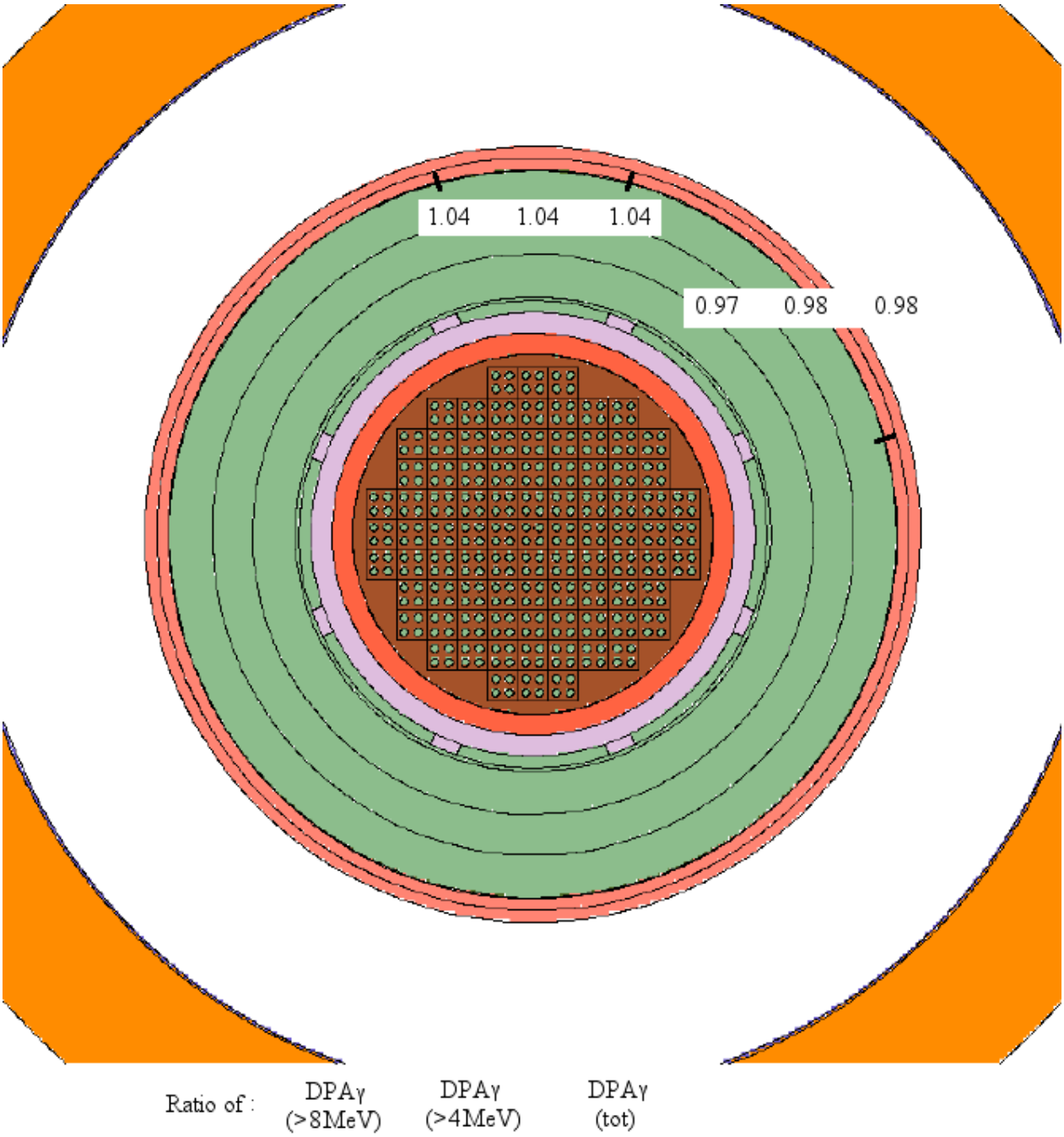

Figure 44. Reference case: Gamma dpa's at a segment of the inner surface of the pressure vessel (between the vessel cladding and the vessel) and averaged over the inner 1/2 depth, at the point where the azimuthal struts rest on the vessel, for 60 years continuous running at 1000 MW.

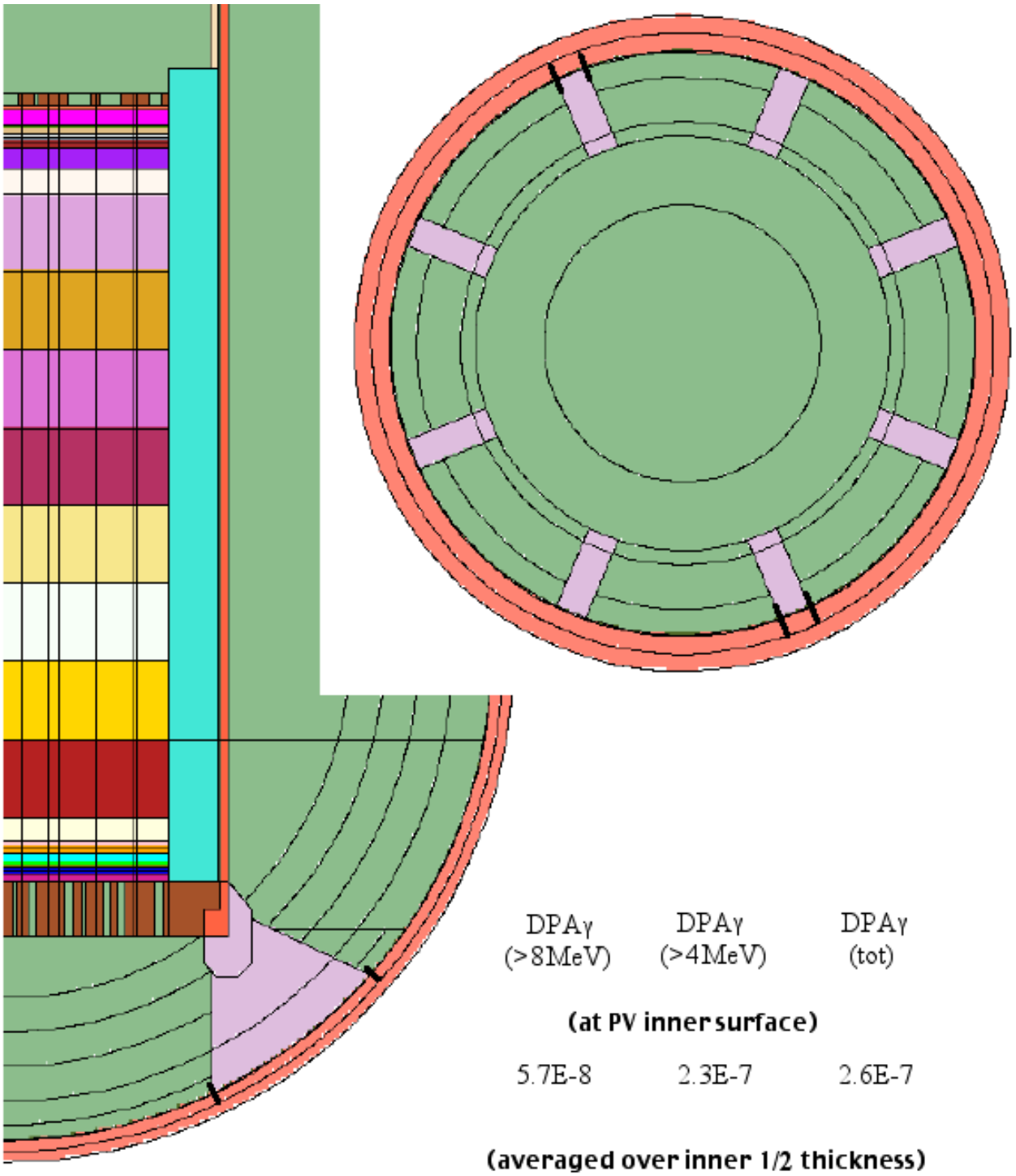

Figure 45. Reference case: Gamma dpa's at a segment of the inner surface of the pressure vessel (between the vessel cladding and the vessel) between the azimuthal struts, for 60 years continuous running at 1000 MW.

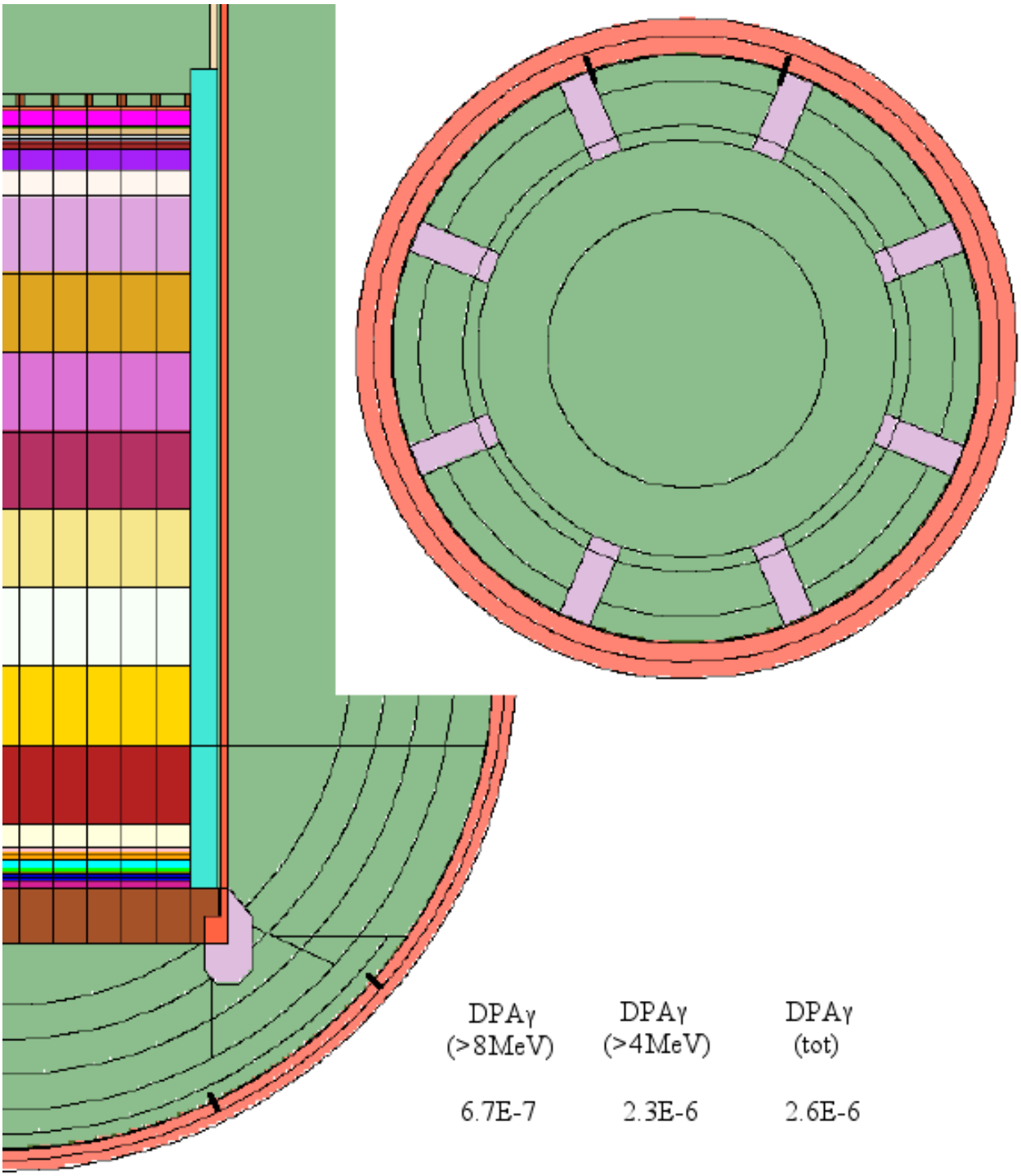

Figure 46. Reference case: Gamma dpa's at two segments of the inner surface of the pressure vessel (between the vessel cladding and the vessel) between the azimuthal struts, for 60 years continuous running at 1000 MW. (Results within brackets denote poor statistical quality.)

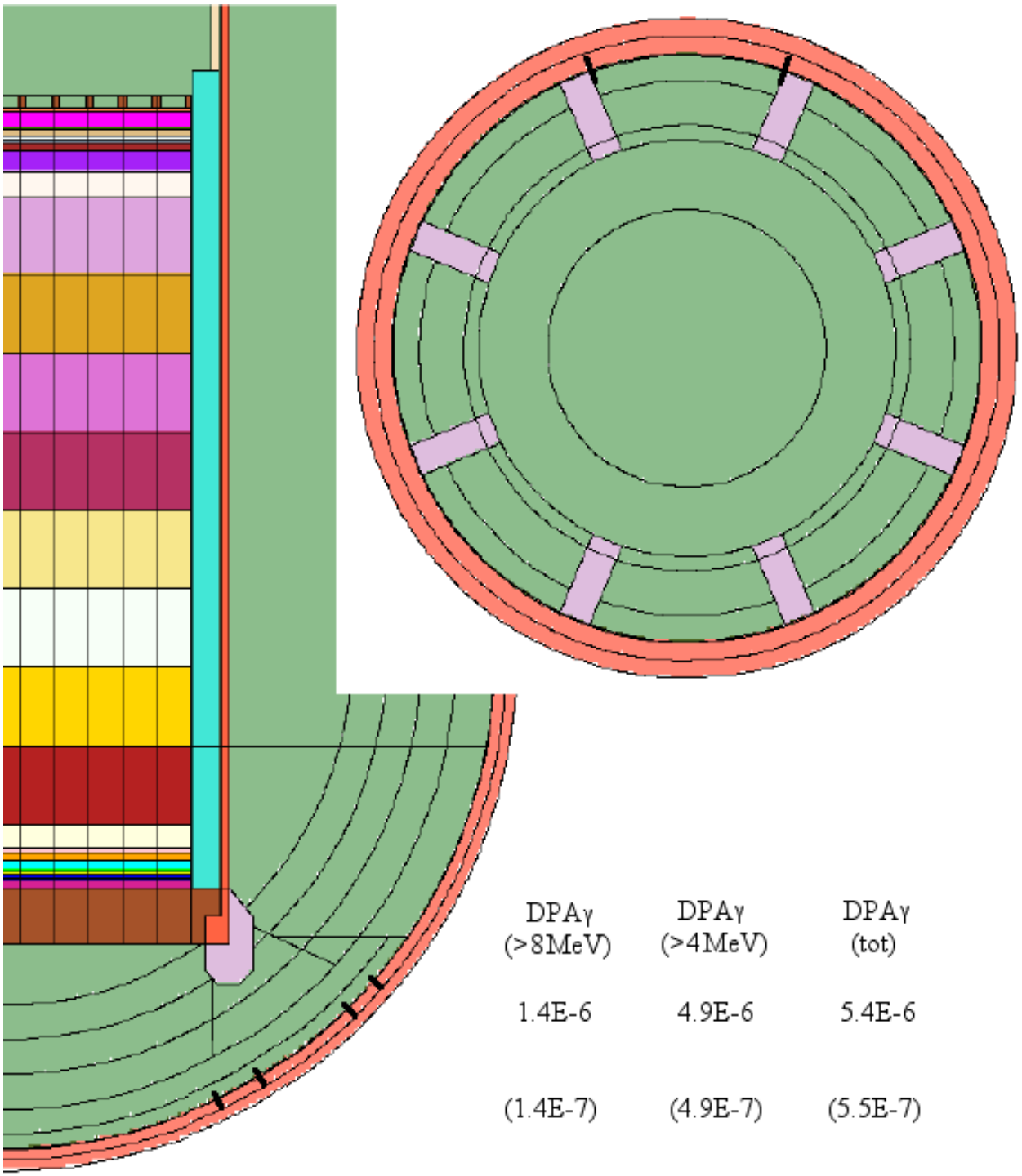

Figure 47. Contribution to the neutron and gamma dpa results on the inner surface of the pressure vessel (see Fig. 27) as a function of the energy of the fission neutrons.

"dpa(n); cyl" = total neutron dpa on cylindrical segment;

"dpa(n); sph" = total neutron dpa on spherical segment;

"dpa(gamma); cyl" = total gamma dpa on cylindrical segment;

"dpa(gamma); sph" = total gamma dpa on spherical segment;

"235U (thermal n)" = thermal neutron-induced fission spectrum from ^{235}U.

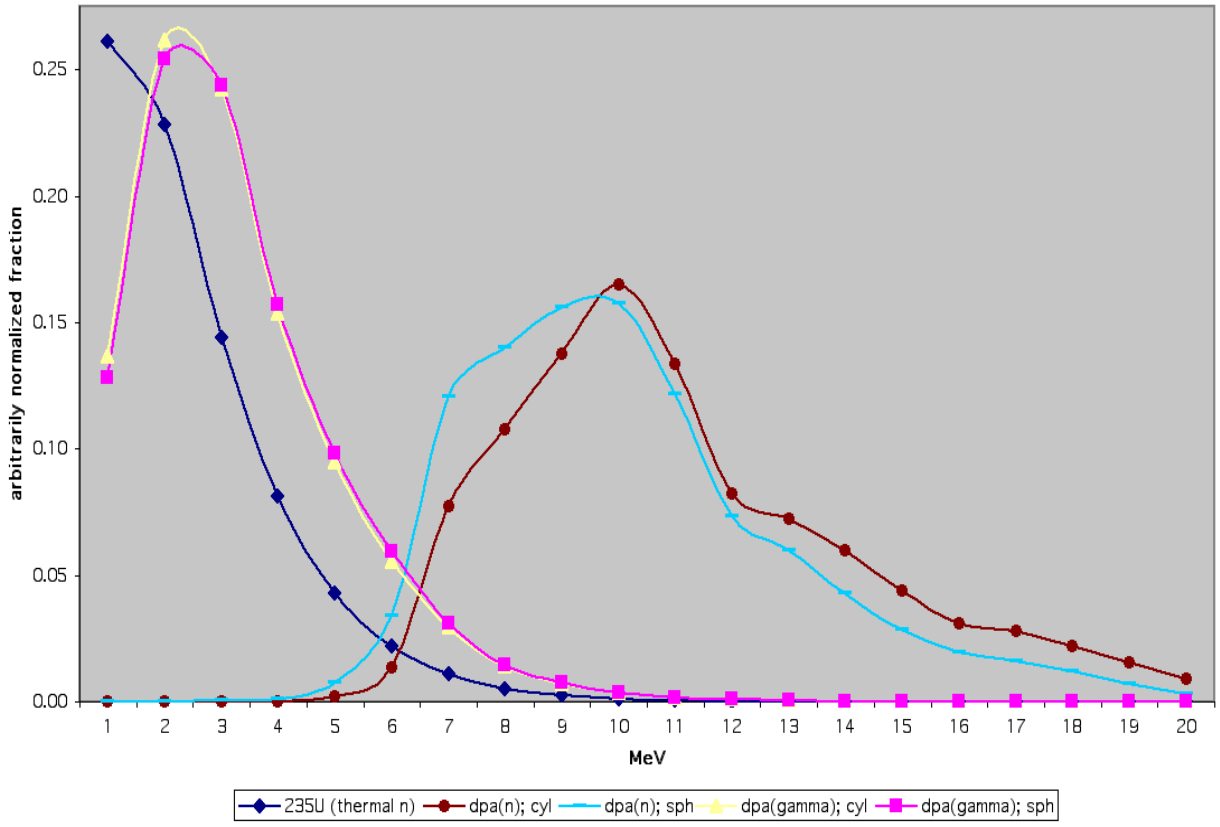

Figure 48. Including steam generators (first model) and with 25 m diameter vessel: vertical section through the inlet nozzles.

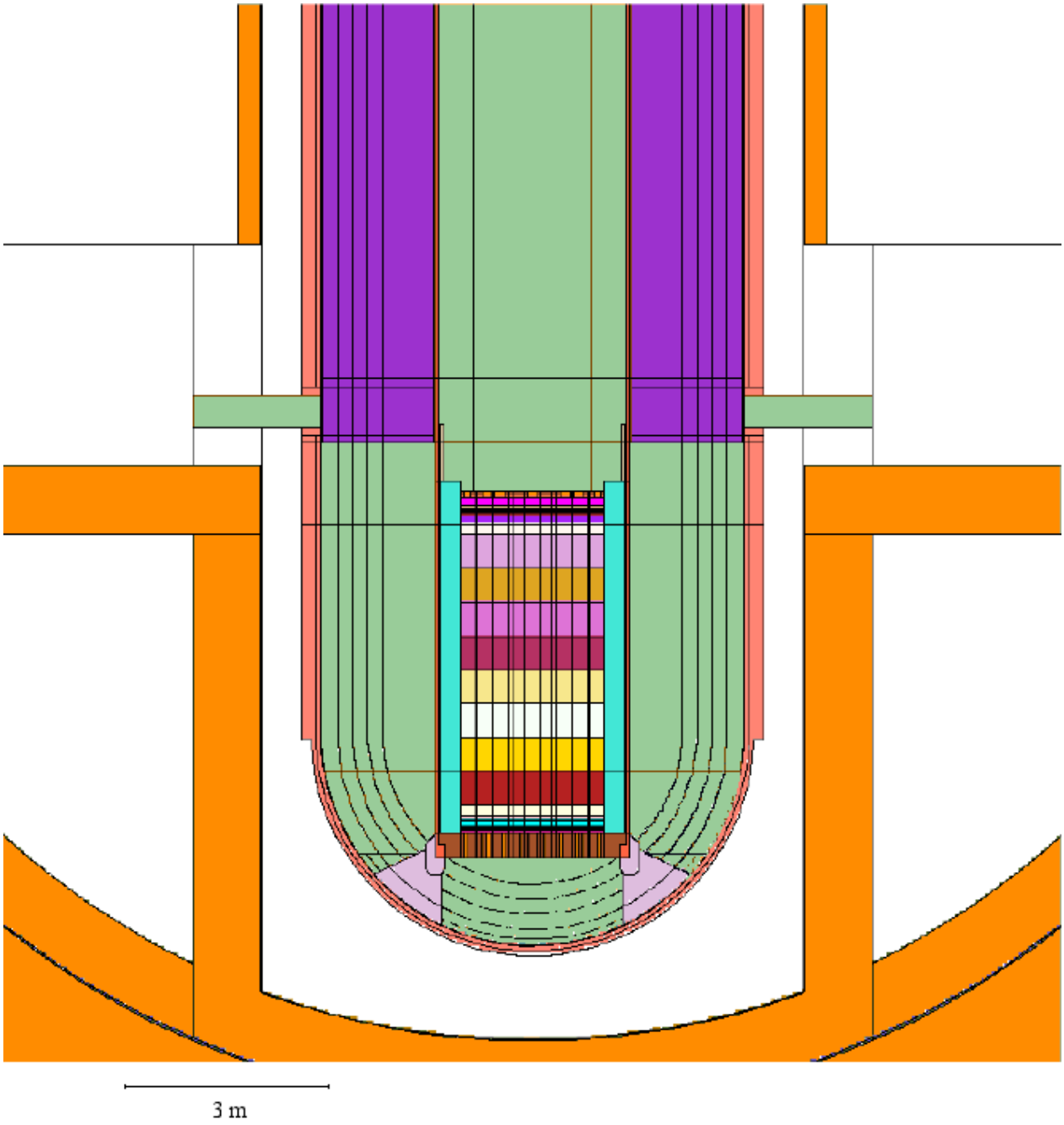

Figure 49. Including steam generators (first model) and with 25 m diameter vessel: vertical section through the inlet nozzles.

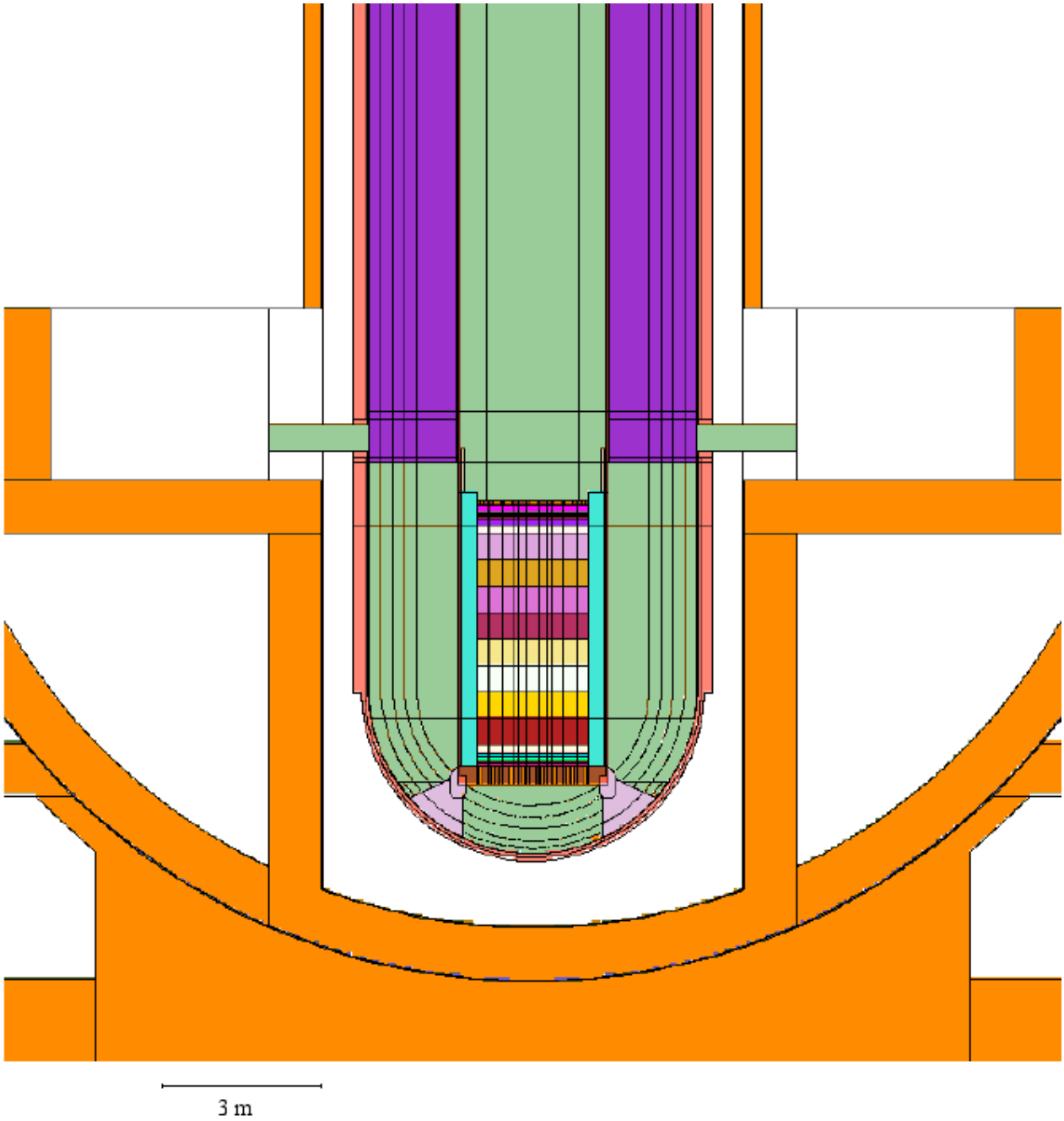

Figure 50. Including steam generators (first model) and with 25 m diameter vessel: vertical section through the inlet nozzles out to the containment vessel.

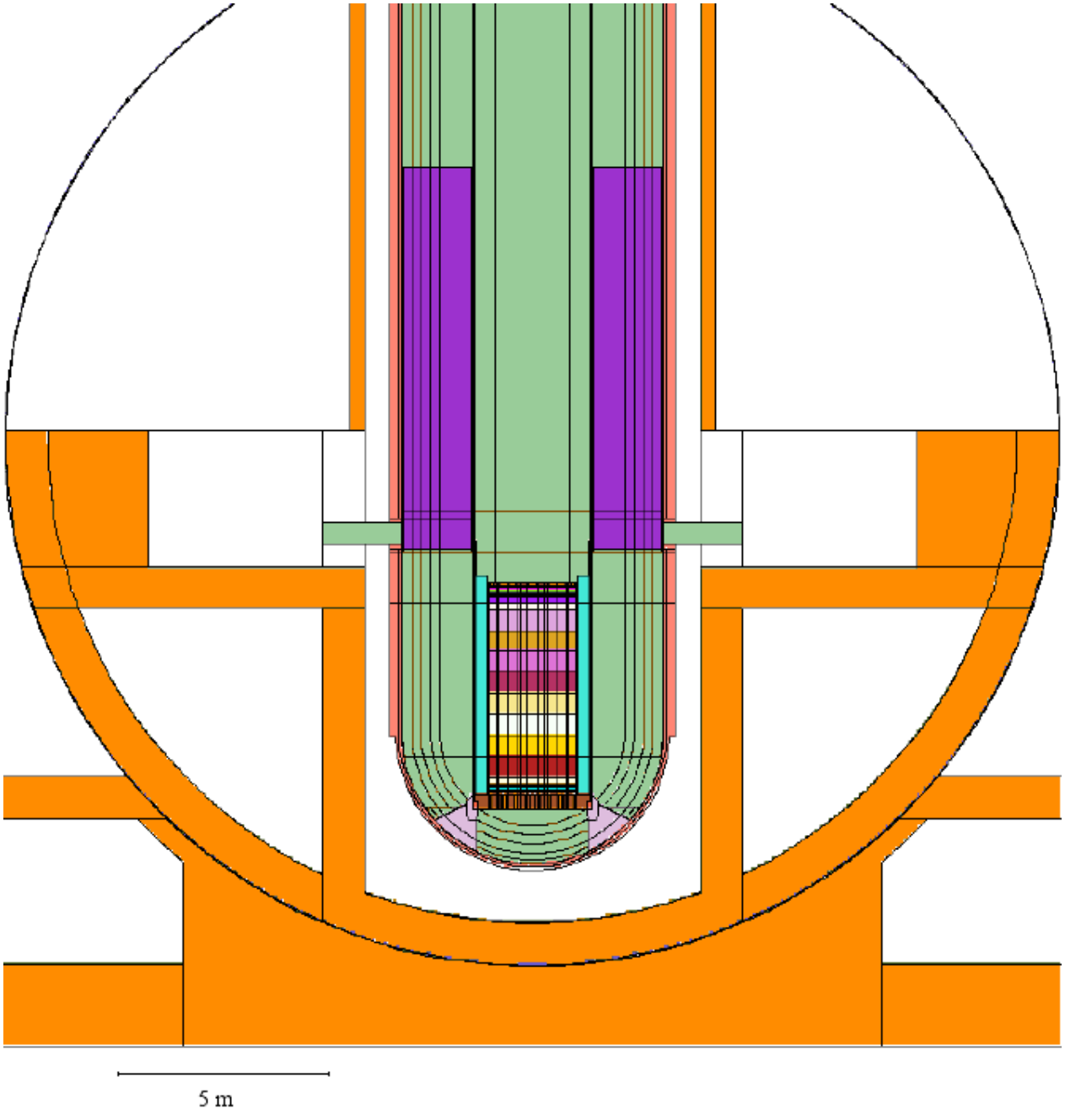

Figure 51. With 25 m diameter vessel: horizontal section through the core centre out to the containment vessel.

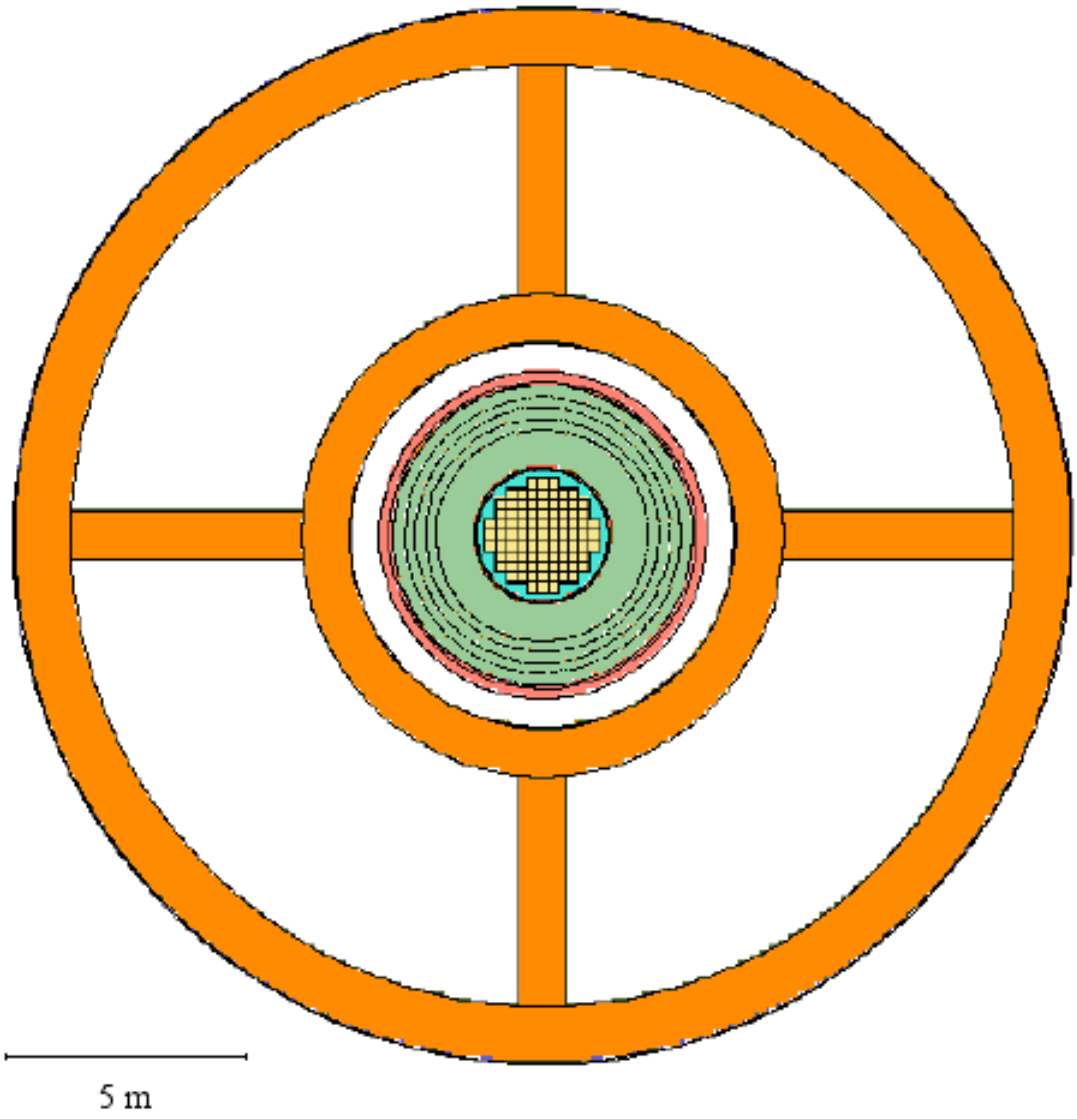

Figure 52. Including steam generators (first model) and with 25 m diameter vessel: horizontal section through the inlet nozzles out to the containment vessel.

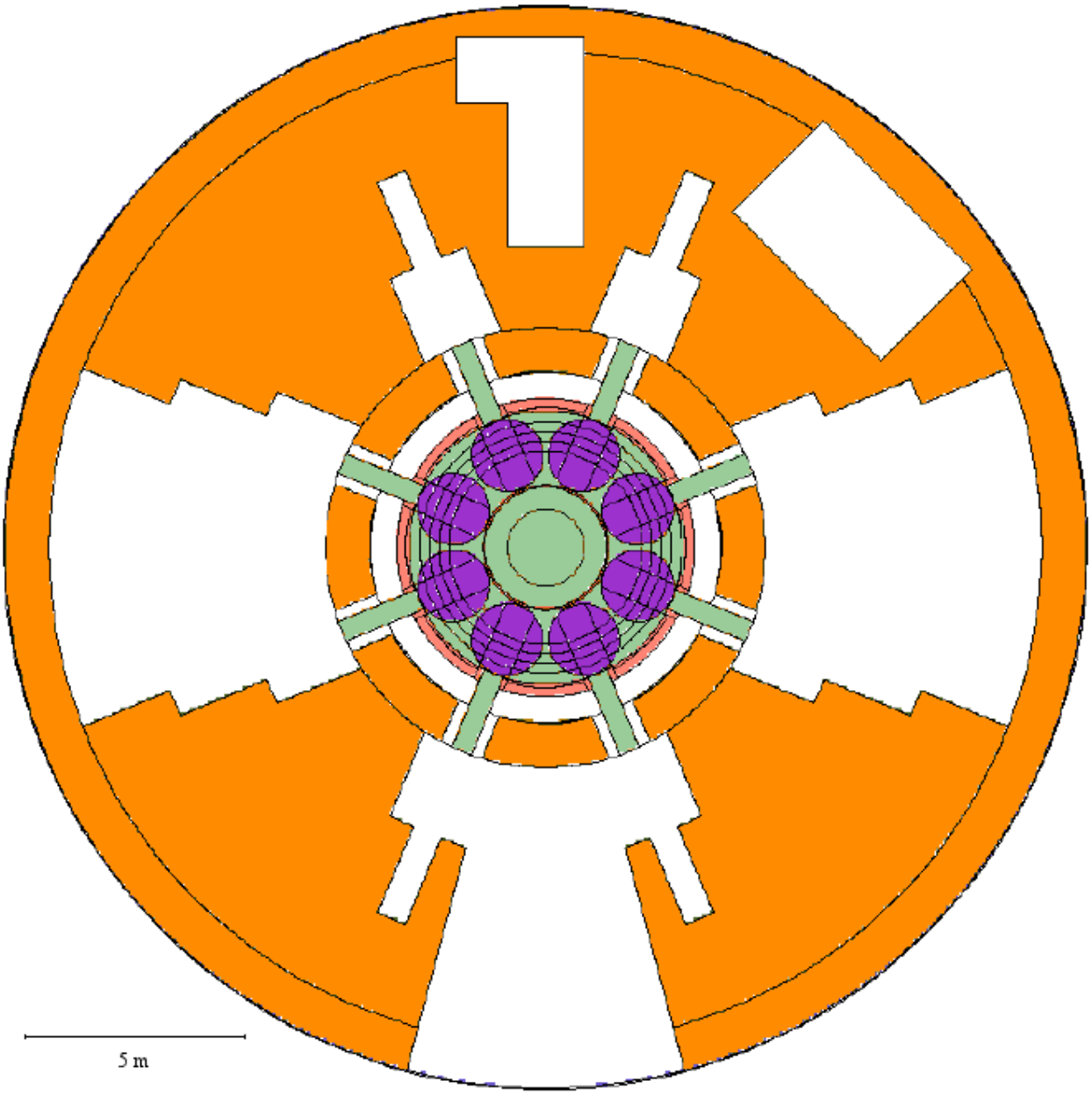

Figure 53. Including steam generators (first model) and with 25 m diameter vessel: horizontal section approximately 2.5 m above the main deck out to the containment vessel.

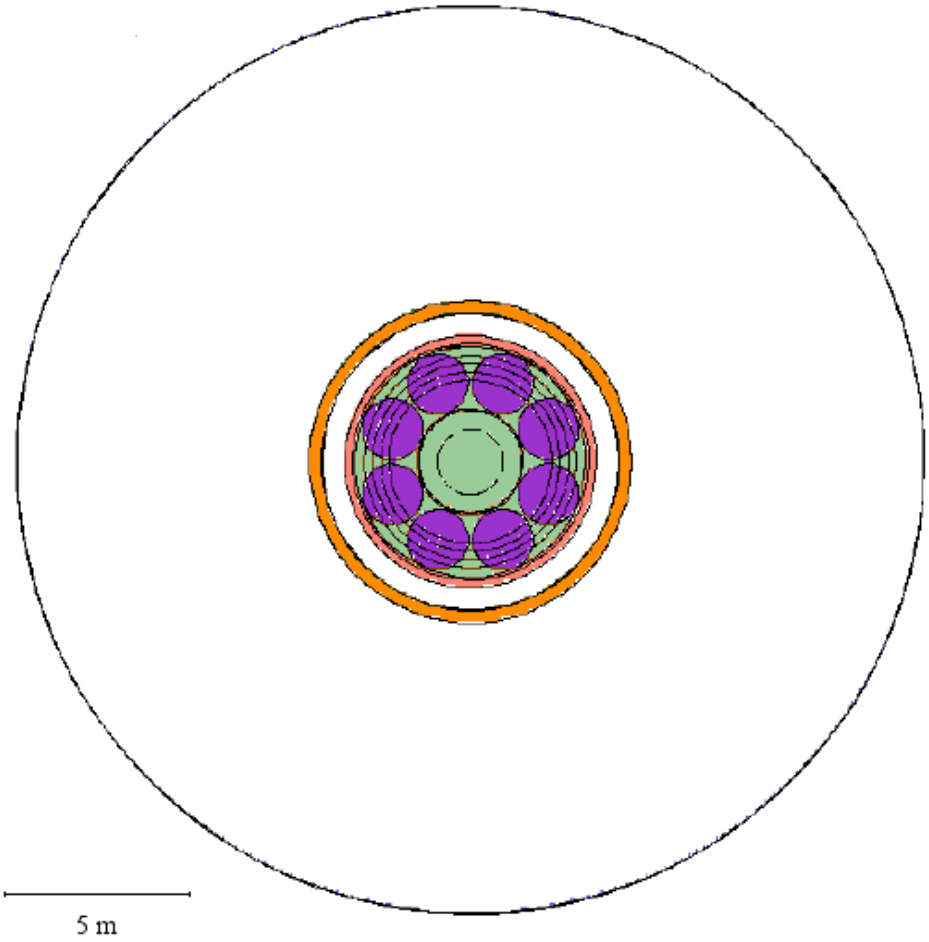

Figure 54. Including steam generators (second model) and with 25 m diameter vessel: vertical section through the inlet nozzles (with nozzle tube walls and flanges).

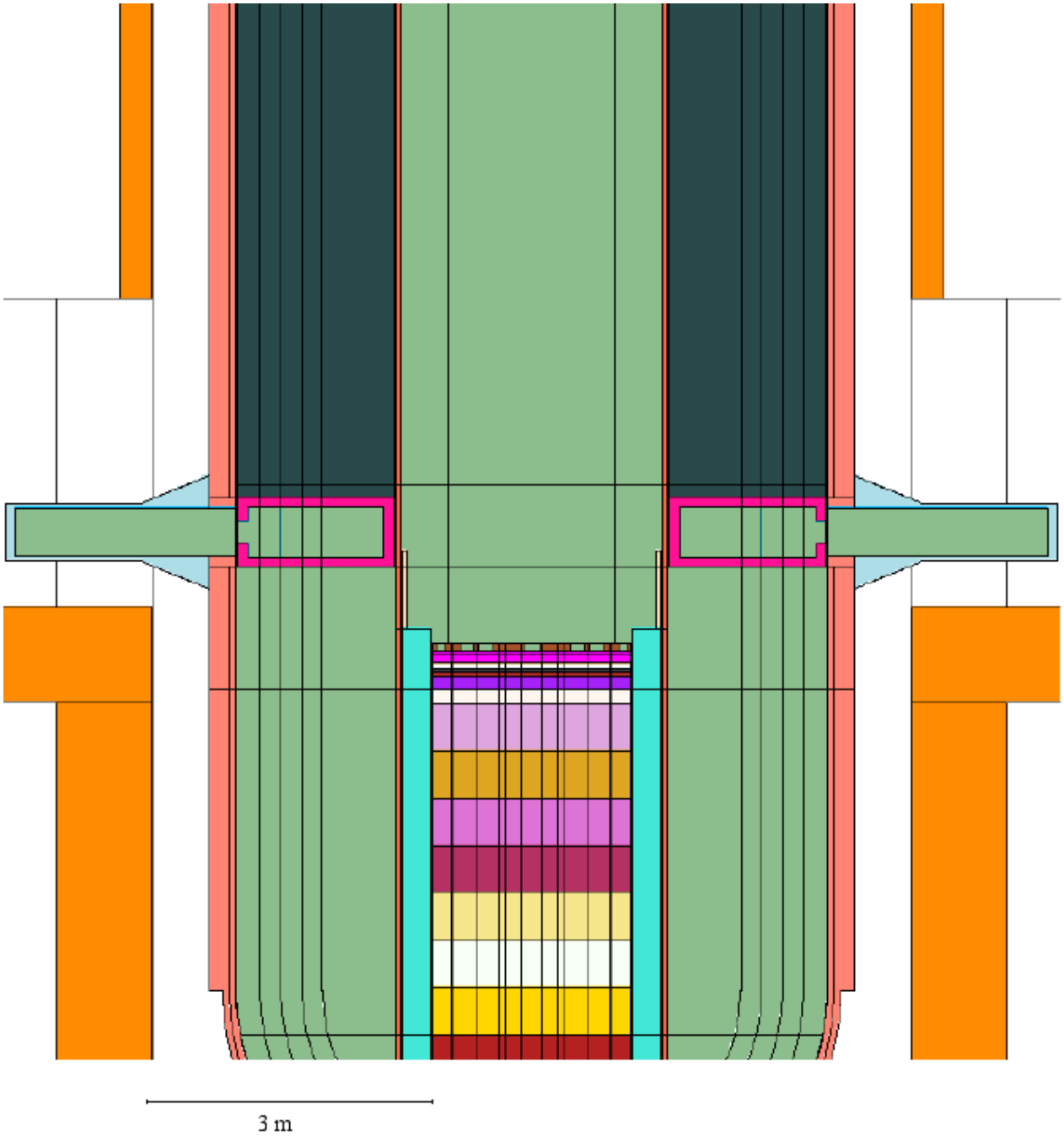

Figure 55. Including steam generators (second model) and with 25 m diameter vessel: vertical section through the inlet nozzles (with nozzle tube walls and flanges).

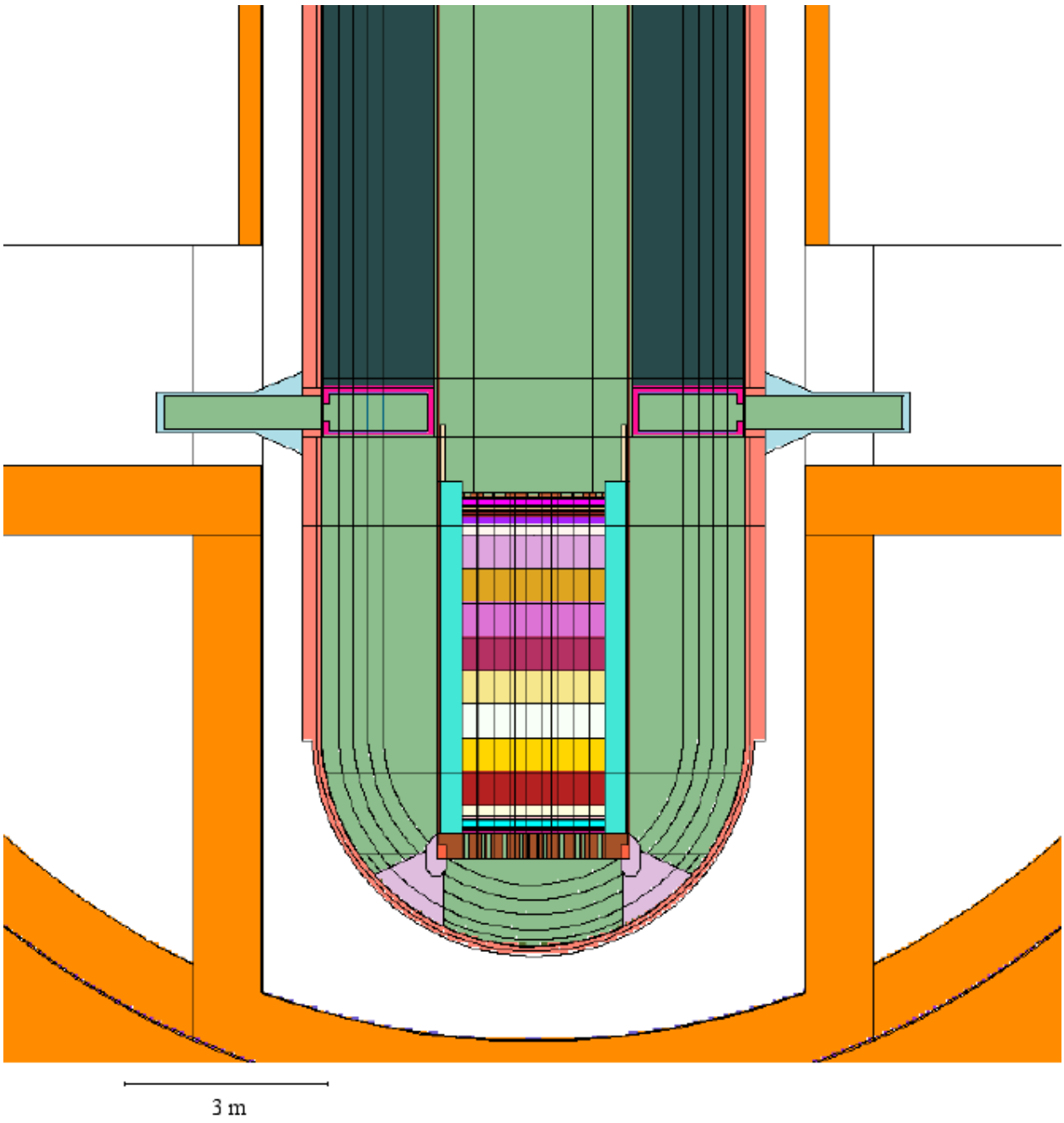

Figure 56. Including steam generators (second model) and with 25 m diameter vessel: vertical section through the inlet nozzles (with nozzle tube walls and flanges).

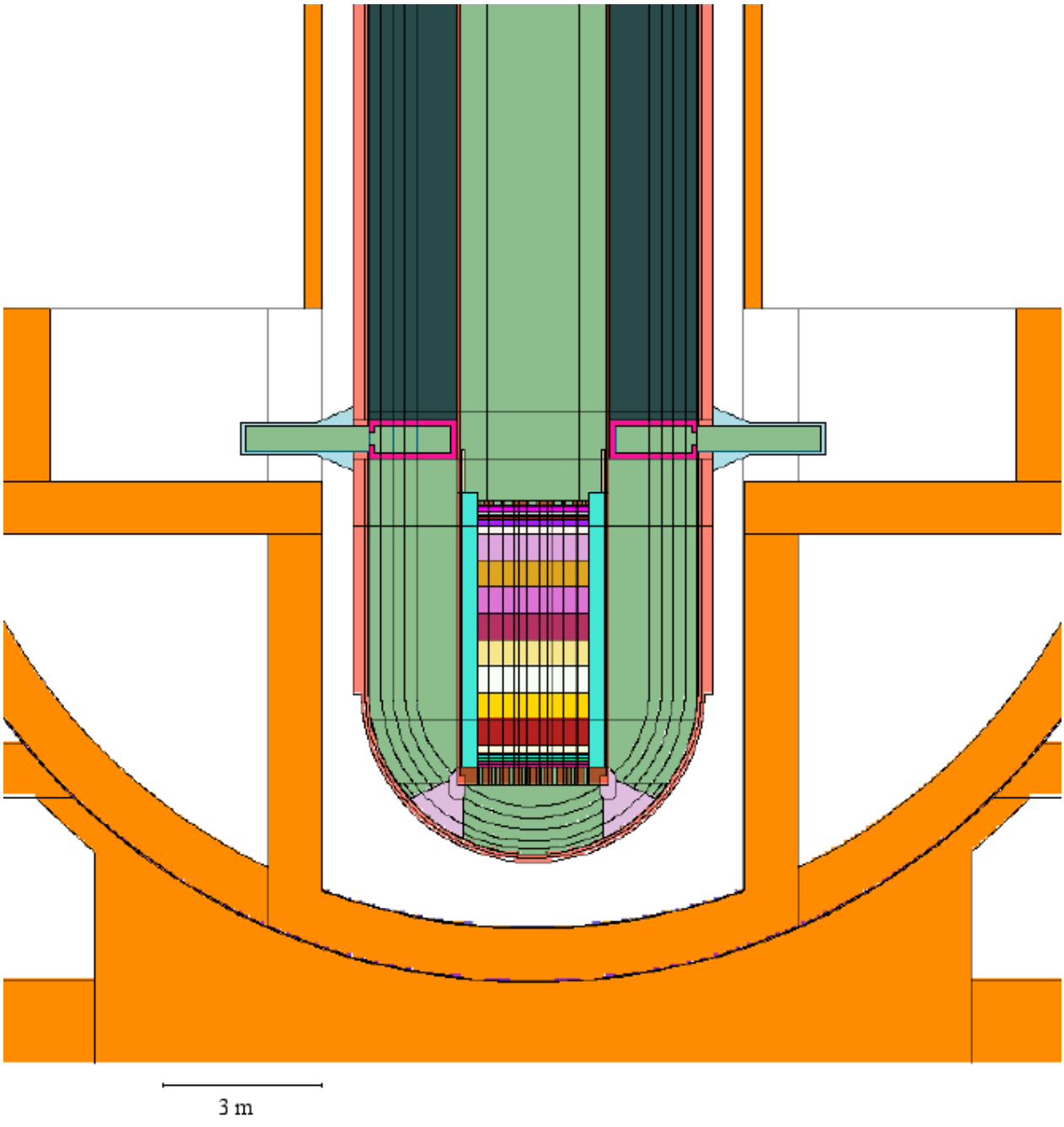

Figure 57. Including steam generators (second model) and with 25 m diameter vessel: vertical section through the inlet nozzles (with nozzle tube walls and flanges) up to containment vessel.

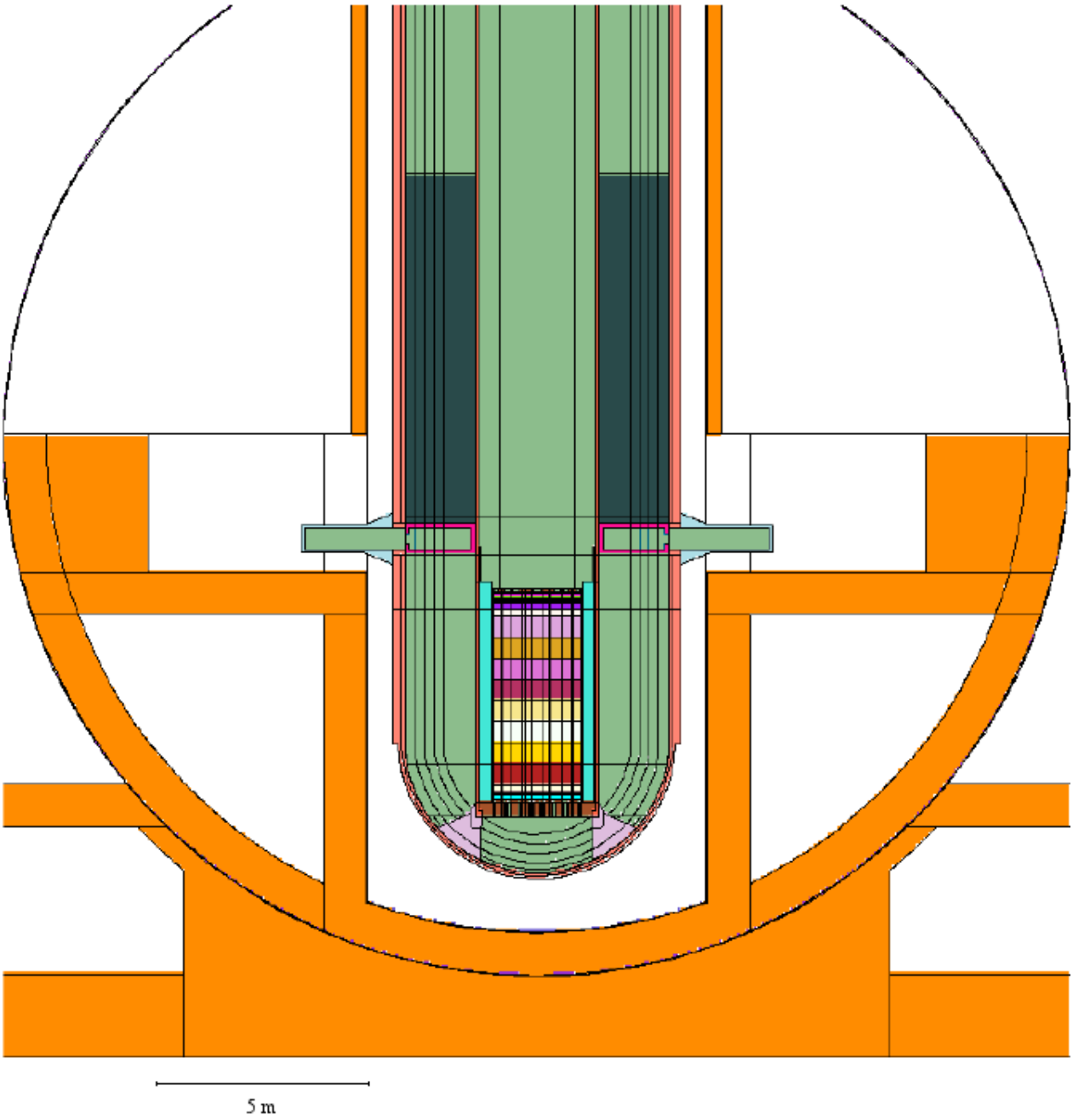

Figure 58. Including steam generators (second model) and with 25 m diameter vessel: horizontal section through the inlet nozzles (with nozzle tube walls and flanges).

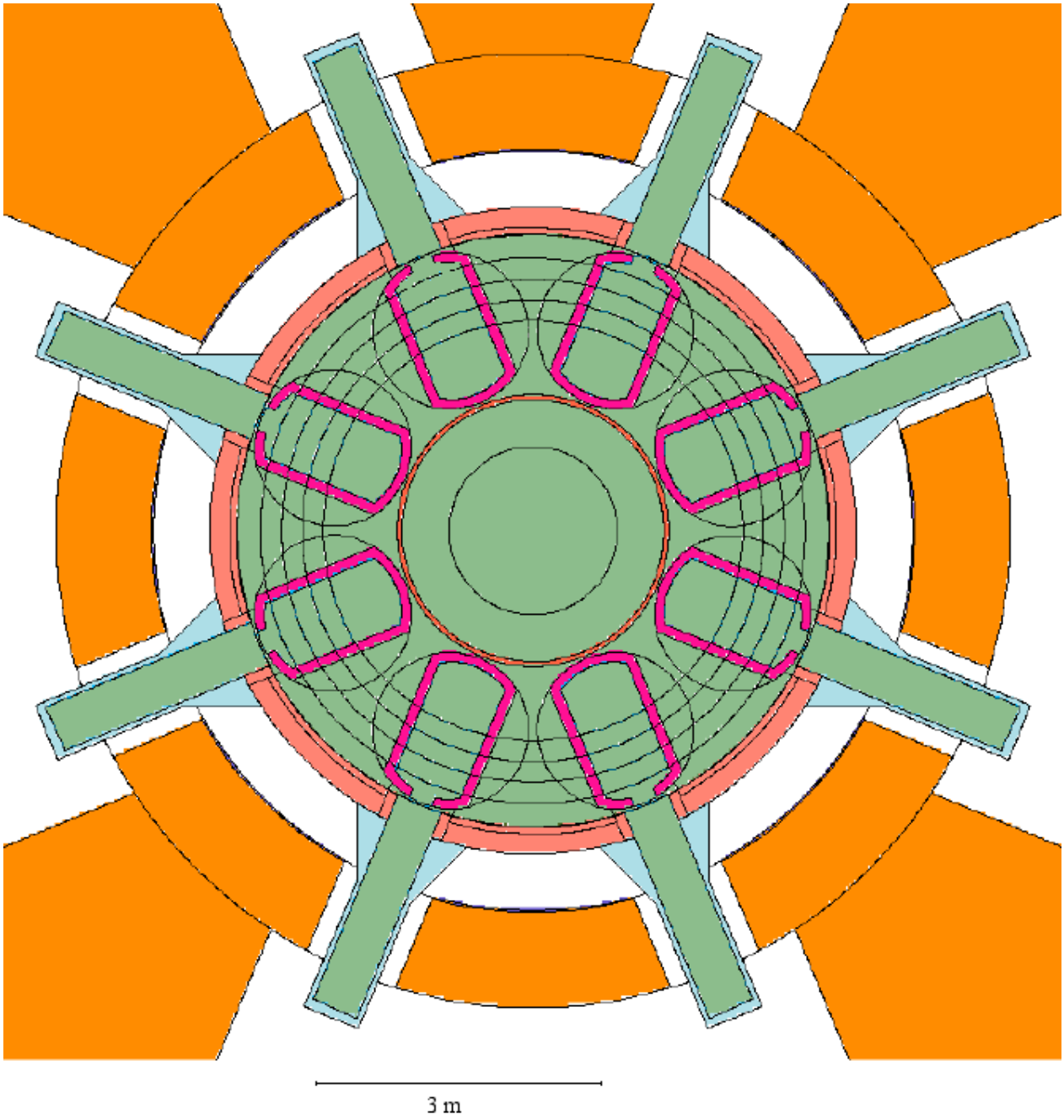

Figure 59. Including steam generators (second model) and with 25 m diameter vessel: horizontal section through the inlet nozzles (with nozzle tube walls and flanges) up to containment vessel.

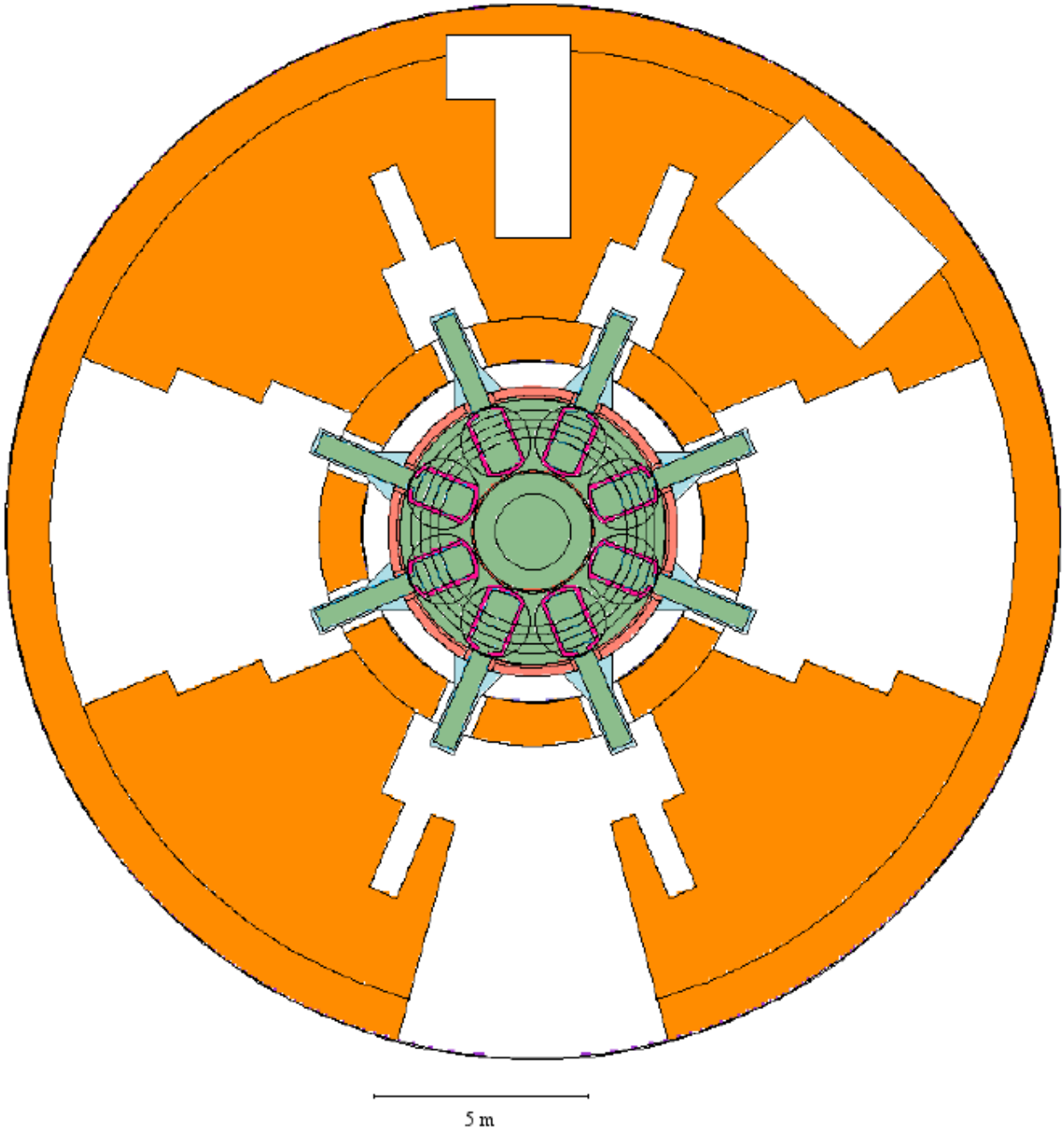

Figure 60. Including steam generators (second model) and with 25 m diameter vessel: vertical section through the inlet nozzles (with nozzle tube walls and flanges) up to wall outside biological shield.

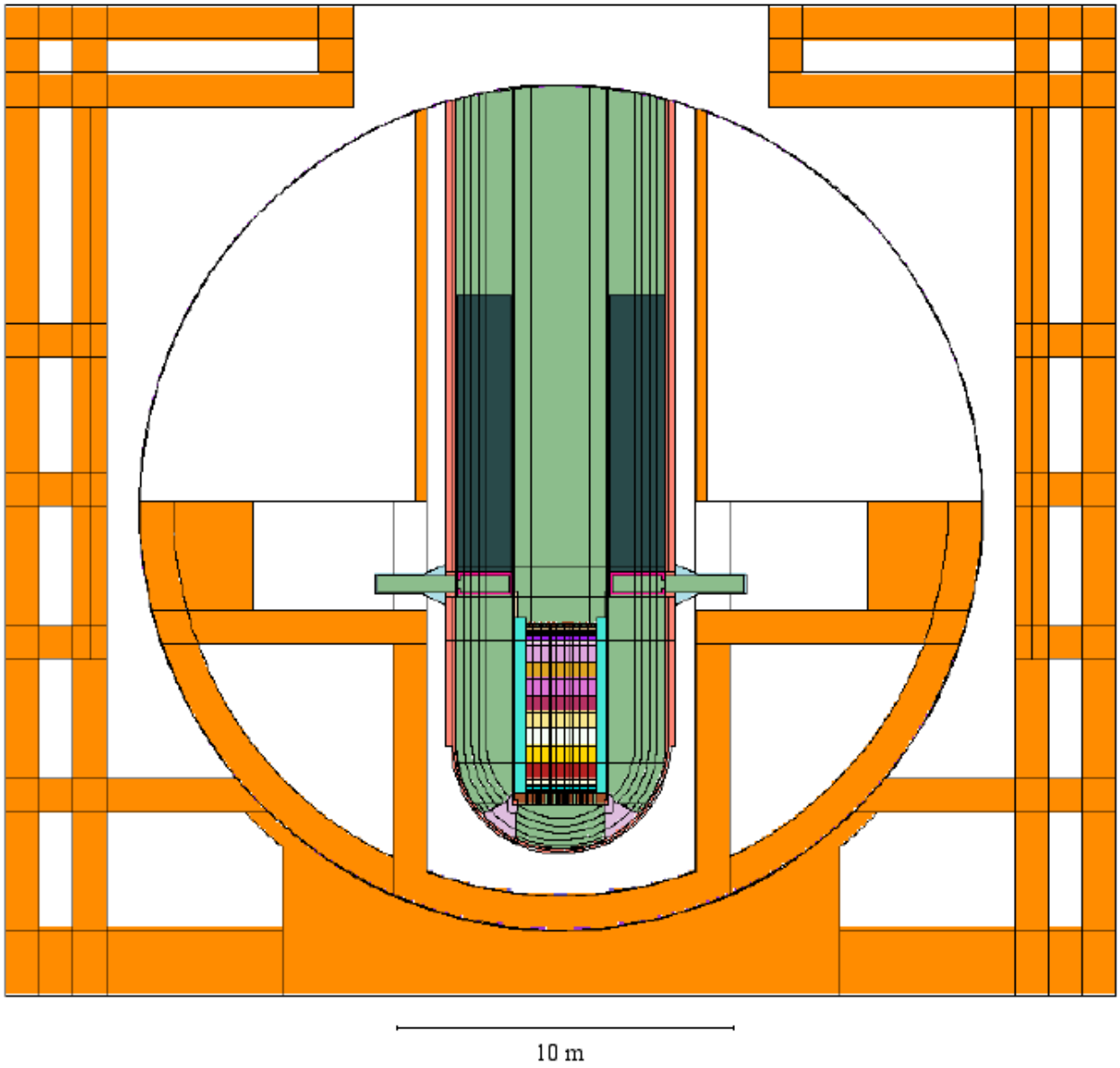

Figure 61. Including steam generators (second model) and with 25 m diameter vessel: horizontal section through the inlet nozzles (with nozzle tube walls and flanges) up to wall outside biological shield.

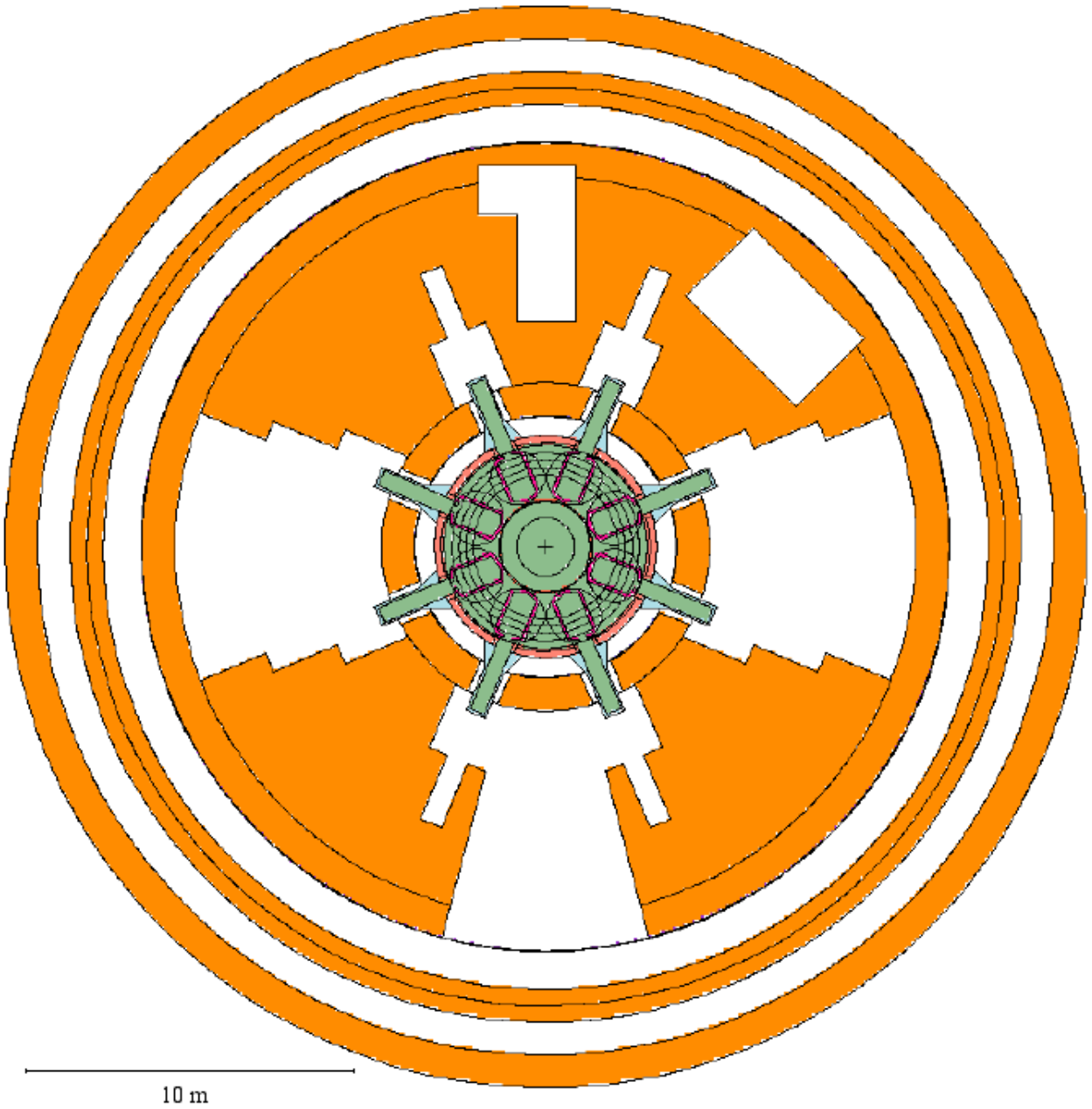

Figure 62. Including steam generators (second model) and with 25 m diameter vessel: horizontal section just above the main deck up to wall outside biological shield.

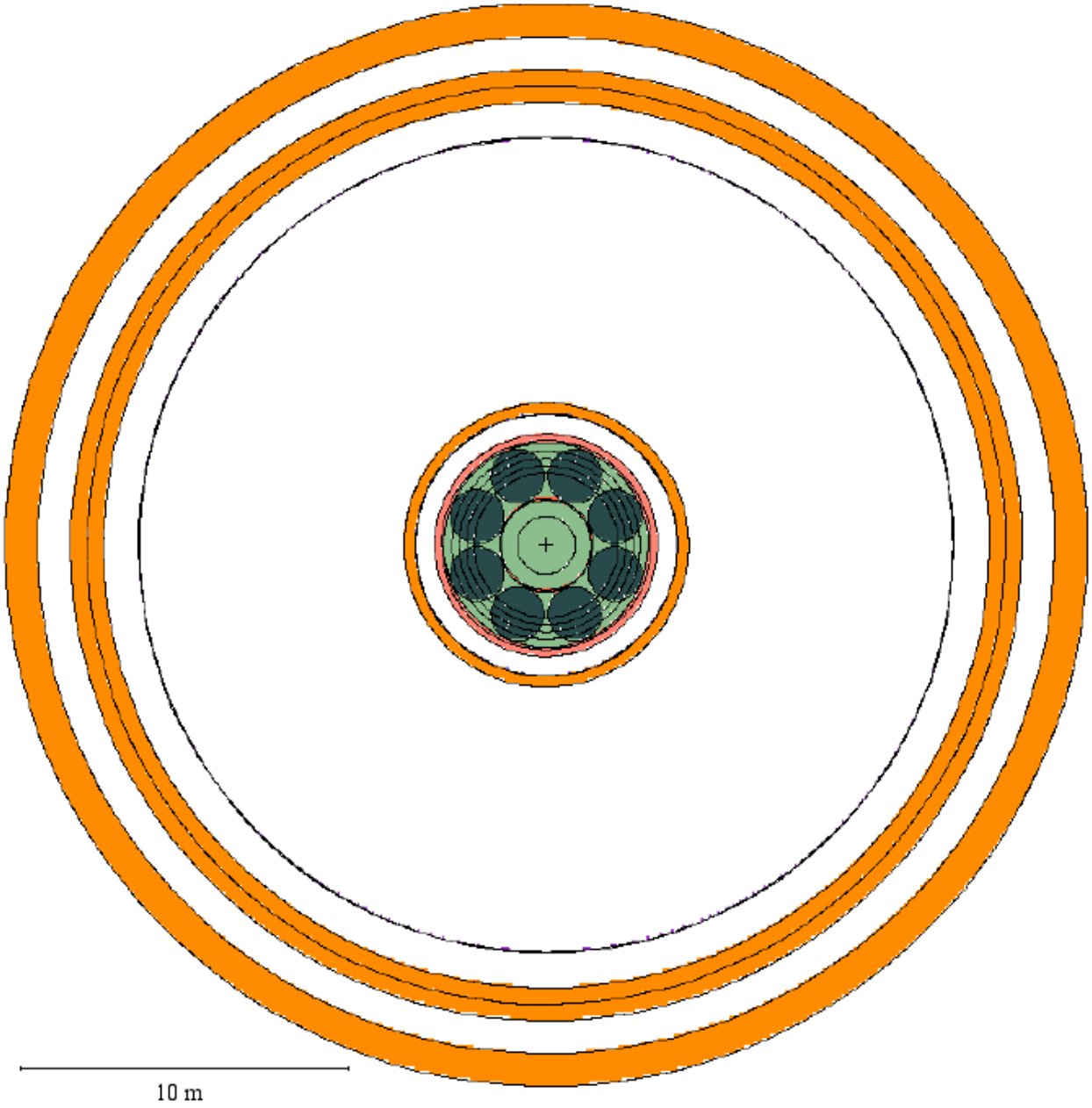

Figure 63. Including steam generators (first model) and with 25 m diameter vessel: vertical section through the inlet nozzles (no walls or flanges) up to wall outside biological shield with coarse grid tally mesh.

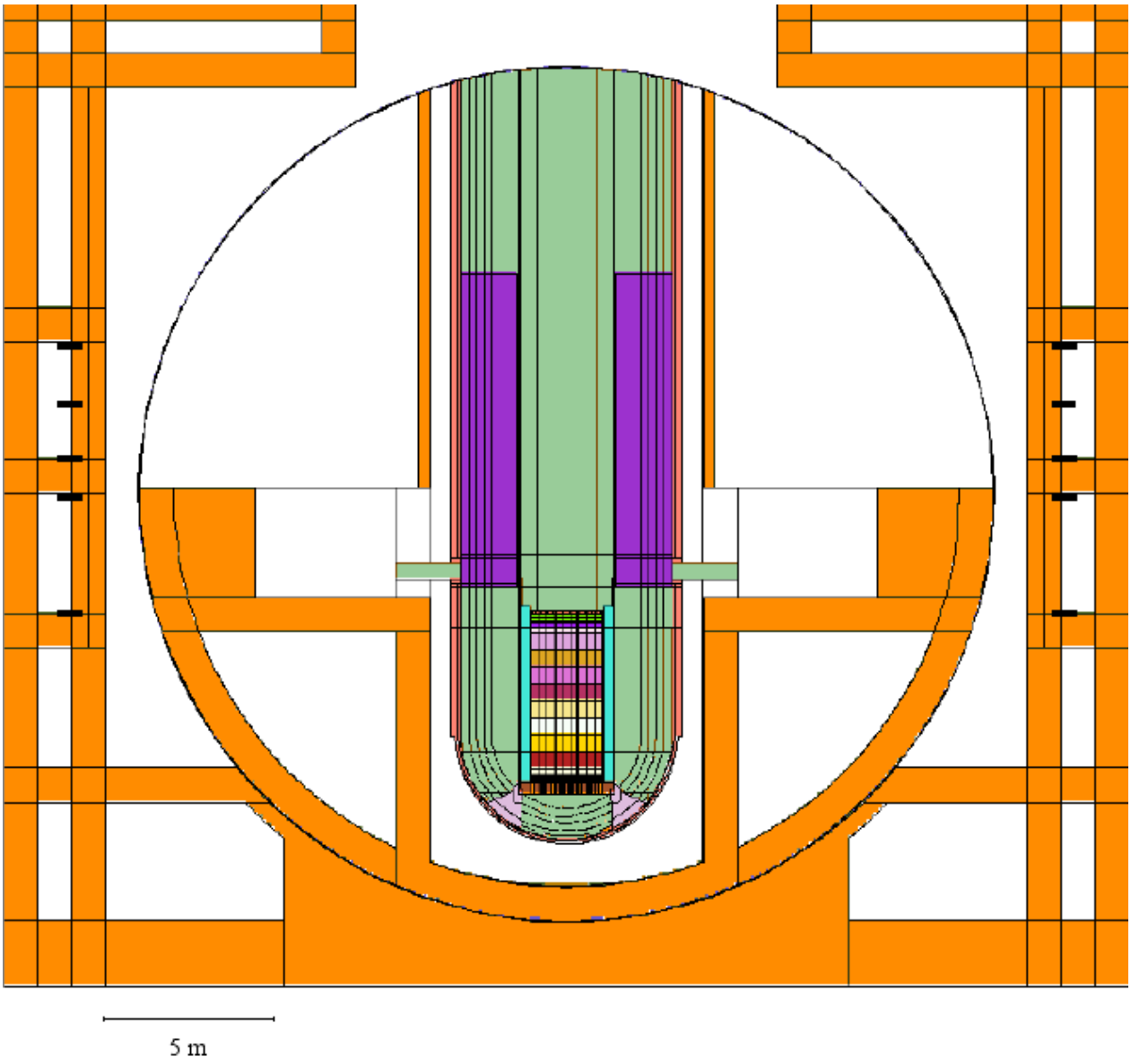

Figure 64. Including steam generators (first model) and with 25 m diameter vessel: horizontal section through the inlet nozzles (no walls or flanges) up to wall outside biological shield with coarse grid tally mesh.

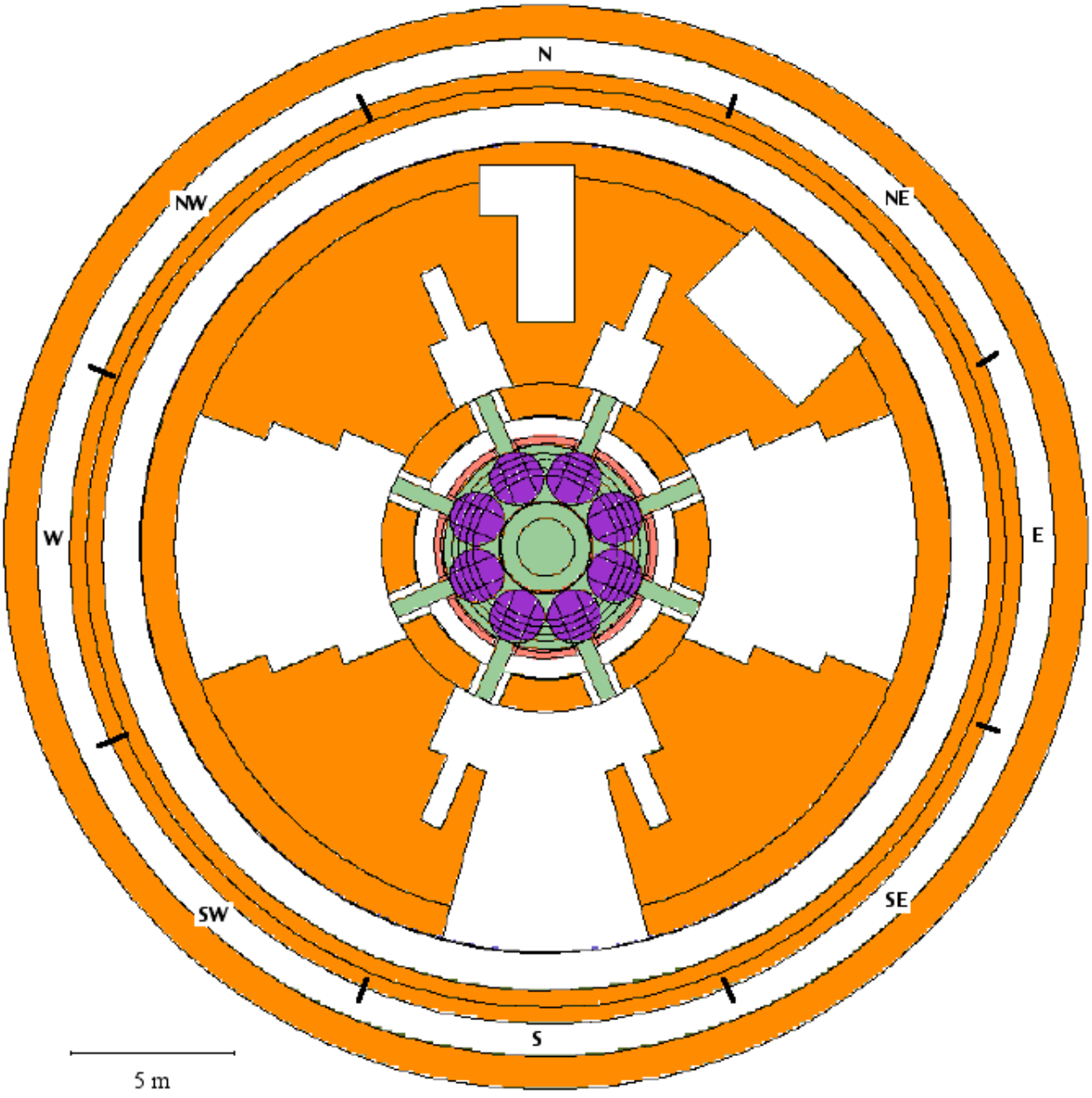

Figure 65. Including steam generators (first model) and with 25 m diameter vessel: horizontal section just above the main deck up to wall outside biological shield with coarse grid tally mesh.

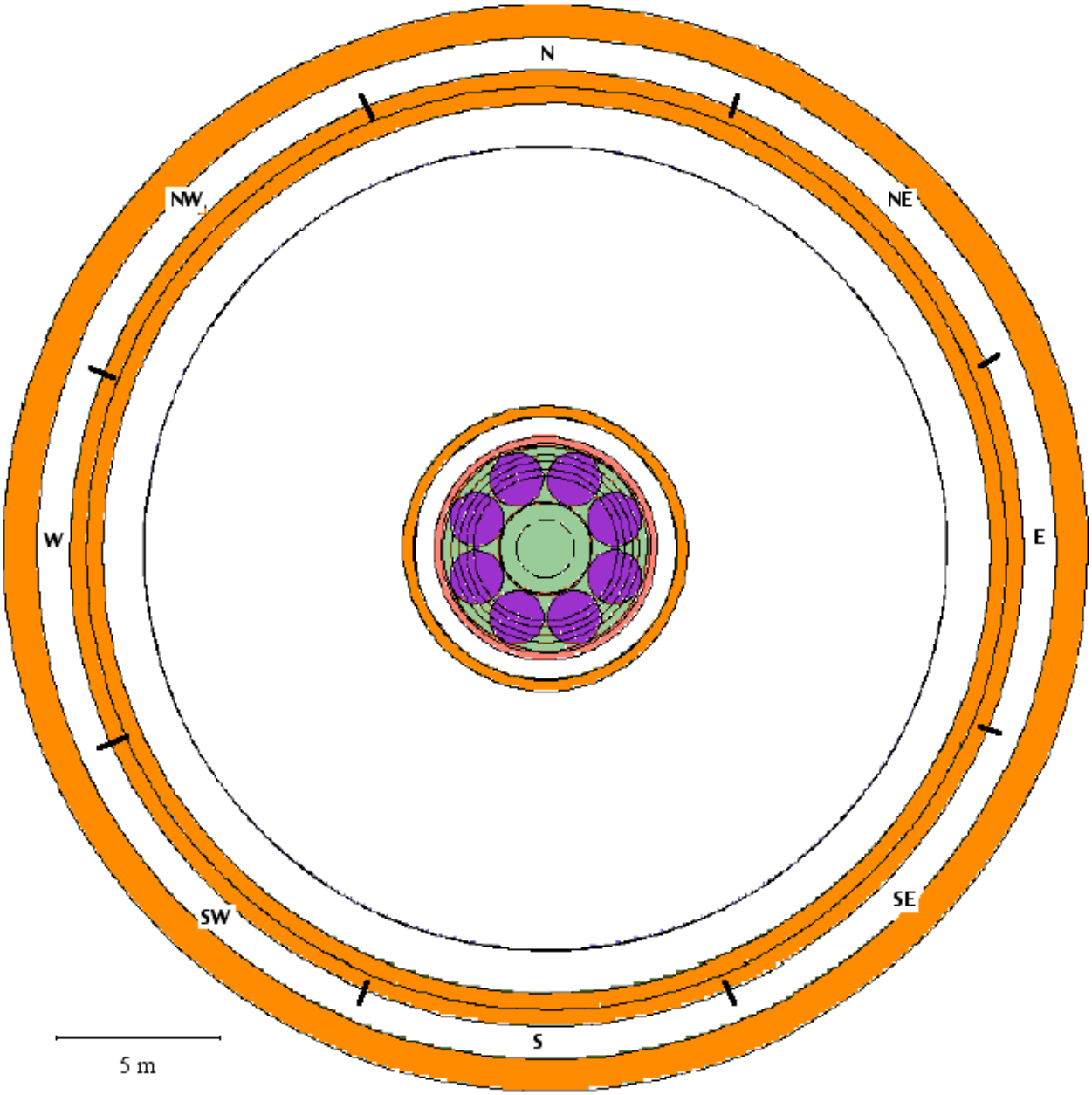

Figure 66. Model of explicit rebar lattice in concrete matrix in semi-infinite geometry.

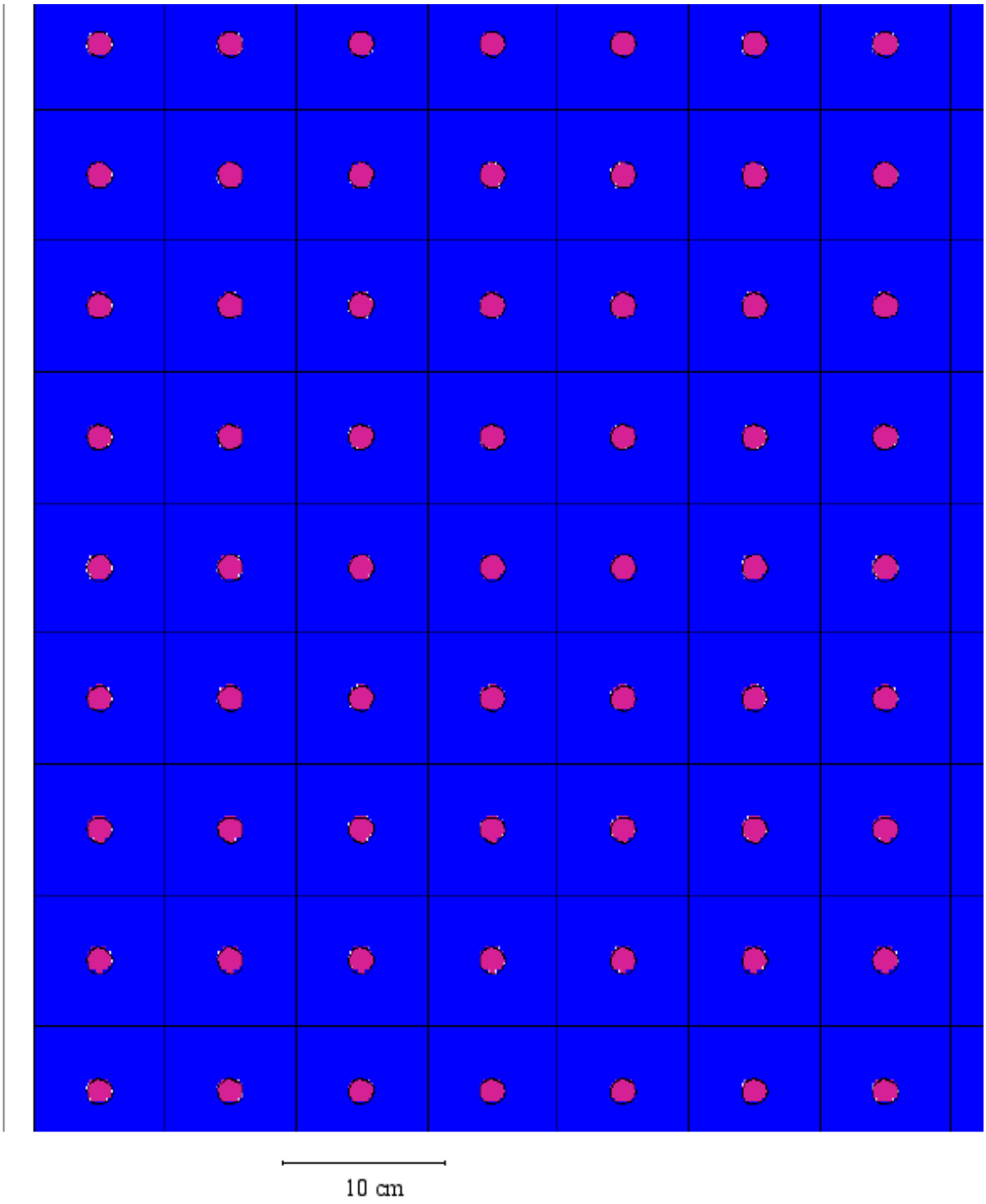

Figure 67. Model of rebar strips in concrete matrix in semi-infinite geometry.

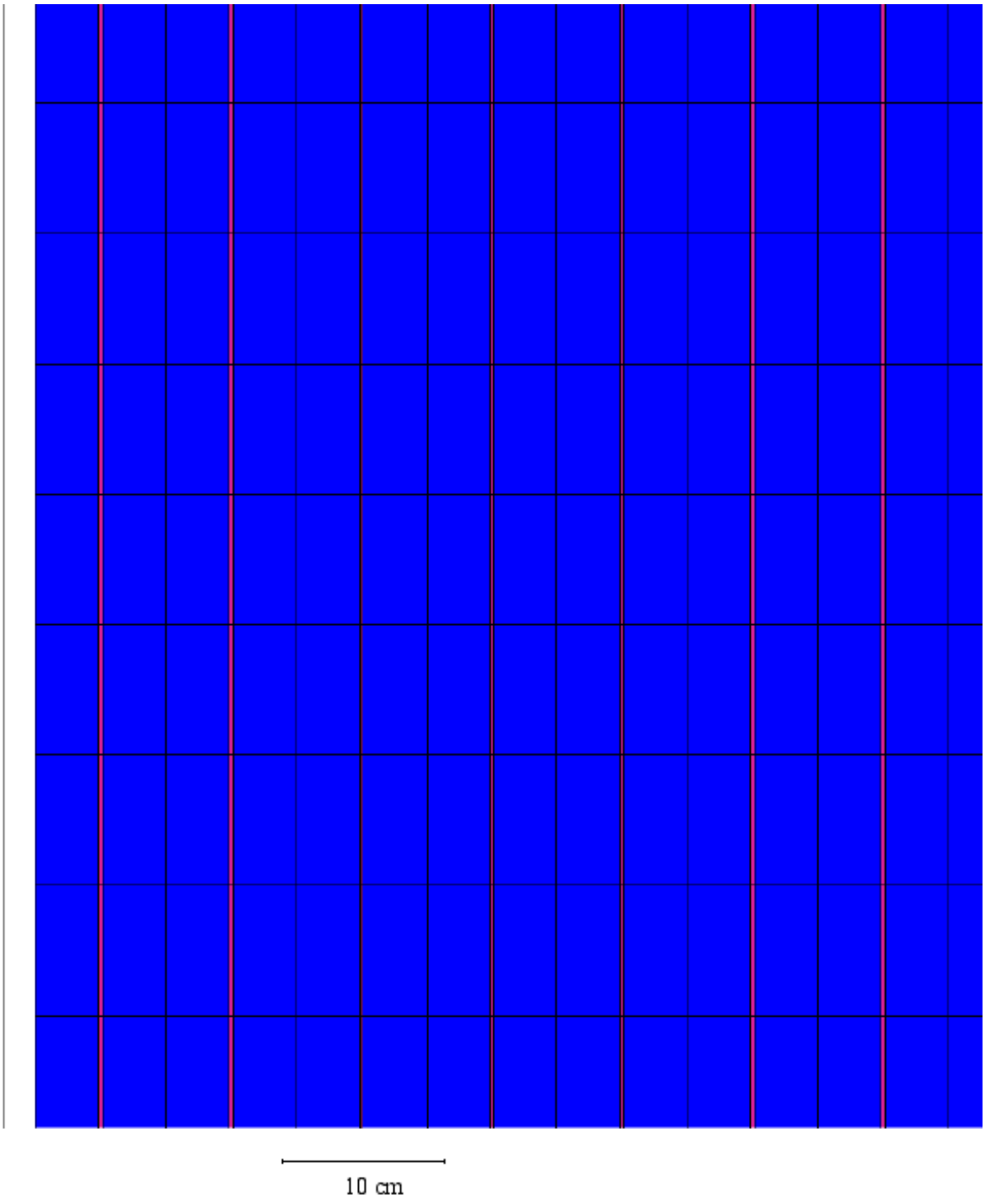

Figure 68. The $^{59}Co(n,\gamma)^{60}Co$ cross-section (barns).

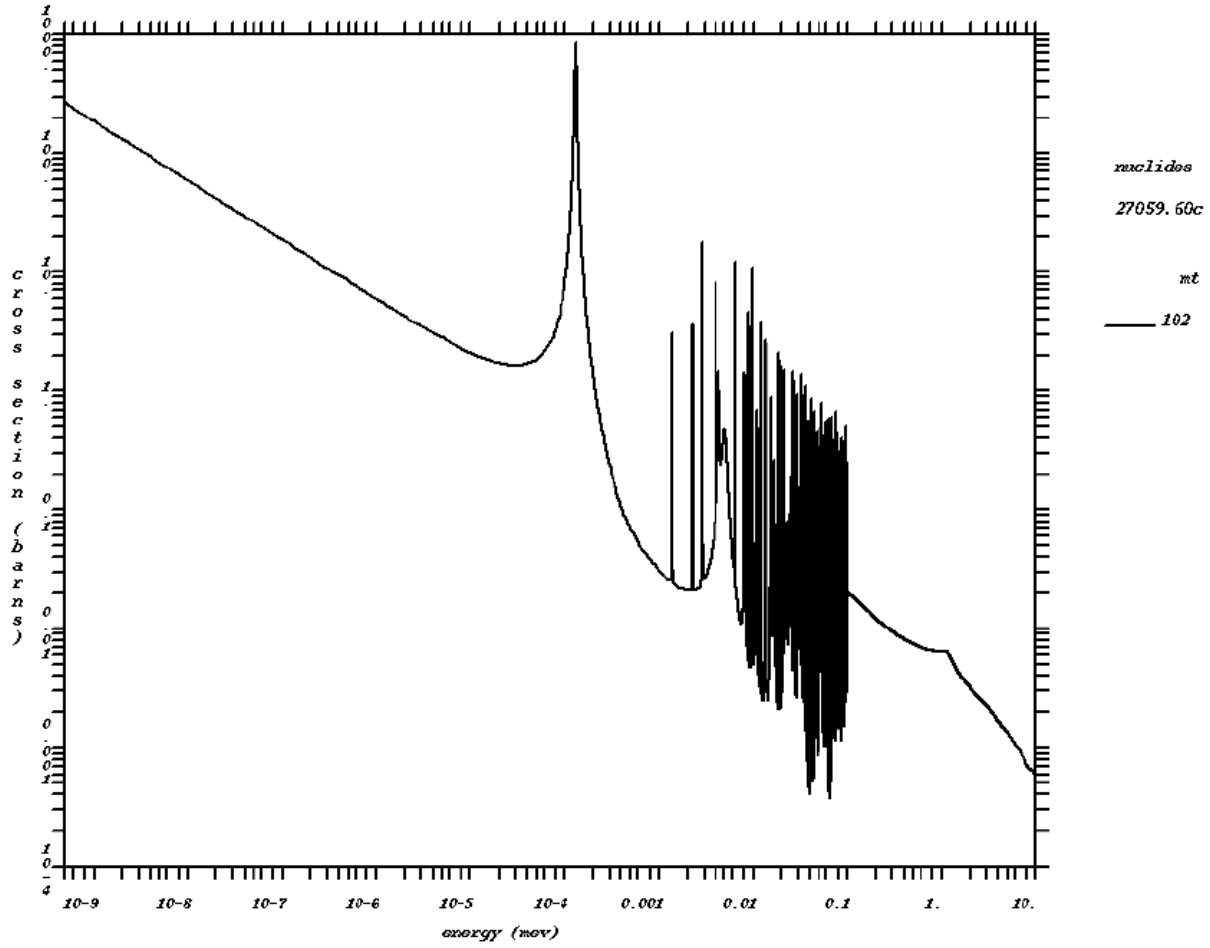

Figure 69. The $^{151}Eu(n,\gamma)^{152}Eu$ cross-section (barns).

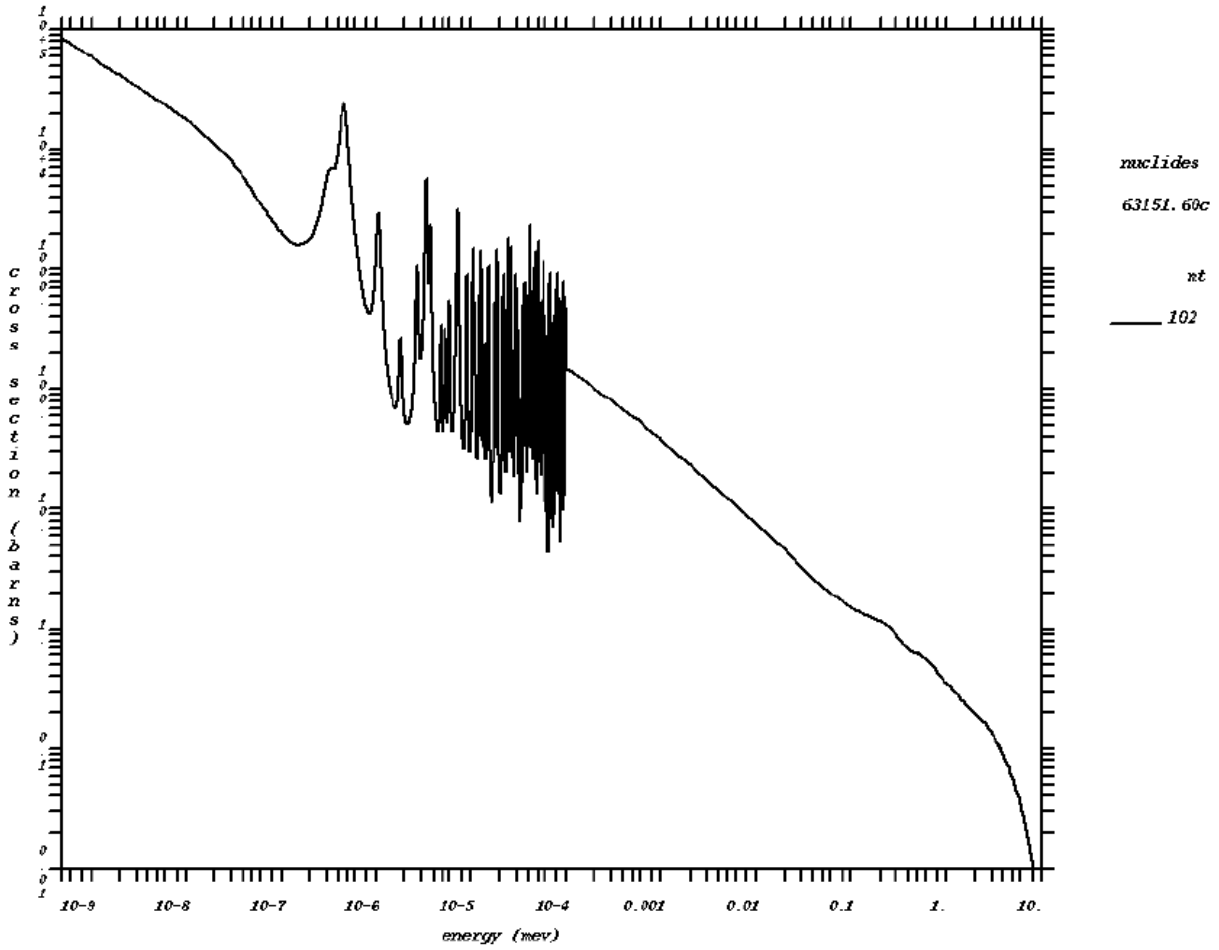

Figure 70. The total cross-section (barns) of the AISI-304L (PV liner, concrete liner).

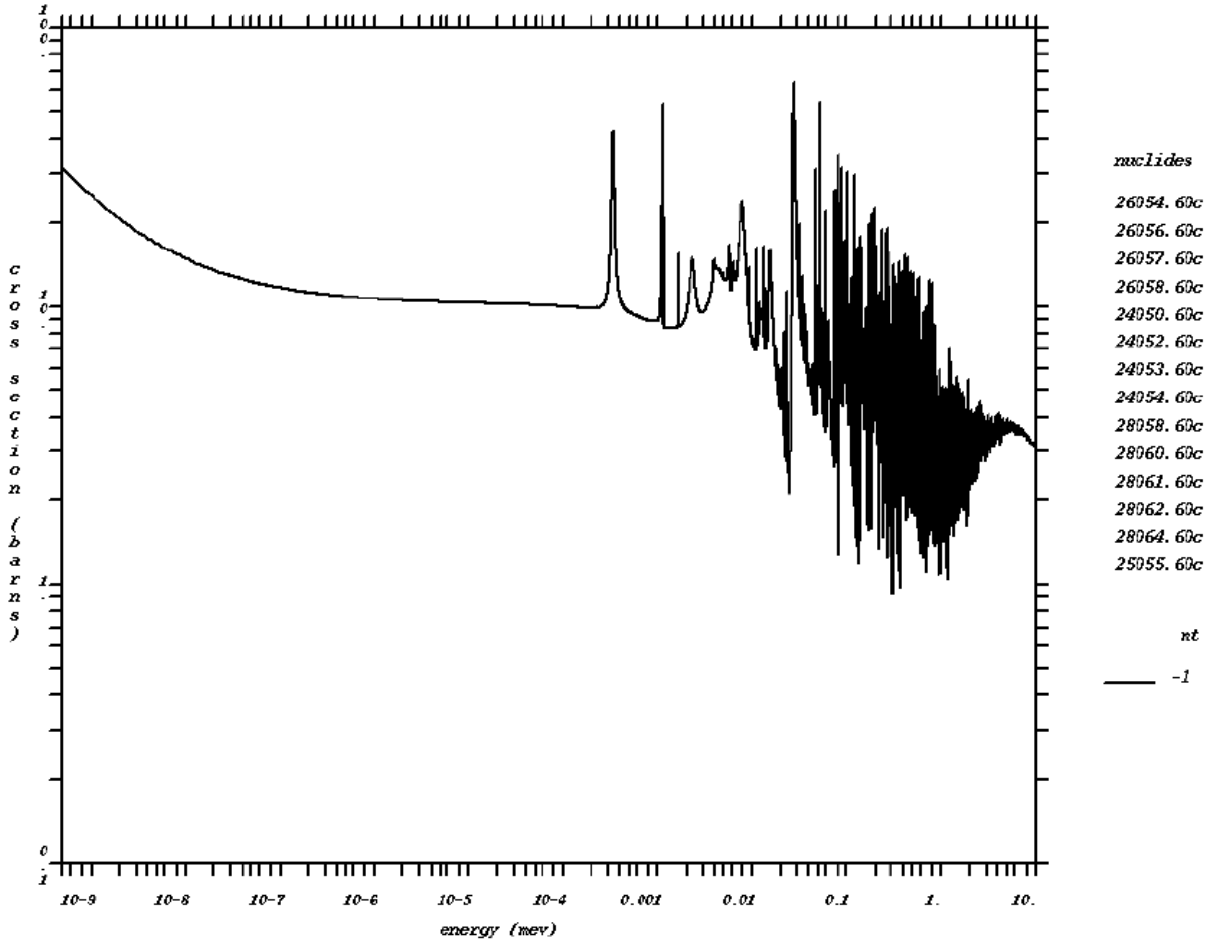

Figure 71. The total cross-section (barns) of the PV steel.

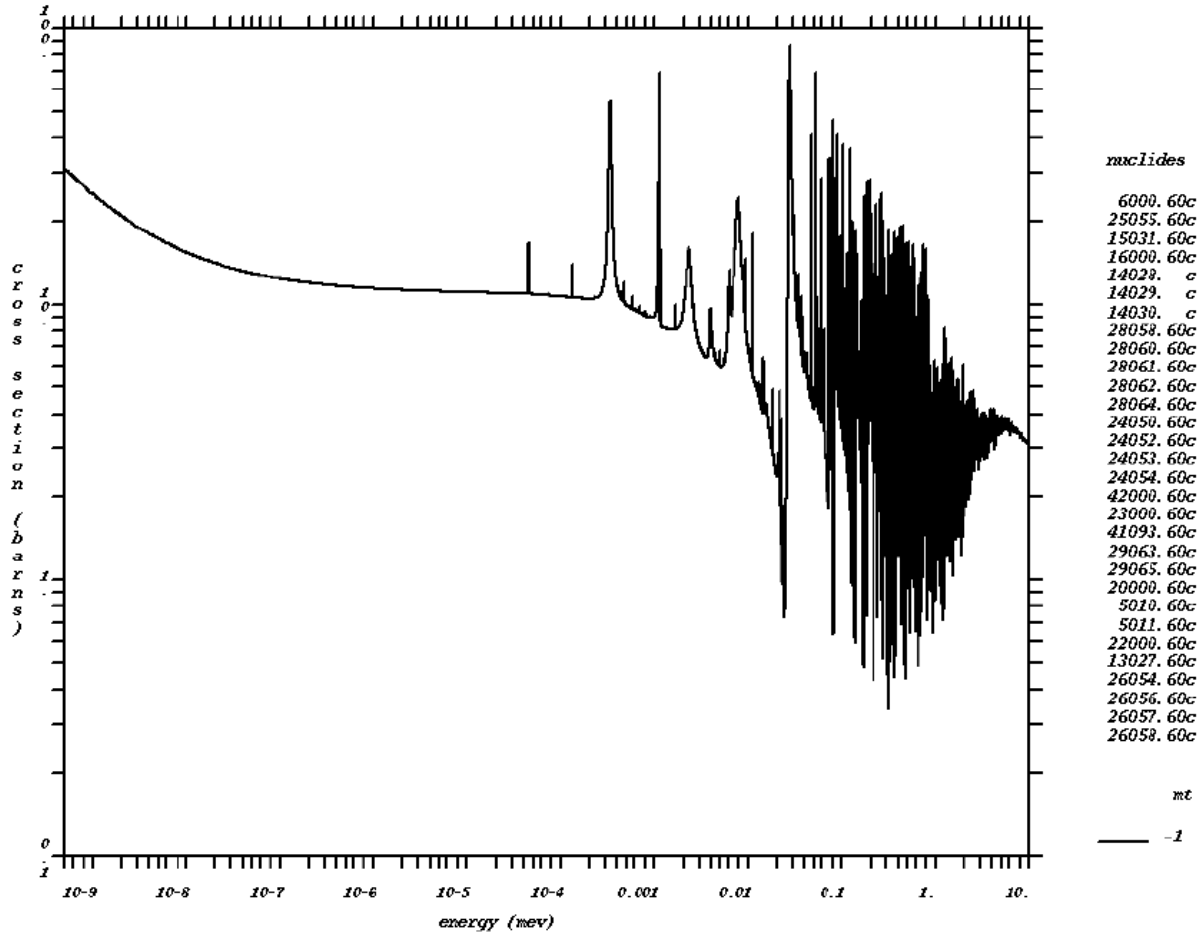

Figure 72. The total cross-section of the homogeneous mix of 97% by vol. Portland concrete, 3% by vol. rebar (§7.1.3) (barns).

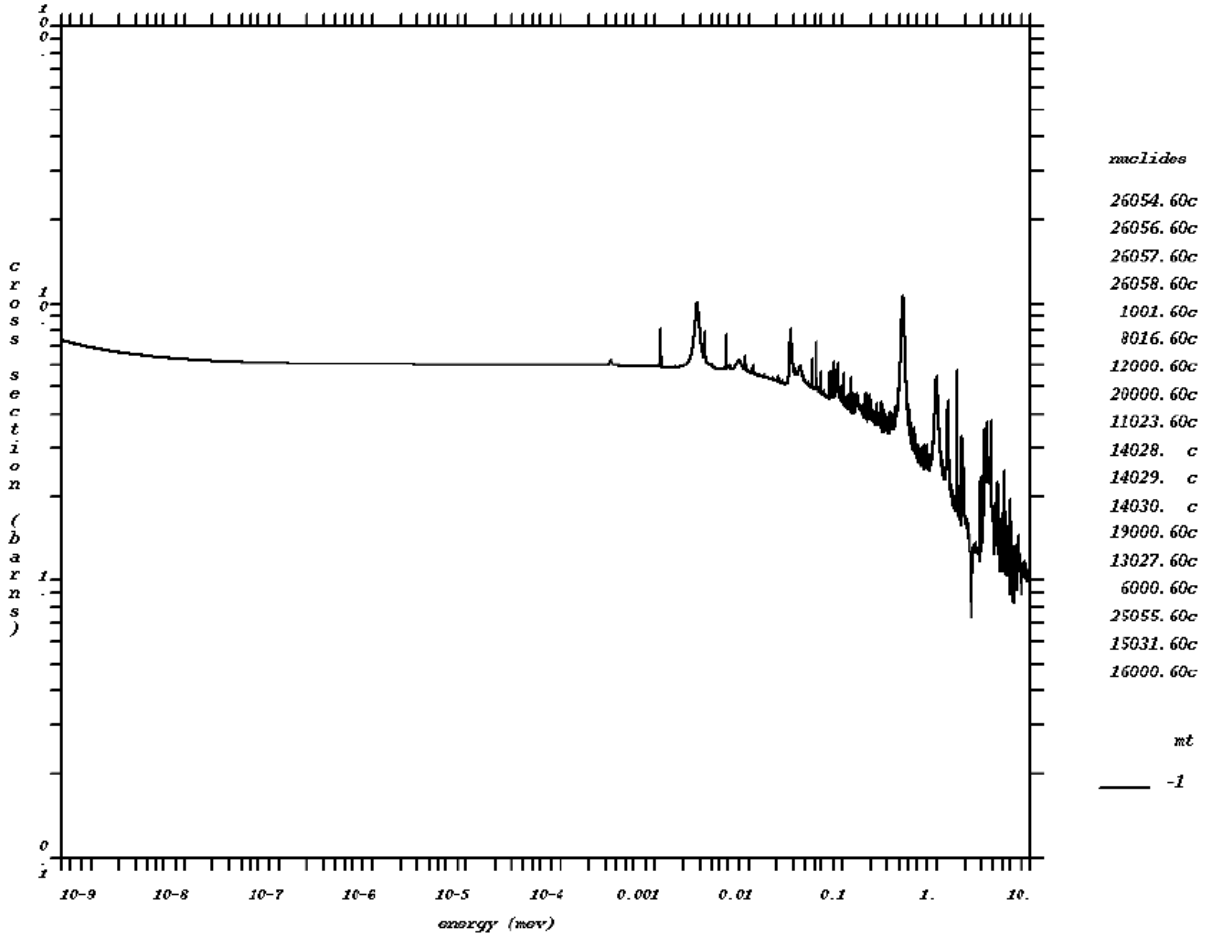

Figure 73. Segmentation of the pressure vessel and concrete and their liners for averaging the neutron fluxes for the search for the maximum EOL activities.

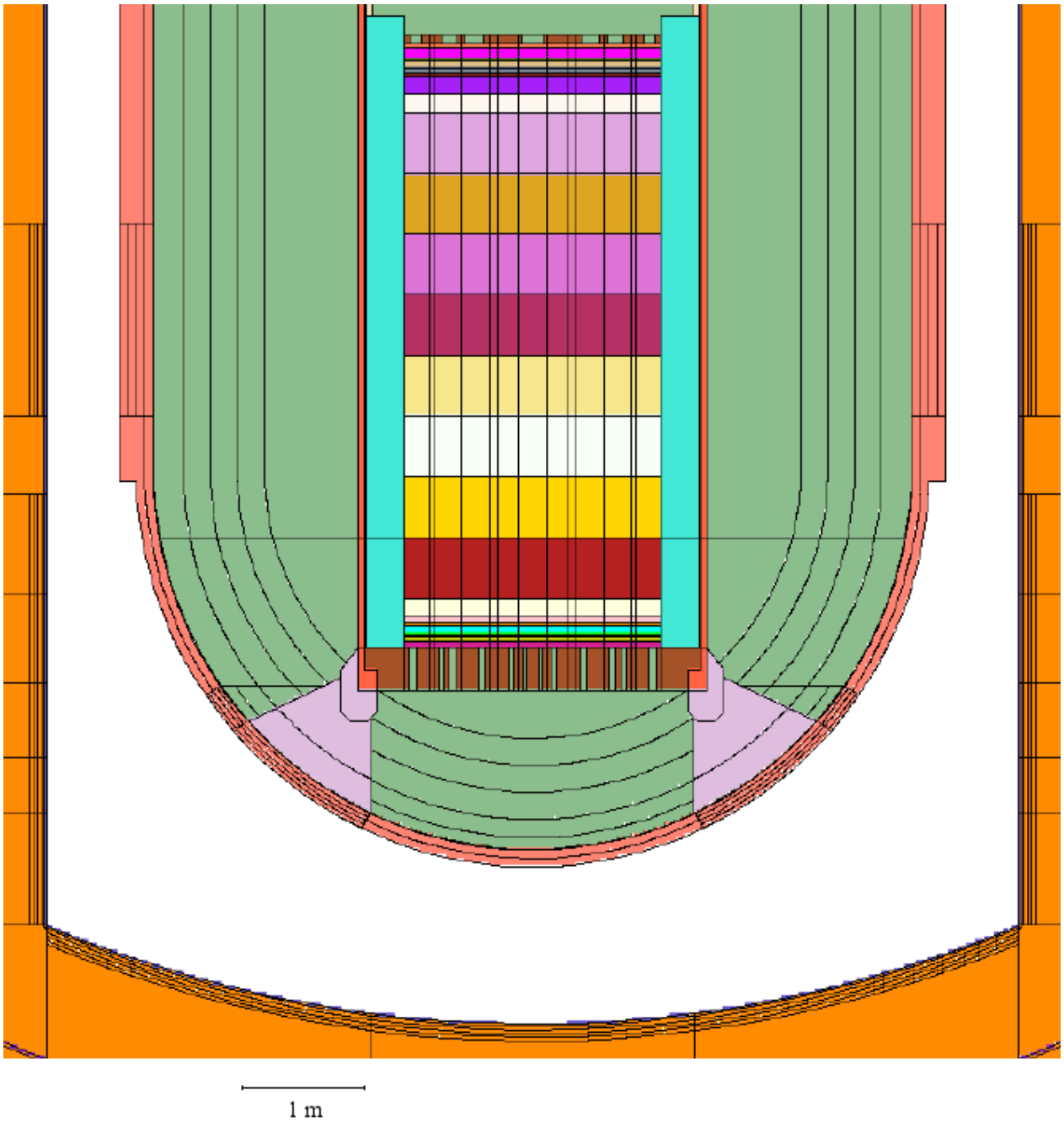

Figure 74. Segmentation of the pressure vessel and concrete and their liners for averaging the neutron fluxes for the search for the maximum EOL activities (larger scale).

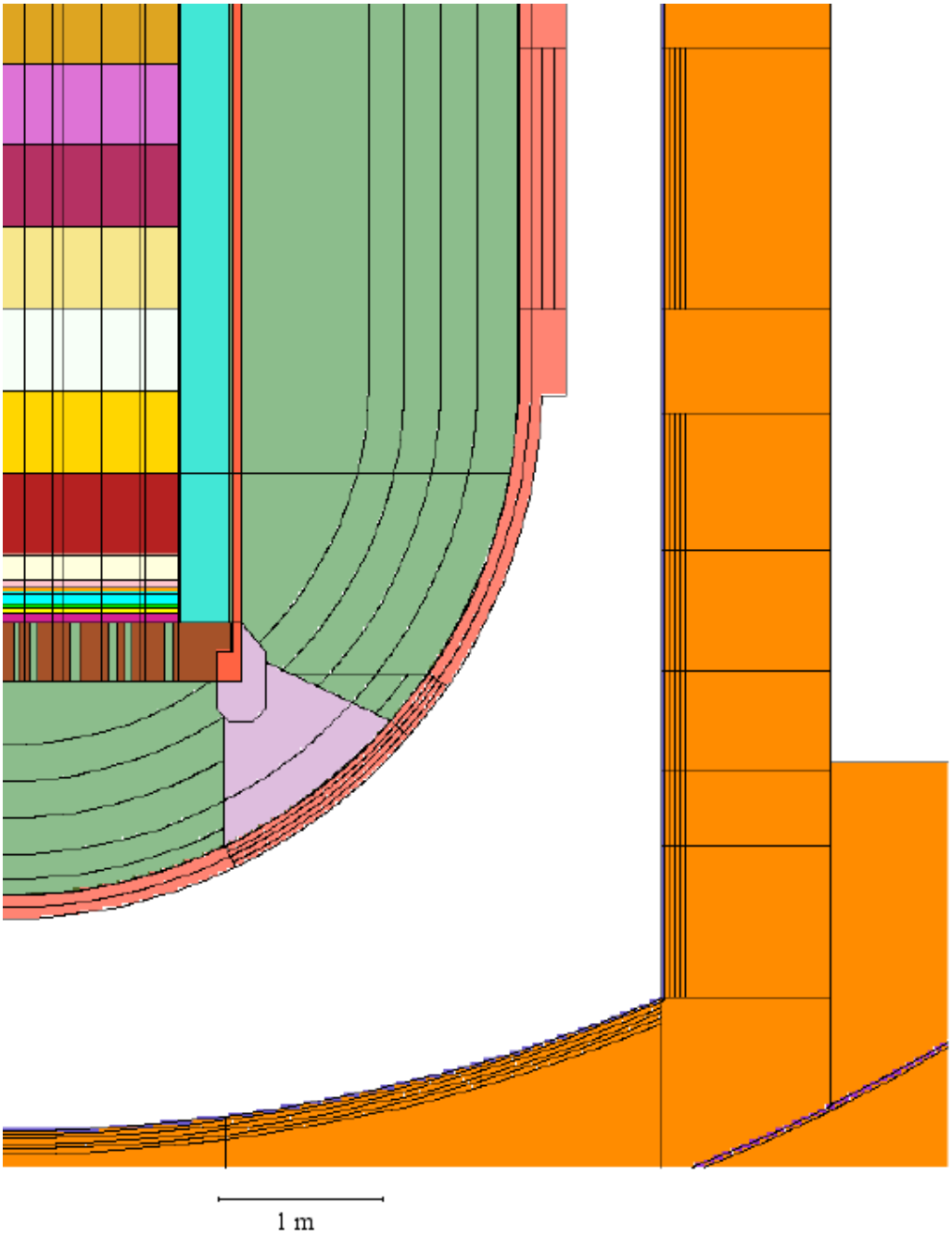

Figure 75. Detail (upper) of Fig. 74.

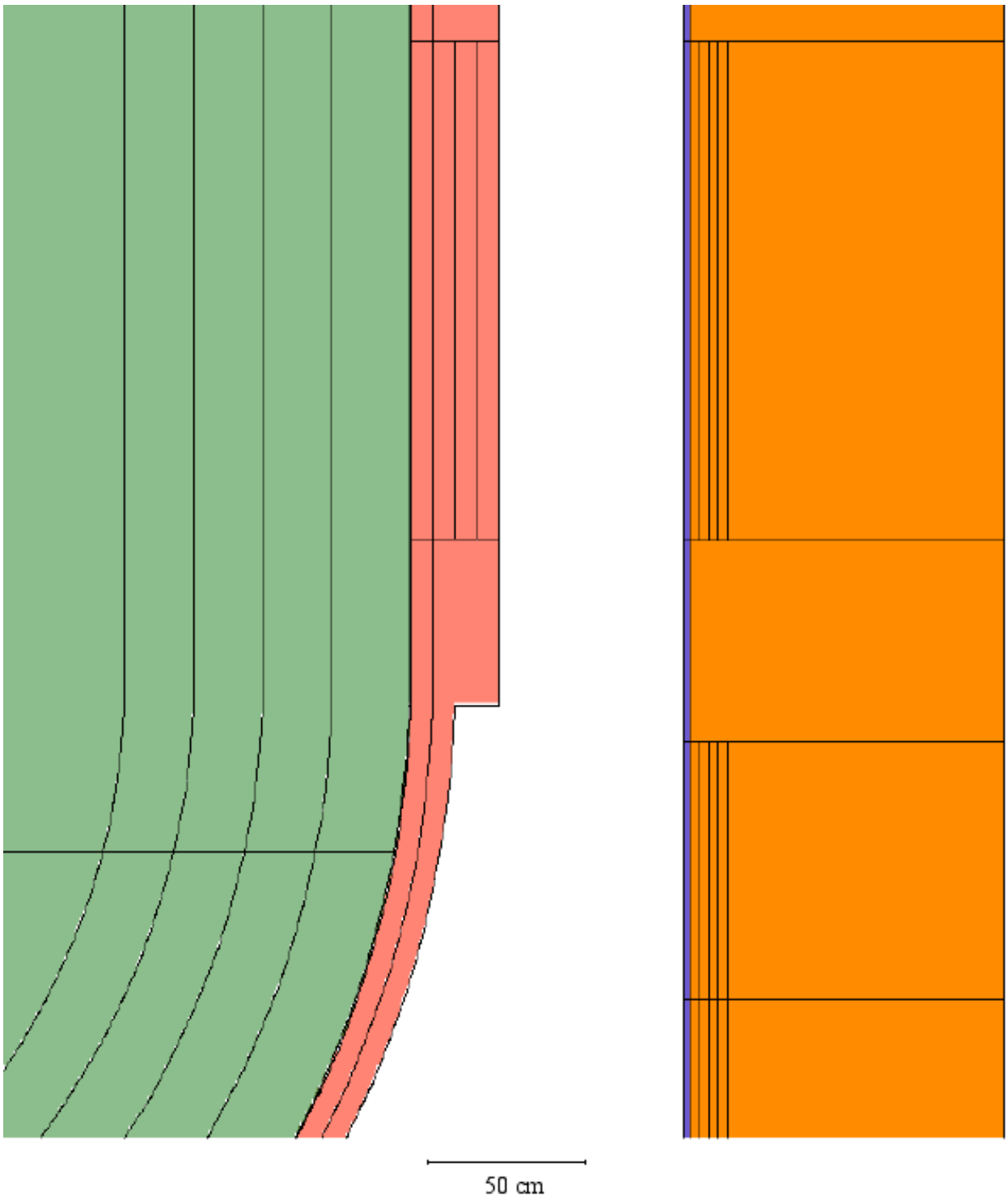

Figure 76. Detail (lower) of Fig. 74.

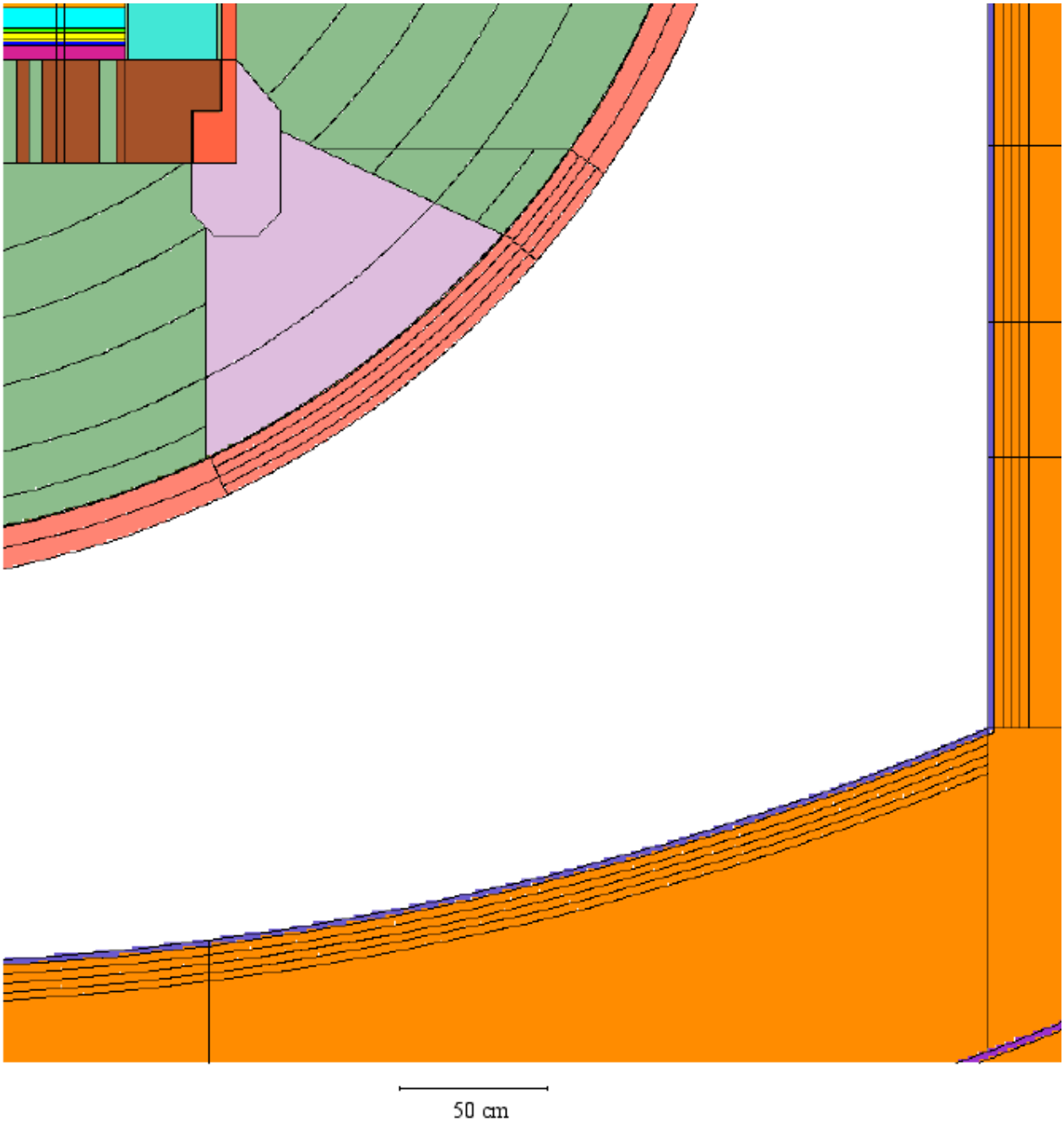

Figure 77. Horizontal section showing the segmentation of the part of the pressure vessel and liner underneath the azimuthal struts at 22.5° to E-W for averaging the neutron fluxes for the search for the maximum EOL activity.

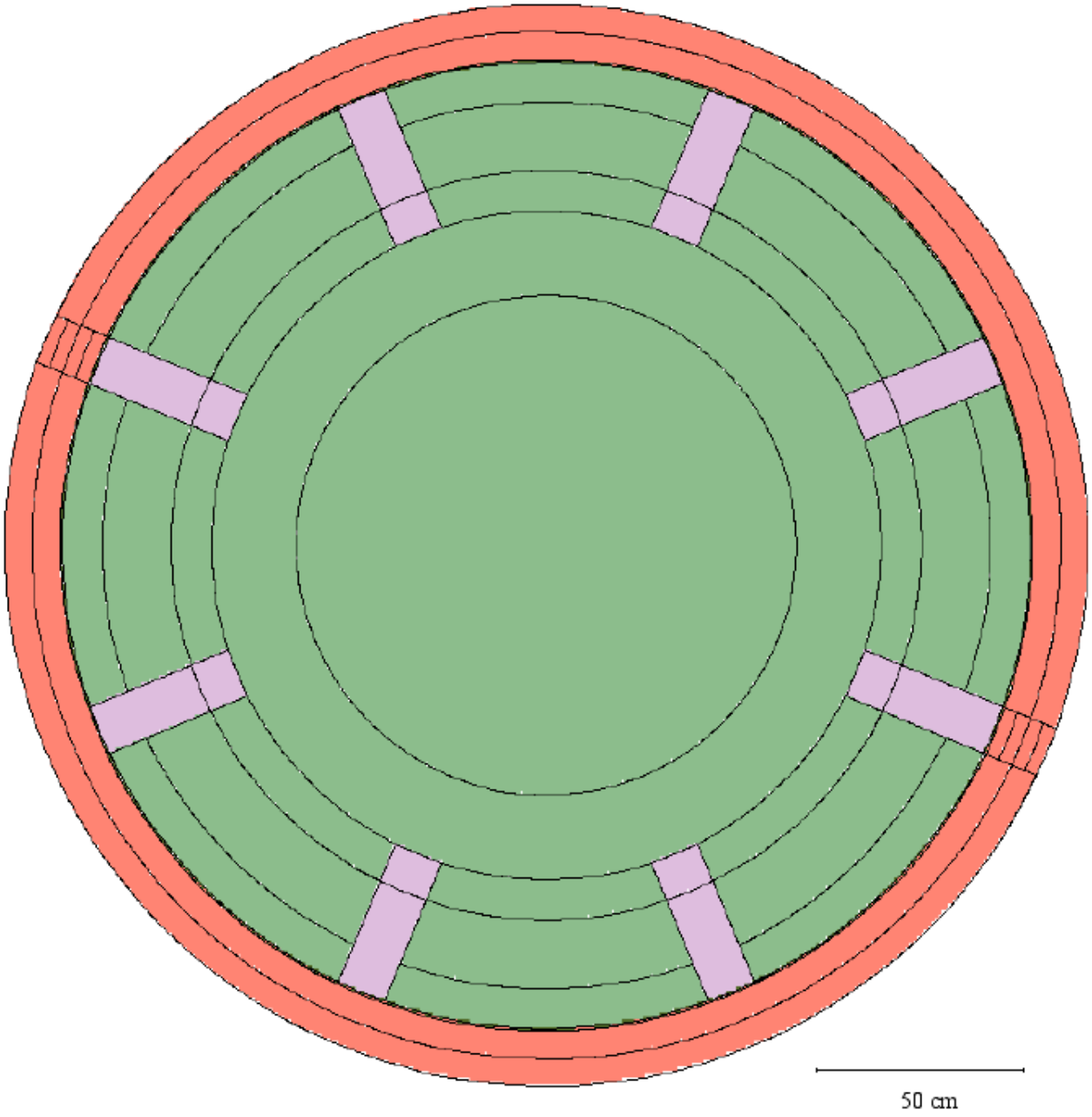

Figure 78. Contribution to the ^{59}Co(n,γ) reaction rate in the first 1/4 thickness of the PV under the azimuthal struts and to the ^{59}Co(n,γ) and ^{151}Eu(n,γ) reaction rates in the outer bottom part of the PV well (see Fig. 74) as a function of the energy of the fission neutrons.

"59Co(n,gamma); under struts, 1/4 T" = ^{59}Co(n,γ) reaction rate in the inner 1/4 thickness of the PV averaged under the azimuthal struts;

"59Co(n,gamma); concrete; bottom well; 6-9 cm" = ^{59}Co(n,γ) reaction rate in the concrete in the outer part of the bottom of the PV well at a thickness of 6-9 cm;

"151Eu(n,gamma); concrete; bottom well; 6-9 cm" = ^{151}Eu(n,γ) reaction rate in the concrete in the outer part of the bottom of the PV well at a thickness of 6-9 cm;

"235U (thermal n)" = thermal neutron-induced fission spectrum from ^{235}U.

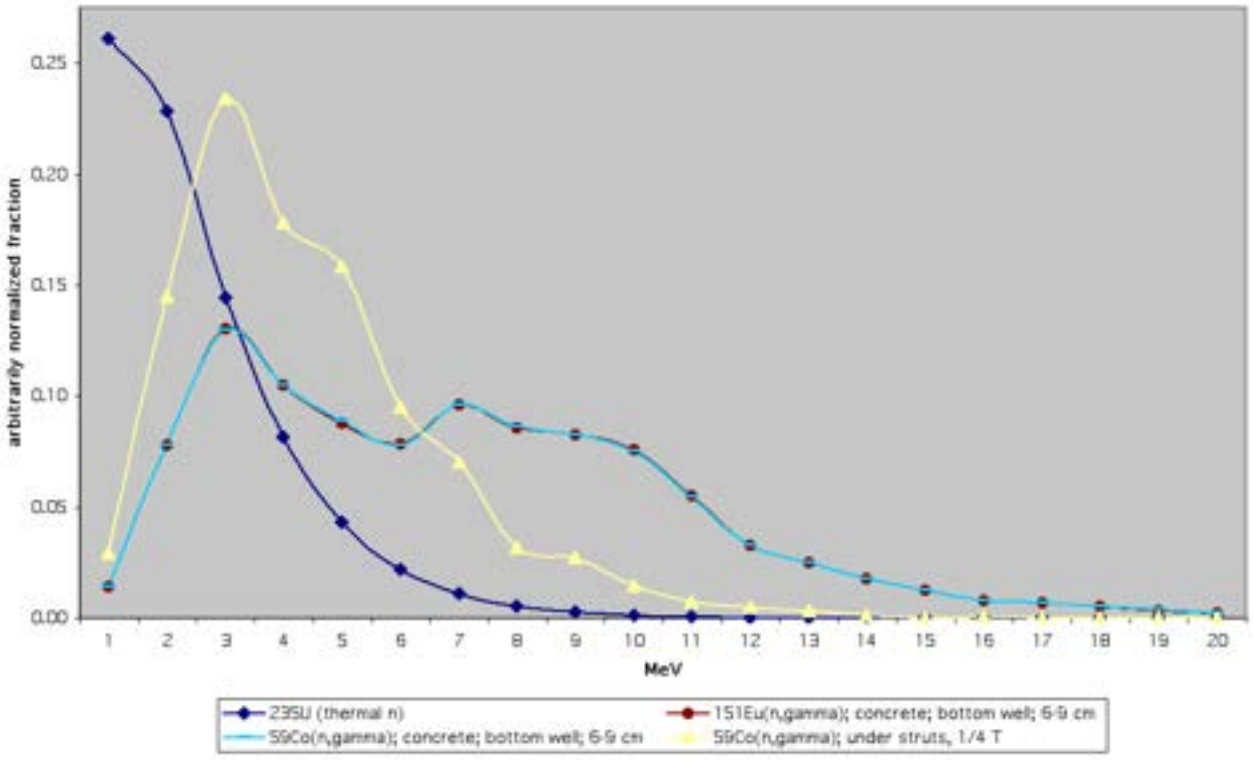

Figure 79. Axial segmentation of the pressure vessel (and pressure vessel liner) for the calculation of the average activities at EOL.

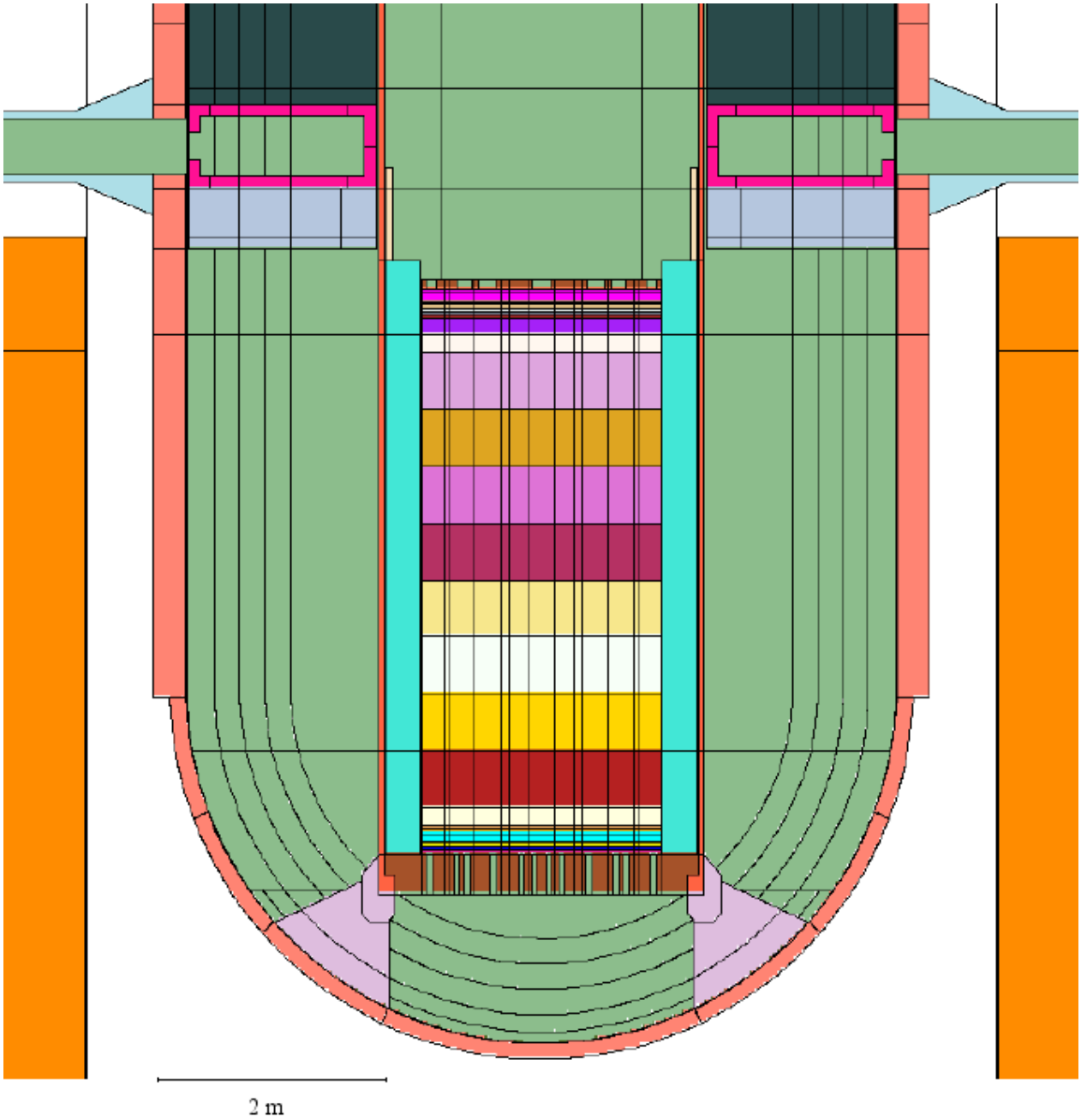

Figure 80. Axial segmentation of the active zone and radial and axial segmentation of the reflector for averaging the neutron fluxes for the calculation of the gamma source and maintenance dose.

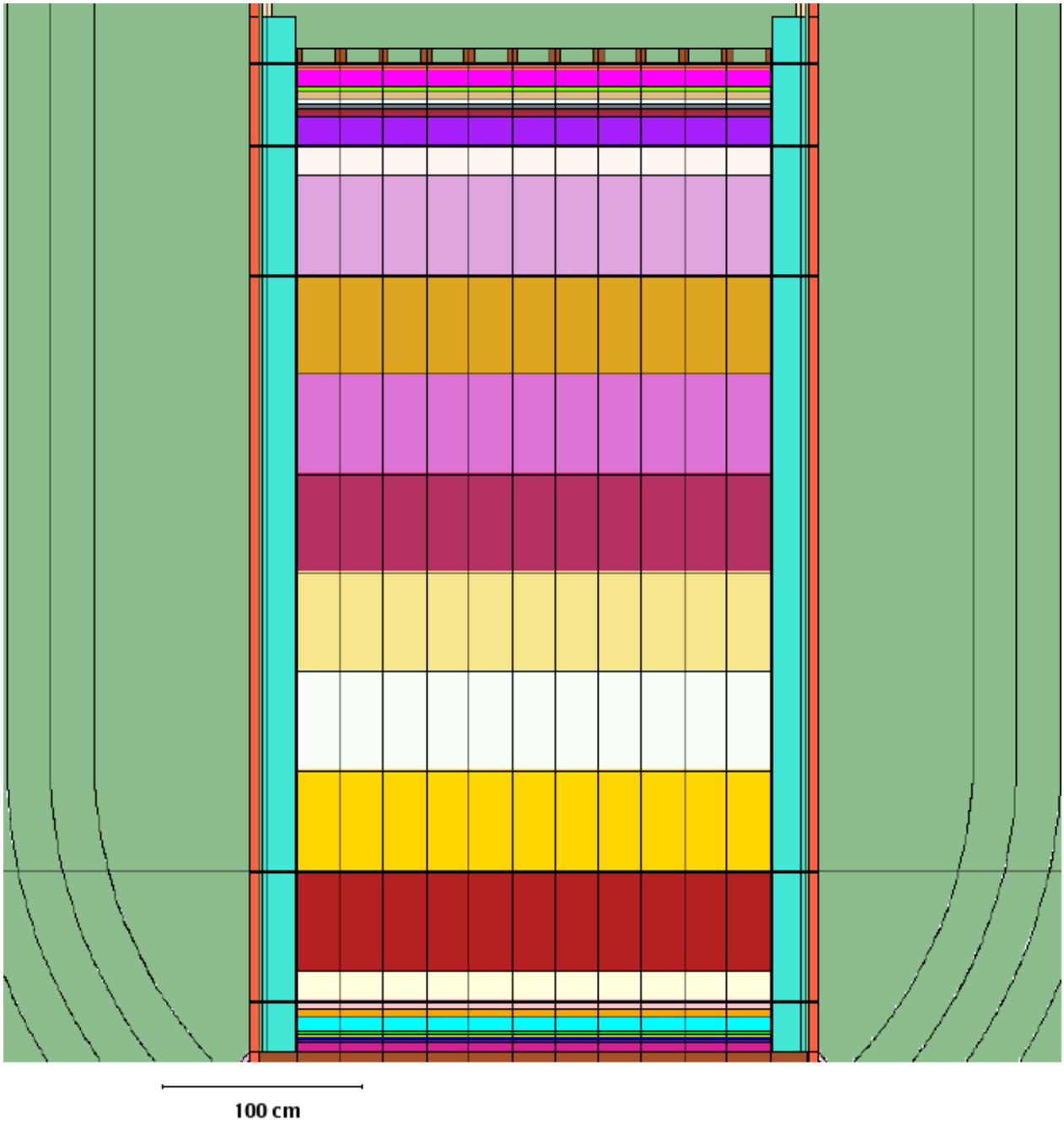

Figure 81. Axial segmentation of the barrel for averaging the neutron fluxes for the calculation of the gamma source and maintenance dose.

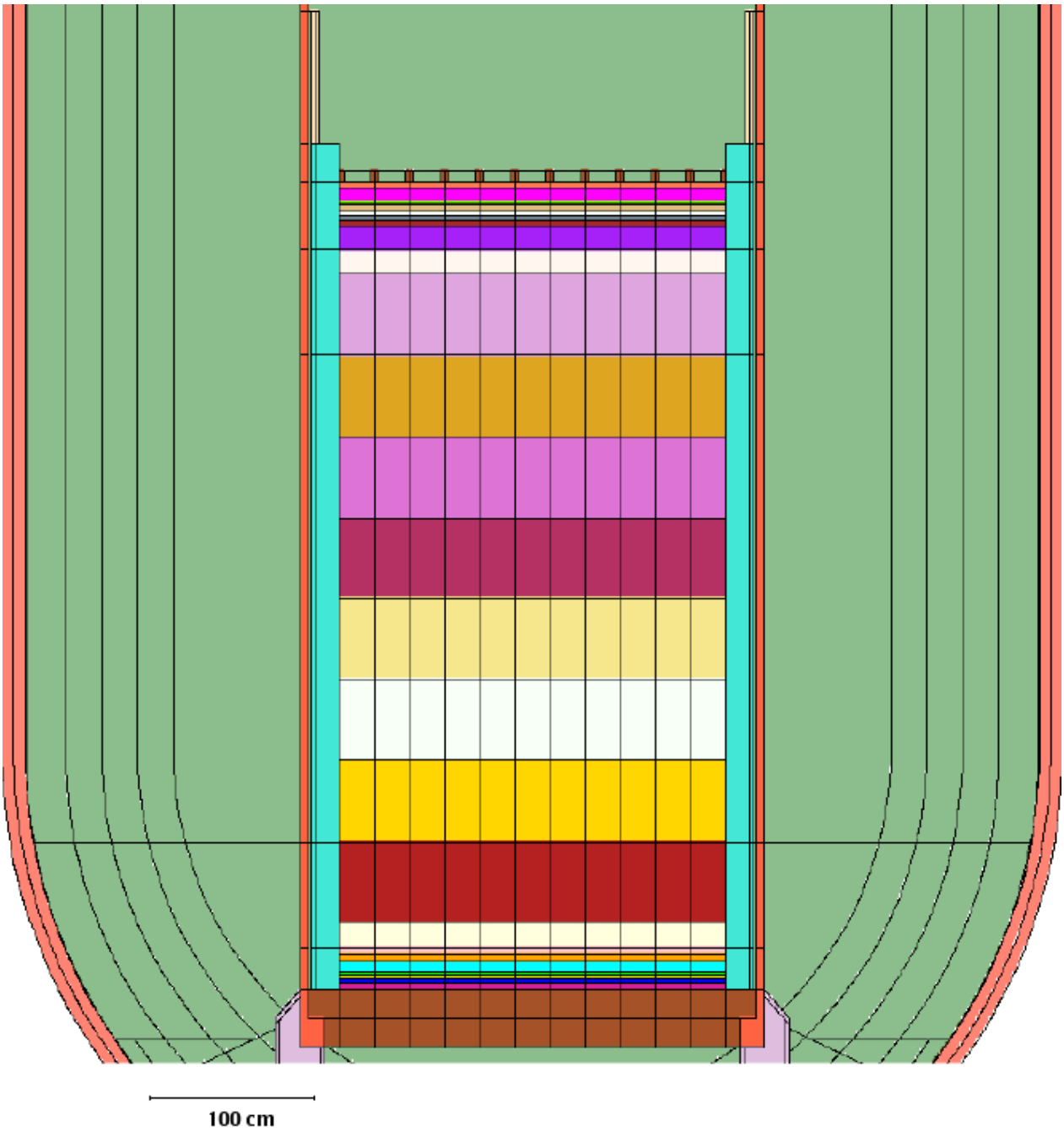

Figure 82. Segmentation of the bottom plate into an upper and lower part and segmentation of the bottom plate annular support for averaging the neutron fluxes for the calculation of the gamma source and maintenance dose.

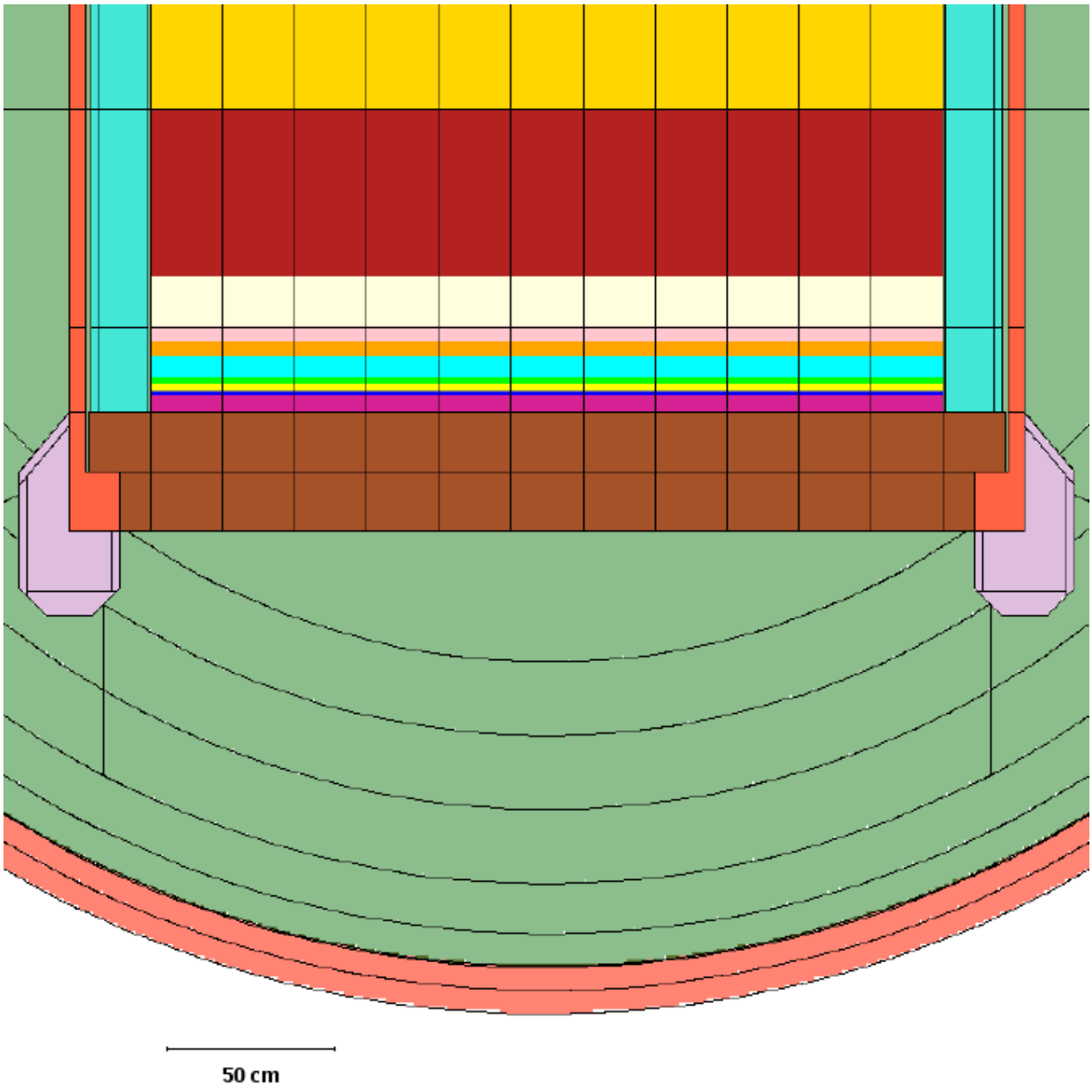

Figure 83. Segmentation of the bottom plate annular support and one of the eight azimuthal supports for averaging the neutron fluxes for the calculation of the gamma source and maintenance dose.

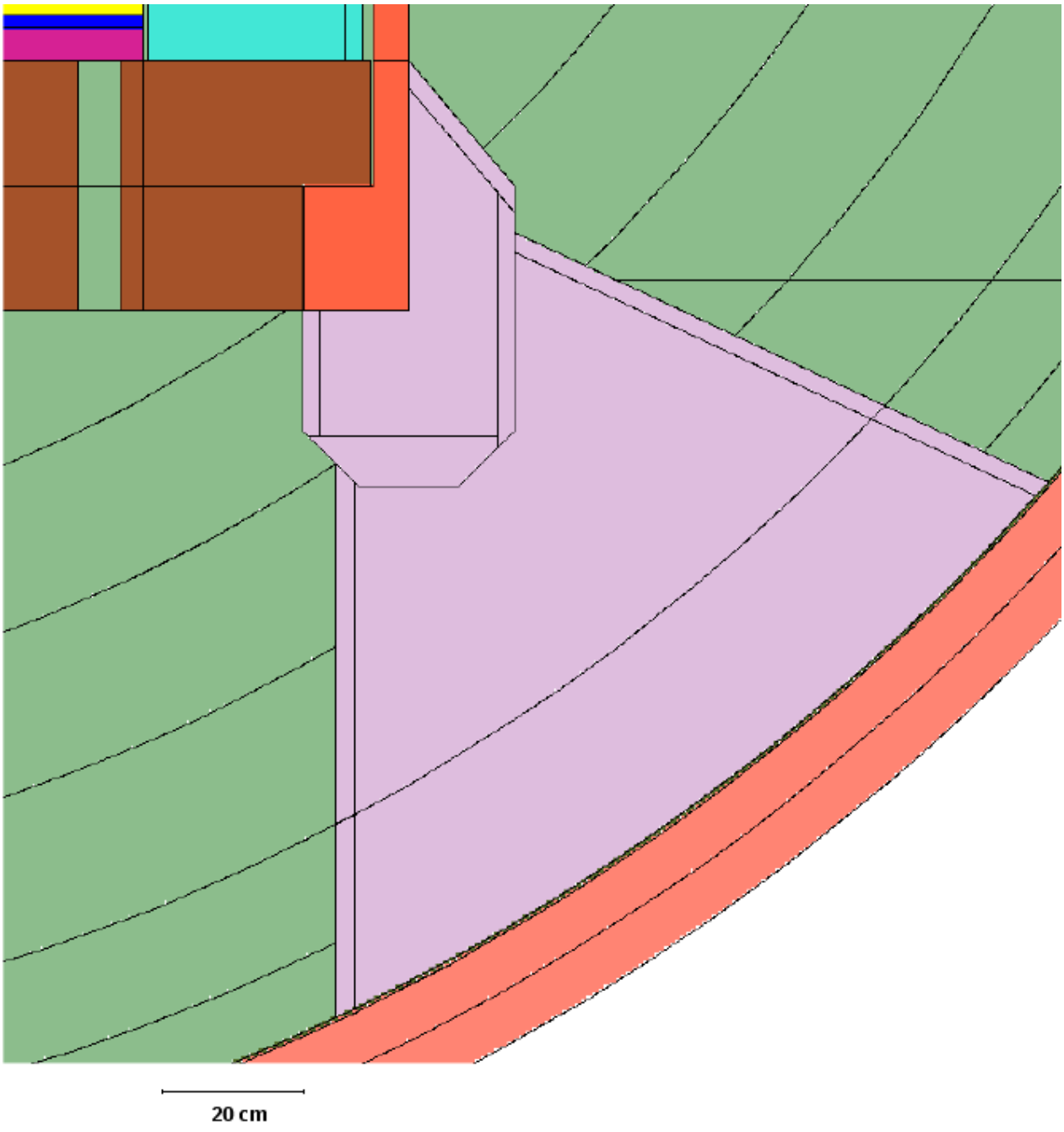

Figure 84. Segmentation of one of the eight azimuthal supports (horizontal cross section) for averaging the neutron fluxes for the calculation of the gamma source and maintenance dose.

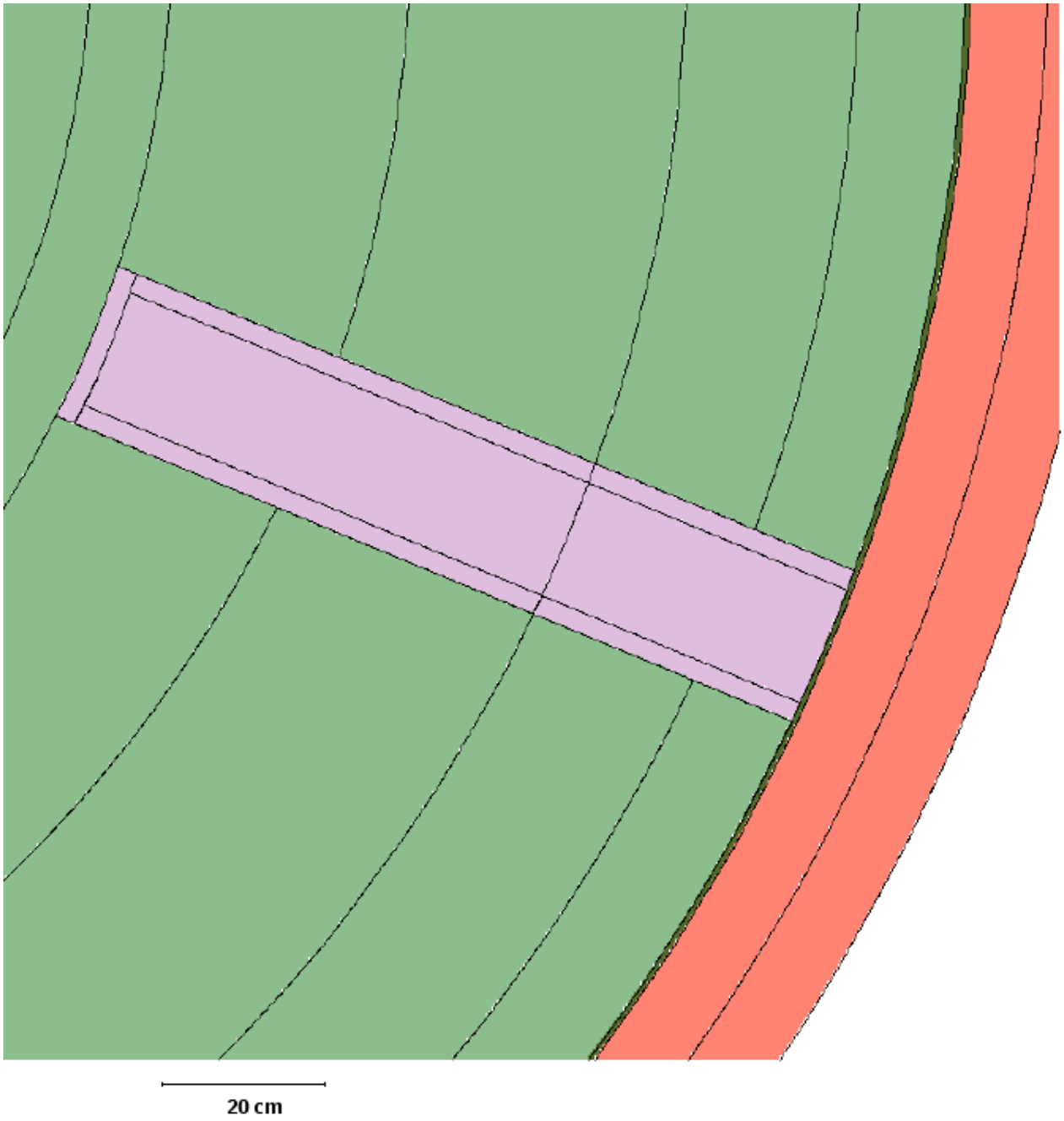

Figure 85. Segmentation of the pressure vessel for averaging the neutron fluxes for the calculation of the gamma source and maintenance dose.

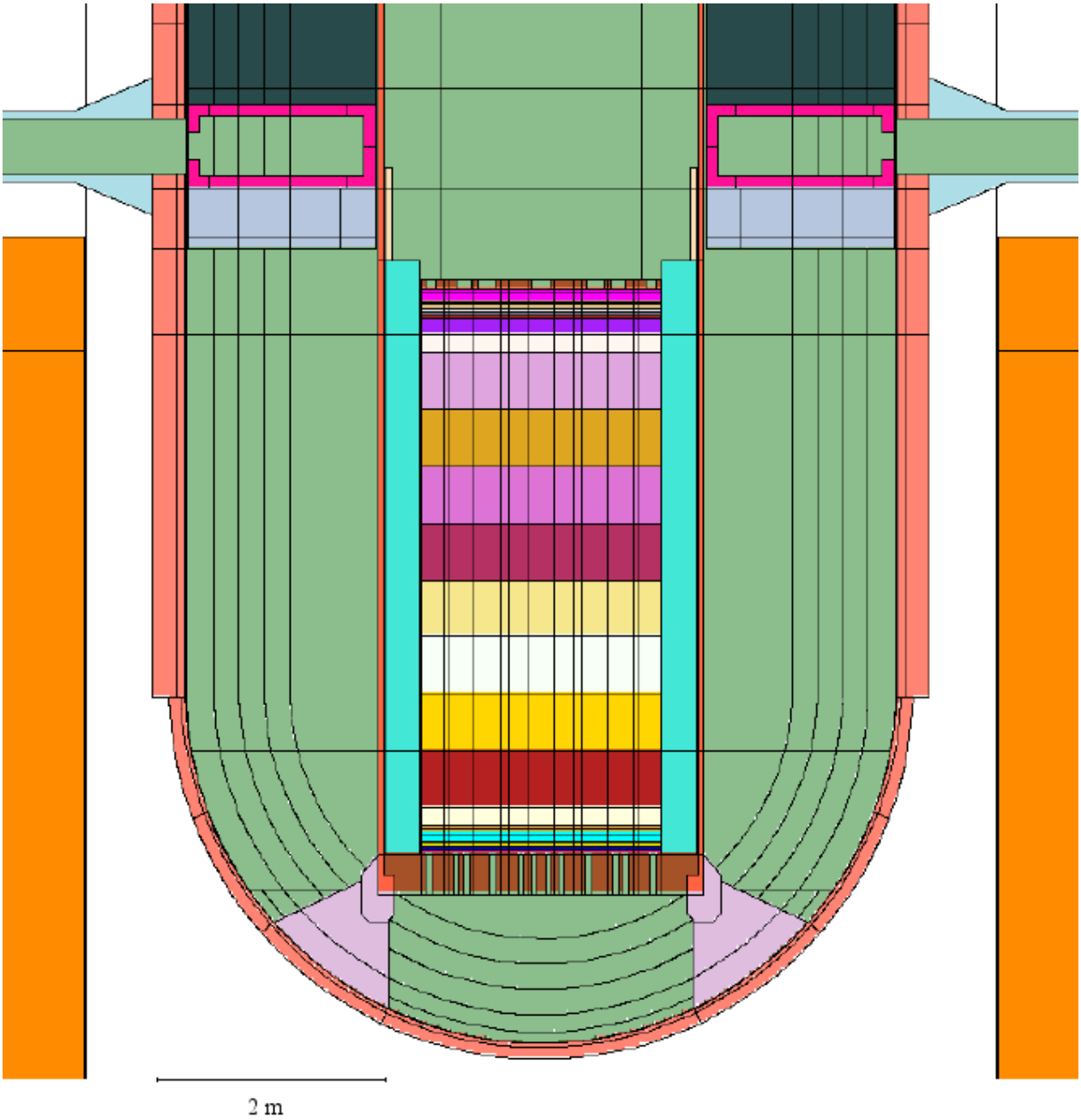

Figure 86. Segmentation of the part of the pressure vessel under the azimuthal struts at 22.5° to EW for averaging the neutron fluxes for the calculation of the gamma source and maintenance dose.

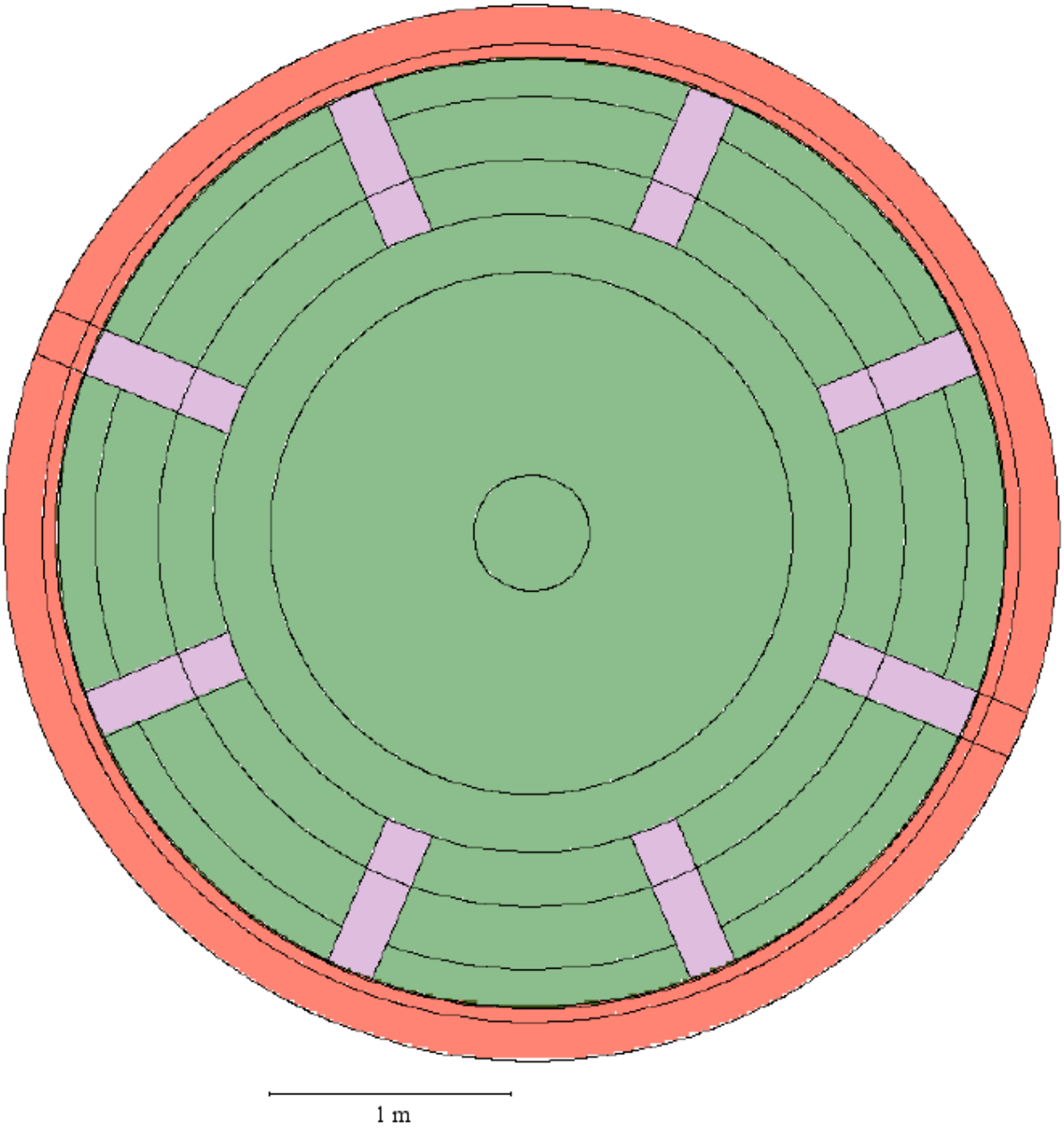

Figure 87. Detail of Fig. 85 around inlet nozzles.

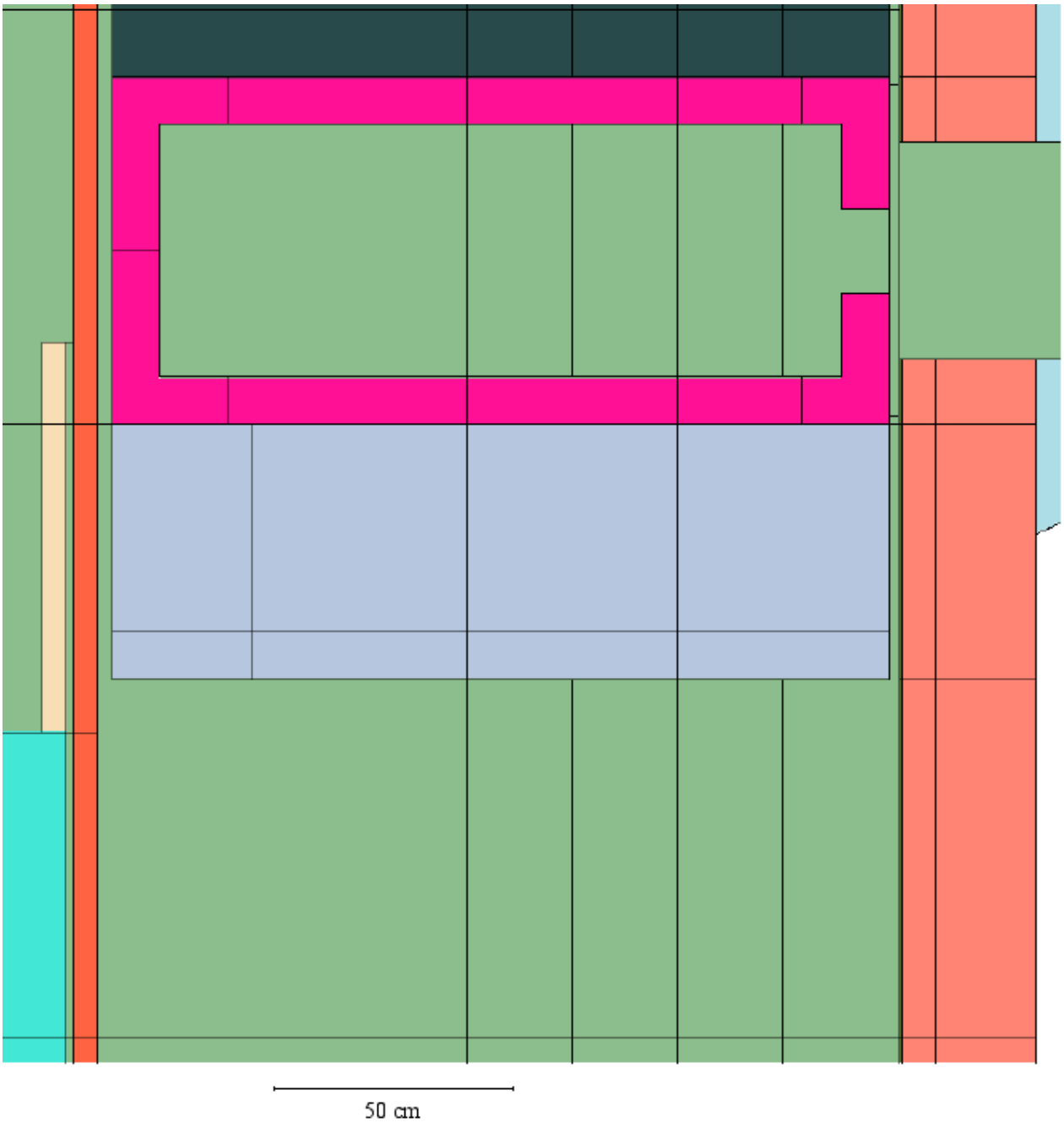

Figure 88. Detail of Fig. 85 where pressure vessel changes from cylindrical to spherical shape.

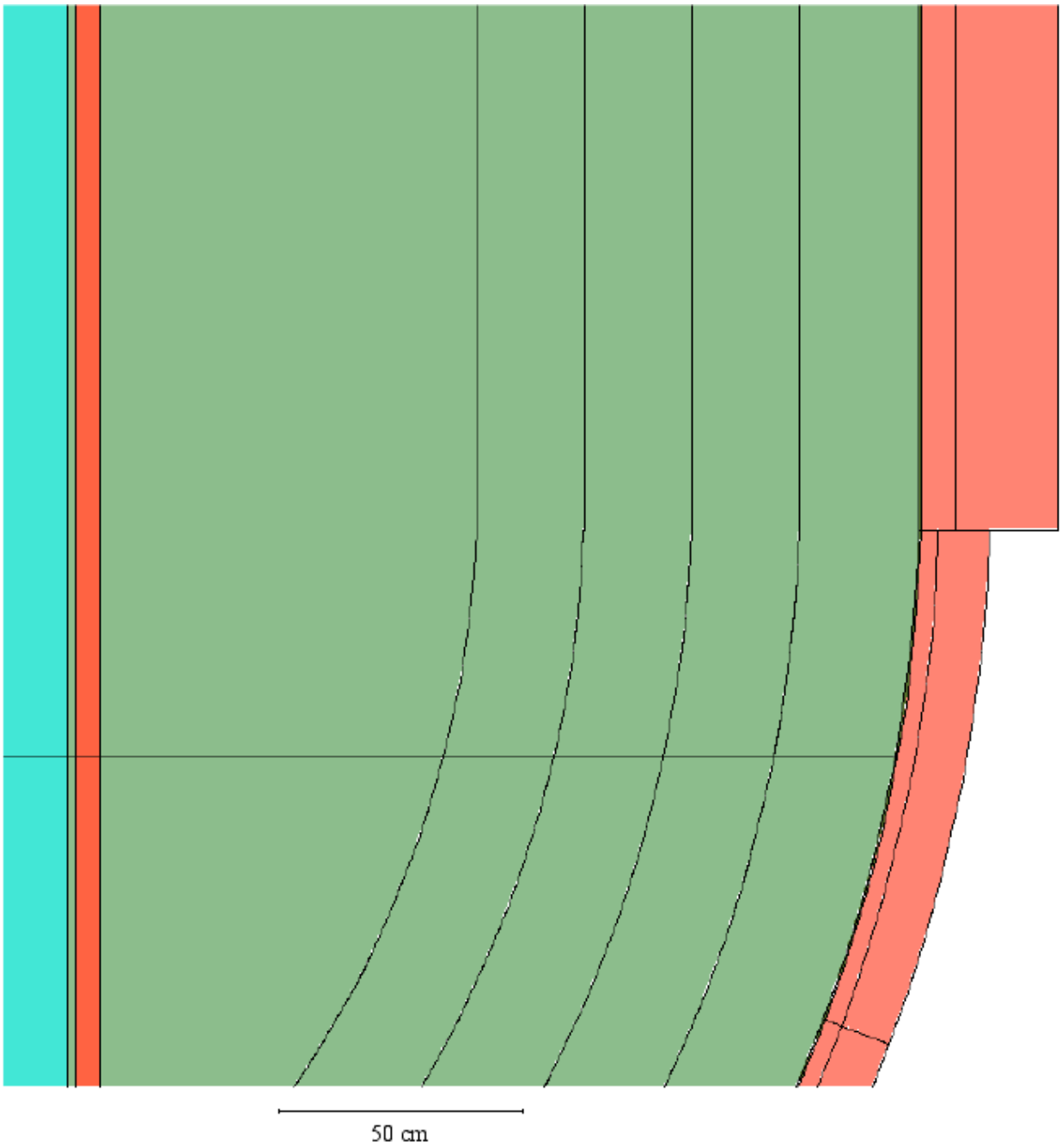

Figure 89. Detail of Fig. 85 just above azimuthal struts.

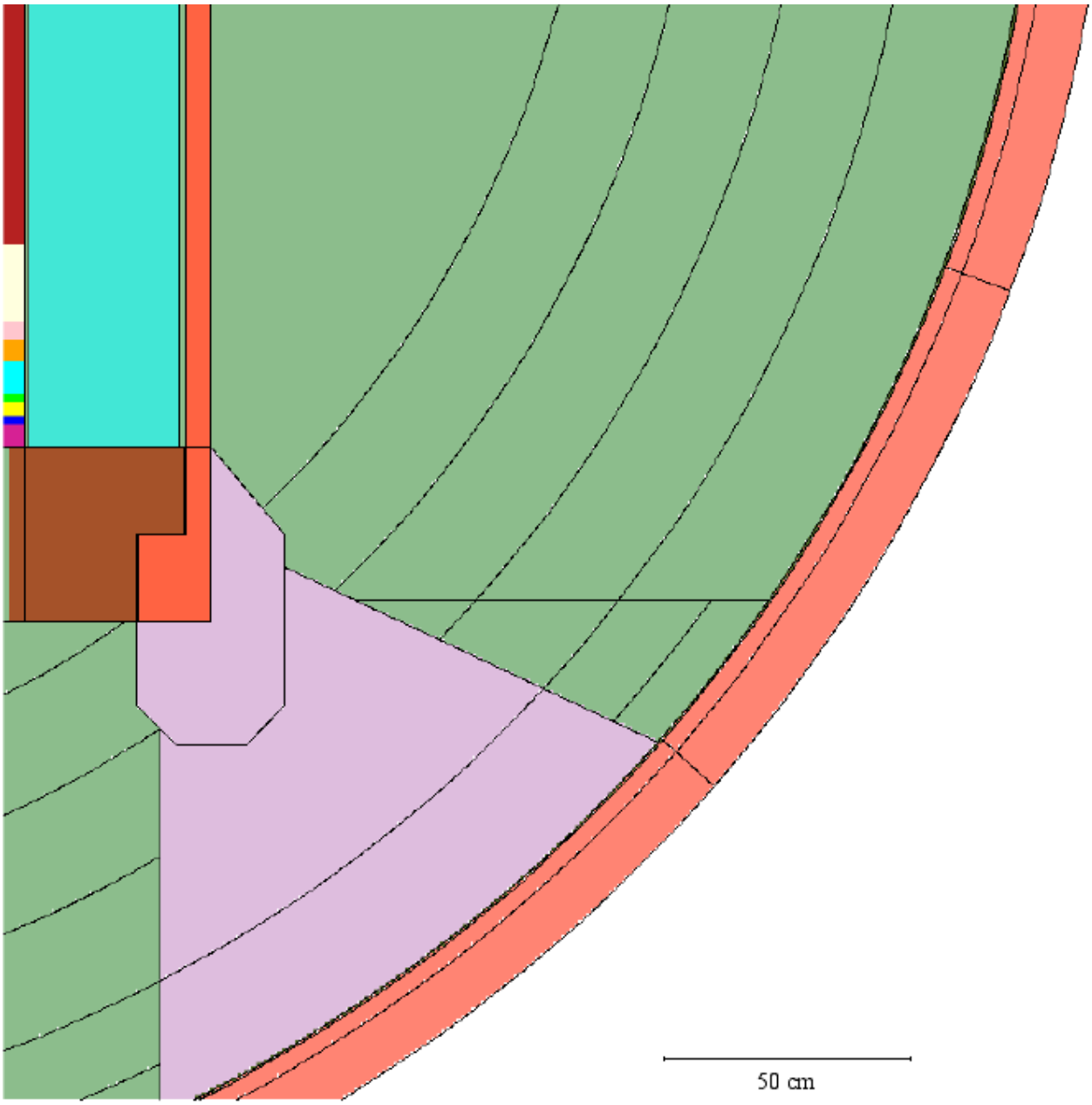

Figure 90. Detail of Fig. 85 just below azimuthal struts.

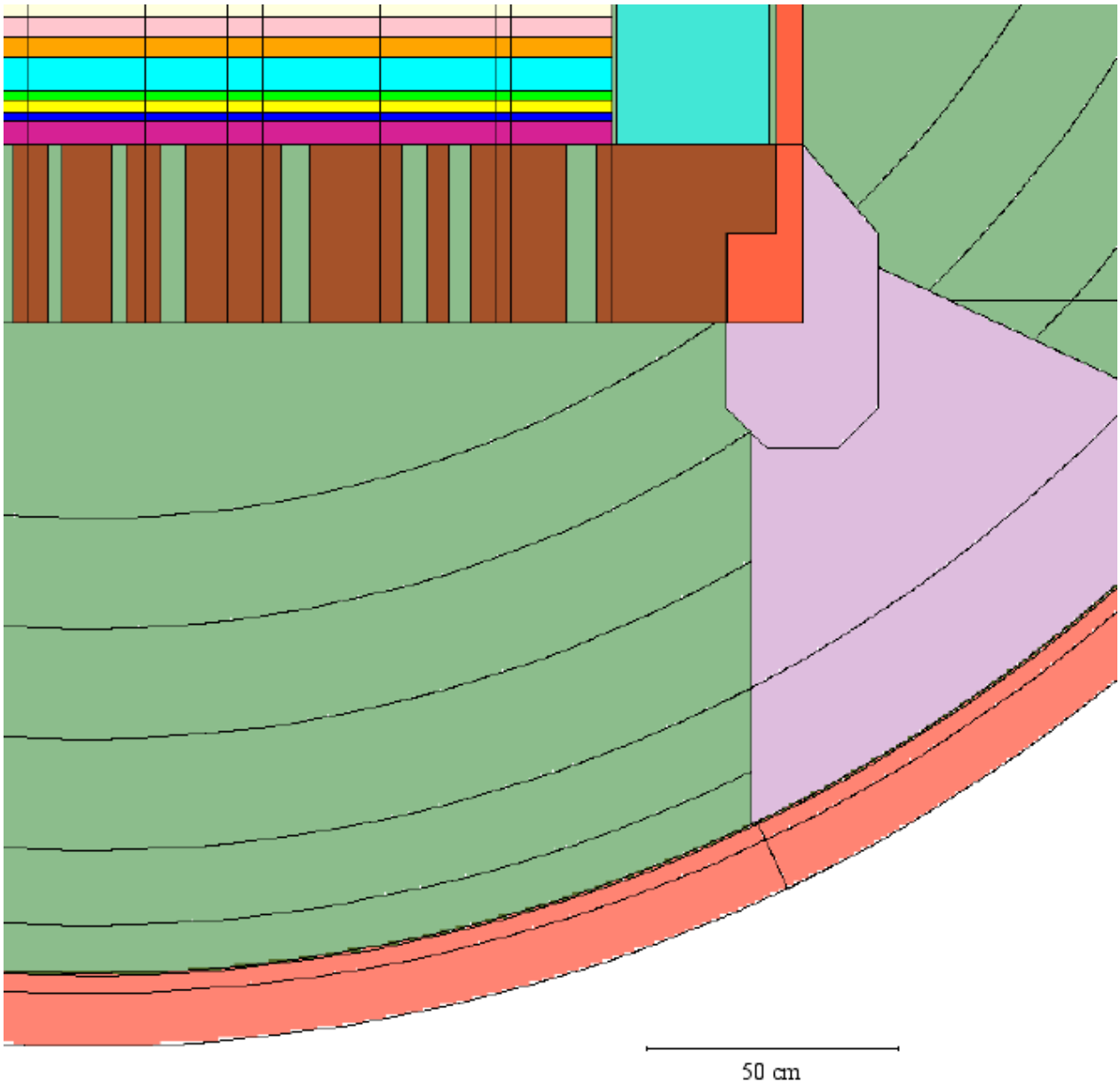

Figure 91. Segmentation of the concrete and concrete liner for averaging the neutron fluxes for the calculation of the gamma source and maintenance dose.

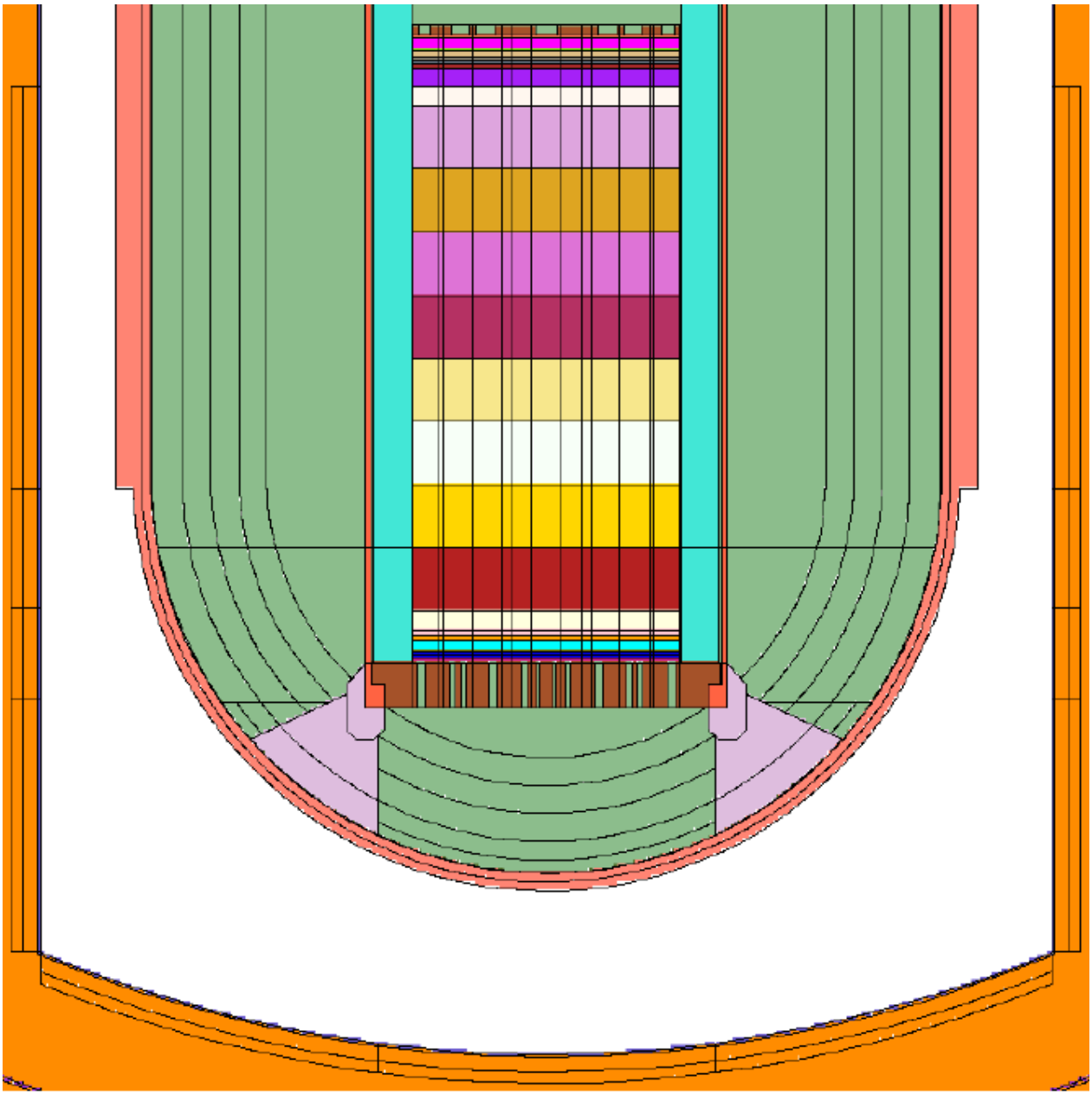

Figure 92. Comparison of the total gamma spectra from the active core at 24 hours after shut-down obtained with FISPACT and with ORIGEN-ARP.

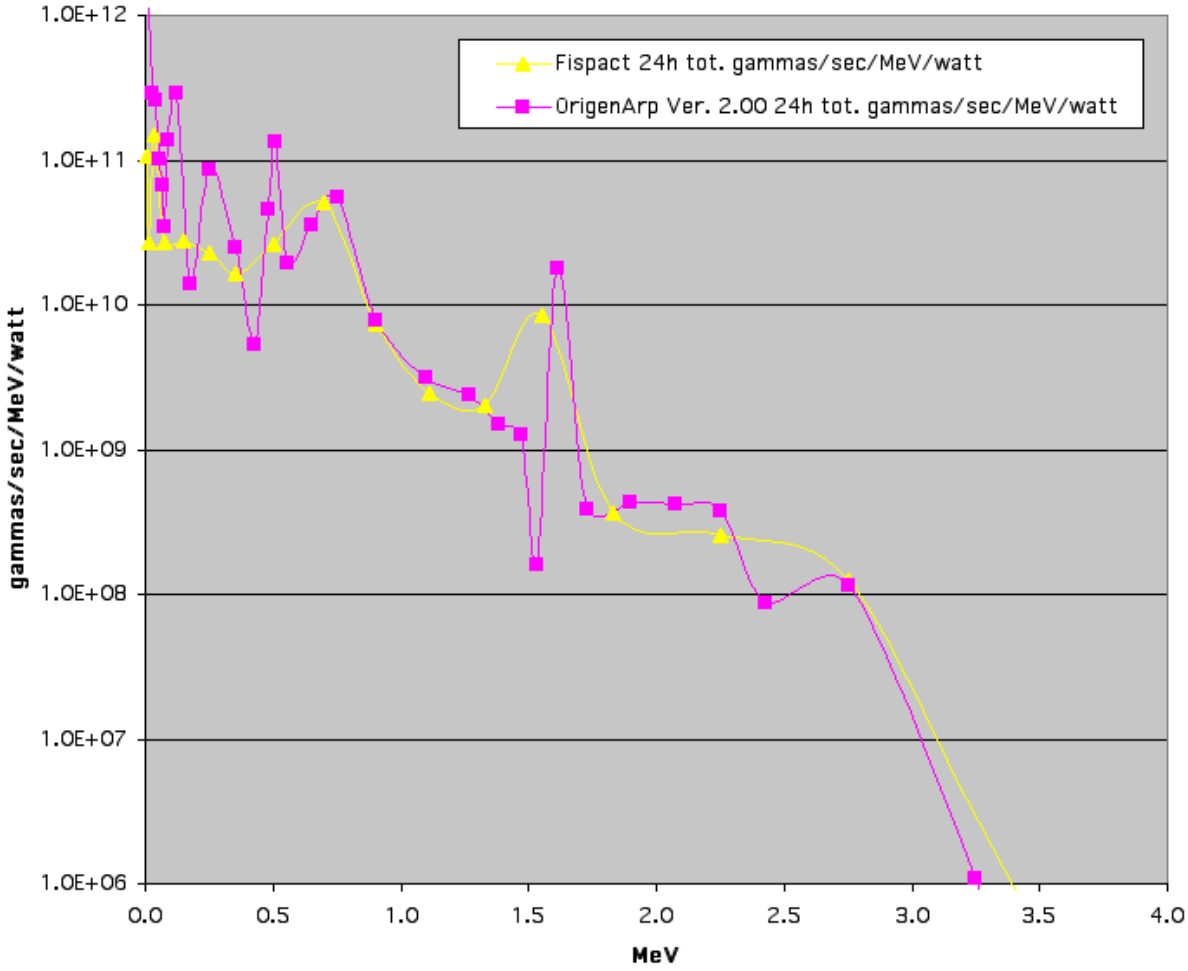

Figure 93. Comparison of the total gamma spectra from the active core at 24 hours after shut-down obtained with FISPACT and obtained with the Westinghouse in-house methodology.

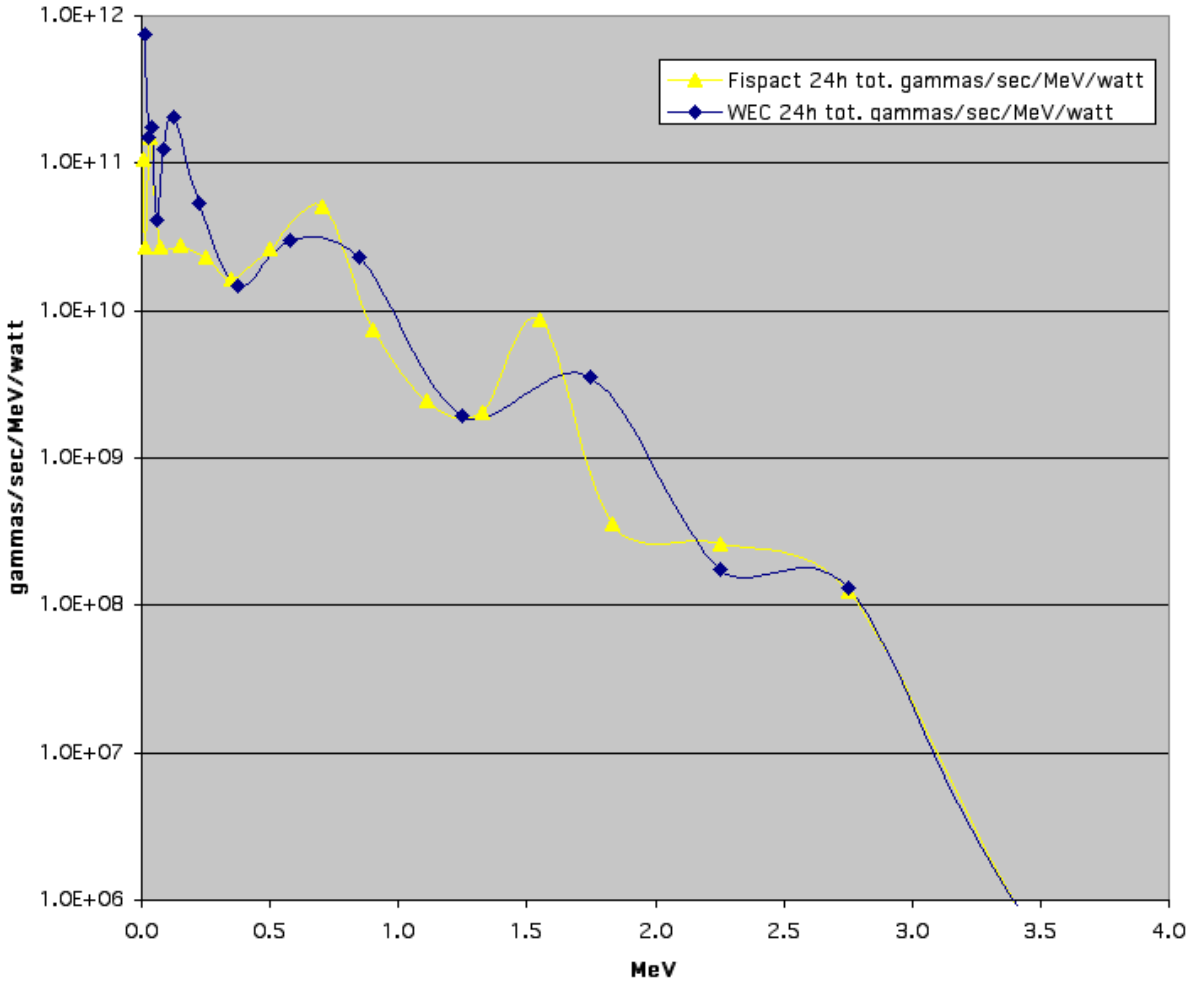

Figure 94. Comparison of the total gamma spectrum from the active core at 24 hours after shut-down with the gamma spectrum at 24 hours after shut-down from gaseous and volatile fission products (Se, Br, Kr, Rb, Cd, Te, I, Xe and Cs), both spectra obtained with FISPACT.

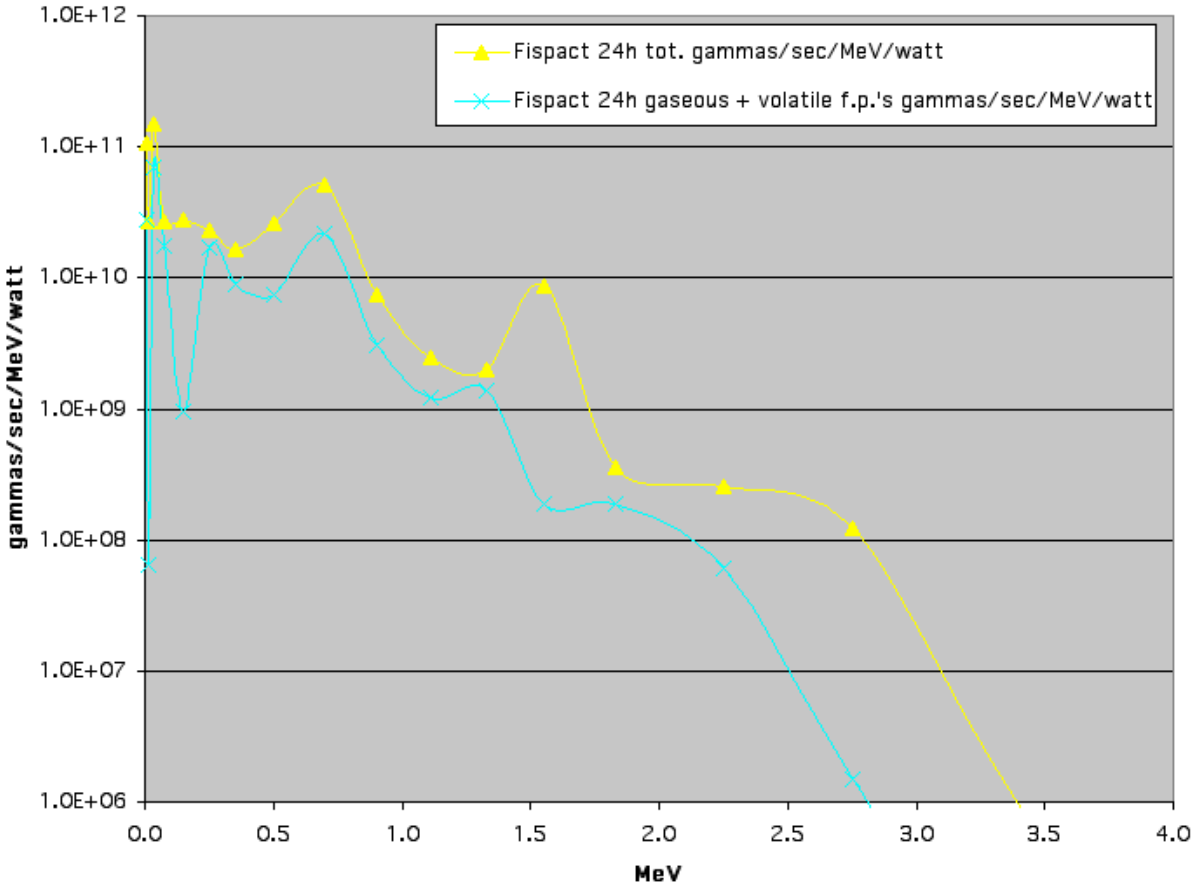

Figure 95. Segmentation of the lower part of the outer surface of the PV (A1 to A5), the lower part of the inner surface of the concrete liner (B1 to B5, C1 and C2) and of the void in the lower part of the PV well (D1 to D7) for averaging the dose from the gamma activation sources.

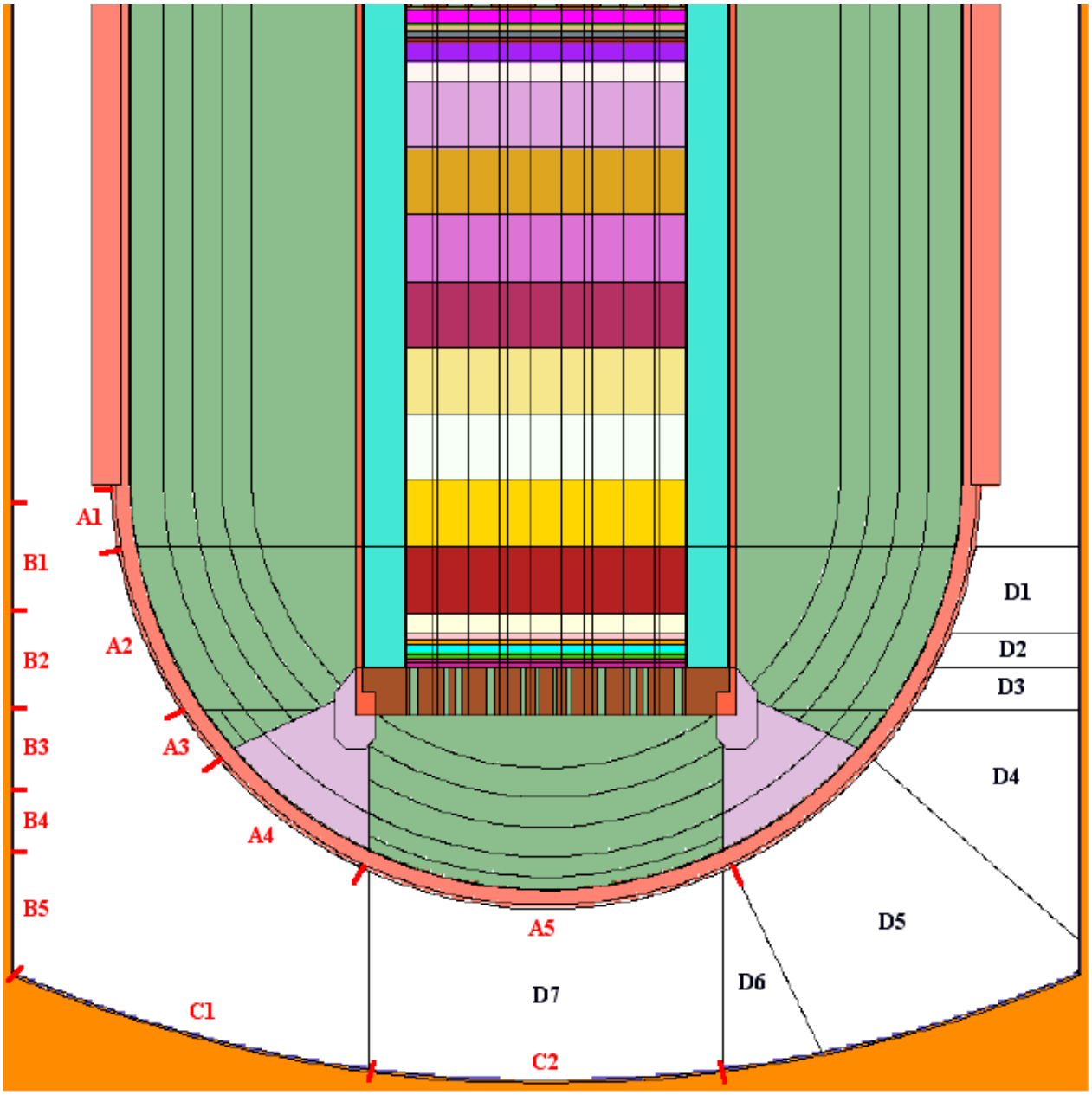

Figure 96. Segmentation of the lower part of the outer surface of the PV for averaging the dose from the gamma activation sources (detail below azimuthal struts).

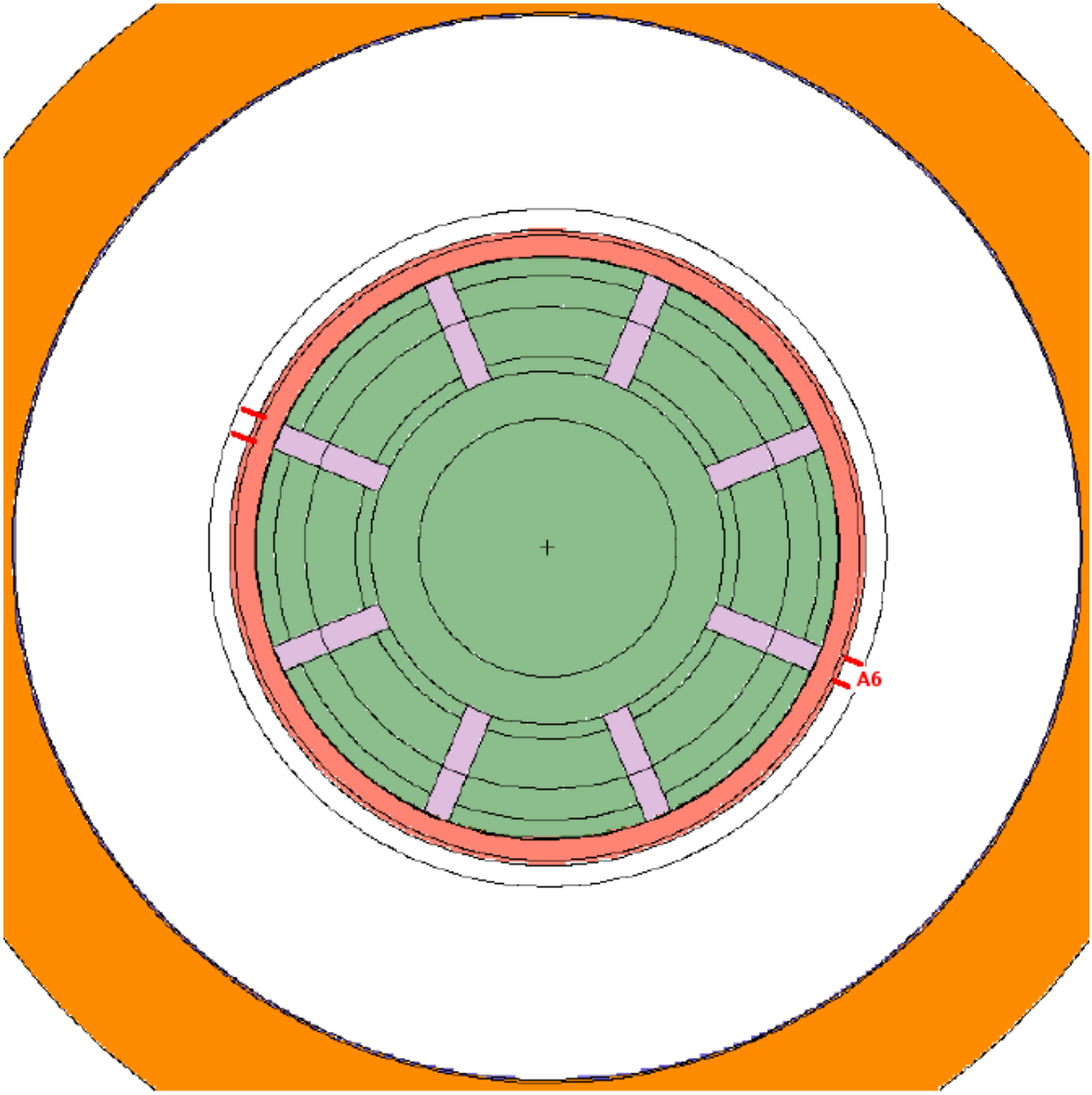

Figure 97. Vertical cross-section showing the homogenized lower support zone of the steam generators.

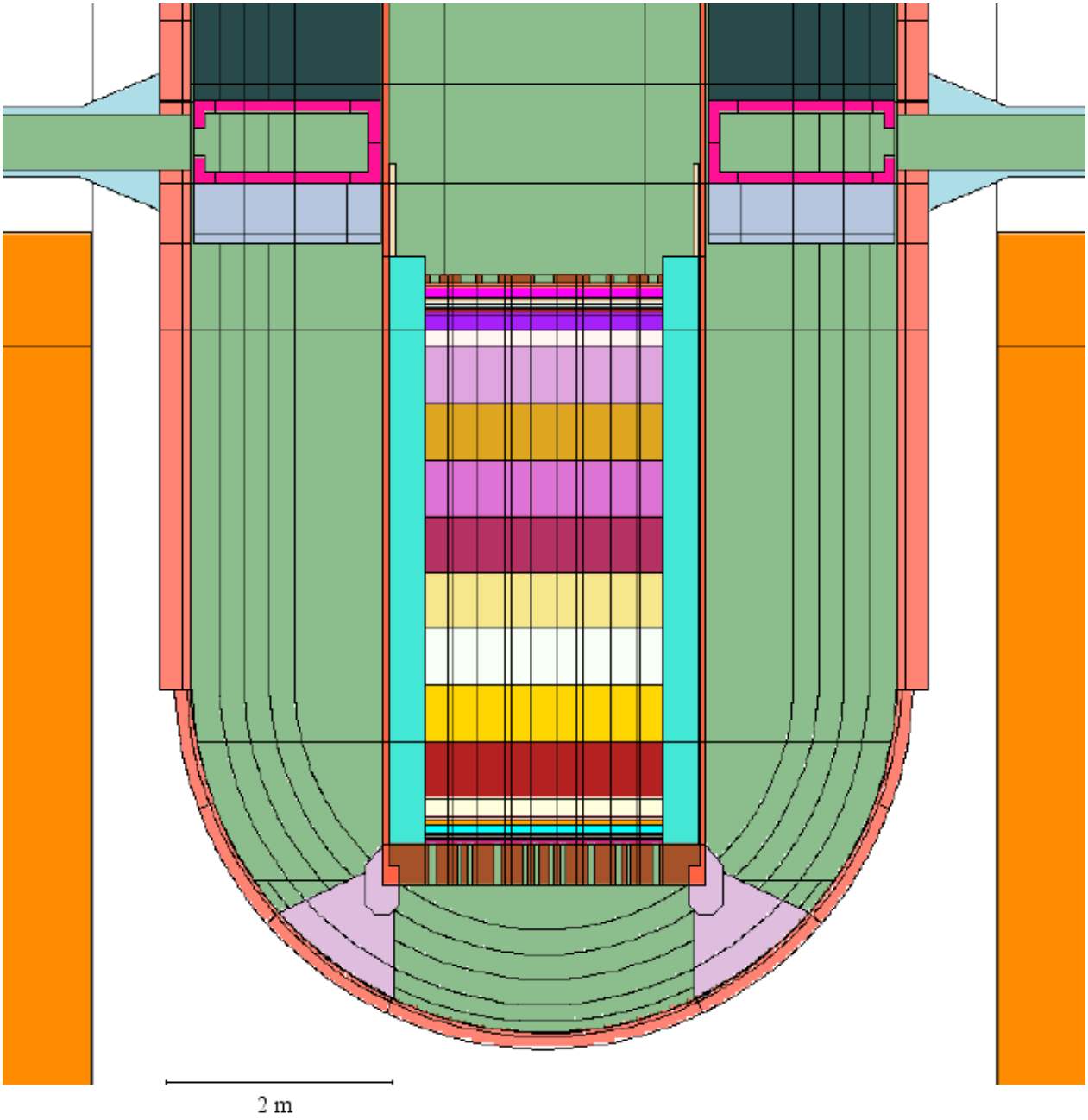

Figure 98. Horizontal cross-section at the homogenized lower support zone of the steam generators.

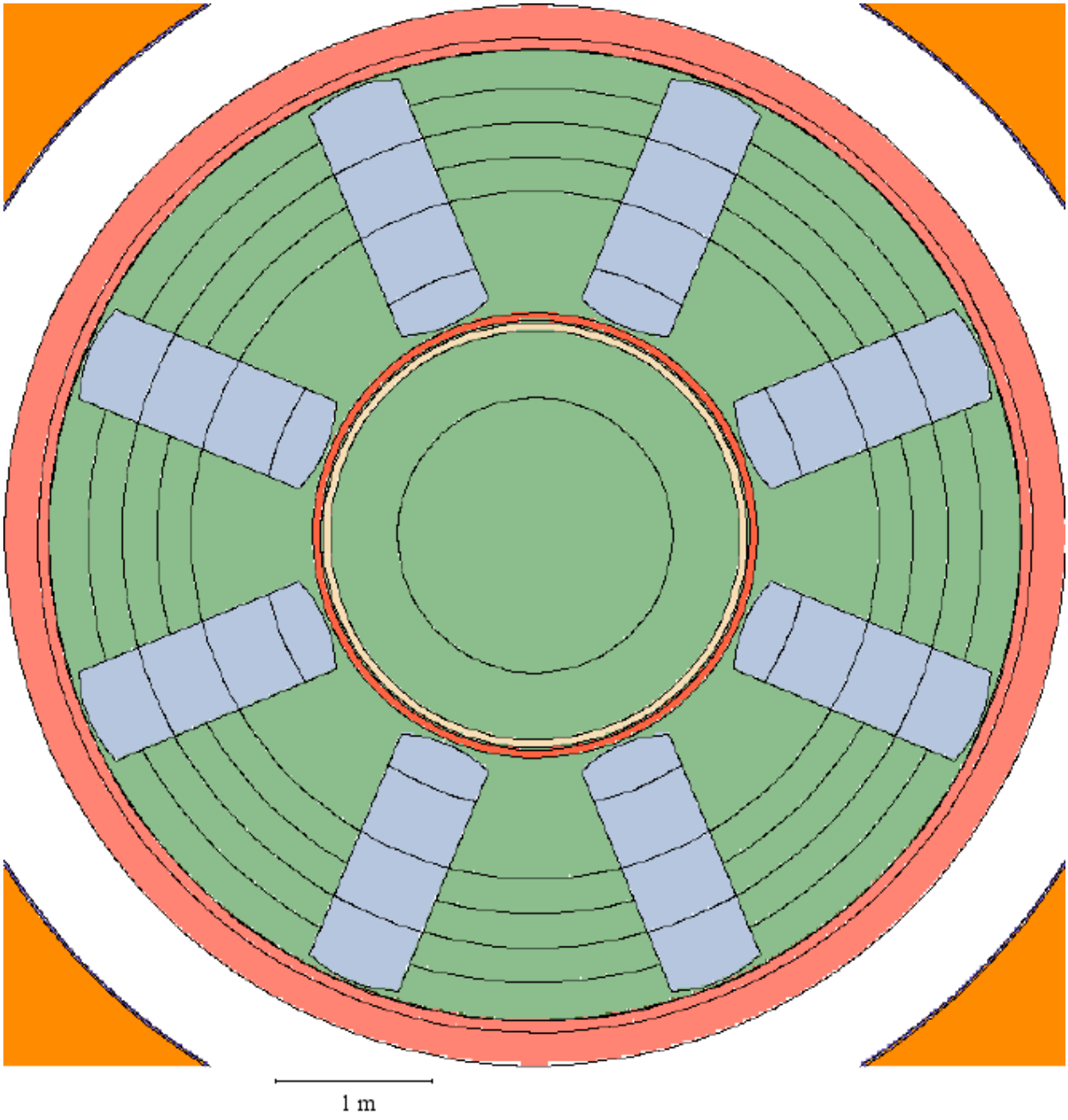

Figure 99. Vertical cross-section of the heterogeneous lower support model of the steam generators.

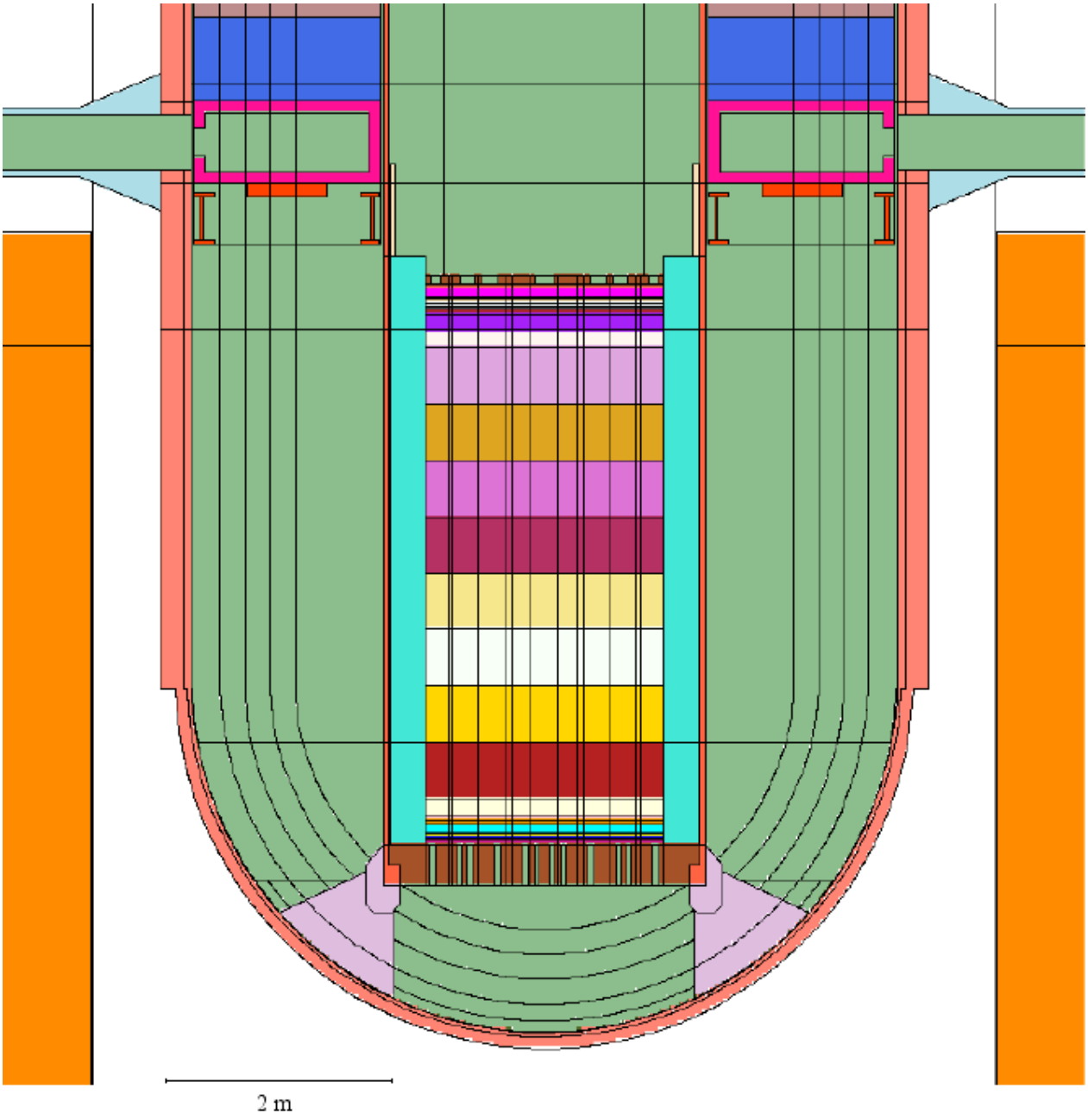

Figure 100. Vertical cross-section of the heterogeneous lower support model of the steam generators (detail).

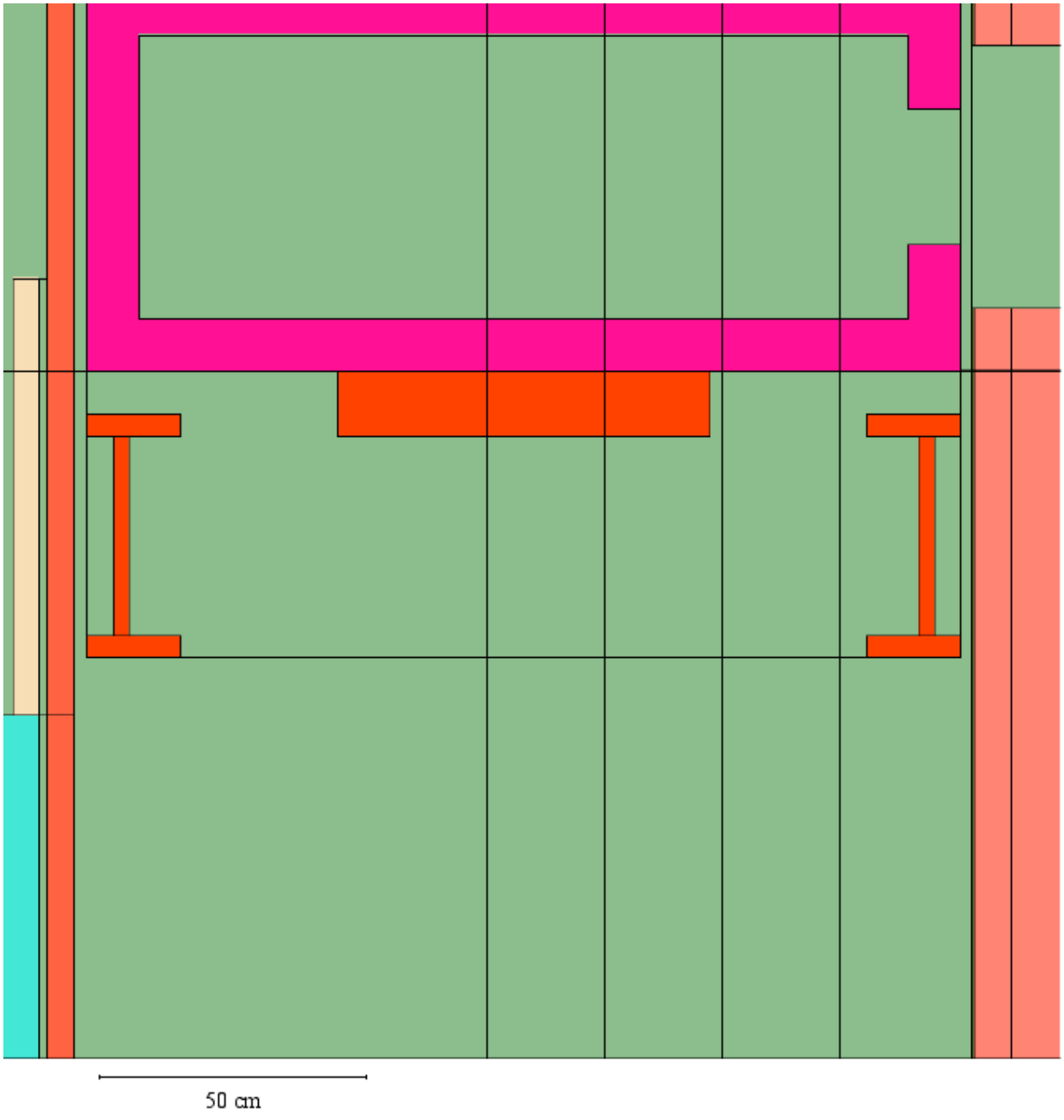

Fig. 101. Vertical cross-section of the heterogeneous lower support model of the steam generators through one of the “T” shaped beams.

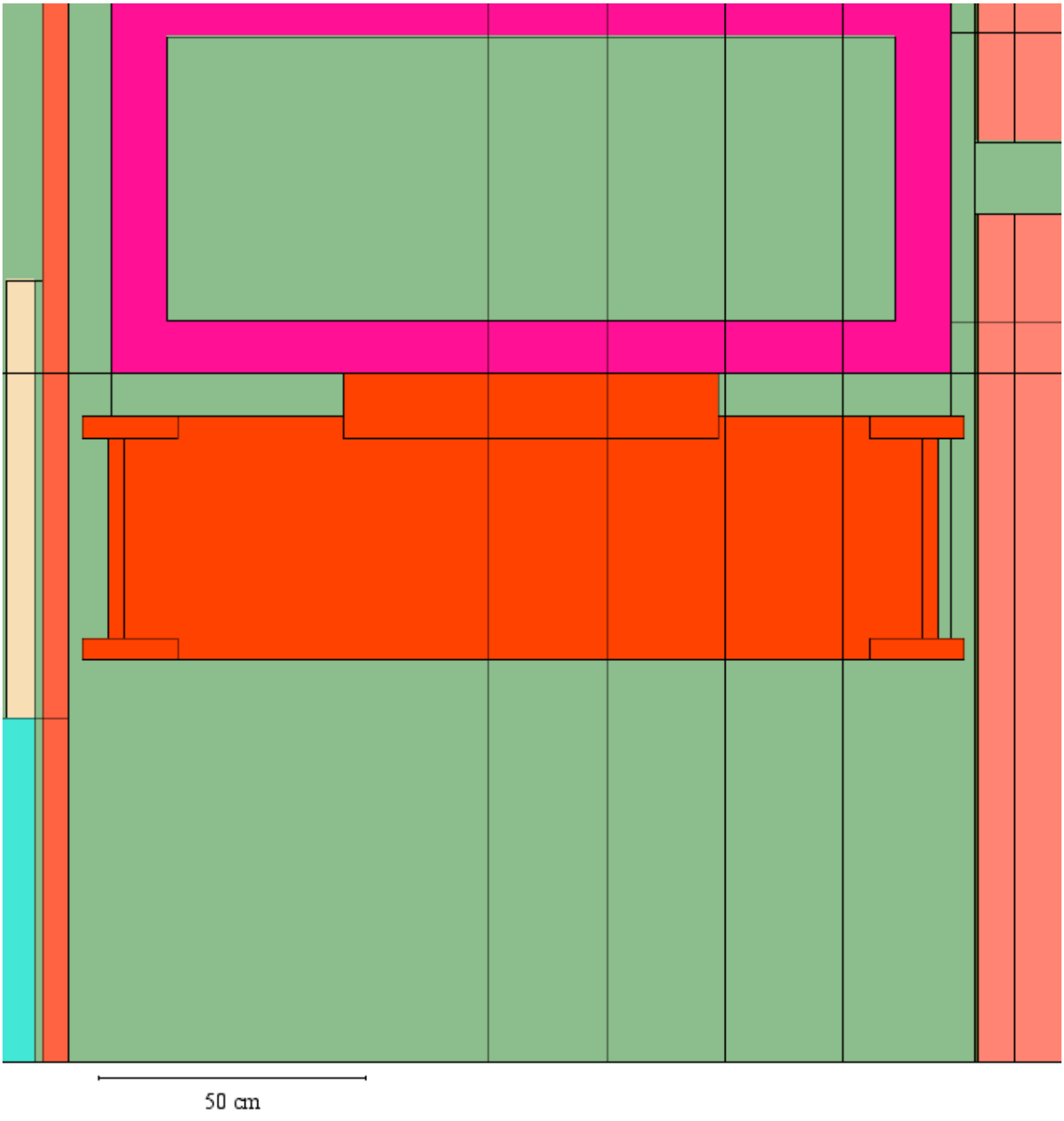

Figure 102. Horizontal cross-section of the heterogeneous lower support model of the steam generators through the lower end of the “I” shaped beams.

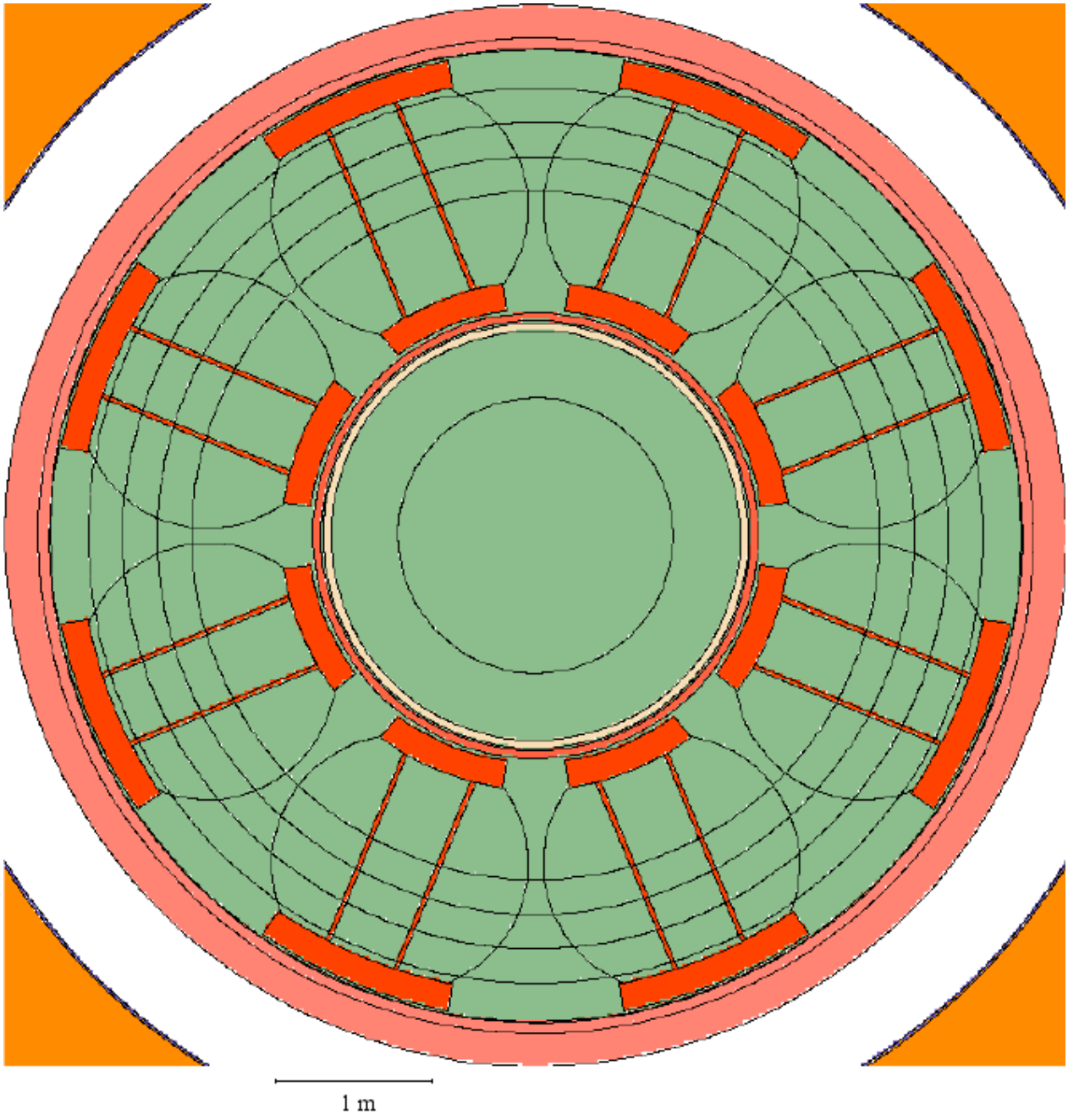

Figure 103. Horizontal cross-section of the heterogeneous lower support model of the steam generators through the middle of the “I” shaped beams.

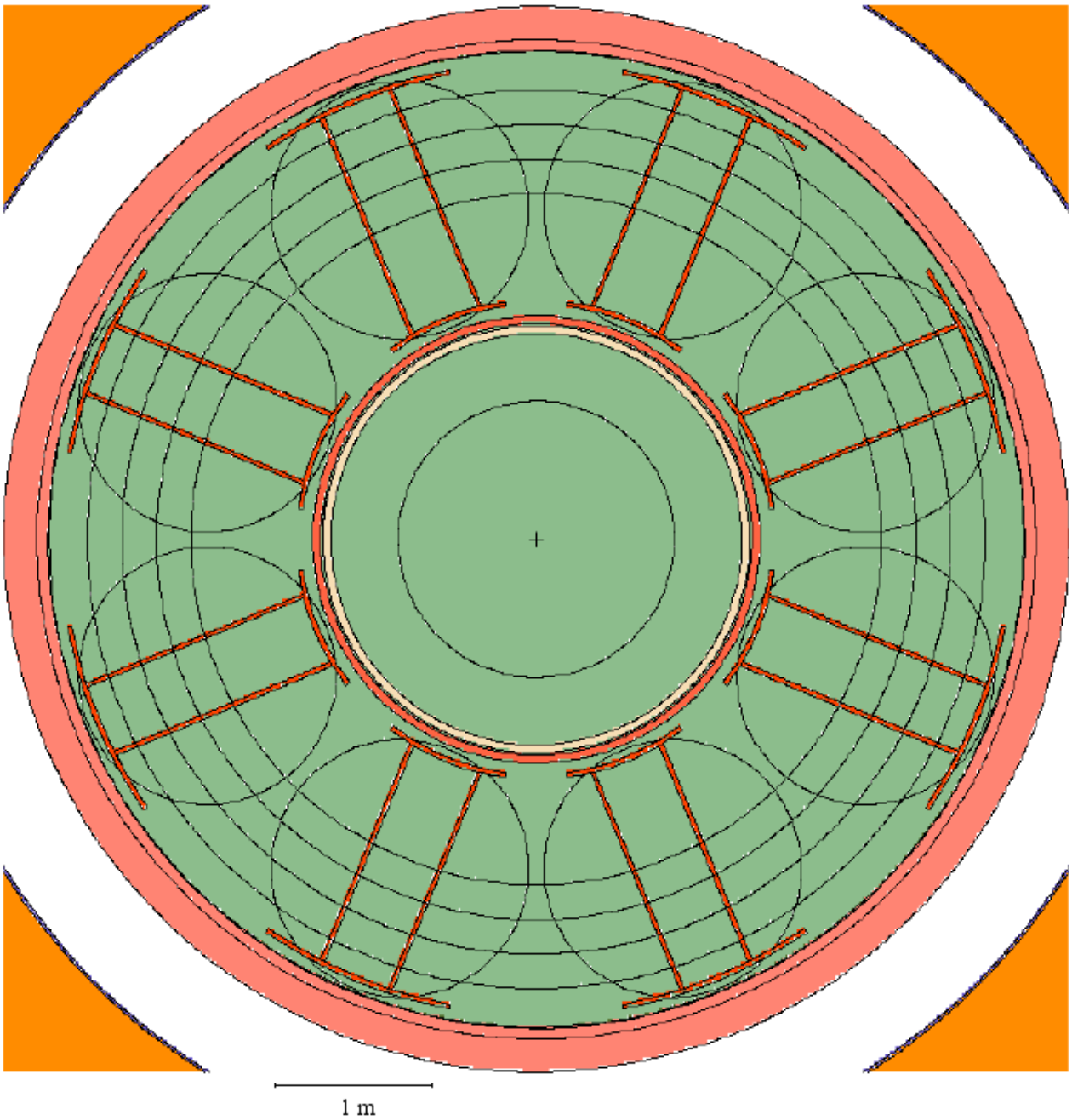

Figure 104. Horizontal cross-section of the heterogeneous lower support model of the steam generators through the upper end of the “I” shaped beams.

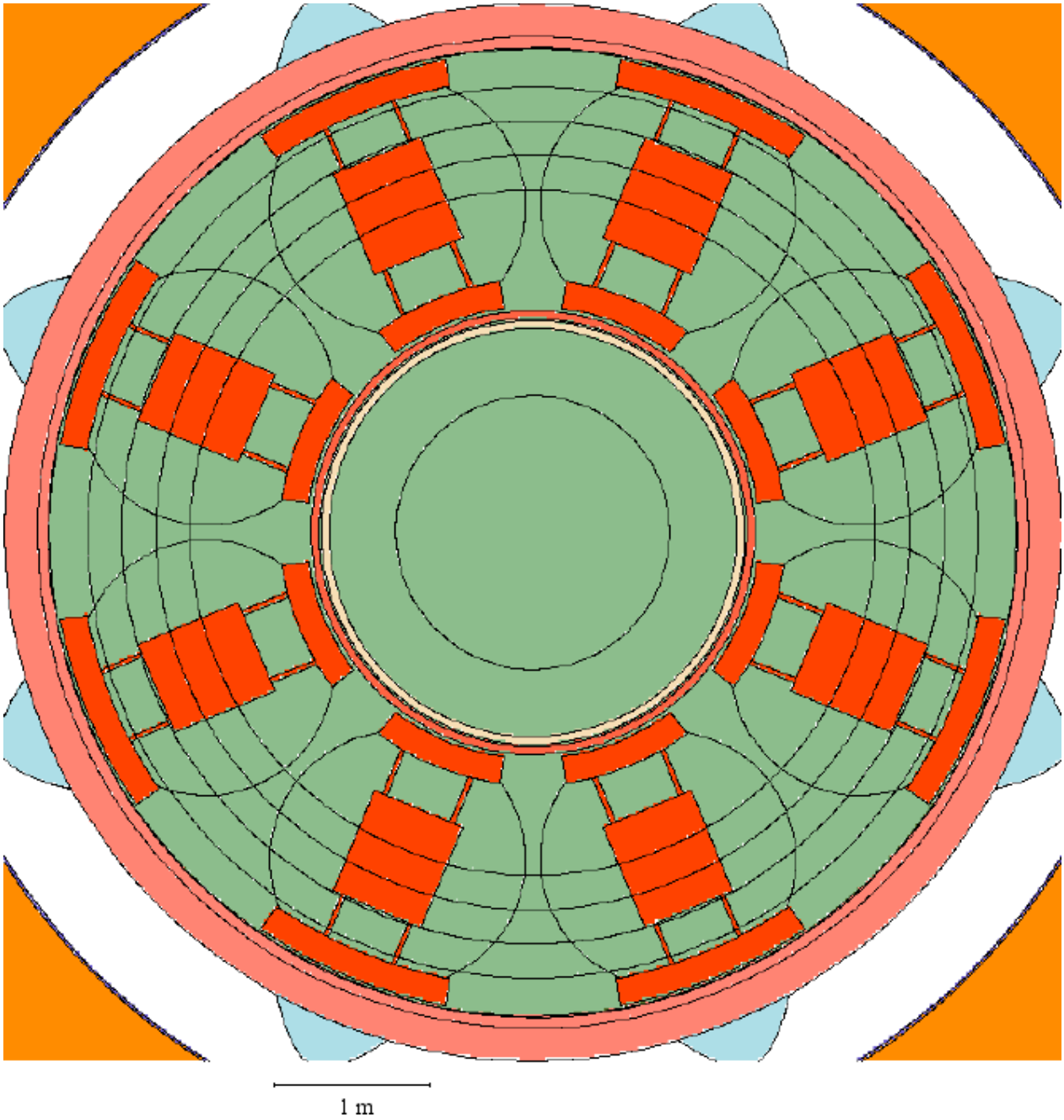

Figure 105. Horizontal cross-section of the heterogeneous lower support model of the steam generators between the “I” shaped beams and the lower header.

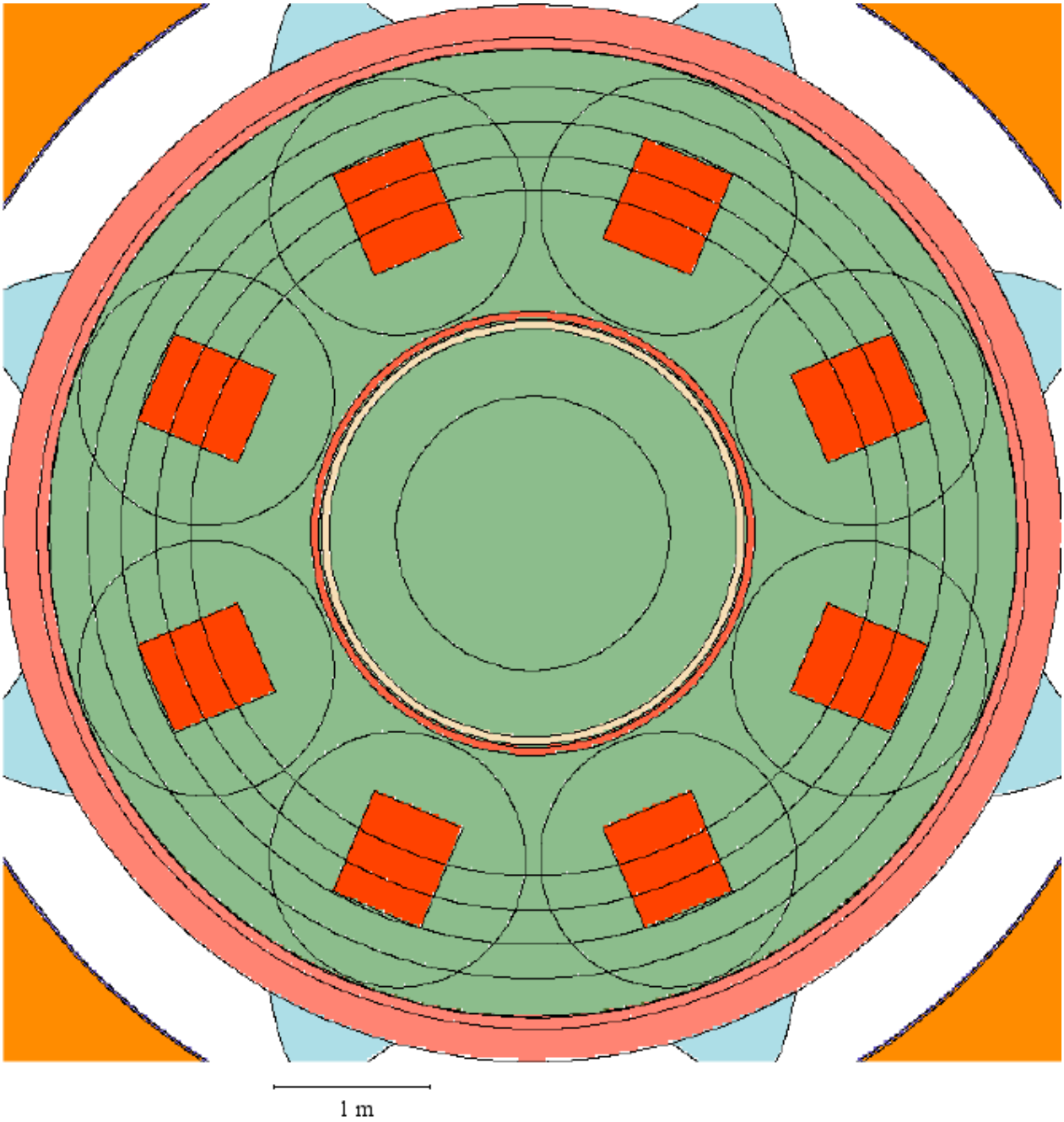

Figure 106. Vertical cross-section of the third model of the steam generators.

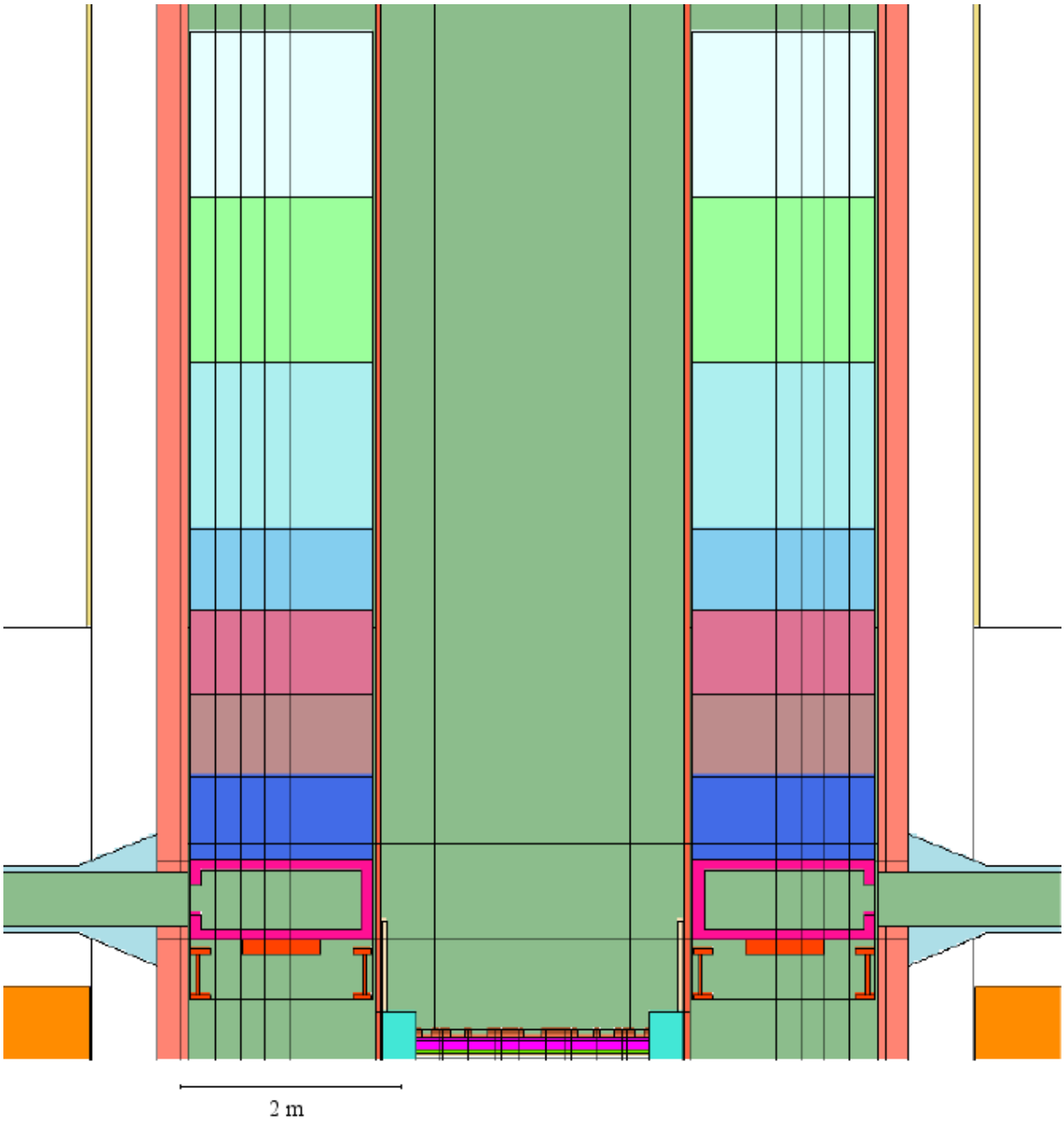

Figure 107. Vertical cross-section of the third model of the steam generators, off-centre of the steam generators, showing the delimitation (red line) between the two bypass water densities.

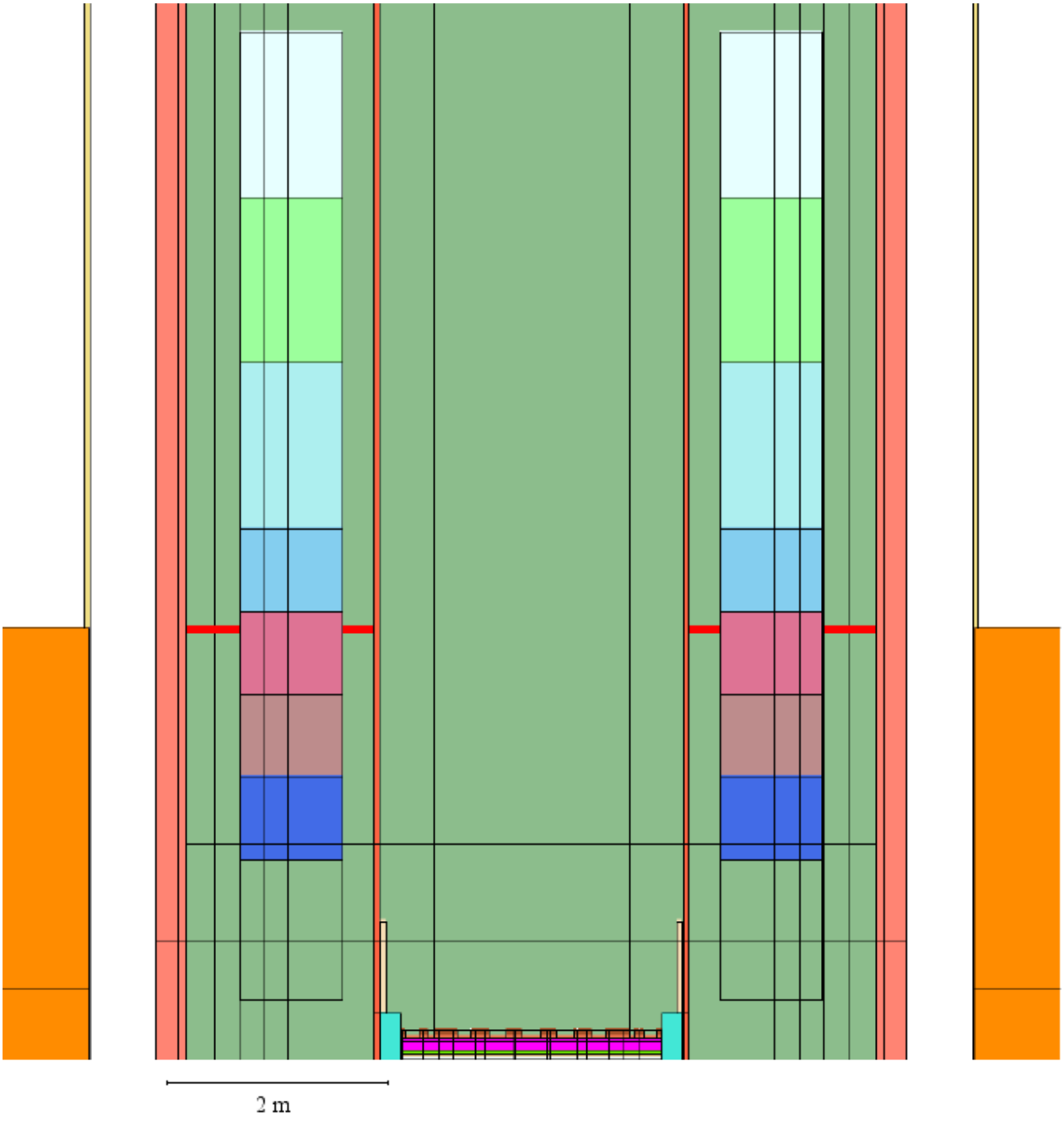

Fig. 108: Steam generator heterogeneous lower support and lower header: vertical section showing the segmentation of the “I” beams and “Centering Ring” model of the lower support for the spatial averaging of the neutron fluxes for the calculation of the activation source.

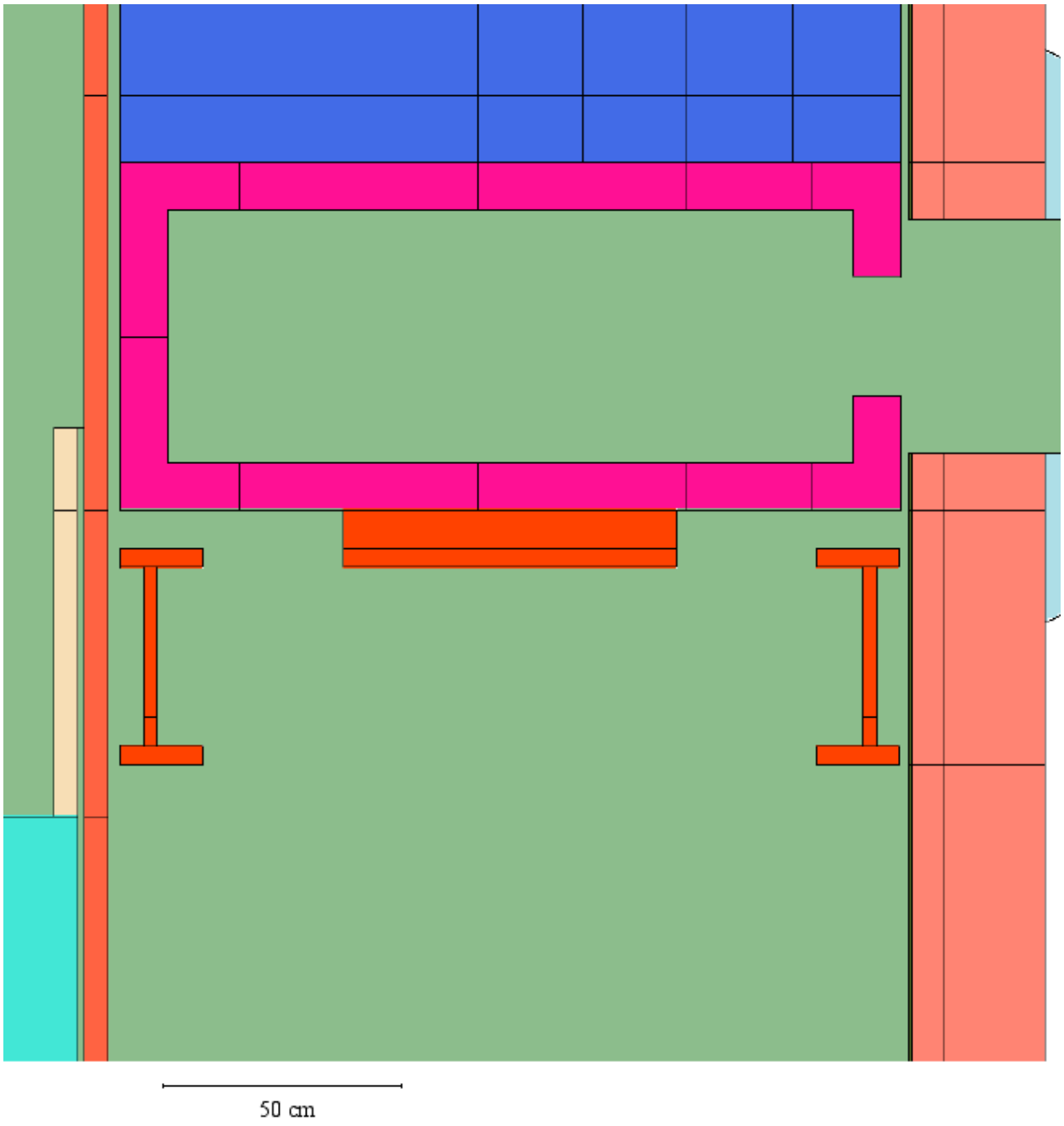

Fig. 109: Steam generator heterogeneous lower support and lower header: vertical section showing the segmentation of the “T” beams of the lower support for the spatial averaging of the neutron fluxes for the calculation of the activation source.

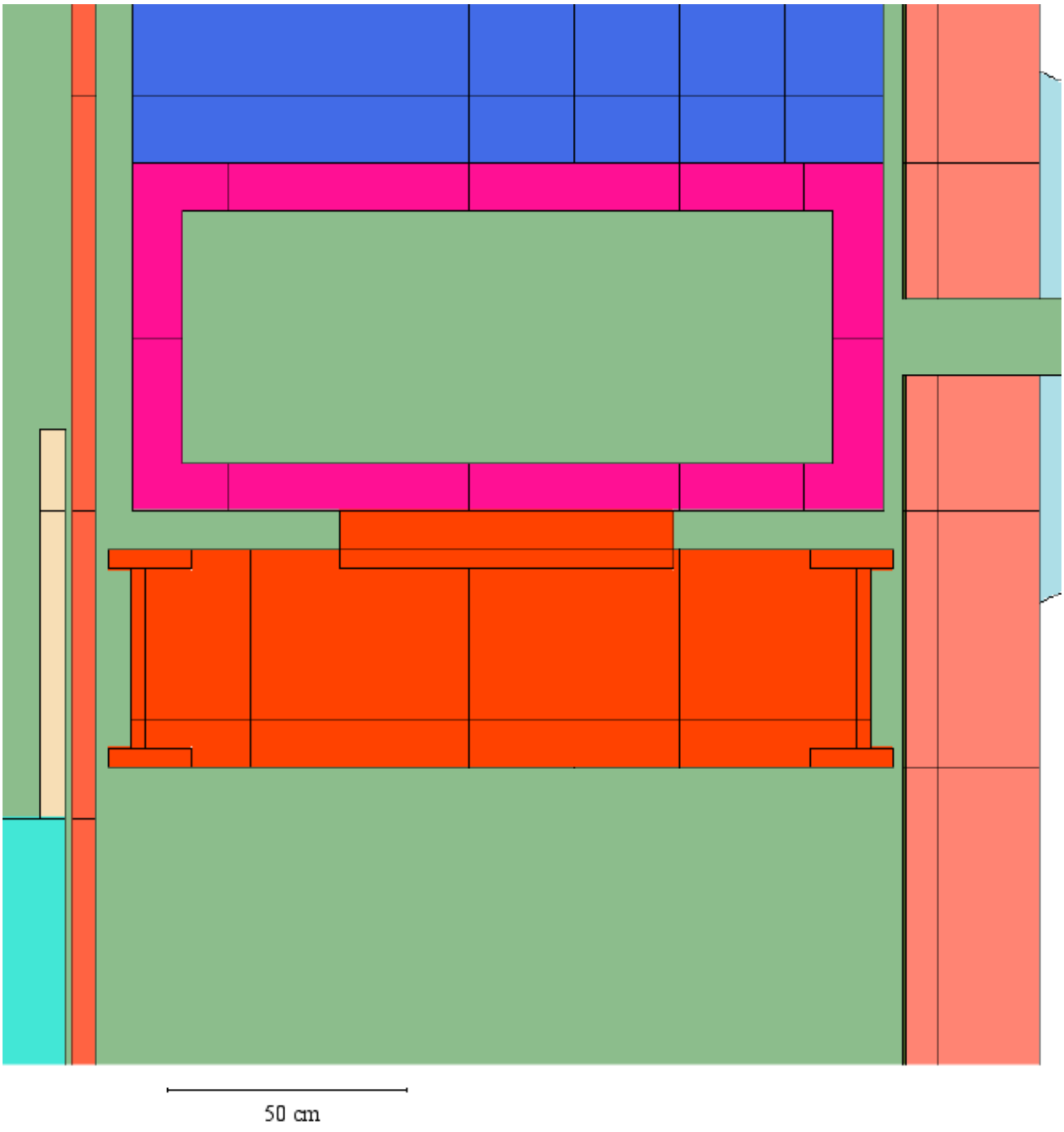

Fig. 110: Steam generator heterogeneous lower support: horizontal cross-section through the lower part of the “I” beams showing the segmentation for the spatial averaging of the neutron fluxes for the calculation of the activation source.

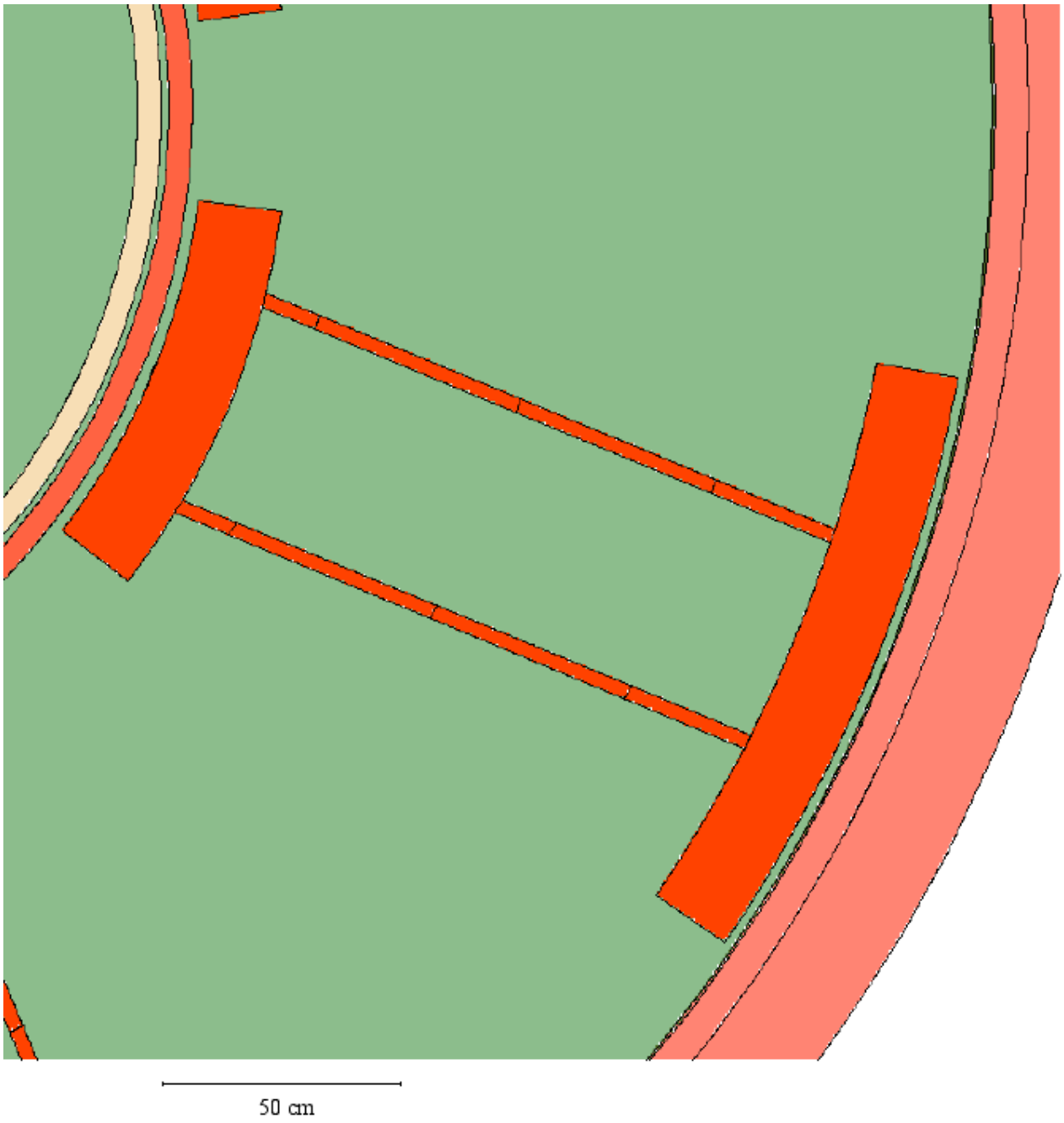

Fig. 111: Steam generator heterogeneous lower support: horizontal cross-section through the middle part of the “I” beams showing the segmentation for the spatial averaging of the neutron fluxes for the calculation of the activation source.

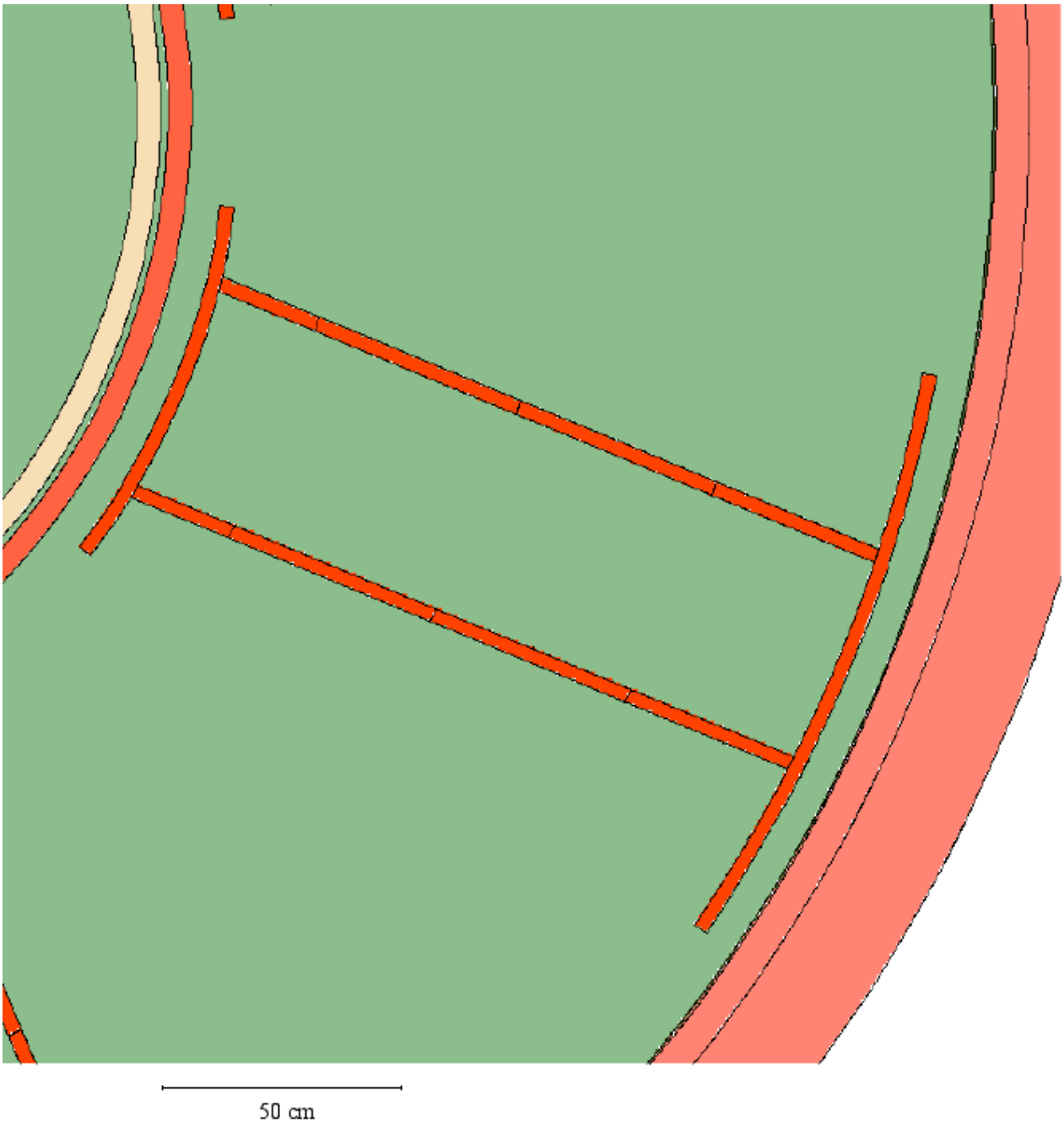

Fig. 112: Steam generator heterogeneous lower support: horizontal cross-section through the upper part of the “I” beams showing the segmentation for the spatial averaging of the neutron fluxes for the calculation of the activation source.

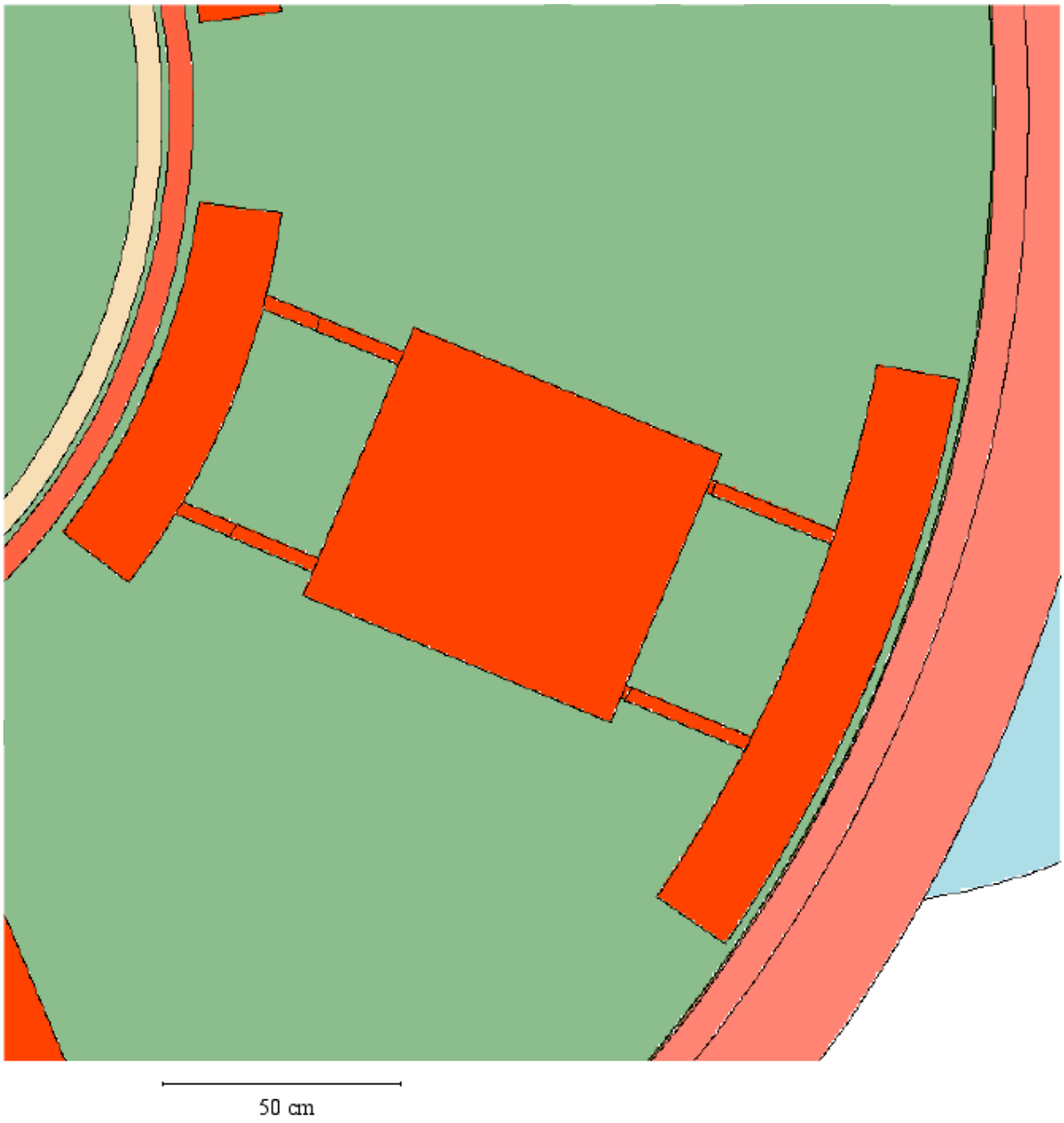

Fig. 113: Steam generator lower header: horizontal cross-section through the bottom wall showing the radial segmentation for the spatial averaging of the neutron fluxes for the calculation of the activation source.

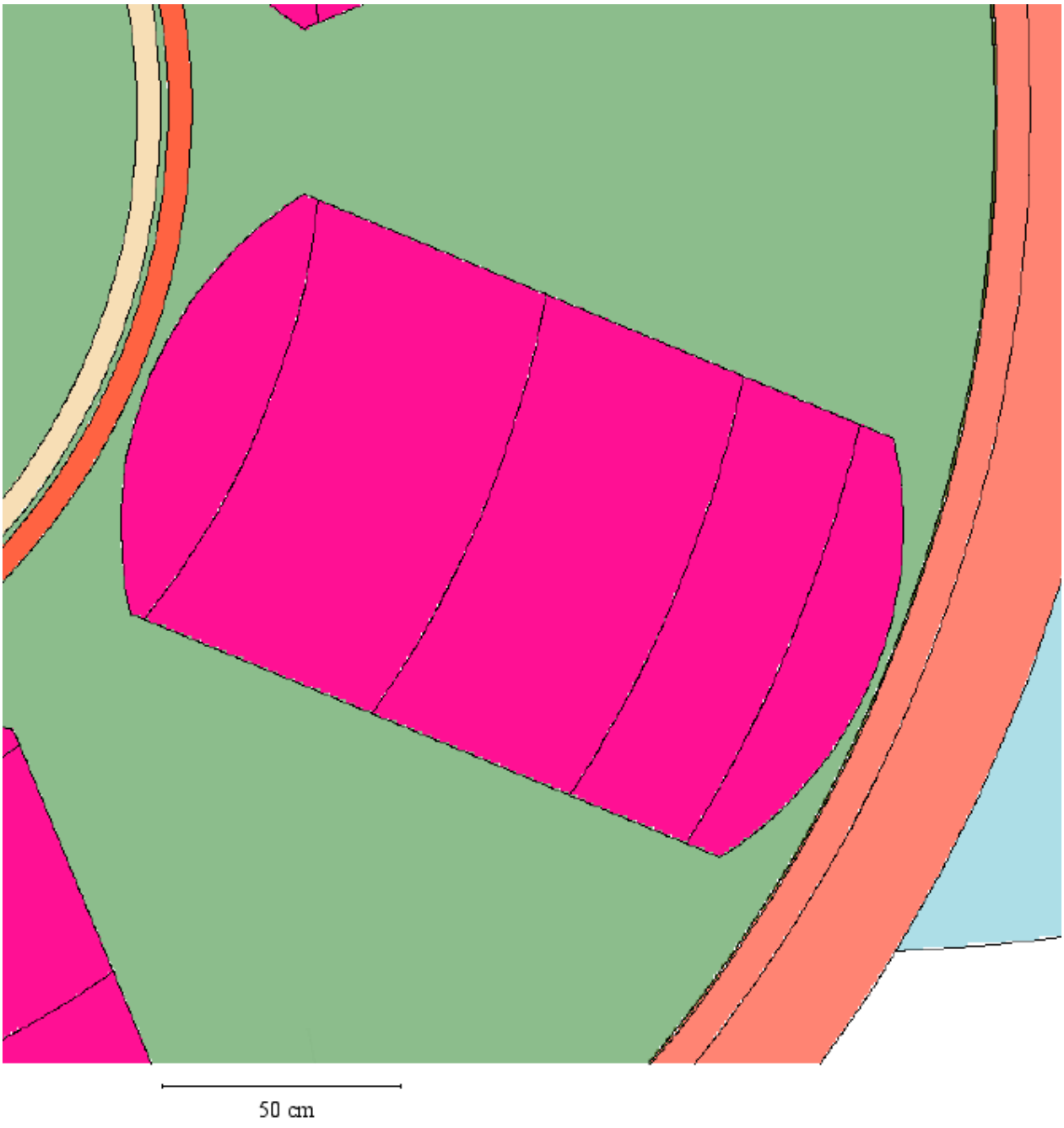

Fig. 114: Steam generator lower header: horizontal cross-section through the lower part showing the radial segmentation for the spatial averaging of the neutron fluxes for the calculation of the activation source.

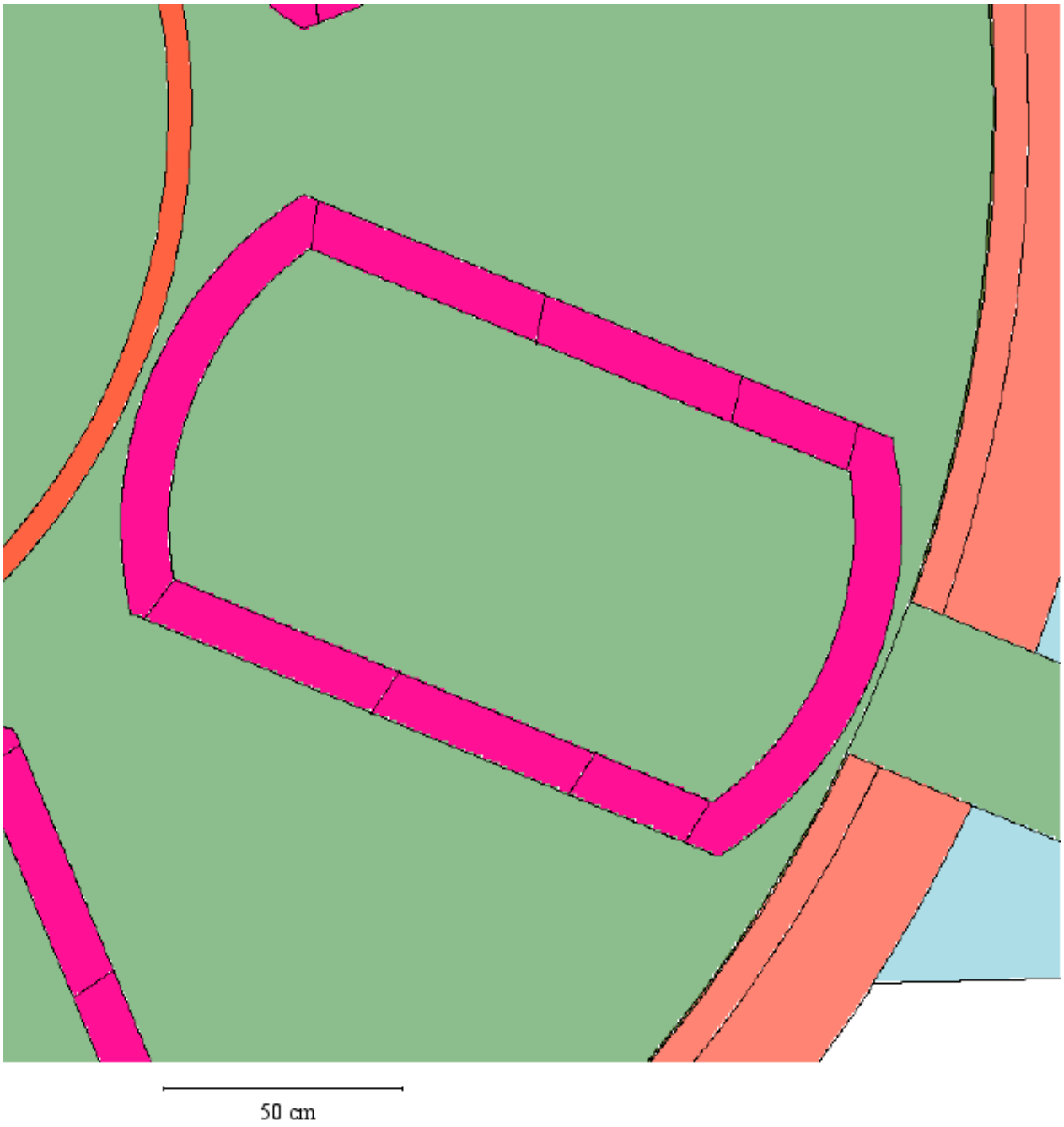

Fig. 115: Steam generator lower header: horizontal cross-section through the middle part showing the radial segmentation for the spatial averaging of the neutron fluxes for the calculation of the activation source.

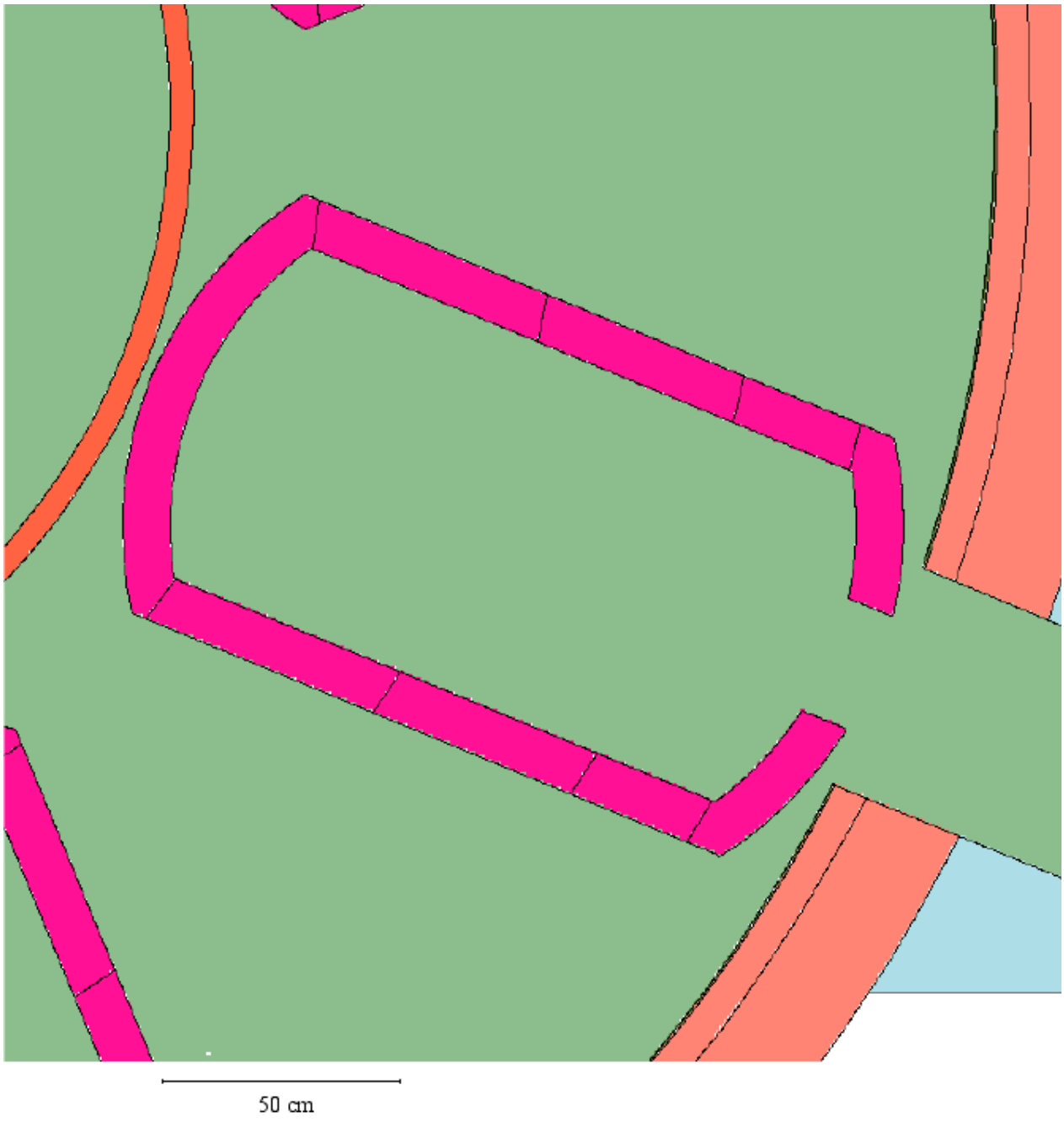

Figure 116. Including steam generators (third model), heterogeneous steam generator supports, explicit steam generator bottom header, ANSALDO data for the inlet nozzles and with 25 m diameter vessel: vertical section through the inlet nozzles (with nozzle tube walls and flanges) up to containment vessel in direction ESE-WNW showing the LGMS tank “B”.

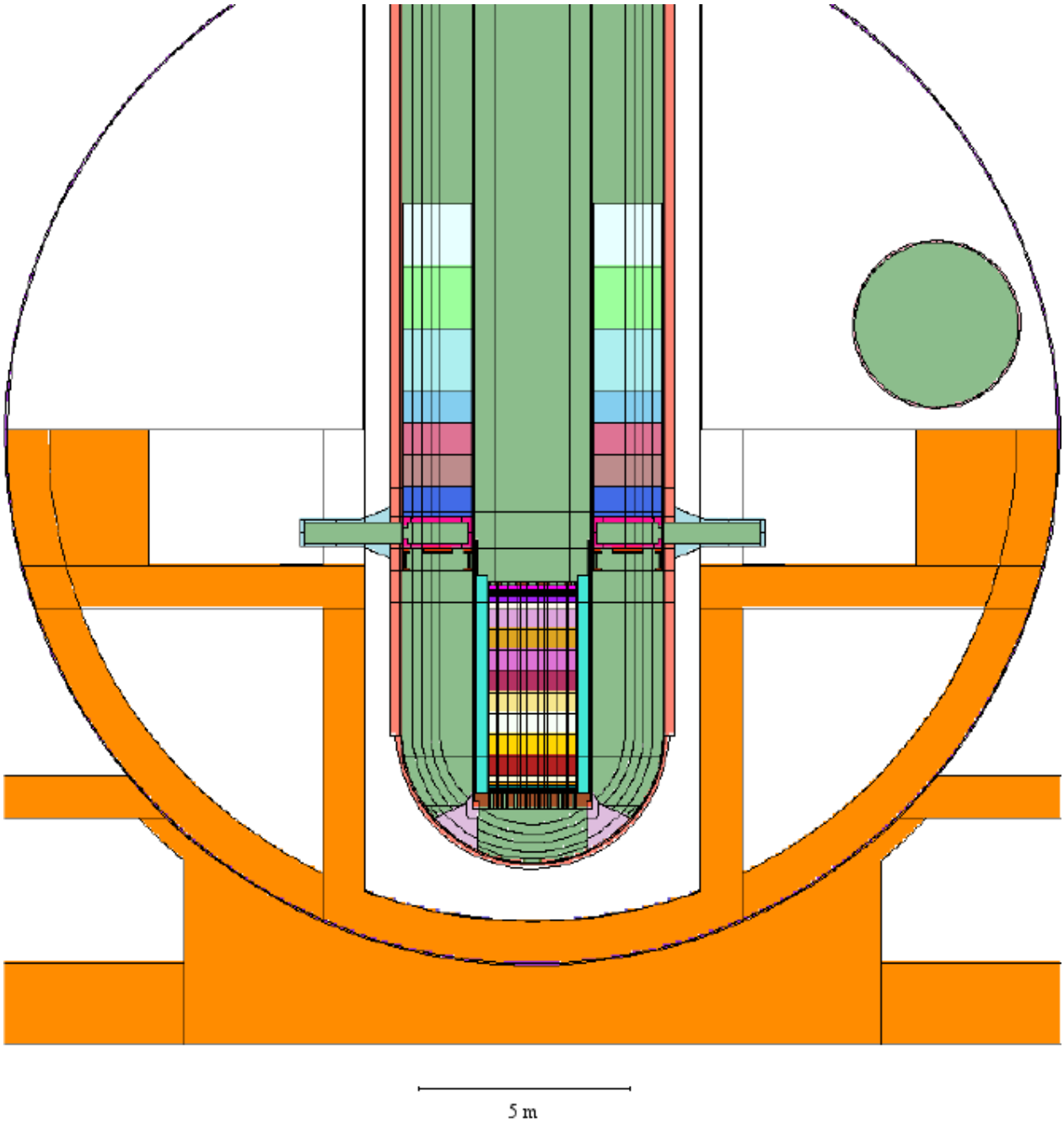

Figure 117. With 25 m diameter vessel: vertical section up to containment vessel in direction SW-NE showing the EBT “B” and LGMS tank “A”.

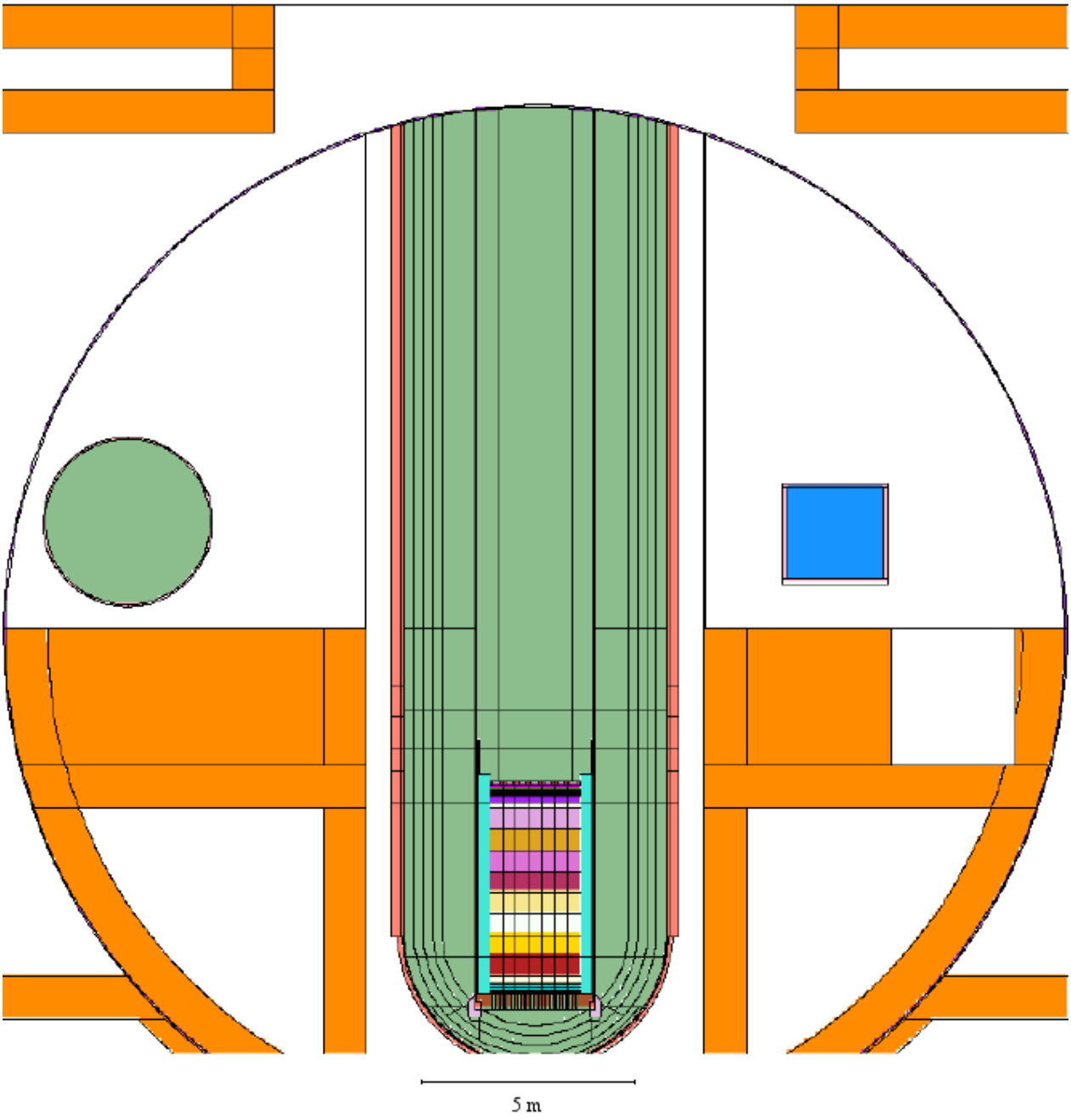

Figure 118. With 25 m diameter vessel: vertical section up to containment vessel in direction W-E showing the ADS Quench tank.

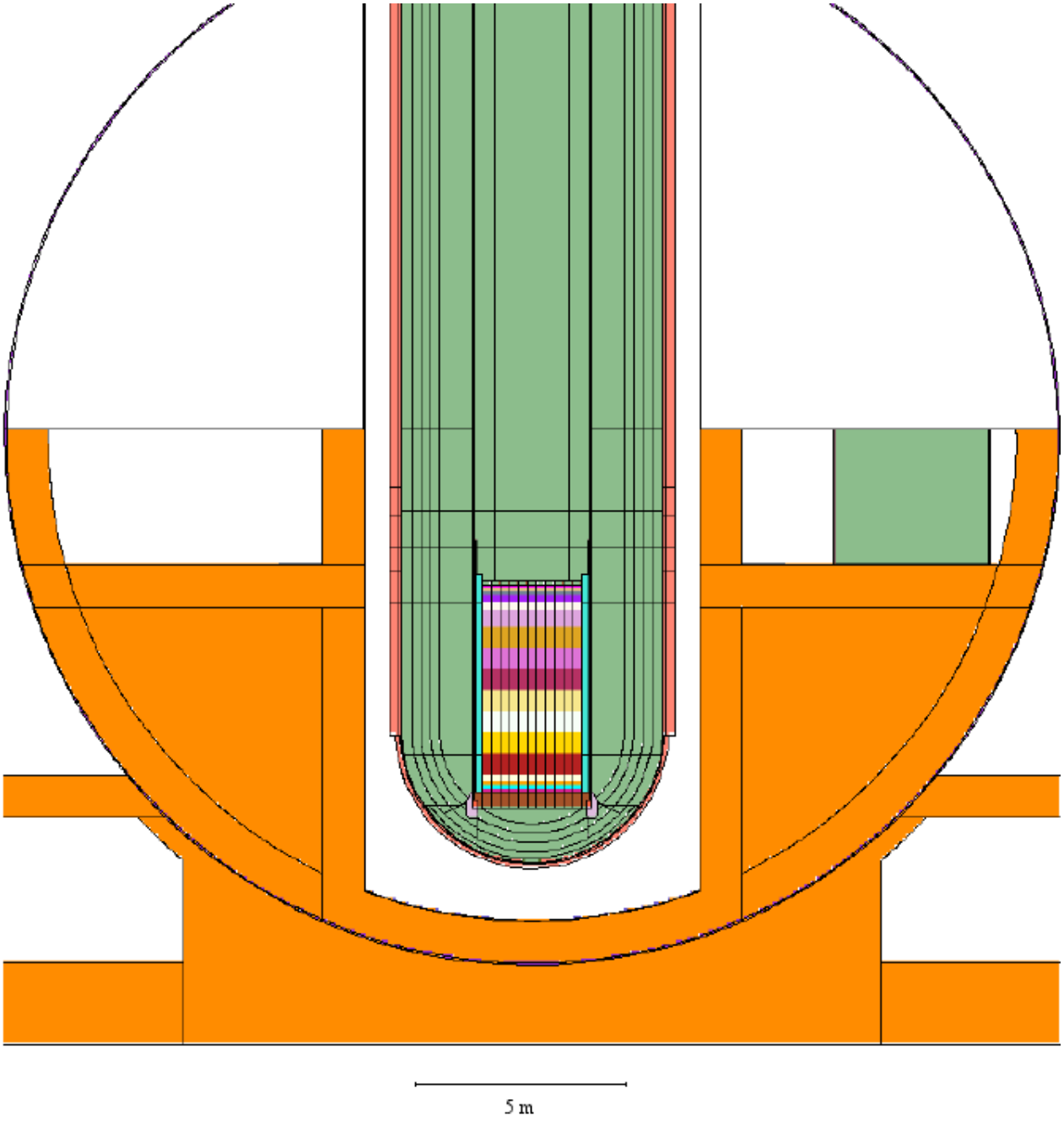

Fig. 119. Including steam generators (third model) and with 25 m diameter vessel: horizontal section up to containment vessel at level of LGMS tanks midplane showing the two LGMS tanks and the two EBT's.

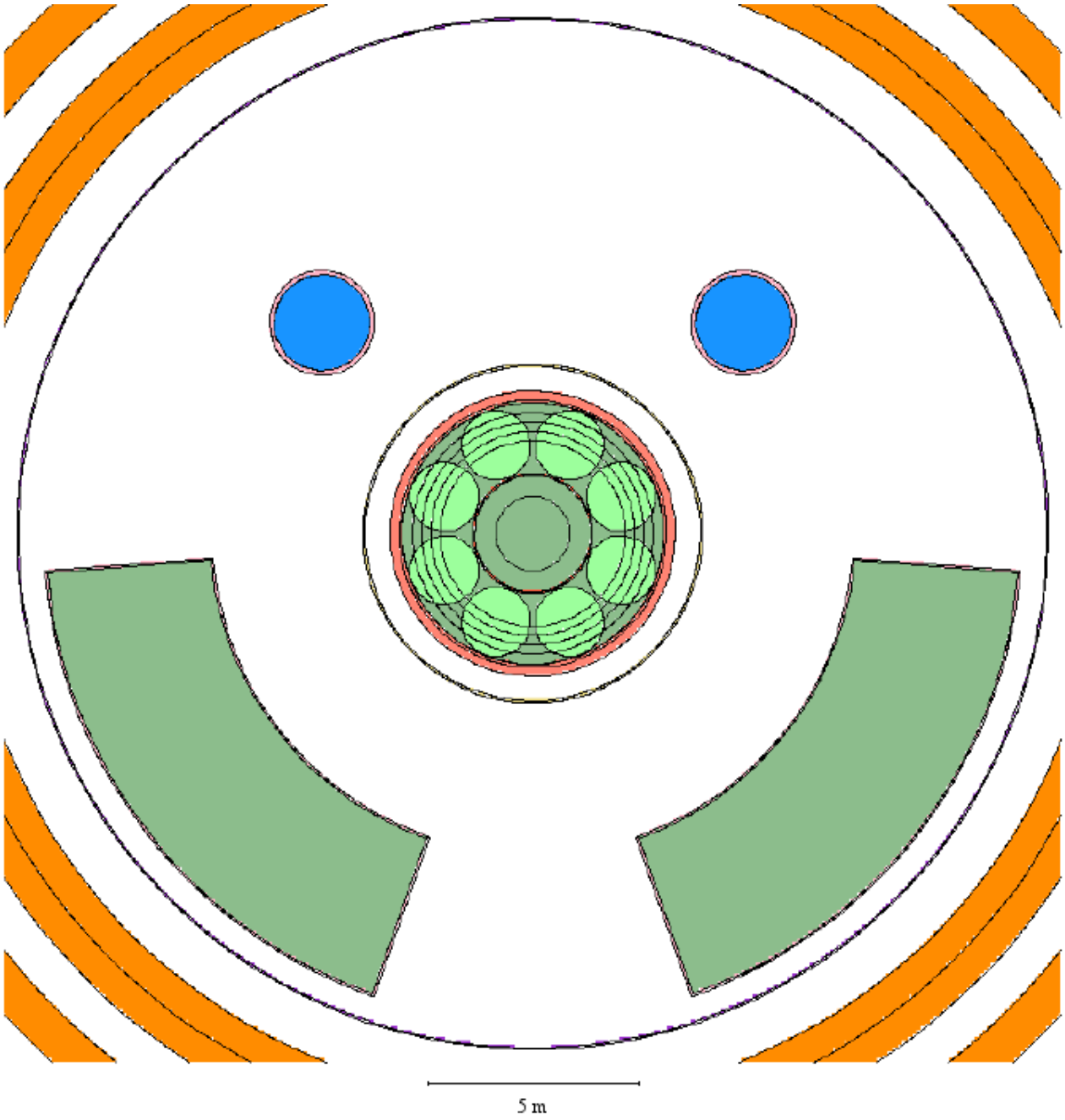

Fig. 120. Including explicit steam generator bottom header, ANSALDO data for the inlet nozzles and with 25 m diameter vessel: horizontal section through the inlet nozzles (with nozzle tube walls and flanges) up to containment vessel showing the ADS Quench tank.

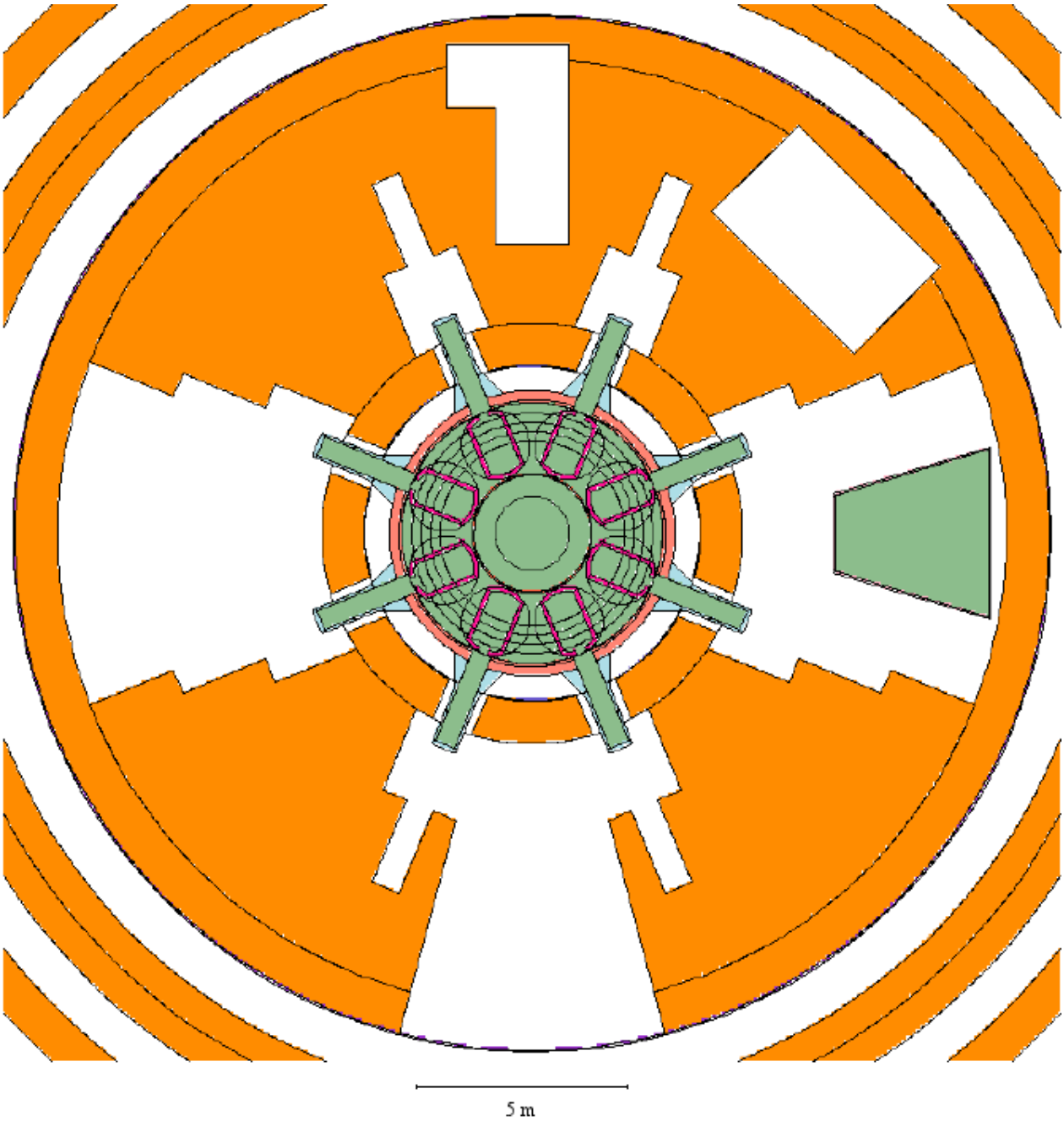

Fig. 121. Three horizontal sections of the ADS Quench tank: just below the top (above), at the inlet nozzles (middle) and just above the base (below).

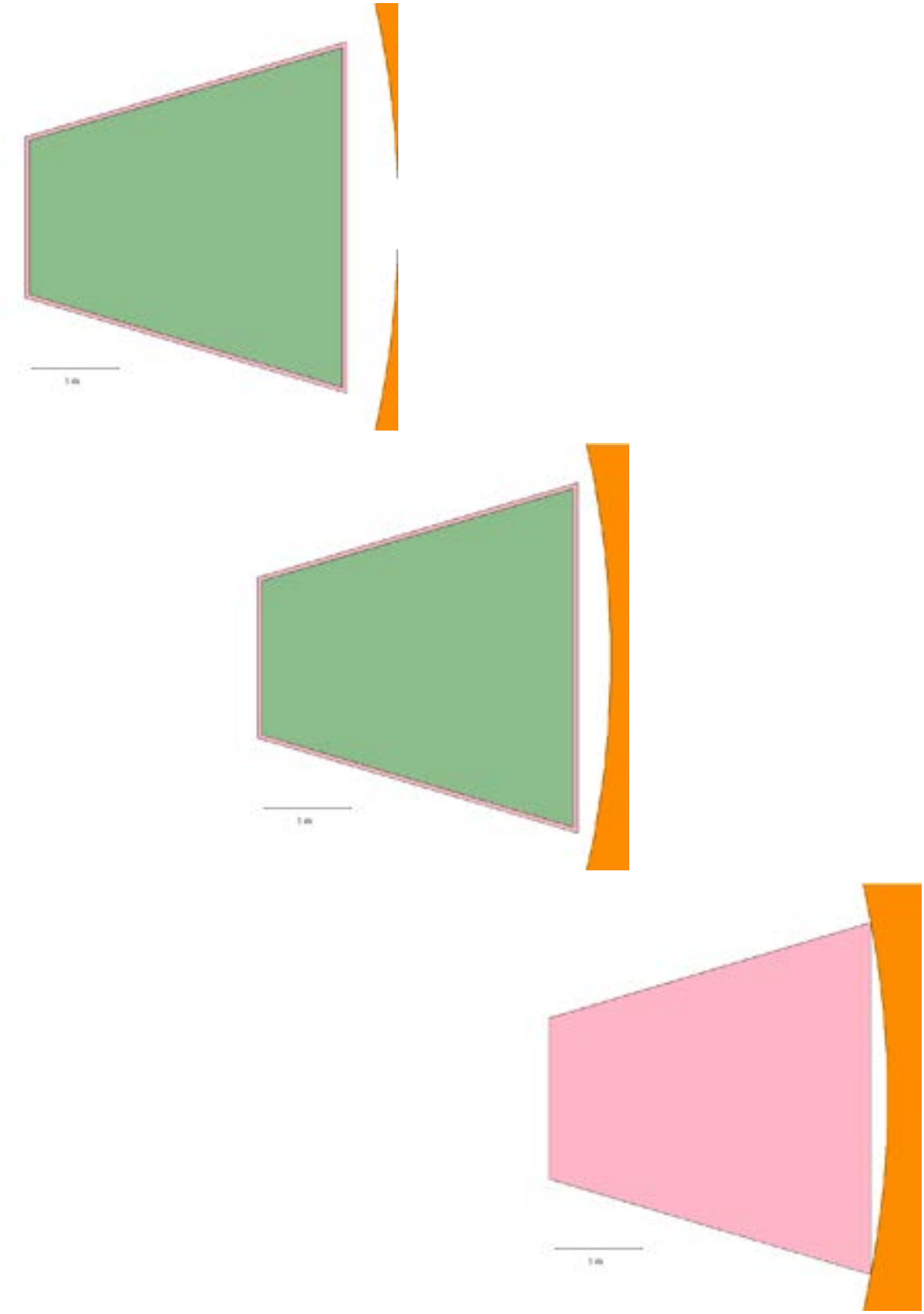

Fig. 122. Including steam generators (third model) and with 25 m diameter vessel: horizontal section up to containment vessel at level of main deck showing the modeled gratings.

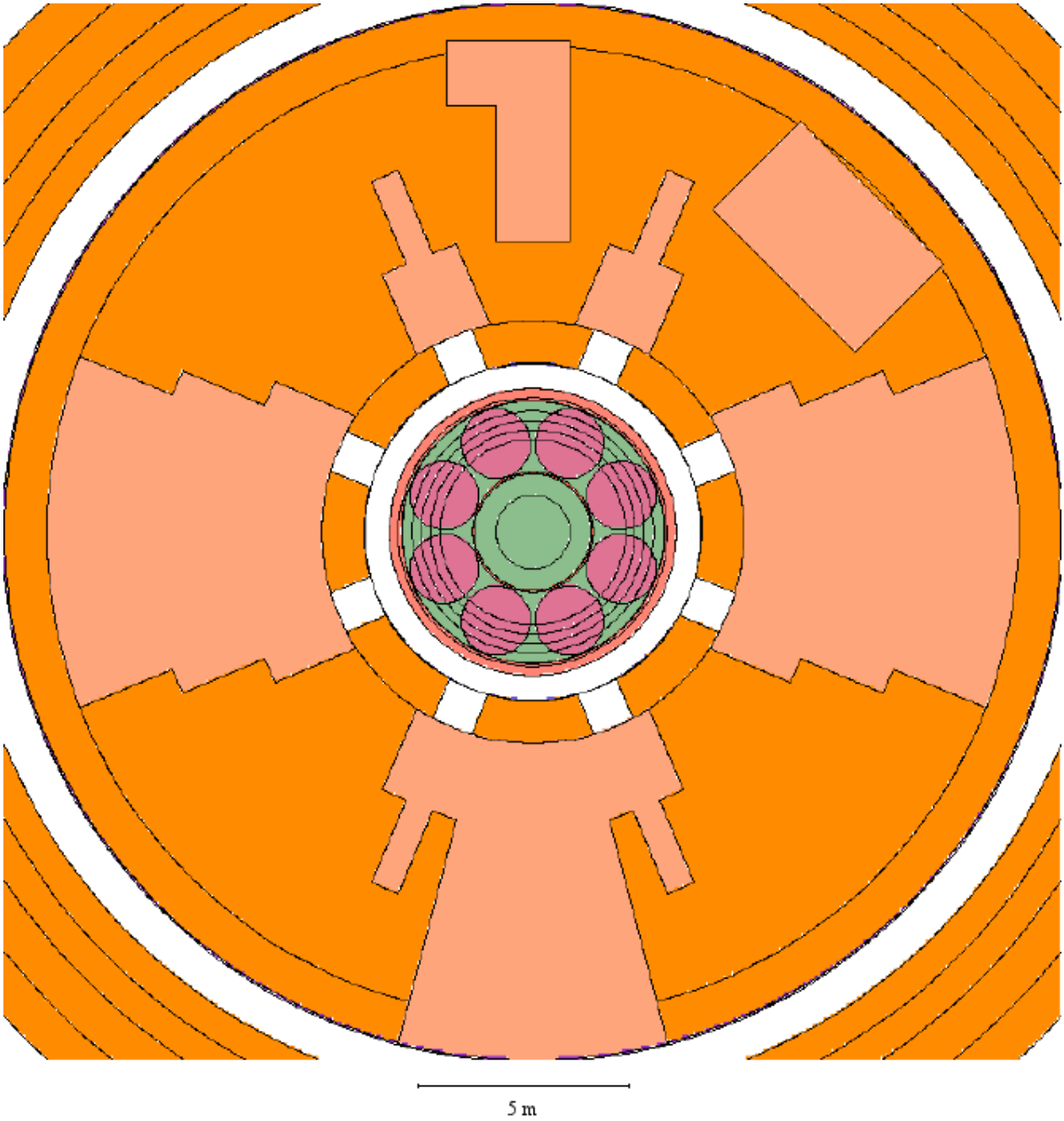

Fig. 123. Including heterogeneous steam generator supports and with 25 m diameter vessel: horizontal section up to containment vessel at level of floor of cavities under main deck showing the steel part of the water pipe model (and the bottom of the ADS quench tank).

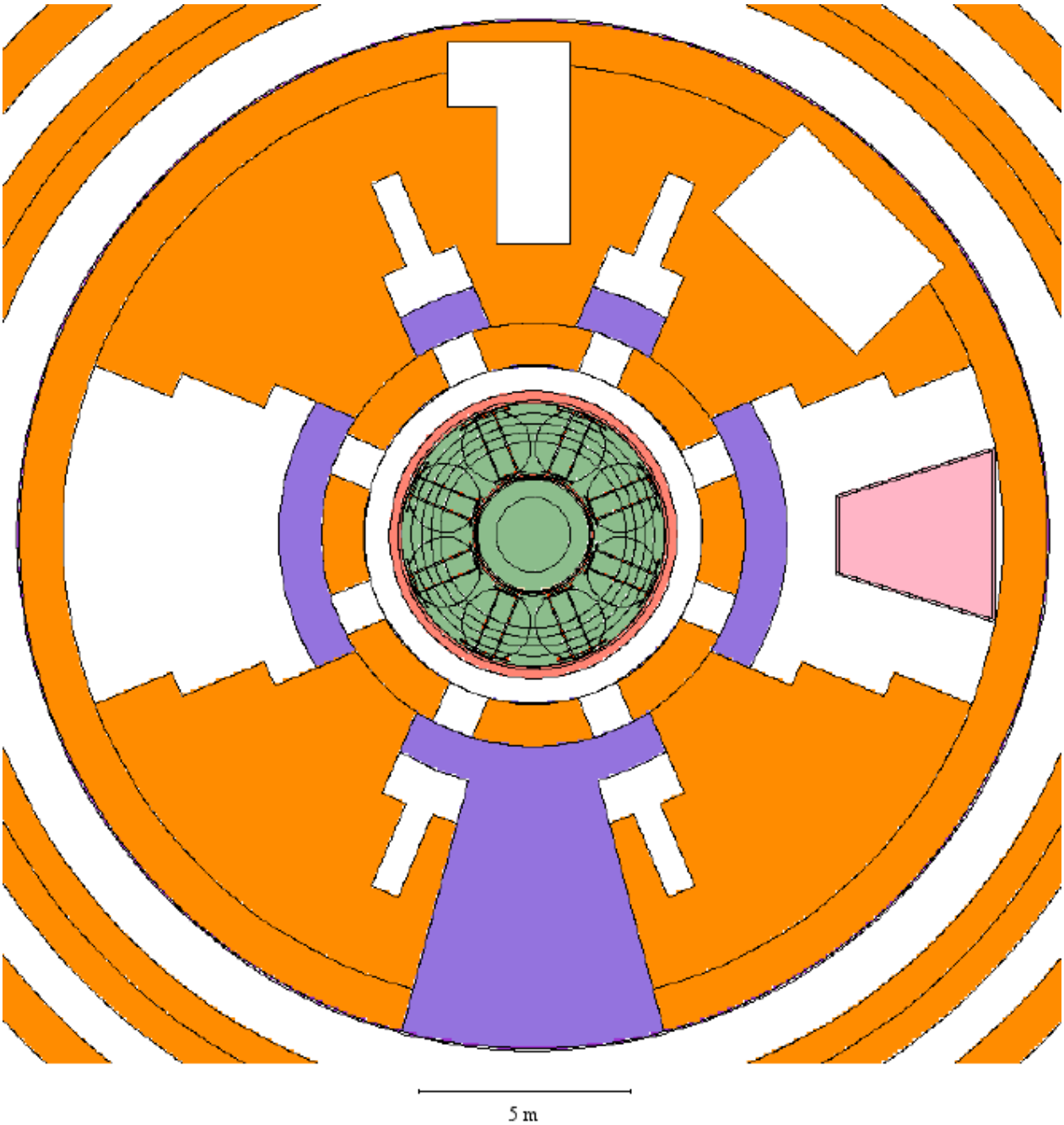

Fig. 124. Vertical section in the ENE direction of the water pipe sandwich model.

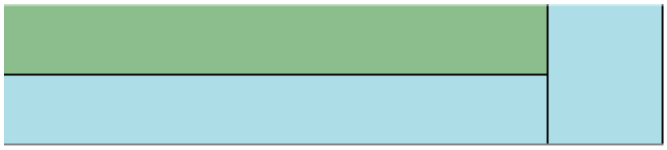

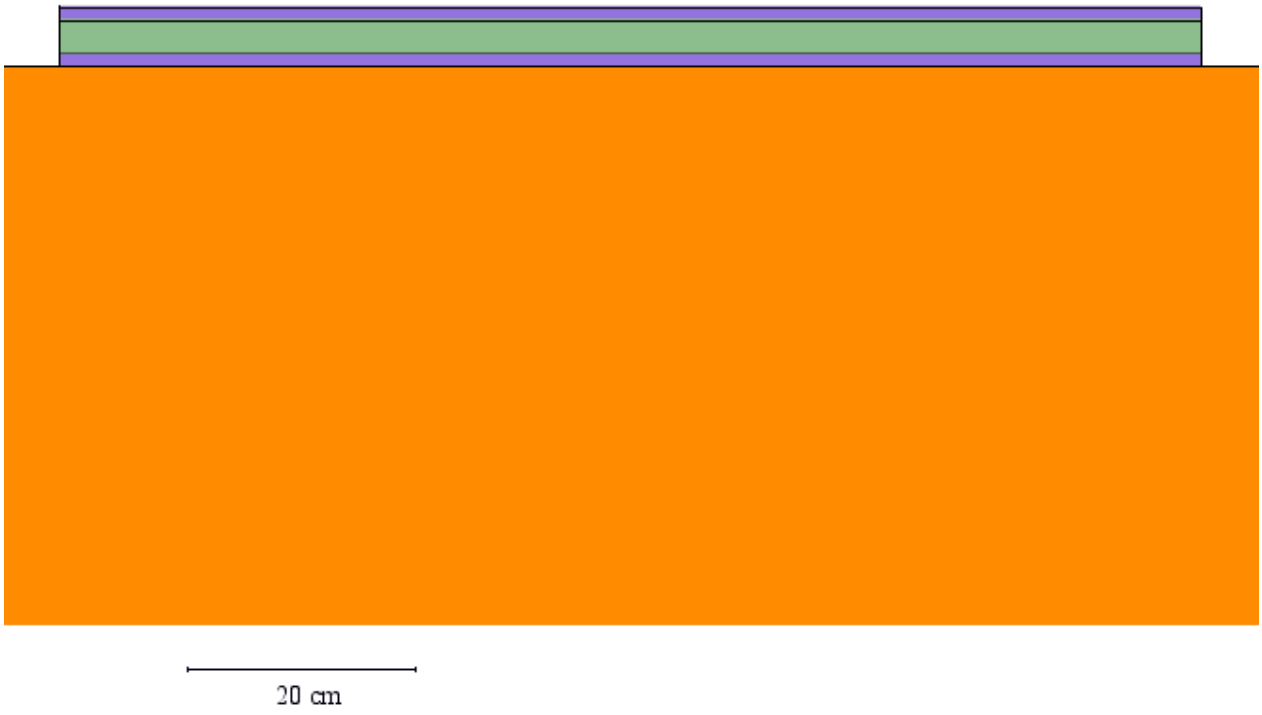

Fig. 125. Horizontal section of one inlet nozzle showing the segmentation for the spatial averaging of the neutron fluxes for the calculation of the activation source.

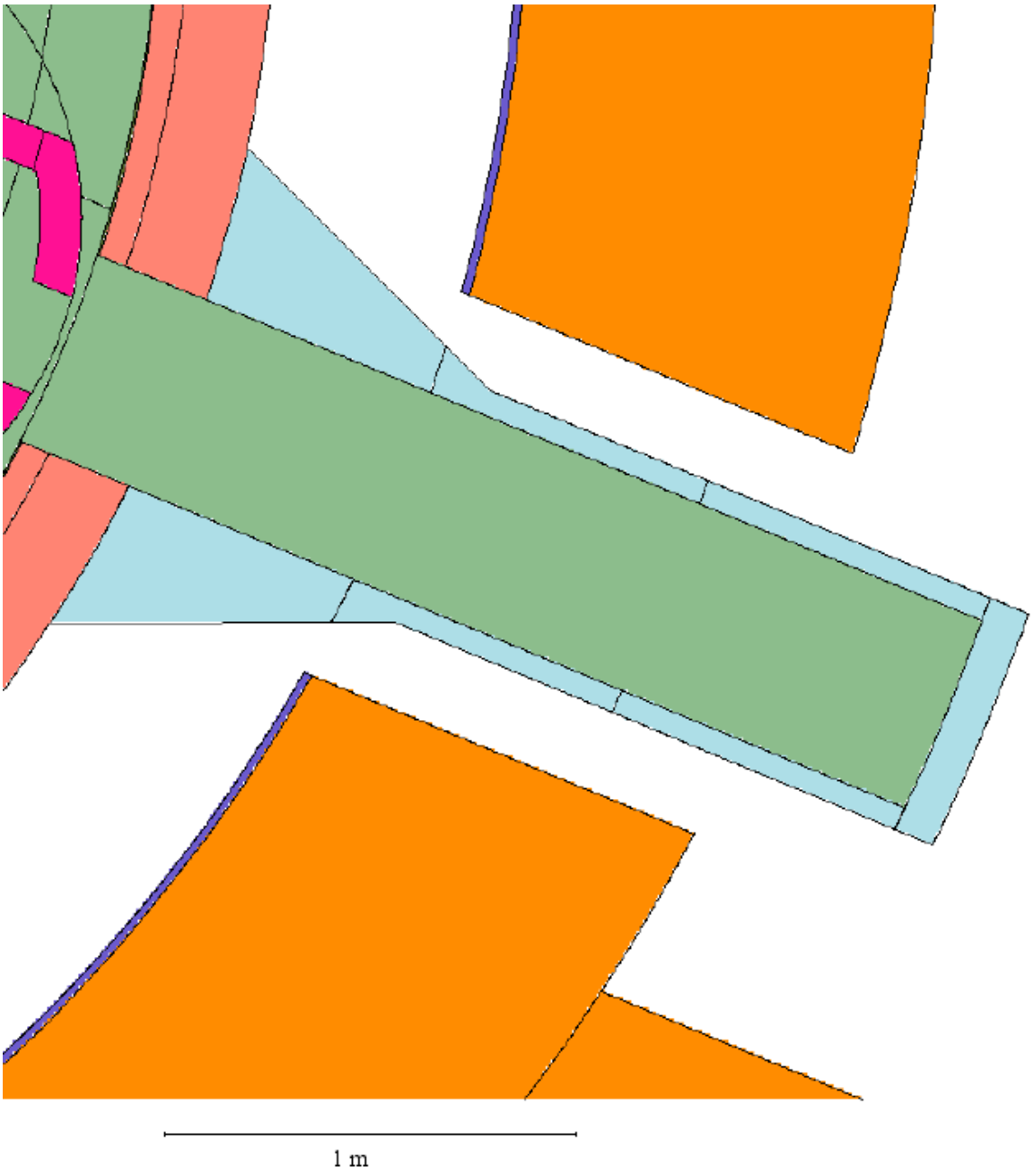

Fig. 126. Vertical section of one inlet nozzle showing the segmentation for the spatial averaging of the neutron fluxes for the calculation of the activation source.

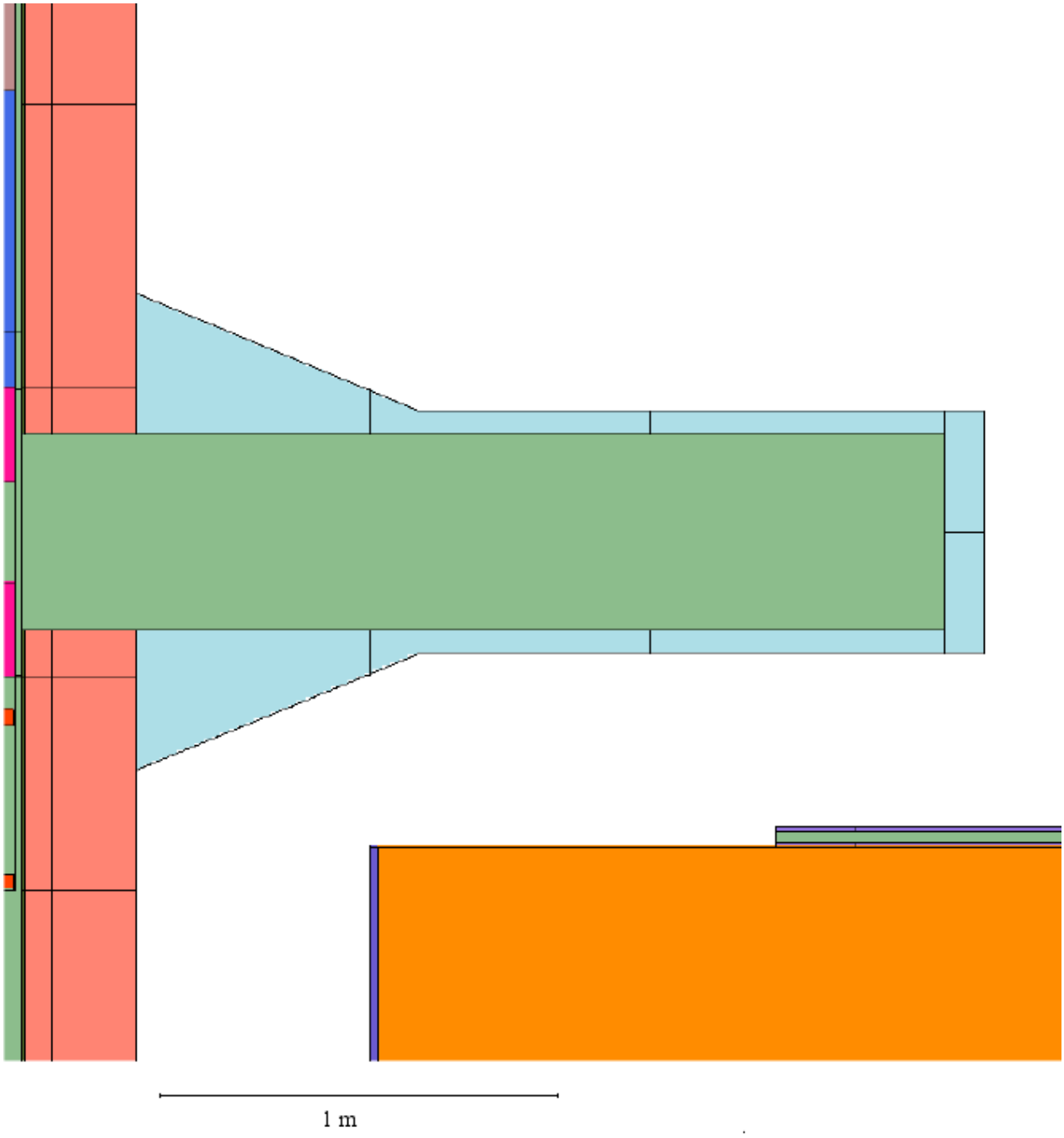

Fig. 127. Vertical section of one inlet nozzle showing the segmentation into an upper and lower part for the spatial averaging of the neutron fluxes for the calculation of the activation source.

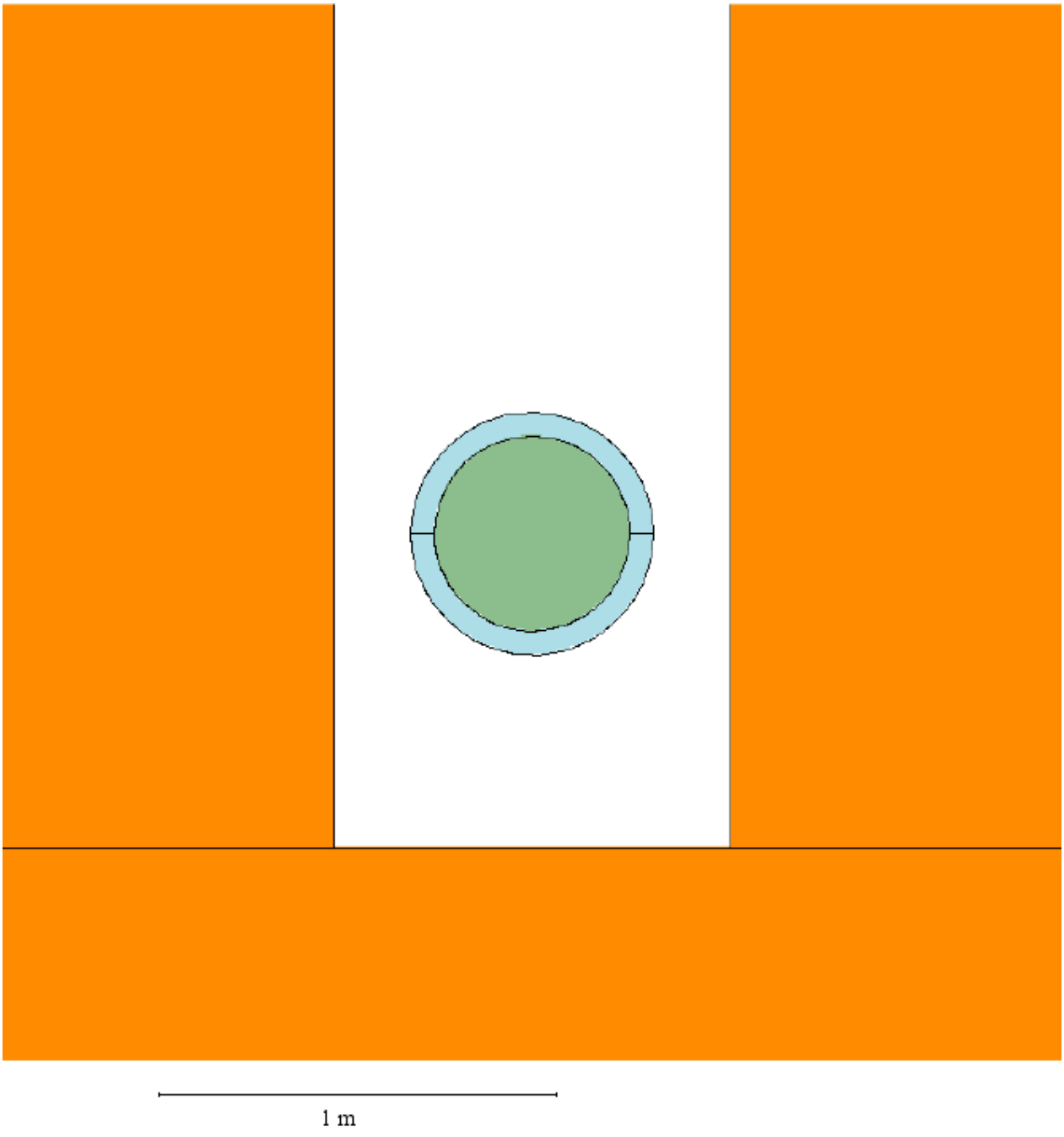

Fig. 128. Segmentation of the anti-missile shield for the spatial averaging of the neutron fluxes for the calculation of the activation source (red lines denote segment delimitation).

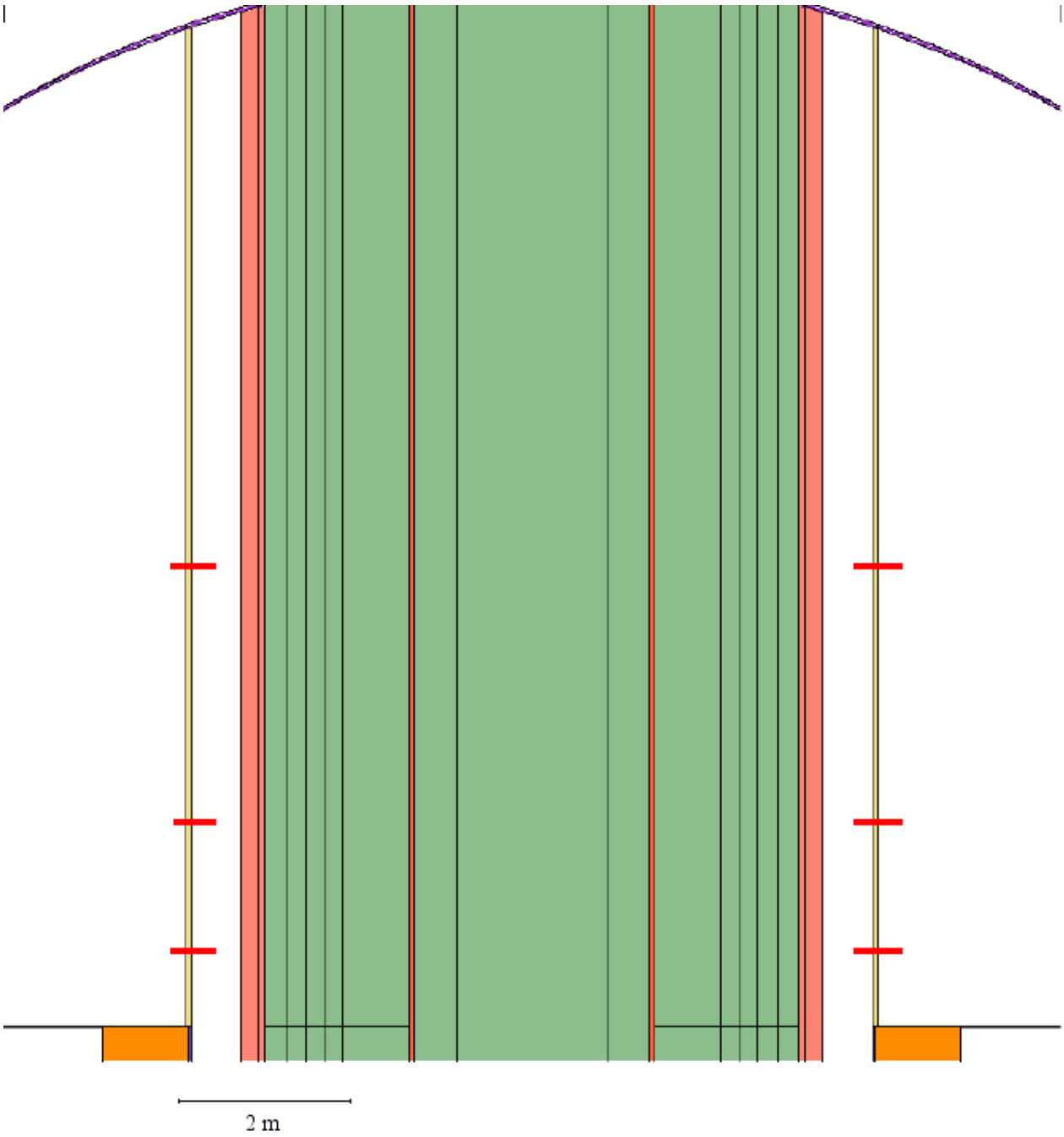

Fig. 129. Segmentation of the water pipe model for the spatial averaging of the neutron fluxes for the calculation of the activation source.

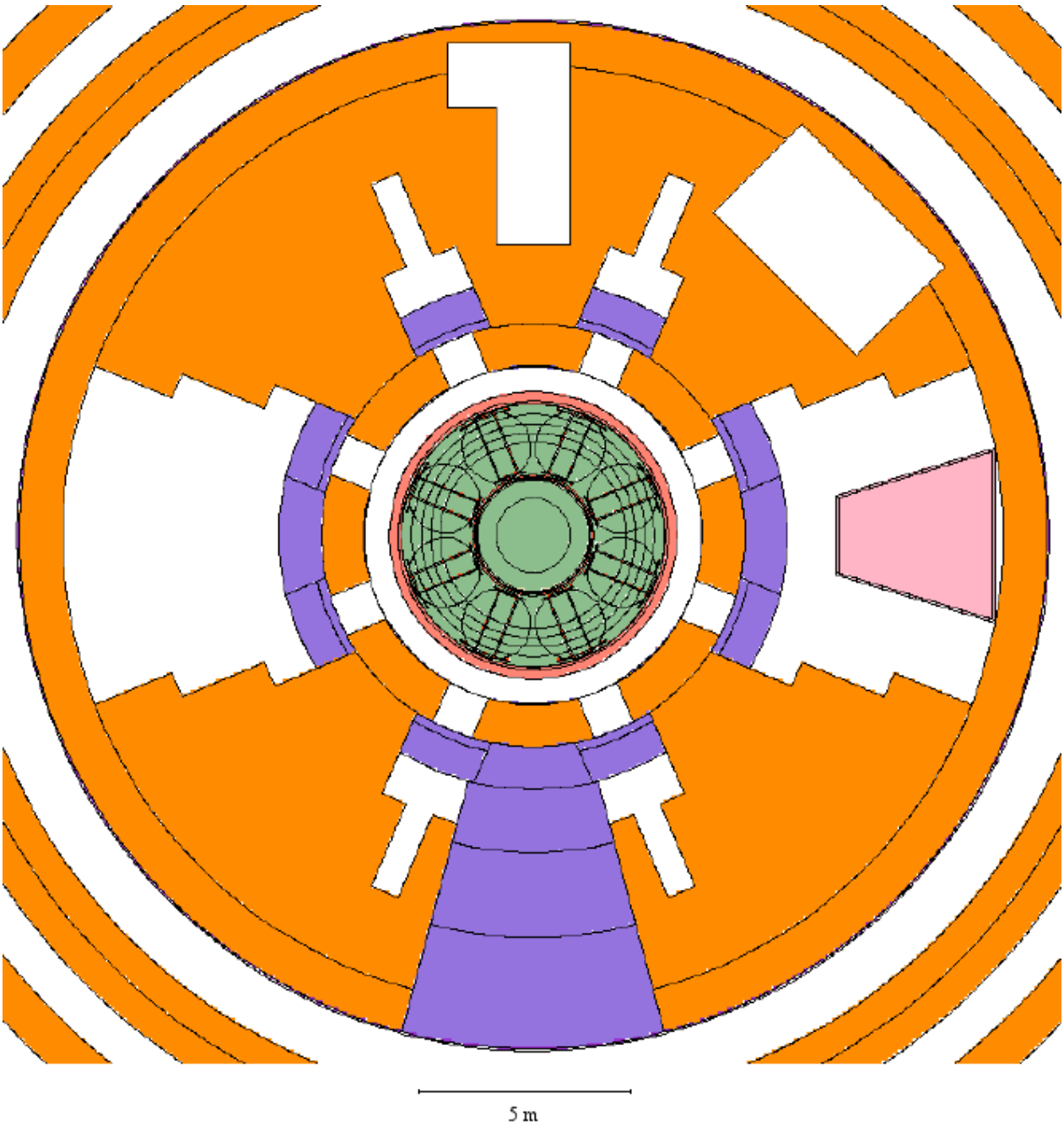

Fig. 130. Segmentation of the water pipe model for the spatial averaging of the neutron fluxes for the calculation of the activation source (detail of inner part).

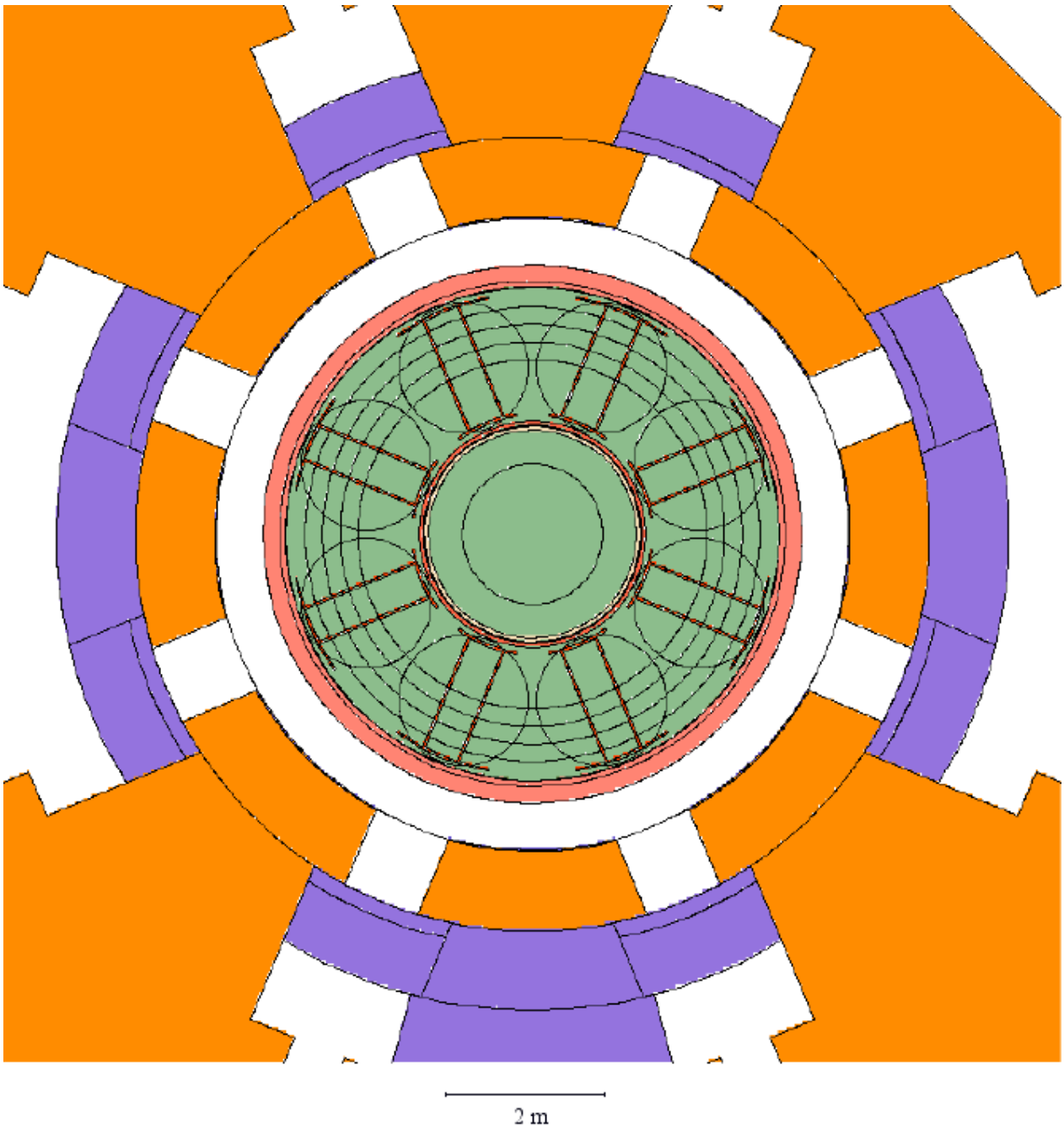

Fig. 131. Segmentation of the main deck gratings for the spatial averaging of the neutron fluxes for the calculation of the activation source.

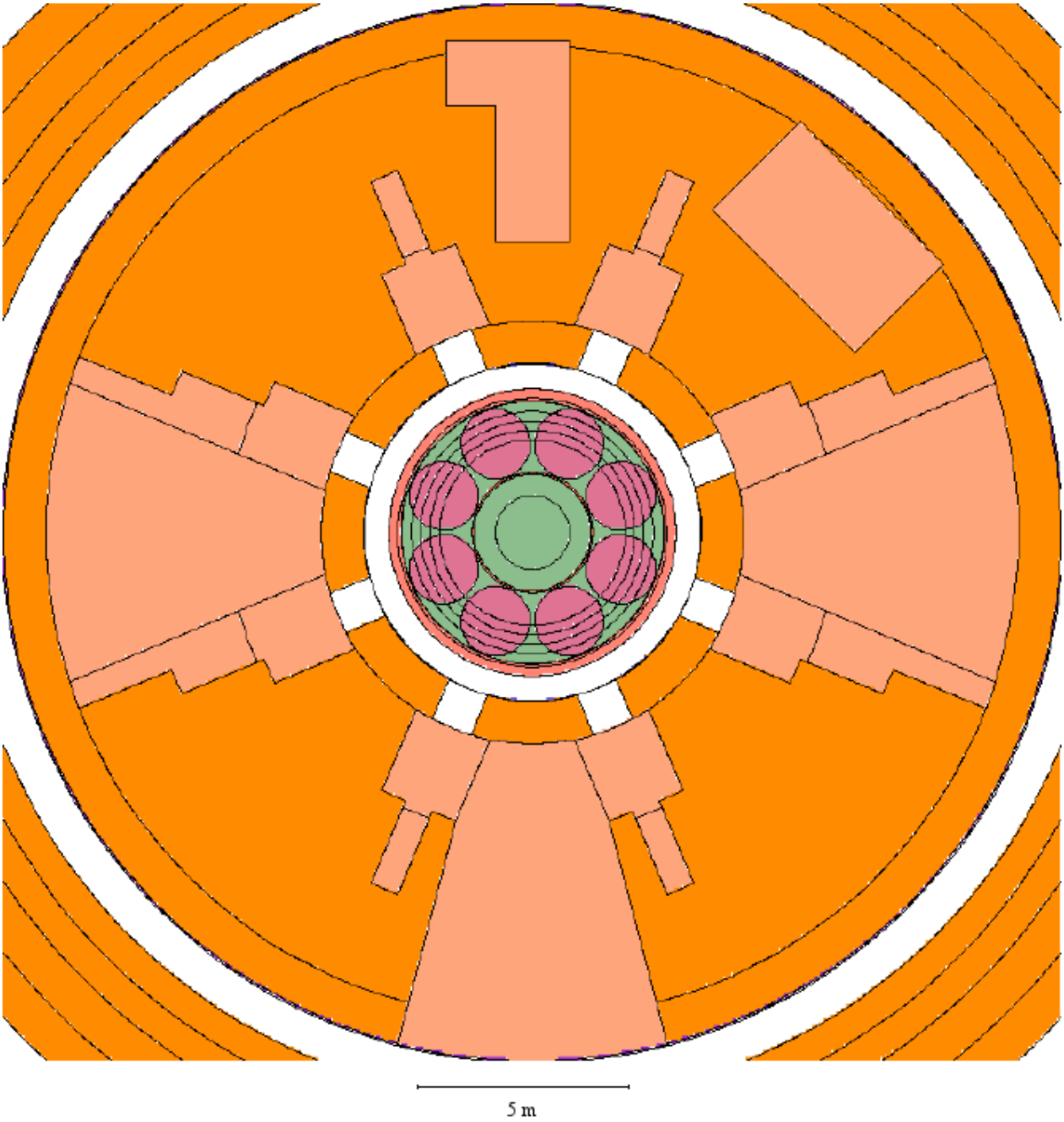

Fig. 132. Vertical section of the ADS quench tank showing the segmentation of the walls for the spatial averaging of the neutron fluxes for the calculation of the activation source: a single front wall, a single bottom and a back wall divided vertically into two parts (red lines denote segment delimitation).

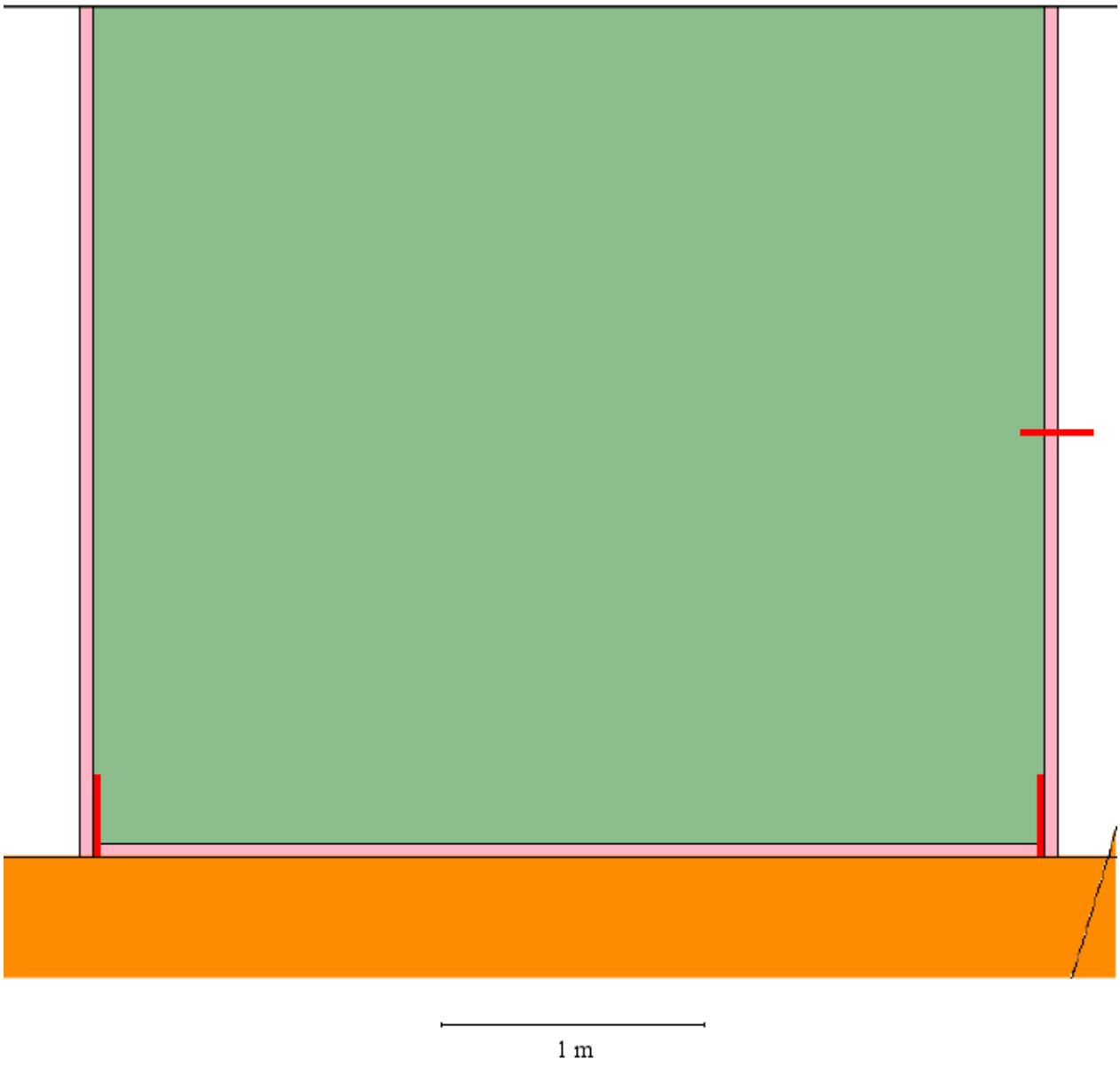

Fig. 133. Vertical section of the ADS quench tank side walls showing the segmentation for the spatial averaging of the neutron fluxes for the calculation of the activation source.

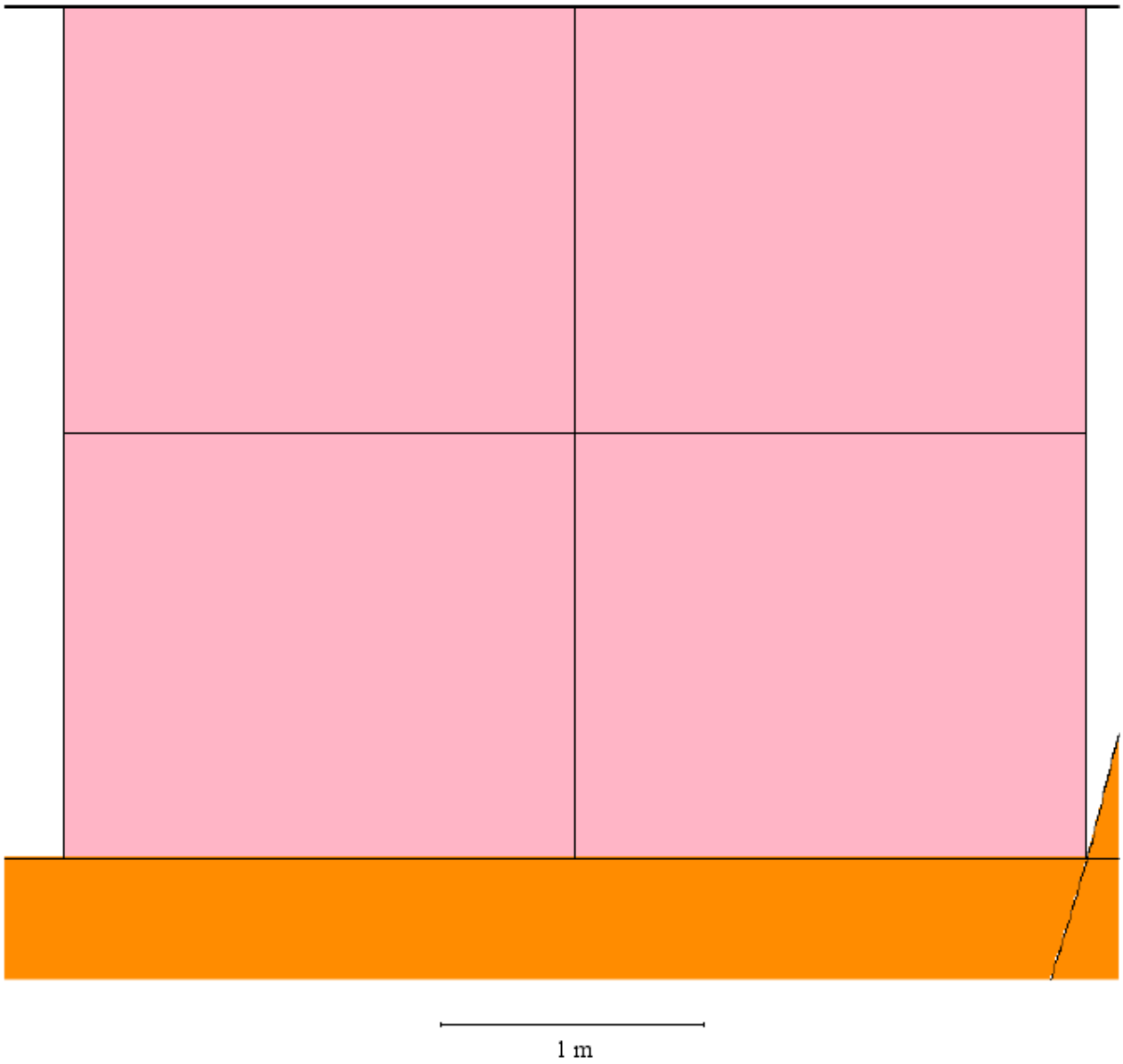

Fig. 134. Vertical section through the ADS quench tank front wall showing the segmentation for the spatial averaging of the neutron fluxes for the calculation of the activation source.

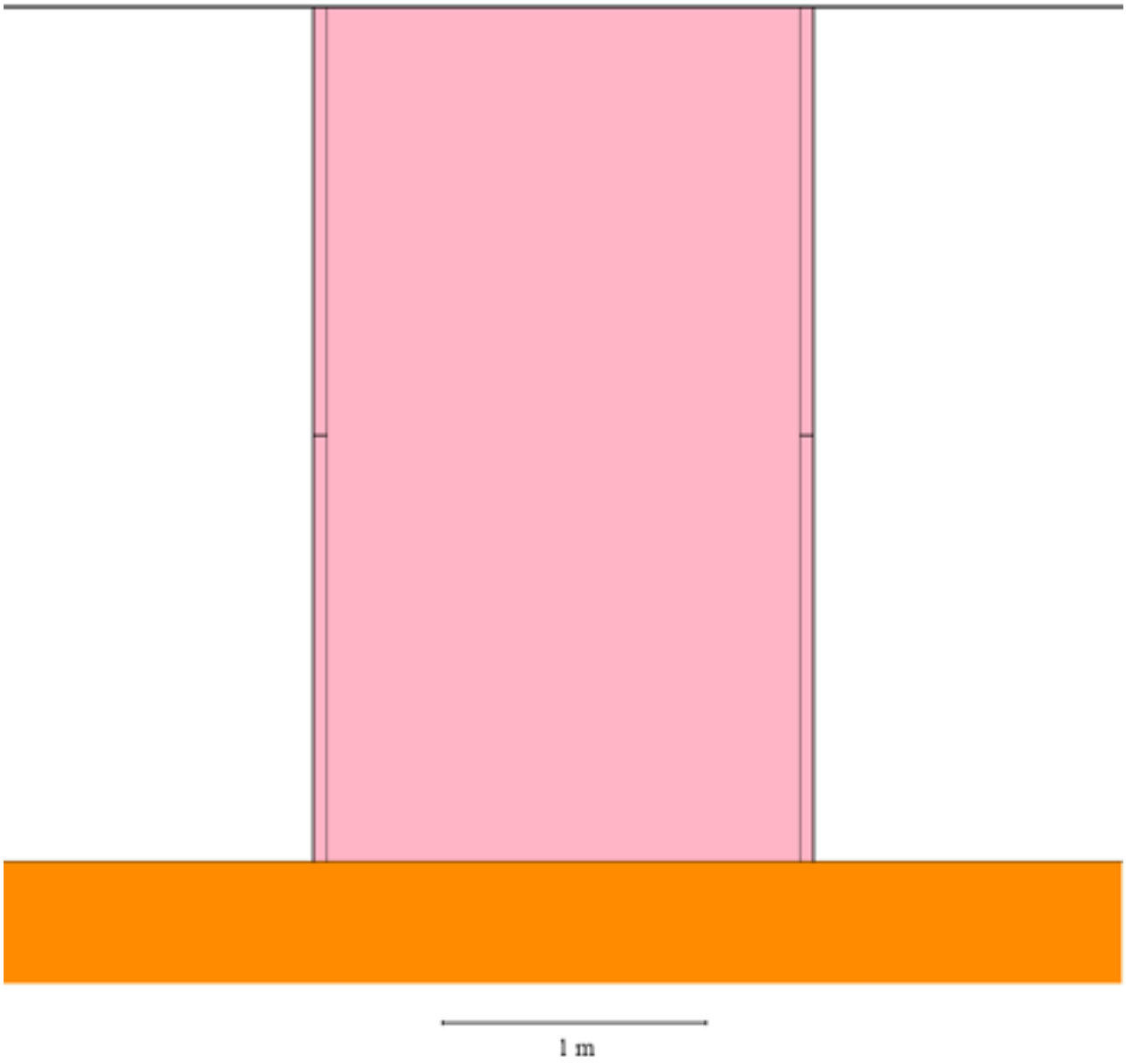

Fig. 135. Vertical section through the ADS quench tank back wall showing the segmentation for the spatial averaging of the neutron fluxes for the calculation of the activation source.

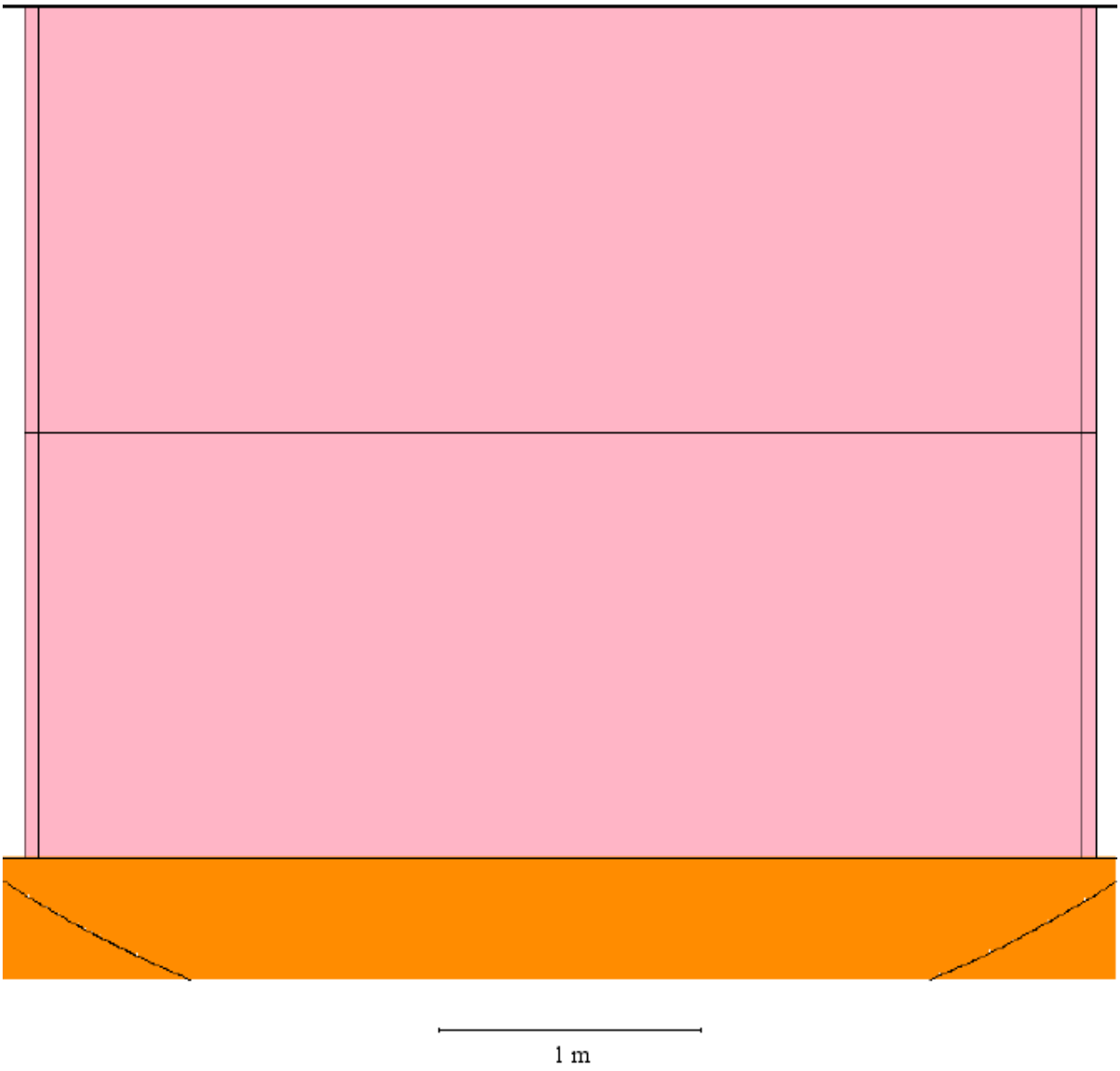

Fig. 136. Horizontal section through the middle part of the ADS quench tank showing the segmentation for the spatial averaging of the neutron fluxes for the calculation of the activation source.

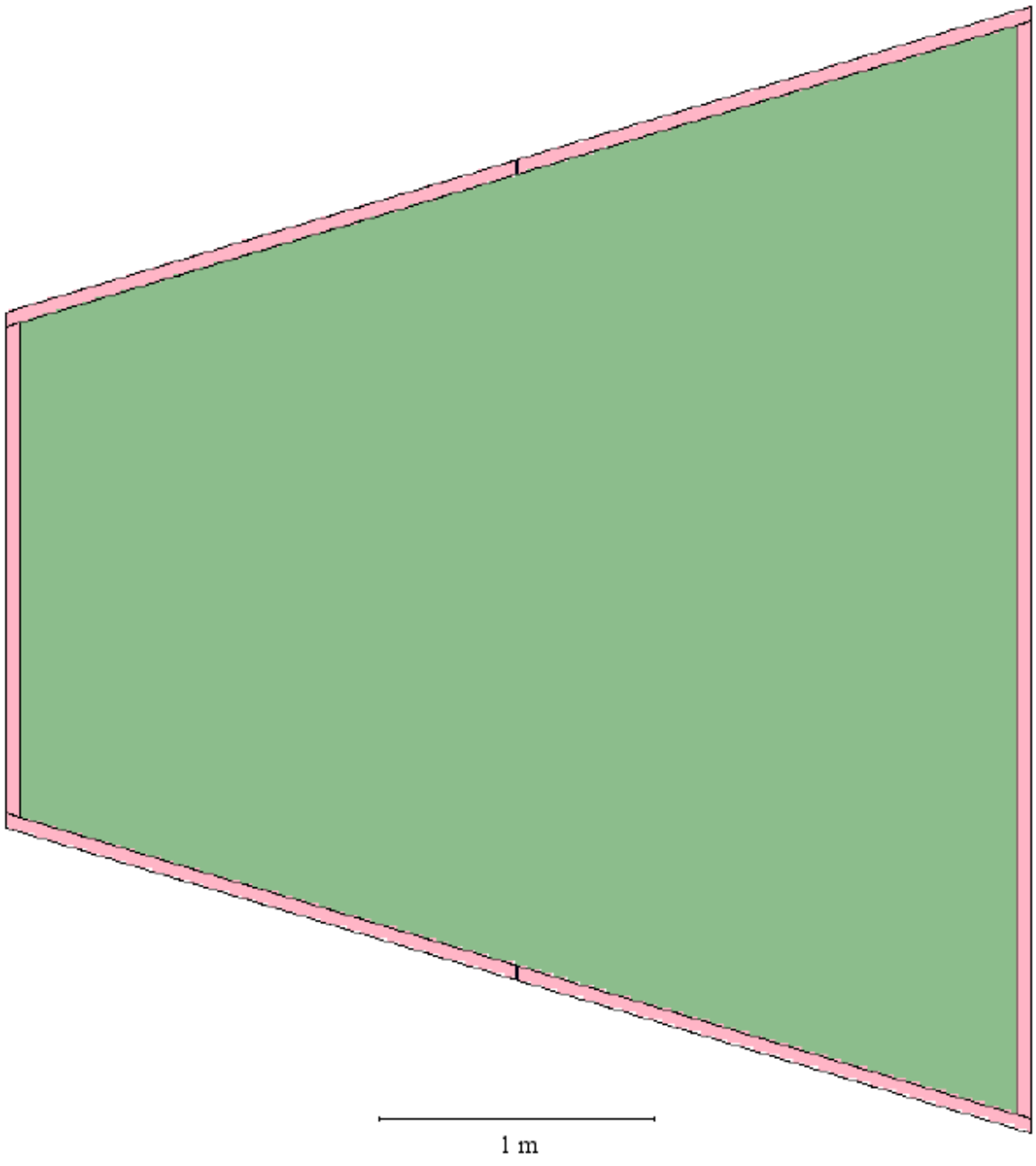

Fig. 137. Horizontal section through the ADS quench tank bottom wall showing the segmentation for the spatial averaging of the neutron fluxes for the calculation of the activation source.

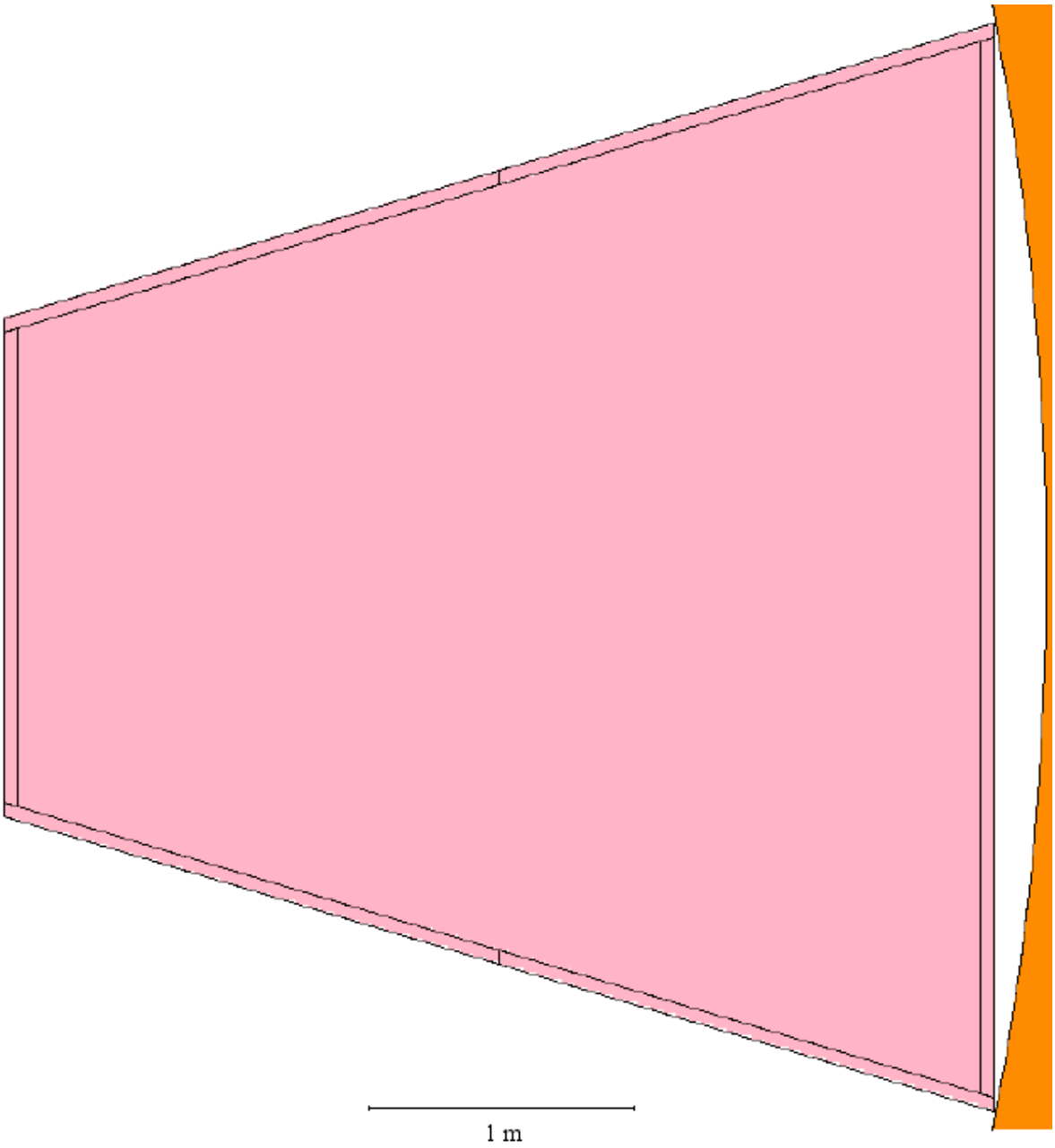

Fig. 138. LGMS tank A (West): delimitation into end caps and four azimuthal segments for the spatial averaging of the neutron fluxes for the calculation of the activation source (red lines denote segment delimitation).

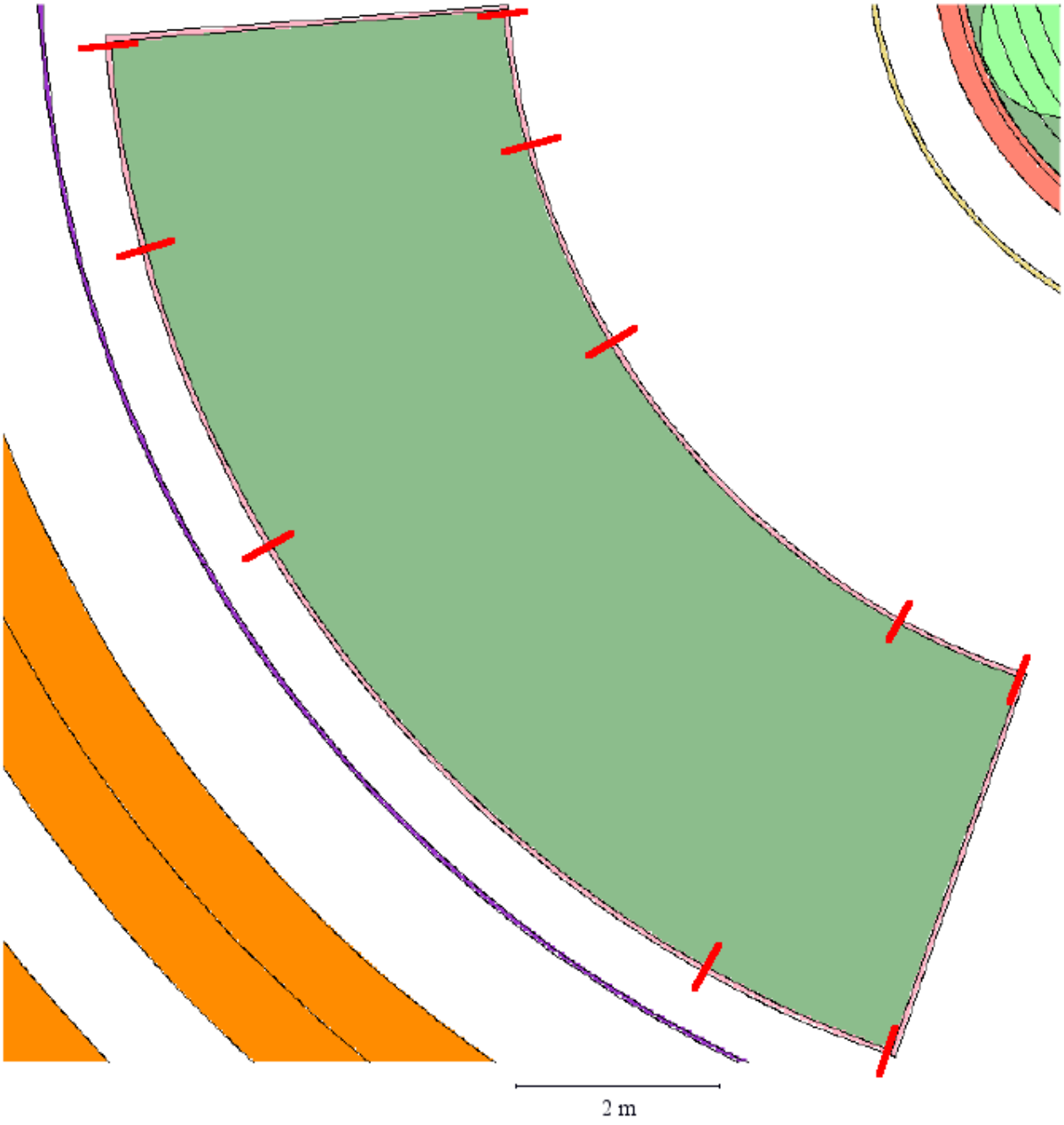

Fig. 139. LGMS tank A (East): division into end caps and four azimuthal segments for the spatial averaging of the neutron fluxes for the calculation of the activation source (red lines denote segment delimitation).

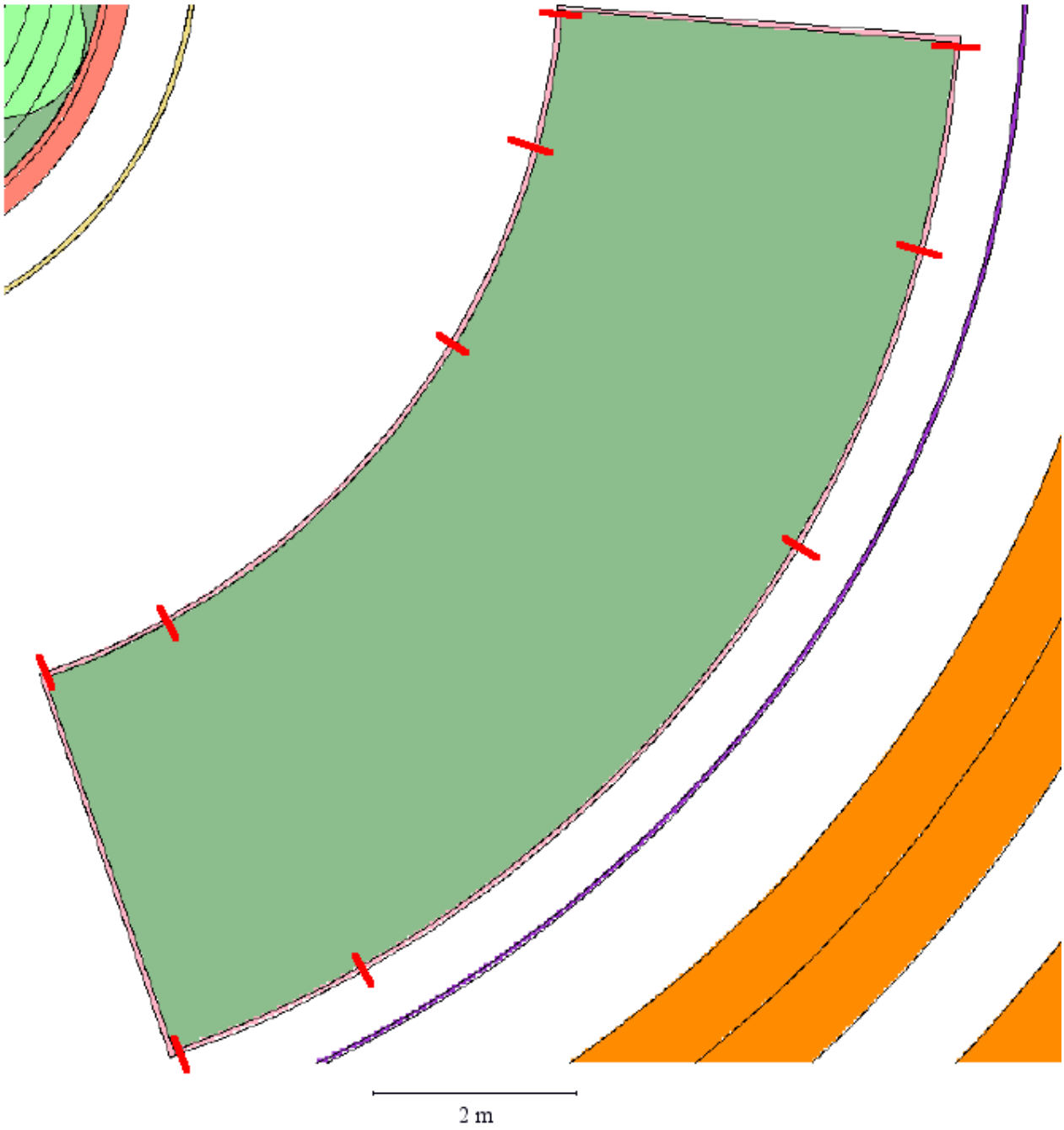

Fig. 140. LGMS tanks: choice of the four azimuthal segments for the spatial averaging of the neutron fluxes for the calculation of the activation source (red lines denote segment delimitation).

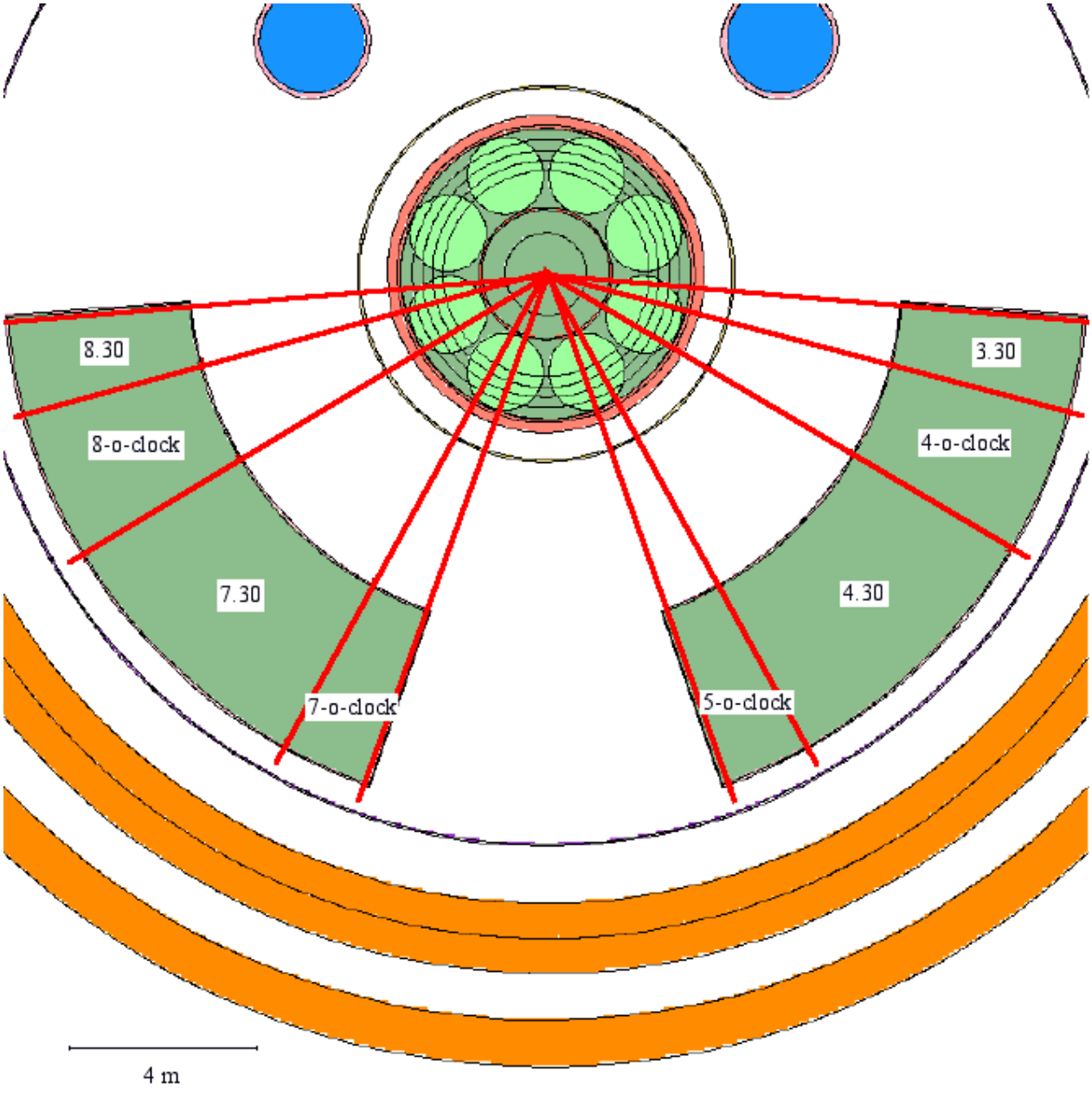

Fig. 141. LGMS tanks: polar segmentation of the azimuthal segments at 4-o-clock, 5-o-clock, 7-o-clock and 8-o-clock (see Fig. 140) for the spatial averaging of the neutron fluxes for the calculation of the activation source (red lines denote segment delimitation).

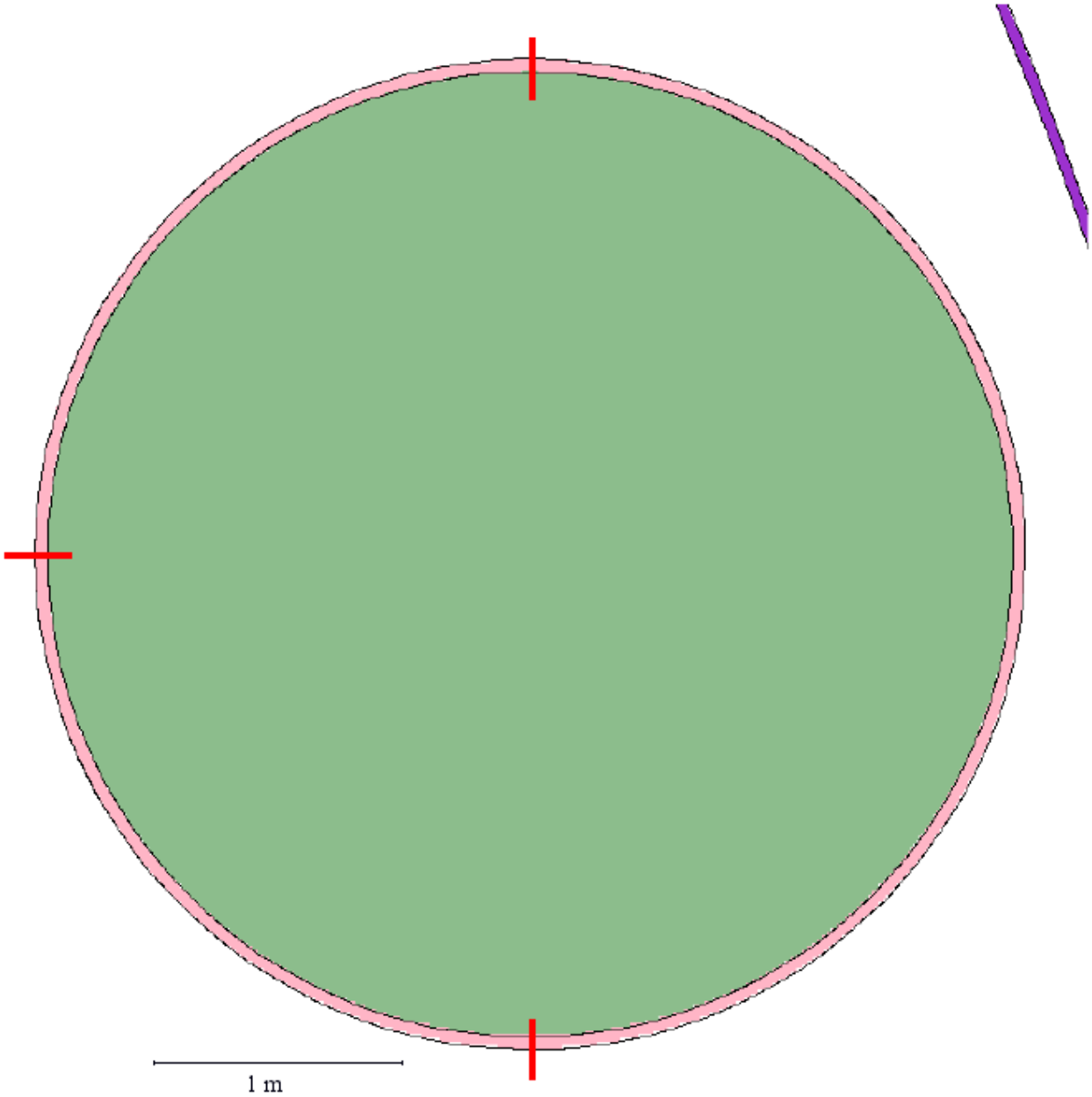

Fig. 142. LGMS tanks: polar segmentation of the azimuthal segments at 3.30, 4.30, 7.30 and 8.30 (see Fig. 140) for the spatial averaging of the neutron fluxes for the calculation of the activation source (red lines denote segment delimitation).

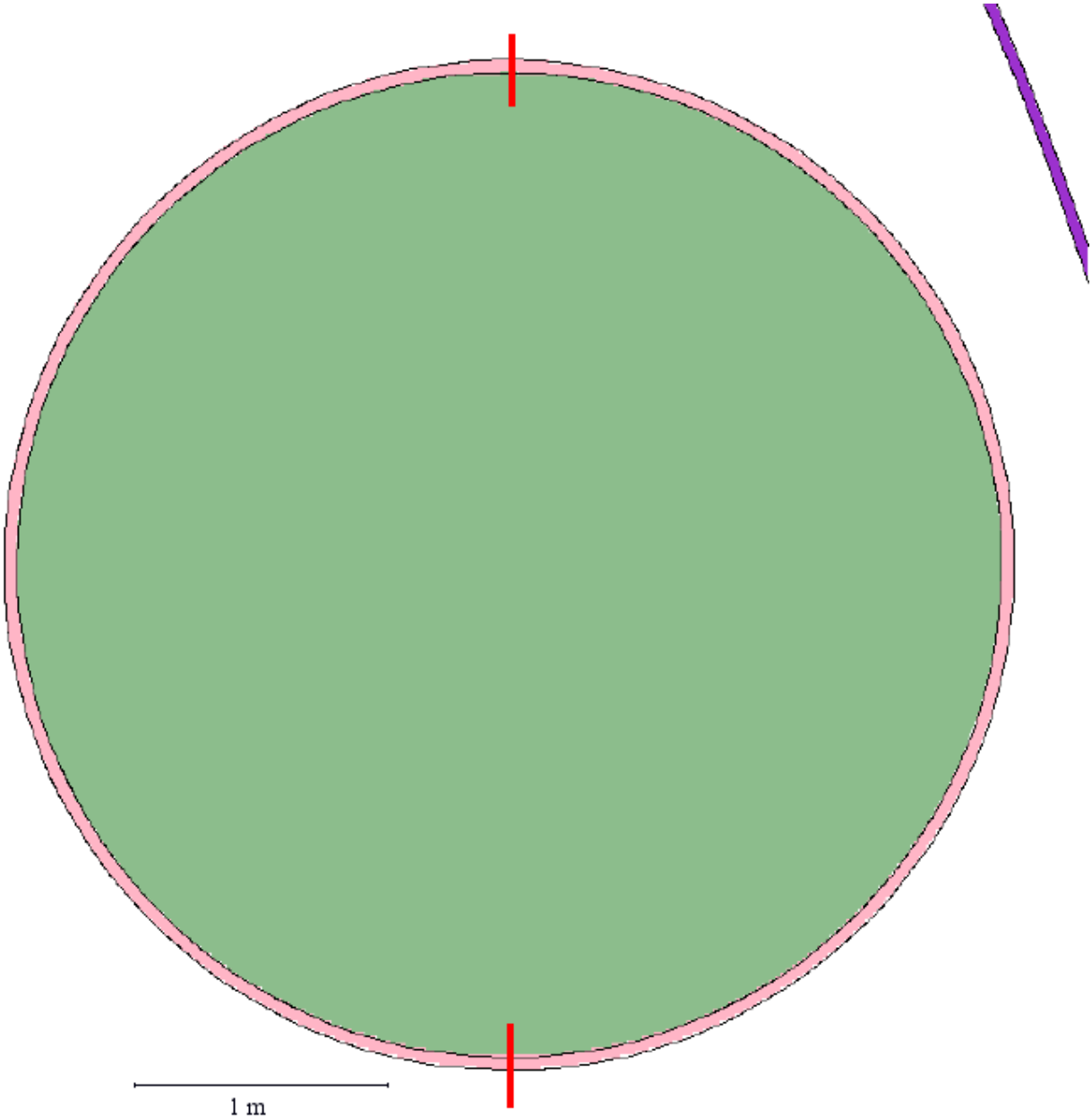

Fig. 143: EB tanks: vertical section showing segmentation into bottom, top and side walls for the spatial averaging of the neutron fluxes for the calculation of the activation source (red lines denote segment delimitation).

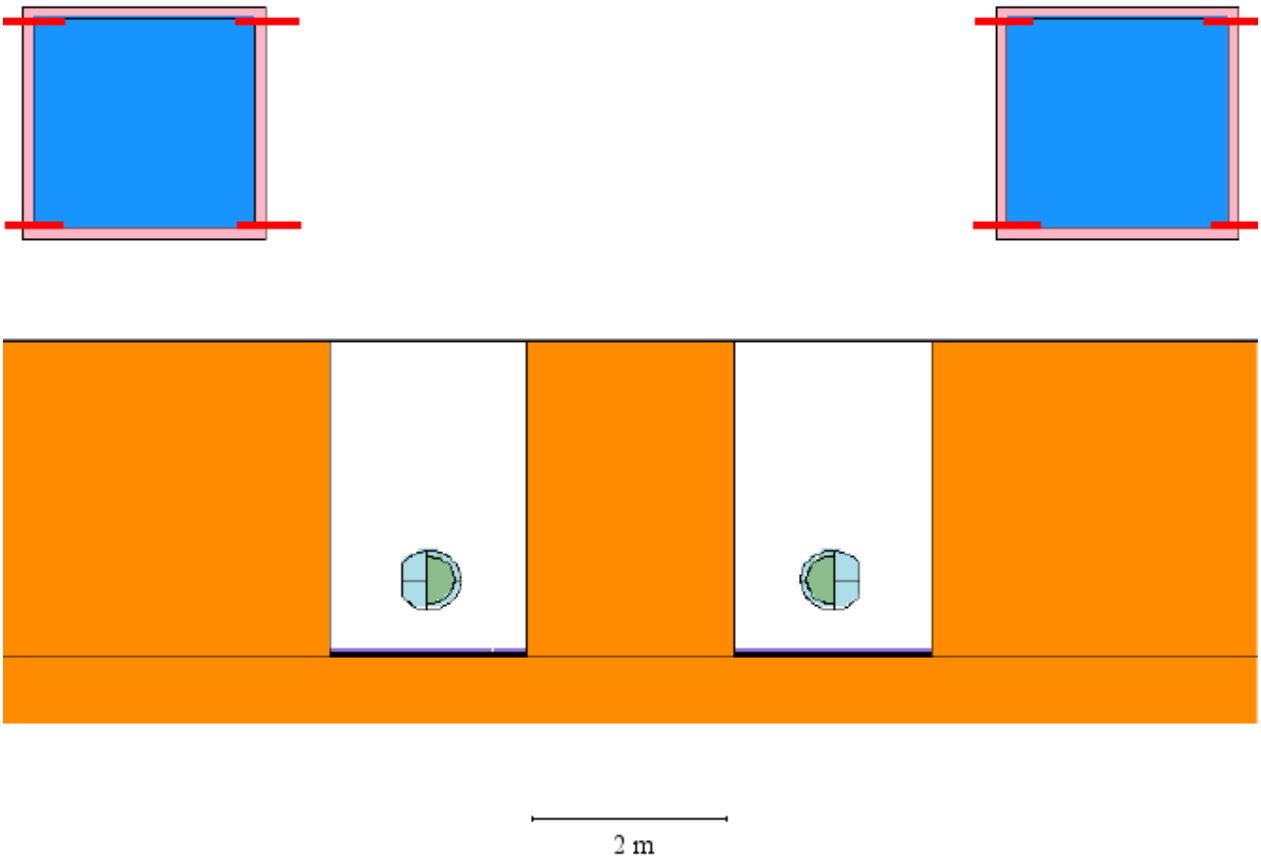

Fig. 144: EB tanks: horizontal section for the spatial averaging of the neutron fluxes for the calculation of the activation source.

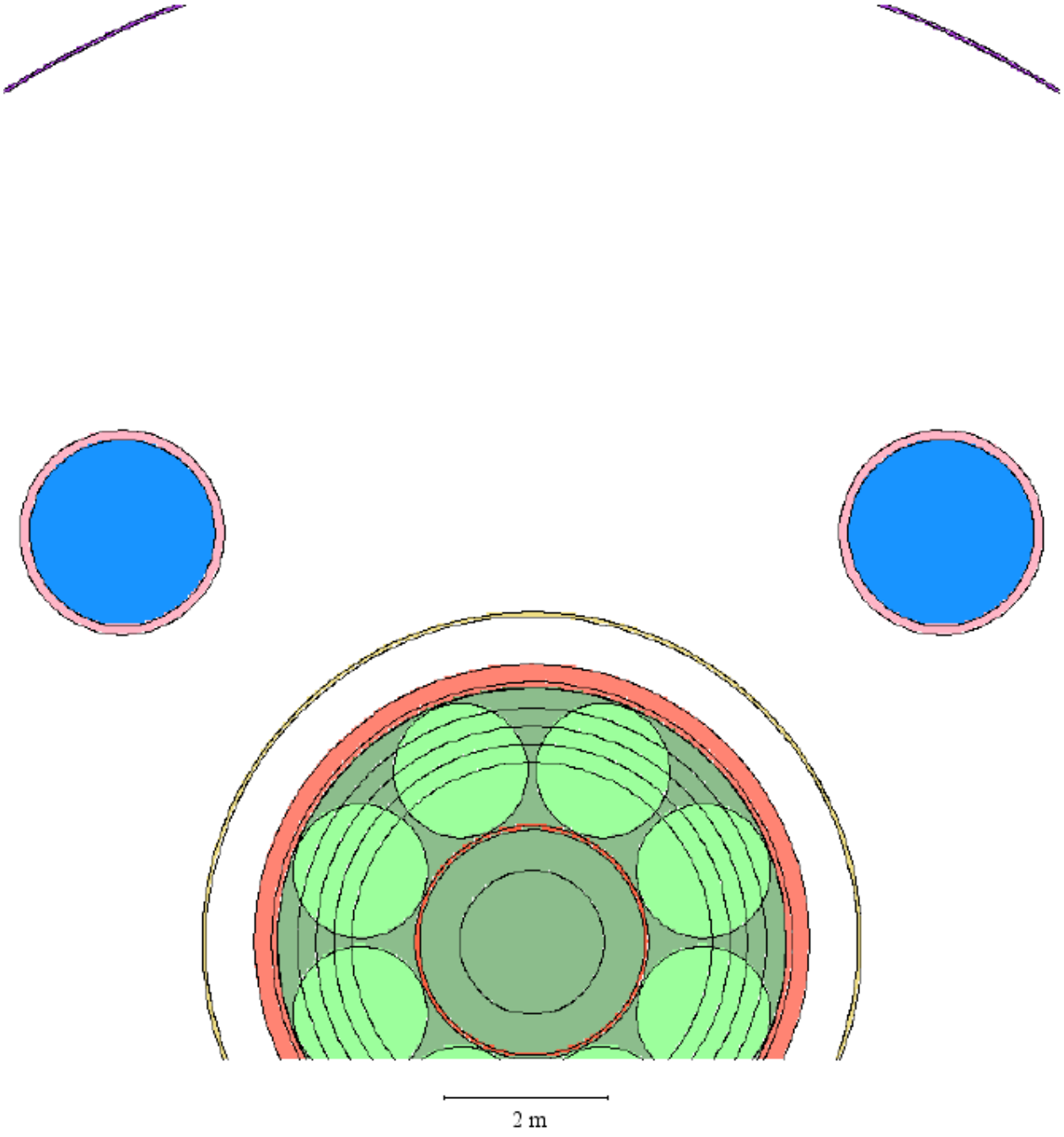

Fig. 145: Containment vessel: vertical section of the part below the main deck in the South direction for the spatial averaging of the neutron fluxes for the calculation of the activation source (red lines denote segment delimitation).

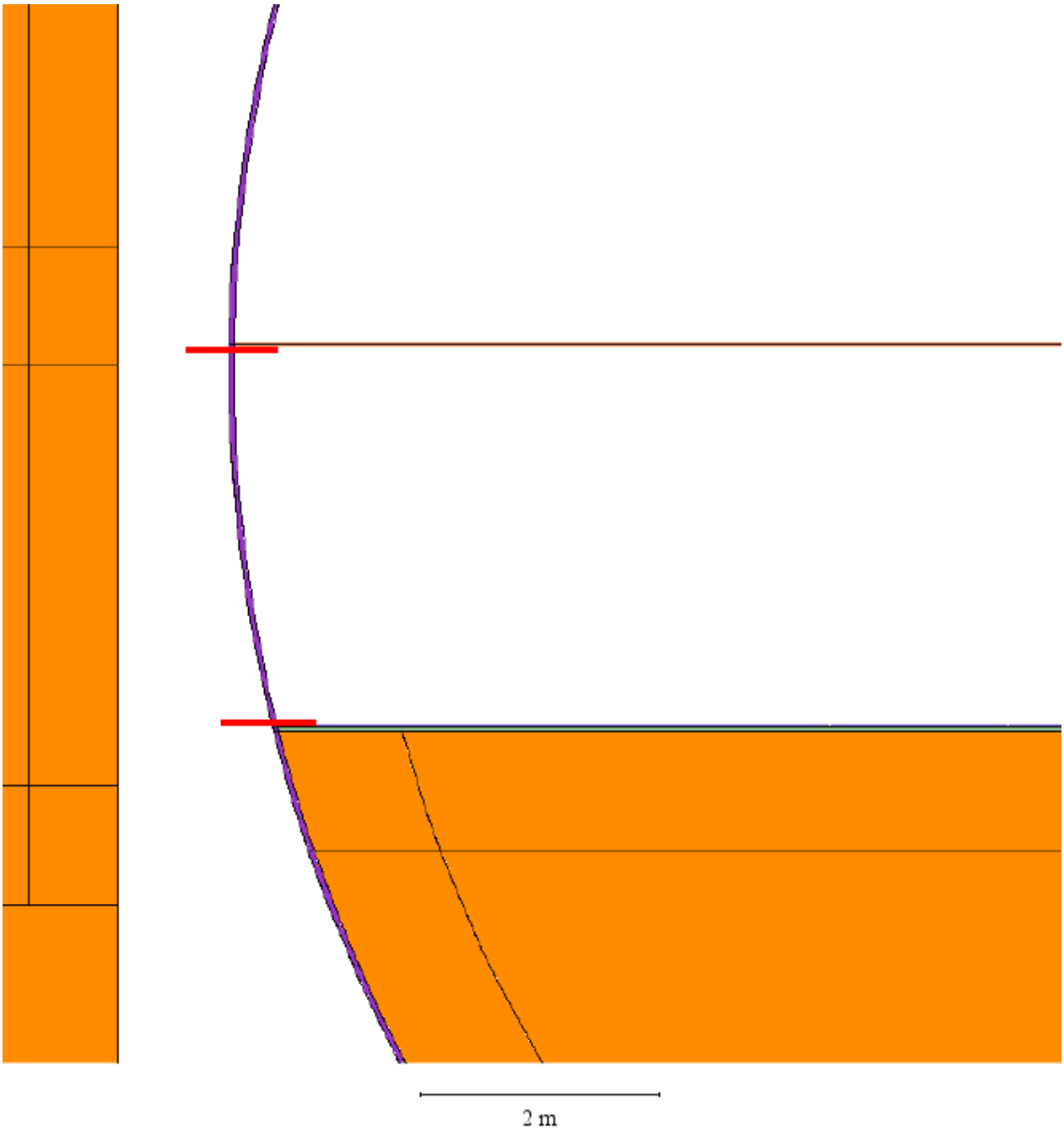

Fig. 146: Containment vessel: horizontal section of the part below the main deck in the South direction for the spatial averaging of the neutron fluxes for the calculation of the activation source (red lines denote segment delimitation).

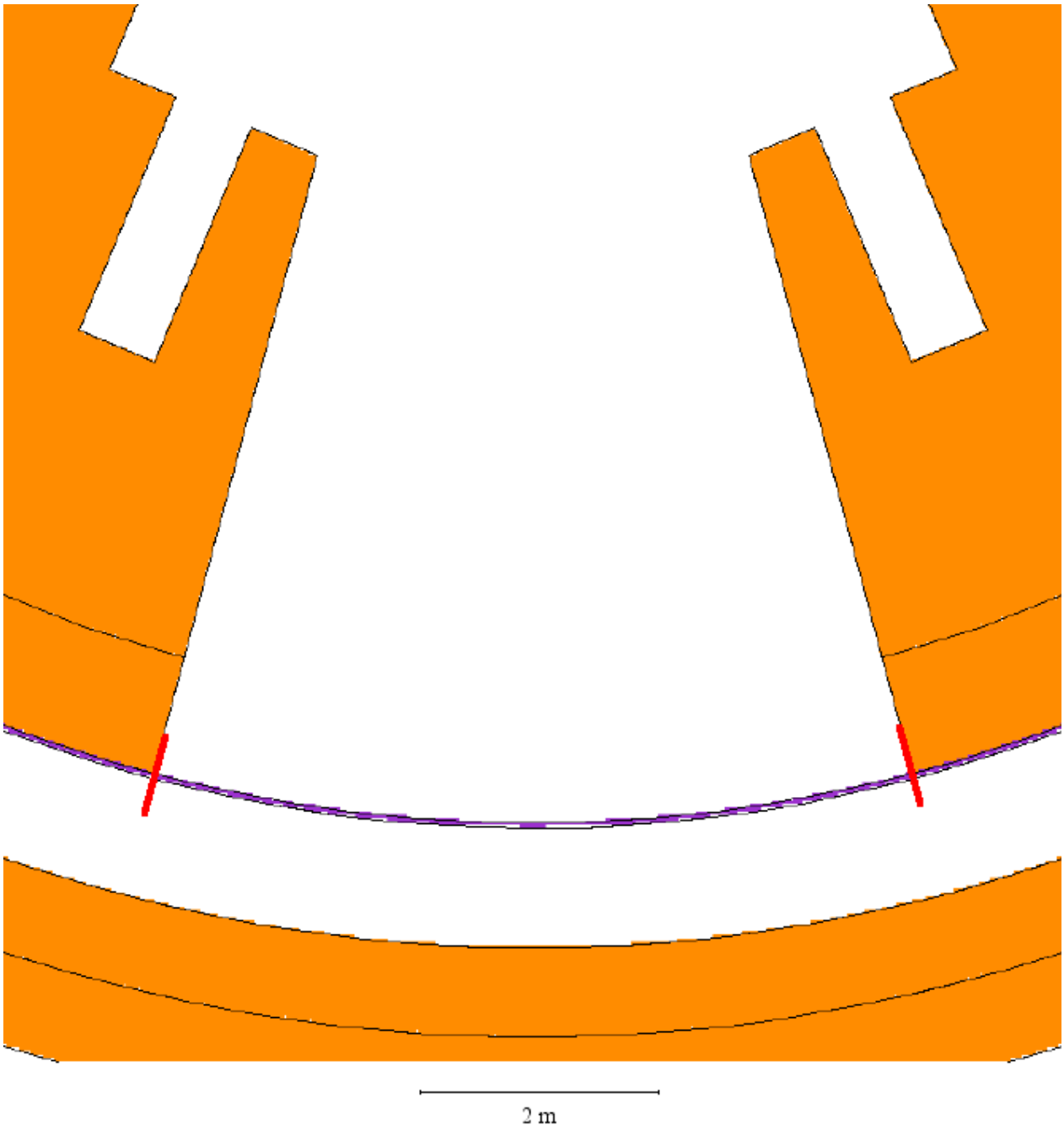

Fig. 147: Containment vessel: vertical section of the segments above the main deck for the spatial averaging of the neutron fluxes for the calculation of the activation source (red lines denote segment delimitation).

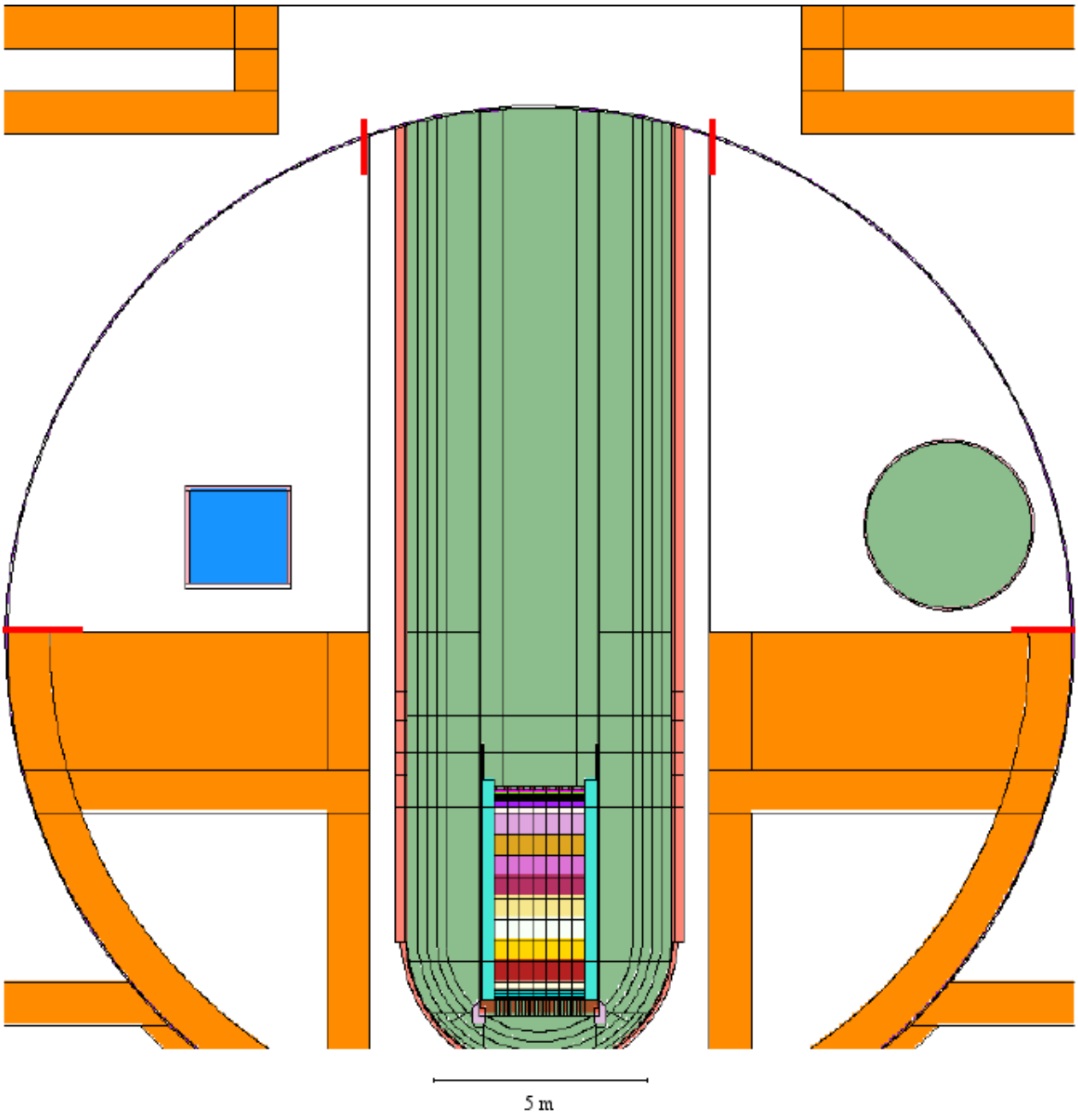

Fig. 148: Containment vessel: horizontal section of the segments above the main deck showing the azimuthal division for the spatial averaging of the neutron fluxes for the calculation of the activation source (red lines denote segment delimitation).

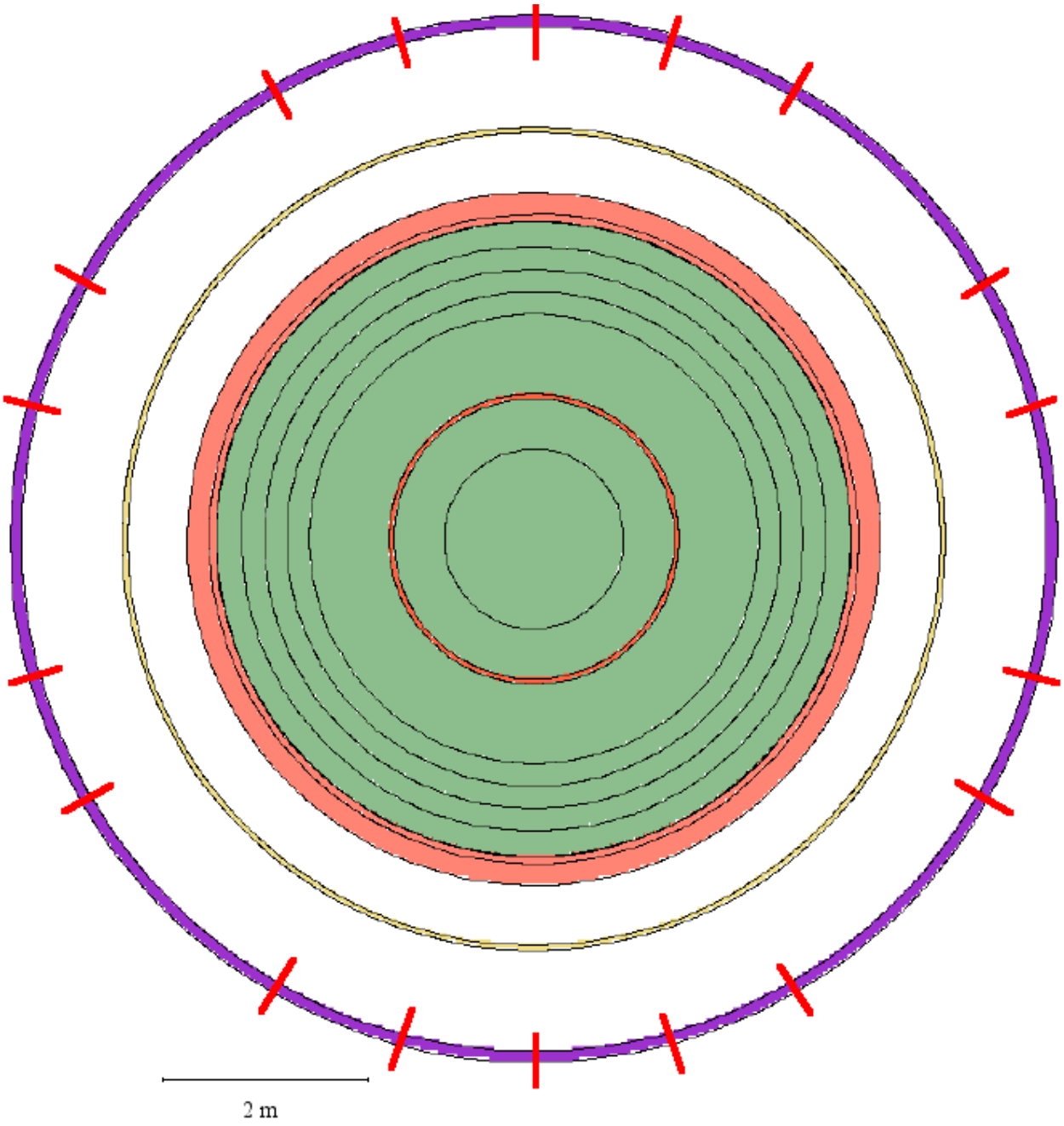

Fig. 149: Pressure vessel: vertical section in the WSW-ENE direction showing the division of the cylindrical part into 5 axial segments (the top segment covers the lowest part of the steam generator just above the bottom header) and 2 radial segments for the spatial averaging of the neutron fluxes for the calculation of the activation source.

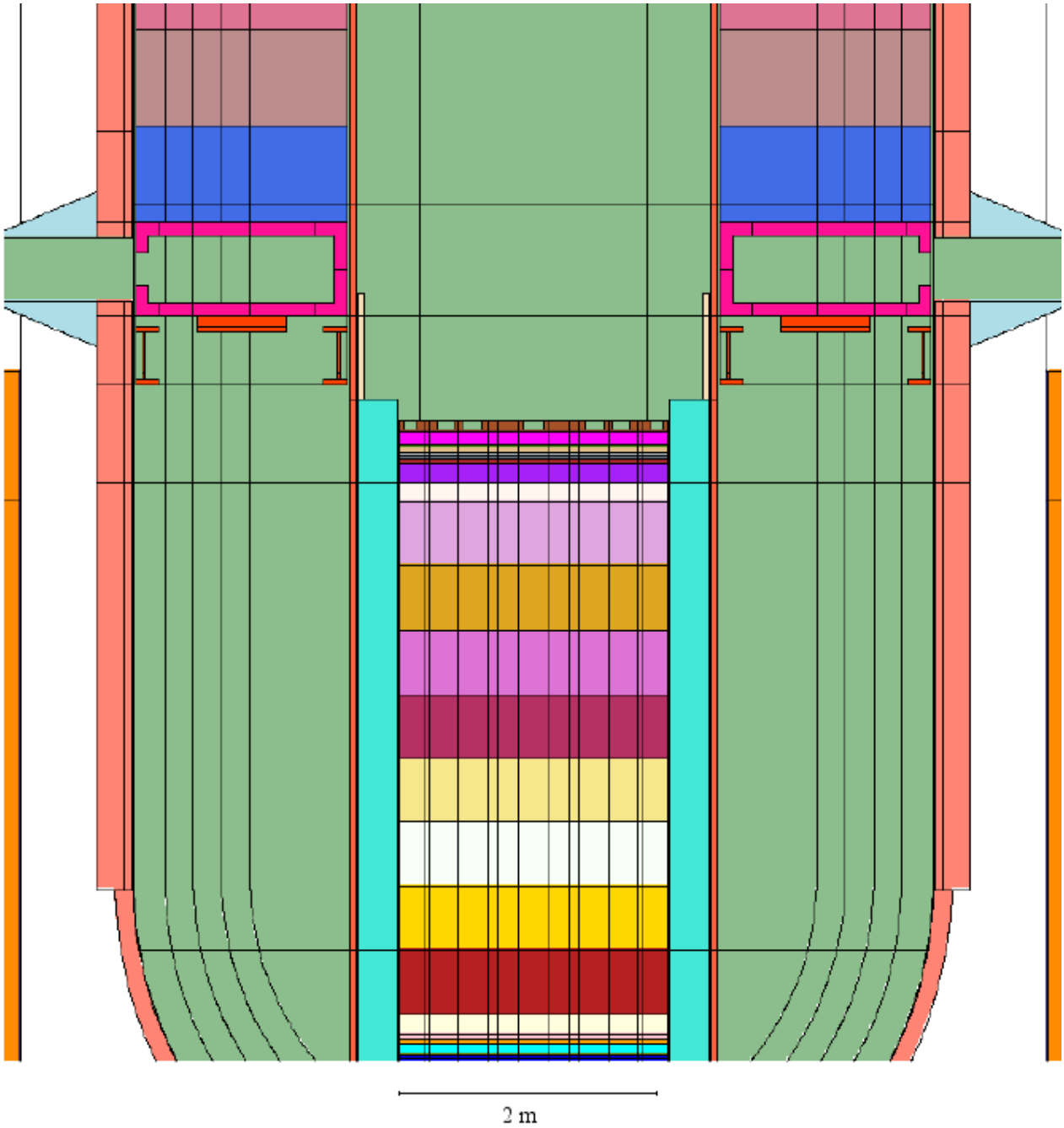

Fig. 150: Pressure vessel: vertical section in the W-E direction showing the division of the cylindrical part into 5 axial segments and 2 radial segments for the spatial averaging of the neutron fluxes for the calculation of the activation source.

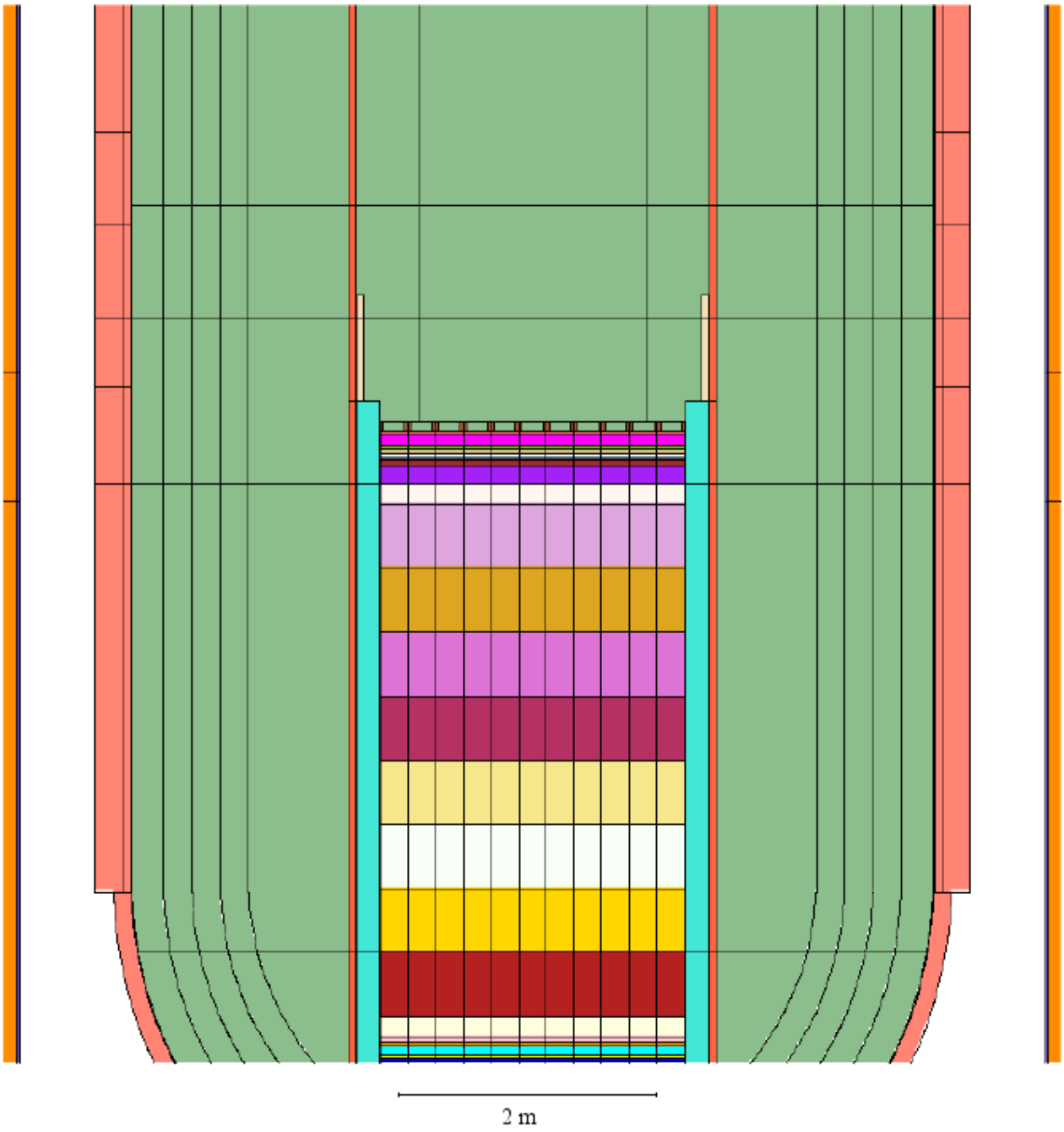

Fig. 151: Segment (in red) showing where the streaming dose from selected active components within the pressure vessel was calculated.

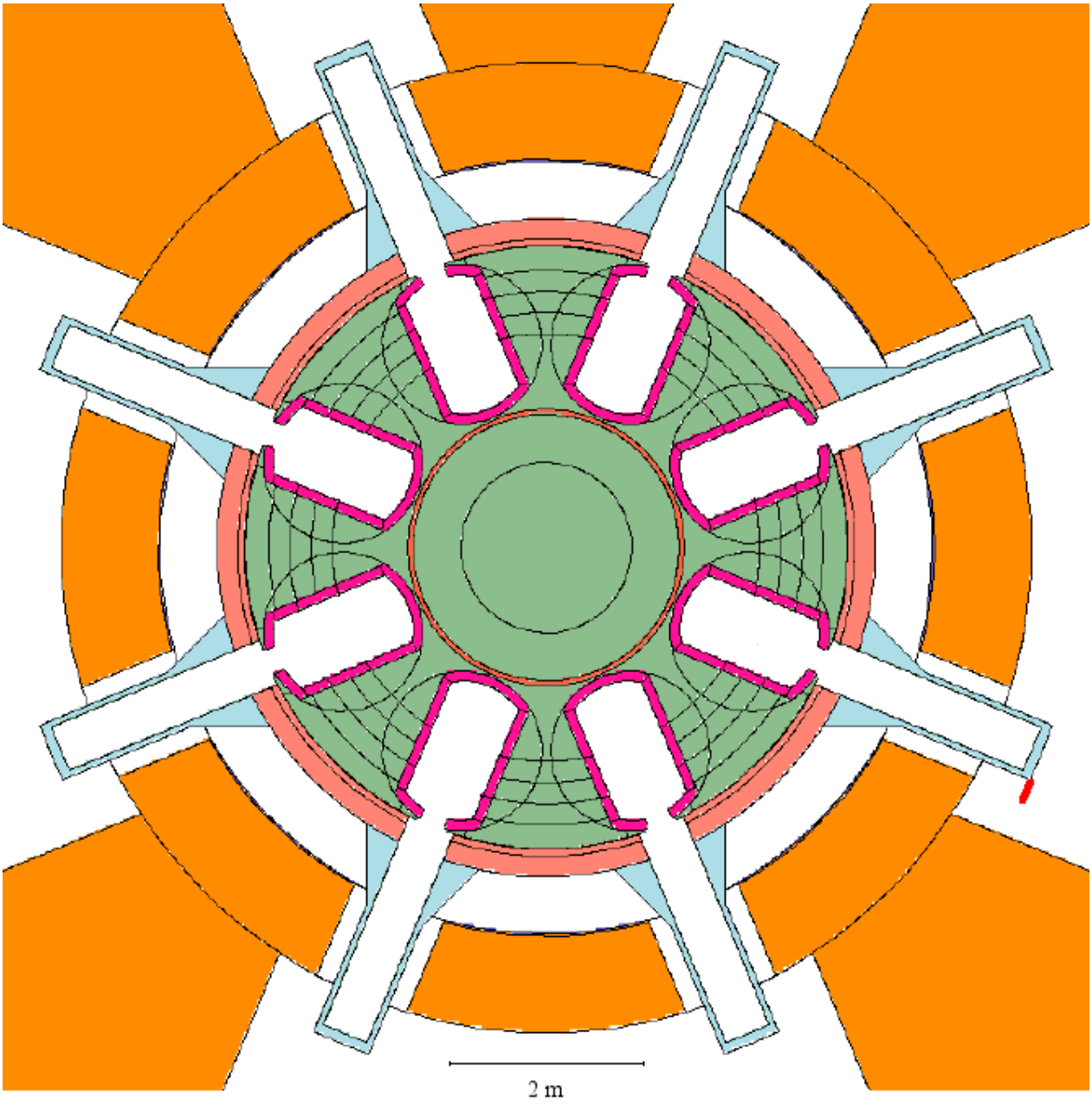

Fig. 152: Segments (in red) showing where the maximum streaming dose from selected active components within the pressure vessel, over the height of the cavities below the main deck level, resulted.

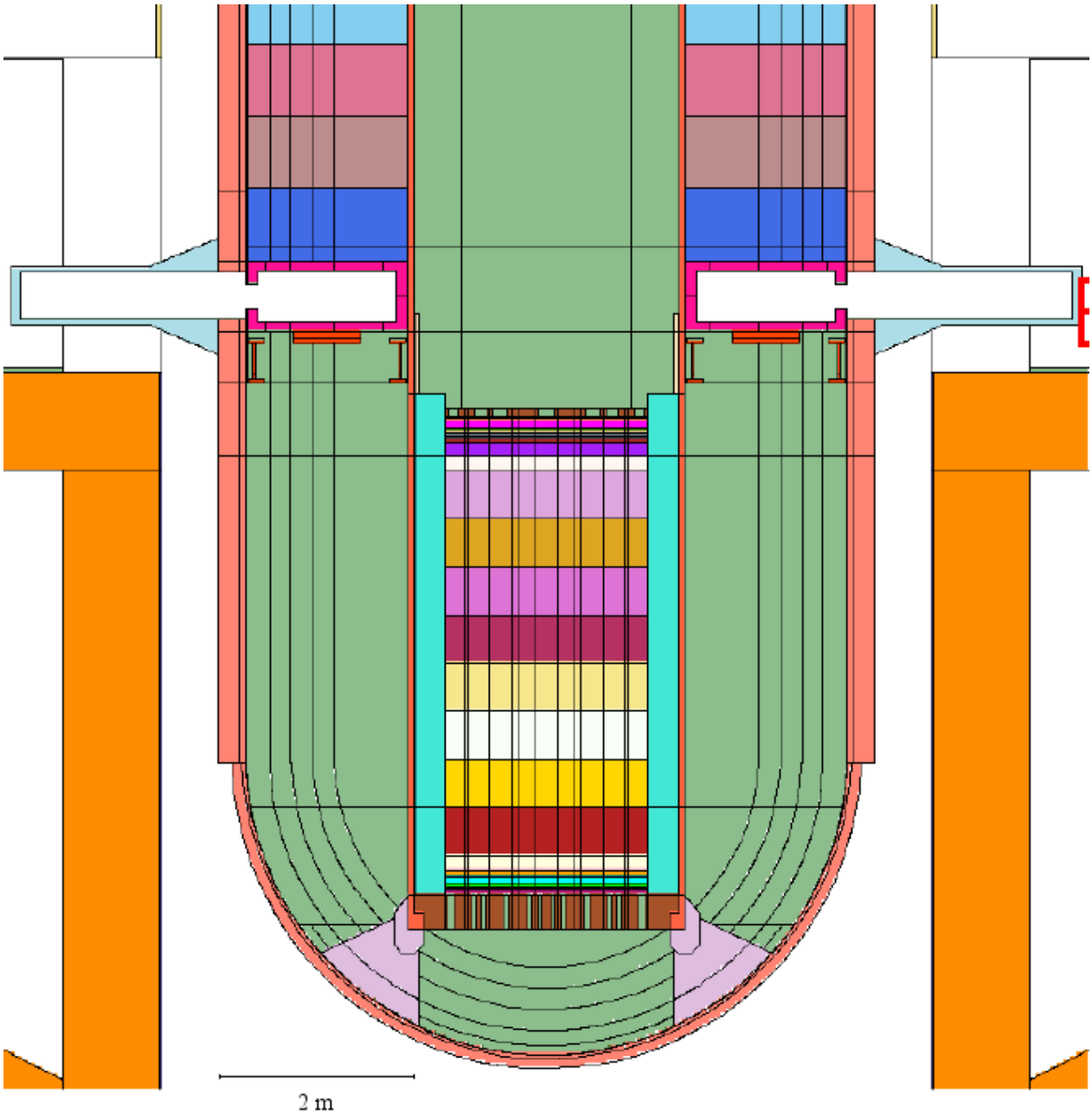

Fig. 153: Dose point (in red) along the path of maximum streaming dose at 1 m radial distance from end of the inlet nozzles, projected onto the plane through the inlet nozzle axes.

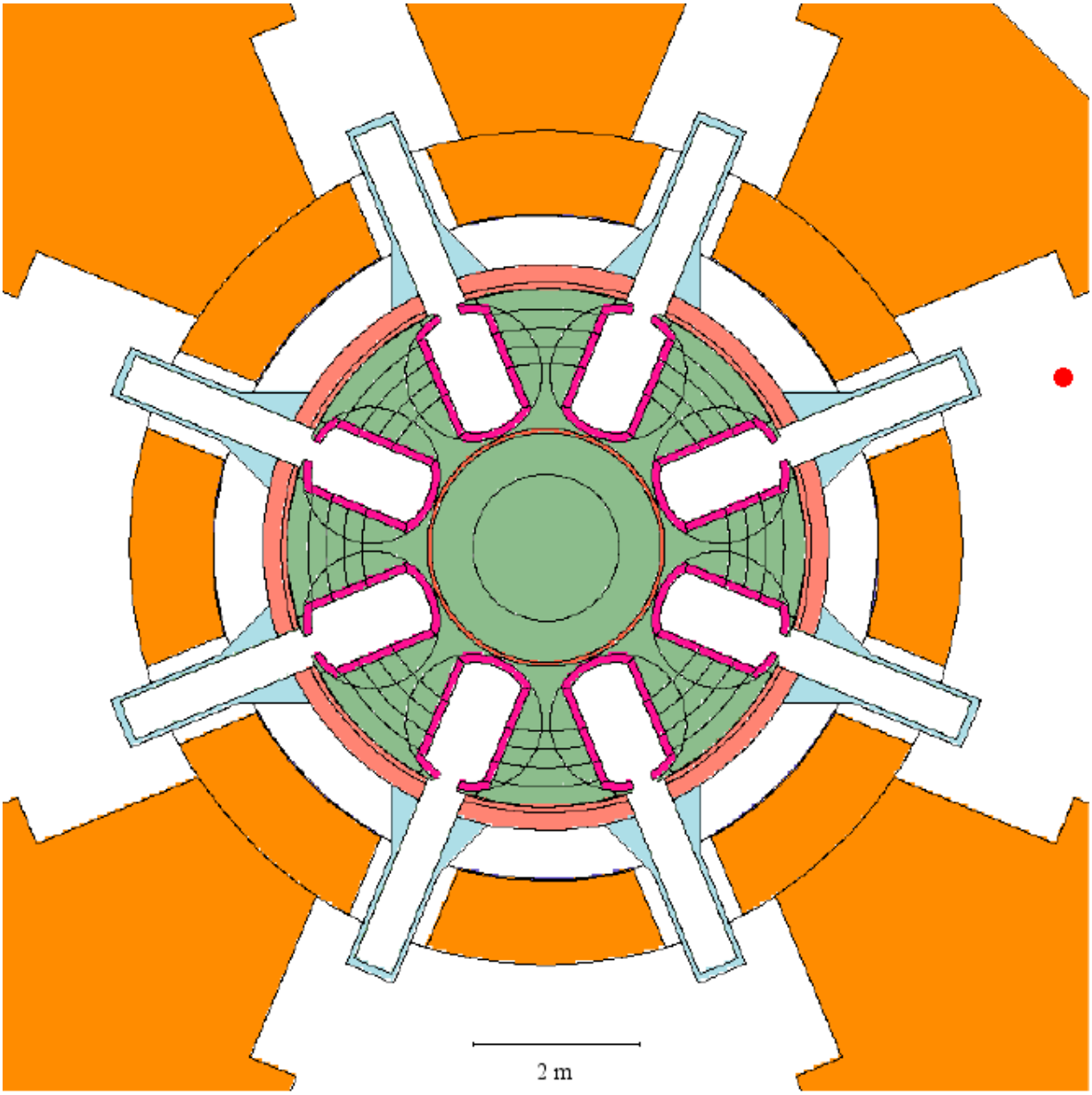

Fig. 154: Dose point (in red) along the path of maximum streaming dose at 1 m radial distance from end of the inlet nozzles at its correct height 40.5 cm above the axes of the inlet nozzles.

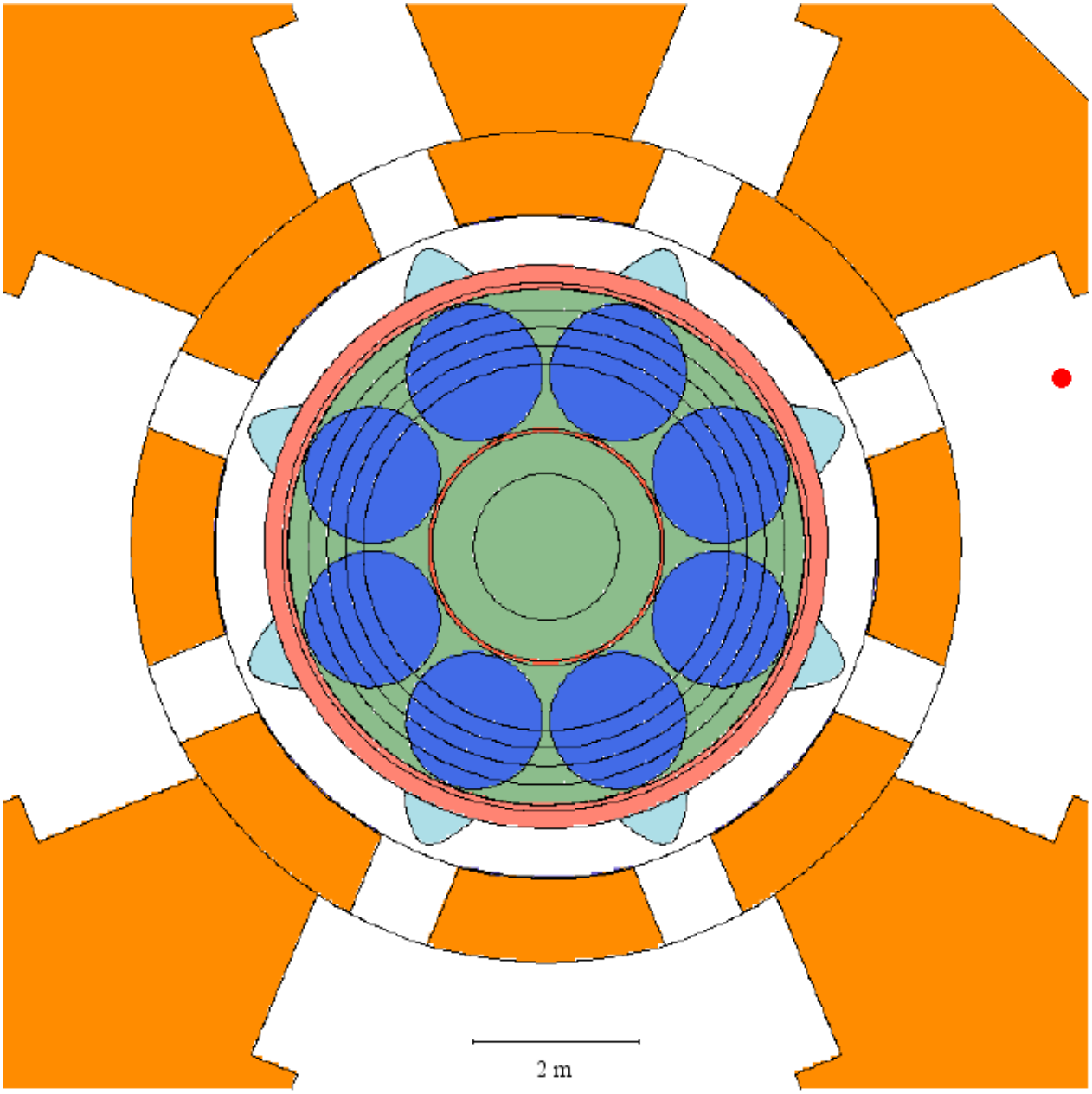

Fig. 155: Dose point (in red) along the path of maximum streaming dose at 1 m radial distance from end of the inlet nozzles at its correct height 40.5 cm above the axes of the inlet nozzles.

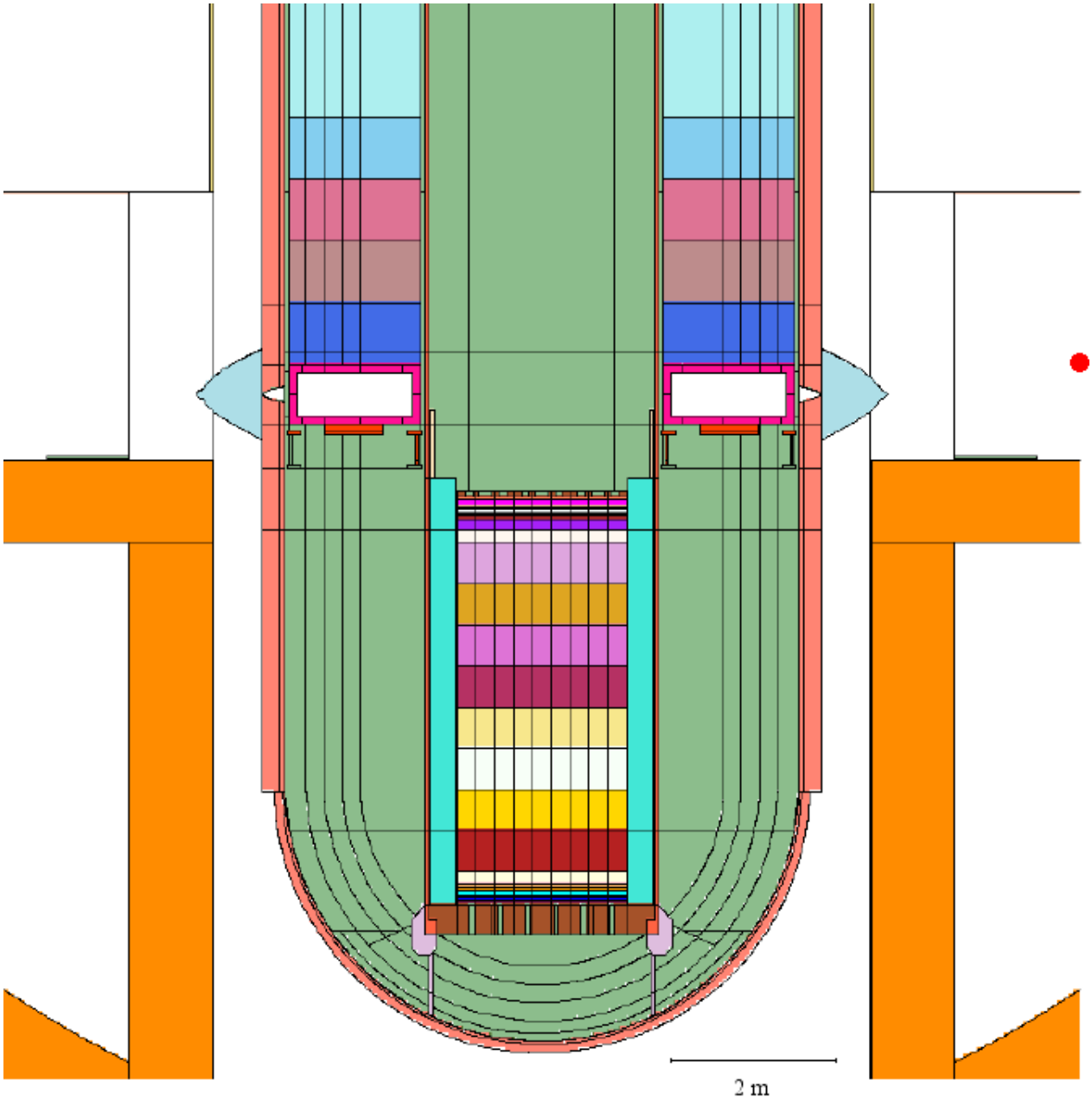

Fig. 156: Dose points (in red) in air in the cavities below the main deck level (where the total dose from all activated components was calculated).

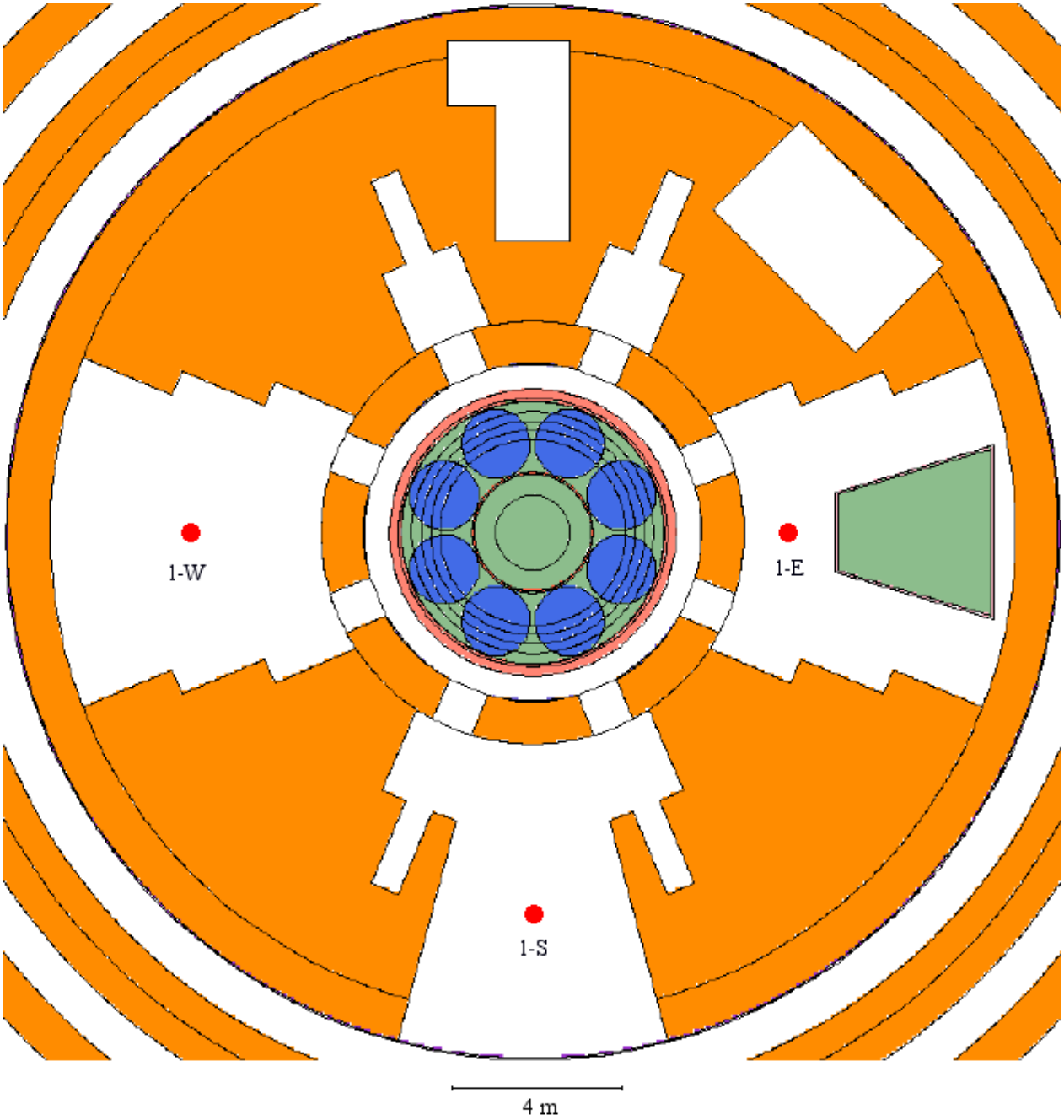

Fig. 157: Dose points (in red) in air in the cavity above the main deck level (where the total dose from all activated components was calculated).

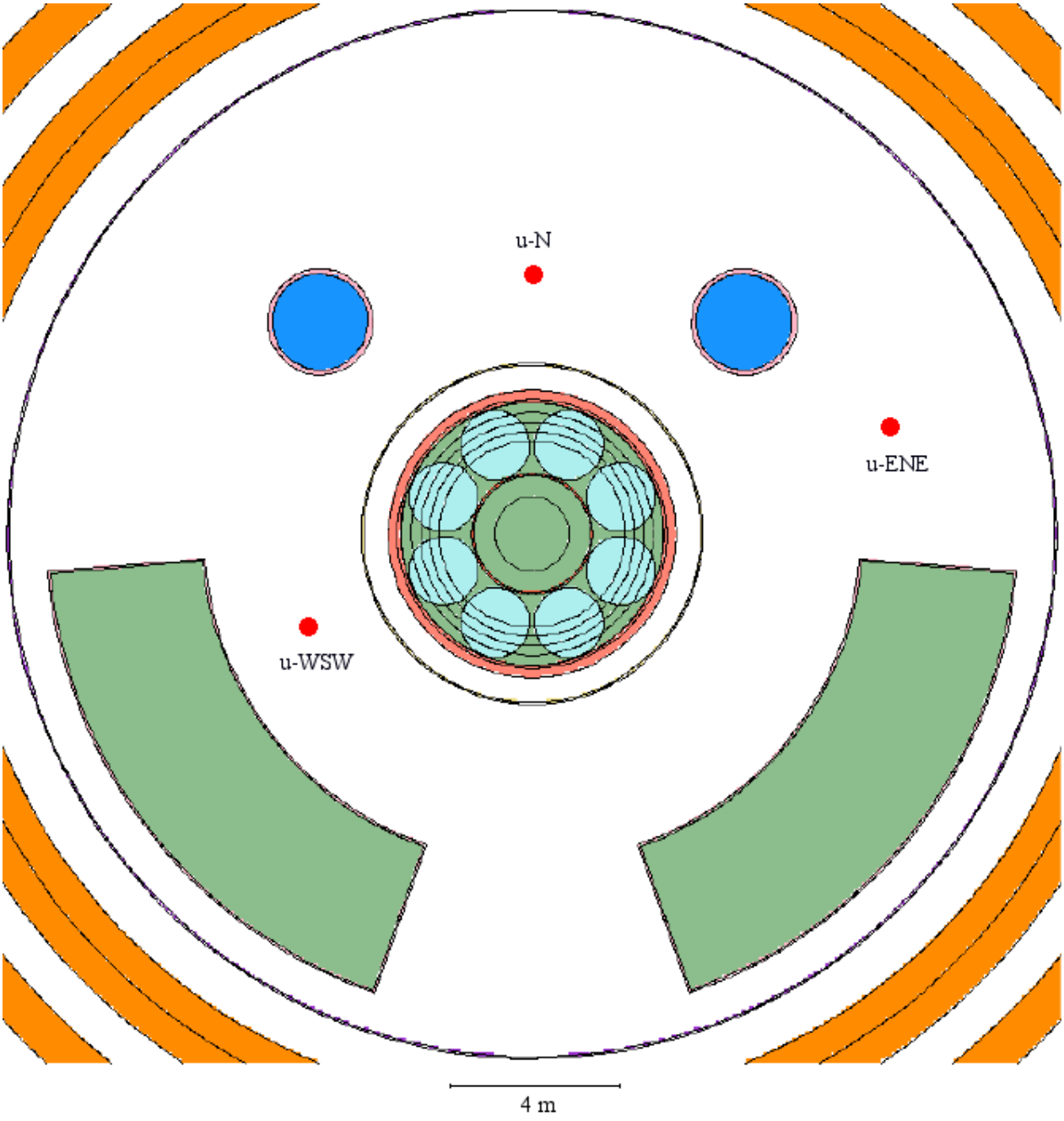

Fig. 158: Vertical section through dose point “u-WSW” and the reactor axis showing possible streaming path.

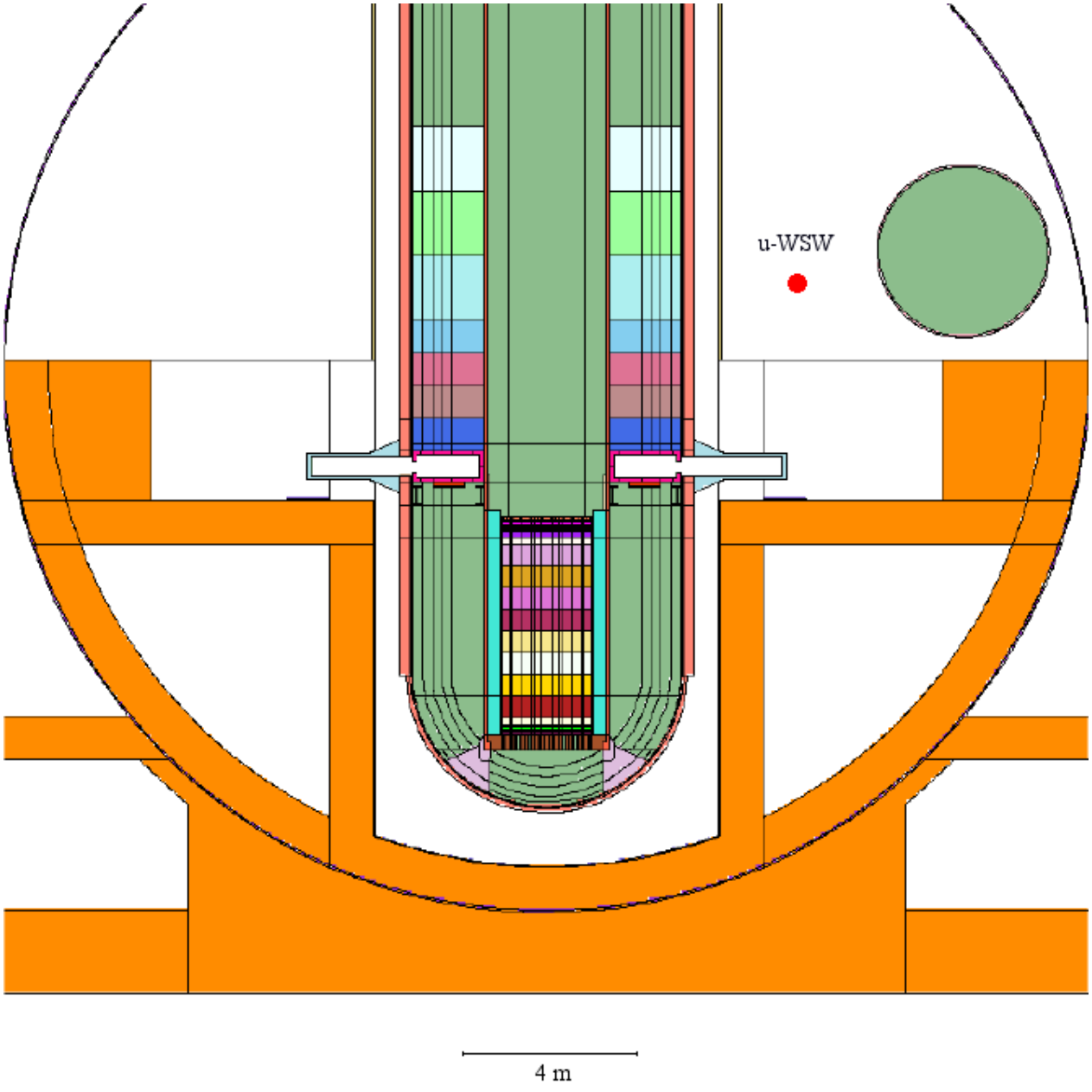

Fig. 159: Vertical section through dose point “u-ENE” and the reactor axis showing possible streaming path.

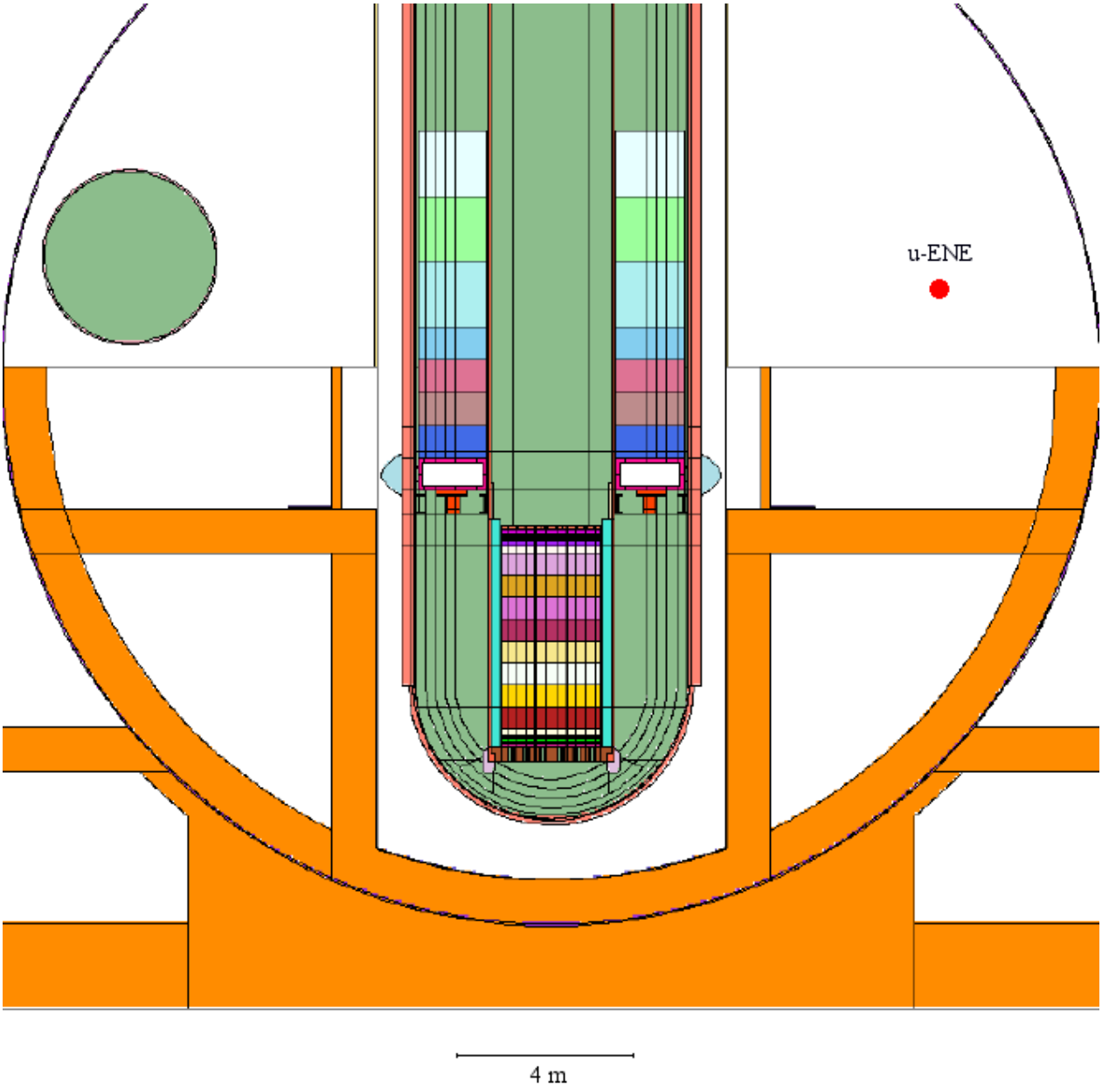

Fig. 160: Vertical section through dose point “u-N” and the reactor axis showing lack of any possible streaming path.

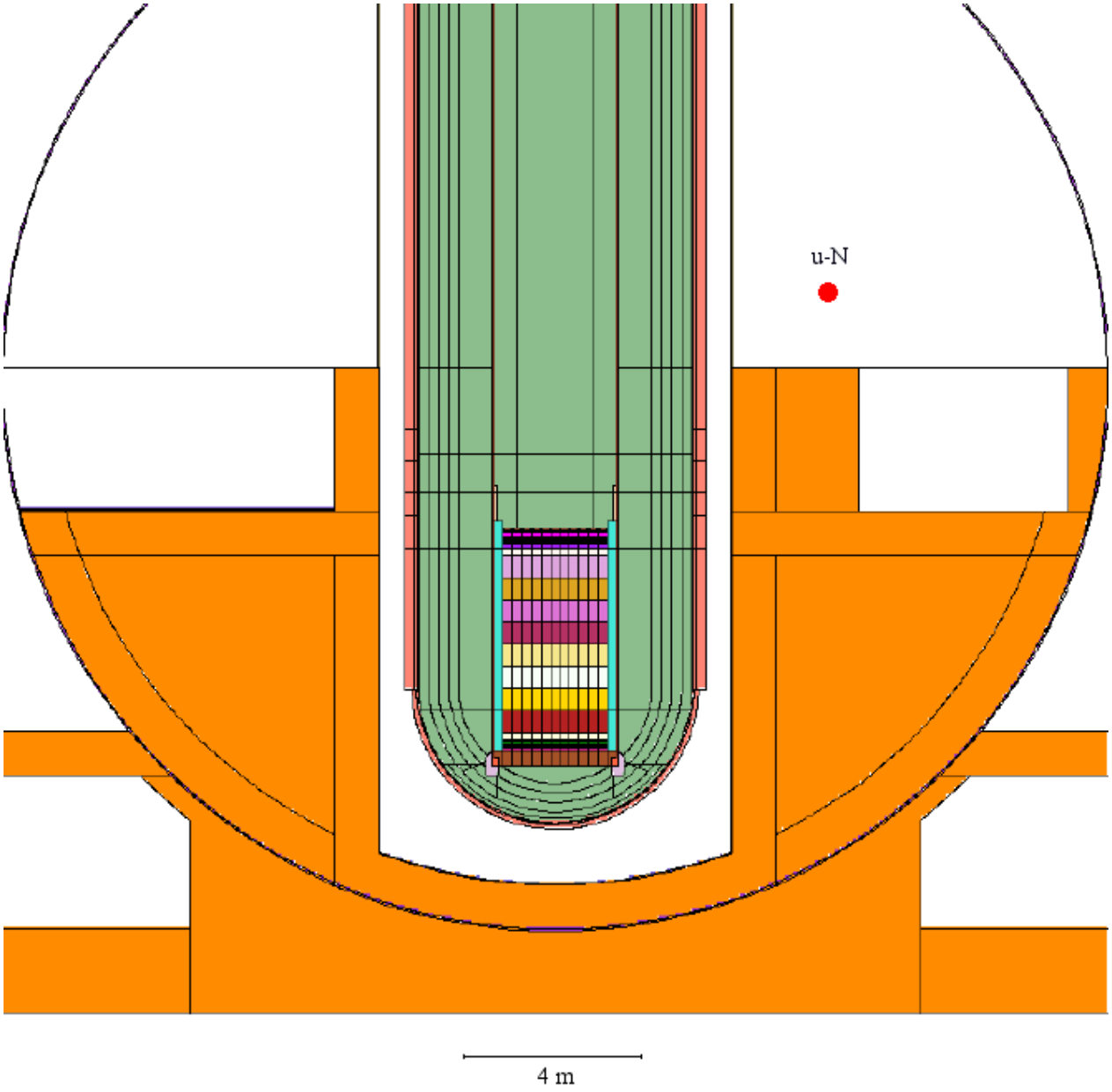

Fig. 161: Horizontal section of inlet nozzle showing (in red) the surface segment used for tallying the activation dose.

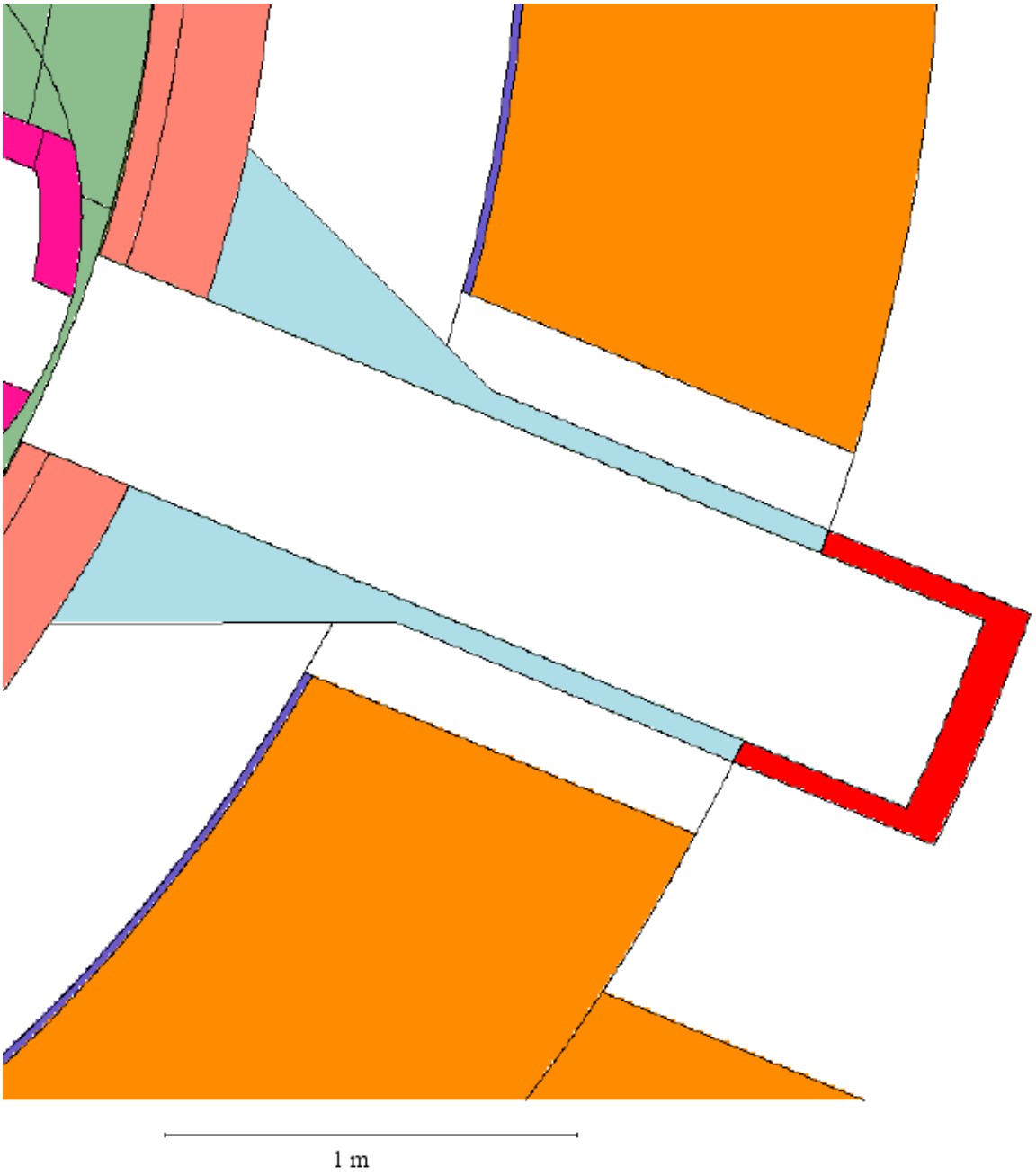

Fig. 162: Vertical section of inlet nozzle showing (in red) the upper and lower surface segments ("IN-u" and "IN-l") used for tallying the activation dose.

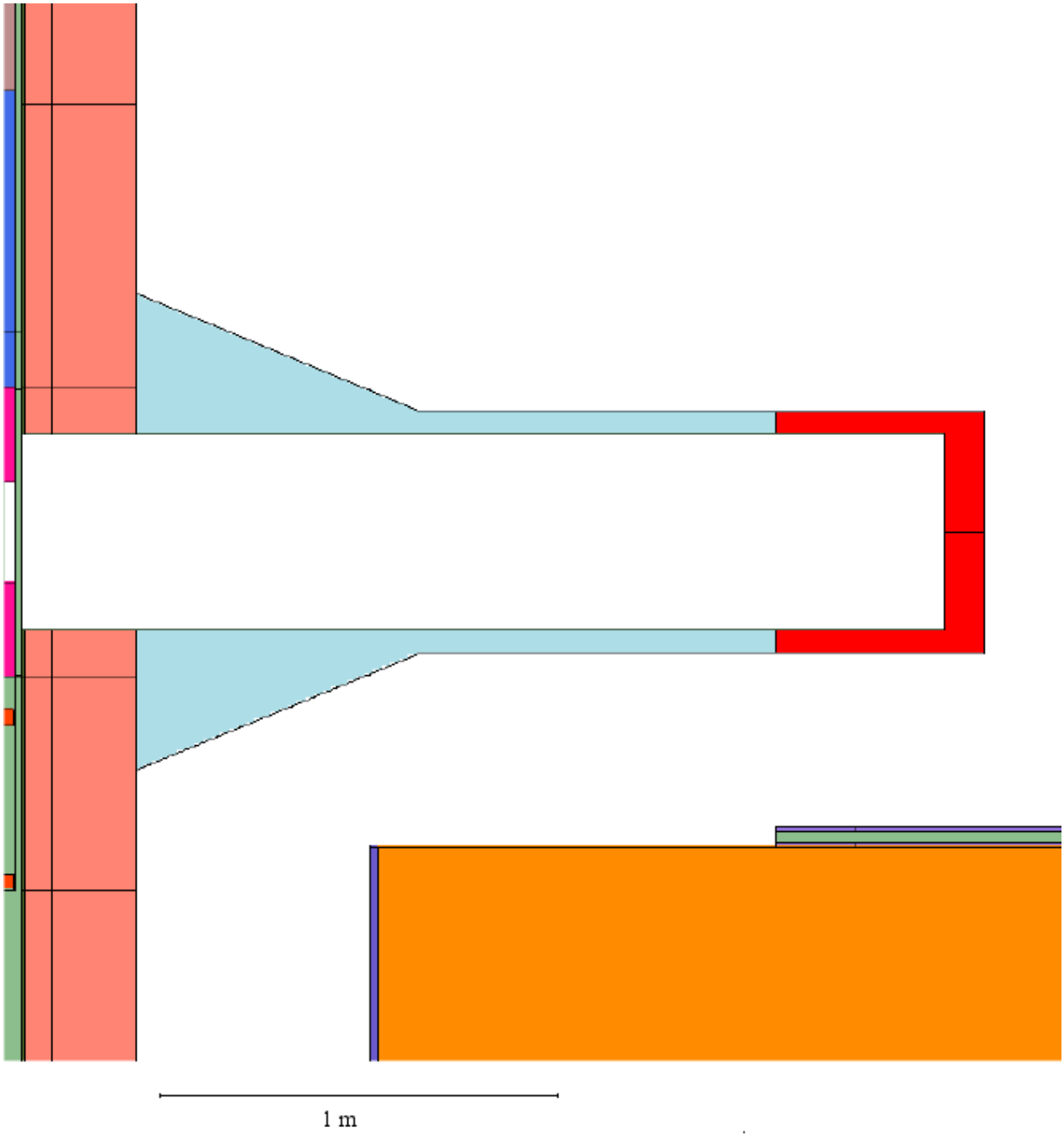

Fig. 163: Two vertical section of inlet nozzle, orthogonal to that in Fig. 162, showing in upper section (in red) the radial surface segments divided into upper and lower parts (“IN-u” and “IN-l”) and in lower section the end axial surface (“IN-cap”), used for tallying the activation dose.

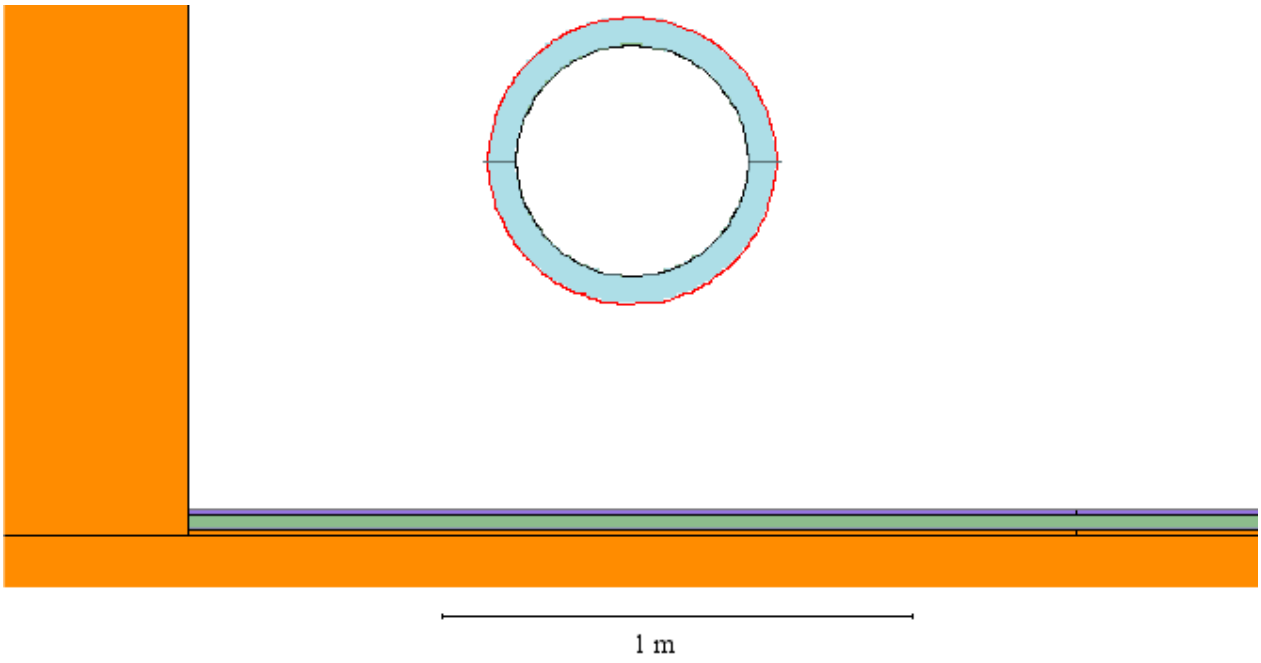

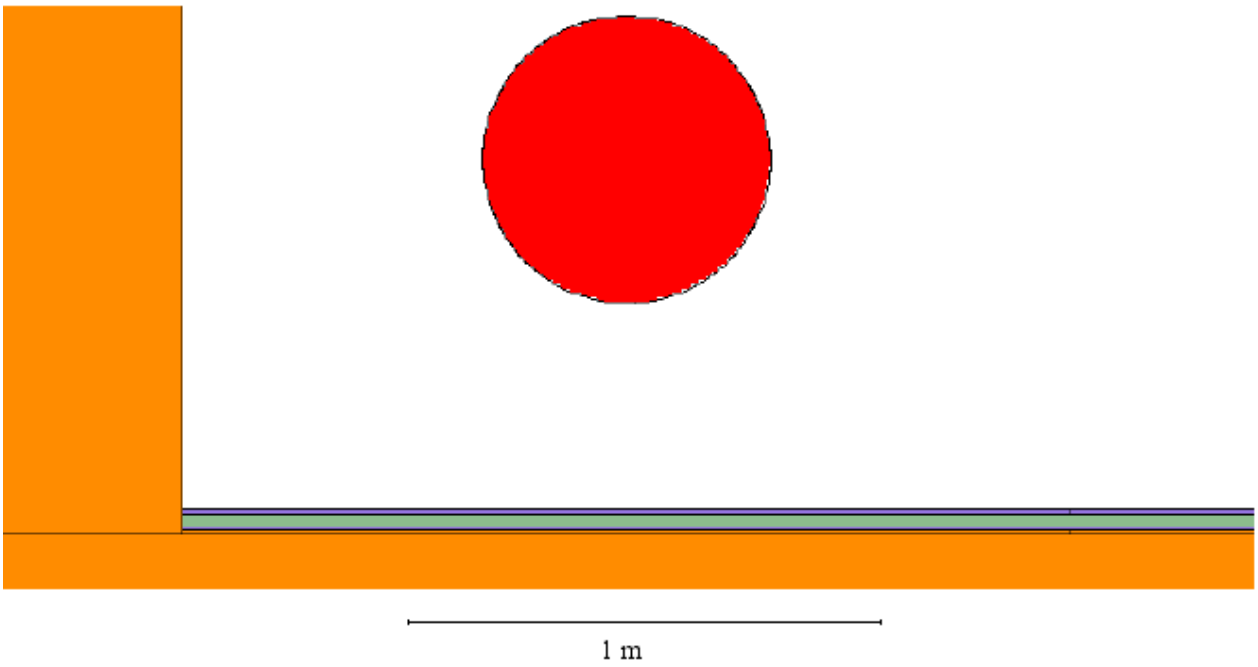

Fig. 164: Horizontal section of water pipe model showing (in red) the surface segment (“WPi”) used for tallying the activation dose.

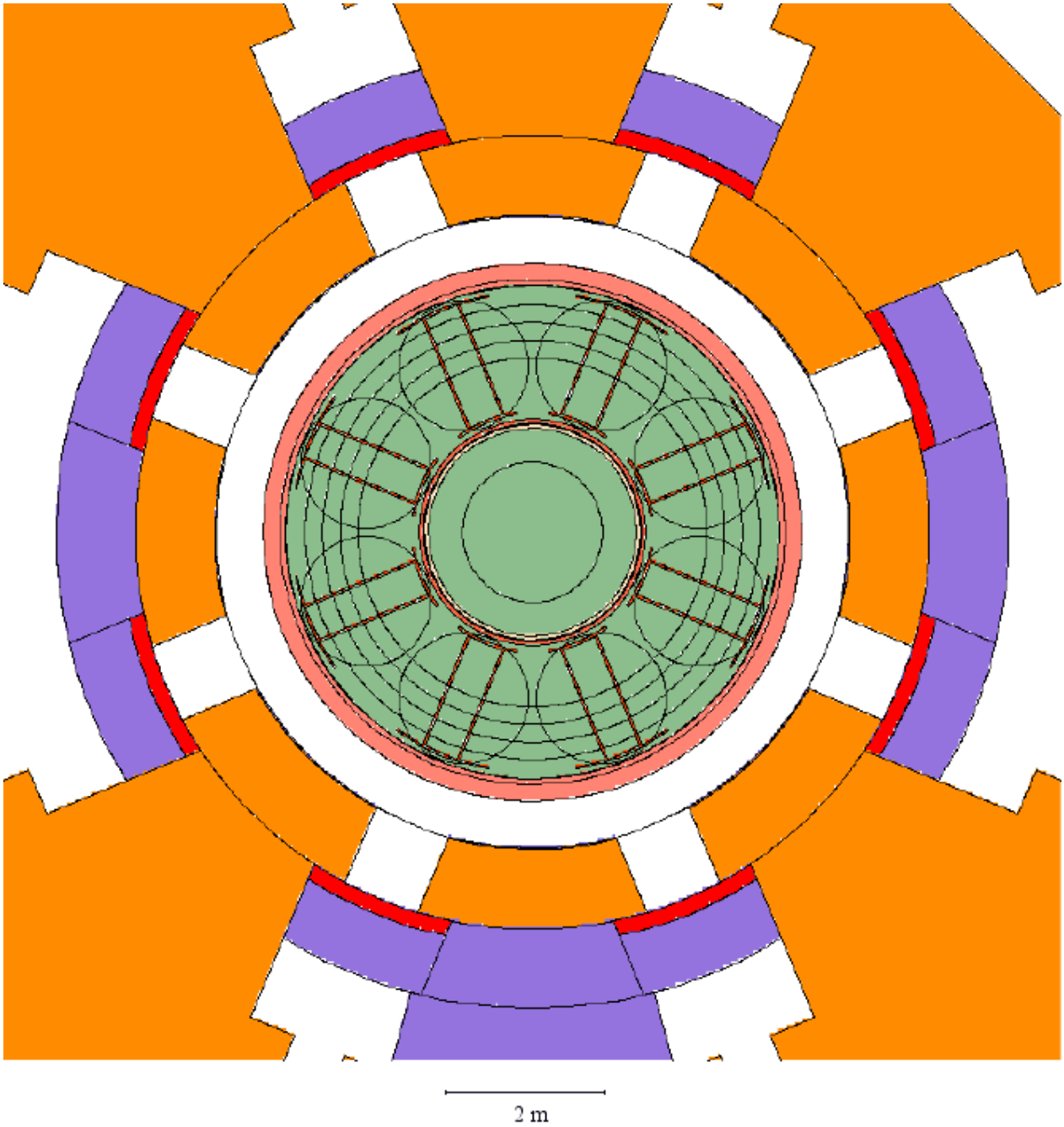

Fig. 165: Vertical section through side surface of ADS quench tank wall showing (in red) quadrant used for tallying the activation dose.

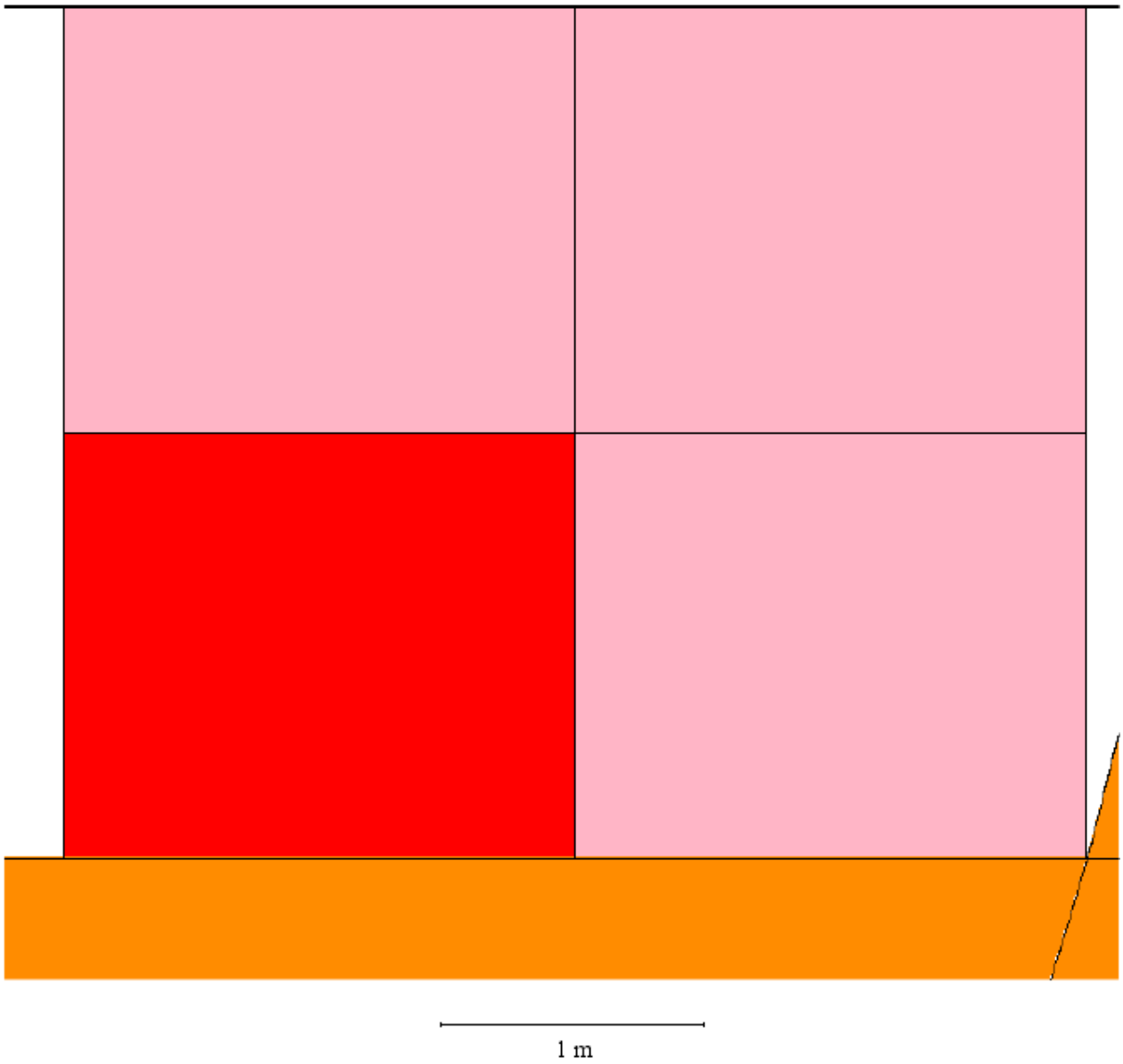

Fig. 166: Horizontal section through ADS quench tank showing (in red) part of side wall used for tallying the activation dose.

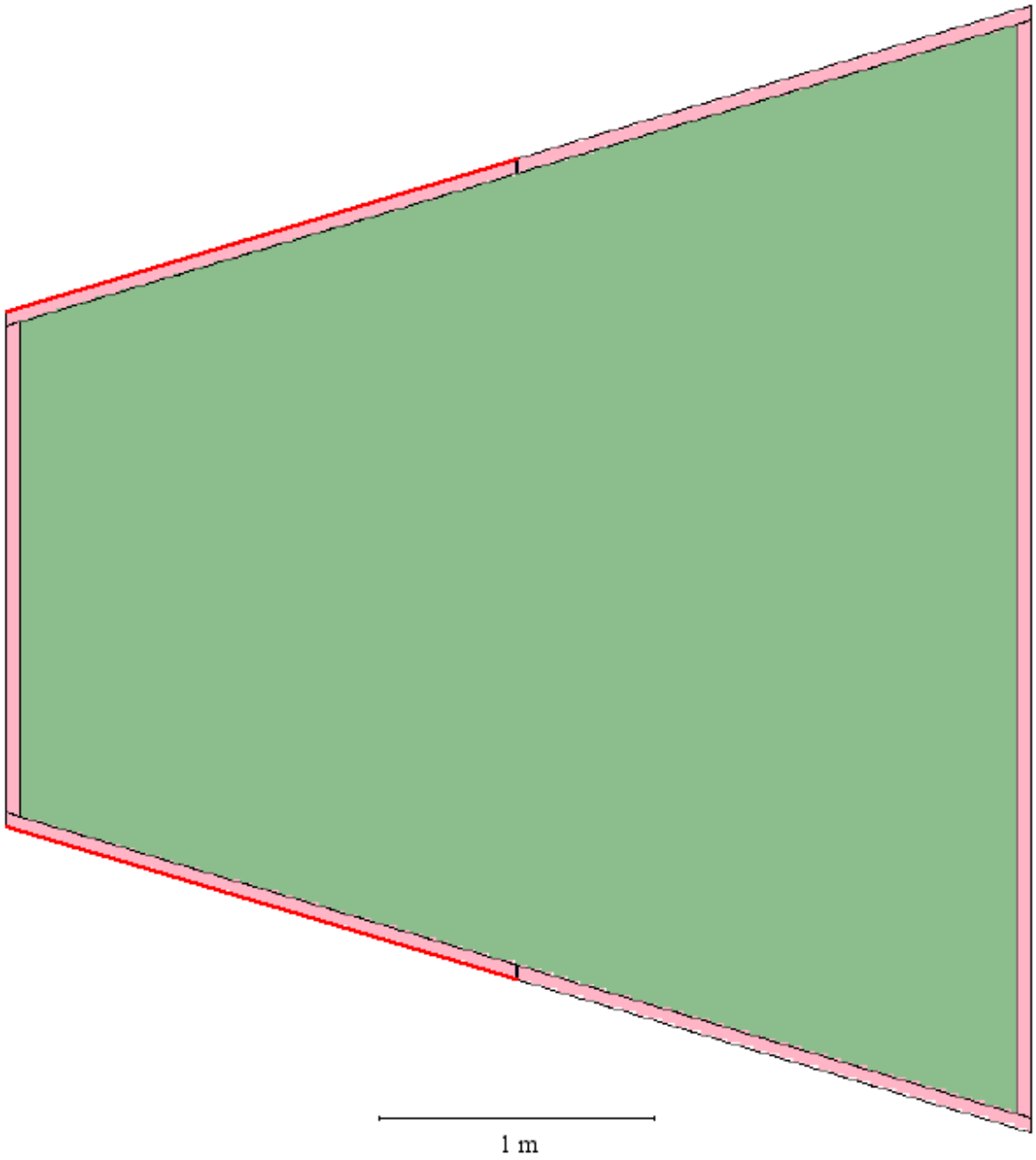

Fig. 167: Horizontal section showing part of containment vessel (in red) in South direction used for tallying the activation dose.

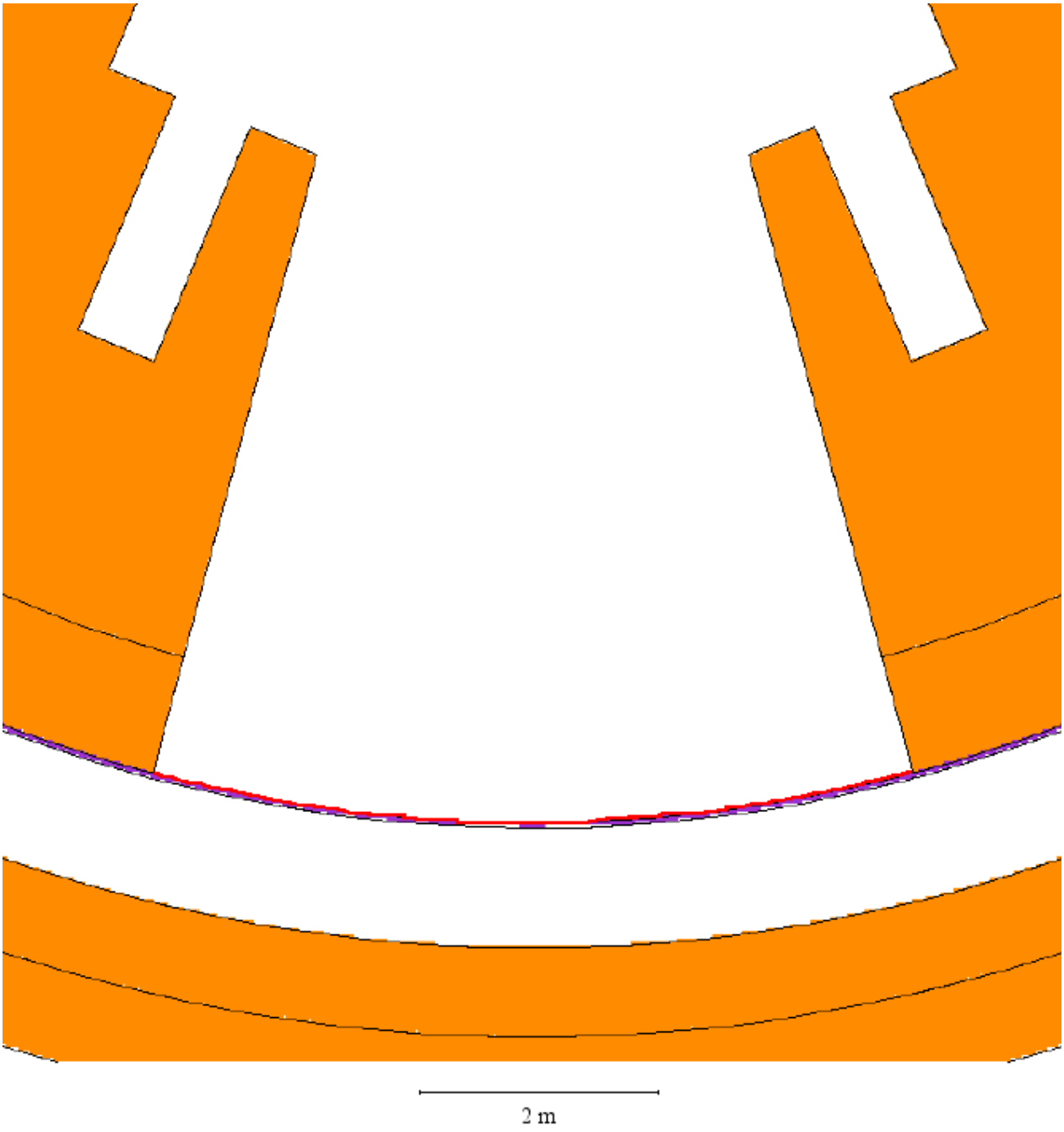

Fig. 168: Vertical section showing part of containment vessel (in red) in South direction used for tallying the activation dose.

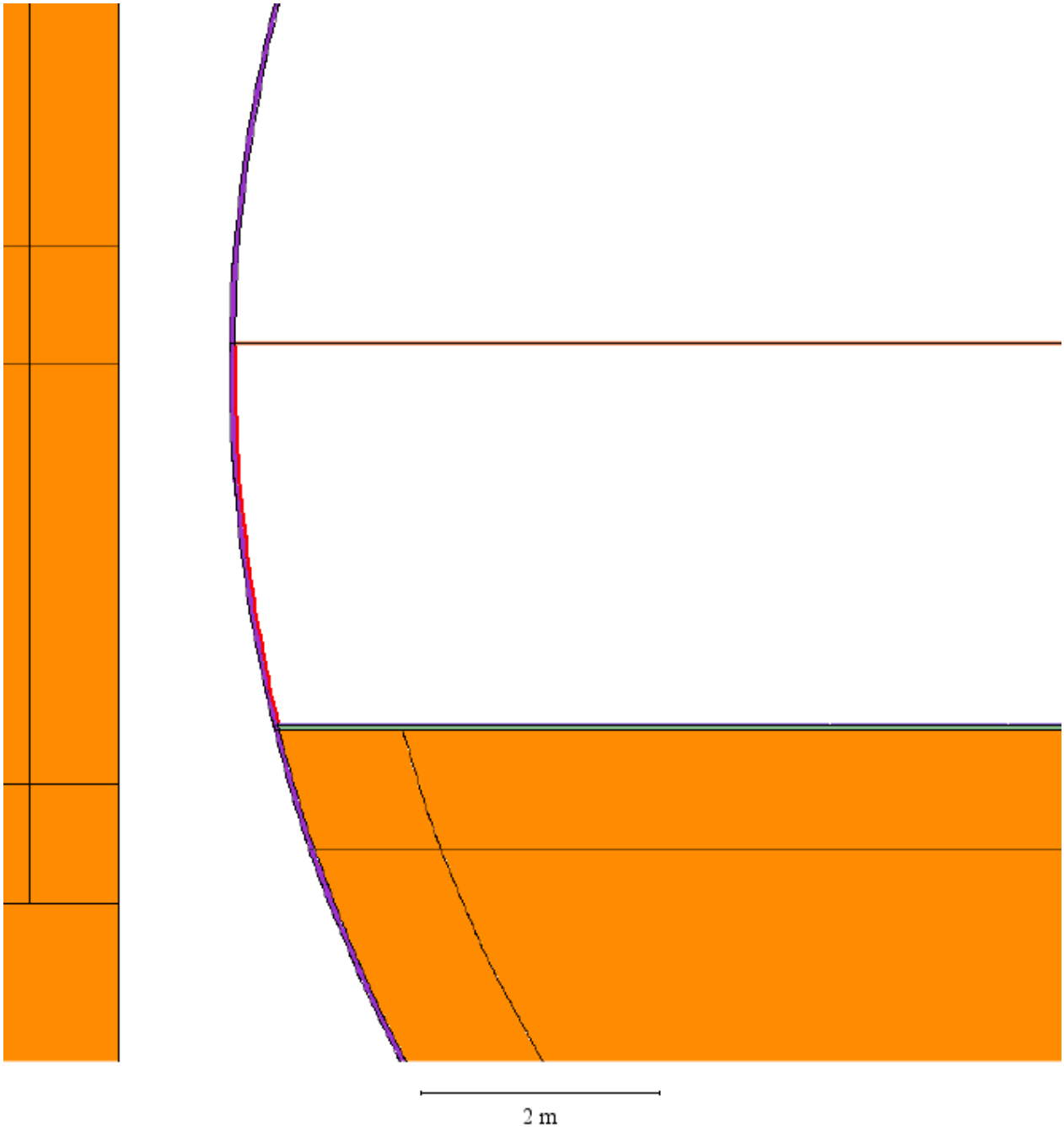

Fig. 169: Horizontal section at main deck level showing part of gratings (in red) used for tallying the activation dose.

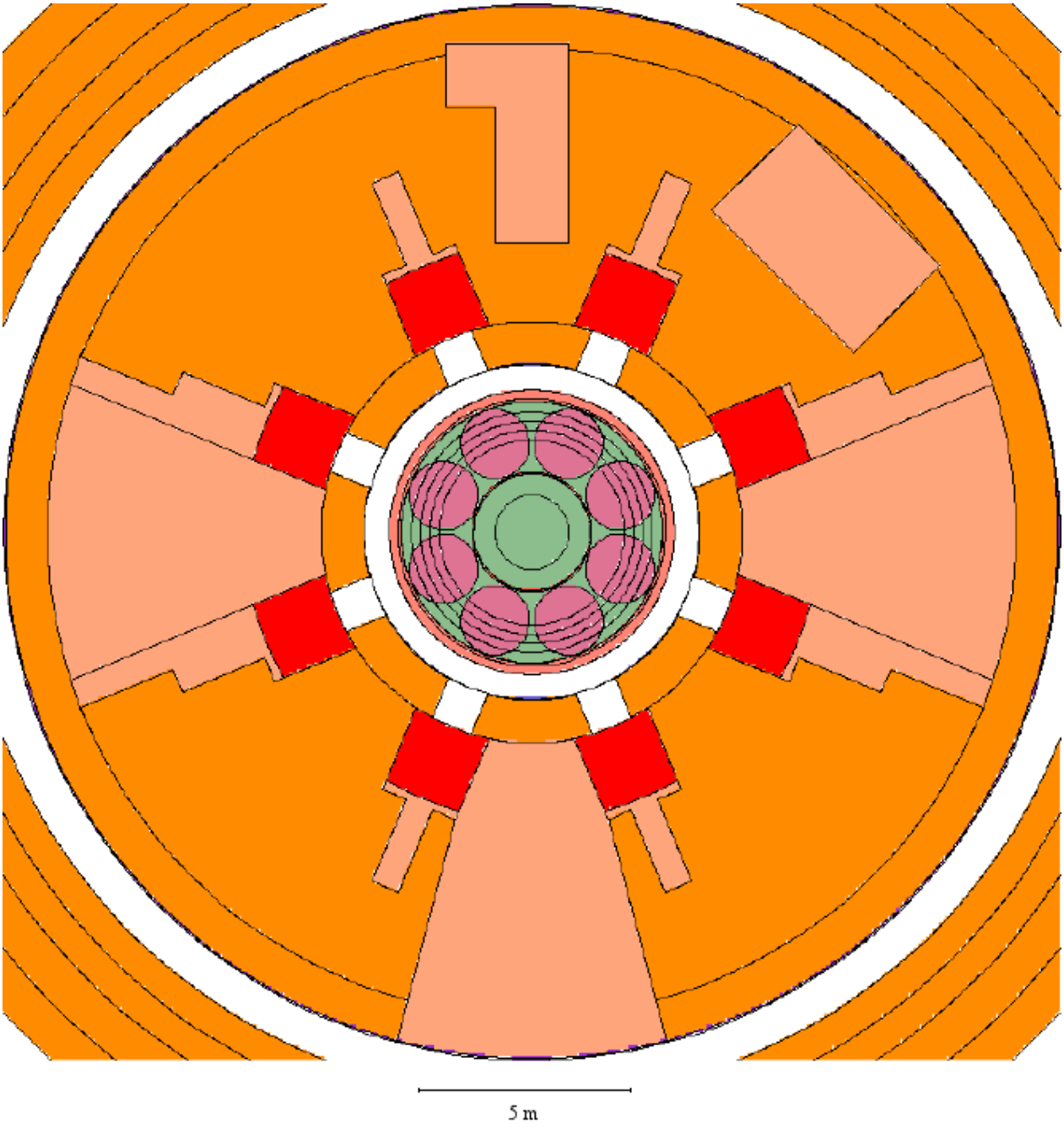

Fig. 170: Vertical section showing lower segment of anti-missile shield (in red) used for tallying the activation dose.

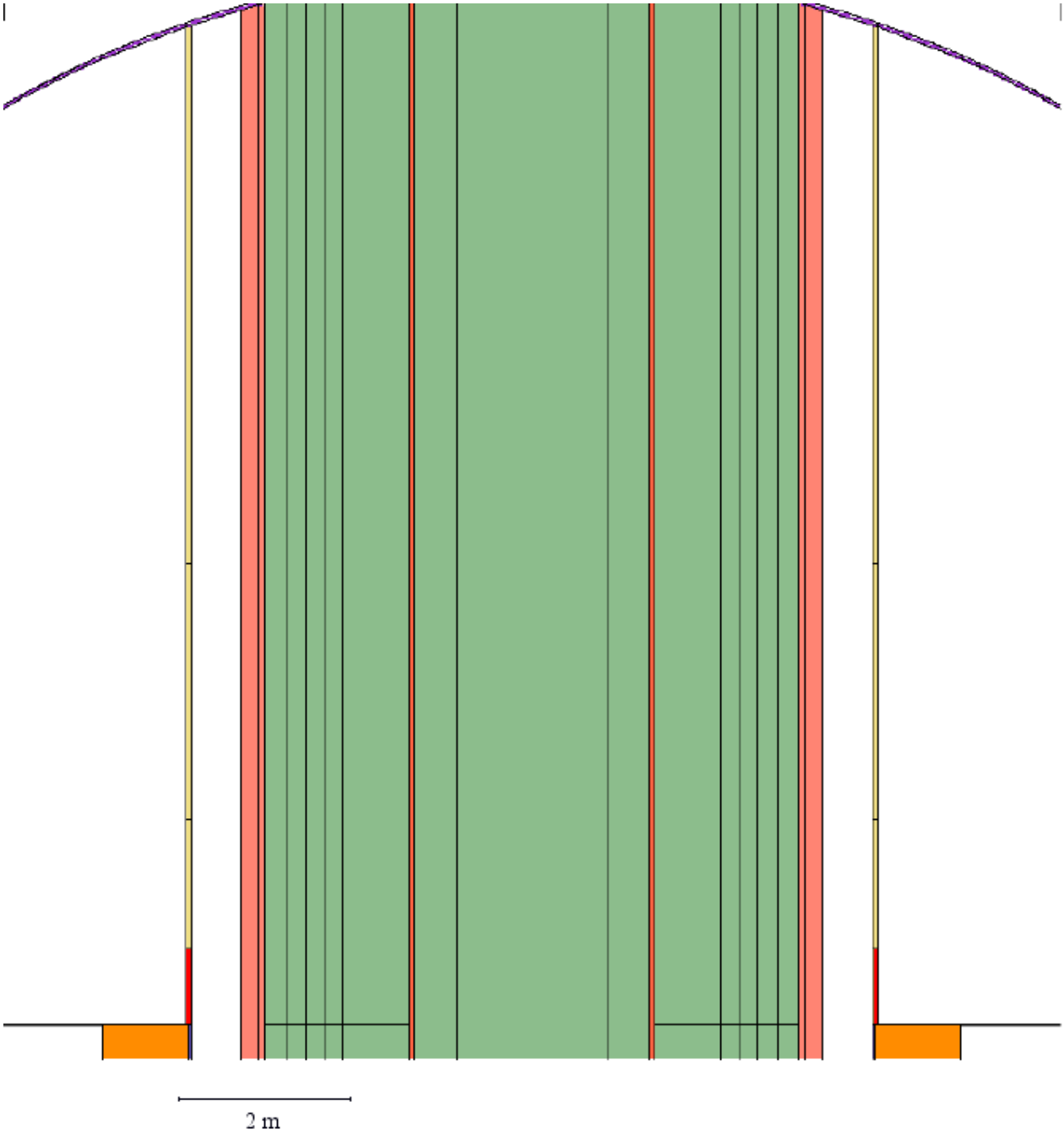

Fig. 171: Horizontal section showing bottom surfaces of EB tanks (in red) used for tallying the activation dose.

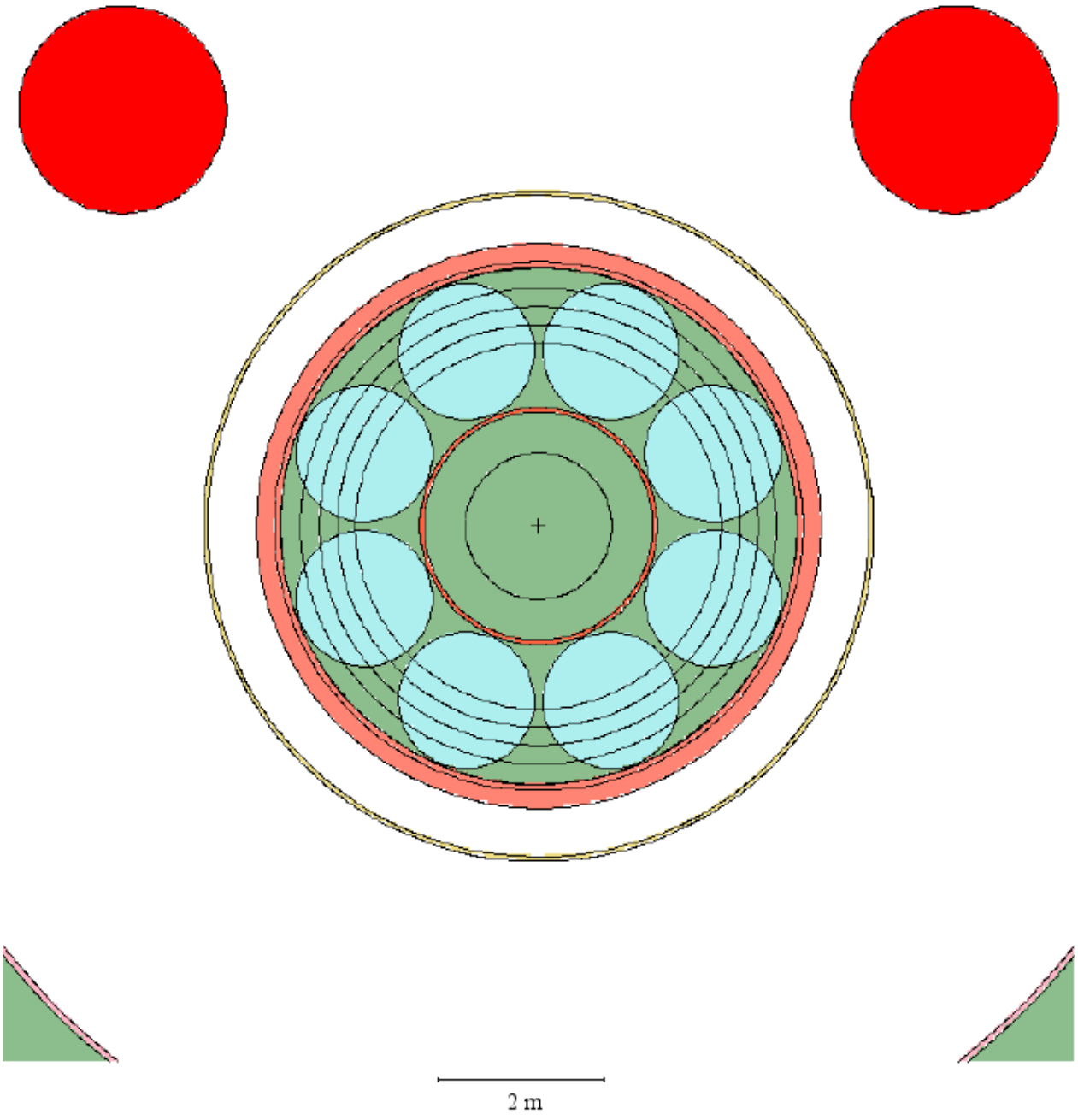

Fig. 172: Horizontal section showing side surfaces of EB tanks (in red) used for tallying the activation dose.

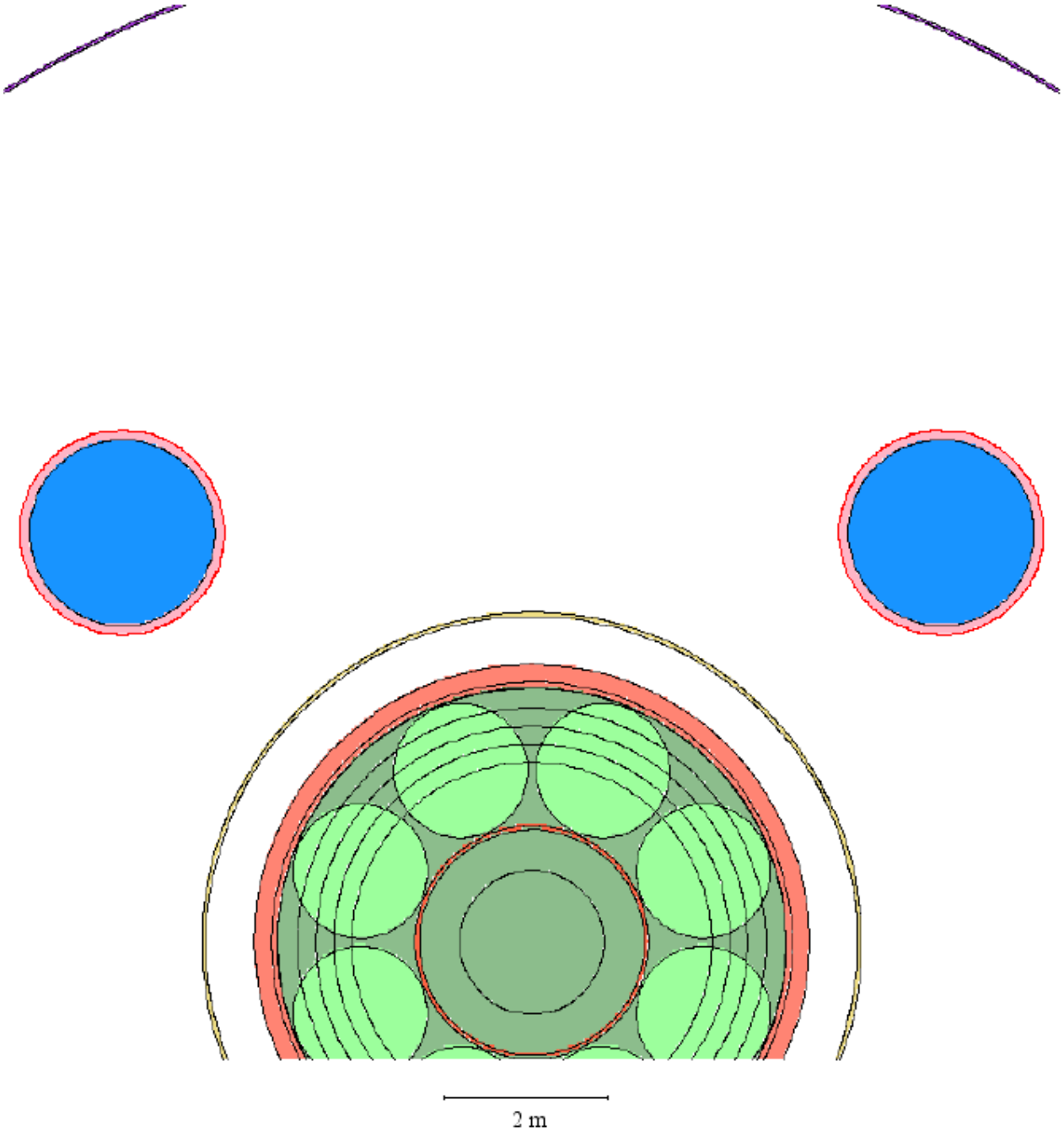

Fig. 173: Horizontal section showing surfaces of LGMS tanks (in red) used for tallying the activation dose.

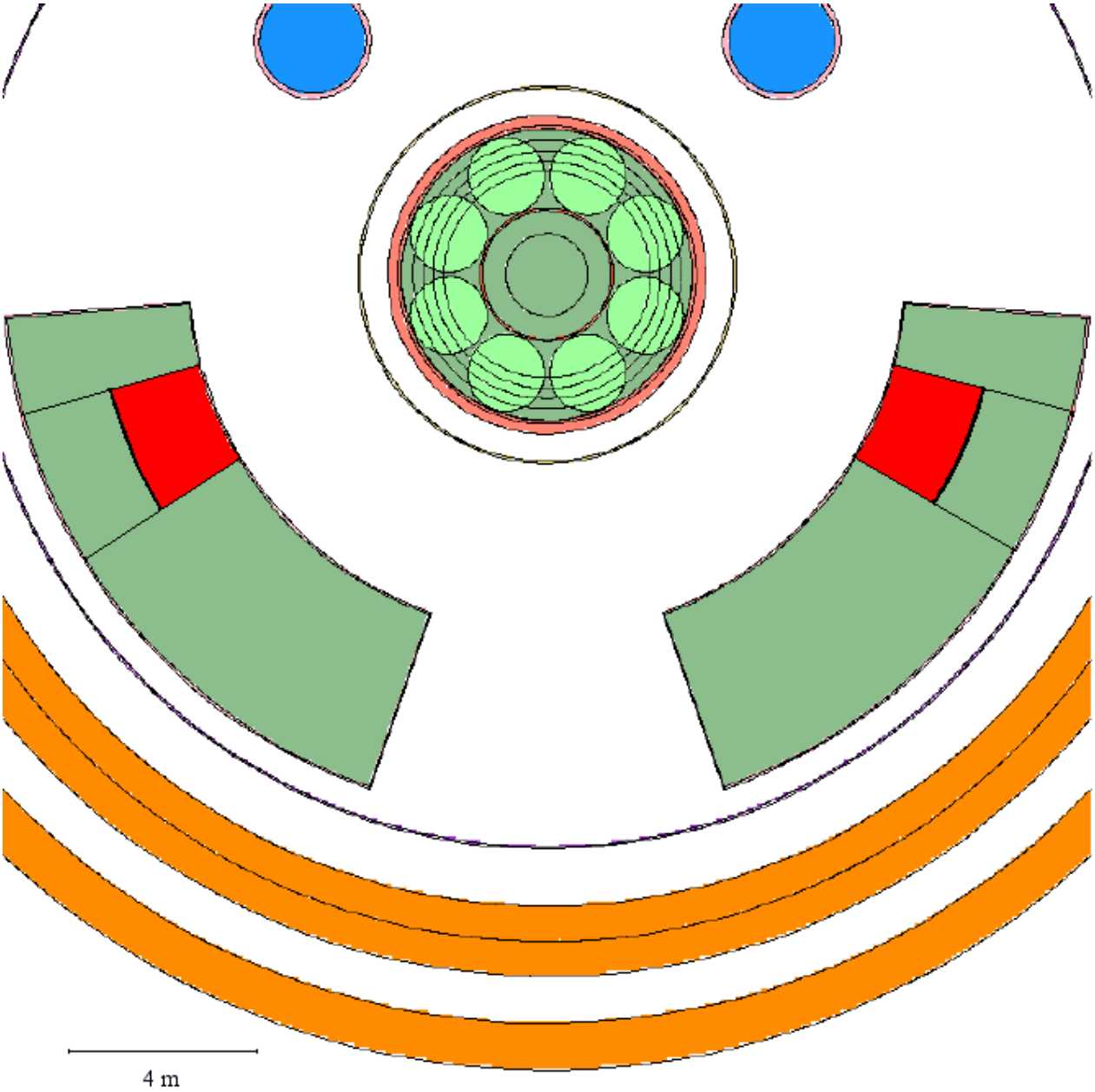

Fig. 174: Vertical section showing surfaces of LGMS tanks (in red) used for tallying the activation dose.

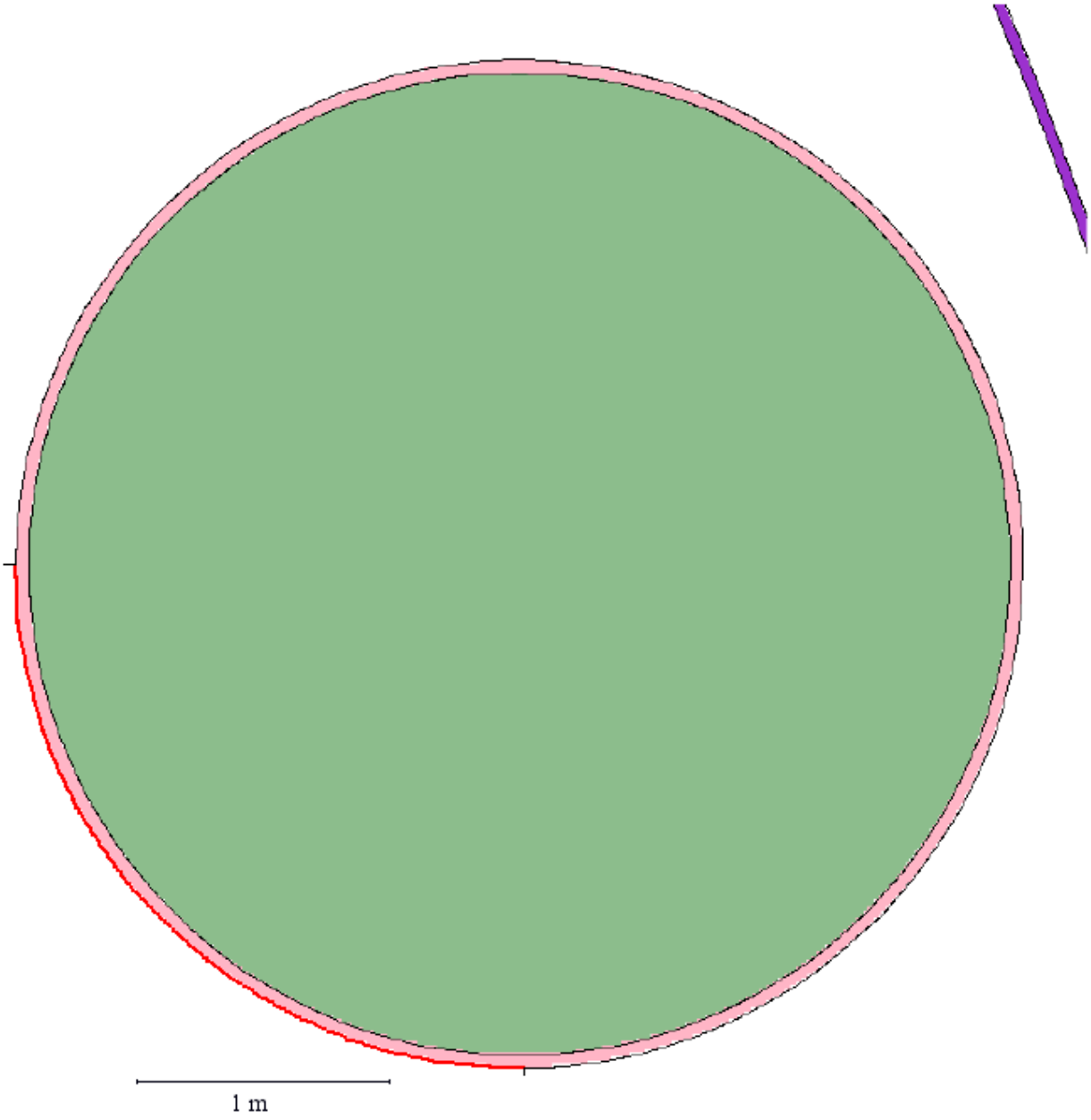

Fig. 175: Vertical section in S-N direction showing inner surface of section of containment vessel (in red) above main deck and outside anti-missile shield used for tallying the activation dose.

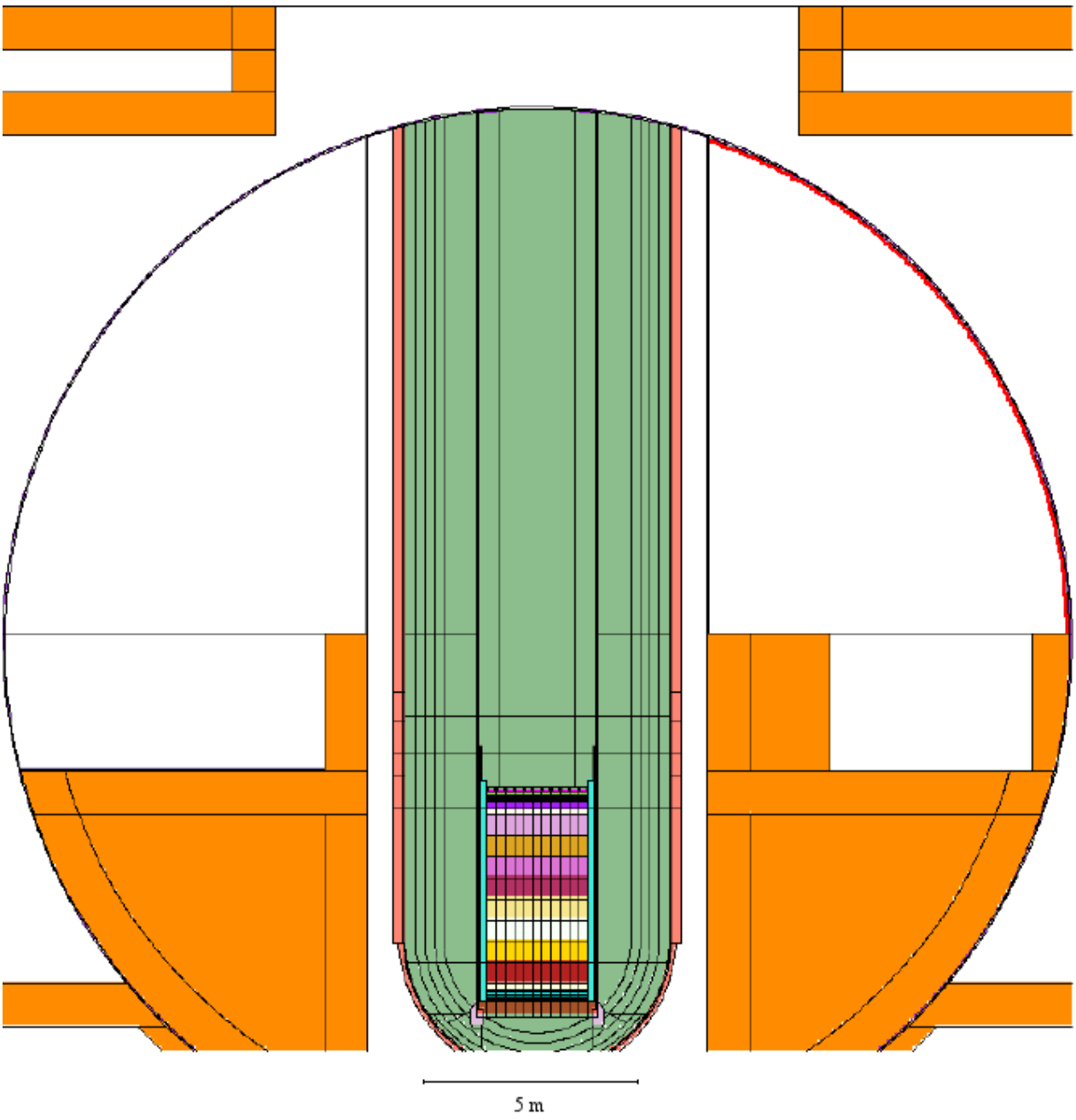

Fig. 176: Horizontal section just below top of anti-missile shield showing inner surface of azimuthal segment of containment vessel (in red) ±15° around North used for tallying the activation dose.

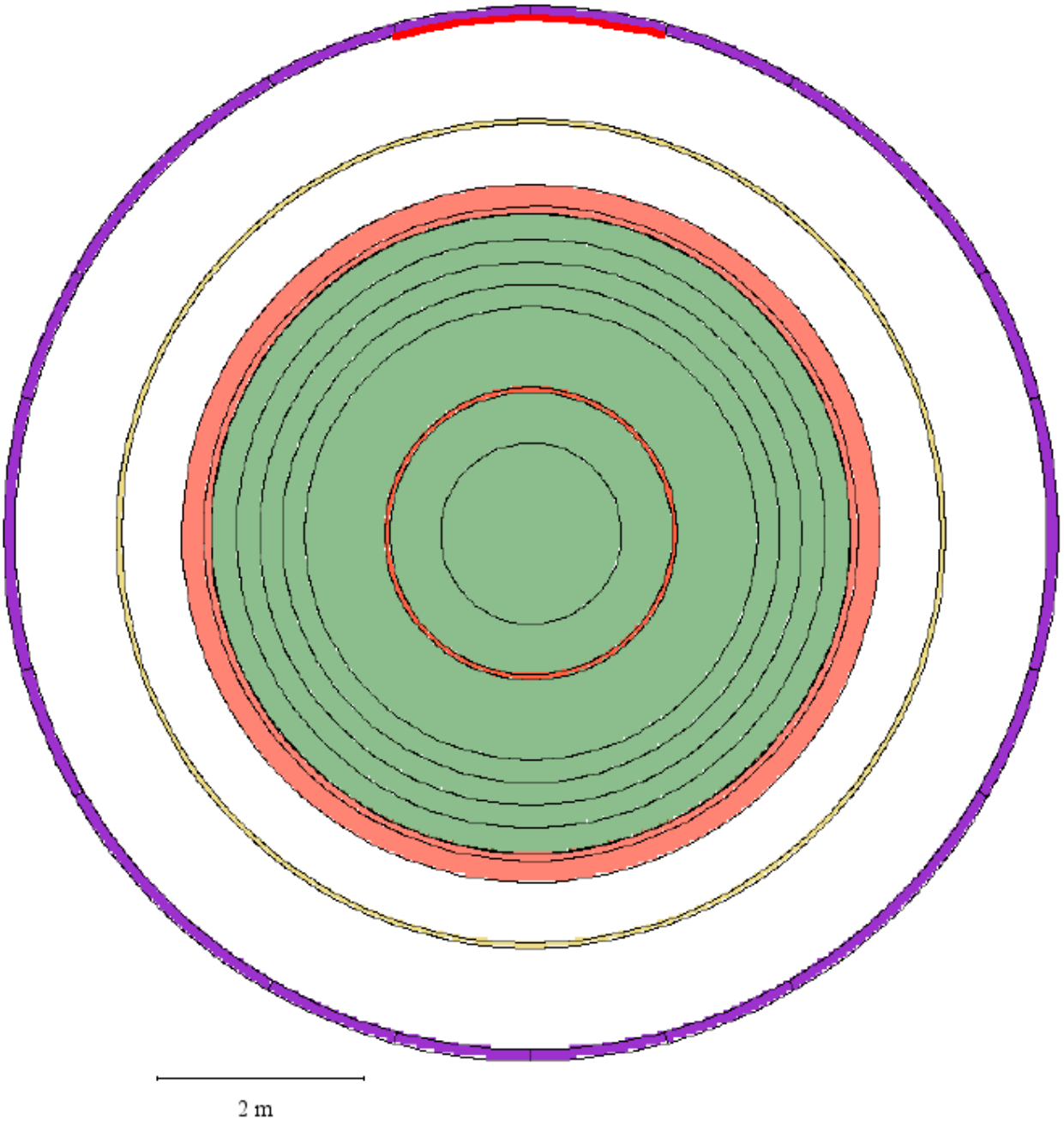

Fig. 177: Vertical section showing outer flange of inlet nozzle removed and surface (in red) used for tallying the activation dose.

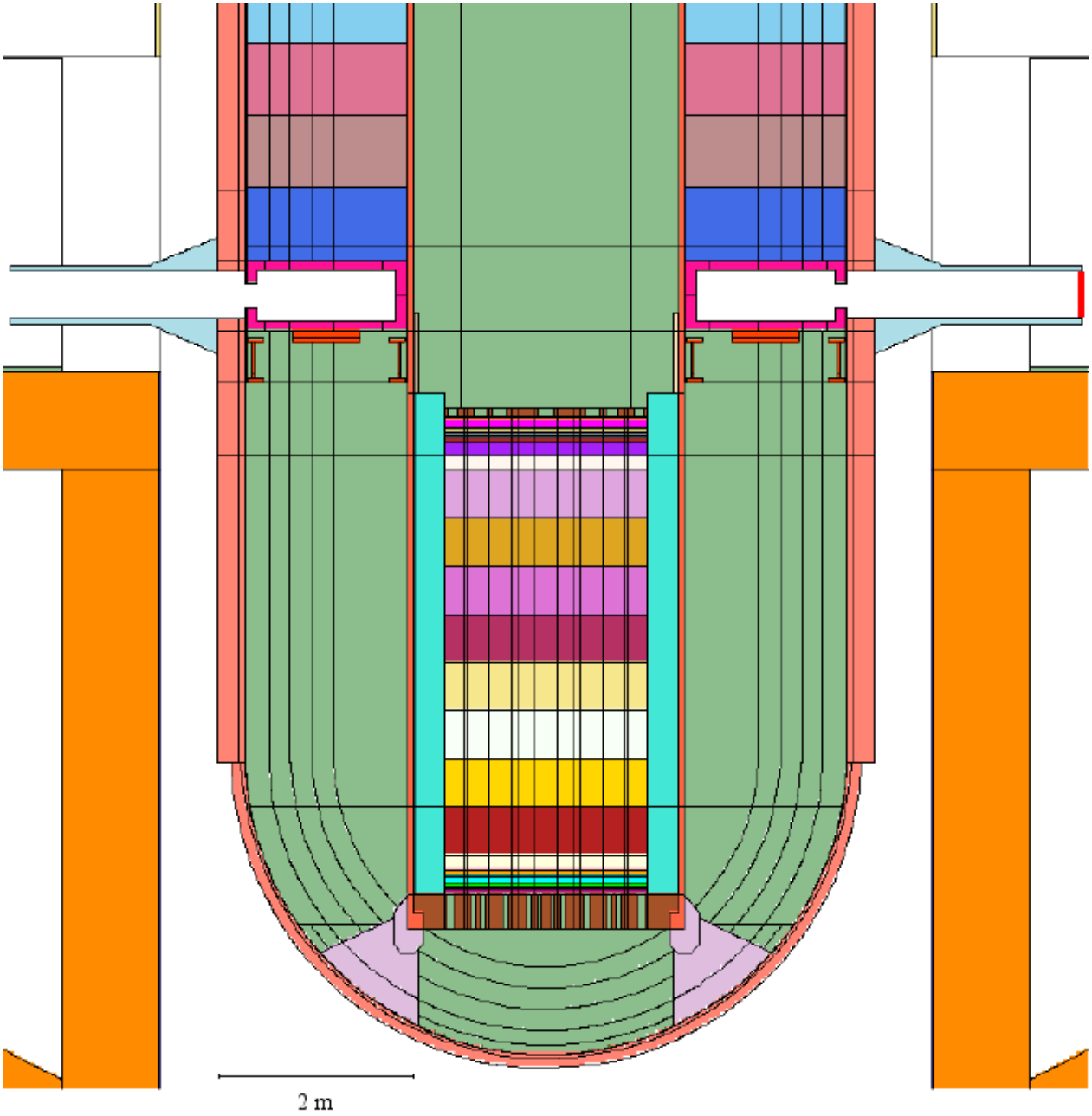

Fig. 178: Horizontal section showing outer flange of inlet nozzle removed and surface (in red) used for tallying the activation dose.

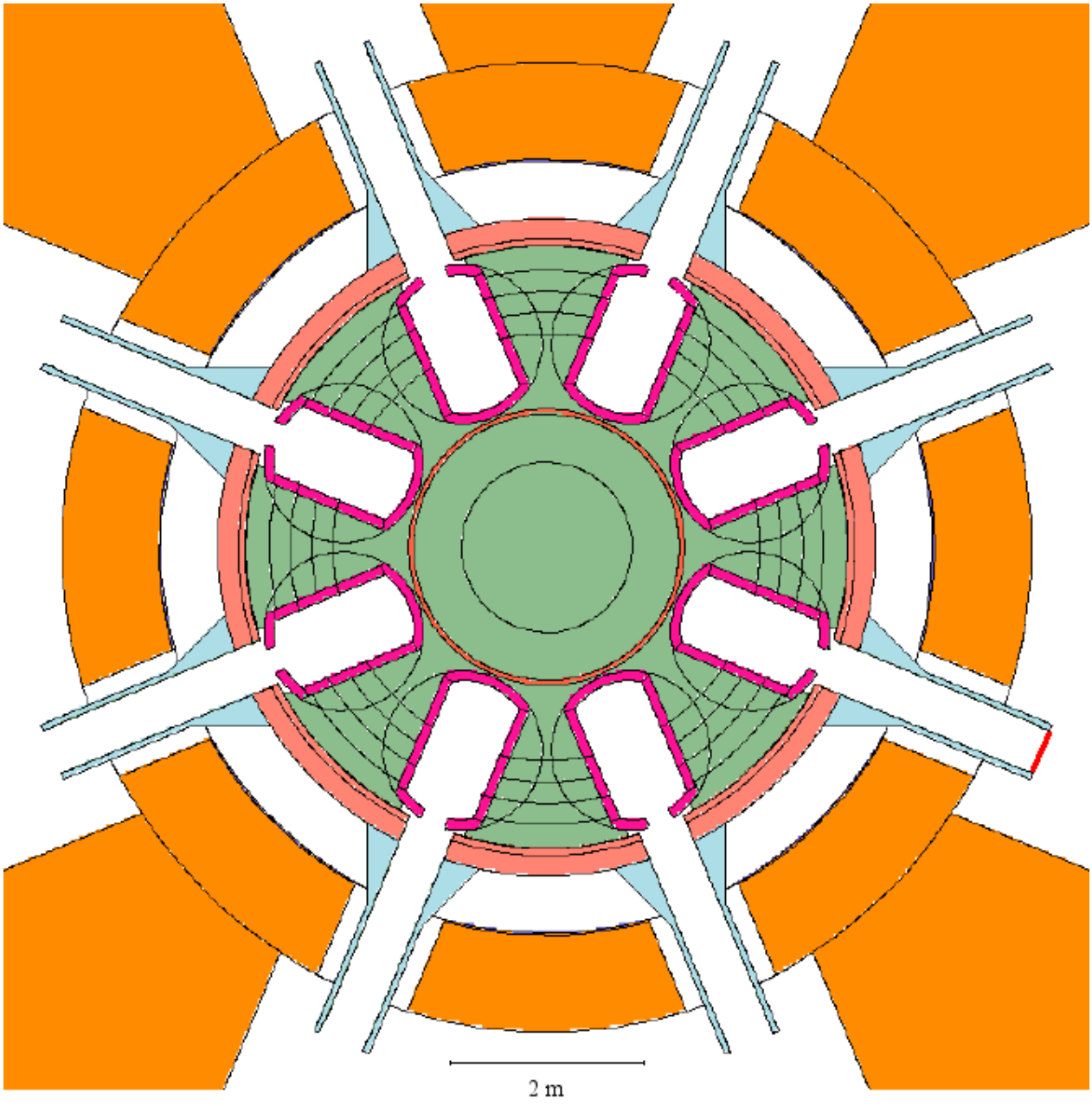

Figure 179. Geometry for the calculation of the dose in the area housing the seismic isolators (scoring surface shown in red with below 1 m of concrete to provide an albedo).

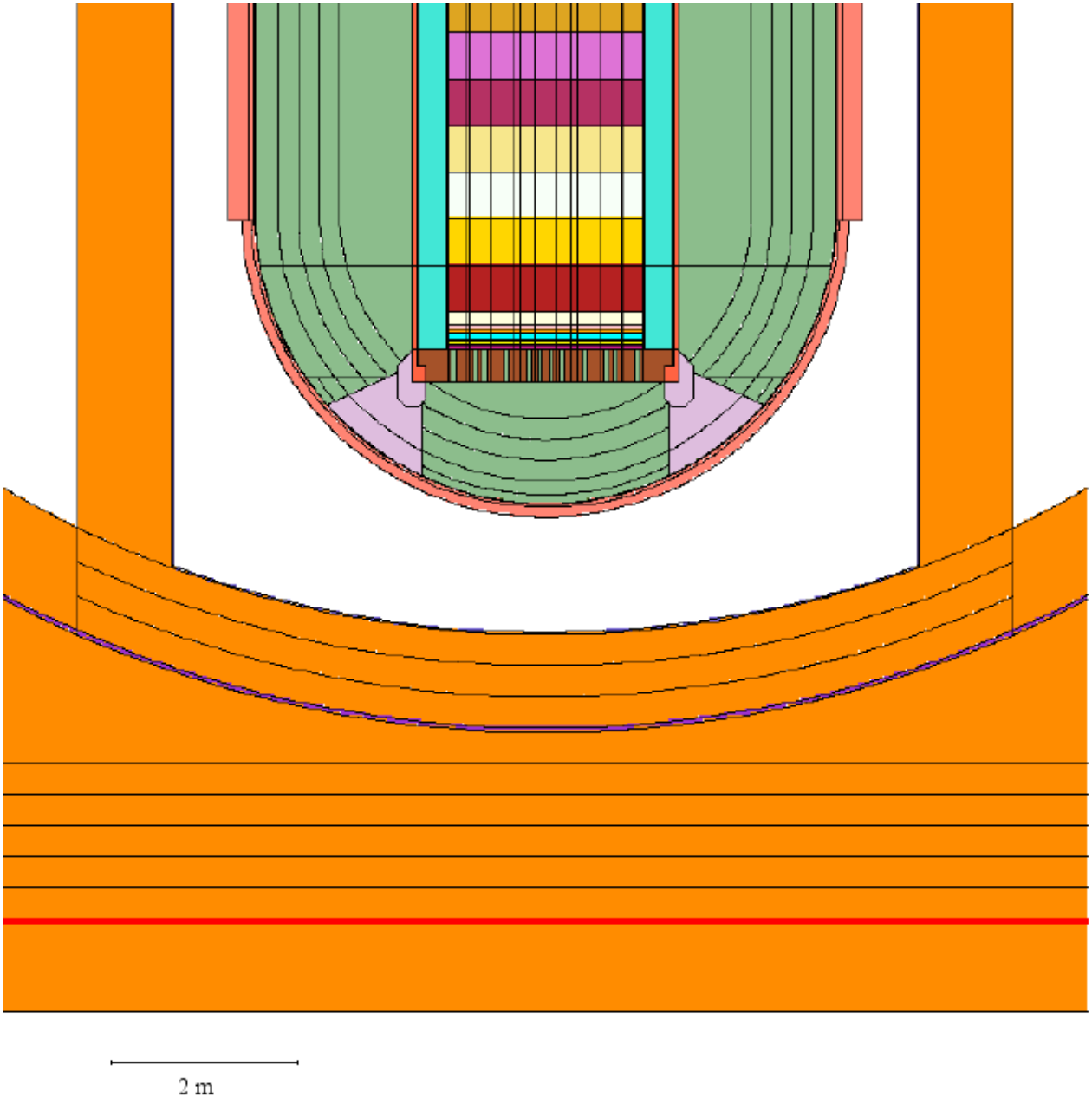

Figure 180. Neutron doses in the seismic isolator cavity under the reactor

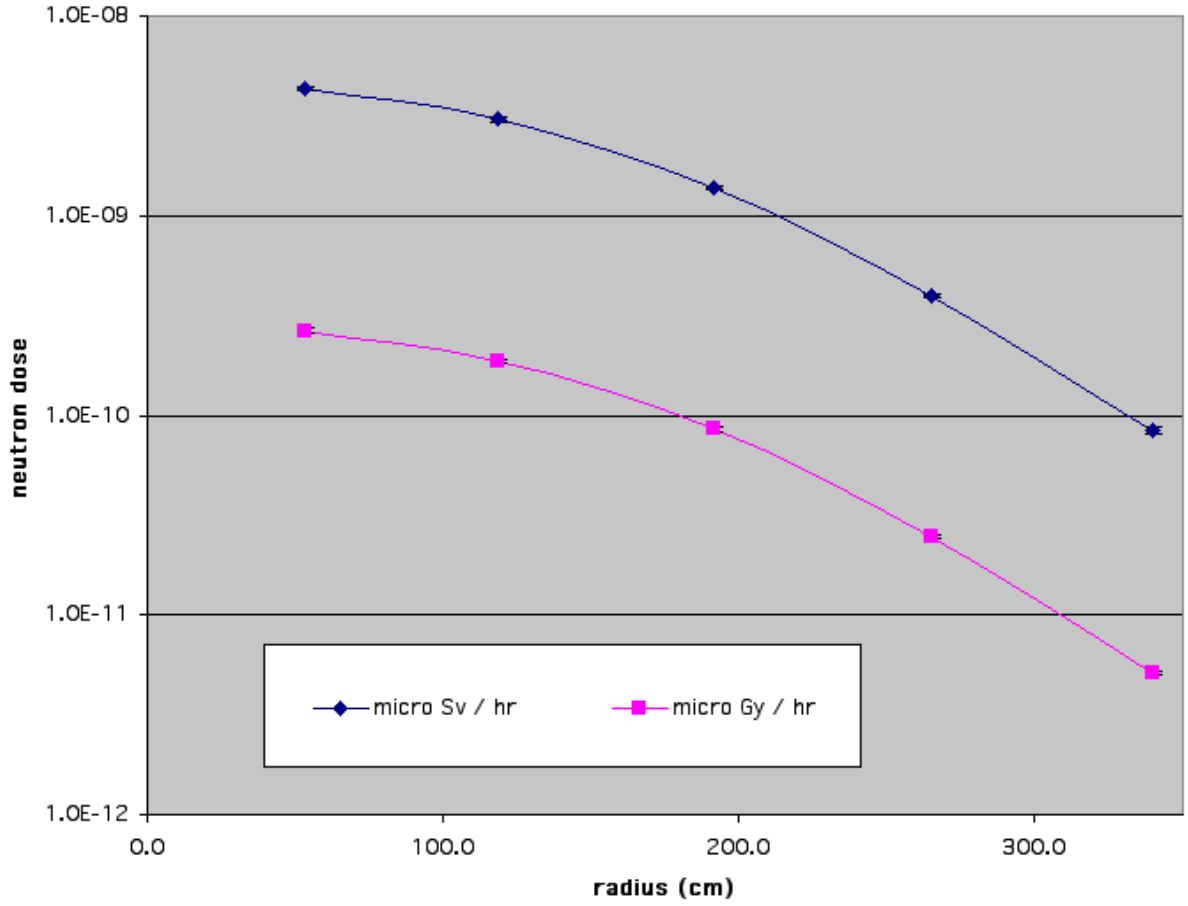

Figure 181. Gamma doses in the seismic isolator cavity under the reactor

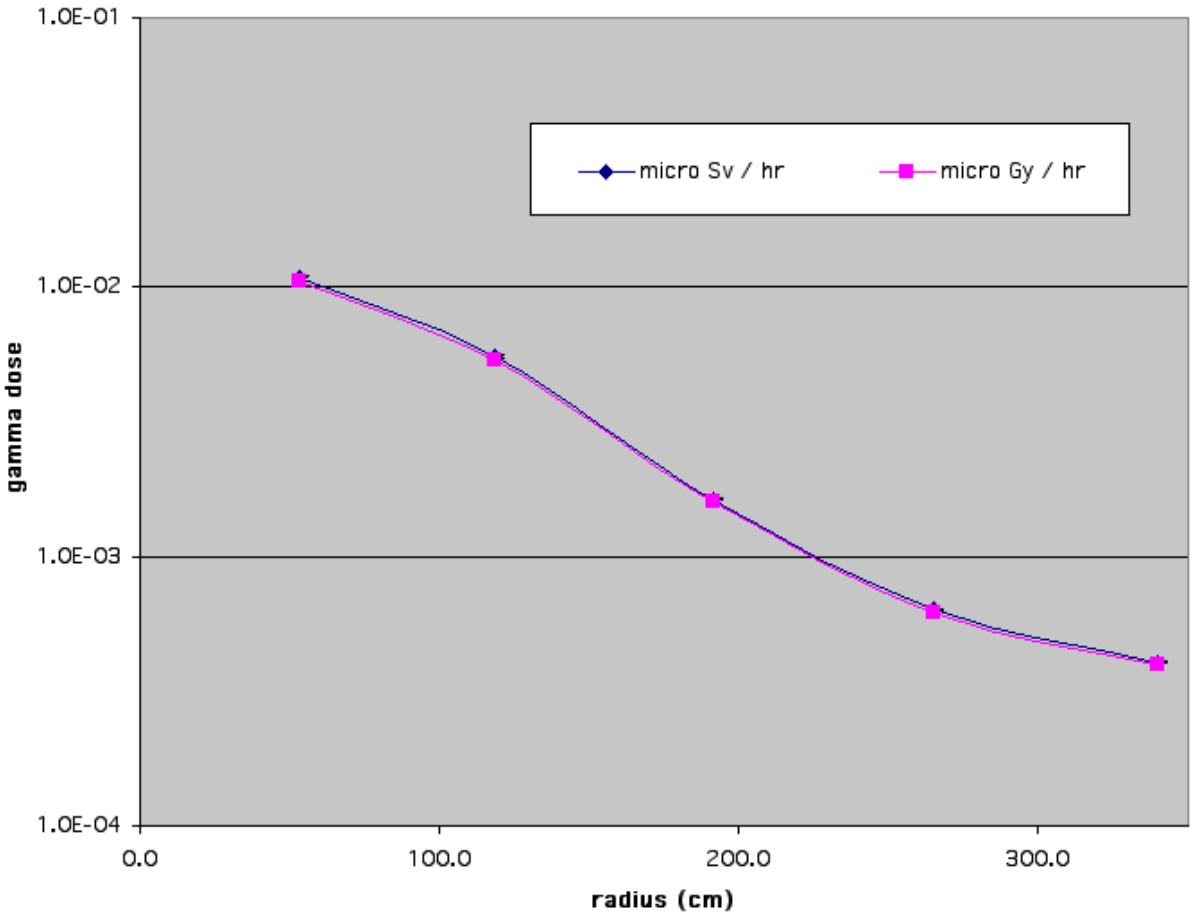

Figure 182. Points at which the dose was calculated around a single extracted steam generator (including bottom header and lower support). Shown are the surface segments and points at 1 m from the surface. Not shown are the points at 10 m from the surface.

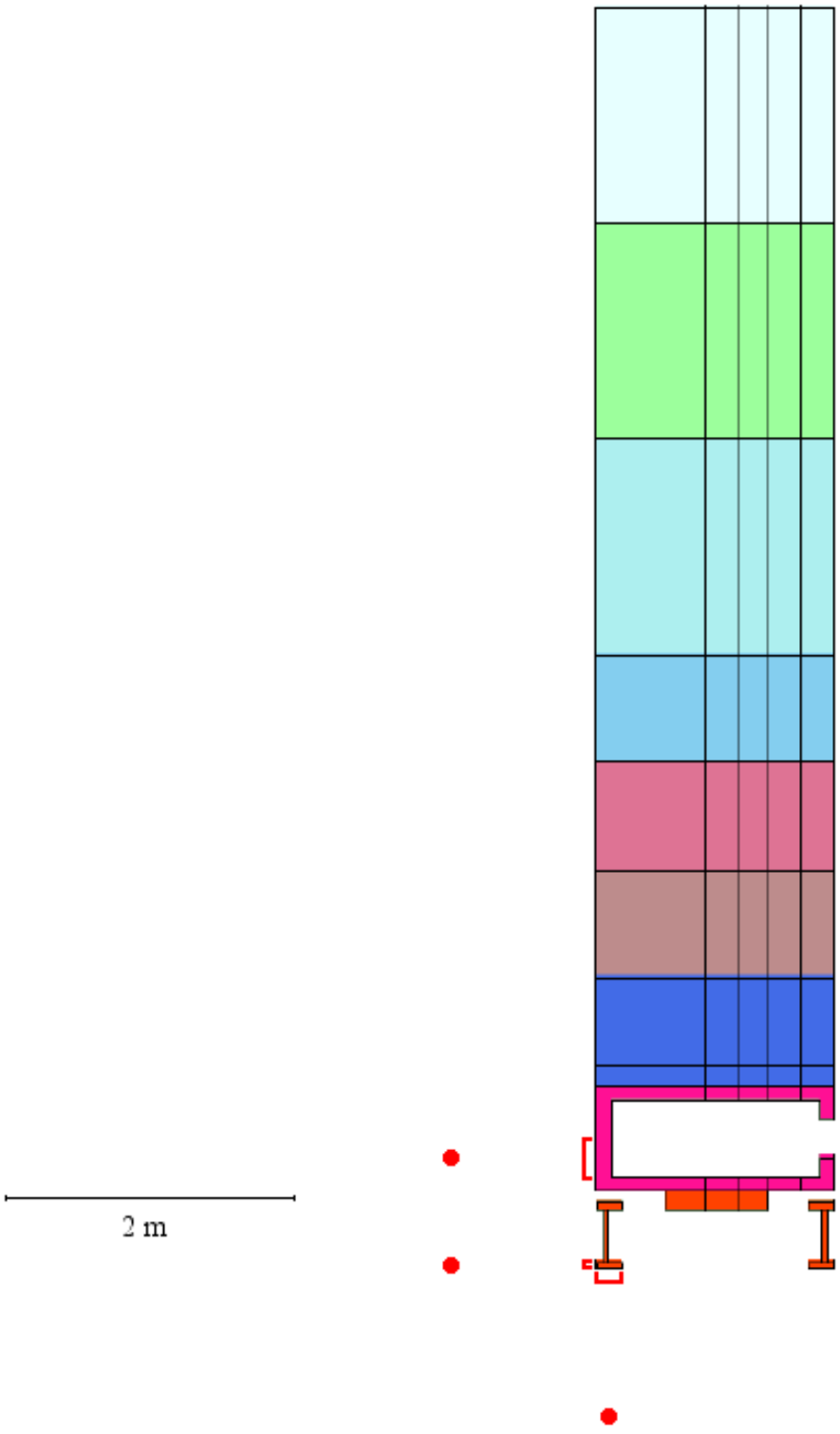

Figure 183. Points at which the dose was calculated around the extracted reflector and barrel. Shown are the surface segments and points at 1 m from the surface. Not shown are the points at 10 m from the surface.

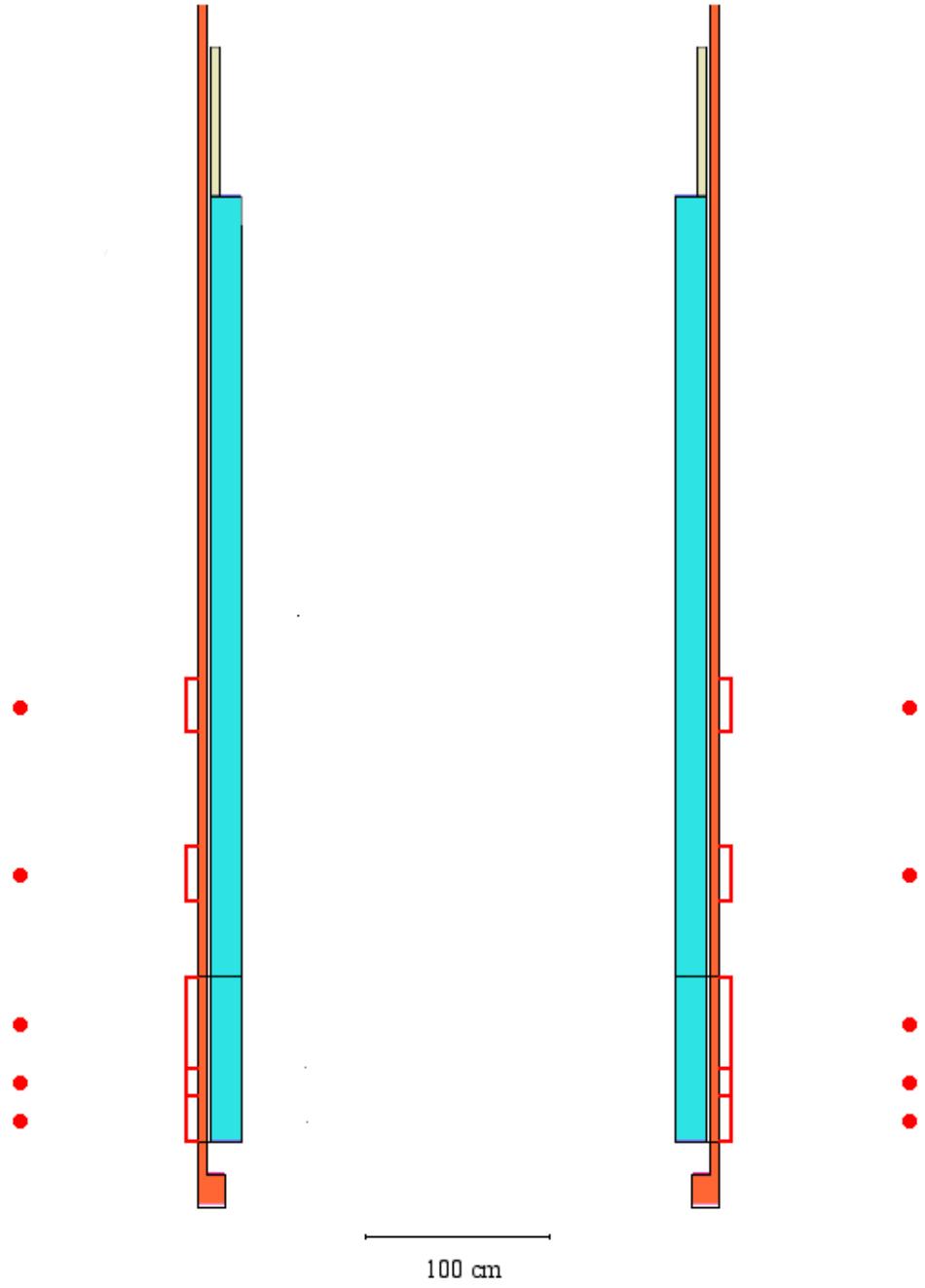

Figure 184. The $^{54}Fe(n,p)^{54}Mn$ cross-section (barns).

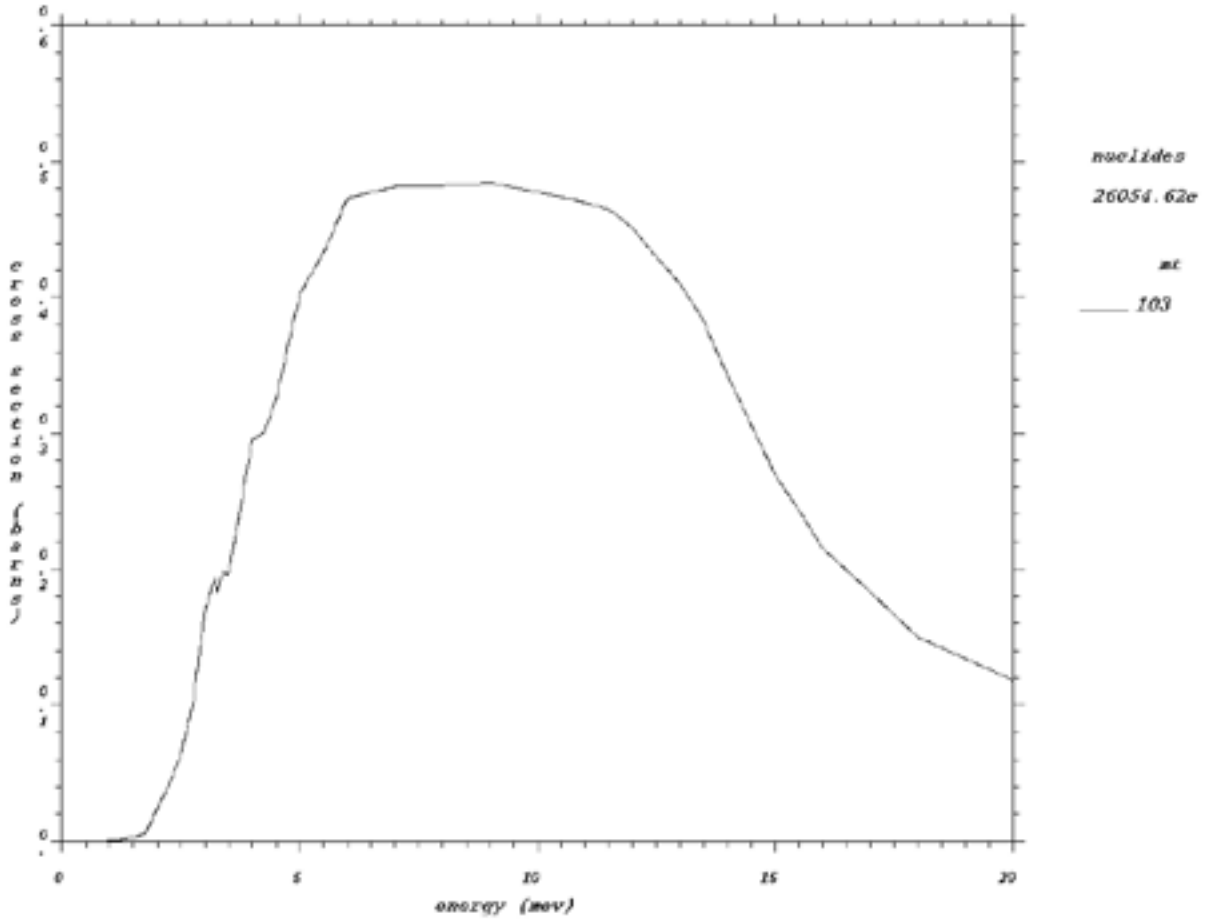

Figure 185. Segmentation of the carbon steel substituting the concrete in the pressure vessel well for averaging the neutron fluxes for the search for the maximum EOL activities.

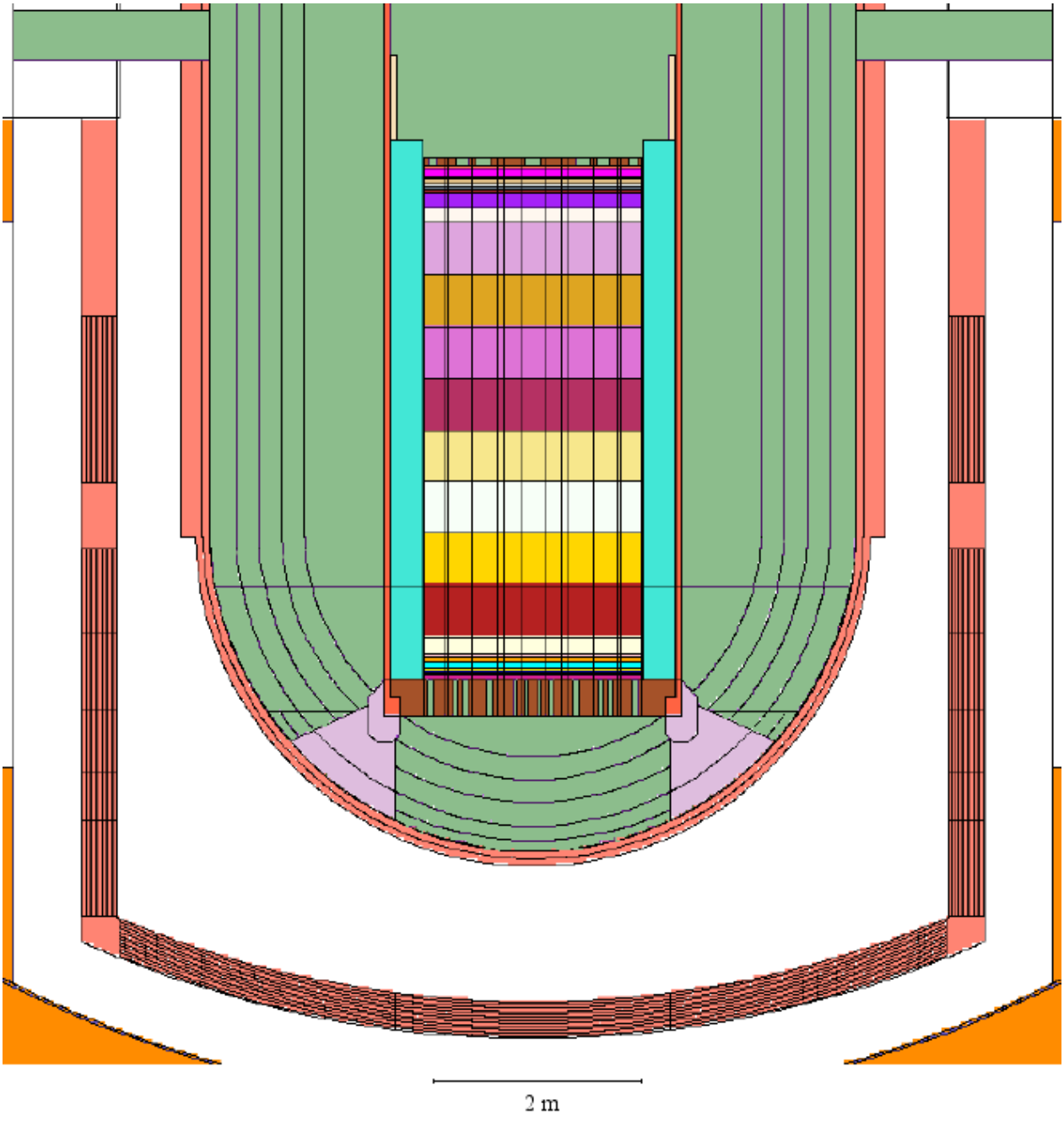

Figure 186. Segmentation of the carbon steel substituting the concrete in the pressure vessel well for averaging the neutron fluxes for the search for the maximum EOL activities (larger scale).

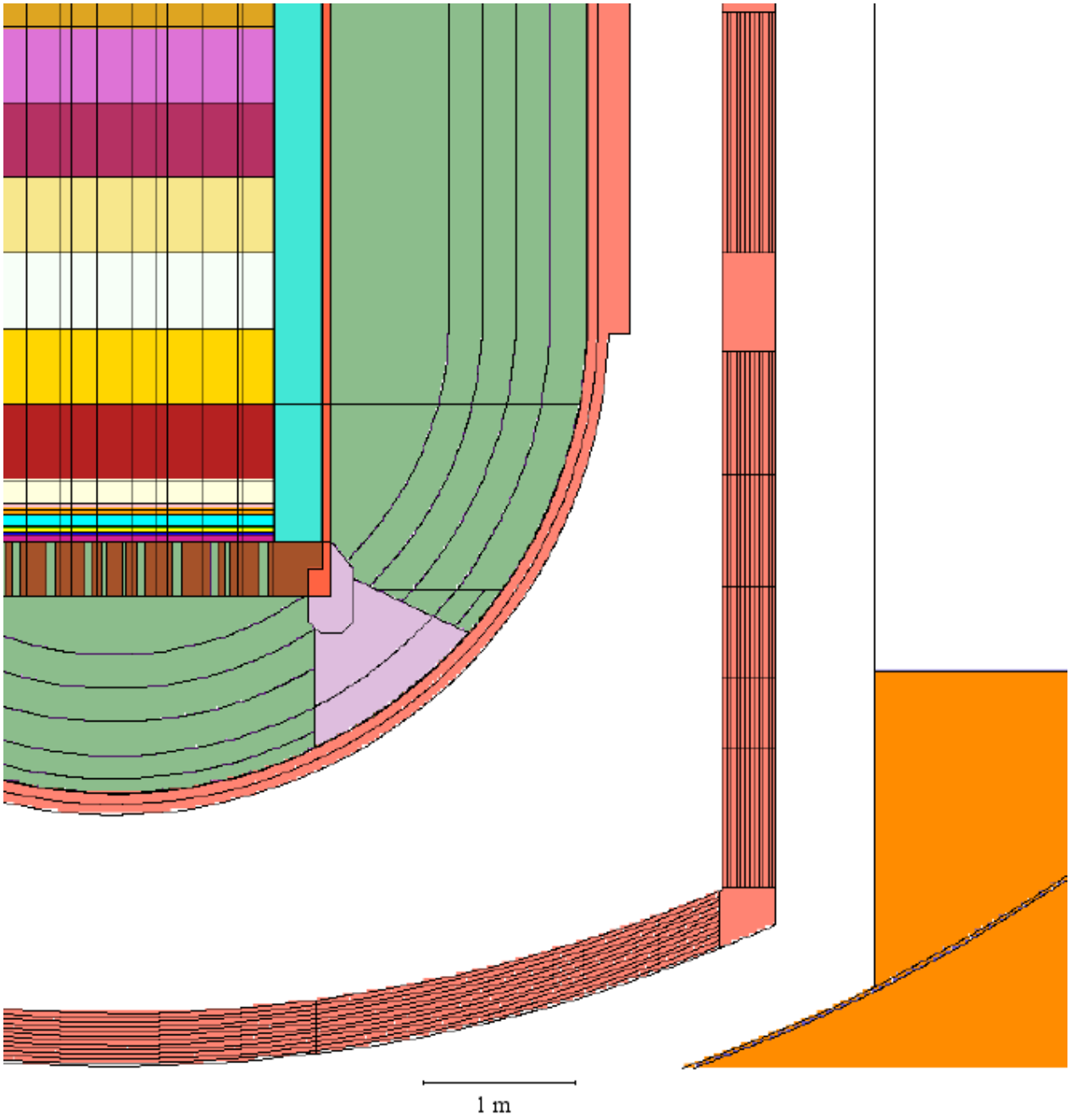

Figure 187. Detail (where the lower spherical part meets the side cylindrical part) of Fig. 186.